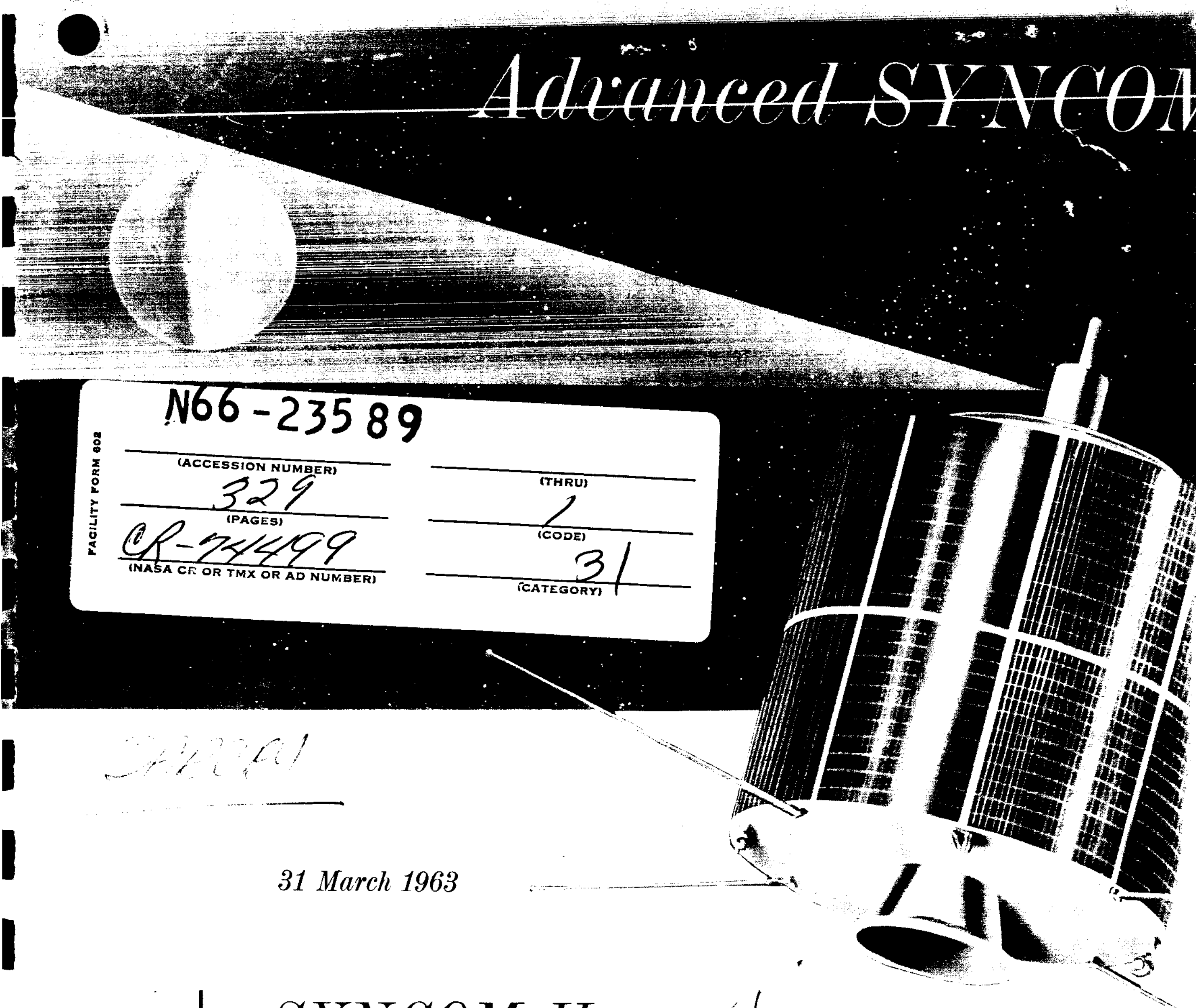

31 March 1963

SYNCOM II SUMMARY REPORT

File

NASA Contract 5-2797
SSD 3128R

AEROSPACE GROUP
SPACE SYSTEMS DIVISION
HUGHES AIRCRAFT COMPANY
CULVER CITY, CALIFORNIA

HUGHES

Advanced SYNCOM

31 March 1963

SYNCOM II SUMMARY REPORT

NASA Contract 5-2797
SSD 3128R

AEROSPACE GROUP
SPACE SYSTEMS DIVISION
HUGHES AIRCRAFT COMPANY
CULVER CITY, CALIFORNIA

HUGHES

CONTENTS

1. INTRODUCTION

The use of communication satellites has been recognized to answer the need for greatly expanded global communications capability. It has been a major effort of the United States Government and of industry to develop a satellite relay system at the earliest possible time.

The National Aeronautics and Space Administration, having management responsibility for developing the space technology leading to a communication satellite system, has investigated nonsynchronous passive satellites and nonsynchronous active repeater satellites. Project Syncom is assigned the synchronous-orbit, active repeater satellite investigations.

Under NASA Goddard Space Flight Center Contract NAS-5-1560, Hughes Aircraft Company developed the Syncom I spacecraft to be orbited by NASA Delta launch vehicles and used in conjunction with Department of Defense Advent ground stations for the performance of inclined synchronous-orbit communication experiments during 1963.

The Syncom I spacecraft will demonstrate a simple spin-stabilized design capable of being placed in a synchronous orbit. At the same time, it will be demonstrated that a simple pulse-jet control system can provide the stationkeeping necessary to maintain a synchronous orbit.

Additional important mission objectives of the NASA communication satellite program include the demonstration of a "stationary" or equatorial, synchronous orbit, conduct of system orbital life tests, demonstration of new wide-band services on a trans-oceanic basis, and demonstration of a system accessible to all nations.

Under NASA Goddard Space Flight Center Contract NAS-5-2797, Hughes has conducted feasibility studies and advanced technological development for an advanced, stationary, active repeater communication satellite. This Summary Report covers the technical progress achieved during the contract period and details the system configuration resulting from the system studies.

2. SYSTEM DESCRIPTION SUMMARY

The global communication system based on the Advanced Syncom stationary active repeater communication satellites will be compatible with all current types of common carrier traffic, typified by voice communications, teletype, and monochrome and color television signals. The system can provide service quality consistent with CCIR standards. Numerous ground stations can be readily accommodated, with each station able to communicate with any or all other stations at any time.

The voice communication capacity of each of the satellite transponders is 600 two-way telephone conversations, with ample margin over CCIR standards, which can be realized by using fixed, nontracking, 85-foot-dish antennas. Each satellite contains four such transponders, providing a total system capacity through the satellite of 2400 two-way voice channels. Alternately, the system can accommodate television or other wide-bandwidth signals through any of the transponders, again with ample margin over available CCIR standards.

The spin-stabilized satellite is launched by the Atlas-Agena D launch vehicle in conjunction with a third-stage apogee injection rocket carried integrally within the spacecraft. Bipropellant rocket reaction jet control systems provide thrust to correct anticipated initial errors in orbit parameters due to launch vehicle guidance tolerances. These bipropellant systems are also used to orient the spin axis of the satellite perpendicular to the orbital (equatorial) plane, and to correct periodically the parameters of the orbit to maintain the satellite stationary to within 0.1 degree throughout the satellite life.

The spinning satellite contains a phased-array transmitting antenna with electronic controls to maintain its highly directional pencil-beam pattern directed toward the earth. Four independent dual-mode communication transponders with efficient traveling-wave tube final power amplifiers provide alternate modes of operation corresponding to the type of communication to be repeated.

Solar cells provide 135 watts of electrical power, which allows a margin over the requirements for continuous, simultaneous operation of all equipment and battery charging circuits.

The satellite, exclusive of apogee motor, weighs 600 pounds when fully loaded with reaction jet control system propellants. The apogee motor and control system tankage are sized to accommodate the maximum payload capability of the Atlas-Agena D for this mission, a satellite weight of 650 pounds, exclusive of apogee motor, fully loaded with control system bipropellants. Apogee motor propellant is off-loaded to the requirements of the less than maximum weight satellite configurations.

3. COMMUNICATION SYSTEM DESIGN

REQUIREMENTS

The communications requirements about which the system has been designed are as follows:

Capacity: The system should accommodate 600 two-way voice channels or one monochrome or color television station in each of the four assigned frequency bands. The voice channels can originate from as many as 100 ground terminals simultaneously and can accommodate multiplexed teletype signals.

Quality: The quality of the communication links should exceed the appropriate standards established by the International Radio Consultative Committee (CCIR) of the International Telecommunication Union (ITU).

The assumed ground station characteristics for which the full communications capacity is achieved are listed in Table 3-1. The spacecraft transponder characteristics are given in Section 6.

TABLE 3-1. GROUND STATION CHARACTERISTICS

Transmitter (for each frequency assignment)	
Saturated power	10 kw
Frequency band	6 kmc
Bandwidth	25 mc
Diplexer loss	−1 db
Frequency stability	1 part in 10^{10}, short term
	1 part in 10^{7}, long term
Antenna	
Diameter	85 feet
Efficiency (transmitting and receiving)	54 percent
Receiver	
Noise temperature (all sources, including antenna)	80°K

Smaller stations can be used with a proportionate reduction in capacity. With 40-foot-diameter antennas and the same transmitters and receivers as in Table 3-1, the voice channel capacity is reduced to 120 two-way channels and the television quality falls below CCIR standards.

The standards used to establish the design of this system are given in Table 3-2.

The use of the CCIR standards in the design of this system follows the procedures recommended by Bray.*

TABLE 3-2. COMMUNICATION SYSTEM STANDARDS

Television signal-to-noise ratio	
Peak-to-peak signal to weighted noise	51 db
Television video bandwidth	
Monochrome	4 mc
Color	4.5 mc
Voice channels	
Test tone/noise ratio	50 db
Total channel bandwidth	4 kc
Voice portion of bandwidth	3.1 kc
Multiplexed teletype signals	
Maximum error in frequency	2 cps

MODES OF OPERATION

The system has two alternate modes of operation possible in each assigned frequency band. The first mode accommodates a wide-band frequency modulated transmission to the spacecraft, which translates the signal carrier frequency and repeats the signal with no conversion in modulation. This mode is used for television or other wide-band data originating from a single station. The spacecraft transponder mode which accommodates such signals is termed the frequency translation mode.

The second mode of operation involves the transmission, simultaneously from a large number of ground stations, of frequency division multiplexed, single sideband, suppressed carrier voice channels. These signals are converted into phase modulation of a single carrier in the spacecraft, and are retransmitted back to all stations in this form. This mode permits simultaneous two-way interconnection of all combinations of the ground stations. The spacecraft transponder mode which accommodates these signals is termed the multiple-access mode.

*W. J. Bray, "The Standardization of International Microwave Radio Relay Systems," Proceedings of the IRE, Part B, March 1961.

SYSTEM CALCULATIONS

FM Frequency Translation (TV)

Tables 3-3 and 3-4 list the signal and noise levels at several key points in the system when used for the relaying of monochrome television signals. It is seen that the overall peak-to-peak signal to weighted noise ratio is 55.2 db, which exceeds the CCIR standard by 4.2 db. The noise weighting factor and the appropriate standard were interpolated from curves given in the previously cited Bray report.

TABLE 3-3. GROUND TO SPACECRAFT, FREQUENCY MODULATION (TV)

Transmitter power	33.0 dbw
Diplexer loss	−1.0 db
Ground antenna gain	62.1 db
Space attenuation	−200.8 db
Receiving antenna gain	8.0 db
Off beam center allowance	−1.5 db
Diplexer loss	−1.0 db
Received carrier power	−101.2 dbw
Receiver noise power density	−195.3 dbw/cps
Receiver noise bandwidth	74.0 db
Receiver noise power	−121.3 dbw
Carrier/noise ratio	20.1 db

TABLE 3-4. SPACECRAFT TO GROUND FREQUENCY MODULATION (TV)

Spacecraft transmitter power	6 dbw
Diplexer and phase shifter losses	−3 db
Spacecraft antenna gain	18 db
Space attenuation	−197.1 db
Off beam center allowance	2 db
Ground antenna gain	58.4 db
Received carrier power	−119.7 db
Receiver noise power density (80°K)	−209.6 dbw/cps
Receiver bandwidth	74.0 db
Receiver noise power	−135.6 dbw
Carrier/noise ratio	15.9 db
Carrier/noise ratio — up link	20.1 db
Carrier/total noise ratio	14.5 db
Top modulation frequency	4 mc
Modulation index, M	2.5
Improvement factor, $3M^2 \frac{25}{4(2)}$	17.7 db
Average signal-to-noise ratio	32.2 db
Noise weighting factor	14 db
Peak-to-peak signal/weighted noise	55.2 db

Single Side Band-Phase Modulation Multiple Access (Voice)

Tables 3-5 and 3-6 list the signal and noise levels at key points in the system for conditions of full channel loading, when 600 two-way circuits are in use in each band. The ground station calculations are for the worst case, with all 600 conversations flowing through

TABLE 3-5. GROUND TO SPACECRAFT. SINGLE SIDEBAND MODULATION (VOICE)

Transmitter peak power capability	40 dbw
Transmitter average power	31.7 dbw
Channel test tone power	18.9 dbw
Diplexer loss	−1.0 db
Ground antenna gain	62.1 db
Space attenuation	−200.8 db
Receiving antenna gain	8.0 db
Off beam center allowance	−1.5 db
Diplexer loss	−1.0 db
Received test tone power	−115.3 dbw
Receiver noise power density	−195.3 dbw/cps
Channel bandwidth	34.9 db
Psophometric noise weighting factor	−2.5 db
Receiver channel noise (weighted)	−162.9 dbw
Test tone/fluctuation noise ratio	47.6 db
Test tone/intermodulation noise ratio	50.5 db
Test tone/noise ratio	45.8 db

TABLE 3-6. SPACECRAFT TO GROUND, PHASE MODULATION (VOICE)

Spacecraft transmitter power	6 dbw
Diplexer and phase shifter losses	−3 db
Spacecraft antenna gain	18 db
Space attenuation	−197.1 db
Off beam center allowance	−2 db
Ground antenna gain	58.4 db
Received carrier power	−119.7 dbw
Receiver noise power density (80°K)	−209.6 dbw/cps
Receiver noise bandwidth (25 mc)	74.0 db
Receiver noise power — total	−135.6 dbw
Carrier/total noise ratio	15.9 db
Weighted channel noise power	−177.2 dbw
Carrier/channel noise ratio	57.5 db
Channel test tone modulation index	0.35
Test tone/noise ratio	48.5 db
Overall link test tone/noise ratio	43.9 db
Compandor improvement factor	15 db
Overall link test tone/effective noise ratio	58.9 db

one station. In computing the noise contributed by various elements of the system, intermodulation noise as well as thermal noise was considered.

Two voice channel signal processing techniques are employed. Echo suppressors are used to prevent the annoying effect on the speaker of delayed echoes produced by long transmission delays and mismatched ground distribution networks. The newer type of suppressor, which allows interruptions to be heard, are used to allow smoother conversational exchanges. Compandors, consisting of a voice dynamic range compressor at the transmitting end and a corresponding expandor at the receiving end, are used to substantially improve the capacity and quality of the voice channels. Although tests have indicated improvements of the order of 22 db in signal-to-noise ratio through the use of compandors, the conservative figure of 15 db is used in the calculations to give adequate allowance for the increased channel loading which occurs.

The calculations are based on the channel loading factors and procedures given by Bray and on the detailed analysis of this system given by Braverman and Williams.* The resulting test tone/noise ratio of 58.9 db exceeds CCIR standards by 8.9 db.

FREQUENCY AND GAIN ADJUSTMENTS

Because of the stringent frequency error tolerances in the single sideband mode, special consideration must be given in the system design to meeting the frequency stability requirements. The major sources of frequency error are associated with the spacecraft — its residual motion relative to the earth produces a small but significant doppler shift, and the transponder receiver oscillator instability must also be taken into consideration. The design philosophy employed has been to accommodate both sources of spacecraft-induced frequency errors by compensating adjustments made continuously and automatically by the ground stations through the use of transponded pilot tones from each station. The same pilot tones used for frequency control are used by the ground stations to maintain gain control as well, to achieve the desired test tone modulation index in the spacecraft.

*D. Braverman and D. D. Williams, "SSB-PM Multiple Access Communication System Analysis." Hughes Aircraft Company TM 721, October 1962.

4. ADVANCED TECHNOLOGICAL DEVELOPMENT PROGRAM

PROGRAM SUMMARY

The Advanced Technological Development Program for an advanced, stationary, active repeater communication satellite included research and development through fabrication and demonstration of engineering models of a multi-element phased-array transmitting antenna and associated control circuits, a collinear array receiving antenna, a dual-mode communication transponder incorporating a traveling-wave tube final power amplifier, a spacecraft structure, and a hot gas reaction control system. Also included were studies of system design feasibility, preparation of performance and test specifications, demonstration planning, and conduct of preliminary engineering acceptance demonstrations.

Initial results of the system design feasibility studies were reported in "Initial Project Development Plan" in August 1962. The studies were continued in parallel with the advanced development work throughout the contract period and form the basis of the system configuration discussions of this report.

Hughes Syncom personnel worked closely with Lockheed Missiles and Space Company personnel studying the Atlas-Agena D launch of Syncom II and similarly provided technical support to the Lenkurt Electric Co., Inc., personnel studying the specification requirements for elements of the communication ground stations for Syncom II.

Hughes is providing assistance to the Goddard Space Flight Center in the technical direction of a program being conducted by the Jet Propulsion Laboratory to develop the apogee injection rocket motor, which will supply the third-stage boost for final orbital injection of the spacecraft. Hughes Syncom personnel have close liaison with JPL apogee motor personnel to ensure rapid definition and satisfactory resolution of all interfaces between the spacecraft and the rocket.

The advanced technological program was initiated on 28 June 1962, and the majority of the program was completed on 31 March 1963 with the submittal of this report. Development of the bipropellant rocket reaction control system was subcontracted to the Marquardt Corporation during February 1963, and the advanced technological development will be completed in May 1963 with the delivery to Hughes of an engineering model unit of the reaction control system.

The engineering model equipment was integrated into the engineering structure and demonstrated to members of NASA and the Department of Defense. The developmental equipment demonstrated included the multi-element 4-kmc phased-array transmitting antenna and associated control electronics, a 6-kmc collinear array receiving antenna, dual-mode communication transponder operating at 6-kmc receiving frequency and 4-kmc transmitting frequency and providing alternate modes of operation as a wide-band FM frequency translation transponder or as a multichannel SSB-PM multiple-access transponder, a traveling-wave tube final power amplifier, and the engineering model structure. The bipropellant rocket reaction control system under development by the Marquardt Corporation will be demonstrated at the vendor's Van Nuys, California, facility during April 1963.

ITEMS DEVELOPED

In addition to the equipment listed above, a transponder test and demonstration panel was developed to provide limited simulation of a communication ground station. Included are SSB and FM transmitters at 6-kmc and an angle modulation receiver at 4-kmc, two audio-baseband transceivers — each providing a voice bandwidth channel frequency translation from audio to baseband and from baseband to audio — and a multitone test generator to simulate heavy traffic conditions over the multiple access transponder link. In support of the preliminary engineering acceptance demonstrations, Syncom I spacecraft telemetry and command equipment was adapted to the requirements of the Syncom II engineering equipment and operated in conjunction with Syncom I system test equipment to permit remote control of Syncom II electronics through RF links.

Several spacecraft configurations were analyzed during the contract period. Initially, the spacecraft design had a 30-inch spherical solid propellant apogee rocket motor. After selection of Jet Propulsion Laboratory for the apogee rocket motor development, the spaceframe and motor mounting provisions were revised to reflect the JPL elliptical end cap, cylindrical motor configuration. Additional configurations studied considered the application of the ABL-248 solid propellant motor for apogee injection or each of four candidate liquid bipropellant rocket injection systems with toroidal or spherical propellant tanks.

Detailed procurement specifications were prepared for the solid propellant apogee injection rocket motor and the liquid bipropellant rocket reaction control system. A spacecraft system performance and test specification was developed, as were probabilistic models for spacecraft availability and replacement rate.

GFE ITEMS SUPPLIED

The apogee injection rocket motor is being procured by NASA separately from this development program. The initial planning called for a NASA-provided, accurately simulated dummy motor for inclusion in limited environmental tests. Subsequent considerations required revision of this plan to reflect supply of the dummy motor casing and auxiliary equipment by Hughes with JPL loading an inert formulation for the tests.

ITEMS SIMULATED FOR ENGINEERING TESTS

The solar cell arrays, electrical storage batteries, ignition timer, flight termination timer, telemetry and command equipment, and portions of the thermal control were not developed during the contract period. During testing when certain of the functions normally accomplished by the missing equipment are essential, functional simulation of missing signals or Syncom I equipment was supplied.

5. LAUNCH AND ORBIT CONSIDERATIONS

GENERAL SEQUENCE OF EVENTS

The Syncom spacecraft will be launched from the Atlantic Missile Range (AMR) (28.5 degree latitude) at 93 degrees azimuth ($\sim$ east), using an Atlas-Agena D with the Atlas and first Agena burn to place the spacecraft in an 85 to 100 nautical mile nominally circular orbit. A second Agena burn at the first ascending node (second equatorial crossing) will place the spin-stabilized spacecraft into an elliptical transfer orbit with an apogee radius equal to the synchronous orbit radius of 22,752.3 nautical miles. An apogee boost is provided by a JPL solid propellant motor fixed in the spacecraft. The JPL motor is sized to the maximum payload injection capability of the Agena for this mission and will be off-loaded to the Syncom payload requirements. After cutoff of the second Agena burn, the Agena guidance package will program a yaw angle of about 54 degrees to the right of the flight path in the horizontal plane to prealign the third stage apogee motor thrust axis (Syncom spin axis) prior to spin-up and separation of the spacecraft from the expended Agena stage. The spacecraft will then be spun at 100 rpm on the spin table mounted on the Agena, and separated.

As it traverses the transfer orbit, the spacecraft will maintain the spin axis attitude established by the Agena guidance system prior to separation. This is the correct attitude for apogee motor thrust to simultaneously accelerate the spacecraft to circular synchronous velocity and remove the 29.1 degree inclination when the spacecraft reaches apogee at the stationary orbital radius. The final longitude attained at apogee motor burnout will be about 93 degrees W (over the Pacific, west of Ecuador). If the apogee motor is ignited at the second apogee crossing, the final longitude will be about 112 degrees E (West Borneo). Other longitudes are also possible, depending on the number of transfer orbit periods allowed before apogee motor ignition or the node at which the Agena begins a second burn to leave the parking orbit. Figure 5-1 illustrates the geometry of the launch for the case in which the transfer ellipse is entered at the second node of the parking orbit, and apogee boost is at the first apogee of the transfer orbit. Figure 5-2 is a ground trace of a similar ascent sequence studied by Lockheed and launched from AMR at 93 degrees azimuth, giving an initial inclination of 29.1 degrees and a longitude at apogee boost of 93 degrees W.

The satellite spin axis attitude and velocity are controlled by a pulsed-jet control system based on the same principles as the control system of the present Delta-launched Syncom satellite. Means for controlling the spacecraft spin speed throughout the lifetime of the vehicle will be incorporated in the form of a spring-restrained centrifugally actuated axial jet. This additional mechanism is described in the orientation and velocity control portion of Section 6.

After apogee motor burning, the spacecraft will be precessed through approximately 65 degrees in yaw until the spin axis is parallel to the earth's spin axis. This attitude permits the transmitting antenna beam to point at the earth at all times, gives efficient solar power supply illumination, and provides control of period and elimination of orbital eccentricity by the velocity control jet system. The orientation control jet system, operated continuously rather than in a pulsed mode, permits elimination of inclination in this attitude.

REQUIREMENTS ON FINAL ORBIT ACHIEVEMENT

The final orbit of the spacecraft must be stationary (zero inclination and zero eccentricity) as well as synchronous (24-hour period). It is desired that the instantaneous angular deviation of the geocentric radius vector be less than ± 0.05 degree (3σ) in latitude and longitude for a minimum time of 3 years. This requirement will greatly reduce the cost and complexity of the communication ground terminal antennas.* It is desirable to choose an initial longitude

*In addition, the residual inclination, i, and eccentricity, e, causing motion relative to the earth should be small enough to produce a tolerable doppler-shifted frequency error in the

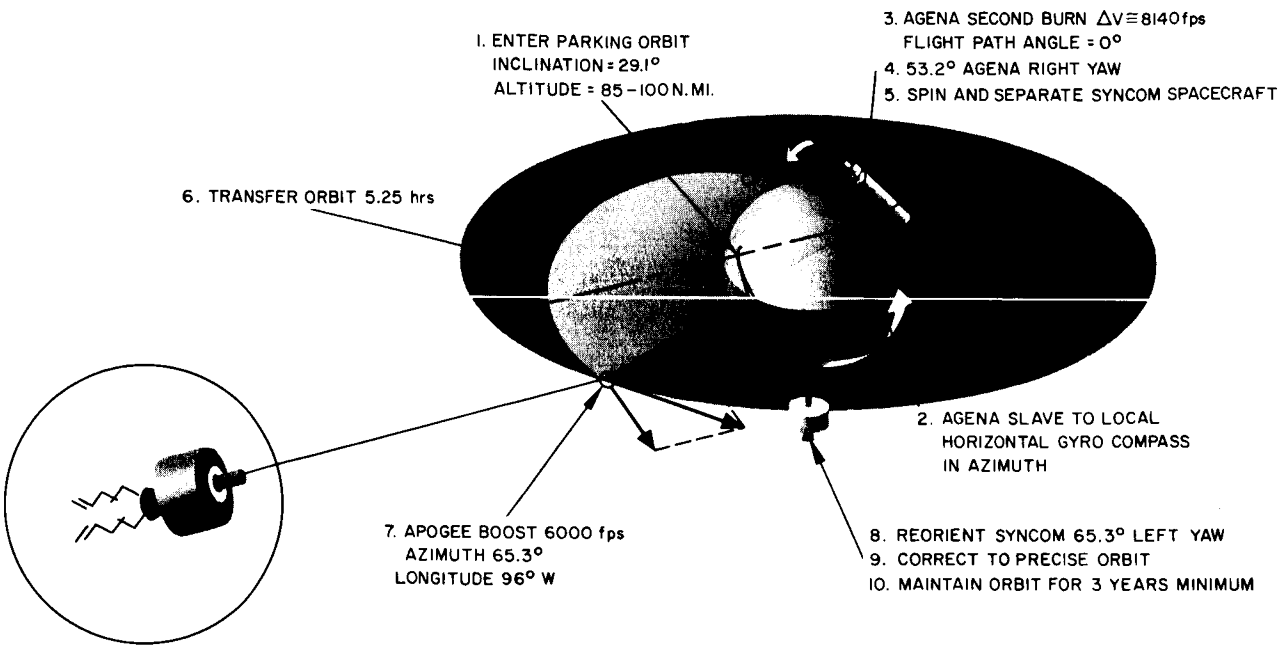

FIGURE 5-1. ADVANCED SYNCOM LAUNCH SEQUENCE

that will provide continuous tracking station visibility and accommodate comunications experiments during the correction of the longitude to the desired final value. The presently planned launch sequence will achieve an acceptable initial longitude position of about 93 degrees W.

To achieve the above goals, it was necessary to study the following sequence of events to enable the proper allocation of performance errors and requirements to the appropriate subsystems.

1) Ascent trajectory sequence
   a) Detailed specification of ascent trajectory sequence of events to apogee motor burnout.
   b) Determination of maximum anticipated ascent guidance and control errors to apogee motor burnout.
   c) Specification of velocity increment required to achieve initial stationary orbit due to in-plane and inclination errors at apogee motor burnout.

2) Initial stationing and vernier correction sequence
   a) Detailed specification of telemetry, tracking, command, and vehicle control sequence of events to achieve final stationary orbit with the ground rules of minimum propellant consumption, reasonable error correction time, and reasonable time to achieve planned longitude placement.

3) Station-keeping sequence
   a) Detailed analysis and specification of perturbing forces and torques on the spacecraft in orbit at planned longitude, including effects of sun-moon and nonradial earth gravitational fields, magnetic fields, solar radiation pressure, and particle impact.
   b) Determination of the orbit due to the above perturbations and specification of telemetry, tracking, command, and vehicle control sequence of events to maintain stationary orbit with ground rules of minimum propellant consumption and correction frequency, and minimum instantaneous angular deviation from initial stationary orbit (latitude and longitude).

---

single-sideband voice mode. For example, if $i(\text{rad}) = e = 0.00175$ (0.1°), the maximum doppler difference, $(\Delta f_d)_{mxa}$, between two ground stations is approximately $(\Delta f_d)_{max} \approx 4.30 \times 10^8 \; e f_o/c \approx 45$ cps at $f_o = 6$ kmc, where c is the velocity of light.

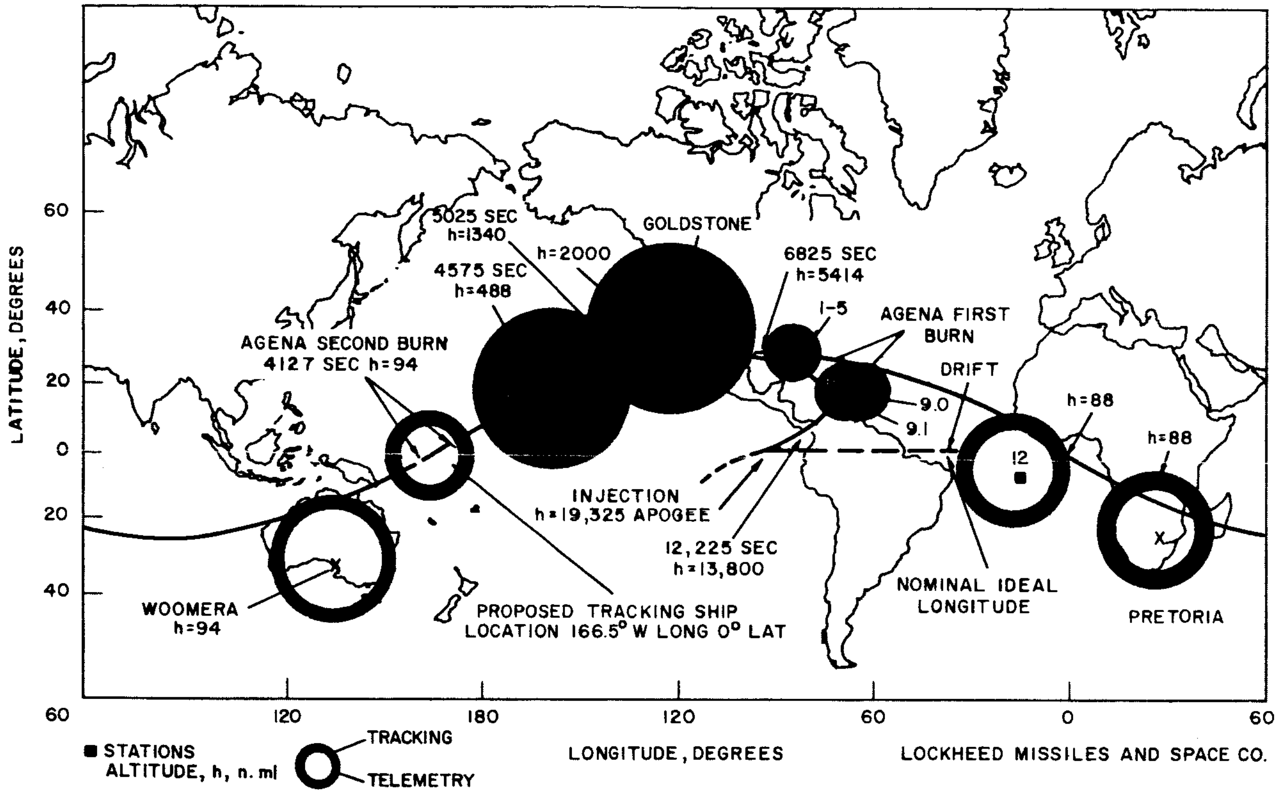

FIGURE 5-2. GROUND TRACE ASCENT SEQUENCE

ASCENT TRAJECTORY SEQUENCE

The exact boost trajectory will be established only after detailed study by the launch vehicle contractor in close conjunction with the NASA and the AMR. However, on the basis of information presently available from Lockheed studies, the trajectory sequence given in Table 5-1 will be used in this analysis.

Parking Orbit

A nominal circular parking orbit injection altitude of 85 nautical miles has been selected to improve the payload capability of the Atlas-Agena booster combination. Alternate parking orbit altitudes that reduce aerodynamic drag and heating will be considered. An average payload increase of 1.67 pounds per nautical mile decrease of injection altitude will be gained from a nominal 100-nautical-mile parking orbit. However, to guard against lower altitudes due to guidance errors, a slight velocity excess over that required for a circular 85-nautical-mile orbit is provided during Agena first burn. This results in a nominal 92-nautical-mile parking orbit apogee and an approximate circular orbital altitude of 88 nautical miles. The perigee of the parking orbit is lowered by about 62 nautical miles per degree of flight path angle at injection. The average gyro pitch error due to 6 deg/hr drift rate (3σ) should be less than 0.1 degree during Agena first burn (6 to 8 minutes from liftoff). Hence, even for the worst Agena guidance error condition of 0.1 degree flight path angle below the horizontal at parking orbit injection, the perigee of the parking orbit will not dip below 85 nautical miles.

The effect of the drag loss due to the low parking orbit altitude will be calculated when more definitive data on the Agena mass, geometry, and projected frontal area due to pitch and yaw error are available. Preliminary discussions with launch vehicle manufacturers indicate that a number of periods can be

TABLE 5-1. ASCENT TRAJECTORY SEQUENCE
AMR Launch, 93 Degrees Azimuth

Event Designation	Nominal Time From Liftoff, seconds	Event Description	Source of Signal
1		Timer reset (set prior to launch) (ground function).	
LO	0	Liftoff.	AGE
BCO	138.5	Atlas D booster engine cutoff.	Atlas guidance
SCO	275	Atlas D sustainer engine cutoff.	Atlas guidance
		Start Atlas programmer sustainer cutoff subroutine.	
SDT	282	Start Agena D SS/D timer.*	Atlas guidance SS/D timer
VCO	292	Jettison H/S fairing. Atlas D vernier engine cutoff, uncage Agena D gyros, arm Atlas/Agena separation circuit, arm nose shroud ejection.	Atlas guidance
VCO (BU)	295	Atlas D vernier engine cutoff (backup), uncage Agena D gyros (backup), arm Atlas/Agena separation circuit (backup), and arm nose shroud ejection (backup)).	Atlas sub-programmer
SEP	296.5	Atlas D/Agena D separation, fire midbody pin pullers and Atlas retro-rockets.	Atlas guidance
	296.7	Start Agena D timer (backup).	Pullaway plug
SEP (BU)	298.5	Atlas D/Agena D separation (backup), fire midbody pin pullers and Atlas retro-rockets (backup).	Atlas sub-programmer
	298.5	Activate pneumatic attitude control.	Separation switch
	298.5	Connect H/S roll signal to IRP roll gyro.	Separation switch
3	305	Command separation (backup), uncage gyros (backup), jettison H/S fairings (backup), connect H/S roll to roll gyro (backup).	SS/D timer
4	320	Remove event 3 backup power. Telemetering calibration and switch from booster to Agena D monitor. Start 180 deg/min pitch rate.	SS/D timer
5	323	Transfer to 2.73 deg/min pitch rate. Connect H/S signals to IRP pitch and roll gyros (H/S bias angle: approx 3.2 degrees).	SS/D timer
6	337	Enable velocity meter and stop telemetering calibration, fire first burn ullage rockets.	SS/D timer
7	349	Arm engine control and deactivate pitch and yaw pneumatic control, fire gas generator starter squib No. 1 (Agena D ignition-first burn), remove telemetering calibration power, and connect pitch H/S.	SS/D timer
PUSH NO. 1	350.3	Steady-state Agena D engine first burn.	
8	355	Eject nose shroud.	SS/D timer
9	359	Open gas generator, arm and fire circuit, arm velocity meter cutoff relay.	SS/D timer
10	503	Remove engine safety No. 1, arm engine shutdown.	SS/D timer
A1CO	513.4	Engine cutoff (first burn), close lip seal pressure valve.	Velocity meter
	513.4	Activate pitch and yaw pneumatic control.	Engine relay
11	523	Engine cutoff (backup), disable velocity meter and connect counter output to telemetry, transfer roll IRP to low gain, terminate —2.73 deg/min pitch rate and initiate —2.88 deg/min pitch rate (transfer ellipse pitch rate), disarm Agena command destruct system.	SS/D timer
12		Fire H/S position squib (H/S bias angle: approx 0 degree).	SS/D timer

TABLE 5-1. (CONTINUED)

Event Designation	Nominal Time From Liftoff, seconds	Event Description	Source of Signal
13	531	Remove stop calibration power, close engine pressure valve, remove power from engine shut-down circuit, transfer flight control to orbit node, transfer to second burn differential velocity, start gyro compassing, start telemetering calibration, and transfer to low pressure.	SS/D timer
14	536	Remove power from engine pressure valve, stop telemetering calibration and turn telemetering off, transfer to second burn engine safety control, remove start calibration power and pneumatics transfer power.	SS/D timer
Coast in parking orbit at 85 n. mi. altitude for ¾ revolution (ascending node)			
15	4024	Stop gyro compassing and transfer flight control to ascent node, turn telemetering on, transfer pneumatics to high pressure and open lip seal pressure valve, remove telemetering off power.	SS/D timer
16	4034	Fire second burn ullage rockets, enable velocity meter and stop telemetering calibration, remove telemetering on power and pneumatics transfer power, terminate —2.88 deg/min pitch rate, initiate —2.14 deg/min pitch rate (second burn pitch rate).	SS/D timer
17	4046	Arm engine control, deactivate pitch and yaw pneumatics, fire gas generator start squib No. 2 (Agena ignition-second burn).	SS/D timer
PUSH NO. 2	4047.3	Steady-state Agena D engine second burn.	
18	4117	Remove power from engine arm circuit and pneumatic shut-down circuit, deactivate engine safety No. 2, arm engine shut-down circuit.	SS/D timer
A2CO	4126.4	Engine cutoff (second burn).	Velocity meter
19	4133	Engine cutoff (backup) and fire oxidizer dump valve squibs (backup), disable velocity meter.	SS/D timer
20	4240	Start telemetering calibration and remove H/S signals from IRP, remove power from engine shut-down circuit.	SS/D timer
21	4249	Initiate 180 deg/min yaw rate (yaw right 54 deg).	SS/D timer
22	4267	Stop 180 deg/min yaw rate.	SS/D timer
23	4270	Actuate third-stage spin-up (approx 100 rpm).	SS/D timer
24	4278	Separate Agena D from third stage (spacecraft) and initiate Agena D retro maneuver.	Centrifugal switch
25		Spacecraft (third stage) — coast to apogee, verify attitude.	Sun sensors/telemetry
Orbit	22968	Fire spacecraft rocket (establish equatorial plane orbit — circular or slightly elliptical).	Spacecraft timer or ground command
Burnout	23014	Spacecraft rocket burnout.	Spin-speed change — sun sensor, solar panel power modulation/telemetry

*SSD = Separation sequence/delay.

spent at this orbital altitude before serious decay results. Other nominal parameters of the parking orbit are:

Velocity	25,620 fps (4.22 n. mi/sec)
Period	5270 seconds (1.468 hours)
Longitude shift eastward per circuit	338 degrees
Inclination	29.1 degrees
Radius	~ 3530.2 nautical miles

Transfer Orbit

The perigee velocity required to achieve apogee at the stationary radius (22,752.3 nautical miles) with a nominal perigee radius of 3,530.2 nautical miles is 33,760 fps. Therefore, the second Agena burn imparts a velocity increment of approximately 8140 fps. The parameters of the transfer orbit are:

Inclination	29.1 degrees
Semimajor axis	13,141.25 nautical miles
Period	37,800 seconds (10.51 hours)
Apogee velocity	5250 fps (0.863 n. mi/sec)
Longitude shift eastward per circuit	202.2 degrees

The attitude of the Agena booster is constrained to the local horizontal after first burn and during second burn by the horizon scanners in the Agena guidance package. The thrust axis is constrained to remain parallel to the flight path by means of gyrocompassing procedure. The estimated error due to this gyrocompassing is 1.5 degrees. This attitude is approximately maintained in the parking orbit until completion of the second Agena burn. The 1.5 degree azimuth error combined with the rest of the Agena-D guidance errors is shown by Lockheed* to contribute an inclination error of about 0.55 degree (3σ) after apogee motor burnout, whereas the resulting longitude drift rate is less than 8 degrees per day (3σ).

Longitude Choice

The spacecraft will enter the parking orbit at approximately 60 degrees W longitude. Table 5-2 shows the effect of the choice of the parking orbit node at which the vehicle is injected into the transfer orbit and also the effect of the choice of transfer orbit apogee at which injection into the 24-hour orbit takes place. The results indicate that, for a satellite for trans-Atlantic service, either an extra half circuit of the parking orbit (boost at second node) or an extra full circuit of the transfer orbit (boost at second apogee) is suitable. Either technique is acceptable but, from a guidance point of view, the former appears to have the following advantages:

*Final Report LMSC-A057612, 30 September 1962.

TABLE 5-2. INITIAL LONGITUDE OF STATIONARY POINT (NOMINAL)

Node of Parking Orbit	Apogee of Transfer Orbit	Longitude (Lockheed Study)*
First	First	101.1° E
Second	First	90.15° W
First	Second	56.70° W
Second	Second	112.05° E
Third	First	78.6° E
Third	Second	79.2° W
Third	Third	123° E
Second	Third	45.8° W
First	Third	145.5° E

*In Lockheed study parking orbit crosses first node at ~ 0°.

1) The additional 45 minutes in the parking orbit will give the Agena guidance package enough settling time for the gyrocompassing procedure. Otherwise, for boost at the first node of the parking orbit, the open-loop inertial quality of the gyros in the Agena guidance package would have to be relied upon to maintain adequate azimuth and attitude accuracy. The nominal 6 deg/hr drift rate of the HIG gyro in the Agena guidance system will yield a 2 degree error in attitude after only 20 minutes, whereas the gyrocompassing procedure will yield a bounded error of less than 1.5 degrees after slaving the Agena attitude to the local horizontal via the horizon scanners.

2) The additional 45 minutes in the parking orbit will also enable the ground tracking system to determine the resulting orbital parameters prior to the ignition time of the second Agena burn. A back-up control is thus provided for the transfer orbit by controlling the second Agena burn as a function of the ground-determined orbital parameters of the parking orbit.

For the ascent sequence yielding a stationary point longitude of 112 degrees E for Asiatic service, Table 5-2 indicates apogee motor ignition at the second apogee crossing of the transfer orbit. This means a spacecraft transfer orbit perigee crossing in the spin-stabilized condition. The possible destabilizing and heating effects of the atmosphere at perigee altitude is being studied and compared with the possible degraded guidance accuracy effects resulting from the first ascent sequence listed in Table 5-2 yielding a station longitude of 101° E. Recommendations will favor the ascent sequence requiring minimum spacecraft design penalty for thermal heating protection and correction of destabilizing effects. The effects of perigee passage or transfer orbit parameters are presented in a later section.

Launch Window

The desired launch time from AMR will be governed by the angle the sun line makes with the spin axis at the selected stationary longitude during the orientation command. The angle between the payload spin axis and the direction to the sun, ϕ, at the start of orientation is determined primarily by the time of day, as well as by the date of firing. The geometry of the spacecraft and the sun at the time of orientation is shown in Figure 5-3, where $\hat{k}$, $\hat{i}$ are body spin axis and a body reference axis normal to $\hat{k}$; ψ is the spin angle from sun sensor maximum output to the center of the axial jet pulse used during orientation; η_i is the initial angle between the spin axis $\hat{k}$ and the X (west)

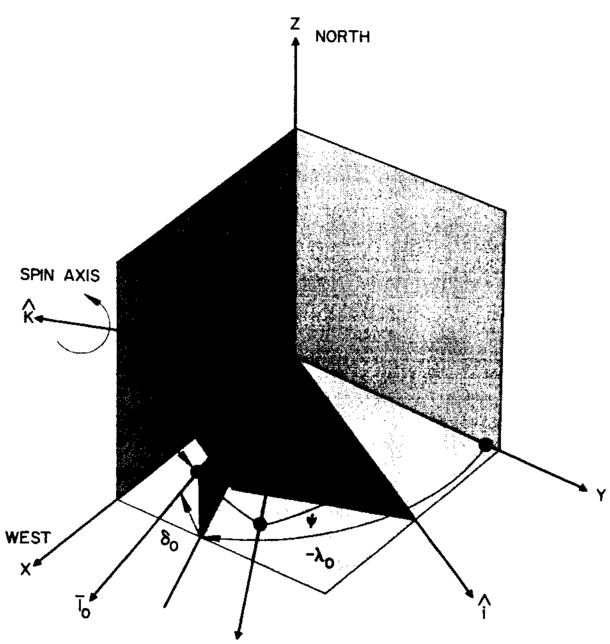

FIGURE 5-3. GEOMETRY AT ORIENTATION

axis measured in the local horizontal plane. For the ascent sequence considered here, the $\hat{k}$ axis will be initially in the southwest quadrant, not as shown.

The spacecraft is at the origin, the Z-axis points north, the X-axis points west, and the Y-axis lies in the meridian through the apogee longitude. The unit vector l_o points toward the sun and has the X, Y, Z components

$$-\sin \lambda_o \cos \delta_o, \quad \cos \lambda_o \cos \delta_o, \sin \delta_o$$

where δ_o is the declination of the sun, tabulated in the Nautical Almanac. The relative longitude of the sun, λ_o, can be found from the relation

$$\lambda_o = (\text{longitude of satellite in degrees west of Greenwich}) + 180 \text{ degrees} - 15 \text{ deg/hr} \; [\text{U.E.} + \text{E}]$$

where U.T. is the Greenwich mean time at which the satellite is oriented (in hours) and E is the "equation of time," evaluated for the day and hour at which orientation is performed, using the tables provided in the Nautical Almanac.

Solar sensor design parameters require a minimum angle, ϕ_{min}, of about 40 degrees. The practical significance of this is that it is undesirable for the satellite to arrive at apogee during the early morning hours, or the late afternoon and early evening hours, in terms of local time at the subsatellite point. On the other hand, apogee arrival times near local noon and midnight at the nadir point are also undesirable because at these times the precession motion takes place about the spacecraft – sun line, which degrades the accuracy of measurement of one of the sun sensor angles that tells when the correct attitude is reached.

The most desirable range of apogee arrival times depends on the time of year, but times of 0100Z, 0700Z, 1300Z, and 1900Z are generally favorable for orientation. (A typical orientation example will be presented later.) These correspond to lift-off times (for 93° W longitude placement) in the vicinity of 1900Z, 0100Z, 0700Z, or 1300Z (6 hours earlier). The local time at AMR is about 5.5 hours less than Greenwich mean time so that lift-off should occur at about 1:30 p.m., 7:30 p.m., 1:30 a.m., 7:30 a.m. Eastern Standard Time. More detailed studies will be made to determine the best launch window width as a function of time of year and selected stationary longitude using the IBM 7090

Launch Window Program generated for the Syncom I orbit. The launch window is further adjusted to take advantage of the period of diminished ionospheric electron density (about 3 a.m., local time at apogee) to facilitate polarization measurements of the electric vector of the radiation from the communication antenna, which provides additional spin axis orientation angular data. The effect of ground station-spacecraft geometery on Faraday rotation measurement is summarized in a later section.

STATIONARY ORBIT INJECTION

As the spacecraft reaches transfer ellipse apogee with velocity V_a and inclination i, the apogee motor will apply a velocity impulse W, the magnitude and direction of which will simultaneously circularize the orbit to synchronous velocity, V_s, and remove the inclination i. An important factor in the successful establishment of a stationary orbit is the attitude of the apogee motor thrust axis, θ, relative to the apogee velocity Vector, V_a. From Figure 5-4,

$$W^2 = V_a^2 + V_s^2 - 2\,V_a V_s \cos i$$

$$\sin\theta = \frac{V_s}{W}\sin i$$

Hence for $i = 29.1$ degrees, $V_s = 10{,}087.5$ fps, the requirements for apogee boost are $W = 6075$ fps and $\theta = 53.8$ degrees. This corresponds to a thrust axis angle η_i of 24.7 degrees northward of the equatorial plane and locally horizontal ($\hat{k}$ axis southward of equatorial plane).

To determine the criticality of the angle θ, an examination of Figure 5-4 shows that the out-of-plane velocity corrections needed to remove an error of $\delta\theta$ in degrees and a boost velocity error, δW, are

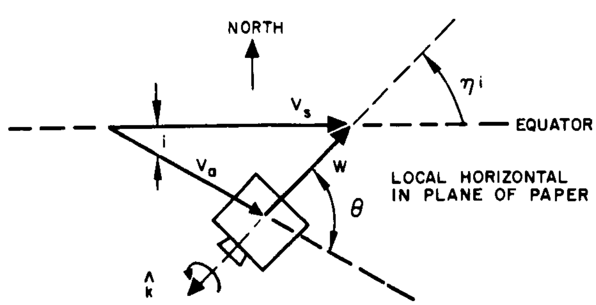

FIGURE 5-4. APOGEE BOOST GEOMETERY

$$\delta V_\perp \cong 95\,\frac{\text{fps}}{\text{deg}}\,\delta\theta \quad ; \quad \delta V_\perp \cong 2500\,\delta W/W$$

Similarly, for the error in synchronous velocity, V_s, due to $\delta\theta$, is

$$\delta V_s \cong -50\,\frac{\text{fps}}{\text{deg}}\,\delta\theta$$

Also, for an error in apogee motor total velocity, δW,

$$\delta V_s \cong 5610\,\delta W/W$$

A worst-case estimate of all the guidance errors is summarized later.

Motor Ignition Time

The accuracy with which the apogee radius of the transfer orbit is known is a function of the amount of tracking data accumulated. Normally, a predetermined timing interval from second Agena burnout of 5.25 hours, based on the nominal value of transfer ellipse semimajor axis, is accurate enough. Should the tracking data indicate a deviation of the semimajor axis corresponding to a time interval change of much more than about 2 minutes, then the ignition time, t, of the apogee motor may be determined by the measured apogee and perigee radii, r_a, r_p.

Guidance Error Estimate

Table 5-3 summarizes the effects of the combined error sources of the Atlas-D/Agena-D apogee motor booster system. Detailed error sources of the Atlas-D/Agena-D guidance and control system are not shown, to keep this report unclassified. As anticipated, most of the longitude drift is caused by apogee motor impulse and attitude errors, whereas the major part of the inclination error is contributed by the Agena-D guidance and control system. The corresponding velocity correction to remove inclination, ΔV_i, and longitude drift, ΔV_d, is given by

$$\Delta V_i \cong 176\,\frac{\text{fps}}{\text{deg}}\,\Delta i = 112 \text{ fps}$$

$$\Delta V_d \cong 9.3\,\frac{\text{fps}}{\text{deg/day}}\,\Delta d = 120 \text{ fps}$$

The 3σ values allocated in Table 5-3 are based on conservative estimates of thrust misalignments and cg shifts, yielding an average torque of 100 ft-lb during

TABLE 5-3. ORBIT DISPERSIONS FOR ASCENT GUIDANCE AND CONTROL ERRORS

Error Source	3 σ Value	Orbital Errors: e, Eccentricity	$\Delta \tau$ Period, minutes	Δ i Inclination, degrees	Δ d Drift, degrees/day
Spacecraft — apogee motor, JPL					
Total impulse error	1.0 percent	0.0113	25.95	0.1110	6.50
Initial weight error	5 lb	0.0043	10.05	0.0196	2.47
Velocity attitude error (pitch and yaw)	1.25 deg	0.0110	24.4	0.2225	6.96
Velocity magnitude loss (spin axis motion)	25 fps	0.0058	12.55	0.041	2.36
Motor ignition time error	2 min	0.0025	0.0648	0.111	0.026
Spacecraft RSS (root-sum-square) error		0.0176	39.05	0.276	10.12
Agena-D RSS error		0.0136	31.09	0.553	7.78
Atlas-D RSS error		0.0025	5.73	0.139	1.44
TOTAL RSS ERROR		0.0223	50.25	0.634	12.85
Velocity correction required, fps				$\Delta V_i = 112$	$\Delta V_d = 120$
Total velocity correction, fps				232	

the apogee motor burning period (~45 seconds). Preliminary estimates of various alignment and balancing tolerances associated with the fabrication and mating of the motor and spacecraft indicate that an average torque of only 50 ft-lb can be readily maintained during apogee boost.

FINAL ORBITAL CORRECTIONS

Because of the sensor and control errors in the transfer phase plus apogee motor design tolerances in the stationary injection phase, it is necessary to correct the final orbit to produce the required precision. Furthermore, the permissible relative motion tolerances imposed to permit the use of fixed, nontracking antennas in the Syncom ground system necessitate repeated velocity pulses in order to compensate for perturbatory drift of the final orbit. Methods of changing the following elements of the 24-hour orbit must therefore be investigated.

$a =$ semimajor axis

$e =$ eccentricity

$\omega =$ angle in orbital plane between ascending node and perigee

$\phi =$ angle in equatorial plane between reference direction and node

$i =$ inclination angle between equatorial and orbital planes

$t_p =$ time of perigee passage

Determination of Orbit

The errors that will be eliminated by these corrections, being in general small, will probably be determined by accurate ground-based sensors making observations over several periods. Therefore, as preliminary considerations to the problem of calculating the final corrections, the pattern of the relative motion of a 24-hour synchronous satellite with respect to the earth is of interest. This ground track may be determined as follows. Consider the case of a circular 24-hour orbit inclined at an angle i to the equator. Let θ and L be the central angle to the node and the latitude of the spacecraft, respectively. Then the spherical trigonometeric relation for i, θ, and Λ, Figure 5-5 is

$$\tan \Lambda = \tan \theta \cos i$$

For a 24-hour circular orbit, $\theta = \omega_e t$ where ω_e is the

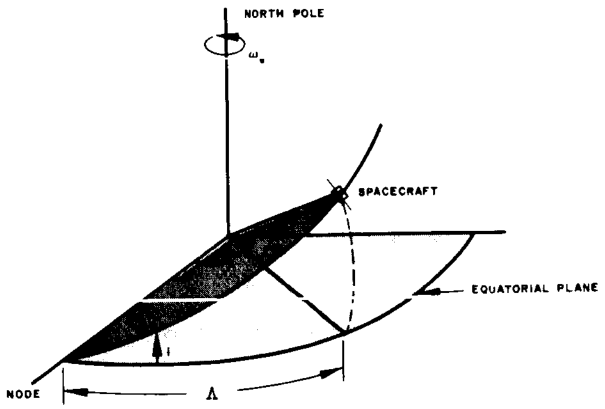

FIGURE 5-5. ORBITAL GEOMETRY RELATIVE TO EARTH

angular velocity of the earth's rotation and t is the time measured from the node. Thus,

$$\Lambda = \tan^{-1} [\tan (\omega_e t) \cos i]$$

The difference between the right ascension of the satellite and that of the nodes is then

$$\Delta \Lambda = \omega_e t - \tan^{-1} [\tan (\omega_e t) \cos i] \qquad (5\text{-}1)$$

The latitude of the spacecraft at any time is

$$L = \tan^{-1} (\sin i \sin \omega_e t) \qquad (5\text{-}2)$$

Equations 5-1 and 5-2 determine the ground plots of the spacecraft in terms of parameters t and i, and show that earth relative motion of an inclined circular orbit is a figure eight, symmetric about the nodes.

For the elliptic orbit case, the central angle from the satellite to the node may be divided into ω (the angle from node to perigee) and $\theta(t)$ (the angle from perigee to the satellite). The equation for the ground track is then

$$\Delta \Lambda = \omega_e t - \tan^{-1} [\tan \{\omega + \theta (t) \} \cos i] \qquad (5\text{-}3)$$

For small eccentricities, e, θ (t) is given by

$$\theta (t) = \frac{2\pi t}{\tau} + 2 e \sin \left(\frac{2\pi t}{\tau}\right) + \frac{5}{4} e^2 \sin \left(\frac{4\pi t}{\tau}\right) + \ldots$$

where τ is the orbital period. The ground track of an elliptical 24-hour orbit relative to the earth is a distorted figure eight. The nodes and the crossover of the figure eight coincide only for $\omega = 0$ degree.

The effect of perturbations will be considered separately since these perturbations are rather small for short periods of time in near stationary orbits and, therefore, can be neglected in the problem of final correction to remove ascent guidance errors after third-stage burnout.

Theoretically, for a stationary orbit, perturbation corrections may be made quasi-permanently by causing the satellite to assume an altitude slightly different from the radius of the unperturbed orbit, so that the drift due to altitude "error" just balances the drift due to the earth's oblateness, the sun, and the moon. The drift rate due to an error in the radius of a circular 24-hour orbit is given by (μ = earth's gravitational constant)

$$\delta\theta = -\frac{3}{2} \frac{\mu^{1/2}}{r^{5/2}} \delta r$$

which gives

$$\frac{\delta\theta}{\delta r} = -0.0237 \text{ deg/day/n.mi}$$

In considering conversions from sensed data to orbital elements, assume that the tracking data includes the slant range from the tracking station to the vehicle (ρ), the elevation angle of the vehicle above the station horizon (α), the azimuth angle from north (β), and the instant of observation (t). The position of the vehicle in inertial space and the six parameters of its orbit are to be determined.

The two Cartesian coordinate systems referred to are an earth-centered inertial coordinate system with the X and Y axes in the plane of the earth's equator and the Z axis directed toward the North Pole, and an earth-fixed coordinate system centered at the tracking station with the z axis directed along the radius vector from the center of the earth to the tracking station and the y axis directed toward the north. These two systems may be related by the following rotations:

$$\begin{Bmatrix} X' \\ Y' \\ Z' \end{Bmatrix} = \begin{bmatrix} -\sin A_0 & -\cos A_0 & 0 \\ \cos A_0 & -\sin A_0 & 0 \\ 0 & 0 & 1 \end{bmatrix} \begin{bmatrix} 1 & 0 & 0 \\ 0 & \sin L_0 & -\cos L_0 \\ 0 & \cos L_0 & \sin L_0 \end{bmatrix} \begin{Bmatrix} x \\ y \\ z \end{Bmatrix} \qquad (5\text{-}4)$$

where X′, Y′, Z′ are axes centered at the tracking station and parallel to X, Y, Z. The latitude, L_o and right ascension, A_o, of the tracking station are known. The following translations complete the transformations of axes:

$$X' - Y = R_e \cos L_o \cos A_o$$

$$Y' - Y = R_e \cos L_o \sin A_o \qquad (5\text{-}5)$$

$$Z' - Z = R_e \sin L_o$$

R_e is the radius of the earth at the tracking station. The complete transformation is then given by the following equations:

$$X = x \sin A_o - y \cos A_o \sin L_o + z \cos A_o \cos L_o + R_e \cos L_o \cos A_o$$

$$Y = x \cos A_o - y \sin A_o \sin L_o + z \sin A_o \cos L_o + R_e \cos L_o \sin A_o$$

$$Z = y \cos L_o + z \sin L_o + R_e \sin L_o \qquad (5\text{-}6)$$

The coordinates of the vehicle in the earth-fixed system are given by

$$x = \rho \cos \alpha \sin \beta$$

$$y = \rho \cos \alpha \cos \beta$$

$$z = \rho \sin \alpha \qquad (5\text{-}7)$$

Then Equation 5-6 becomes the rectangular coordinates of the vehicle in inertial space at time t in terms of measured values.

In order to solve for the radius vector, r, to the vehicle in the inertial system as well as the latitude, L_v, and right ascension, A_v, of the vehicle at time t,

$$X = r \cos L_v \cos A_v$$

$$Y = r \cos L_v \sin A_v$$

$$Z = r \sin L_v \qquad (5\text{-}8)$$

The equations resulting from combining Equations 5-6, 5-7, and 5-8 determine r, L_v, and A_v. However, r is more readily determined from the law of cosines

$$r^2 = \rho^2 + R_e^2 + 2\rho R_e \sin \alpha \qquad (5\text{-}9)$$

The expression for A_v and L_v becomes

$$\tan A_v = \frac{\rho \left[\dfrac{\sin \beta}{\cos L_o} - \tan A_o (\tan L_o \cos \beta + \tan \alpha) \right] + \dfrac{R_e \tan A_o}{\cos \alpha}}{\rho \left(\tan \alpha - \dfrac{\tan A_o \sin \beta}{\cos L_o} - \tan L_o \cos \beta \right) + \dfrac{R_e}{\cos \alpha}} \qquad (5\text{-}10)$$

$$\sin L_v = \frac{\rho (\cos L_o \cos \alpha \cos \beta + \sin L_o \sin \alpha) + R_e \sin L_o}{(\rho^2 + R_e^2 + 2\rho R_e \sin \alpha)^{1/2}} \qquad (5\text{-}11)$$

Obtaining three positions in this manner theoretically determines the orbit completely. Let these three positions be denoted by P_1 (r_1, L_{v1}, A_{v1}), P_2 (r_2, L_{v2}, A_{v2}), and P_3 (r_3, L_{v3}, A_{v3}). Actually, many data points are taken, and the results of the following parameter computations are averaged to reduce errors.

Two data points are theoretically sufficient to determine the node and inclination of the orbit.

$$r = A_{v1} - \tan^{-1} \left[\frac{\sin (A_{v1} - A_{2v})}{\dfrac{\tan L_{v2}}{\tan L_{v1}} - \cos (A_{v2} - A_{v1})} \right] \qquad (5\text{-}12)$$

$$i = \tan^{-1} \left[\frac{\tan L_{v1}}{\sin (A_{v1} - r)} \right] \qquad (5\text{-}13)$$

The angles in the orbital plane from node to P_1, P_2, and P_3 are given by

$$\sin \theta_{nj} = \frac{\sin L_{vj}}{\sin i}, \; j = 1, 2, 3$$

The orbital central angle from node to perigee is shown to be

$$\omega = \tan^{-1} \left(\frac{Q}{S} \right)$$

where

$$Q = (r_1 - r_2)(r_1 \cos \theta_{n1} - r_3 \cos \theta_{n3}) - (r_1 - r_3)(r_1 \cos \theta_{n1} - r_2 \cos \theta_{n2}) \qquad (5\text{-}14)$$

$$S = (r_1 - r_3)(r_1 \sin \theta_{n1} - r_2 \sin \theta_{n2}) - (r_1 - r_2)(r_1 \sin \theta_{n1} - r_3 \sin \theta_{n3})$$

The expressions for e and a are

$$e = \frac{r_2 - r_1}{r_1 \cos(\theta_{n1} - \omega) - r_2 \cos(\theta_{n2} - \omega)} \tag{5-15}$$

$$a = \frac{r_1 [1 + e \cos(\theta_{n1} - \omega)]}{1 - e^2} \tag{5-16}$$

Finally, the time of perigee passage, t_p, is determined from Kepler's equation.

$$t_p = t_1 - \frac{a^{3/2}}{\mu^{1/2}} \left[\sin^{-1}\left(\frac{1 - e^2 \sin \theta_1}{1 + e \cos \theta_1}\right) - \frac{e(1 - e^2)^{1/2} \sin \theta_1}{1 + e \cos \theta_1} \right] \tag{5-17}$$

If the values $\dot{r}$ and $\dot{\theta}$ are obtained by comparing successive readings of r and θ, the following conversions are useful:

$$a = \frac{r\mu}{2\mu - r^3 \dot{\theta}^2 - r \dot{r}^2} \tag{5-18}$$

$$e = \frac{1}{\mu} (r^4 \dot{\theta}^2 \dot{r}^2 + r^6 \dot{\theta}^4 - 2\mu r^3 \dot{\theta}^2 + \mu^2)^{1/2} \tag{5-19}$$

$$p = \frac{r^4 \dot{\theta}^2}{\mu} = \text{semiparameter of ellipse} \tag{5-20}$$

$$\gamma = \tan^{-1}\left[\frac{r \dot{r}}{(\mu p)^{1/2}}\right] = \text{flight path angle relative to local horizontal} \tag{5-21}$$

$$V = (r^2 \dot{\theta}^2 + \dot{r}^2)^{1/2} \tag{5-22}$$

Orbit determination programs including the effect of earth oblateness are being generated at Hughes for Syncom I orbits and should be applicable to Advanced Syncom launches.

Calculation of Corrections

For a near stationary orbit, the ground track of the incorrect orbit will be small because the plot of the nominal orbit is a point. The advantages of a linear expansion about this point will be examined during continuing studies. Programs have been generated to predict the effect of a specified velocity correction for Syncom I and should be directly applicable to the Advanced Syncom orbit.

Initial measured data may be selected as the apogee altitude (h_a), perigee altitude (h_p), and time of perigee crossing (t_p). To determine the corrections for the most general condition, the problem is considered in three cases:

1) $r_a > r_s > r_p$

2) $r_a > r_p > r_s$

3) $r_s > r_a > r_p$

The r_s is the stationary radius at which the satellite is motionless with respect to the earth when perturbation effects are considered.

Case 1: $r_a > r_s > r_p$

Consider first the velocity pulse necessary to change an initially elliptical orbit to a circular synchronous orbit. From Figures 5-6 and 5-7 and the law of cosines,

$$\Delta V_\epsilon^2 = V_s^2 + V_{24}^2 - 2V_s V_{24} \cos \gamma$$

where $V_s \cong (\mu/r_s)^{1/2} = 10{,}087.5$ fps, V_{24} is the velocity in the incorrect orbit at r_s, and γ is the change in flight path during correction. Although it is possible to correct V_{24} with a single velocity pulse ΔV_ϵ directed at angle ϕ_{te} at time t (a, E, t_p), the calculation of t is somewhat complex. A simpler method (if not optimum) would be to use two tangential velocity pulses, $V_{\epsilon 1}$ and $V_{\epsilon 2}$, applied at times t_1, t_2 where

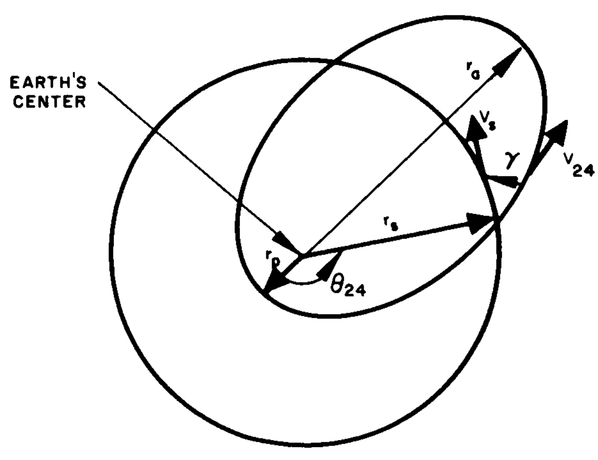

FIGURE 5-6. PARAMETERS FOR ORIBITAL CORRECTION

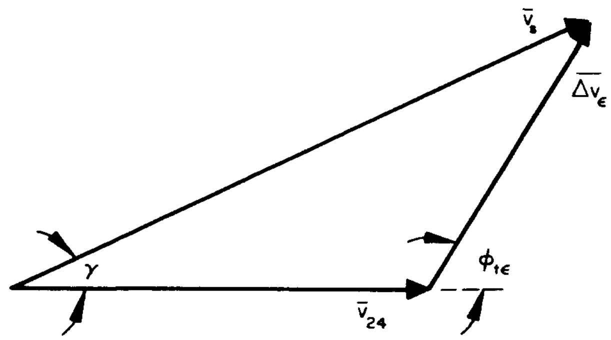

FIGURE 5-7. VERNIER VELOCITY CORRECTION GEOMETRY

$$\frac{\Delta V_{\epsilon 1}}{\sqrt{2V_a}} = \frac{1}{\left(\frac{r_a}{r_s}+1\right)^{1/2}} - \frac{1}{\left(\frac{r_a}{r_p}+1\right)^{1/2}};$$

$$V_a \cong \left(\frac{\mu}{r_a}\right)^{1/2} \qquad (5\text{-}23)$$

$$\frac{\Delta V_{\epsilon 2}}{V_s} = 1 - \left(\frac{2}{1+\frac{r_s}{r_a}}\right)^{1/2}$$

$$t_1 = t_p + \frac{\pi}{\mu^{1/2}}\left(\frac{r_a+r_p}{2}\right)^{3/2} \qquad (5\text{-}24a)$$

$$t_2 = t_p + \frac{2\pi}{\mu^{1/2}}\left(\frac{r_a+r_p}{2}\right)^{3/2} \qquad (5\text{-}24b)$$

To correct for inclination i, let i to be removed be determined as the maximum latitude excursion of the vehicle (L_m) at time t_m. Then the corrective maneuver to be signalled at time $t_i = t_m + \tau/4$ is (where τ = period)

$$\Delta V_i = 2V_s \sin\frac{L_m}{2} \qquad (5\text{-}25)$$

directed at

$$\phi_{ti} = \pm\ (1/2\,L_m + 90 \text{ degrees}) \qquad (5\text{-}26)$$

from the initial direction of motion in the horizontal plane. The sign is positive for L_m north latitude.

To correct for position in the stationary orbit plane, assume the vehicle is displaced $\Delta\Lambda$ from the desired longitude; then the time in which the satellite passes through $\Delta\Lambda$ in the 24-hour orbit is

$$\Delta t = \frac{\tau\Delta\Lambda}{2\pi} \qquad (5\text{-}27)$$

This Δt must be lost or made up, depending upon whether the satellite is ahead or behind its desired zenith. A computationally simple solution is to cause the vehicle to enter an elliptical orbit possessing a period $\tau = \pm\Delta t/n$ by a velocity pulse tangent to the original orbit, and to reenter the original orbit by an equal and opposite pulse after n periods of the transfer orbit. Then, if τ_t and "a" are properties of the transfer orbit, and assuming the satellite leads its correct zenith, with n = 1,

$$\Delta t = \tau_t - \tau = \tau\left[\left(\frac{a}{r_s}\right)^{3/2} - 1\right] \qquad (5\text{-}28)$$

Combining Equations 5-27 and 5-28 and noting that

$$a = \frac{\mu r_s}{2\mu - r_s V_{24}^2}$$

V_{24} is determined as

$$\left(\frac{V_{24}}{V_s}\right)^2 = 2 - \frac{1}{\left(\frac{\Delta\Lambda}{2\pi}+1\right)^{2/3}}$$

Then

$$\frac{\Delta V_{\lambda 1}}{V_s} = \frac{V_{24}}{V_s} - 1 = \left[2 - \left(\frac{\Delta\Lambda}{2\pi}+1\right)^{-2/3}\right]^{1/2} - 1 \qquad (5\text{-}29)$$

and $\Delta V_{\lambda 2} = -\Delta V_{\lambda 1}$, where $\Delta V_{\lambda 1}$, $\Delta V_{\lambda 2}$ are the first and second corrective velocity pulses applied tangentially at an interval $\tau\ (1 + \Delta\Lambda/2\pi)$. The same corrections indicated above apply to Case 2: $r_a > r_p > r_s$.

Case 3: $r_s > r_a > r_p$

Proceeding in a manner similar to Case 1,

$$\frac{\Delta V_{\epsilon 1}}{\sqrt{2V_p}} = \left(1+\frac{r_p}{r_s}\right)^{-1/2} - \left(1+\frac{r_p}{r_a}\right)^{-1/2} \qquad (5\text{-}30)$$

$$\frac{\Delta V_{\epsilon 2}}{\sqrt{2}\,V_s} = 1 - \sqrt{2}\left(\frac{r_s}{r_p}+1\right)^{-1/2} \qquad (5\text{-}31)$$

where $\Delta V_{\epsilon 1}$ and $\Delta V_{\epsilon 2}$ are applied tangentially at times

$$t_1 = t_p + \frac{2\pi}{\mu^{1/2}}\left(\frac{r_a + r_p}{2}\right)^{3/2} \qquad (5\text{-}32)$$

$$t_2 = t_p + \frac{3\pi}{\mu^{1/2}}\left(\frac{r_a + r_p}{2}\right)^{3/2} \qquad (5\text{-}33)$$

The subsequent corrections for i, $\Delta\Lambda$ proceed exactly as in Case 1.

Orientation and Vernier Velocity Control Requirements

Following injection into an approximate stationary orbit, the Syncom vehicle uses its hot gas jet system to station the satellite accurately at the desired longitude and to correct orbital error due to ascent guidance and control errors. A total velocity increment of 232 fps is allowed for this purpose, as estimated previously.

For command simplicity the velocity correction for inclination errors will be made with the axial jet (after vehicle orientation of 65.3 degrees to align the spin axis to the earth's polar axis) firing continuously. The in-plane velocity corrections will be made with the lateral (velocity) jet (in pulsed operation). Although the continuous firing mode is more efficient, the effect of lateral pulsed jet operation on extra fuel consumption will be small, since less than 15 percent of all the velocity increment required for orientation, initial trimming, and station keeping is developed in the pulse mode.

Except for the consideration of orientation and station-keeping requirements, discussed later, the foregoing discussions lead to a specification of the correction procedure to be employed, as well as an estimate of the velocity increment required to complete the correction. Table 5-4 delineates the effect of the major system performance requirements on the sizing of hot gas jet system. Although the values of some of these velocity requirements will change as more refined trajectory, guidance, and spacecraft data become available, it is believed that the total velocity requirement is conservative. For instance, the 5 fps value allotted for spin speed control and residual precession is based on jet thrust misalignments (due to nonsymmetrical exhaust with respect to the nozzle axis, center-of-gravity shifts, and nonradial spaceframe flexing under spin loads) of 2 degrees or about 1 inch with respect to the nominal center of gravity and the perturbation corrections shown exceeds the calculated yearly requirement for the worst-case longitude and sun-moon location.

Orientation Example

As shown in Figures 5-3, 5-4, and 5-8, the initial angle between the spin axis $\hat{k}$ and the sun line $\bar{I}_o$ is designated by ϕ_I and satisfies the relation

$$\cos\phi_I = -\cos\eta_i \sin\lambda_o \cos\delta_o - \sin\eta_I \sin\delta_o \qquad (5\text{-}34)$$

if no attitude errors are induced by apogee boost. In practice, this angle will be determined from a measurement of ψ_2 and the relation

$$\cot\phi = \sin\psi_2 \cot I = \sin\psi_2 \cot 35 \text{ degrees}$$
$$= 1.42815 \sin\psi_2 \qquad (5\text{-}35)$$

where ψ_2 denotes the angle through which the spacecraft must rotate about the spin $(\hat{k})$ axis from maximum output of the "ψ" sun-sensor "beam" to maximum output from the "ϕ" sensor "beam" inclined to the ψ beam at an angle $I = 35$ degrees, as in Figure 5-9.

From Figure 5-3 it is seen that the precession will cease when the $\hat{k}$ axis is along the north-south axis pointing south to that the final angle ϕ_F is found from

$$\cos\phi_F = -\sin\delta_o \quad ; \phi_F = 90 \text{ degrees} + \delta_o \qquad (5\text{-}36)$$

If the spin angle ψ defined earlier is held constant throughout the precession sequence, the motion of the spin axis will generate a rhumb line or loxodrome on a unit sphere as in Figure 5-8. Thus the precession angle P and spin angle ψ are defined by the relations

$$\Delta\theta' = \theta_F' - \theta_I' = \tan\psi \ln\left(\frac{\tan \frac{1}{2}\phi_F}{\tan \frac{1}{2}\phi_I}\right) \leq 180 \text{ degrees} \qquad (5\text{-}37)$$

$$\Delta\phi = \phi_F - \phi_I = -P\cos\psi \qquad (5\text{-}38)$$

TABLE 5-4. CORRECTION PROCEDURE AND VERNIER VELOCITY REQUIREMENTS

Correction Function	ΔV Required, fps	Jet	Mode	ΔV Total (5 years), fps Pulsed	Continuous	Comments
Reorient 65.3 degrees	~18	Axial	Pulsed	18		Impulse ≈ 415 lb-sec
Ascent guidance In-plane (ΔV_d)	120	Lateral	Pulsed	120		3 σ requirement
Inclination (ΔV_i)	112	Axial	Continuous		112	
Perturbations Triaxiality (In-plane)	≦7/yr	Lateral	Pulsed	35		~ 1 correction/5 days
Sun-moon (Inclination)	<180/yr	Axial	Continuous		900	5 fps/correction as often as needed to keep i <±0.05 degree
Spin speed and precession Due to thrust misalignments (~ 1 inch or 2 degrees) and/or cg shifts	0.6: spin speed	Axial	Continuous		0.6	Centrifugally actuated axial jet nozzle angle
	~4: precession	Axial	Pulsed	4		
			Subtotal	177	1013	$\frac{\Delta V \text{ pulsed}}{\Delta V \text{ total}} \approx 15$ percent
			Total vernier velocity		1190 fps	

where $\Delta\theta'$ is the angular rotation of the plane $(\hat{k}, \bar{I}_o)$ about $\bar{I}_o$ during the precession sequence, resulting in a total precession angle P. The angle $\Delta\theta'$ is inferred from knowledge of λ_o, δ_o, (assumed constant during precession sequence) and burnout attitude, η_i, from the expressions

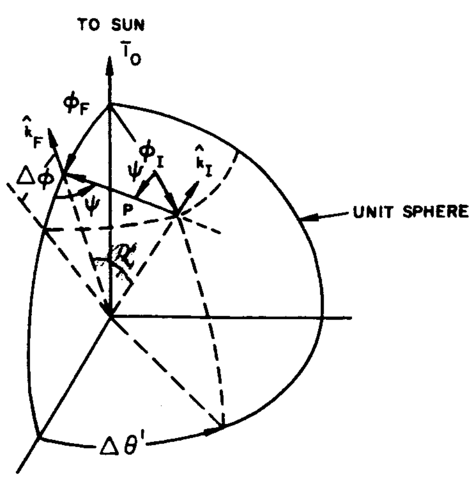

FIGURE 5-8. SPIN AXIS RHUMB LINE MOTION

$$\cos \Delta\theta = \frac{\bar{N}_I \cdot \bar{N}_F}{\sqrt{N_I^2 N_F^2}} \tag{5-39}$$

where, if $\hat{I}, \hat{J}, \hat{K}$ are unit vectors along the X, Y, Z axes of Figure 5-13,

$$\bar{N}_I \equiv (\hat{k} \times \bar{I}_o)_I = \begin{vmatrix} \hat{I} & \hat{J} & \hat{K} \\ \cos \eta_i & 0 & -\sin \eta_i \\ -\sin \lambda_o \cos \delta_o & \cos \lambda_o \cos \delta_o & \sin \delta_o \end{vmatrix} \tag{5-40}$$

$$\bar{N}_F \equiv (\hat{k} \times \bar{I}_o)_F = \begin{vmatrix} \hat{I} & \hat{J} & \hat{K} \\ 0 & 0 & -1 \\ -\sin \lambda_o \cos \delta_o & \cos \lambda_o \cos \delta_o & \sin \delta_o \end{vmatrix} \tag{5-41}$$

If the initial orientation takes place on 15 July 1964 at 7.0000^h U.T., at longitude, $\lambda_{sat} = 93$ degrees W, then from the Nautical Almanac (at 0^h U.T.)

$E \equiv$ equation of time $= -$ 5 minute 49.70 seconds
$\cong -0.097$ hr

$\delta_o = +$ 21 degrees, 33 minutes, 38.6 seconds $\approx$
$+$ 21.57 deg

and from apogee burnout conditions $\eta_I = 24.7$ degrees so that Equation 5-34 gives

$$\cos \Delta\phi_I = -0.3082;$$

$$\phi_I = 180 \text{ degrees} - 72 \text{ degrees},$$

$$= 107.95 \text{ degrees}$$

whereas from Equation 5-36

$$\phi_F = 90 \text{ degrees} + 21.57 \text{ degrees}$$

$$= 111.57 \text{ degrees}$$

$$\Delta\phi = \phi_F = \phi_I = +3.62 \text{ degrees}$$

The relative longitude of the sun, λ_o, is given by

$$\lambda_o = \lambda_{sat} + 180 \text{ degrees} - 15 \text{ deg/hr (U.T.} + \text{E)}$$

$$= 93 \text{ degrees W} + 180 \text{ degrees}$$

$$-15\ (7.000 - 0.097) = +169.46 \text{ degrees},$$

so that from Equations 5-39, 5-40, and 5-41

$$\cos \Delta\theta' = \frac{+0.306}{0.898} = 0.341;$$

$$\Delta\theta' = -70.1 \text{ degrees} = -1.2234 \text{ rad}$$

From Equations 5-37 and 5-38

$$\tan \psi = \frac{-1.2234}{\ln 1.07} = -18.1;\ \cos \psi < 0$$

so that

$$\psi = 180 \text{ degrees} - 86.84 \text{ degrees}$$

$$= 93.16 \text{ degrees}$$

$$\cos \psi = -0.0552$$

$$P = \frac{\Delta\phi}{\cos \psi} = \frac{3.62 \text{ degrees}}{0.0552}$$
$$= 65.6 \text{ degrees}$$

It is of interest to note that the efficiency of the rhumb line precession angle P_{rl} relative to the great circle precession angle $P_{gc} = 90$ degrees $- \eta_I$ 65.3 degrees, for this example is estimated by

$$\frac{P_{gc}}{P_{rl}} \cong \frac{65.3 \text{ degrees}}{65.6 \text{ degrees}} = 99.5 \text{ percent}$$

To estimate the precession time t_p, and hot gas propellant consumed, Wp, an estimate is formed of the angular impulse, Nt_p (torque $\times$ time).

$$\bar{I}_z\, \omega_z\, \bar{P} \cong \bar{N} t_p \tag{5-42}$$

$$N = \frac{\omega_z}{2\pi} \int_{-\pi/n\omega_z}^{+\pi/n\omega_z} Fl \cos (\omega_z t)\, dt = \frac{Fl}{2\pi} \sin \omega_z t \Big]_{-\pi/n\omega_z}^{+\pi/n\omega_z}$$

$$\equiv \text{average torque/rev}$$

$$N_{60} = \frac{Fl}{2\pi} \text{for } n = 6 \text{ (60 degrees jet pulse width)} \tag{5-43a}$$

$$N_{45} = \frac{Fl}{\pi} (0.3827)\text{; for } n = 8 \text{ (45 degrees jet pulse width)} \tag{5-43b}$$

where

I_z = moment of inertia about spin axis, slug-ft^2
= 70.76 slug-ft^2

ω_z = spin speed, rad/sec
= 10.47 rad/sec (100 rpm) (assumed constant)

F = thrust of axial jet, pounds
= 5.0 lb (constant during precession)

l = moment arm of axial jet to spin axis, feet
= 2.16 feet

P = precession angle, radians
= 65.6 degrees/57.3 = 1.145 radians

Thus for a 60 degree jet pulse width Equations 5-42 and 5-43a give

$$t_p = \frac{I_z\, \omega_z\, P}{N_{60}} = \frac{(70.76)\ (10.47)\ (1.145)}{1.72}$$

$$= \frac{849}{1.72} = 493 \text{ seconds} \quad = 8.21 \text{ minutes}$$

and for a 45 degree jet pulse width

$$t_p = \frac{849}{1.317} = 645 \text{ seconds} = 10.76 \text{ minutes}$$

For a specific impulse $I_{sp} = 260$ seconds, the weight of the hot gas propellant consumed, Wp, is, for a 60 degree jet pulse

$$W_p = \frac{F\,t_p}{I_{sp}}\frac{\pi/3}{2\pi} = \frac{(5)\ (493)}{260}\frac{1}{6} = 1.58 \text{ pounds}$$

which is almost the same propellant weight, W_p, for a 45 degree jet pulse, i.e.,

$$W_p = \frac{(5)\ (645)}{260}\left(\frac{\pi/4}{2\pi}\right) = 1.55 \text{ pounds}$$

The 2.5 minute increase in t_p may be acceptable for the 45 degree jet pulse angle design since this angle is simpler to mechanize electronically as an integral multiple of a time base.

Since the maximum impulse I_T required for orientation is

$$I_T = I_{sp}\,W_p = (260)\ (1.58) = 411 \text{ lb-sec}$$

the equivalent velocity correction required for orientation is approximated by

$$\Delta V = g\,I_{sp} \ln\left(\frac{W_s}{W_s - W_p}\right) \approx \frac{g\,I_{sp}\,W_p}{W_s - W_p}$$

$$= \frac{g\,I_T}{W_s - W_p} = \frac{(32.2)\ (411)}{(764.62)} = 17.35 \text{ fps}$$

where W_s = weight of spacecraft at time of orientation

$\cong$ 766.2 pounds

ANALYTIC ESTIMATE OF MISALIGNMENT EFFECTS DURING APOGEE MOTOR THRUST

The effects of thrust misalignment during burning of the third-stage motor have been estimated to predict the subsequent attitude change, α_1, of the angular momentum vector, the rotation, γ_1, of the incremental velocity vector, and the induced nutation angle, θ_1. The analytic model developed by R. H. Edwards (Reference 5-1, Section 5K) was used and checked against machine solution results given in Section 7 of Reference 5-2.

Using assumptions comparable to those of Reference 5-2, reasonable bracketing of values was obtained except in the prediction of the postburnout α_1 angle, where the model predicted a maximum angle, $|\alpha_1|_{max}$, of 1.47 degrees, compared with 1.7 degrees from Reference 5-2. Further discussion with LMSC is planned in this area. In this study the effect of dynamic unbalance on γ_1 was estimated analytically and compared with results in Reference 5-2. In a later section the effect of fuel sloshing is summarized with emphasis on possible resonance conditions.

General Discussion, Definitions, and Assumptions

If the spacecraft is treated as a spinning symmetrical top with principal moments of inertia, $I_x = I_y < I_z$, along pitch, yaw, and roll body axes x, y, z whose unit vectors are $\bar{1}_x$, $\bar{1}_y$, $\bar{1}_z$ respectively, then the angular momentum vector $\bar{H}$, the instantaneous angular velocity vector $\bar{\omega}$, and $\bar{1}_z$ all lie in one plane. In general, the following can be written (Reference 5-3):

$$\bar{\omega} = \omega_x\bar{1}_x + \omega_y\bar{1}_y + \omega_z\bar{1}_z = \bar{\omega} + \omega_z\bar{1}_z \tag{5-44}$$

$$\bar{H} = I_x\,(\omega_x\bar{1}_x + \omega_y\bar{1}_y) + \bar{I}_z\omega_z\bar{1}_z = I_x\bar{\omega} + I_z\omega_z\bar{1}_z \tag{5-45}$$

Eliminating $\bar{\omega}$ gives

$$\bar{\omega} = \frac{\bar{H}}{I_x} - \left(\frac{I_z}{I_x} - 1\right)\omega_z\bar{1}_z \tag{5-46}$$

Equation 5-46 is shown graphically in Figure 5-10. Later, the practical fact that for Syncom $|\bar{\omega}| << |\bar{\omega}|$ will be used. The angle θ in Figure 5-10 will be the induced nutation angle after apogee motor burnout.

It is now assumed that a slightly misaligned thrust vector F acting through an effective moment arm β about the center of gravity of the spacecraft will generate a torque $|\bar{N}| = F\beta$ for a time t such that $N = N_x + i\,N_y$, $(i^2 = -1)$ – i.e., $N_z \cong 0$ and $\omega_z \approx$ constant.

The reasonableness of this assumption for Syncom II is shown below by submitting typical 3σ values for N_z that arise from various misalignments. The resulting spin speed change $\Delta\omega_z$ is only about 1 percent of the initial spin rate ω_z.

If, in addition, the pitch-to-roll moment of inertia ratio I_x/I_z varies slowly during the burning time t, or more precisely, if

$$\frac{d}{dt}\ln\frac{I_x(t)}{I_z(t)} << \omega_z \approx 10.5 \text{ rad/sec} \tag{5-47}$$

(as verified numerically below), then, from Reference

5-1, the change α of the direction of H due to torque N is approximated by

$$\alpha = \frac{I_x \omega_o}{I_z \omega_z} + \frac{I_x}{I_z \omega_z} \int_o^t \exp(i\omega_z \tau) \frac{N}{I_x} d\tau \quad (5\text{-}48)$$

where $\omega_o = (\omega_x + i\omega_y)_o$ is the initial angular velocity in pitch and yaw due to tipoff at Agena separation. For Syncom II, $\omega_o \approx 0$ as a result of the more than 5-hour effect of nutation damper action from perigee separation to transfer ellipse apogee motor ignition.

Assuming further that F begins almost instantaneously (≤ 1 second) and the acceleration (F/M) varies almost linearly until start of tailoff, the two principal contributions to α are those due to the impulse at the start of thrust and the thrust tailoff effects at the end of burning.

Constant Spin Speed Assumption. From the equation of motion about the spin axis

$$I_z \dot{\omega}_z = N_z \approx F_{av} \epsilon_F \delta_{cg}$$

it is seen that if the misalignment torque is directed to change the spin speed, the change in spin speed $\Delta\omega_z$ will be

$$\Delta\omega_z \approx \frac{F_{av} \epsilon_F \delta_{cg} \Delta t}{I_{zav}}$$

$$= \frac{(7000)(4.4 \times 10^{-3})(8.33 \times 10^{-3})(30)}{73} \text{ rad/sec}$$

$$\approx 0.105 \text{ rad/sec}$$

where the values given in Table 5-5 later in this section and the (3σ) estimates of Reference 5-2 for ϵ_F and δ_{cg} are used. Thus it is seen that, conservatively

$$\frac{\Delta\omega_z}{\omega_z} \leq \frac{0.105}{10.47} \approx 1 \text{ percent}$$

during the 30-second burning period, and ω_z may be assumed constant.

Constant (I_x/I_z) Assumption. In the derivation of Equation 5-48 carried out in Reference 5-1, the assumption

$$\frac{I_x}{I_z} = \text{a constant} \quad (5\text{-}49)$$

was made to evaluate the integral

$$\int_o^t \omega \exp(i\omega_z \tau) d\tau$$

in the form

$$\int_o^t \omega \exp(i\omega_z \tau) d\tau \approx \left(\frac{I_x}{I_z}\right)\left[\left(\frac{\omega}{i\omega_z}\right)\exp(i\omega_z \tau) - \left(\frac{\omega_o}{i\omega_z}\right) - \left(\frac{1}{i\omega_z}\right)\int_o^t \exp(i\omega_z \tau) \cdot \frac{\dot{N}}{I_x} d\tau\right]$$

This approximation is applicable provided

$$\frac{d}{dt} \ln \frac{I_x(t)}{I_z(t)} << \omega_z \approx 10.5 \text{ rad/sec}$$

From Reference 5-2, it is seen that I_x/I_z varies linearly with t during burning; that is,

$$\frac{I_x(t)}{I_z(t)} = \left[\frac{I_x}{I_z}(t_1) - \frac{I_x}{I_z}(o)\right]\frac{t}{t_1} + \frac{I_x}{I_z}(o)\,;\; o \leq t \leq t_1$$

$$it_1 = 30 \text{ sec}$$

$$= mt + b;\; m = -0.00164;\; b = 0.769$$

$$\left|\frac{d}{dt}\ln(mt + b)\right|_{t=t_1} = \left|\frac{d}{dt}\ln\frac{I_x}{I_z}(t)\right|_{max} = \frac{m}{mt_1 + b}$$

$$= 0.0023 << \omega_z \text{ rad/sec}$$

Thus the assumption of Equation 5-49 is valid.

Angular Momentum Direction, α_I. If $\tau = 0+$, $\tau = t_1$, and $\tau = t_2$, correspond respectively to start of full thrust, start of tailoff, and time of burnout (pressure ≤ 50 psig), then, from Reference 5-1, for an impulsive tailoff, α_1 becomes

$$\alpha_1 = \frac{I_x}{I_z}\left\{\frac{\omega_o}{\omega_z} + \frac{1}{\omega_z}\left[\left(-\frac{N}{i\omega_z I_x}\right)\Big|_{o+} + \frac{1}{i\omega_z}\left(\frac{N}{I_x}\right)\Big|_{1-} \exp(i\omega_z t_1)\right]\right\} \quad (5\text{-}50)$$

For a linear tailoff,

$$\alpha_1 = \frac{I_x}{I_z}\left\{\frac{\omega_o}{\omega_z} + \frac{1}{\omega_z}\left[\left(-\frac{N}{i\omega_z I_x}\right)\Big|_{o+} + \left(\frac{N}{I_x}\right)\Big|_2 \cdot \frac{(e^{i\omega_z t_1} - e^{i\omega_z t_2})}{\omega_z^2 (t_2 - t_1)}\right]\right\} \quad (5\text{-}51)$$

where the subscripts adjacent to the vertical bars indicate the times at which the preceding parenthetical expressions are evaluated. Assuming an impulsive tailoff (to yield a conservative estimate) and letting $N(t) = N_{av} = F_{av}\beta$, (a constant), $\omega_o = 0$, Equation 5-50 becomes

$$\alpha_1 \cong \left(\frac{I_x}{I_z}\right)_{av} \cdot \left(\frac{1}{I_x}\right)_{1-} \frac{i\,N_{av}}{\omega_z^2}\left[\frac{(I_x)_{1-}}{(I_x)_{o+}} - e^{i\omega_z t_1}\right] \tag{5-52}$$

Rotation of Incremental Angular Velocity Vector, γ_1. If the incermental velocity component normal to the initial z axis is designated by V_n and the incremental velocity in the initial z-direction by V_b, the angle between the incremental velocity vector at burnout (subscript 1) and the initial z-direction (desired incremental velocity direction) is given in Reference 5-1 as

$$\gamma_1 = \frac{V_{n_1}}{V_{b_1}} = \frac{V_{no}}{V_{b_1}} + \frac{1}{V_{b_1}} \int_o^{t_1} \frac{F}{M} \frac{I_x}{I_z \omega_z} \left\{ \omega_o \left(1 - e^{i\omega_z \frac{I_z}{I_x} t}\right) + \int_o^t \frac{N}{I_x} e^{i\omega_z \tau} \cdot \left[1 - \exp\left(i\omega_z \frac{I_z}{I_x}[t-\tau]\right)\right] d\tau \right\} dt \tag{5-53}$$

where M is the mass of the spacecraft. The term of the form

$$\int_o^{t_1} \frac{F}{M} \left\{ \frac{I_x}{I_z \omega_z} \omega_o \left(1 - e^{i\omega_z \frac{I_z}{I_x} t}\right) \right\} dt$$

can be adequately approximated by

$$\int_o^{t_1} \frac{F}{M} \frac{I_x}{I_z \omega_z} \omega_o \, dt \cong V_{b_1} \frac{I_x \omega_o}{I_z \omega_z} \tag{5-54}$$

if

$$\omega_z \frac{I_z}{I_x} t_1 >> 1 \tag{5-55}$$

Similarly,

$$\int_o^{t_1} \frac{F}{M} \frac{I_x}{I_z \omega_z} \int_o^t e^{i\omega_z \tau} \cdot \frac{N}{I_x} \left[1 - \exp\left(i\omega_z \frac{I_z}{I_x}\left[t - \tau\right]\right)\right] d\tau \, dt$$

can be approximated by

$$\int_o^{t_1} \frac{F}{M} \frac{I_x}{I_z \omega_z} \int_o^t e^{i\omega_z \tau} \cdot \frac{N}{I_x} d\tau \, dt$$

$$= \int_o^{t_1} \frac{F}{M} \frac{I_x}{I_z \omega_z} \left\{ \frac{1}{i\omega_z} e^{i\omega_z \tau} \frac{N}{I_x} \Big|_o^t - \frac{1}{i\omega_z} \int_o^t e^{i\omega_z \tau} d\left(\frac{N}{I_x}\right) \right\} dt \tag{5-56}$$

The first term within the braces is zero since $N(t) = N(O) = 0$. From the previous assumptions made in the evaluation of α_1, the second term in the braces is approximated in Reference 5-1 by

$$-\frac{1}{i\omega_z} \int_o^t e^{i\omega_z \tau} \, d\left(\frac{N}{I_x}\right) \approx \left(-\frac{1}{i\omega_z} \frac{N}{I_x}\Big|_{o+}\right) \tag{5-57}$$

so that Equation 5-56 becomes

$$\int_o^{t_1} \frac{F}{M} \frac{I_x}{I_z \omega_z} \left(-\frac{1}{i\omega_z} \frac{N}{I_x}\Big|_{o+}\right) dt \cong V_{b_1} \frac{I_x}{I_z \omega_z} \left(\frac{-1}{i\omega_z}\right) \frac{N}{I_x}\Big|_{o+} \tag{5-58}$$

Thus from Equations 5-58 and 5-54, Equation 5-53 reduces to

$$\gamma_1 \approx \frac{V_{no}}{V_{b_1}} + \frac{I_x}{I_z \omega_z} \left[\omega_o + \frac{i}{\omega_z} \left(\frac{N}{I_x}\right)\Big|_{o+}\right] \tag{5-59}$$

The component V_{no} is in general due to an initial thrust attitude error generated by the Agena guidance system during the programmed yaw maneuver prior to spinup and separation of the spacecraft at transfer ellipse perigee. Since V_{no} is not an apogee motor spacecraft misalignment effect, it will be considered zero in this analysis, as will ω_o.

Induced Nutation Angle, θ_1. In a similar manner, after an impulsive burnout, the complex angular rate $\omega_1 = (\omega_x + i\omega_y)_1$ about the pitch and yaw axes induced by the thrust misalignment torque $N = F\beta$ is given by

$$\omega_1 = e^{-i\Omega t_1}$$

$$\cdot \left\{ \omega_o - \frac{1}{i\Omega}\left(\frac{N}{I_x}\right)\bigg|_{o+} + \frac{1}{i\Omega}\left(\frac{N}{I_x}\right)\bigg|_{1-} \cdot e^{i\Omega t_1} \right\} \tag{5-60}$$

where

$$\Omega = \omega_z\left(1 - \frac{I_z}{I_x}\right) < 0 \tag{5-61}$$

and the last term of Equation 5-60 is zero for a linear tailoff.

For $\omega_o = 0$, and $N(t) = N_{av} = F_{av}\beta =$ constant, Equation 5-60 becomes

$$\omega_1 \approx \frac{iN_{av}}{\Omega}\left[\left(\frac{1}{I_x}\right)\bigg|_{o+} e^{-i\Omega t_1} - \left(\frac{1}{I_x}\right)\bigg|_{1-}\right] \tag{5-62}$$

Referring to Figure 5-10, it is seen that at burnout $|\bar{\omega}_\perp| = \omega_1$, so that

$$\tan\theta_1 \approx \theta_1 = \frac{\omega_1}{\omega_z}\left(\frac{I_x}{I_z}\right)_1 \tag{5-63}$$

Substituting Equation 5-63 into 5-62 and rearranging gives

$$\theta_1 \approx \frac{iN_{av}}{\omega_z\Omega(I_z)_1}\left[\frac{(I_x)_{1-}}{(I_x)_{o+}} e^{-i\Omega t_1} - 1\right] \tag{5-64}$$

Misalignment Torque, N_{av} Estimate. As Figure 5-11 shows the principal sources of error that give rise to a misalignment torque are uncertainties in:

1) The cg location in the spacecraft, δ_{cg}, from nominal
2) The average thrust direction with respect to the z-axis, ϵ_F
3) The concentricity of the nozzle with respect to the z-axis, δ_N

Although in general these independent random error sources will each generate torques in different directions with respect to a body-fixed coordinate system, a conservative estimate of their combined effect will result if the 3σ values of each of these errors are root-sum-squared as if their torque contributions were all about the x-axis, for example. Thus a 3σ estimate of N_{av} is approximated to first order by

$$N_{av} = F_{av}\left[(r\,\epsilon_F)^2 + \delta_N^2 + \delta_{cg}^2\right]^{1/2} = F_{av}\beta \text{ ft-lb} \tag{5-65}$$

where the thrust F_{av} is measured in pounds; the moment arm, r, from the exit plane to the nominal cg in feet; ϵ_F in radians; and δ_N, δ_{cg}, and β in feet. The value β can now be considered as the *effective* moment arm through the cg and normal to F_{av}.

Dynamic Unbalance Torque, N_u, and Principal Axis Misalignment, ϵ (Reference 5-4). A disturbance torque N_u due to a mass unbalance M_u can be treated as follows.

From Figure 5-11, it is assumed that the mass element M_u causing the dynamic unbalance can be placed a distance Y_u from the nominal spin axis and a distance Z_u from the cg along the spin axis. The torque about the cg due to this mass element is

$$N_x = \omega_z^2 Y_u Z_u M_u = \omega_z^2 I_{yz} \tag{5-66}$$

where I_{yz} is the equivalent product of inertia component about the x-body axis. Now from the properties of moments of inertia, the angle ϵ_x between the principal axis and the axis about which the moments and products of inertia are computed is given by*

$$\tan 2\epsilon_x = \frac{2 I_{yz}}{I_z - I_x} \approx 2\epsilon_x \tag{5-67}$$

Thus, for $I_{yz} \approx I_{xz}$, $\epsilon_x \approx \epsilon_y$

$$\epsilon \cong \sqrt{\epsilon_x^2 + \epsilon_y^2} = \frac{\sqrt{2}\, I_{yz}}{I_z - I_x} \tag{5-68}$$

Now, if I_{yz} is written

$$I_{yz} = k\, I_x,\ 0 \leq k << 1 \tag{5-69}$$

Equation 5-68 becomes

$$\epsilon \approx \frac{\sqrt{2}\,k}{\frac{I_z}{I_x} - 1} \tag{5-70}$$

and, from Equation 5-66

$$\frac{N_u}{I_x} = \frac{\sqrt{2}\,N_x}{I_x} = \sqrt{2}\,\omega_z^2 k = \omega_z^2 \epsilon \left(\frac{I_z}{I_x} - 1\right) \tag{5-71}$$

---

*Note: $I_x = I_y >> I_{yz}$.

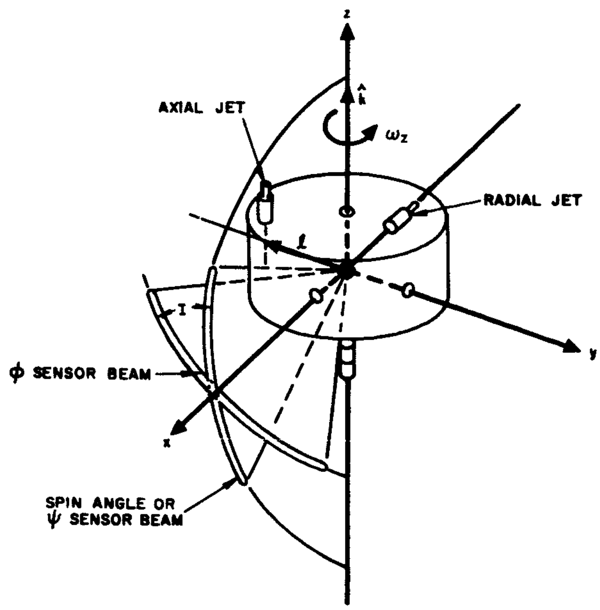

FIGURE 5-9. SUN SENSOR AND CONTROL JET GEOMETRY

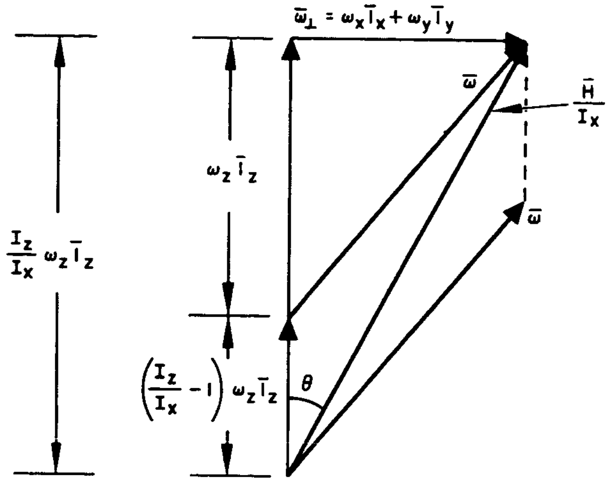

FIGURE 5-10. INSTANTANEOUS VECTOR GEOMETRY

In general, the ratio I_z/I_x will vary slowly enough during apogee motor burning to be considered a constant, whereas I_x and thus ϵ will vary (linearly) with time during burning.

Numerical Check with LMSC Data. Table 5-5 lists the parameters for one of the spacecraft configurations studied by LMSC in Reference 5-2 on an IBM 7090. In addition, an impulsive tailoff at $t = t_1 = 30$ seconds was assumed.

Attitude Change, α_1, after Burnout. From Equation 5-52 and Table 5-5.

$$\alpha_1 = i\,\frac{(0.774)\ (100)}{(47)\ (109.62)}\left(0.702 - e^{i\frac{10}{3}\pi t_1}\right)$$

$$= i\,0.015\left(0.702 - e^{i\frac{10}{3}\pi t_1}\right)$$

At $t_1 = 30$ seconds exactly, $(10/3\ \pi t_1) = 100\,\pi$ and the exponent is 1, so that $|\alpha_1| = |\alpha_1|_{min} = (0.015)\ (0.3) = 0.0045$ radian ≈ 0.26 degree.

However,

$$\frac{\delta t_1}{t_1} \approx \pm 0.01$$

$$\delta t_1 = \pm 0.3 \text{ second}$$

and

$$\frac{10}{3}\,\pi\,(t_1 + \delta t_1) = 100\,\pi \pm \pi$$

in which case the exponent may be equal to -1, so that

$$|\alpha_1| = |\alpha_1|_{max} = (0.015)\ (1.7) = 0.0256 \text{ radian} \approx 1.47 \text{ degrees}$$

TABLE 5-5. LMSC SPACECRAFT CONFIGURATION PARAMETERS

t, seconds	I_z, slug-ft²	$I_x = I_y$, slug-ft²	$\frac{I_z}{I_x}$	$\left(\frac{I_z}{I_x}\right)_{av}$	N_{av}, ft-lb	F_{av}, pounds	ω_z, rad/sec	$\Omega\|_{t-}$, rad/sec	k
0	82.1	66.7	1.23	0.774	100	6967	10.47	1.2π	0.01
30	63.9	47.0	1.36						

The value given in Reference 5-2 is $|\alpha_1|_{LMSC} = 1.7$ degrees. Thus in this instance the model predicts somewhat optimistically even if the value $(I_x/I_z)_{max} = 0.813$ were used instead of $(I_x/I_z)_{av} = 0.774$ (to yield $|\alpha_1|_{max} = 1.54$ degrees).

Incremental Velocity Vector Rotation, γ_1, After Burnout. From Equation 5-59 with $V_{no} = \omega_o = 0$ and from Table 5-5.

$$|\gamma_1| = \frac{(0.774)\ (100)}{(109.62)\ (66.7)}$$

$$= 0.0106 \text{ radian} \approx 0.61 \text{ degree}$$

whereas from Reference 5-2, it is seen that

$$|\gamma_1|_{LMSC} = 0.64 \text{ degree}$$

The effect due to dynamic unbalance of 1 percent I_x (a severe unbalance) at $t = 0$ is obtained from Equations 5-59 and 5-71

$$|\gamma_1|_u = \left(\frac{I_x}{I_z}\right)_{av} \frac{1}{\omega_z^2} \left(\frac{N_u}{I_x}\right)\Bigg|_{0+}$$

$$\cong \left(\frac{I_x}{I_z}\right)_{av} \sqrt{2}\,k = (0.774)\ (1.414)\ (0.01)$$

$$= 0.0109 \text{ radian} = 0.625 \text{ degree}$$

compared with

$$|\gamma_1|_{u \atop LMSC} = 0.58 \text{ degree}$$

It may be of interest to note thay by forming the sums

$$|\gamma_1| + |\gamma_1|_u = 0.61 + 0.625 = 1.235 \text{ degrees}$$

$$(|\gamma_1| + |\gamma_1|_u)_{LMSC} = 0.64 + 0.58 = 1.22 \text{ degrees}$$

while the rotation γ_1 due to the simultaneous effect of thrust misalignment and dynamic unbalance is given by Reference 5-2 as

$$|\gamma_{1,u}|_{LMSC} = 1.24 \text{ degrees}$$

in close agreement with the algebraic sum of the model.

Nutation Angle, θ_1. From Equation 5-64 and Table 5-5,

$$\theta_1 = -0.0396\, i\ (0.702\, e^{-i\, 1.2\pi t_1} - 1) \text{ radian}$$

$$|\theta_1|_{max} = (0.0396)\ (1.7) = 0.0675 \text{ radian}$$

$$\approx 3.9 \text{ degrees}$$

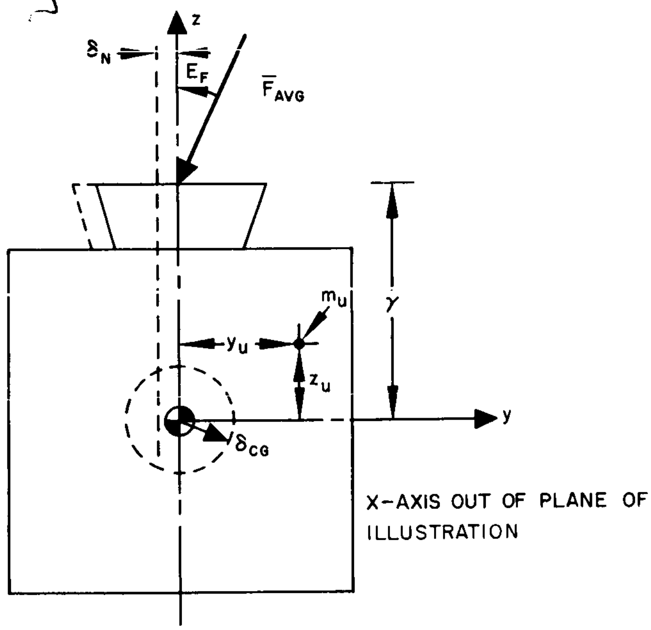

FIGURE 5-11. MISALIGNMENT AND MASS UNBALANCE GEOMETRY

$$|\theta_1|_{min} = (0.0396)\ (0.3) = 0.0119 \text{ radian}$$

$$\approx 0.7 \text{ degree}$$

whereas from Reference 5-2 it is noted that

$$|\theta_1|_{LMSC} \approx 1.2 \text{ degrees}$$

whose value is bracketed by the model.

Conclusions

Considering the number of simplifications and assumptions made, the model gives good enough prediction of the important dynamic parameters α_1 and γ_1 at burnout to be useful as a preliminary design tool, subject to computer verification when the design parameters are known precisely. Initial application of this model to preliminary JPL motor design data (February Progress Report) shows that an average misalignment torque of $\leq$ 50 ft-lb will yield acceptable values of attitude change α_1 incremental velocity vector rotation γ_1, and principal axis rotation ϵ_1. A general FORTRAN Rigid Body Program has been generated to analyze the effects of more realistic thrust, torque, and moment-of-inertia histories on the subsequent vehicle motion (Reference 5-5).

Lunar and Solar Perturbations of Inclination

An analysis of the inclination buildup due to sun-moon effects shows that over an interval of time represented by the angle ϕ, [the angle between the vernal equinox of date and the moon's line of nodes (intersection of lunar orbital plane and equatorial plane)], the component values of inclination for the lunar effect can be represented by

$$\Delta i_y = \frac{F_m}{\omega_{reg}}$$

$$\left(\sin I^* \cos I^* \cos \epsilon \cos \phi - \sin^2 I^* \sin \epsilon \frac{\cos 2\phi}{4}\right)\Bigg|_{\phi_i}^{\phi_f}$$

$$\Delta i_x = \frac{F_m}{\omega_{reg}}\Bigg[\sin I^* \cos I^* \cos 2\epsilon \sin \phi + \sin \epsilon \cos \epsilon$$

$$\left\{\phi\left(\cos^2 I^* - \frac{\sin^2 I^*}{2} - \frac{\sin^2 I^*}{4} \sin 2\phi\right)\right\}\Bigg]\Bigg|_{\phi_i}^{\phi_f}$$

where (see also Figure 5-12)

$$F_m = \frac{3}{4}\frac{k_m^2}{R_m^3}\frac{1}{n_o} = 1.6425 \text{ deg/yr}$$

k_m^2 = constant of attraction of moon

$= 0.0123\, k^2;\ k^2 = 62{,}627.75\ \dfrac{\text{n.mi}^3}{\text{sec}^2}$

n_o = mean motion of the stationary satellite

$= \omega_e = 360$ deg/day

ω_{reg} = rate of regression of moon's line of nodes

$= 19.341$ deg/yr

I^* = inclination angle of the lunar orbital plane to the plane of the ecliptic ≈ 5 degrees

ϵ = inclination angle of the plane of the ecliptic to the equatorial plane ≈ 23.4 degrees

X, Y, Z = coordinate frame formed by X along the vernal equinox, Y normal to X in the equatorial plane, Z normal to the equatorial plane

x', y', z' = coordinate frame formed by $x' = X$, y' normal to x' in the lunar orbital plane, z' normal to lunar orbital plane

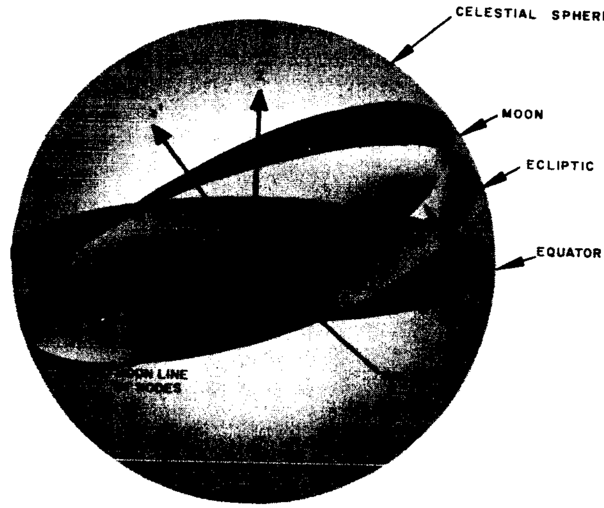

FIGURE 5-12. SPATIAL GEOMETRY OF PERTURBING ORBITS

A similar expression holds for the perturbation of the sun in terms of F_s, where

$$F_s = \frac{3}{4}\frac{k_s^2}{R_s^3}\frac{1}{n_o} = \frac{3}{4}\frac{n_s^2}{n_o}$$

$$\approx \frac{0.75}{365} n_s = 0.7391 \text{ deg/yr}$$

k_s^2 = constant of attraction of the sun $= 333{,}000\, k^2$

R_s = radial distance from center of sun to center of earth

n_s = angular velocity of the earth in its orbit around the sun

This corresponds to an average inclination of change due to the sun of

$$\left(\frac{di}{dt}\right)_{\substack{ave\\sun}} = \frac{3}{4}\sin\epsilon\cos\epsilon\,\frac{n_s}{365} < \frac{3}{4}(0.40)\left(\frac{2\pi}{365}\right)$$

$$= 0.00516 \text{ rad/yr} = 0.30 \text{ deg/yr}$$

For each year, beginning with 12 January 1962, and its associated ϕ, Table 5-6 lists the integrated inclination component buildup, i_x, i_y, in the X and Y directions due to the moon, and the integrated inclination buildup in the X direction due to the combined effects of the sun and the moon. This table gives the value of the expression for i_x, i_y at the upper end point, so that the difference in tabulated values represents the perturbations over the associated time interval.

For example, if initial satellite injection takes place in July 1964 and it is desired to compute the velocity correction to remove the sun-moon induced inclination for a period of at least 5 years (~ 1970), from Table 5-6 (by interpolation):

Year	ϕ, degrees	i_y (Moon), degrees	i_x (Sun + Moon), degrees
July 1964	268.267	— 0.006	8.575
January 1970	375.003	0.381	11.549

$$\Delta i_y = 0.387 \text{ degree}$$

$$\Delta i_x = 2.974 \text{ degrees}$$

$$\Delta i = [(\Delta i_y)^2 + (\Delta i_x)^2]^{1/2} \cong 3.0 \text{ degrees}$$

The velocity increment required for this inclination is $\Delta V_i = 176.06$ fps/deg Δi; $\Delta V_i = 528$ fps for the 5.5 year period.

Although the above example corresponds to only 96 fps/yr, the value of 180 fps/yr indicated in Table 5-4 corresponds to the time at which the maximum rate of change of inclination occurs due to moon only, i.e., April 1969, whence $(d\,i_m/d\,t)_{max} = 0.689$ deg/yr.

If the value of the maximum rate of change of inclination due to the sun (0.30 deg/yr) is added, then

$$\left(\frac{d\,i}{d\,t}\right)_{max} = 0.989 \text{ deg/yr}$$

$$\left(\frac{\Delta V_i}{yr}\right)_{max} = 174 \text{ fps}$$

The frequency with which this correction is to be made will, of course, depend on the year of satellite operation, which determines the instantaneous rate of change of inclination. However, for the worst average case, the maximum correction frequency will be

$$\frac{1 \text{ deg/yr}}{0.05 \text{ deg}} = 20 \text{ times/yr}$$

The velocity increment per correction is nominally chosen at 5 fps, to be made as often as necessary to keep $|\,i\,| > 0.05$ degree.

Perturbation Due to Triaxiality of Earth

Analysis of the earth's surface indicates that the earth's gravitational field is not rotationally symmetric about the polar axis. There will be, therefore, a tangential component of the gravity field along the orbit of a stationary satellite. According to available geodetic data, the resulting perturbation, if not corrected, would cause an oscillation whose amplitude depends on the initial longitude but can be as large as ± 90 degrees, with a period of over 5 years as discussed later, in the section on Ground Control Loss. Correction for this perturbation will require a control system velocity increment of the order of 7 fps per year.

NASA and RAND studies (References 5-6 and 5-7) give, for the tangential acceleration, F_λ/m, in the longitudinal direction, the following expression for an equatorial satellite

$$\frac{\overline{F}_\lambda}{m} = \frac{-6\,J_2^{(2)}\,k^2\,R_e^2 \sin 2\,(\lambda - \lambda_o)}{r_c^4}\,\overline{i}_\lambda$$

where

$J_2^{(2)}$ = coefficient of tesseral harmonic = 2.2×10^{-6}

k^2 = constant of attraction = 62,627.747 ni mi^3/sec^2

R_e = earth radius = 3441.7 n. mi (1 n. mi = 6080 feet)

λ = instantaneous satellite longitude (positive eastward)

λ_0 = longitude of minor axis of equatorial ellipse

r_c = synchronous radius = 22,752.5 n. mi

Thus for $(\lambda - \lambda_0)$ = 45, 135, 225 and 315 degrees $|\,F_\lambda\,|$ is maximum

$$\left|\frac{F_\lambda}{m}\right|_{\lambda = 45°}$$

$$= \frac{(6)\,(2.2 \times 10^{-6})\,(6.26277 \times 10^4)\,(3441.7)^2}{(22{,}752.5)^4}$$

$$\approx 3.625 \times 10^{-11} \text{ n. mi/sec}^2$$

$$= (3.625 \times 10^{-11} \text{ n.mi./sec}^2)$$

$$(315 \times 10^7 \text{ sec/yr})\,(6080 \text{ ft/n.mi})$$

$$\approx 6.95 \text{ fps/year} = \Delta V_d/t$$

TABLE 5-6. LUNAR AND SOLAR PERTURBATIONS OF INCLINATION

Year (12 January)	ϕ degree	i_y° (Moon)	i_x° (Moon)	$_x^\circ$ (Sun + Moon)
1962	220.275	−0.304	6.526	6.526
1963	239.616	−0.199	7.050	7.319
1964	258.957	−0.073	7.606	8.144
July 1964	268.267	−0.006		8.575
1965	278.298	0.061	8.198	9.005
1966	297.639	0.187	8.825	9.901
1967	316.980	0.291	9.481	10.826
1968	336.321	0.362	10.161	11.775
1969	355.662	0.393	10.854	12.737
1970	375.003	0.381	11.549	13.701
1971	394.344	0.327	12.236	14,657
1972	413.655	0.237	12.904	15.594
1973	433.076	0.119	13.545	16.504
1974	452.367	−0.013	14.153	17.381
1975	471.708	−0.144	14.725	18.222
1976	491.049	−0.261	15.263	19.029
1977	510.390	−0.348	15.772	19.807
1978	529.731	−0.395	16.262	20.566
1979	549.072	−0.396	16.746	21.319
1980	568.413	−0.352	17.223	22.065
1981	587.754	−0.267	17.743	22.854
1982	607.095	−0.152	18.279	23.659

GROSS EFFECTS OF GROUND CONTROL LOSS ON ADVANCED SYNCOM

Several perturbation studies have been made to predict the gross behavior of an initially stationary orbit after loss of ground control commands that normally remove the effects of the two perturbation sources, the triaxality of the earth and the sun-moon gravitational attraction. In addition, the effect of using mean instead of apparent sun position as a despinning reference for positioning the antenna pencil beam over the earth after loss of ground control has been examined. In addition the maximum magnitudes of attitude disturbing torques due to the effects of gravity gradient, magnetic field, and solar radiation pressure unbalance have been estimated. Although some of the spacecraft design parameters (e.g., moment of inertia) have changed somewhat from the values indicated in these analyses, the results are not enough affected to warrant recalculation.

Triaxiality of the Earth

The effects of the nonspherical mass distribution of the earth on a nominally stationary satellite have been examined at Hughes (Reference 5-8), RAND Corporation (Reference 5-7), and NASA (Reference 5-6), among others. Of particular importance is the effect of the ellipticity of the earth's equatorial section. If the earth's gravitational potential in the equatorial plane at the synchronous radius r_c is given by

$$U_{eq} = \frac{g_o R_e^2}{r_c}\left[1 - J_2 \frac{R_e^2}{2r_c^2} + 3 J_2 \frac{R_c^2}{r_c^2} \cos 2 (\lambda - \lambda_o)\right]$$

where

R_e = earth's radius $\cong$ 3441.7 nautical miles

r_c = synchronous radius $\cong$ 22,752.5 nautical miles

g_o = gravitational acceleration at the earth's surface

$g_o R_e^2 = k^2$ = earth's constant of attraction = 62,627.75 n. mi.^{3}/sec^2

J_2 = coefficient of zonal harmonic (earth oblateness) $= + 1.08219 \times 10^{-3}$

$J_2^{(2)}$ = coefficient of tesseral harmonic (Reference 5-6) (equatorial ellipticity)
$= -2.2 \times 10^{-6}$

λ = instantaneous satellite longitude (positive eastward)

λ_o = longitude of minor axis of equatorial ellipse

The RAND study shows that the time t to drift through a longitude change $|\Delta\lambda| \leq 10$ degrees is given approximately by

$$\Delta\lambda \cong 9\, J_2^{(2)} \frac{R_e^2}{r_c^2}\, \omega_e{}^2 t^2 \sin 2\,(\lambda_i - \lambda_o)$$

where

ω_e = earth's rate = 2π rad/day

λ_i = initial longitude of satellite at time of control loss, $t = 0$

Since the exact location of λ_o is yet to be determined, the worst case drift rate (e.g., $|\lambda_i - \lambda_o| = 45$ degrees) will be considered, using the latest reported value of $J_2^{(2)}$ (Reference 5-6). Thus,

$$|\Delta\lambda|_{max} = (9)\ (2.2 \times 10^{-6})\ (0.15127)^2\ (6.28)^2\ (57.3)\left[\frac{deg}{day^2}\right] t^2$$

$$= 1.025 \times 10^{-3}\left[\frac{deg}{day^2}\right] t^2$$

Figure 5-13 is a log-log plot of the above expression showing that the satellite will drift 0.05 and 0.1 degree after 7 and 10 days, respectively, due to the ellipticity of the earth's equatorial section. The drift is toward the minor axis λ_o or $\lambda_o + \pi$, whichever is closer, since these locations represent positions of stable equilibrium. In general, the satellite will execute large-angle oscillations in the equatorial plane about the minor axis. The period of oscillation will depend on the initial longitude of the satellite relative to the longitude of the minor axis, i.e. $|\lambda_i - \lambda_o|$. For $|\lambda_i - \lambda_o| = 45$ degrees, the period T is about 2.4 years. This period reduces to a little over 2 years as $|\lambda_i - \lambda_o|$ approaches zero and increases rapidly to over 5 years as $|\lambda_i - \lambda_o|$ approaches 90 degrees. The semiamplitude of these oscillations is equal to the initial longitude difference between the satellite and the nearest minor axis, $|\lambda_i - \lambda_o| \leq 90$ degrees.

It is interesting to note that as $|\lambda - \lambda_o|$ is increasing, the orbital radius r_c decreases by an amount δ_r; conversely, when $|\lambda - \lambda_o|$ is decreasing, δ_r is positive. The maximum change in δ_r occurs when the satellite passes the location of the minor axis and is given by

$$\left|\frac{\delta_r\, max}{r_c}\right| = 4\sqrt{-J_2^{(2)}}\,\frac{R_e}{r_c}\,\sin\left|\lambda_i - \lambda_o\right|$$

or

$$|\delta_{r_{max}}| \cong 20.4 \sin|\lambda_i - \lambda_o| \text{ nautical miles}$$

$$0 \leq |\lambda_i - \lambda_o| \leq 90 \text{ degrees}$$

Finally, the triaxiality of the earth causes no change in the inclination of an equatorial synchronous orbit, and the maximum control system velocity increment

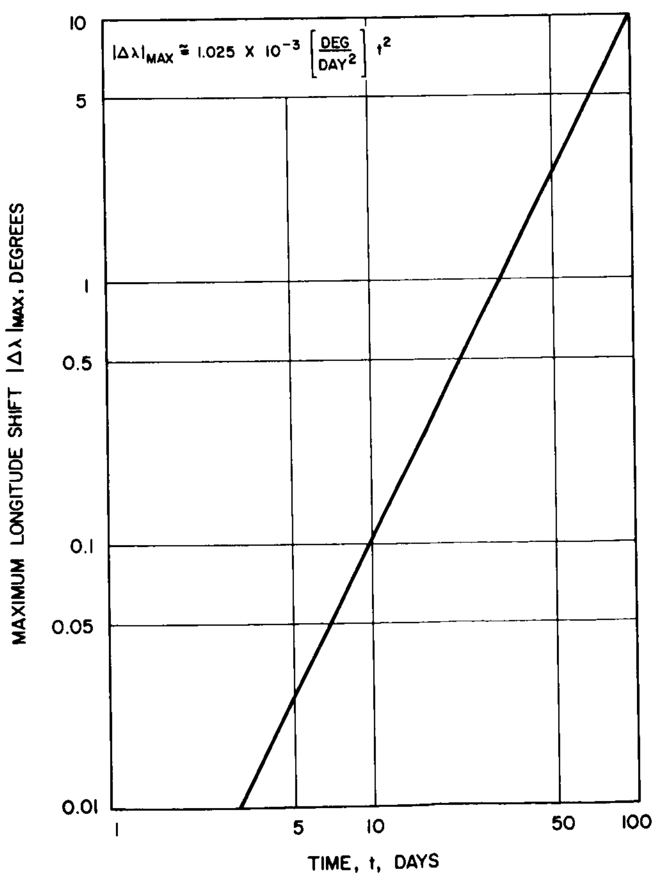

FIGURE 5-13. MAXIMUM LONGITUDE SHIFT OF STATIONARY SATELLITE DUE TO EARTH TRIAXIALITY PERTURBATION

required to correct to in-plane effect is about 7 fps per year as reported in Reference 5-6. In the Project Development Plan, 15 August 1962, the value used for $J_2^{(2)}$ was about (-5.5×10^{-6}), yielding 17.7 fps for the required velocity correction.

Sun-Moon Effects

The main effect of the sun and the moon is to cause the inclination of the stationary orbit to increase at the maximum rate of about 0.95 degree per year (0.8525 degree per year, according to Reference 5-7) for the first 10 to 15 years after ground control loss. This results in a north-south oscillation of the satellite with a period of one sidereal day and with an amplitude that increases with the above rate. Of this amplitude rate, the moon contributes a maximum of about 0.685 degree per year, and the sun contributes 0.27 degree per year.

An approximate expression for the inclination increase, Δi_p, with time, t, for a perturbing body p is given by

$$\Delta i_p \cong A_p \left[(n_p t)^2 + \sin^2 (n_p t) - 2\, n_p t \cos (n_p t + 2 v_{po}) \right]^{1/2}$$

where

$$A_p = \frac{3}{4} \frac{k_p^2}{n_o R_p^3 n_p} \sin I_p \cos I_p$$

k_p^2 = constant of attraction of perturbing body

n_o = stationary satellite angular velocity $= \omega_e = 2\pi$ rad/day

n_p = perturbing body angular velocity

R_p = distance between centers of earth and perturbing body

I_p = inclination angle of perturbing body orbit plane to earth equatorial plane

v_{po} = initial polar angle of perturbing body relative to satellite at $t = 0$

For the moon

$$k_p^2 = k_m^2 = 0.0123\, k^2$$

$$n_p \cong \frac{2\pi}{27.3} \text{ rad/day} = n_m$$

$I_p = I_m$ where 18.317 degrees $\leq I_m \leq$ 28.584 degrees

$$R_p = R_m \cong 60.267\, R_e$$

$$A_p = A_m \leq 0.00814 \text{ degree}$$

For the sun,

$$k_p^2 = 333{,}000\, k^2$$

$$n_p = n_s \cong \frac{2\pi}{365.25} \text{ rad/day}$$

$$I_p = I_s = 23.45 \text{ degrees}$$

$$R_p = R_s \cong 2.34 \times 10^4\, R_e$$

$$A_p = A_s \cong 0.0432 \text{ degree}$$

Figure 5-14 is a plot of the inclination increase due to the sun and moon as a function of the polar angle of the perturbing body where $v_{po} = 0$. The effect of the diurnal motion has been averaged out over one orbital period (24 hours). The figure shows that the moon will induce an inclination increase of about 0.05 degree at the end of one sidereal month (27.3 days), while the sun will cause this inclination change at the end of 68.5 days. It will take approximately twice as long to accrue an inclination of 0.1 degree due to the sun and moon.

It should be noted, however, that even if the inclination magnitude exceeds the ground antenna pointing angle limits with respect to satellite latitude deviations, the diurnal oscillation will cause the satellite to cross the equator twice a day and come within the pointing angle limits of the ground antennas for at least a fraction of each day (assuming no longitudinal drift due to triaxiality). Thus, if the satellite initial longitude is located close enough to a minor axis of the equatorial ellipse so that the resultant longitudinal drift rate is made comparable to the rate of increase of inclination due to the sun and moon, with respect to the ground antenna pointing limita- the useful continuous communication period (after ground control loss) of the satellite can be optimized tions. A similar argument holds for providing communication periods equal to some minimum fraction of a day (resulting in a required satellite longitudinal placement closer to the minor axis than for the continuous communication case).

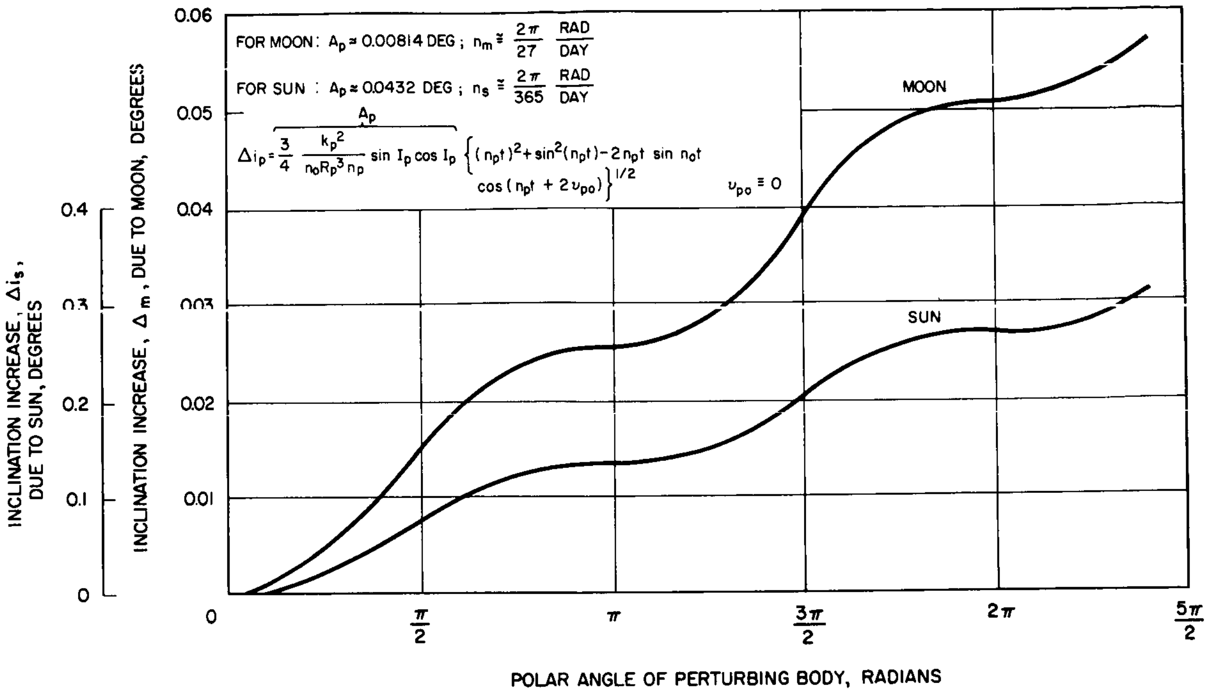

FIGURE 5-14. STATIONARY SATELLITE INCLINATION CHANGE DUE TO SUN-MOON PERTURBATIONS

Finally, the in-plane effect of the sun-moon perturbation on the satellite orbit is shown to be small from a ground antenna tracking standpoint (Reference 5-7). In particular, the maximum possible tangential deviation from an initial longitudinal position is less than 39 nautical miles, or about 7 minutes of arc as seen from the earth's surface.

Effect of Equation of Time on Syncom Pencil-Beam Pointing

The relative longitude of the sun with respect to the satellite is shown to be (Reference 5-1)

$$\lambda_s = \lambda_i - 180 \text{ degrees} - \omega_e (UT + E) (\text{degrees})$$

where

λ_i = initial longitude of satellite in degrees east of Greenwich

ω_e = earth's rate of rotation = 15 deg/hr

UT = Greenwich mean time (Universal Time), hours

E = equation of time

= apparent (true) minus mean right ascension of sun, hours

Thus, λ_s is the angle between the projection of the satellite-sun line onto the equatorial plane and the upward local vertical of the satellite location. This is used as the despinning reference angle for pointing the maximum gain of satellite pencil-beam pattern along the local vertical toward the earth. When the ground control link is operative, the correct value of E can be periodically commanded to make up for the seasonal changes in the difference between the mean and apparent sun position. If, at t = o, ground control is lost, the subsequent pointing error $\delta\lambda$ of the pencil-beam maximum is given by

$$\delta\lambda = \omega_e \int_o^t \frac{\delta E}{\delta t} dt$$

where

$\delta E/\delta t$ = daily rate of change of E tabulated in the

American Ephemeris and Nautical Almanac

ω_e = earth's rate

= 15 deg/hr

Although $\delta E/\delta t$ is essentially a periodic function for each year of the form (where $|a_o|, |a_3|, |a_4| < |a_1| < |a_2|$)

$$\frac{\delta E}{\delta t} = a_o + a_1 \cos 2\pi \frac{(t - t_o)}{365} + a_2 \cos \frac{4\pi\,(t - t_o)}{365}$$

$$+ a_3 \cos \frac{6\pi\,(t - t_o)}{365} + a_4 \cos \frac{8\pi\,(t - t_o)}{365}$$

it cannot be directly integrated until the reference date $t = 0$ is known relative to the beginning of the year t_o. However, some upper bounds can be established. An examination of the American Ephemeris for 1962 and 1963 shows that the position of the hour angle of the mean sun is never more than 16 minutes (of time) or 4 degrees from the true sun, with a peak-to-peak variation δE_{max} of 29.5 minutes (1770 seconds) or 7.4 degrees. Furthermore, the maximum value of the rate of change of E is

$$\left(\frac{\delta E}{\delta t}\right)_{max} = 30 \text{ sec/day}$$

Thus, under the worst conditions, such as ground control loss when $\delta E/\delta t$ is maximum,

$$\delta\lambda_{max} = \omega_e \left\{ \min \left[\left(\frac{\delta E}{\delta t}\right)_{max} t,\ \delta E_{max} \right] \right\}$$

$$= 0.004167 \{ \min [30\,t, 1770] \} \text{ (degrees)}$$

$$= \text{minimum } [0.125\,t, 7.4] \qquad \text{(degrees)}$$

where t is in days. Now for a sin k θ/k θ pencil-beam pattern whose gain is 3 db down at $\theta = 8.6$ degrees, the 2-db downpoint occurs at $\theta = 7$ degrees from the local vertical. If this angle constitutes the allowable pointing error $\delta\lambda_a$ for usable communication signal strength, it will take at least 56 days after ground control loss to accrue 7 degrees. If a pointing error of 7.4 degrees still provides useful signal strength for certain land masses (east or west of the satellite nadir, depending upon the direction of the shift of the pencil beam which, in turn, depends on the year and season of ground control loss), the maximum useful time interval for operation after ground control loss will be determined only by ground antenna tracking limitations in the face of perturbation-induced drifts, as discussed earlier.

Incorporation of a single spacecraft-body-mounted IR earth sensor to remove the dependence of the despinning reference signal on the equation of time is being investigated. Preliminary results show that a thermistor element sensor using two lenses squinted 13 degrees apart ($\pm$ 6.5 degrees relative to the spin axis normal), each with a field of view of 1.3 degrees square, will yield an attitude sensing error of $\pm$ 0.1 degree (3σ). Dimensions and weight are $1.5 \times 3 \times 5$ inches and ≤ 1 pound.

Disturbing Torques

Gravity Gradient. Since the spin axis is normal to the plane of the orbit, the dominant inverse squared term of gravitational attraction does not give rise to any torque on the satellite. Furthermore, since the initial orbit is in the equatorial plane, the torque, due to oblateness, will be initially zero. To estimate the order of magnitude of gravity gradient precession rate due to the sun-moon induced inclination increase of the satellite orbit, Williams (Reference 5-9) observes that in the inverse square field this rate is given by

$$|\dot{\psi}_g| \cong 3\, g_o \frac{R_e^2}{r_c^3} \frac{(I_z - I_x)}{I_z\, \omega_z} \left(\frac{\delta i}{\delta t}\right) t$$

$$= 3.6 \times 10^{-10} \left[\frac{\text{deg}}{\text{sec-yr}}\right] t$$

where

R_e = earth's radius

g_o = surface gravity at R_e

r_e = stationary orbital radius

I_z = moment of inertia about the spin axis

= 50.6 slug-ft^2 (half-life value) (Reference 5-10)

I_x = moment of inertia about normal to spin axis

= 37.8 slug-ft^2 (half-life value) (Reference 5-10)

ω_z = satellite spin rate

= 100 rpm = 10.5 rad/sec

$\frac{\delta i}{\delta t}$ = sun-moon induced inclination rate of stationary orbit

≤ 0.95 deg/yr $= 1.66 \times 10^{-4}$ rad/yr

The maximum precession rate due to oblateness is shown to have the order of magnitude of

$$|\psi_{g_o}|_{max} = \frac{3\, g_o R_e^4}{2\, \omega_z r_c^5} J_2 = 19.2 \times 10^{-6} \text{ deg/yr}$$

Magnetic Field. Two effects result from eddy currents in the satellite induced by the presence of a magnetic field:

1) The spin speed ω_z is damped, $d\,\omega_z/dt < 0$.

2) The spin axis precesses toward the instantaneous magnetic field.

For an electrically symmetrical structure, Williams (References 5-1, 5-9, and 5-11) shows that the precession rate θ and spin speed ω_z can be conservatively represented by

$$\dot{\theta} = \frac{-\sin\theta\cos\theta}{\tau_o}$$

$$\dot{\omega}_z = \frac{-\sin^2\theta}{\tau_o}\omega_z$$

$$\tau_o = \frac{2\rho}{\sigma B_o^2} = \text{minimum damping constant}$$

where

θ = angle between spin axis and magnetic field

ρ = density of idealized satellite cylindrical shell (with massless perfectly conducting end planes)

$= 2650$ kg/m^3 for aluminum

σ = specific surface conductivity

$= 3.54$ mhos/m for aluminum

B_o = magnetic field induction at r_c due to earth's magnetism

$$\leq 0.630 \left(\frac{R_e}{r_c}\right)^3 \text{ gauss}$$

$$\leq 2.18 \times 10^{-7} \text{ Webers/m}^2$$

Thus,

$$\tau_o = \frac{1.5 \times 10^{-4}}{4.74 \times 10^{-14}} = 3.165 \times 10^9 \text{ seconds}$$

$$= 100 \text{ years}$$

$$\dot{\theta} = -\frac{0.56}{2 \times 100} = -2.8 \times 10^{-3} \text{ rad/yr}$$

$$= -0.16 \text{ deg/yr}$$

$$\dot{\omega}_z/\omega_z = -\frac{0.0852}{100} = -0.852 \times 10^{-3} \text{ rad/yr}$$

Hysteresis effects may contribute additionally to the damping of spin, but predictions at this time may be premature. However, a conservative estimate may be made by comparing with some spin speed decay data of Telstar due to hysteresis (Reference 5-12). If the spin speed ω_z obeys an exponential decay law

$$\omega_z = \omega_{zo}\, e^{-t/\tau_h}$$

the Telstar data exhibits a time constant, τ_h, of

$$\tau_h = 320 \text{ days}$$

Now, since the perigee and apogee altitudes of Telstar are about 515 and 3043 nautical miles respectively, the field strength is about 300 times that of a synchronous satellite, so that the hysteresis decay time constant should be considerably longer for Syncom.

The precession rate due to the torque created by the magnetic moment of the satellite and the earth's magnetic field B_o is also expected to be small at the synchronous radius. If the magnetic moment is expressed in (ampere-turns-square meters), the precession rate θ_m may be estimated by (Reference 5-11)

$$\dot{\theta}_m \approx \frac{B_o niA \sin\theta}{I_z\, \omega_z};$$

$$\frac{\dot{\theta}_m}{niA \sin\theta} \approx 3 \times 10^{-10} \frac{\text{rad/sec}}{\text{amp-turn-m}^2}$$

$$= \frac{0.053 \text{ deg/yr}}{\text{amp-turn-m}^2}$$

where

ni = magnetic-moment-inducing current (ampere turns)

A = area enclosed by current loop (square meters)

θ = angle between B_o and normal to A

B_o = earth's field strength at r_c

$= 2.18 \times 10^{-7}$ Weber/m^2

$I_z \cong 50.6$ slug-feet^2 $= 50.6 \times 1.36$

$= 69$ kg-m^2 $= 69$ Newton-meter-second^2

$\omega_z = 10.5$ rad/sec

Solar Radiation. Solar radiation pressure unbalance is the most significant torque yet estimated. A simple model for calculating this effect is a cylinder with perfectly reflecting ends and completely absorbing sides. Consideration of the varying geometry during the course of a year shows that there is an average precession of the spin axis in the direction of the intersection of the orbital (equatorial) plane (normal to the initial spin axis) and the ecliptic plane. By integrating the precession rate, Williams (Reference 5-1) shows that the magnitude is

$$\dot{\psi} = \frac{\pi}{8} \frac{S}{C} a^2 h \frac{\sin 2i}{I_z \omega_z}$$

where

S/C = ratio of solar constant to speed of light

$= 0.957 \times 10^{-7}$ lb/ft^2

$= 0.957 \times 10^{-7}$ slug/ft — sec^2

a = radius of the cylinder

= 23.5 inches = 1.96 feet

h = height of the cylinder

= 25 inches = 2.08 feet

i = inclination of the orbit to the ecliptic

= 23.6 degrees

$I_z = 50.6$ slug-ft^2

$\omega_z = 10.5$ rad/sec

Thus, the maximum precession rate magnitude is

$$\dot{\psi} = 4.13 \times 10^{-10} \text{ rad/sec} = 0.013 \text{ rad/yr}$$

$$= 0.75 \text{ deg/yr}$$

ADDITIONAL ATTITUDE REFERENCE STUDIES

Bendix Photodetector for Syncom Attitude Reference

In this section the physical properties of a miniature photodetector and a nonmechanical scanning system described in Reference 5-13 are examined to show their feasibility as a body-mounted detector of the star Polaris and therefore a more precise attitude reference for Syncom. It is assumed that the existing Syncom attitude reference and control system will bring the spacecraft spin axis to within 2.5 degrees of the line of sight to Polaris, i.e., half the field of view of the detector.

A simplified, single-channel, PPI scanning method with angle referenced to the sun sensor pips may be more suitable than the two-channel linear raster scan indicated in Reference 5-13, since the rotation of the satellite about its spin axis naturally provides the angular sweep motion of a polar coordinate system. In either case, however, some degradation of spin angle resolution results for star images near the center of the field due to overlap of the scanning line, which is 0.5 degree wide. A linear raster scan outlined by Bendix does not preclude this difficulty, although some extra electronics will be needed to despin the rotating field of view.

Optics of 1.5 inches diameter and a video bandwidth of about 10 kc should provide adequate signal-to-noise ratio, ≥ 2 at the input to a video amplifier with a resolution of 15 minutes of arc when aimed at Polaris. The attitude control precision, however, will not be directly limited by the available spin angle resolution, (360 degrees/512 $\approx$ 0.7 degree) plus sun sensor errors ($\sim$ 0.2 degree) and should be better than 0.2 of the resolution element or ($0.2 \times \frac{1}{4}$ degree) about 0.05 degree. The direction of the angular difference ($\sim$ 0.9 degree) between the earth's polar axis and the line of sight to Polaris can be determined from a knowledge of Polaris mean right ascension and the sun ephemerides at the satellite longitude. In addition, the telemetered video information of the field of view (e.g., in the form of a video display on a multimode storage tube referenced to the satellite-sun line) can be used to readily discriminate against fainter stars appearing in the 5-degree field, (e.g., δ —Ursa Minor), by visual inspection, by using some suitably prepared star-field mask, or automatically.

A solid-state (no moving parts) phototropic screen is proposed as an alternate to a mechanical shutter to protect the photocathode from possible damage due to sun imaging during the initial ascent and orientation sequence. The phototropic screen is claimed to go from a transparent to an opaque state within a few microseconds after exposure to strong ultraviolet light; transparency is regained in a few seconds after removal of the ultraviolet light.

Bendix Photodetector, Electron Multiplier, and Proposed Tracker

The Bendix channel photomultiplier (photodetector and electron multiplier) weighs 1.2 ounces, occupies 2.5 cubic inches, and has provisions for image scanning. Bendix proposes to build a tracker (using coarse and fine scans) with this tube per specifications listed in Table 5-7).

TABLE 5-7. PROPOSED BENDIX TRACKER SPECIFICATION

Weight	3 pounds
Volume	95 cubic inches
Power	5 watts (1 to 2 kilovolts at 2×10^{-7} ampere needed for channel multiplier)
Field of view	5 degrees total 0.5 degree instantaneous (coarse scan) with 50 percent overlap
Pointing accuracy	
Coarse scan	± 0.25 degree (linear raster scan, saturated output)
Fine scan	± 9 seconds of arc (cross scan, proportional output, when viewing third magnitude stars or brighter)
Output saturation level	± 6 volts (15 minutes of arc error)
Sensitivity	0.4 v/min of arc to saturation
Linearity	10 percent over 30 minutes of arc
Sampling rate	25 frames/sec
Photocathode characteristic	S-11 (see text)

PHOTODETECTOR

When an image of a star falls on the photocathode, the electron stream emitted at that spot is focused to a fine bundle in the plane of the aperture by means of the electrostatic lens (Figure 5-15). Should the electron stream enter the aperture, it undergoes a process of amplification by the electron multiplier, shown schematically.

In general, owing to pointing error, the image will not fall exactly on the optical axis but will be displaced some radial distance r and angle θ (with respect to a reference) on the cathode. For this case the electron stream would miss the aperture and the output of the electron multiplier would be zero. However, the magnetic deflecting scanning fields applied to the region behind the cathode are such that an off-axis electron stream is eventually introduced into the aperture, and

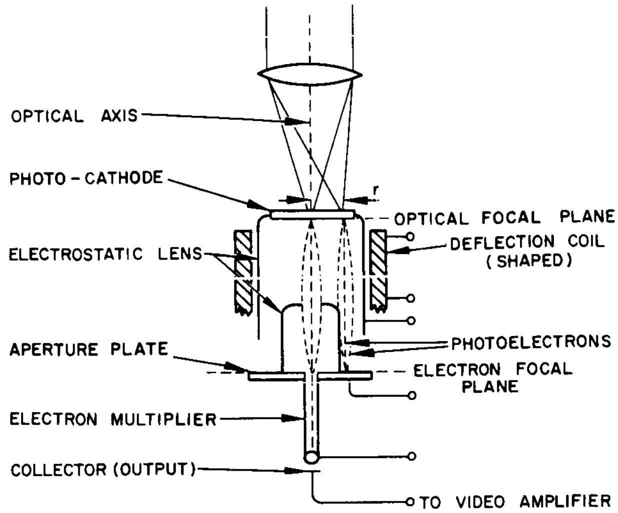

FIGURE 5-15. PHOTODETECTOR SCHEMATIC DIAGRAM

an output signal is obtained at a time during the scan that corresponds uniquely to the radial and angular image position on the photocathode. (Bendix gives no details on the electron-ballistic description of the focusing or deflection mechanism except to cite a reference to a Farnsworth Image Dissector Tube (1939), which uses similar techniques. A brief description, taken from Reference 5-14 is given at the end of this section.)

ELECTRON MULTIPLIER

A hollow glass tube with a high resistivity inner surface is connected through suitable applied electrodes to a voltage source of 1000 to 2000 volts, as shown in Figure 5-16. A small continuous current is established along the inner surface from one end to the other; thus a uniform electric field is established down the tube. If a primary photoelectron strikes the inner surface, a secondary electron will be generated with a small transverse velocity that will tend to carry it across the tube while the longitudinal electric field accelerates it down the tube. By proper proportioning of the diameter and field strength, enough energy is imparted to a typical electron so that it will, on the average, generate more than one secondary upon collision with the opposite wall of the tube. Thus, a cascading action is instigated, which can produce electron gain.

For this proposal Bendix chose a channel measuring d = 0.018 inch inside diameter and l = 0.9 inch in

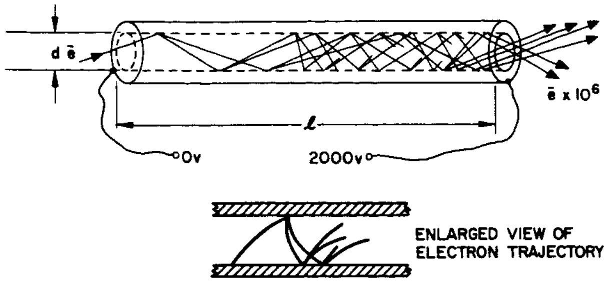

FIGURE 5-16. CHANNEL ELECTRON MULTIPLIER

length. The resistance of the channel is approximately 10^{10} ohms; therefore, a strip current of about 2×10^{-7} ampere may be realized at 2000 volts. Output currents up to about 10^{-8} ampere may be obtained before current saturation is noticed.

PHOTOCATHODE

A semitransparent photocathode (Reference 5-13 and 5-15) consisting of a thin film of antimony with cesium deposited on the optically treated face of the tube will be used. Its characteristics will be similar to S-11, which is tabulated in Table 5-8.

TABLE 5-8. S-11 PHOTOMISSIVE CHARACTERISTICS (CsSbO)

Radiant sensitivity at peak, S_{max}				$0.05 \frac{\text{microamp}}{\text{microwatt}}$				
Wavelength at peak, λ_{max}				4400 Å				
Luminous sensitivity				$70 \frac{\text{microamp}}{\text{lumen}}$ (calibrated with 2870° K color temperature tungsten lamp)				
Typical dark current emission				10^{-14} to 10^{-15} amp/cm² at 25°C				
10 percent response points				3200 to 6200 Å				
Relative spectral sensitivity, S/S_{max} versus λ, Å								
S/S_{max}	0	0.62	0.9	0.99	0.85	0.58	0.2	0.01
λ, Å	3000	3500	4000	4500	5000	5500	6000	6500
Window				Visible light transmitting; lime glass or Kovar sealing borosilicate glass				

Star Field Near Polaris

In order to examine possible methods of discrimination among the stars that may appear in the 5-degree star field with Polaris, a selected star catalog whose locations are within 6 degrees declination of the north celestial pole is given in Table 5-9 (References 5-16 and 5-17). It should be noted that Polaris is a Cepheid variable star whose magnitude varies from 2.08 to 2.17 with a period of pulsation of 3.97 days. Thus, for design purposes the output signal-to-noise ratio of the photodetector should be based on the magnitude value of 2.17. A study of Table 5-9 shows that except for Polaris there are no magnitude 2 or 3 stars in this region. The next brightest star is δ Ursa Minor which is more than 2 magnitude numbers "dimmer" than Polaris. Since the Bendix photodetector is designed for use with magnitude-3 stars or brighter, a discrimination technique based only on star brightness appears feasible. The video content of the scanned star field referenced to the sunline can be telemetered to the ground control station and displayed on a multimode (selective erasure) storage tube. Polaris can be identified by inspection or by comparison with some predetermined video level. An attitude error signal may then be generated by comparison with a superposed star field pattern (directly on the multimode storage tube face), which is driven by the local sun ephemeris at the satellite longitude (with propagation delays calibrated out). Alternatively, selection and location of Polaris relative to the optical axis may be made aboard the satellite and only the location data need be telemetered. Attitude error signals may then be determined by comparing the measured data with a computed location derived from sun position and the right ascension and declination of Polaris. The former approach, however, would reduce the extra on-board electronics needed for star location at the moderate expense of additional telemetering bandwidth.

Scanning Methods

LINEAR RASTER SCAN

In an attempt to attain precision pointing (9 seconds of arc) within a 5-degree field of view, Bendix uses a coarse scan with low pointing accuracy (0.25 degree), which is switched to a fine resolution scan after the target image has been positioned to within the limit of resolution of the coarse scan (Reference 5-13). The proposed scanning system starts with a coarse linear raster in which an instantaneous field of view of 30 minutes of arc is swept over the 5-degree image field in 1/25 second. A 50-percent overlap is employed so that the image may be positioned to within 15 minutes of arc of the center of the field. When this occurs, the coarse scan is electronically switched to a small cross scan having an amplitude of 45

TABLE 5-9. SELECTED STAR CATALOG WITHIN 6-DEGREE DECLINATION OF NORTH CELESTIAL POLE

Name	Magnitude (Visual)	Spect.	Mean R. A. h	m	s	Mean Declination Degrees	Minutes	Seconds	Relative Order of Decreasing Brightness
Na 43 H. Cephei	4.52	K0	1	03	02.18	+86	02	56.56	3
Nbα Ursae Minoris (Polaris)	2.12 (var.)	F8	1	56	25.23	+89	04	58.05	1
Nβ Bradley 402 (Cephei)	5.78	K0	3	22	44.17	+84	46	42.74	7
Nc Groombridge 750 (Cephei)	6.7	F8	4	23	14.91	+85	26	35.42	15
Nγ B. D. +85° 74 (Cephei)	6.54	A5	5	17	45.39	+85	54	21.74	12
Nδ Groombridge 944 (Cephei)	6.41	K0	5	49	02.15	+85	10	39.62	11
Nd 51H Cephei	5.26	M0	7	22	57.90	+87	06	18.38	5
Nε Groombridge 1359 (Camelopardi)	6.39	A0	8	07	50.48	+84	10	35.02	10
Nξ B. D. +84° 196 (Camelopardi)	6.26	F0	9	07	32.67	+84	20	30.37	8
Nη B. D. +86° 161 (Camelopardi)	7.17	A2	11	10	06.69	+85	51	08.48	16
Nθ Groombridge 1850 (Camelopardi)	6.38	F5	12	02	41.06	+85	48	11.35	9
Nηδ Ursae Minoris	4.44	A0	17	44	44.67	+86	36	22.47	2
Niλ Ursae Minoris	6.55	M3	18	07	06.46	+89	03	17.19	13
Nυ Groombridge 3212 (Draconis)	6.61	A2	20	05	15.75	+84	33	31.15	14
Nξ 32 H. Cephei	5.38	A0	22	16	39.42	+85	54	46.22	6
No 36 H. Cephei	4.96	K5	22	54	47.62	+84	08	15.85	4

minutes of arc along the X and Y axes, centered at the origin. This produces a 30- by 30-minute overlapped field of view (from the X and Y portions of the cross scan) at the center and an additional nonoverlapped 15 by 30 minutes extended along each axis, not used in the data processing.

Since, for the present Syncom application it is not necessary to attain a pointing accuracy much better than 0.25 degree, and also since it is desired to point the optical axis parallel to the north celestial pole and not directly at Polaris (~0.9 degree from pole), the fine scan mode will not be considered at this time.

PPI SCAN

Because of the advantages of using the rotational motion of the spinning satellite to simplify the on-board sweep circuitry to one channel, a PPI scan suggests itself. Here the satellite spin angle referenced to the sun line will mechanically cause a linear, single-channel scan line (passing through the optical axis) to sweep through the star field in π radians. The frame time for a spin speed, W_s, is then

$$\text{Frame time} = \frac{\pi}{W_s} \approx \frac{3.14}{10.5} = 0.3 \text{ second}$$

However, the geometry yielding the spin angle location of a star may lead to some excessive spin angle ambiguity due to the apparent angular broadening (in the spin angle direction) of a star image located near the optical axis. This is caused by the constant thickness of the scan line. For example, consider a 5-degree field of view focused on a photocathode with diameter $2\,r_0$. To cover adequately the periphery of the field with a 0.5-degree line scan thickness using 50-percent overlap to yield a resolution element of 0.25 degree, the equivalent spot size $\delta\epsilon$ at the periphery of the photocathode will be approximately

$$\delta\epsilon \cong \frac{0.25 \text{ degree}}{5 \text{ degrees}}\, 2\, r_0 = 0.1\, r_0$$

The spin angle subtended by this spot size at any other distance $r < r_o$ from the tube center will be of the order

$$\frac{\delta\epsilon}{r} = 0.1 \frac{r_o}{r}$$

If a star image is located a distance $r = r_o/5$ from the tube center (equivalent to a star located 1 degree from the optical axis, e.g. Polaris, when the optical axis is almost parallel to celestial pole), the spin angle subtended by the star image becomes (after five successive PPI line scans)

$$\frac{\delta\epsilon}{r} = (0.1)\ (5)\ \frac{r_o}{r_o} = 0.5 \text{ radian} = 28.7 \text{ degrees}$$

Although this integration effect of the PPI mode enhances the signal-to-noise ratio for stars near the optical axis, some processing (such as image bisecting via angle gating of image arc) will be desirable after initial detection by the ground control equipment to facilitate the timing of precession torque pulse directions with respect to the sun line.

Scan Frequency and Bandwidth Requirements

LINEAR RASTER SCAN

Scanning through a field $\theta = 5$ degrees at a frame rate of 25 frames/sec with a line resolution of $\delta\,\theta = 0.25$ degree, the scan frequency, f_{scan}, is given by

$$\frac{1}{f_{scan}} = \tau_{scan} = \frac{\delta\theta}{\text{angle scan rate}} = \frac{\delta\theta}{\theta\ (\text{frame rate})}$$

$$= \frac{0.25 \text{ degree}}{5 \text{ deg/frame } 25 \text{ frames/sec}} = 0.002 \text{ second}$$

$$f_{scan} = 500 \text{ cps}$$

For a linear sawtooth scan voltage waveform with fly-back time, $\tau_{fb} << \tau_{scan}$, the rate, $\delta\theta/\delta t$, at which a resolution element is scanned through may be approximated by

$$\frac{\delta\theta}{\delta t} = \frac{\theta}{\tau_{scan} - \tau_{fb}} \approx \frac{\theta}{\tau_{scan}}$$

so that the bandwidth requirement Δ_f becomes

$$\Delta_f \approx \frac{1}{\delta t}\ \frac{\theta}{\delta\theta\ \tau_{scan}} = \frac{\theta\, f^2 \text{ scan}}{\text{angle scan rate}} = \frac{f^2 \text{ scan}}{\text{frame rate}}$$

$$= \frac{(500)^2}{25} = 10 \text{ kc}$$

PPI SCAN

Using the criteria developed earlier for peripheral coverage of the field of view, namely, for a cathode radius r_o, a field of view θ, and resolution element $\delta\theta$

$$\frac{\delta\epsilon}{2\,r_o} = \frac{\delta\theta}{\theta} = \frac{0.25 \text{ degree}}{5 \text{ degrees}}$$

the scan frequency f_{scan} required for a satellite spinning at a rate $\omega_s \leq 13.1$ rad/sec is (nominally $\omega_s = 10.5$ rad/sec)

$$f_{scan} = \frac{\omega_s}{\delta\epsilon/r_o} \leq \frac{13.1}{0.1} = 131 \text{ cps}$$

As before, the bandwidth may be determined from the rate $\delta\epsilon/\delta t$ at which a resolution element is scanned through, i.e.,

$$\Delta f \cong \frac{1}{\delta t} = \frac{2r_o}{\delta\epsilon} f_{scan} = \frac{2f^2_{scan}}{\omega_s} \leq \frac{2(131)^2}{13.1} = 2600 \text{ cps}$$

Compared with the linear raster scan values, the relatively lower f_{scan} and Δf for the PPI scan are obviously due to the inherently lower nominal frame rate of 3.3 frames/sec as opposed to 25 frames/sec for the raster scan. Other scan geometries and rates should be investigated.

Signal-to-Noise Ratio Considerations

The rms signal-to-noise ratio produced in the current delivered to the video amplifier after passing through the multiplier channel is claimed to be independent of the assumption of energy distribution of the cathode electrons (Reference 5-13). For low, dark currents (see Table 5-8) and threshold signals, the theory of the shot effect in the absence of space change is applicable to determine the noise levels limiting the information content of the signal. On this basis the current signal-to-noise ratio is given by

$$\frac{i_s}{i_n} = 865 \times 10^{-m/5}\, d \left(\frac{S}{\Delta f}\ \frac{G\text{-}1}{G}\right)^{1/2}$$

where

m = astronomical magnitude of star whose image is considered ≤ 2.17 for Polaris
d = diameter of objective lens, cm
S = sensitivity of the photocathode, microamp/microwatt
= 0.05 microamp/microwatt for S-11 (see Table 5-8)

Δf = bandwidth of signal considered
= 10 kc for linear raster scan proposed by Bendix
≤ 2.6 kc for PPI scan

G = gain per electron collision with channel wall
≅ 2 for Bendix proposed design

Substituting values for m, S, and G and rearranging to solve for d gives

$$d \leq 4.46 \times 10^{-3} \left(\frac{i_s}{i_n}\right) \left(\frac{\Delta f}{0.05}\right)^{1/2}$$

Using $\Delta f = 10$ kc (raster scan) and a desired $(i_s/i_n) \cong 2$, the required objective lens diameter becomes

$$d \Big|_{\Delta f = 10\text{ kc}} \leq 4.46 \times 10^{-3} (2) \left(\frac{10^4}{5 \times 10^{-2}}\right)^{1/2}$$

$$= (4.46)(0.448)(2) = 4\text{ cm}$$

$$\cong 1.575\text{ inches}$$

For $\Delta f = 2.6$ kc (PPI scan) and $(i_s/i_n) \cong 2$

$$d \Big|_{\Delta f = 2.6\text{ kc}} \leq 4.46 \times 10^{-3} (2) \left(\frac{2.6 \times 10^3}{5 \times 10^{-2}}\right)^{1/2}$$

$$= (4.46)(0.228)(2) = 2.03\text{ cm}$$

$$= 0.8\text{ inch}$$

These values for d indicate the feasibility of using the Bendix photodetector and channel amplifier design to detect and display Polaris with reasonably sized optics.

Physical Placement and Environmental Considerations

No knowledge is yet available on the vibration and steady-state load factor limits of this device. A recommendation that can be made at this time is to qualify the device in the same way as an existing, physically similar Syncom component, e.g., the traveling-wave tube. To minimize the possible degrading effect of the steady-state spin load factor, the optical axis may be placed (parallel to the spin axis) at a radial distance from the spin axis that would just barely prevent the 5-degree field of view from being obstructed by the antenna structure near the spin axis. The objective lens may be slightly recessed below the satellite surface structure to take advantage of spacecraft temperature control and to minimize possible lens contamination by propellant exhaust products. Similar comments apply for shading the lens from direct sunlight (where ecliptic is north of equator).

Attitude Reference for Third-Stage Thrust Alignment

A launch window study is suggested to determine how often the field of view of the photodetector will contain the sun just prior to third-stage ignition. If this direct-sunlight interval does not constrain the possible launch interval too severely, a priori knowledge of the star field (associated with the preignition attitude of the third stage) may be used to finely align the third-stage thrust axis, resulting in a lower error residual of the final orbit as indicated in Reference 5-18. In Advanced Syncom, for example, the out-of-plane δV_1 and in-plane δV_s velocity residuals due to thrust attitude error, $\delta\theta \cong 2$ degrees, will be reduced from nominally

$$|\delta V_1| \cong 96 \frac{\text{fps}}{\text{deg}} \delta\theta = 96\ (2) = 192\text{ fps}$$

$$|\delta V_s| \cong 49.2 \frac{\text{fps}}{\text{deg}} \delta\theta = 49.2\ (2) = 58.4\text{ fps}$$

to about

$$|\delta V_1| \cong 96\ (0.25) = 24\text{ fps}$$

$$|\delta V_s| \cong 49.2\ (0.25) = 12.3\text{ fps}$$

for a $\delta\theta$ of about 0.25 degree.

General Conclusions

The foregoing brief examination indicates that

1) It is feasible to adapt the Bendix photodetector for use in Syncom II to locate Polaris with reasonably sized optics.
2) Attitude error may be determined from the telemetered video content of the star field when compared with a priori ephemerides of Polaris and local sun.
3) A PPI scan geometry appears to require the simplest satellite-borne sweep circuitry.

4) Ground control video data processing, discrimination, and display techniques should be further investigated to facilitate timing of vernier control jets at the appropriate spin angle relative to the sun line.
5) Further tradeoffs between instantaneous field of view and bandwidth requirements should be made to determine the bandwidth cost of improving resolution to, say, 0.1 degree by reducing the collecting aperture area of the photodetector.

Image Dissector (Nonstorage) Tube

PRINCIPLE OF OPERATION

The image dissector operates on the principle of an electron-collecting aperture which is scanned by an electron image from a photo-emitting surface upon which an optical image is focused (References 5-19, 5-20, and 5-21). The aperture collects the electrons emitted by the photosensitive material of the photocathode. The electron streams forming the electron image from the photocathode are caused to move past the aperture by externally applied magnetic deflection fields. The electrons collected by the aperture are introduced into the first stage of an electron multiplier and subsequently amplified by secondary multiplication to a sufficiently high level to develop a signal appreciably higher than the noise generated in the following (conventional) video amplifier stage.

The stream of electrons emitted by the photocathode of the image dissector are brought to a focus on a plane passing through the multiplier aperture and perpendicular to the axis of the tube. This is accomplished by the action of an axial magnetic focusing field and the electrical field produced by the accelerator rings. Therefore, as the entire raster is deflected across the multiplier aperture, the aperture intercepts the sharply focused stream of electrons produced by each illuminated area, and translates the light image into a stream of electrons forming the video signal information, as illustrated in Figure 5-17.

OPTICAL INPUT ARRANGEMENT AND PARAMETERS

The useful area of the commercial image-dissector photocathode is a circle of 2.75-inch diameter, permitting the use of a scanned area of 2.2 by 1.65 inches. The light from the scene to be televised is focused directly on the photocathode, which is deposited directly on the inside of the faceplate of the image dissector. The lens should be designed to cover this area since the resolution varies directly with the size of the image used on the photosurface.

ELECTRICAL ARRANGEMENTS AND PERFORMANCE CHARACTERISTICS

Resolution. The resolution of the image dissector is determined by the aperture size of the collector and the magnification of the image from the photocathode to the plane on which the image is focused. The curves of Figure 5-18 give the resolution of the tube as a function of the aperture size (square aperture) for an image magnification of one. For different magnifications to the line numbers are multiplied by the magnification ratio. This curve gives the response of the tube to a square-wave test pattern in terms of peak signal amplitude and television line number.

Image dissectors are made to the specifications of the customer with respect to the size of the aperture, which ultimately controls the sensitivity and the resolving capabilities. The signal-to-noise ratio of the reproduced picture with a given illumination varies as the square root of the aperture area or directly with the aperture width. The resolution varies inversely as the width of the collecting aperture.

The signal-to-noise ratio of the signal developed can be expressed as

$$\frac{\text{peak signal}}{\text{rms noise current}} = \left(\frac{SLa\ (R-1)}{2Rm^2e\ \Delta f}\right)^{1/2}$$

where

S = photosensitivity of photosurfaces, amp/lumen

L = light intensity, foot-candles (on photosurface)

a = aperture area, square feet

m = linear magnification of image within tube

R = secondary-emission ratio of first multiplier dynode

e = electron charge

Δf = bandwidth, cps

The scene illumination necessary to produce this illumination on the photocathode of the tube can be determined by the following relationship

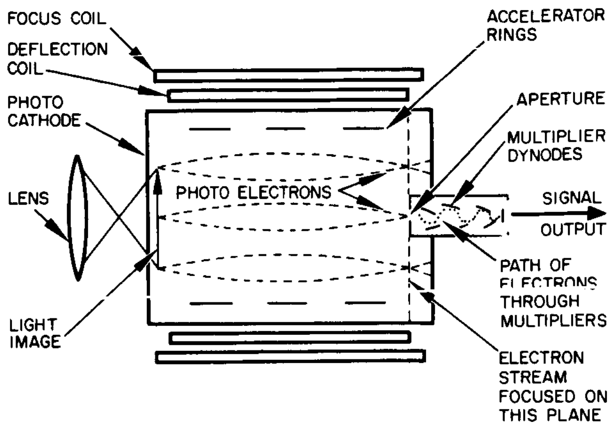

FIGURE 5-17. IMAGE DISSECTOR TUBE

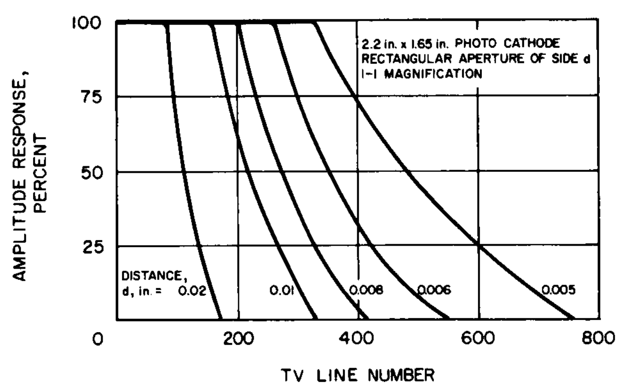

FIGURE 5-18. AMPLITUDE RESPONSE OF IMAGE DISSECTOR AS FUNCTION OF APERTURE SIZE

$$I_s = \frac{4f^2L}{TR}$$

where

I_s = scene illumination, foot-candles

f = effective aperture of lens

T = transmission factor of lens

R = highlight reflectance of scene

L = illumination of photocathode

Light Transfer Characteristics. The signal output is directly proportional to the input light for all signal levels below the point where the final stages of the multiplier saturate. Saturation can be guarded against by the use of 1) variable potentials on the multiplier stages, or 2) a controlled multiplier stage to control the overall amplification of the multiplier. For low-resolution systems (that is, systems employing large apertures) the signal output will be linear up to the point where peak signal currents approach 5 milliamperes, at which point the last dynode stage tends to saturate. When high photocurrents are drawn from the photocathode, in high-resolution tubes where high light levels are necessary to achieve the proper signal-to-noise ratio, saturation of the multiplier or lack of conductivity of the photosurface may distort the picture and alter the light transfer characteristics.

Output Impedance. The multiplier of the image dissector can be considered a constant current generator with a very high value of shunt impedance. The capacity to ground of the multiplier itself is 10 micro-microfarads. Sufficient gain is obtained in the multiplier to permit the use of a low value of load impedance. Therefore, the signal need not be corrected by a peaking stage. The output signal can be determined by

$$I_o = \frac{SLaR^z}{m^2}$$

where

S = sensitivity of photosurface, amp/lumen

L = illumination of surface, foot-candles

a = aperture area

z = number of stages

R = multiplier stage gain

m = magnification from photocathode to aperture

Black-level Setting. Absence of signal from the image dissector represents black-level. Black-level setting can best be achieved by shunting the output electrode to ground during the retrace interval, producing a zero output voltage, which represents black signal. An appropriate blanking signal is also inserted at this point to fix the blanking level with respect to the black-level information of the picture.

Multiplier Gain. The average stage gain of the multiplier is a function of the voltage applied across the stages. This varies between approximately 2.5 for 100 volts per stage and 4 for 200 volts per stage. The usual number of multiplier stages is 11.

AUXILIARY CIRCUITS

Focus Coil. A long-focus solenoid reduces the geometric distortion of the picture and produces unity magnification. The average field strength required is 20 gauss.

Deflection Coils. The deflection coils located adjacent to the tube and under the focus coil produce a cross component of deflection field in the order of 4 gauss for full deflection.

Focusing Electrodes. Focusing electrodes consisting of a series of rings along the path of the electron image produce a uniform accelerating field for the electron image. Connection to these electrodes is made through terminals on the periphery of the faceplate. Each of these rings is maintained approximately 100 volts positive with respect to the preceding one. The anode of the tube is maintained at ground potential and the photocathode at approximately —2000 volts, while the aperture of the multiplier is maintained at approximately —1400 volts.

Effect of Syncom-Tracking Station Geometry on Faraday Rotation Angle

Since the polarization angle of the transponder signal is used to provide additional attitude information, the component due to Faraday rotation must be included. To facilitate the advanced planning of suitable tracking station locations relative to the spacecraft longitude, some results are presented showing the effect of the line-of-sight geometry on the magnitude of the Faraday rotation component of the polarization angle.

SUMMARY

A Keplerian ephemeris program, augmented to provide a measure of Faraday rotation, θ, has had its constant of attraction modified to cause a longitude drift of Syncom at the synchronous radius. The subsequent change in the visible line-of-sight elevation angle (from a number of tracking stations to the drifting satellite) was used to generate the values of Faraday rotation for different Syncom longitudes. Results, plotted in Figures 5-19 and 5-20, show that the variation of Faraday rotation with satellite longitude for different tracking stations is not more than 2.6 degrees for Rosman, N.C., (latitude 35.13° N, longitude, 82.83° W), 2.3 degrees for Cocoa Beach, Florida, (latitude, 28.4° N, longitude, 80.5° W), 2.45 degrees for Honolulu, (latitude, 21.3° N, longitude, 157.87° W), and 1.5 degrees for Ascension Island, (latitude, 7.975° S, longitude, 14.39° W). For a tracking station located at the subsatellite longitude, L, the

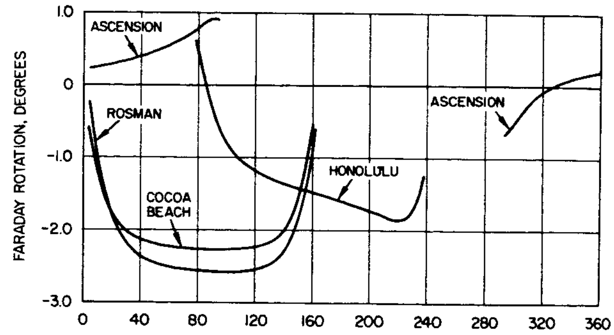

FIGURE 5-19. FARADAY ROTATION VERSUS SATELLITE LONGITUDE

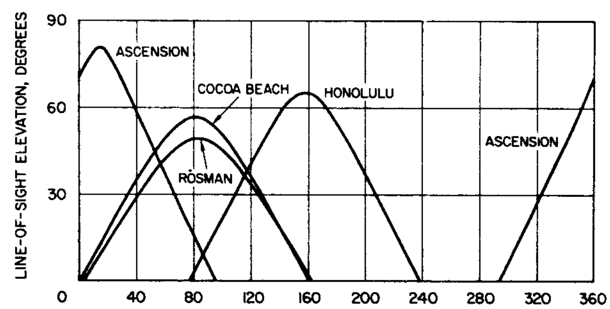

FIGURE 5-20. LINE-OF-SIGHT ELEVATION VERSUS SATELLITE LONGITUDE

Faraday rotation θ_{ss} may be approximated by (Reference 5-22).

$$\theta_{ss} \cong 0.88 \cos (78.6° \text{ W} - \text{L}) \text{ (degrees)}$$

so that for an Atlantic service Syncom located at L = 25° W, $\theta_{ss} \cong 0.52$ degrees. Comparison with the corresponding values for Ascension, Rosman, and Cocoa Beach (from Figure 5-19) shows that

$$\theta_{\text{ASCENSION}} \cong 0.30 \text{ degrees}$$

$$\theta_{\text{COCOA BEACH}} \cong -1.9 \text{ degrees}$$

$$\theta_{\text{ROSMAN}} \cong -2.0 \text{ degrees}$$

The above values of θ assume a spacecraft transmission frequency of 4 kmc and an integrated electron density of 4.8×10^{17} electrons/m^2 (a conservative value).

Similarly for a Pacific service Syncom located at L = 175° W

$$\theta_{ss} \cong -0.01 \text{ degree}$$

$\theta_{HONOLULU} \cong -1.56$ degree

Additional tracking stations (especially in Western Europe) will be studied in the future.

MATHEMATICAL MODEL

From References 5-23 and 5-24, the Faraday rotation θ is given by

$$\theta = 23.7 \frac{\overline{B} \cdot \overline{U}_\rho}{f^2} \int N \, d\rho \qquad \text{(radian)} \tag{5-72}$$

where

$\overline{B}$ = magnetic flux density vector of earth (Gauss)
$\overline{U}_\rho$ = unit vector along station-spacecraft line-of-sight
f = spacecraft transmitter frequency in 100 mc
$= 40$ (100 mc)
N = electron density in 10^{17} electrons/m^3

The integral in Equation 5-72 is approximated by

$$\int N \, d\rho \cong \left\{ 1 - \frac{\cos^2 \epsilon}{[1 + (h/R_0)_{av}]^2} \right\}^{-1/2} \cdot \int N(h) \, dh \tag{5-73}$$

where

ϵ = elevation angle of line-of-sight to spacecraft

$\left(\frac{h}{R_0}\right)$ = ratio of average altitude of ionosphere to earth radius

$$\approx \frac{\Delta h}{2 R_0} = \frac{500 \text{ km}}{(2)\ (6380) \text{ km}} \cong 0.039$$

$\int N(h) \, dh \approx 4.8 \times 10^{17}$ electrons/m^2

≈ 2.5 times the average quiet noon value of integrated electron density

EFFECT OF FUEL SLOSHING ON A SPIN STABILIZED VEHICLE

The motion of a spin stabilized vehicle that contains a store of liquid fuel, the mass of which is significant compared to the mass of the vehicle, must be considered. Two possible configurations have been studied. In the first, the fuel is stored in four identical spherical tanks symmetrically placed about the spin axis. In the second, the fuel is placed in a toroidal tank with its axis along the spin axis of the vehicle.

It is well known that the fuel will act as an energy damper, and that the vehicle will, with no external moment applied, eventually spin about the principal axis of maximum moment of inertia. The problem to be considered will be primarily associated with vehicle response when external forces and moments such as thrusting and control moments are applied.

Many investigations have been made of the normal modes and frequencies of fuel sloshing in spherical and cylindrical tanks (for example, Reference 5-25). One investigation of the energy absorption of a fluid in annular tank attached to a spinning vehicle was made (Reference 5-26); in it the mass of the fluid was considered to be so small that it could not affect the short time motion of the vehicle, but was effective over a long time in acting as a nutation damper.

In the short time sense, the fluid may be considered to be inviscid. Various tests have indicated good agreement between measured fundamental frequencies and those predicted by an inviscid analysis (Reference 5-25). Consequently, viscosity will be ignored in what follows.

Four Tank Configuration

The system considered is a spinning vehicle with four spherical fuel containers. It is assumed that the vehicle, without fuel, is inertially symmetrical about the spin axis and that the centroid of the fuel tanks will be located on a plane perpendicular to this axis.

The fuel in the tank is assumed to act as a mass attached to a universal joint at the center of the tank. Since the resultant of the force applied by the fluid to the tank must pass through the center of the tank, the fuel will be assumed to act as a point mass. The model pendulum will then be assumed to be of length defined by the fundamental frequency, and with mass equal to the mass of the liquid. The ratio of the pendulum length L to the tank radius R is given in Figure 5-21 as a function of the fuel level. This curve is based on Budiansky's Figure 14.

An (x, y, z) coordinate system is introduced with origin at the vehicle cg and the z-axis along the spin axis. The tank centers are assumed to be placed at (l, o, h), (o, l, h), (—l, o, h) and (o, —l, h), respectively. These will be referred to as 1, 2, 3, and 4 respectively. The corresponding concentrated masses

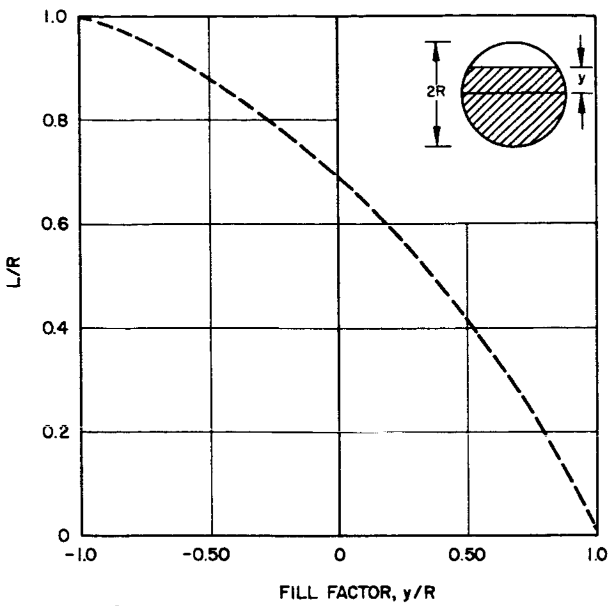

FIGURE 5-21. DEPENDENCE OF PENDULUM LENGTH — TANK RADIUS RATIO, L/D, ON FILL FACTOR FOR SPHERICAL TANK

will be located in the equilibrium position at (b, o, z_o), (o, b, z_o), $(-b, o, z_o)$, and $(o, -b, z_o)$.

$$b = l + L \cos \theta$$

$$z_o = h - L \sin \theta$$

and

$$\theta = \tan^{-2} \frac{T}{(M_o + 4_m)\ \omega_o^2\, b}$$

where

$T =$ thrust of rocket engine (assumed to act along spin axis)

$M_o =$ mass of vehicle

$m =$ mass of single fluid slug

If displacement of the fuel masses and angular rate deviations from equilibrium are linearized, the following displacements are retained:

Mass No.: 1 $(\delta t_1 \sin \theta, \delta y, \delta t_1 \cos \theta)$

2 $(\delta x_2, \delta t_2 \sin \theta, \delta t_2 \cos \theta)$

3 $(-\delta t_3 \sin \theta, \delta y_3, \delta t_3 \cos \theta)$

4 $(\delta x_4, -\delta t_4 \sin \theta, \delta t_4 \cos \theta)$

and the angular rates retained are:

$$(\delta\omega_x, \delta\omega_y, \omega_o + \delta\omega_z)$$

Define

$$\delta y_1 + \delta y_3 = Y$$

$$\delta x_2 + \delta x_4 = X$$

$$\delta t_1 - \delta t_3 = T_1$$

$$\delta t_2 - \delta t_4 = T_2$$

and

$$\delta\omega_x + i\delta\omega_y = \Delta\omega$$

$$X + iY = \psi$$

$$T_1 + iT_2 = \Omega$$

The pertinent equations become:

$$\begin{aligned} I_x' \Delta\omega + i\,(I_x' - I_z')\ \omega_o \Delta\omega &= -m\,[ih'\,(\ddot{\psi} + 2\, i\omega_o \dot{\psi} - \omega_o^2 \psi) \\ &\quad + i \sin \theta\, h'\,(\ddot{\Omega} + 2\, i\, \omega_o \dot{\Omega} - \omega_o^2\, \Omega) \\ &\quad - il \cos \theta\, \ddot{\Omega}] + M \end{aligned}$$

$$\begin{aligned} &\ddot{\psi} + \left(\frac{a_o}{L} - \omega_o^2\right)\psi + 2\, \omega i \sin \theta\, \Omega \\ &\quad + 2\, \omega_o\, (1 - 2\, \alpha)\ z_o\, \Delta\omega - 2\,[z_o\, (1 - 2\, \alpha)]\ i\Delta\dot{\omega} \\ &\quad - \alpha\, [\psi + 2\, \omega_o\, i\dot{\psi} - \omega_o^2\, \psi + \sin \theta \\ &\qquad (\Omega + 2\, \omega_o\, i\Omega - \omega_o^2\, \Omega)] = 0 \end{aligned}$$

$$\begin{aligned} &\ddot{\Omega} + \left(\frac{a_o}{L} - \sin^2 \theta\, \omega_o^2\right)\Omega + 2\, i\omega_o \sin \theta\, \dot{\psi} \\ &\quad + 2\, \omega_o\, [z_o'\, (1 - 2\, \alpha) \sin \theta + b \cos \theta]\ \Delta\omega \\ &\quad + 2\, i\, [b \cos \theta - z'\, (1 - 2\alpha) \sin \theta]\ \Delta\dot{\omega} \\ &\quad - \alpha \sin \theta\ [\ddot{\psi} + 2\, \omega_o\, i\dot{\psi} - \omega_o^2\, \psi + \sin \theta \\ &\qquad \times (\ddot{\Omega} + 2\, \omega_o\, i\dot{\Omega} - \omega_o^2\, \Omega)] = 0 \end{aligned}$$

where a_o is the magnitude of the total steady-state acceleration on the fluid slug (i.e., ω_o^2 b sec θ), $\alpha = 2m/(4m + M)$ $h' = h\ [1 - (4m)/(4m + M_o)]$,

$$I_x' = I_x + m(4\, h'z + 2\, lb)$$

$$I_y' = I_y + m\, (4\, h'z + 2\, lb)$$

$$I_z' = I_z + m\, 4\, lb$$

(I_x, I_y, I_z) are principal moments of inertia of the vehicle alone.

Values approximating those of the design vehicle are:

$$I_x' = 43.8 \text{ slug ft}^2$$

$$I_z' = 58.9$$

$$\omega_0 = 100 \text{ rpm} = 10.5 \text{ rad/sec}$$

$$l_o = 1.67 \text{ feet}$$

$$L = 0.5 \text{ foot}$$

$$M_o = 19.35 \text{ slugs}$$

$$m = 1.1 \text{ slug}$$

$$T/(M_o + 4m) \sim 238 \text{ ft/sec}^2$$

$$a_r = 10.5^2 \times 2.17 = 238 \text{ ft/sec}^2$$

$$\theta = 45 \text{ degrees}$$

$$a_o = 337 \text{ ft/sec}^2$$

$$h' = 0$$

$$z_o = -0.353$$

$$\alpha = 2m/(M + 4m) = 0.95$$

$$b \sim 2.17$$

The preceding equations then become:

$$\Delta\dot{\omega} - 3.62\, i\Delta\omega = i\, 0.04\, \ddot{\psi} + 0.023\, M$$

$$\ddot{\psi} + 564\, \psi + 14.8\, i\dot{\Omega} - 6\, \Delta\omega + 0.57\, \Delta\omega i - 0.095\, (\ddot{\psi} + 21\, i\dot{\psi} - 110\, \psi) - 0.067\, (\ddot{\Omega} + 21\, i\dot{\Omega} - 110\, \Omega) = 0$$

$$\ddot{\Omega} + 619\, \Omega + 14.8\, i\dot{\psi} + 27.9\, \Delta\omega + 2.66\, i\Delta\omega + 0.067 \times (\ddot{\psi} + 21\, i\dot{\psi} - 110\, \psi) - 0.0475\, (\ddot{\Omega} + 21\, i\dot{\Omega} - 110\, \Omega) = 0$$

From the foregoing, it would appear that the coupling between $\Delta\omega$ and the other two variables is slight since the cross coupling coefficients are small and since there would be no steady-state coupling term in the $\Delta\omega$ equation.

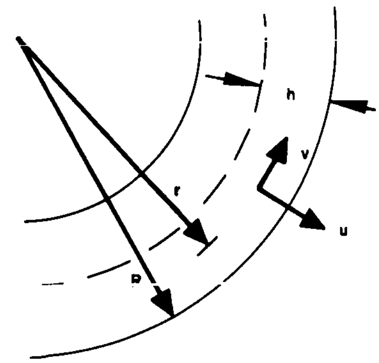

FIGURE 5-22. TOROIDAL GEOMETRY

Toroidal Configuration

The spinning vehicle is assumed to contain a toroidal fuel tank, and the spin axis is taken to be coincident with the axis of the toroid. Carrier and Miles (Reference 5-26) have studied the fluid motion in the tank under the assumptions that the vehicle was freely precessing and that the fluid action on the vehicle was of secondary magnitude. The tank itself was considered to be effectively two dimensional, and annular rather than toroidal. The only driving motion considered was the lateral acceleration of the center of the annulus. This type acceleration occurs with nutation if the plane of the annulus does not contain the cg of the vehicle. Furthermore, since they were concerned with energy absorption, they, of necessity, considered viscosity in their solution. However, the inviscid part of the solution should be usable here. A second type of solution, in which the toroid undergoes angular acceleration about an axis in the plane of the toroid, is needed. Furthermore, a coupling of the resulting fluid motion with the motion of the vehicle is essential.

Following the notation of Reference 5-26, the coordinate system (Figure 5-22), rotates with the mean speed ω. (U, V) then represents fluid velocity in this rotating coordinate system. Again following a slight modification of the material in Reference 5-26, a solution to the dynamical equations that satisfy boundary conditions $u = -ike^{i(pt + \phi)}$ at $r = R$ and the free surface conditions

$$\frac{\partial}{\partial t}\left(\frac{p}{2} - \frac{1}{2}\omega^2 r^2\right) = -\omega^2 (R-h)\, u$$

$$\text{at } r = (R-h)$$

was found to be

$$u = -ik\left(A + B\left(\frac{R}{r}\right)^2 \right) e^{i(pt+\phi)}$$

where A and B are defined by

$$A + B = 1$$

$$mA + nB = 0$$

where

$$m = \left(1 - \frac{p}{\omega}\right)^2 \left(1 - \frac{h}{R}\right)^2$$

$$n = \left(1 - 2\frac{p}{\omega} - \frac{p^2}{\omega^2}\right)$$

It is apparent that when $m = n$, resonance will occur. It is unlikely that such resonance will occur in this version of the Syncom. This is so because the cg of the vehicle is close to the centroid of the toroid and consequently it is doubtful that this mode will be driven. Since $I_z/I_x \sim 1.3$, the driving frequency will be -0.3ω. Then

$$m = 1.69\left(1 - \frac{h}{R}\right)^2$$

$$n = 1.51$$

These two values could be coincident if $h/R = 0.06$. Further work on the second mode in which the toroid tilts will be expected to follow.

PERTURBATION OF TRANSFER ORBIT DUE TO DRAG

An analytical drag model has been generated to predict the effects of atmospheric drag on apogee and perigee altitude of the presently planned Syncom transfer orbit (85-90 n.mi perigee altitude). This is the first part of a study to determine whether any deleterious effects exist during a possible second (or more) perigee passage. Results show that above 80 n.m. perigee altitude the effects of perigee passage are negligible for a moderate number of orbits.

Almost all of the theories developed for the effect of atmospheric drag on earth satellites have been limited to orbits of small eccentricity ($e < 0.1$) and for perigee distances that do not cause the vehicle to enter far into the earth's atmosphere. The purpose of this discussion is to remove some of these restrictions and to consider elliptic orbits of large eccentricity and low perigee passage. The theory proceeds exactly analogous to the usual development which leads to the following set of integrals for the variations in the perigee and apogee distances per revolution:

$$\Delta r_p = \frac{-r_p^2\, \delta\, \rho_p}{(1-e)} \exp\{\beta(a_o - a - x_o)\} \int_0^{2\pi} (1 - \cos E)\left(\frac{1 + e\cos E}{1 - e\cos E}\right)^{1/2} \exp\{\beta\, x \cos E\} dE \tag{5-74}$$

$$\Delta r_a = \frac{-r_a^2\, \rho_p\, \delta}{(1+e)} \exp\{\beta(a_o - a - x_o)\} \int_0^{2\pi} (1 + \cos E)\left(\frac{1 + e\cos E}{1 - e\cos E}\right)^{1/2} \exp\{\beta\, x \cos E\} dE \tag{5-75}$$

where

$\delta = FC_DA/m = F$ (drag coefficient) (spacecraft projected area normal to velocity) /spacecraft mass

$\beta =$ reciprocal of atmospheric density scale height

$x = ae =$ (semimajor axis) (eccentricity)

$x_o = = a_oe_o$ (initial values)

$\rho_p =$ density at initial perigee height

$$F = \left(1 - \frac{r_p\, \omega_a}{v_p} \cos i\right) \approx 0.92 \text{ (see later text)} \tag{5-76}$$

The integrals in Equations 5-74 and 5-75 cannot be integrated in "closed form." The usual technique is to expand the integrals in a power series of the form

$$M = \int_0^{2\pi} \sum_n C_n(e) \cos nE \cdot \exp\{\beta\, x \cos E\}\, dE \tag{5-77}$$

Because the interest is usually concentrated in the region of small eccentricities, the series are often terminated with terms of $0(e^2)$. Termwise integration is straightforward because the individual terms are recognized as the integral representation of the modified Bessel function. That is

$$I_n(z) = \frac{1}{2\pi}\int_0^{2\pi} \cos n\theta \exp\{z\cos\theta\}\, d\theta \tag{5-78}$$

Hence, Equation 5-77 can be written as

$$M = 2\pi \sum_n C_n(e)\, I_n(\beta x) \tag{5-79}$$

Applying the following three-term recurrence relation, all the modified Bessel functions can be expressed as combinations of I_o and I_1:

$$I_{n-1}(z) - I_{n+1}(z) = 2nz^{-1} I_n(z) \tag{5-80}$$

For large values of the argument $z = \beta x$, (i.e., $\beta x > 2$), and I_o and I_1 can be represented by their asymptotic expansions:

$$I_o(z) = \frac{\exp\{z\}}{(2\pi z)^{1/2}}\left[1 + \frac{1}{8z} + \frac{9}{128z^2} + \cdots\right]$$

$$I_1(z) = \frac{\exp\{z\}}{(2\pi z)^{1/2}}\left[1 - \frac{3}{8z} - \frac{15}{128z^2} - \cdots\right] \tag{5-81}$$

The preceding technique results in an excessive number of terms for larger eccentricities, e.g., $0.2 \leq e < 1$. Therefore, an alternate theory was developed which does not depend upon assuming small eccentricities. The new theory depends upon formulating an asymptotic expansion which is valid within the range of interest specified by the Syncom II system parameters.

Consider the integral in Equation 5-74 and make the change of variables

$$z = \beta x \qquad y = \cos E \tag{5-82}$$

The integral becomes

$$N = 2\int_{-1}^{+1} (1-y)\left(\frac{1+ey}{1-ey}\right)^{1/2} e^{zy} \frac{dy}{(1-y^2)^{1/2}} \tag{5-83}$$

Now let $y = 1 - u$ and Equation 5-83 becomes

$$N = 2\sqrt{\frac{1}{2}\frac{(1+e)}{(1-e)}}\; e^z \int_0^2 u^{1/2}\left(1-\frac{u}{2}\right)^{-1/2} (1-Au)^{1/2}\,(1+Bu)^{-1/2}\, e^{-uz}\, du \tag{5-84}$$

where

$$A = \frac{e}{1+e} \qquad B = \frac{e}{1-e} \tag{5-85}$$

The magnitude of the parameter $z = \beta ae$ is critical in the following expansion. For example, using design parameters for the Syncom II transfer orbit:

$r_p = 3{,}530$ n.mi.
$r_a = 22{,}752$ n.mi.
$e = 0.735$
$a = 13{,}141$ n.mi.
$H = 1/\beta = 15$ n.mi.
$z = \beta ae = 644$

Because z is a large number, Equation 5-84 can be integrated by the formal process of expanding the binomial series in the integrand, multiplying series and collecting terms of the same order of $u^{-(2n+1)/2}$. The resulting series can then be formally integrated as "incomplete gamma" functions. However, it can be readily demonstrated that because of the large values of z, the incomplete gamma functions can be replaced by the complete gamma functions with no loss of accuracy.

For example, it can be shown that Equation 5-84 becomes

$$N = 2\sqrt{\frac{1}{2}\left(\frac{1+e}{1-e}\right)}\, e^z \left[\Gamma\left(\frac{3}{2}\right) z^{-3/2} + a_1\Gamma\left(\frac{5}{2}\right) z^{-5/2} + a_2\Gamma\left(\frac{7}{2}\right) e^{-7/2}\right] \tag{5-86}$$

where

$$a_1 = \frac{1}{2}\left(\frac{1}{2} - A - B\right)$$

$$a_2 = \frac{1}{4}\left(\frac{3}{8} - \frac{A}{2} - \frac{A^2}{2} - \frac{B}{2} + AB + \frac{3}{2}B^2\right) \tag{5-87}$$

The curves in Figures 5-23 and 5-24 were computed from equations developed in the preceding fashion. In each case r_a was held fixed at the transfer value of 22,752 n. mi.

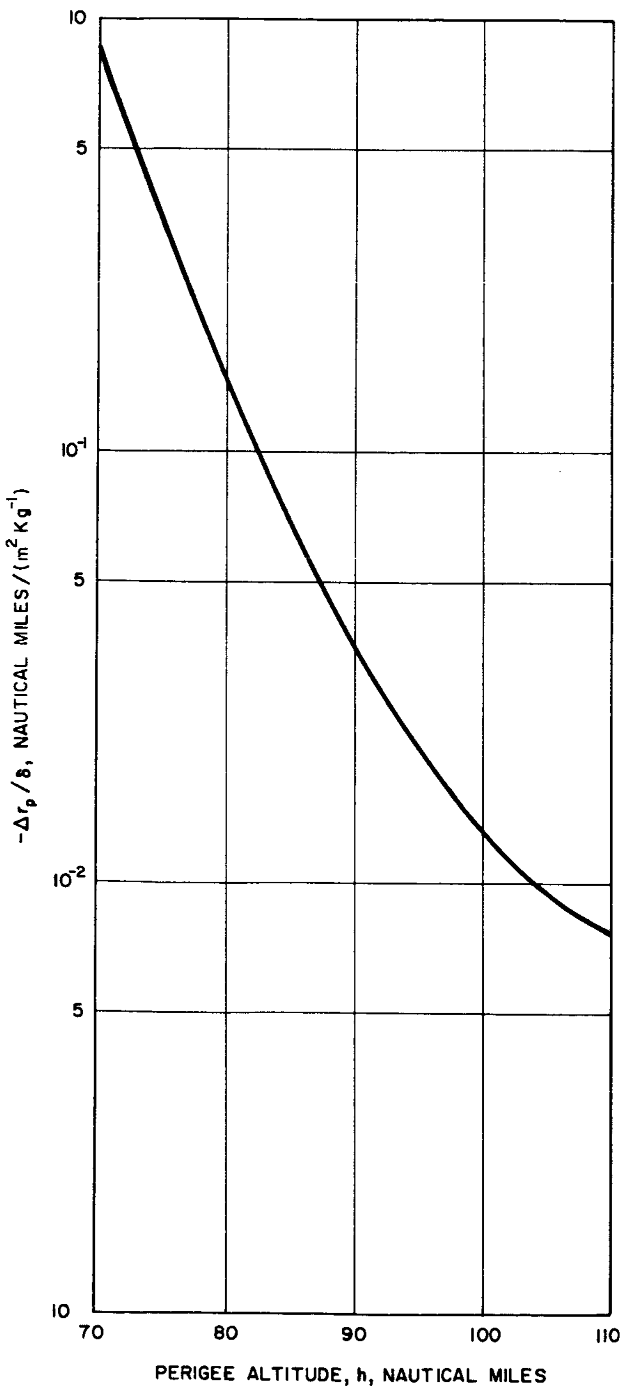

FIGURE 5-23. CHANGE IN PERIGEE ALTITUDE DUE TO DRAG

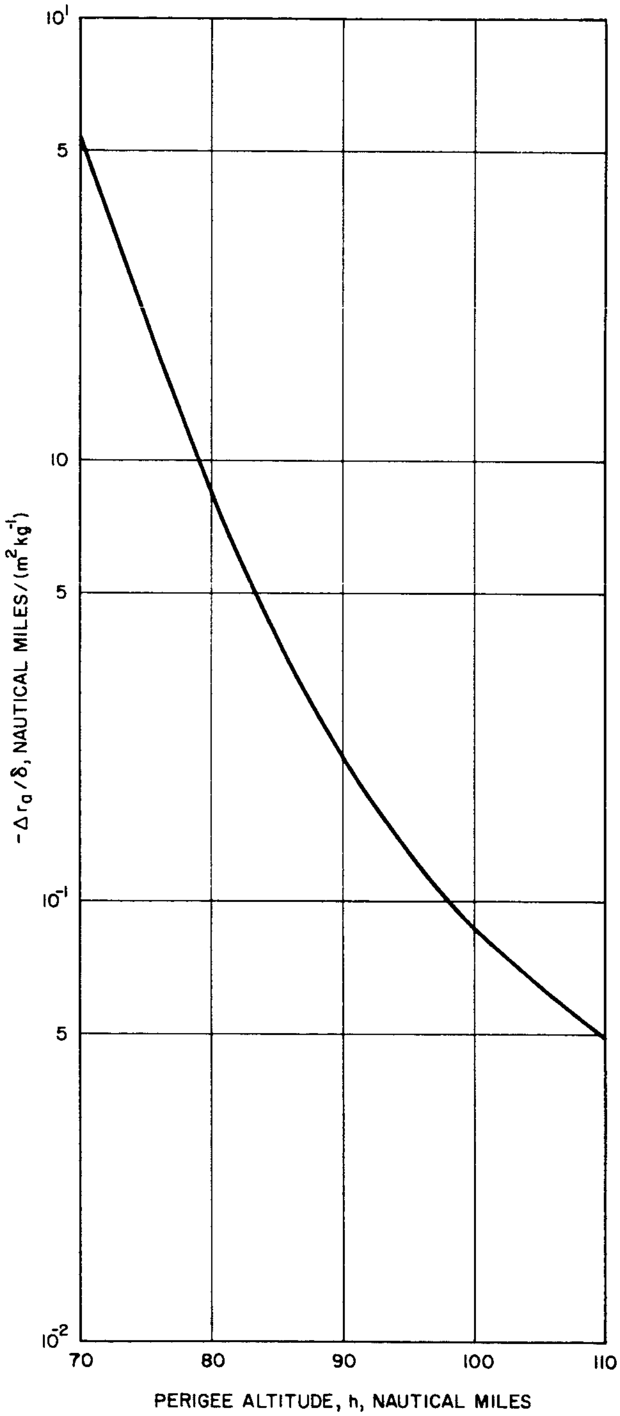

FIGURE 5-24. CHANGE IN APOGEE ALTITUDE DUE TO DRAG

A theoretical problem arises because the integrand in Equation 5-84 has a singularity at the value 1/B. It has been demonstrated that for $0.5 \leq e < 1$, the integrals can be terminated at 1/B without affecting the value of the integral. It is felt that this restriction is a little severe and further work should establish the validity of the asymptotic expansion for values of eccentricity in the range $0.2 \leq e < 1$.

Since this work was initiated, a paper on a similar subject has been published by King-Hele (Reference 5-27). His development is quite similar to that developed independently in the Hughes study. King-Hele does not explicitly prove the validity of his asymptotic expansion, and, in fact, does not point out that his results are indeed asymptotic expansions.

A report being prepared will contain the explicit formulations used for the calculations as well as a discussion of the domain of validity for the expansions.

Estimate of δ

From Equation 5-76 it is noted that

$$\delta = FC_D\,A/m \qquad , \qquad 0.9 \leq F \leq 1.1$$

$$\text{with } F = \left(1 - \frac{V_p\,\omega_a}{v_p}\cos i\right)^2.$$

The factor F (King-Hele, Reference 5-28) allows for the difference between the spacecraft inertial velocity v_p at perigee and the velocity relative to the atmosphere which is rotating with the earth at the angular rate $\omega_a \approx \omega_e = 2\pi$ rad /day. The inclination angle i for this transfer orbit is 29.1 degrees with respect to the equator. Thus for perigee radius $v_p =$ 3530 n. mi. and velocity $v_p = 5.55$ n. mi./sec, the value for F is

$$F = \left(1 - \frac{(3530)\,(7.35 \times 10^{-5})\,(0.874)}{5.55}\right)^2 \cong 0.92$$

A conservative estimate of C_D for a cylindrical satellite of length l and diameter d at or above the altitudes considered for the transfer orbit (free-molecular flow), is taken as 2.2 (Reference 5-28), based on the mean cross section seen by the remote molecular stream. For $l = 4.16$ feet, $d = 4.75$ feet, the rectangular (A_r) and circular (A_c) cross-sectional areas of the spacecraft are, respectively,

$$A_r = ld = (4.16)\,(4.75) = 19.75 \text{ ft}^2 = 1.835 \text{ m}^2$$

$$A_c = \frac{\pi d^2}{4} = \frac{(3.14)\,(22.5)}{4} = 17.65 \text{ ft}^2 = 1.64 \text{ m}^2$$

Since at perigee passage the nominal angle between the spin (k) axis and the velocity vector relative to the atmosphere v_{pa} is about 54 degrees (neglecting the F factor) from Figure 5-4, the mean value, $A = 1.74$ m,[2] of A_r and A_c appears to be a reasonable value for the effective cross-sectional area.

Finally, with the mass of the spacecraft (before apogee motor ignition) m = 1518 pounds = 688 kg the estimate of δ is

$$\delta \approx \frac{(0.92)\,(1.74)\,(2.2)}{688} = 5.12 \times 10^{-3}\left(\frac{m^2}{kg}\right)$$

Using the above value for δ, Table 5-10 shows the effect of perigee passage per orbit for perigee altitudes bracketing the planned altitude of 90 n.mi. It is seen that for perigee altitudes above 80 n.mi. the shape of the orbit is changed by a negligible amount up to about 50 orbits, for example. After this many circuits the apogee radius will have changed by an amount comparable to the effect of earth's oblateness (~0.3 n.mi.).

TABLE 5-10. EFFECT OF DRAG ON TRANSFER ORBIT PER PASSAGE

Perigee Altitude (h), n. mi	Normalized Apogee Change ($-\Delta V_a/\delta$, n. mi./m^2-kg^{-1}	Apogee Change ($-\Delta V_a$), n. mi. x 10^3	Normalized Perigee Change ($-\Delta V_p/\delta$), n. mi./m^2-kg^{-1}	Perigee Change ($-\Delta V_p$), n. mi. x 10^3
70	5.559	28.45	8.859	45.4
80	0.9136	4.67	0.1415	0.725
88.3	0.2789	1.43	0.0433	0.222
90	0.2101	1.08	0.0326	0.167
100	0.0871	0.446	0.01396	0.0715
110	0.0492	0.252	0.007682	0.0393

REFERENCES

5-1. Williams, D.D., "Dynamic Analysis and Design of the Synchronous Communication Satellite," Hughes Aircraft Company TM 649, May 1960.

5-2. "Syncom Booster Feasibility Study Final Report," LMSC A057612, Contract No. AF 04(647)-592, 30 September 1962 (Confidential).

5-3. Joos, G., "Theoretical Physics," Hafner Publishing Company, 1950, page 151.

5-4. Buglia, J. J., *et al.*, NASA Technical Report R-110, Langley Research Center, Virginia, 1961.

5-5. Williams, D. D., "General FORTRAN Rigid Body Program," Hughes Aircraft Company IDC 2280-03/76, 18 March 1963.

5-6. Fleig, A. J., "Effect of Nonsphericity of Earth's Gravitational Potential on an Equatorial Synchronous Satellite," NASA Goddard Space Flight Center, Guidance and Control Section Report No. 43, June 15, 1962.

5-7. Frick, R. H. and T. B. Garber, "Perturbation of a Synchronous Satellite," RAND Corporation R-399 NASA, Contract NASr-21(02), May 1962.

5-8. William, D. D. "Triaxiality of the Earth and Its Effect on a Stationary Satellite," Hughes Aircraft Company TIC 4120.7/13, 30 December 1960.

5-9. Williams, D. D., "Torques and Attitude Sensing in Spin-Stabilized Synchronous Satellites," American Astronautical Society, Goddard Memorial Symposium, Washington, D. C., 16, 17 March 1962.

5-10. Lotta, J. G., "Syncom II Weight Status, Hughes Aircraft Company IDC 2243.11/183, 18 September 1962.

5-11. Williams, D. D., "Precession in Magnetic Field," Private Notes, 3 November 1960.

5-12. "TELSTAR Symposium," Bell Telephone Laboratories, Goddard Space Flight Center, Greenbelt, Marland, 18 September 1962.

5-13. "Optical Tracker," Engineering Proposal No. 9011-62-51, Sales File No. 1554, Eclipse-Pioneer Division, Bendix Corp., October 17, 1962.

5-14. Fink, D. G., "Television Engineering Handbook," McGraw-Hill Television Series, Section 5.5, 1957.

5-15. "Typical Absolute Spectral Response Characteristics of Photoemissive Devices," Chart, ITT Components and Instrumentation Laboratory, Fort Wayne, Indiana.

5-16. Payne-Gaposchkin, C., "Introduction to Astronomy," Chapter XIV, Prentice-Hall, 1955.

5-17. "Apparent Places of Fundamental Stars, 1961," Astronomisches Rechnen-Institut, Heidelberg, 1960 (under auspices of International Astronomical Union).

5-18. "Advanced Syncom, Initial Project Development Plan, Vol. 1, Technical Plan," Hughes Aircraft Company SSD 2380R, NASA Contract 5-2797, 15 August 1962.

5-19. Larson, C. C. and B. C. Gardner, "The Image Dissector," Electronics, Vol. 12, No. 10, October 1939, pp. 24-27, 50.

5-20. Schaetti, N., "An Image Dissector Without Storage for Film Scanner," Bull. assoc. suisse elec., Vol. 40, No. 17, 1949, pp. 569-570.

5-21. Schaetti, N., "An Image Dissector of the Non-storage Farnsworth Type," Helv. Phys. Acta, Vol. 24, No. 2, 1949, pp. 225-232.

5-22. Levine, D., "Radargrammetry," McGraw-Hill, 1960, pp. 74-75.

5-23. Williams, D. D., "Addition of Faraday Rotation to Keplerian Ephemeris," Hughes Aircraft Company IDC 2280.03/46, 15 August 1962.

5-24. "Technological Considerations Concerning Satellite Communication Systems," Hughes Aircraft Company Communications Div. Report R-73, October 1958.

5-25. Bernard Budiansky, "Sloshing of Liquids in Circular Canals and Spherical Tanks," Journal of the Aerospace Sciences, Vol. 27, No. 3, March 1960, pp. 161-174.

5-26. G. F. Carrier and J. W. Miles, "On the Annular Damper for a Freely Precessing Gyroscope," Journal of Applied Mechanics Paper No. 59-A-44.

5-27. King-Hele, D.G., "The Contraction of Satellite Orbits Under the Influence of Air Drag III. High eccentricity orbits ($0.2 \leq e < 1$)." Proc. Royal Soc. Ser. A 267 (1962), 541-557.

5-28. King-Hele, D.G., "Properties of The Atmosphere," Chapter I, § 2, *Progress In The Astronautical Sciences, Volume I*, S. F. Singer, Ed., North Holland Pub. Co., 1962.

6. SPACECRAFT SYSTEMS DESIGN

The Syncom II spacecraft employs advanced systems developed from the corresponding techniques and equipments used in the spin-stabilized Syncom I. The spacecraft is larger than Syncom Mark I by approximately a factor of two in linear dimensions and a factor of eight in volume and weight.

REQUIREMENTS

The basic requirements established by NASA include the following:

1) The launch vehicle is the Atlas-Agena, using the Nimbus shroud, plus a third-stage apogee injection motor.
2) Spin axis orientation and vernier orbital corrections will be performed by a hot gas reaction jet control system.
3) The spacecraft communication system will employ a high-gain phased array antenna for transmission.
4) The spacecraft communication transponders will utilize traveling-wave tube final power amplifiers and will provide for the alternate modes of operation (dual mode) of multiple access and frequency translation.
5) The communication frequencies will be in the 6000-mc band for ground-to-spacecraft transmissions and the 4000-mc band for spacecraft-to-ground transmissions.
6) Redundant equipments, communications repeaters, command receivers, and telemetry transmitters shall be provided.
7) The spacecraft structure, apogee injection motor, and control system design should take cognizance of the maximum payload capabilities of the Atlas-Agena for this mission.
8) The useful lifetime design objectives are 3 years in orbit and 1 year storage. Potential opportunities to extend the objective lifetime will be given consideration.

The spacecraft equipment design approaches implementation techniques, and investigations are described in the following discussion.

COMMUNICATION TRANSPONDERS

Block diagrams of the two types of communication transponders are shown in Figure 6-1. A pair containing one of each type constitutes a dual mode transponder; four dual mode transponders operating at different carrier frequencies are included in the spacecraft.

A bandwidth of 25 mc is available for each signal. Identical carrier frequencies are used in both modes of a transponder, but only a 5-mc bandwidth is needed for the ground-to-spacecraft link of the multiple access mode. In addition to the communication carriers, the spacecraft will radiate an unmodulated beacon at 4080 mc.

The general arrangement of the transponders in the spacecraft is similar to that of Syncom I. The receiver mixers and preamplifiers are located in the antenna electronics compartment just aft of the apogee rocket. This compartment will also contain the multiplexers and the power splitter and phase shifters for the phased array antenna. The transmitters will be mounted on structural ribs between the quadrant packages and the antenna; the remainder of the transponders are in the quadrant electronic compartments.

Frequency Translation Transponder

Both modes of the transponders have been designed to incorporate Syncom I components with a minimum of modification and addition. The frequency translation transponder, which is the same type as the Syncom I transponder, is described with reference to Figure 6-1.

The input and output frequency assignments required the addition of a doubler to the transmitter branch of the varacter diode frequency multiplier chain and the substitution of a tripler for the two doublers in the receiver branch. The design of the doubler was derived from that of the first receiver doubler of Syncom; the tripler was a new development. A second isolator has been added ahead of the tripler to eliminate a system impedance adjustment. The remainder of the frequency multiplier design involved increasing the center frequency of the Syncom I units by about 12 percent. Some adjustment of line lengths was involved, but no changes in diode types. The dual filter-hybrid and isolator required similar retuning.

The input mixer, high level mixer, and interconnection hybrid required frequency scaling. The wide band IF amplifiers have been designed to meet the delay distortion specifications appropriate for color television signals. The injection of the beacon signal imposes different design considerations from those in Syncom because of its considerable separation in frequency from the communication carrier. New units — a 14-db coupler, a beacon mixer, and a 144-mc beacon oscillator — are needed. The single sideband filter following the high level mixer will have two separated passbands.

The output RF power switch used to connect the ON transmitter to the antenna required a new approach to operate satisfactorily at 4000 mc. A ferrite circulator whose field direction can be switched electronically, thus eliminating the moving parts of the relay employed in Syncom I, has been designed to fulfill this function.

The frequency translation mode is more suitable for relaying a single carrier modulated by wideband data, of which television is an outstanding but not unique example. It may also be used for experimental tests of the feasibility of a limited multiple access system using time division multiplex but is not compatible with a more practical, high channel capacity frequency-division-multiplex multiple access system.

Multiple Access Transponder

The multiple access transponder is designed to permit the interconnection of a large number of ground stations with high quality communication channels in a manner that provides a simple, reliable spacecraft electronic system and inexpensive ground stations. The constraints considered in the transponder design were minimization of spacecraft power requirements, minimization of intermodulation products, and ability to meet the frequency stability requirements of the system at the assigned carrier frequencies. The desire to use Syncom I components with minimum modification determined some design choices. The multiple access transponder shown in Figure 6-1 represents the system that evolved from these considerations. The spectrum of the signals at several stages of the transponder is shown in Figure 6-2.

The reference signal for the receiver mixer is the 192nd harmonic of the receiver master oscillator, a crystal oscillating at 66.223 mc. The long-term stability of this oscillator is not critical to the communication system, and it will be designed to operate without temperature-controlled ovens but with a high degree of thermal isolation. The major constraint on the oscillator relates to its short-term stability, which is controlled largely by its thermal and power supply design. The multiplication is accomplished in two sections: a factor of 32 in a unit similar to the Syncom I multiplier and a tripler identical to the tripler in the new frequency translation transponder.

The received signals are amplified in a 5.8 mc bandwidth amplifier centered at approximately 35 mc. The amplitude of the composite signal fluctuates in the same manner as band limited noise; hence this amplifier must be linear to prevent excessive intermodulation. The output power of this amplifier averages less than a microwatt, however, and the required linearity is achievable. It would be difficult to produce intermodulation levels of importance at such low signal levels even if the attempt were made to do so.

The amplified received signals and the transmitter master oscillator reference are the inputs to the IF phase modulator which performs the modulation conversion. The operation of this modulator is described with reference to Figure 6-3. The composite signal and reference carrier are introduced into a hybrid transformer arranged so that the signal produces in-phase vectors and the carrier out-of-phase vectors at output terminals A and B. The limiters restrict the resultant vectors to a constant amplitude, so that its modulation is low index phase modulation. This action of the limiters creates the second sideband characteristic of a phase-modulated carrier. The limited resultant vectors are added in the output summing network in the ratio $\mu + 1/\mu - 1$, causing the resultant vector's phase shift to be increased by the factor μ. This arrangement permits the ratio of carrier to signal to be high enough prior to limiting to keep intermodulation products low, while permitting the modulation index to be subsequently adjusted to the level corresponding to the communication system requirements. A detailed analysis of this modulator is given in TM 721, "SSB-PM Multiple Access Communication System," October 1962.

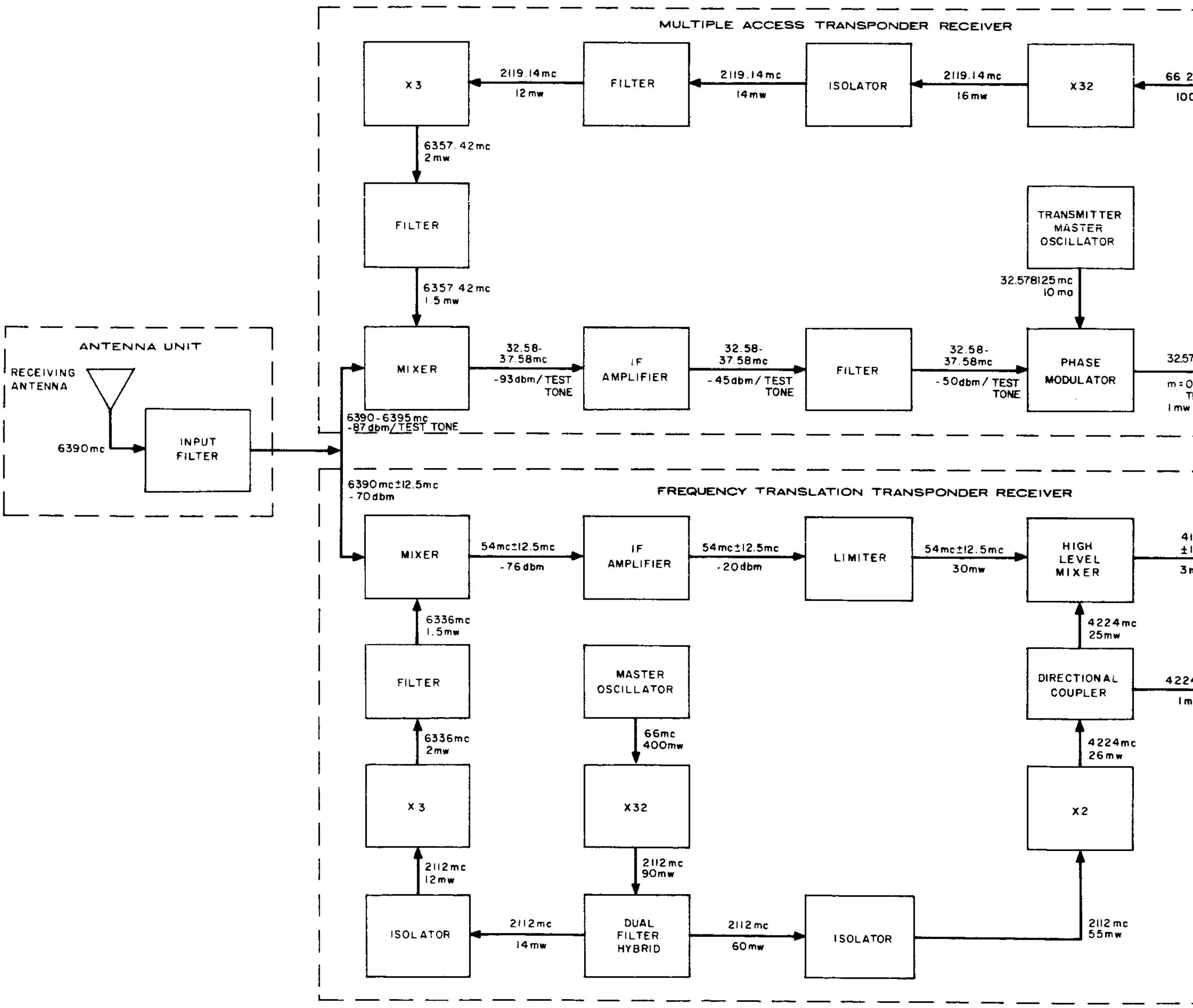

FIGURE 6-1. FREQUENCY TRANSLATION

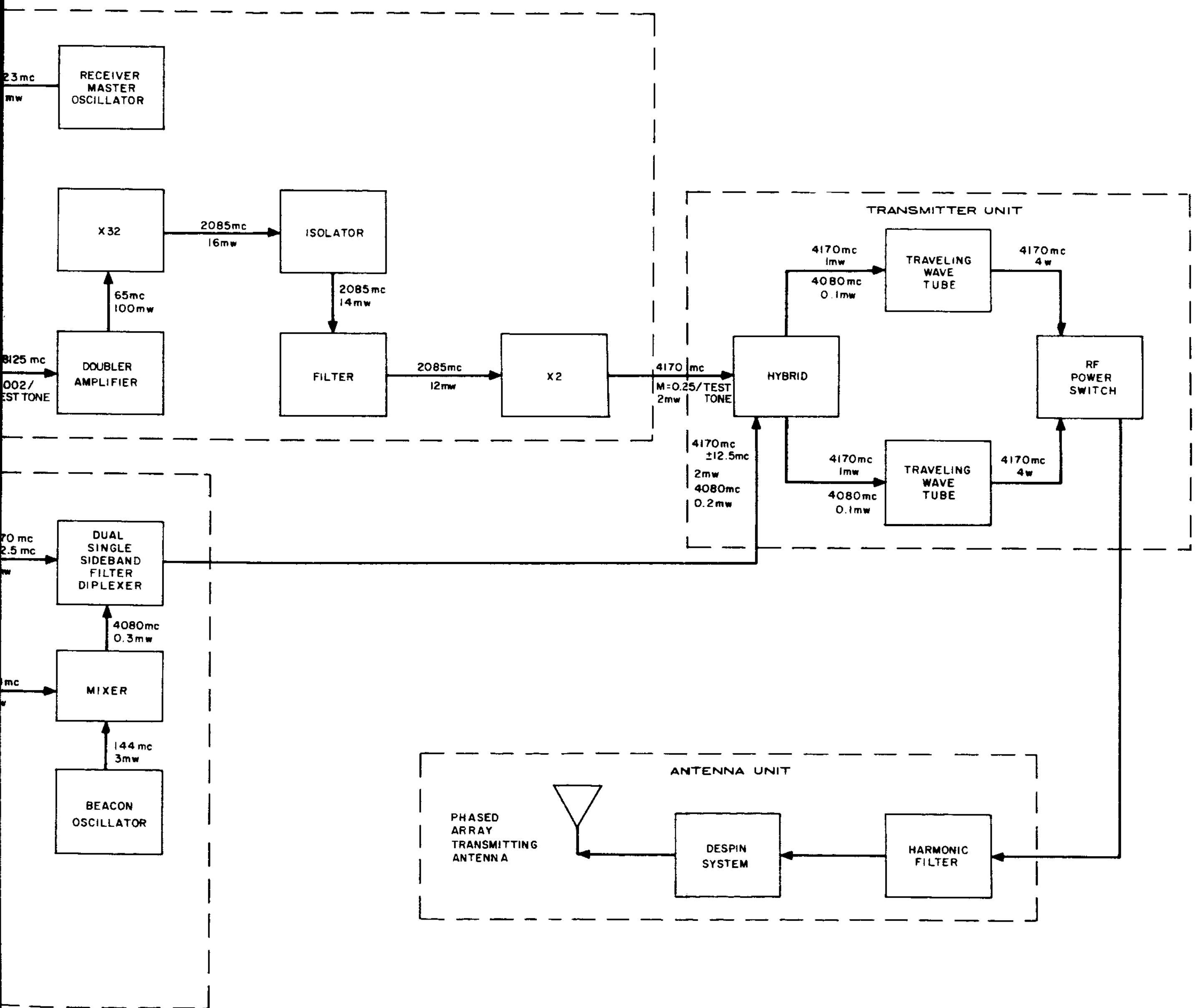

ND MULTIPLE ACCESS TRANSPONDERS

V

The output of the phase modulator is doubled in frequency and amplified to a power level of 100 mw with transistors. It is then multiplied further in varactor diode circuits by a factor of 32 in a unit identical to the corresponding multiplier in the receiver chain and finally by a factor of 2 in a doubler similar to a doubler in the Syncom I transponder. The output of the chain is amplified to 4.0 watts in the traveling-wave tube power amplifier. The conversion of the signals to phase modulation permits both the transistor amplifier and the traveling-wave tube amplifier to operate saturated — hence at maximum efficiency — without introducing intermodulation products caused by nonlinearity of their amplitude characteristics.

Multiplexers

Multiplexers are used to connect all the transmitters through low loss paths to the power splitter of the phased array antenna and all the receivers to the receiving antenna. Waveguide hybrids and directional filters will be used in the branching filters, and waveguide interconnections will be used between them, to allow an acceptable multiplexer loss. A design study of the 4 and 6 kmc multiplexers is summarized in subsequent portions of this section.

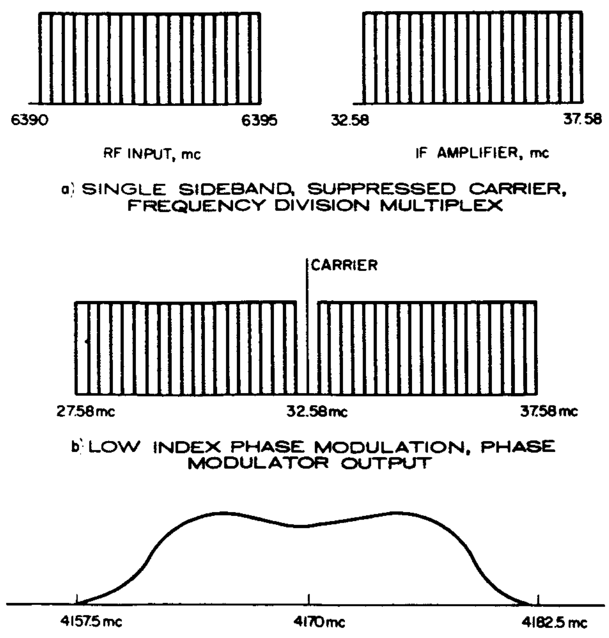

FIGURE 6-2. MULTIPLE ACCESS TRANSPONDER SIGNALS

Summary of Transponder Characteristics

Some important characteristics of the transponders, applicable to each of the four, are listed in Table 6-1. These values are the design objectives and are used in the communication system design. Details of development accomplished on the units that comprise the two transponder types are presented in the following paragraphs.

FERRITE RF POWER SWITCH

The ferrite switch utilized to switch the multiplexer input to the selected traveling-wave tube is essentially a three-port circulator with provisions for reversing the magnetic field polarity (Figures 6-4 and 6-5). In this configuration, the circulator operates as a single-pole double-throw switch.

This switch requires 24 watts of power for a computed switching speed of about 0.5 millisecond. The microwave characteristics over a 200 mc bandwidth are 0.2 db maximum insertion loss between transmission terminals and 25 db minimum isolation. Power is needed only to reverse the ferrite magnet polarity; and once this is accomplished, no further power is required.

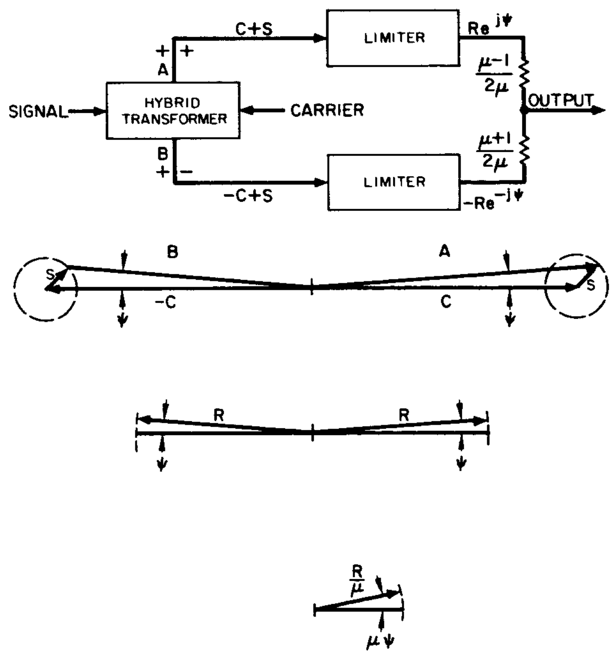

FIGURE 6-3. PHASE MODULATOR

Low insertion loss and switching power were the main design objectives. Assuming optimum circulator design, the limiting factor for lowest possible insertion loss is determined by the dielectric and magnetic losses of the garnet. For low switching power, the number of ampere turns per inch around the ferrite magnet must be a minimum, which would require a low coercive force ferrite magnet with good square loop properties. For the switch to operate with a low coercive force magnet, the internal garnet must have a low saturation magnetization and airgaps in the magnetic circuit must be minimized.

TABLE 6-1. TRANSPONDER CHARACTERISTICS

Characteristic	Frequency Translation Mode	Multiple Access Mode
Transmitter		
Power, watts	4.0	4.0
Frequency band, megacycles	4000	4000
Bandwidth, megacycles	25	25
Antenna gain, decibels	18	18
Losses, decibels	3	3
Receiver		
Noise figure, decibels	9	9
Frequency band, megacycles	6000	6000
Bandwidth, megacycles	25	5.8
Antenna gain, decibels	8	8
Losses, decibels	1.5	1.5

The airgap in the magnetic circuit was decreased to 0.010 inch by using soft iron wherever possible. The lowest saturation magnetization garnet was used consistent with low dielectric and magnetic losses and temperature stability. A coercive force of 40 oersteds and residual magnetism of 2040 gauss was specifically synthesized for use in this switch. The proper flux density was obtained by varying the cross-sectional area of the magnet; and, by winding 600 turns of No. 33 wire around the magnet, the switch requires one ampere at 24 volts.

DUAL MIXER (6 KMC)

Hardware development of this dual mixer, which operates approximately 1000 mc below that of Syncom I, has included completion of a test fixture to permit optimization of the match of the two mixer diodes, RF choke, RF filter, and the RF hybrid ring. Three alternate materials were tested (revolite, tellite, and duroid) for the hybrid rings, to minimize losses and simplify fabrication processes. The dual mixer is shown in Figure 6-6 as compared to the Syncom I unit.

The final configuration of this unit is composed of two single mixers (6390 mc), one for each of the transponder receivers, plus a junction and two transmission lines. The lengths of the interconnecting cables

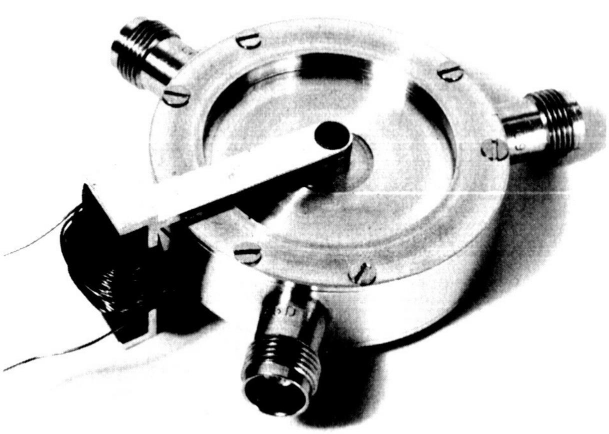

FIGURE 6-4. NEWLY DESIGNED COAXIAL POWER RELAY FOR MARK II ANTENNA CONFIGURATION

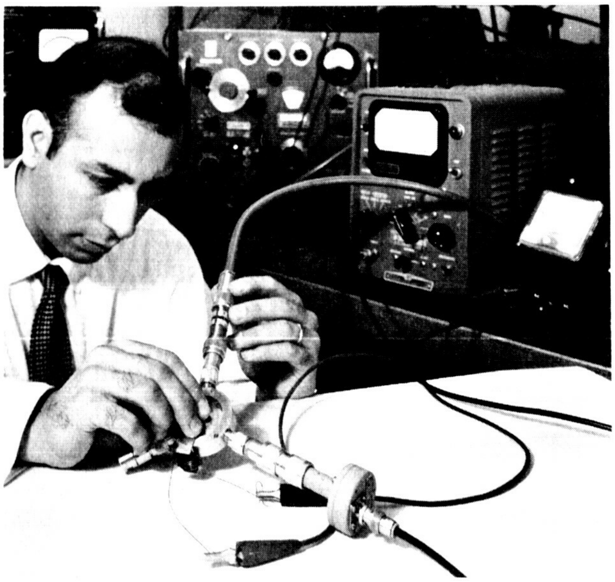

FIGURE 6-5. RF COAXIAL POWER SWITCH BEING TESTED

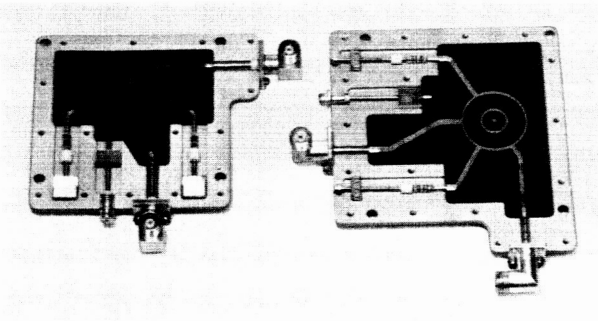

FIGURE 6-6. COMPARISON OF SYNCOM I (LEFT) AND SYNCOM II (RIGHT) INPUT MIXERS

were adjusted to provide half-wavelengths of transmission line between the input junction and the mixers. The crystal detector of the "off" receiver is back-biased, causing a high impedance to appear at the input junction. Thus the signals supplied from the receiving antenna are introduced into the mixer of the "on" receiver with only the loss of the interconnecting cabling.

X32 MULTIPLIER AND BIAS

The required units were completed and employed in the spacecraft with an additional unit integrated into the ground checkout equipment. Latest development efforts have been directed toward improvement of the stability of the X32 frequency multiplier chain. This includes an increase in the range, temperature, voltage, and load mismatch, over which stable operation can be achieved. These improvements also will allow the multipliers to be more readily reproducible. (See Figure 6-7.)

X3 MULTIPLIER

All required X3 multipliers were fabricated and checked out, meeting all design requirements. These units have a fixed length line for the input tuning. Effort was concentrated on the circuit development for these units. The X3 multiplier raises the frequency of the output of the X32 multiplier to that required for the input mixer. The input frequency to the X3 multiplier is 2112 or 2119 mc and the output frequency is 6336 or 6357 mc. This multiplier is a waveguide structure with a fixed line length for input tuning and self-biased diodes as varactor multipliers. Input power is 12 mw and output power is 3 mw. (See Figure 6-8.)

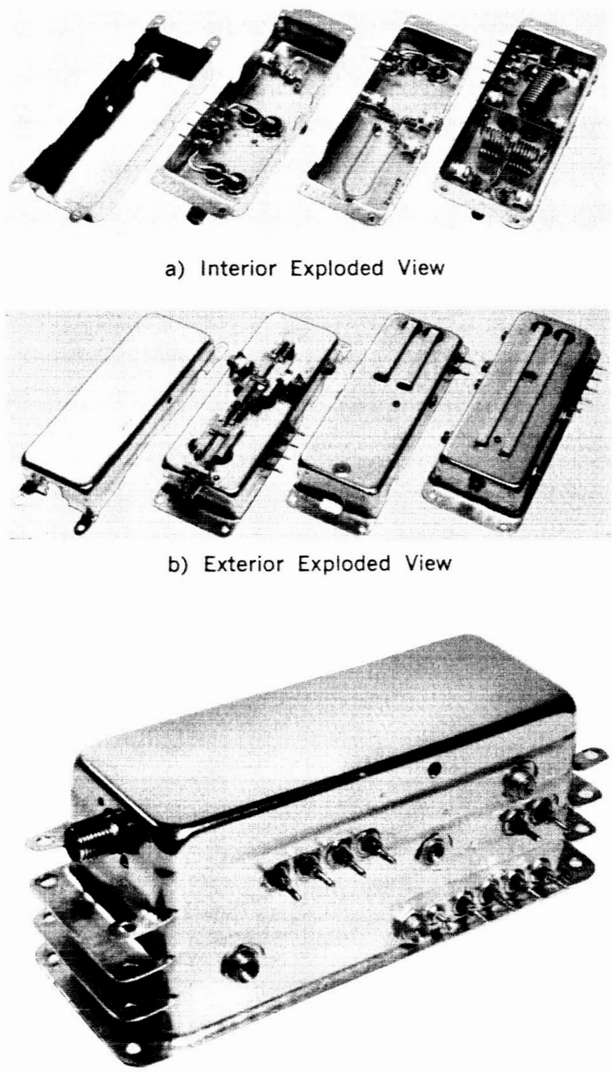

a) Interior Exploded View

b) Exterior Exploded View

c) Assembled

FIGURE 6-7. X32 MULTIPLIER

X2 MULTIPLIER

The units required for the spacecraft transponders and test panel equipment are now in service.

In the frequency translation transponder this unit is used with the X32 multiplier and the master oscillator to provide high level mixer and beacon mixer reference signal input.

In the multiple access transponder it doubles the phase modulated signal to the output frequency prior to transmission by the traveling-wave tube. (See Figure 6-9.)

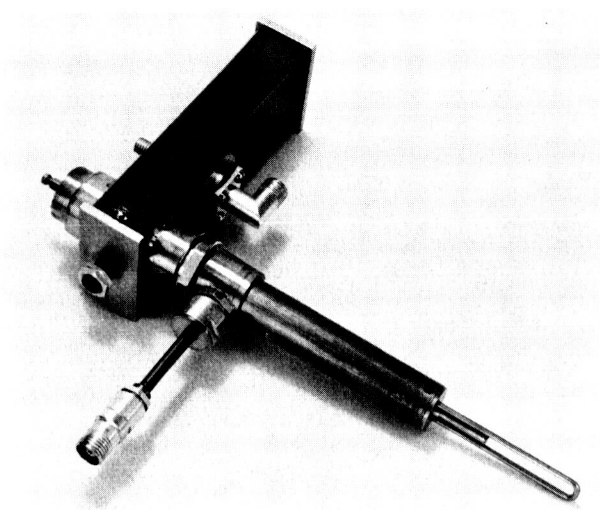

a) Assembled

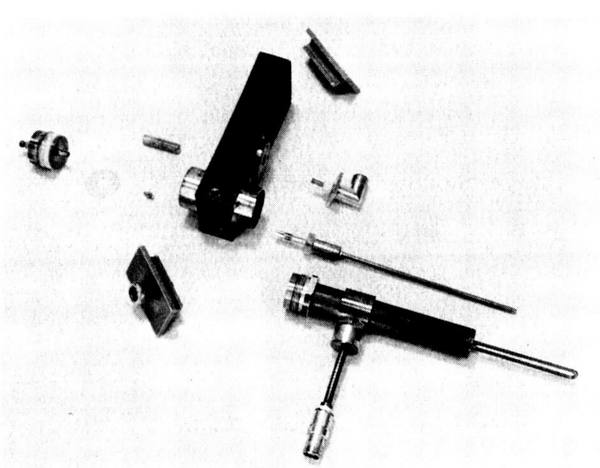

b) Exploded

FIGURE 6-8. BREADBOARD X3 MULTIPLIER

4-KMC HYBRID

Design fabrication and checkout of the 4-kmc hybrid has been completed. It will be used as an isolating junction for driving the traveling-wave tube. In addition, the unit is employed in the beacon and high-level mixers. As shown in Figure 6-10, the square portion of the unit comprises the 4-kmc hybrid; with the crystal mounts attached, this unit becomes either the 4-kmc high-level mixer or the beacon mixer.

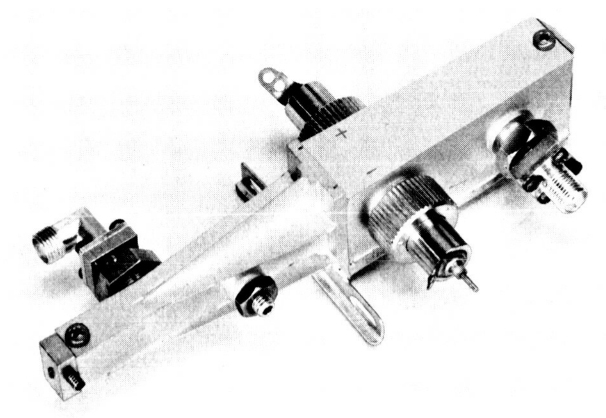

FIGURE 6-9. X2 MULTIPLIER

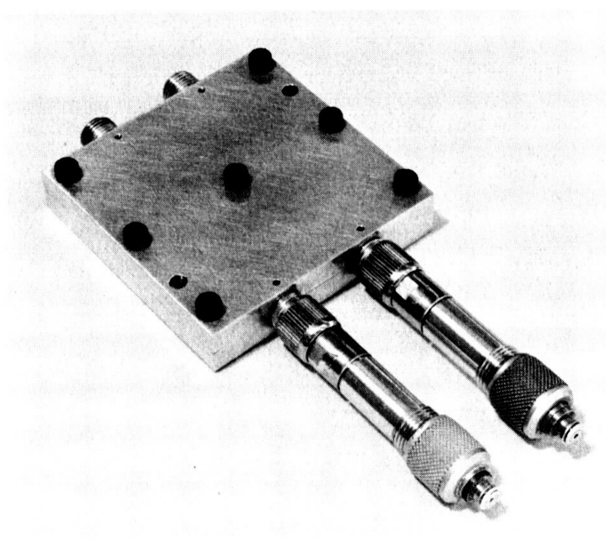

FIGURE 6-10. 4 KMC HYBRID WITH CRYSTAL MOUNTS ATTACHED

LOCAL OSCILLATOR FILTER

The local oscillator filter will be used between the X3 multiplier and the input mixer. Design and fabrication was completed, with the basic design patterned after the Syncom I local oscillator filters. Frequency range and bandwidth modifications comprised the basic changes from the Syncom I units.

INPUT FILTER

All required input filters for use between the receiving antenna and the input mixer were completed. The

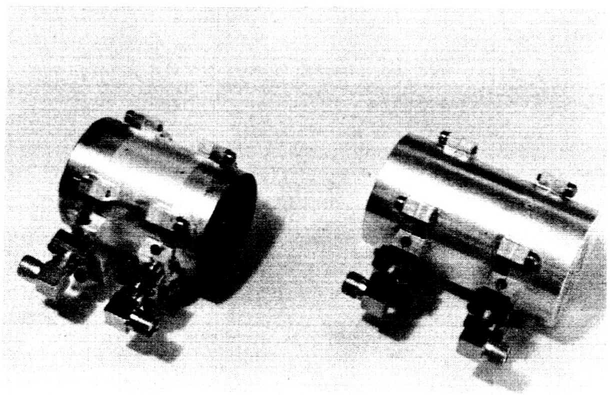

FIGURE 6-11. INPUT FILTER
Local oscillator filters are same in exterior appearance

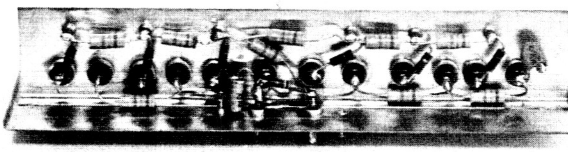

a) Back View

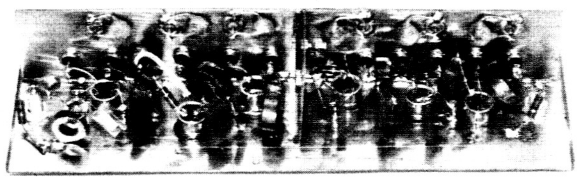

b) Front View

FIGURE 6-12. 54-MC IF AMPLIFIER

basic design of these filters is that of the Syncom I filters, with linear dimensions scaled to frequency. Changes from the Syncom I units consisted of frequency range and bandwidth modifications. (See Figure 6-11.) When the transponders are operated in conjunction with the receiving multiplexer, this filter should not be required.

Circuits for FM Frequency Translation Transponder

54-MC PREAMPLIFIER/54-MC IF AMPLIFIER

Initial effort for these units was directed toward development of 25-mc bandwidth circuits applying the circuit techniques developed for Syncom I and using the same transistors (Figure 6-12). However, difficulties encountered with this transformer-coupled approach created a parallel consideration of an alternate transistor and RC-coupled circuits. Subsequently, the preamplifier and the amplifier were combined into one operating unit. This configuration consisted of two staggered tuned three-stage amplifiers utilizing six 2N1405 transistors. Basic advantages of this design approach appeared to be: reduction in difficulty of adjusting the tuning and availability of adequate gain. This new design used only one triple (which determined the bandpass and noise figure) followed by a wide-band video-type amplifier (consisting of three pairs of ground-emitter and emitter-follower stages). These stages were not tuned, but were only frequency-compensated against the dropoff in beta. However, final design investigation showed that combining these two units would be less effective than their operation as separate units, because separate configurations would provide an improved gain distribution and packaging design.

54-MC IF LIMITER

The three-stage breadboard for this unit exhibited excellent linearity over the 25-mc bandwidth. An additional three-stage structure was constructed to test reproducibility of this circuit. The final configuration employs six stages to obtain the required gain. A signal-level monitor will be included to provide an operational measurement of system performance. All required units were completed and checked out satisfactorily. (See Figure 6-13.)

ISOLATOR

Syncom I isolator design was modified to meet Syncom II requirements (Figure 6-14). For operation at the new frequencies, the garnet diameter was decreased and the transverse magnetic field increased. A typical performance curve is shown in Figure 6-15. The 2119-mc isolator is used in the local oscillator channel of the multiple-access transponder.

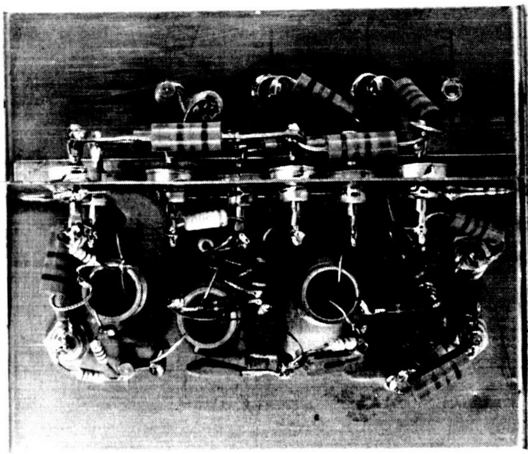

FIGURE 6-13. TOP VIEW OF 54-MC IF LIMITER

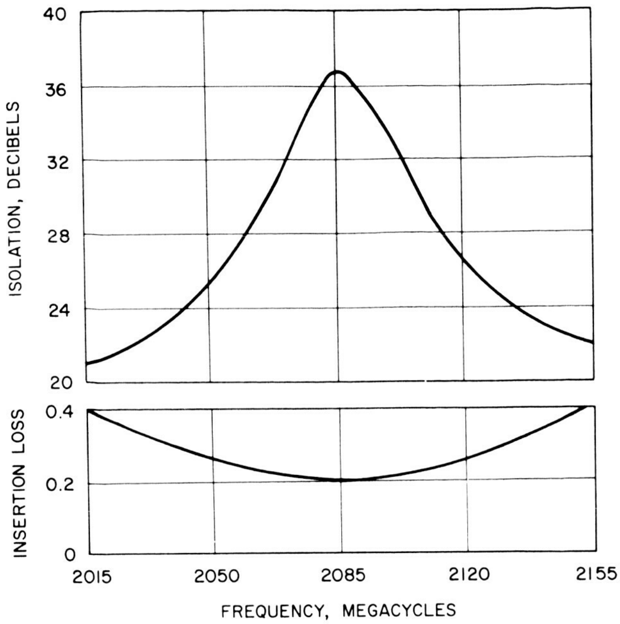

FIGURE 6-15. TYPICAL SYNCOM II ISOLATOR PERFORMANCE

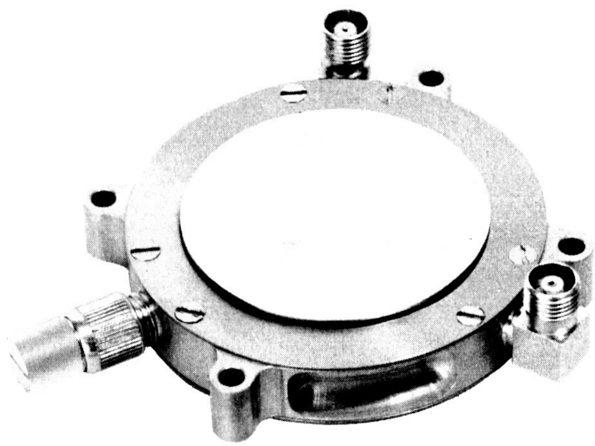

FIGURE 6-14. ISOLATOR REDESIGNED FOR MARK II TRANSPONDERS

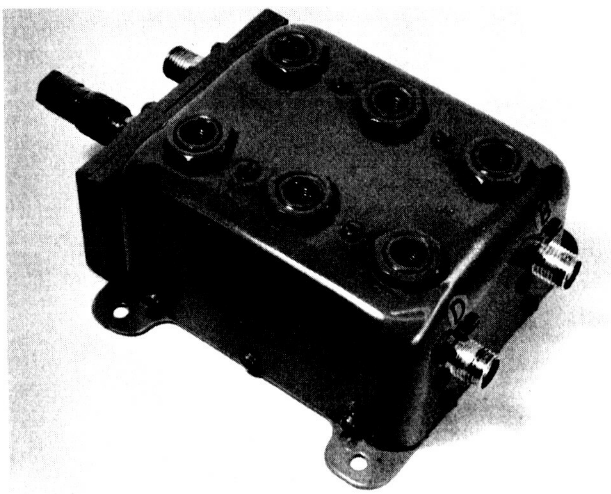

FIGURE 6-16. 2112 MC DUAL FILTER HYBRID

DUAL-FILTER HYBRID (2112 MC)
(Rantec Subcontract)

A purchase order was released to Rantec to supply the 2112-mc dual-filter hybrid (Figure 6-16). Delivery of the engineering model units was made on schedule. This hybrid is scaled from the 1849-mc dual-filter band of Syncom I, with the additional change of level difference between the two output arms.

Specifications are as follows:

Center frequency (f_o)	2112 mc
Insertion loss (f_o)	1.25 db maximum
VSWR (f_o)	1.20:1 maximum
Rejection ($f_o \pm 40$ mc)	40.0 db minimum
Hybrid output ratio	6.0 db $\pm$ 0.5 db
Hybrid directivity (f_o)	20.0 db minimum
Isolation between filters ($f_o \pm 40$ mc)	90.0 db minimum
Weight	8 ounces maximum

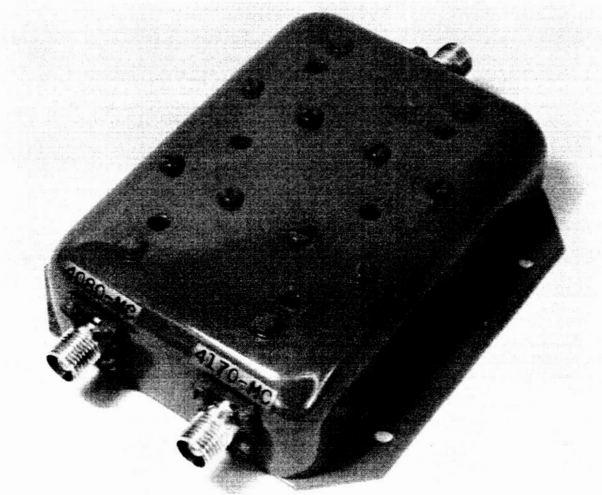

FIGURE 6-17. 4080 AND 4170-MC DUAL-SINGLE SIDEBAND FILTER DIPLEXER

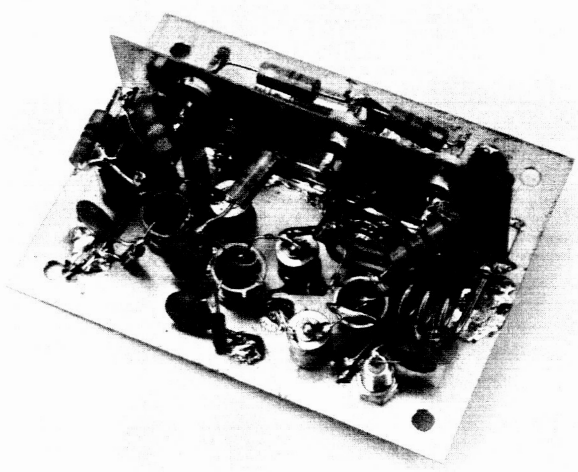

FIGURE 6-18. 144-MC BEACON OSCILLATOR

DUAL SINGLE-SIDEBAND FILTER-DIPLEXER (4080-4170) (Rantec Subcontract)

All of these units were delivered and checked out, and although they did not optimally meet specifications, they operated within acceptable limits. This filter-diplexer will select the 4170-mc modulation sideband from the high-level mixer and diplex this signal with the 4080-mc beacon signal (Figure 6-17).

Specifications are as follows:

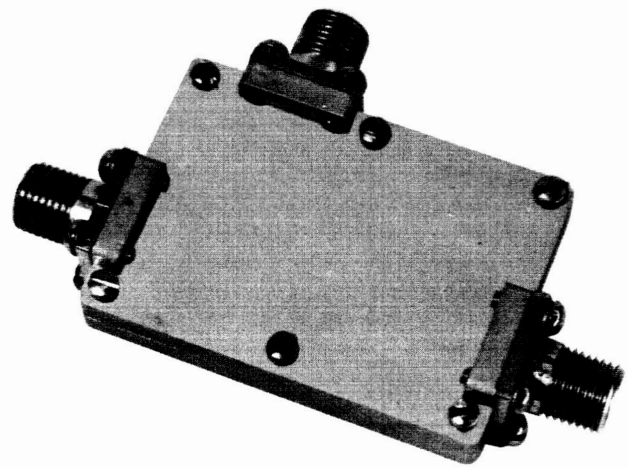

FIGURE 6-19. 14-DB COUPLER

Frequency ($f1_0$)	4080 mc
Insertion loss	1.0 db maximum
Bandwidth at 1.2 VSWR	25 mc minimum
Rejection at 4170 mc	25 db minimum
Frequency ($f2_0$)	4170 mc
Insertion loss	1.0 db maximum
Bandwidth at 1.2 VSWR	25 mc minimum
Rejection at 4080 mc	25 db minimum
Weight	6.5 ounces maximum

BEACON OSCILLATOR (144-MC)

All required beacon oscillators were designed, fabricated and checked out satisfactorily (Figure 6-18). The circuits provide the desired 3 milliwatts at 144 mc.

Test specifications are as follows:

Beacon oscillator	
Power output:	6.2 mw
Power input:	237 mw (9.87 ma at — 24 volts)
Frequency:	144 mc nominal

14-DB COUPLER

Design, fabrication, and checkout of the required couplers was satisfactorily completed. (See Figure 6-19.)

HIGH-LEVEL AND BEACON MIXERS

Initial hardware development of the high level mixer was initiated using Syncom I types. An alternate mixer approach was considered in parallel to this development; it consisted of a varactor diode modulator as the first stage of a two-stage mixer. The required 4224-mc drive power was to be reduced sufficiently to permit a common (power level) design for all three X32 multiplier application in the dual-mode transponder. The next development phase consisted of modification of Syncom I mixer mounts for compatibility with Syncom II frequencies. A branch-line hybrid was developed for use in this mixer. The design of the 4-kmc mixers (Syncom I technique) permitted interchangeable usage for high-level and beacon mixer operation. Hybrids for the high-level mixer were fabricated and placed in service. They were integrated with the diodes to complete the combined high-level and beacon mixer configurations. These units were checked out and met the high-level mixer requirements.

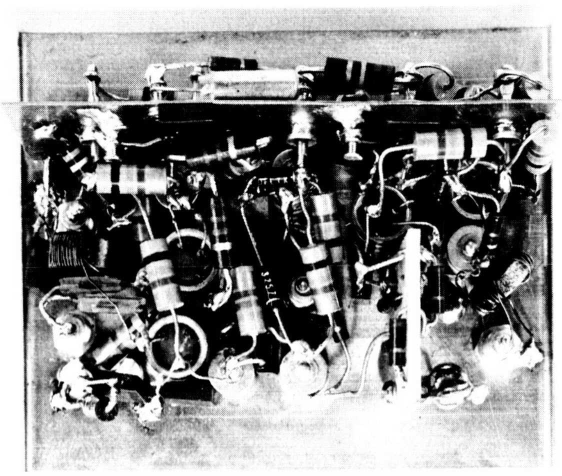

FIGURE 6-20. 32.5 — mc PHASE MODULATOR

RECEIVER MASTER OSCILLATOR (66.223 MC)

The receiver master oscillator was fabricated and checked out electrically. The power and frequency met design requirements.

Test specifications:

Master oscillator

Power output:	400 mw
Power input:	1.3 watts (55.6 ma at —24 volts)
Frequency:	66 mc nominal

IF PHASE MODULATOR

The IF phase modulator (Figure 6-20) is employed in the multiple-access transponder to convert, without demodulation, the received band of single-sideband signals to a low deviation phase-modulated signal at 32.5 mc. The 32.5-mc signal is subsequently multiplied up in frequency to produce a wide-deviation phase-modulated 4-kmc signal which is amplified for transmission by the traveling-wave tube.

The required IF phase modulators were designed and fabricated. These units were subsequently checked out and met all requirements.

Test specifications are as follows:

Power output with 2 mw from transmitter master oscillator: 1.0 mw

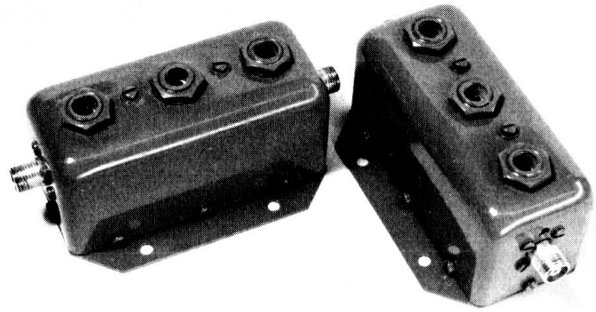

a) 2085 mc b) 2119 mc

FIGURE 6-21. SINGLE SIDEBAND FILTERS

Power input:	745 mw (31 ma at —24 volts)
Modulation sensitivity for index of 0.002 with —50 dbm:	IF input
Bandwidth:	32.578125 ±4.5mc

SINGLE-SIDEBAND FILTER (2085 MC)
(Rantec Subcontract)

Delivery of three single-sideband filters was completed on schedule (Figure 6-21). The filters were tested and met the following specifications.

Resonant frequency	2085 mc
Bandwidth	
120 : 1 VSWR	16 mc minimum
25.0 db	110 mc minimum

Insertion loss	0.75 db maximum
VSWR	1.20 : 1 maximum
Weight	2.5 ounces maximum

TRANSMITTER MASTER OSCILLATOR (32.5-MC)

All required transmitter master oscillator units were designed, fabricated, and checked out according to design requirements (Figure 6-22). Additional testing now in process consists of determination of the short term stability. This oscillator was mated to the phase modulator. The test specifications are as follows:

Transmitter master oscillator

Power output:	2 mw
Power input:	105 mw (4.4 ma at —24 volts)
Frequency:	32.578125 mc nominal

FILTER-ISOLATOR (2085 AND 2119 MC) (Rantec Subcontract)

A purchase order was released to Rantec to supply these filters. Delivery of all engineering models was completed. The filters have been tested and meet the following specifications:

FILTER (2119 MC)

Resonant frequency	2119 mc
Bandwidth	
1.20 : 1 VSWR	6.0 mc minimum
50.0 db	132 mc maximum

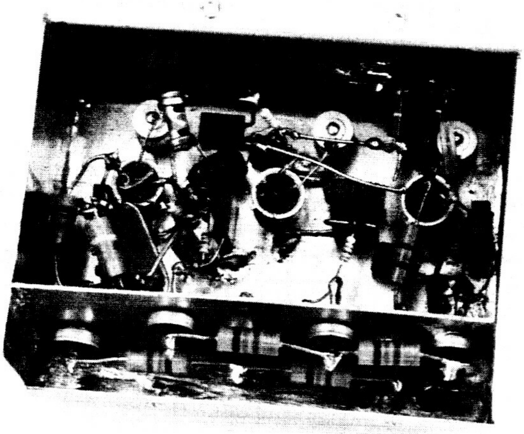

FIGURE 6-22. 32.5 mc TRANSMITTER MASTER OSCILLATOR

Insertion loss	1.25 db maximum
VSWR	1.20 : 1 maximum
Weight	2.5 ounces maximum

DOUBLER/AMPLIFIER (32.5/65 MC)

These units were completed on schedule and incorporated in the engineering model. The test specifications are as follows:

Power output with 1 mw drive:	100 mw
Power input:	985 mw (41 ma at — 24 volts)
Bandwidth:	65 mc $\pm$4.5 mc

5.8-MC BANDWIDTH PREAMPLIFIER

The two required units were designed, fabricated, and checked out. Only slight modification from the original design was necessitated to increase gain.

4 GC AND 6 GC MULTIPLEXERS (Rantec Subcontract)

Investigation was undertaken to determine an optimum design approach and basic electrical and mechanical parameters for a pair of four-channel multiplexers operating in the 4 and 6 Gc regions. These multiplexers must combine the desirable qualities of low loss, good impedance match, low weight, convenient configuration, and stability under vibration, shock, and temperature changes. After evaluating the various types of multiplexer circuits, a circuit consisting of four directional filters in cascade was selected and details of layout, size, and electrical performance were determined.

Two types of waveguide directional filters that would be suitable for the Syncom II application are shown in Figure 6-23. The one in (a), utilizing two 3-db hybrid couplers and an identical pair of rectangular waveguide bandpass filters, has been widely used in microwave communication systems for many years. The one in (b), utilizing a dual-mode circular waveguide filter coupled to the broad walls of two rectangular waveguides, has had considerable application in more recent years. Comparatively, type (a) is simpler to develop and tune, while (b) is more compact and less heavy. Because of the importance of the latter advantages in the Syncom II application, (b) is the preferable directional filter configuration.

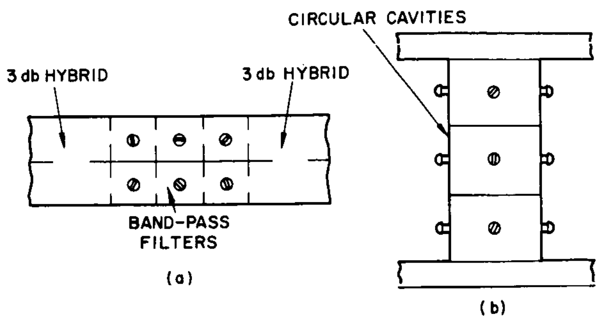

FIGURE 6-23. ALTERNATE WAVEGUIDE DIRECTIONAL — FILTER STRUCTURES

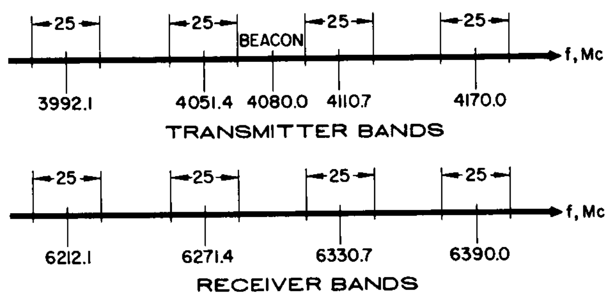

FIGURE 6-24. FREQUENCY BANDS OF TRANSMITTER AND RECEIVER MULTIPLEXER

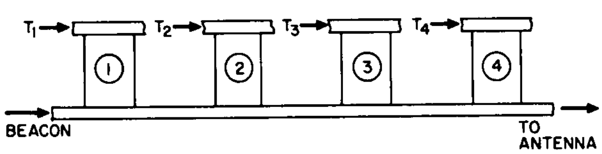

FIGURE 6-25. TRANSMITTER MULTIPLEXER CIRCUIT

FILTER RESPONSE PARAMETERS

The specified frequency bands for the transmitter and receiver multiplexers are shown in Figure 6-24. In both cases the channel bands are 25 mc wide. However, the design of the filters must take account of temperature effect on the center frequencies. Since the coefficient of linear expansion of aluminum is $26(10)^{-6}/°C$, the filter center frequencies will change by $-26(10)^{-6}f_0/°C$. Assuming a temperature range of $\pm 25°F$, or $\pm 14°C$, then at $f_0 = 4100$ mc, f_0 varies by ± 1.3 mc, and at $f_0 = 6300$ mc by ± 2.0 mc. In order to allow for this variation, the filter bands should be widened on each side by 1.3 mc in the transmitter case and 2.0 mc in the receiver case. A further widening should be made to allow for errors in alignment and in the operating frequencies.

Therefore, the channels were assumed wider by a total of 2.0 mc on each side in the transmitter case and 3.0 mc in the receiver case. Thus, in the transmitter case the passband was assumed to lie between $f_0 \pm 14.5$ mc, while the edges of the adjacent channels were assumed at $f_0 = 44.8$ mc. In the receiver case these frequencies are $f_0 \pm 15.5$ and $f_0 = 43.8$ mc, respectively.

Figure 6-25 shows the directional-filter circuit for the transmitter multiplexer. Note that energy from each transmitter except T_4 passes at least one of the other directional filters. Consider T_1 at f_1, for example. Since filters 2, 3, and 4 have finite stop band loss at f_1, some of the energy at f_1 will pass through these filters and be absorbed in their loads. For example, if filter 2 has 17 db stop band loss at f_1, 2 percent of the f_1 power will be removed from the main waveguide, causing a transmission loss of 0.1 lb. If the filter 2 stop band loss is 27 db at f_1, the transmission loss for f_1 will be 0.01 db.

In order to minimize power loss into the adjacent channel, an insertion loss of 27 db at $f_0 \pm 59.3$ mc was assumed. It was also desirable that the insertion loss exceed 17 db at $f_0 \pm 44.8$ mc. After examining the theoretical response curves of various filters, it was determined that a three-cavity design was necessary to achieve these adjacent-channel insertion losses, while maintaining low loss in the passband. The design selected was one based on a loss-less three-element low-pass filter prototype having an 0.01 db equal-ripple response. The theoretical insertion losses at various frequencies of interest are listed below.

$\Delta f/0$ *mc*	*L/0 db*
± 12.2	0.01
± 12.5	0.02
± 14.5	0.1
± 15.5	0.2
± 23.0	3.0
± 29.7	8.2
± 43.8	18.5
± 44.8	19.5
± 59.3	27.0

The same filter parameters are suitable in both the transmitter and receiver cases.

LOSSES IN THE MULTIPLEXER

There are a number of significant sources of loss in the multiplexer. Consider first the transmitter multiplexer case. The losses are examined individually below.

Dissipation Loss in Bandpass Filter. The center frequency dissipation loss, L_o, can be computed easily in terms of the filter bandwidth and the cavity unloaded Q, Q_u.[3]

$$L_o = \frac{4.34\ \omega_1'}{Q_u\ w_1} \sum_{1}^{3} g_i \qquad (6\text{-}1)$$

where the various symbols are as defined in Reference 3.* At 4200 mc the theoretical Q_u of a cylindrical copper TE_{111}-mode cavity is about 19,000. A *practical* value of Q_u would be about 20 percent less, or about 15,000. Substituting this and the various filter and bandwidth parameters into Equation 6-1 yields

$$L_o = 0.11 \text{ db}$$

for the transmitter case. At the band edges, the dissipation loss will be about 1.5 times this, or about 0.16 db.

In the receiver case, the estimated center frequency loss is 0.22 db at f_o and 0.30 db at the band edges.

Scattered-Wave Loss in Directional Filter. With reference to Figure 6-26, the desired path for the energy at f_1 is from ports 1 to 3. However, due to imperfections in the directional filter, a small amount of the f_1 energy will be reflected back toward the transmitter at port 1, and other small amounts will be lost at port 2 and port 4. An estimate of the loss due to these three scattered waves is 0.09 db at f_o and 0.25 db at ± 14.5 mc in the transmitter case. In the receiver case, the estimated loss is 0.10 db at f_o and 0.35 db at ± 15.5 mc.

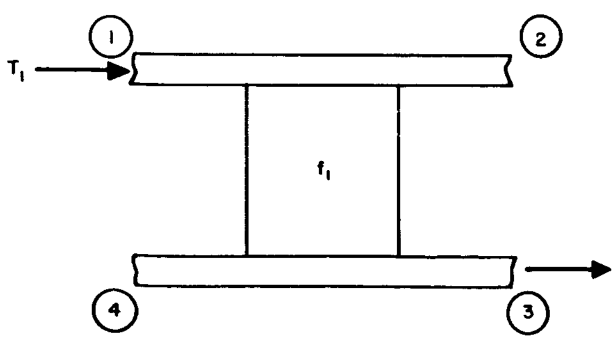

FIGURE 6-26. TRANSMITTER DIRECTIONAL FILTER

Loss in Load of Adjacent-Channel Filter. Consider one of the transmitter directional filters in Figure 6-25, such as filter 2, and assume that an adjacent channel filter (filter 3) is located between filter 2 and the antenna. At the center frequency of filter 2, filter 3 has 27 db insertion loss. Therefore, the power passing through filter 3 into its load will cause a loss of 0.01 db for f_2. At the band edge of filter 2 nearest f_3, this loss will be 0.06 db. In the receiver case a safer value is 0.07 db at the band edge.

The losses into the loads of nonadjacent filters will be negligible.

Dissipation Loss in Other Filters. As energy from one transmitter passes other directional filters on the way to the antenna, some of the transmitter energy will enter the input cavities of these other filters resulting in dissipation loss on the cavity walls. For the adjacent-channel filter this loss is estimated to be less than 0.01 db, while for nonadjacent channels the loss would be considerably less. For T_1 the total loss due to dissipation in filters 2, 3, and 4 is estimated to be less than 0.02 db for f_1 at band center, and 0.04 db at the most unfavorable band edge. In the corresponding receiver case, 0.04 and 0.08 db respectively are more appropriate.

Rectangular Waveguide Loss. In the transmitting case, assuming a reasonable length of 2 x 0.5 inch aluminum waveguide, the estimated rectangular waveguide loss is 0.09 db between T_1 and the antenna port. In the receiving case, assuming 1½ x ¾ inch waveguide, this loss is estimated at 0.10 db.

Beacon Transmitter Loss. The beacon transmitter emits a narrow-band signal at $f_b = 4080$ mc. This lies almost half way between the frequencies of filters 2 and 3 in the transmitter multiplexer. If the beacon signal is inserted as shown in Figure 6-25, the principal loss will result from beacon power diverted by filters 2 and 3 into their loads. On the average, f_b lies $59.3/2 = 29.7$ mc away from the center frequencies f_2 and f_3. At this point the filter insertion loss is 8.2 db. As a result, each of these filters causes an 0.7 db loss of beacon power in the main waveguide, or 1.4 db for the two filters. When waveguide and other losses are added, 2.0 db loss seems reasonable for the beacon transmitter.

*S. B. Cohn, "Dissipation Loss in Multiple-Coupled-Resonator Filters," Proc. IRE, Vol. 47, No. 8, pp. 1342-1348 (August 1959).

Total Loss. In addition to the above losses, about 0.1 db for the transmitter case and 0.15 db for the receiver case should be added to allow for various other unaccountable losses, such as flange contact loss, coax-to-waveguide-junction loss, etc. When all the losses are added along the multiplexer, the following theoretical estimates are obtained.

Estimated Losses for Transmitter Multiplexer

Transmitter	*Estimated Loss at f_o*	*Estimated Loss at ± 14.5 mc*
1	0.42 db	0.70 db
2	0.40	0.67
3	0.37	0.63
4	0.27	0.53
Beacon	2.0	—

Estimated Losses for Receiver Multiplexer

Receiver	*Estimated Loss at f_o*	*Estimated Loss at ± 15.5 mc*
1	0.61 db	1.04 db
2	0.58	1.01
3	0.55	0.98
4	0.49	0.82

In the above tables, the numbering of the transmitters and receivers starts at the end of the multiplexer farthest from the antenna. Of course, specified losses for these multiplexers must include some allowance for manufacturing tolerances.

RECOMMENDED PHYSICAL SPECIFICATIONS

Figures 6-27, 6-28, and 6-29 show sample layouts for the transmitter and receiver multiplexers. Type TNC connectors would be used at all ports. Note that three directional filters are sufficient for the receiver case (Figure 6-29). However, the fourth directional filter of Figure 6-24 might be desired to provide off-channel rejection and impedance match for R_1. In the transmitter case, the four directional filters of Figure 6-27 are necessary to enable injection of the beacon signal.

In the layout shown, the transmitter multiplexer falls inside a cylindrical space of 26-inch diameter and 3¾ inch height. Its weight, not including mountng structure, is estimated at 5.5 pounds.

In computing the weight of the transmitter multiplexer, it was assumed that aluminum parts would be used throughout. The rectangular waveguide would be 2 x 0.5 inch outside diameter by 0.064 inch wall, while the circular cavities would be machined with 0.125 inch walls. The miniaturized flanges are needed

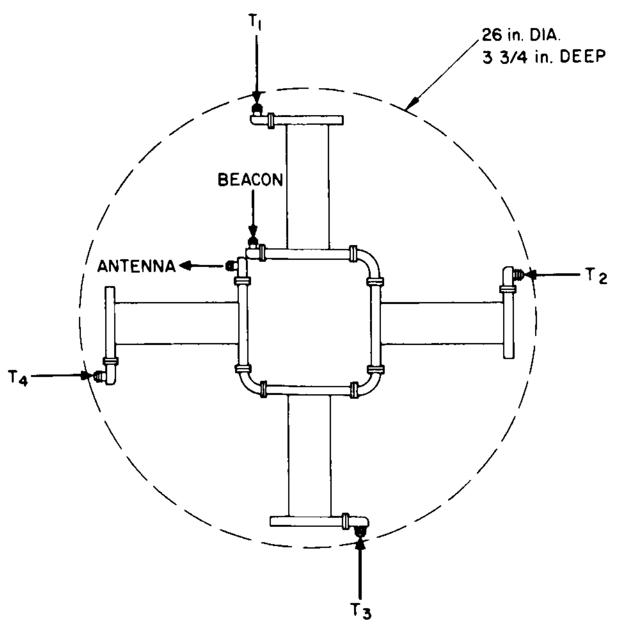

FIGURE 6-27. TRANSMITTER MULTIPLEXER

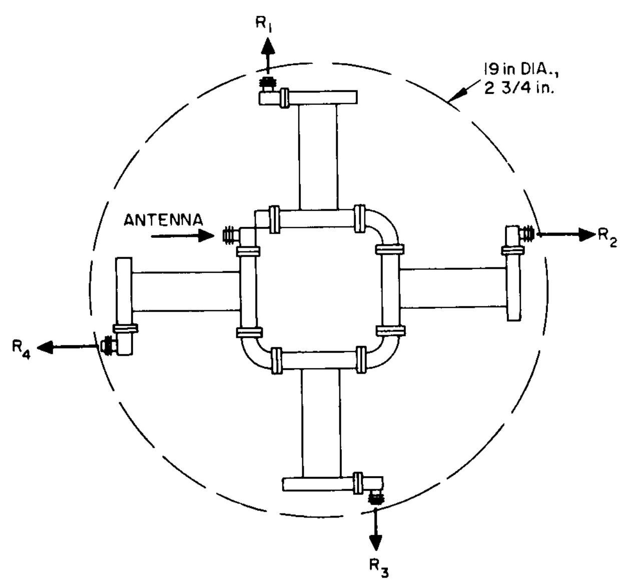

FIGURE 6-28. RECEIVER MULTIPLEXER UTILIZING FOUR DIRECTIONAL FILTERS

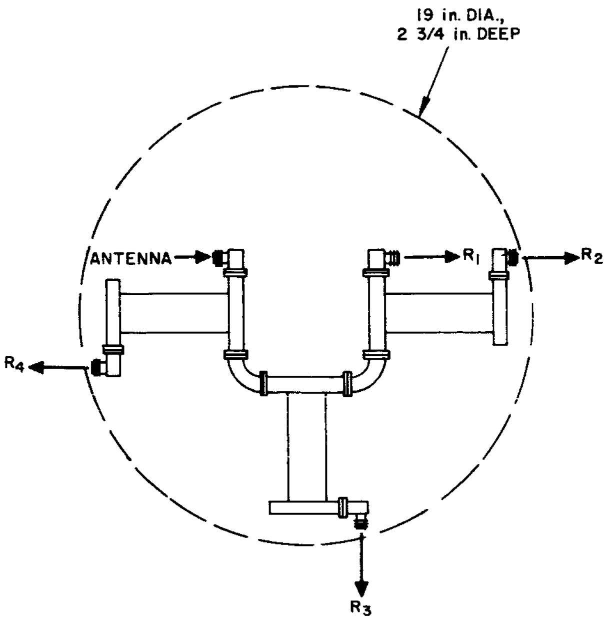

FIGURE 6-29. RECEIVER MULTIPLEXER UTILIZING THREE DIRECTIONAL FILTERS

so that the individual directional filters can be aligned and tested before assembly into the multiplexer. The weight breakdown is as follows:

Transmitter Multiplexer

Rectangular waveguide	1.80 pounds
Circular cavities	2.40
Miniature flanges	0.55
Irises, end pieces, connectors, screws, etc.	0.70
	5.45 pounds

In the layout shown, the receiver multiplexer will fall inside a cylindrical space of 19-inch diameter and 2¾ height. If four directional filters are used, (Figure 6-28), the estimated weight, not including mounting structure, is 3.0 pounds. If three directional filters are used (Figure 6-29), the estimated weight is 2.3 pounds.

The weight computation of the receiver multiplexer assumes 1½ x ¾-inch outside diameter rectangular waveguide with 0.064-inch walls. The walls of the cylinders are assumed 0.100 inch in thickness. The breakdown of weight is as follows for Figure 6-28:

Receiver Multiplexer

Rectangular waveguide	1.13 pounds
Circular cavities	0.84
Miniature flanges	0.45
Irises, end pieces, connectors, screws, etc.	0.55
	2.97 pounds

The wall thicknesses assumed in the weight calculations would provide the dimensional stability needed in these relatively narrow-bandwidth, highly sensitive filters. It is possible that thinner walls might suffice; however, the resulting weight saving should be compared to the increase of weight that might then be necessary in the supporting structure.

TRAVELING-WAVE TUBE

The initial goals of the traveling-wave tube program were to develop a tube having a minimum power output of 2.5 watts at 4.080 Gc with a bandwidth of ± 102.5 mc. Efficiency, including the heater power, was to be greater than 20 percent and saturated gain greater than 36 db. The ruggedness and environmental capabilities of the Syncom I traveling-wave tube were to be reproduced and improved upon at the higher frequency. A minimum of 3 years life with a designed life of 5 years was also required. The first ten tubes were constructed to these specifications. Spacecraft changes then required that the tube output power be raised to a minimum of 4 watts; also, because of the high efficiency obtained in the early tubes, the minimum beam efficiency was raised to 30 percent which, with heater power included, would give a tube efficiency of 27 to 28 percent. Somewhat later it was also requested that the saturated gain be raised to about 40 db. Several experimental tubes were made to facilitate these design changes. Some of the tubes were designed to obtain even greater power output and gain, thereby enabling complete evaluation of the tube capabilities. Several major accomplishments are summarized here and discussed in more detail subsequently.

1) The mechanical design, structural integrity, and reliability of the Syncom I tube have been reproduced at C-band and several improvements have been added.
2) A new gun design has been used to obtain better focusing and lower cathode loading than obtained in the Syncom I traveling-wave tube.

3) The current intercepted by the helix has been reduced to less than 2 ma.
4) It has been shown that, with minor changes, the tube design is capable of 20 watts of power-out and-gain up to 50 db without instability.
5) Beam efficiency (tube efficiency, which includes the heater power, is about 2 percent lower than beam efficiency) as high as 45 percent has been achieved and it appears that 35 to 40 percent can be expected through production with minor additional development effort.
6) A review of tube bakeout, cathode activation schedule, and parts processing and heat treatment has been completed to assure that the 5-year life is reasonable. Also, accuracy calculations have been made to better determine the life expectancy through cathode "wearout."
7) An experimental study has been made of the encapsulating material based on a goal of 5 years life.
8) Additional controls and inspection procedures have been initiated to improve quality control. Parts traceability from the final tube to the raw material lot is now possible.

Approximately 30 tubes have been made. One tube, 384H-13, has been subjected to qualification tests as severe as those of the Syncom I tubes. Two designs have been achieved, accomplishing all the desired electrical performance specifications. However, not enough tubes of either design have been fabricated to ascertain final production tube configuration. Also, further optimization efforts of both designs will be made prior to production phase.

Tube 384H-13, now undergoing qualification tests, is shown in Figure 6-30. This tube is 9 inches long

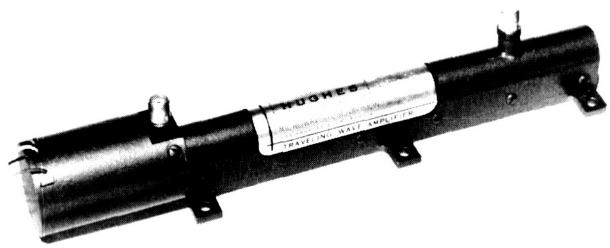

FIGURE 6-30. 384H-13 TRAVELING-WAVE TUBE

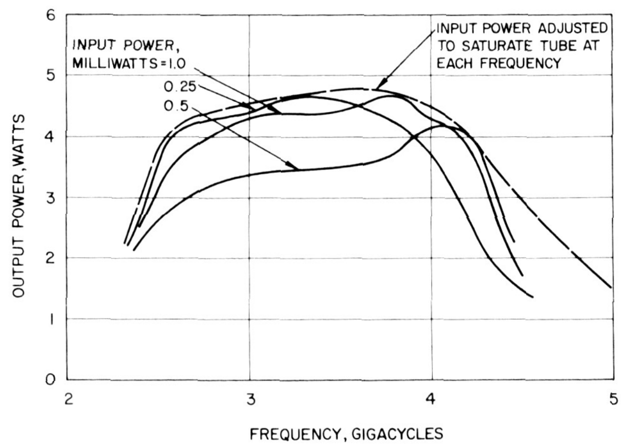

FIGURE 6-32. POWER OUTPUT AS FUNCTION OF FREQUENCY FOR VARIOUS INPUT POWER LEVELS

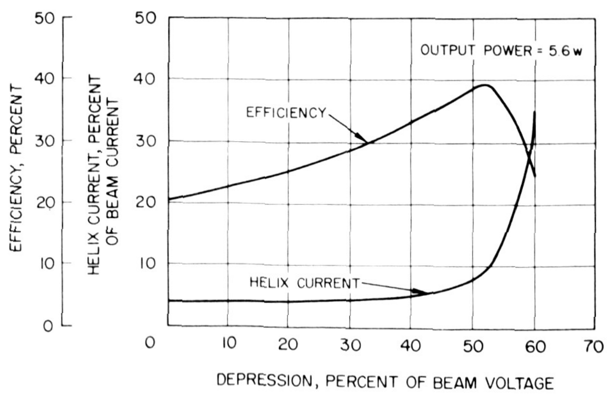

FIGURE 6-31. EFFICIENCY AND HELIX INTERCEPTOR AS FUNCTION OF COLLECTOR DEPRESSION

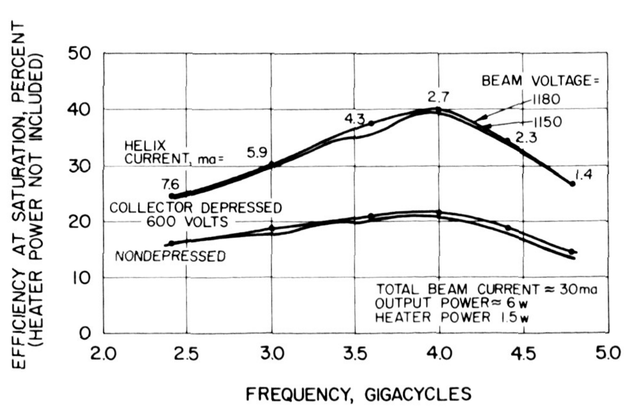

FIGURE 6-33. EFFICIENCY AT SATURATION VERSUS FREQUENCY EFFICIENCY optimized at desired frequency

and weighs 17.5 ounces. At 4 Gc, the power-out is 5.5 watts with 1 mw RF power-in. The tube voltages (with respect to the helix) and currents are:

Element	*Voltage*	*Current*
Cathode	− 1160	23.62 ma
Anode	+ 300	0.32 ma
Helix	0	1.80 ma
Collector	− 600	21.5 ma
Heater	4.5	0.260 amp

The gain at 1 mw input is 37.4 db and the tube efficiency is 35 percent including the heater power.

The considered-excellent depression characteristics of tube 384H-13 (accounting for the high efficiency) are shown in Figure 6-31. Power-out as a function of frequency with input power as the parameter is shown in Figure 6-32, and the corresponding efficiency at saturation for a nondepressed and a depressed collector is shown in Figure 6-33. The latter two figures illustrate a tube characteristic which has been concentrated upon to obtain the high efficiency of the 384H tube series. This series has, inherently, a bandwidth much greater than required for the Syncom mission. The required operating frequency range can be chosen anywhere within the tube's inherent bandwidth. For most applications (including narrow-band space missions) the operating range is usually chosen from within the tube's inherent bandwidth. However, in the present case there is a definite advantage to centering operation at the high end of the natural band, as illustrated in Figures 6-32 and 6-33. Although the tube power output is relatively constant over a broad band, the beam transmission, in a manner characteristic of defocusing effects in the presence of RF, improves toward the high end of the band. This is important since the power to the helix stays constant or increases with collector depression and represents a larger proportion of the dissipated power as the collector is depressed further. Thus, when the collector is depressed, efficiency is greater at the high end of the inherent passband. For this reason, operating in that region has been stressed.

Recorder tracings of the power output as a function of power input, with beam voltage as a parameter (compression curves) are shown in Figure 6-34. It be seen that the curves rise rapidly as the input power is increased, then flattens out at saturation and drops again rather rapidly. Because the power-out drops

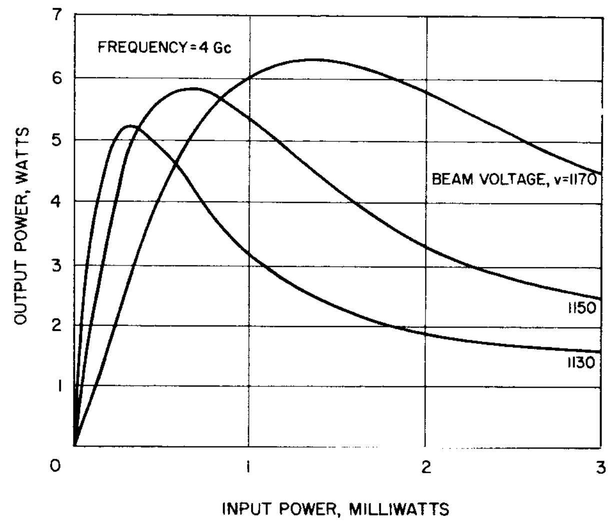

FIGURE 6-34. POWER OUT VERSUS POWER IN FOR VARIOUS BEAM VOLTAGES

when the tube is oversaturated, the power-out varies rapidly with changes in beam voltage. Essentially, the same variation occurs when frequency is changed instead of voltage and the reason is the same. Performance would be much less sensitive to changes in voltage, frequency, and input power if the power-out did not drop in the oversaturation region. Experiments with the other tubes show that the compression curves can be flattened by lengthening the loss region of the helix, and this should accordingly be accomplished in the production tube.

It has been found that the output power of the tube can be varied from 1 to about 15 watts without adversely affecting the performance of the tube (except that life will possibly be shorter at the higher powers) by simply changing the anode voltage. The fact that this can be done is mainly attributable to the excellent gun optics. Changing the anode voltage changes the current in the beam; i.e., beam perveance is changed. As perveance is increased, the power-out and the gain increase, and generally the efficiency, will also increase slightly. It is thus possible with this tube to match the power-out characteristics of tubes in the production run if the anode voltage is allowed to vary. This feature can significantly increase the yield of the production. In contrast, the power output of the 314H Syncom I tube could also be varied by changing the anode voltage, but the helix current generally changed so rapidly with anode voltage that a low-power tube could seldom be salvaged without a critical tradeoff in reliability.

A list of tubes made with a summary of their characteristics is given in Table 6-2.

Five more tubes are in progress or have parts ready for assembly. Three of these tubes will have small helices and will be similar to No. 23 and 24; two tubes will be like No. 21 and 22. Table 6-2 shows that

TABLE 6-2. 384H TRAVELING-WAVE TUBES

Tube No.	Major Changes from Previous Tubes	Some Test Results	Status
1	....	Best operating frequency was too low (3.4 kmc). Beam voltage was also low causing low output power (1.9 watts). Focusing and depression characteristics were good. (Efficiency = 31.8 percent)	In storage. Will be scrapped to recover the magnets.
2	Same as tube No. 1. This was a backup tube. Slightly different loss distribution.	Same as tube No. 1 except somewhat lower power-out.	Scrapped.
3	Helix pitch was changed to raise the frequency and power.	Operating frequency raised as expected but a construction error limited the usefulness of the experiment.	Scrapped.
4	This was a backup to Tube No. 3.	Same as tube No. 3.	Scrapped.
5	Same as tube No. 3.	Focusing was poor. Test results were of little value.	Scrapped.
6	Same as Tube No. 3 with minor adjustments in the gun and the loss distribution.	Leak occurred in the output window. Problem was traced to poor metalization of the ceramic.	Scrapped.
7	Same as tube No. 6 except for the loss distribution.	This tube met the initial specifications except for being slightly low in power (2.4 instead of 2.5 watts). The tube had 40 percent efficiency before packaging, 25 percent after packaging. This problem was traced to potting material seeping into the output RF coupler.	Used as developmental model.
8	Change in pitch to raise power slightly. Tube was lengthened to 9 inches; previous tubes were 8 inches long.	This tube as well as No. 9 and 10 were in work when the power level was raised to 4 watts. The anode voltage was raised to obtain the power and the tube operated well. Extensive testing was done to determine the effect of anode voltage on tube operation. The tube efficiency at 4 watts out was 38 percent, but the frequency was somewhat low. At 5 watts out 45 percent efficiency was achieved.	Tube was being prepared for environmental testing when a leak developed. Problem was traced to a poor pinch-off from the ion pump.
9	Slightly different loss distribution.	Anode current was high when the tube was depressed. This is due to secondary electrons from the collector region. Experiments were run to shape the magnetic field in the collector to trap the secondary electron. The experiments were only partially successful.	Scrapped.
10	Pitch was changed and the helix diameter was made smaller to raise the frequency.	Tube operated at the proper frequency and gain was about 50 db. The match was poor and efficiency was low (28 percent).	Storage.
11	Helix diameter changed back to original value but the tube length was left at 9 inches.	Tube had a bad cathode and also oscillations due to poor match.	Scrapped.
12	Helix pitch changed to experiment with much higher power.	Tube did not focus too well, power-out was about 16 watts. Tube started to oscillate during focusing causing a deterioration in the loss.	Scrapped.
13	Similar to no. 11.	Tube met performance specifications. Beam efficiency = 39 percent at 4 kmc. Focusing was excellent with beam interception low.	Tube is being subjected to environmental testing.
14	Similar to 12.	This tube operated well at up to 13 watts power-out. However, the gain was very high and some difficulty with oscillation occurred.	Storage.

TABLE 6-2. 384H TRAVELING-WAVE TUBES (Cont'd)

Tube No.	Major Changes from Previous Tubes	Some Test Results	Status
15	Tube was lengthened to determine how high gain could be raised and stability retained.	Testing on this tube and tube No. 16 is not completed.	Awaiting further testing.
16	Same as No. 15.	See No. 15 above.	Awaiting further testing.
17	Same as No. 13.	This tube had about the same characteristics as No. 13 but had a somewhat greater bandwidth. Efficiency = 38 percent.	This tube was pinched off a day later than No. 8 and also developed a leak. Trouble was traced to the pinch-off tool which has since been reworked. Tube is being reworked.
18	Same as No. 13.	Tube developed a leak and has not yet been RF checked.	Tube is being reworked.
19	Design was changed slightly to optimize the frequency. Small helix design similar to No. 10.	Tube was accidentally broken during focusing.	Scrapped.
20	Similar to tube Nos. 10 and 19; this was an attempt to optimize the smaller helix diameter tubes.	Bandwidth was well centered but beam voltage was low.	Storage.
21	Similar to No. 13 but with improved RF match.	Construction difficulties have held up the testing.	Tube is being reworked.
22	Same as No. 21.	Tube meets specifications but efficiency is lower than tube No. 13 (34 percent at 4 Gc).	Tube will undergo further testing to evaluate the effect of the match change.
23	Modification of No. 20 to raise the power.	Tube is undergoing test. Initial data is good.	....
24	Small helix tube similar to No. 23.	Tube is on bakeout.	....

two designs have been developed. The first is similar to tube No. 13; this series of tubes meets the specifications but requires a relatively high anode voltage, 300 to 500 volts. The second design has a smaller helix diameter and is centered somewhat higher in frequency; these tubes will have a lower anode voltage, below 300 volts, but will also have somewhat less efficiency. Upon completion of the tubes listed and after detailed evaluation of the data, the design will be finalized. If the desired tube differs, but not greatly, from the two designs already achieved, then two or three tubes will be needed for design finalization.

Tube Life

The 384H tube has been designed to have a "wear-out life" of greater than 5 years. However, several critical factors are considered for assurance that the expected life is reasonable. The most critical factor is the life of the cathode. One secondary consideration is the tube's packaging. A study of the encapsulating material has therefore been initiaited.

Cathode Life

In a properly designed vacuum tube, the ultimate, or wearout life, is determined by eventual deterioration of electron emission from the cathode. The initial estimate of cathode life was based on the relation of expected life directly to cathode current density. This relationship is shown in Figure 6-35. However, Figure 6-35 does not distinguish between two cathodes operated at the same current density but having different base metal additives, different cathode thicknesses, different coating volumes, or operating at different temperatures and in different poisoning environments. Also, the only extensive life test results available on traveling-wave tubes (the Bell Relay Tube shown on Figure 6-35) indicate that initial estimates are pessimistic or possibly inaccurate. Because of the 384's

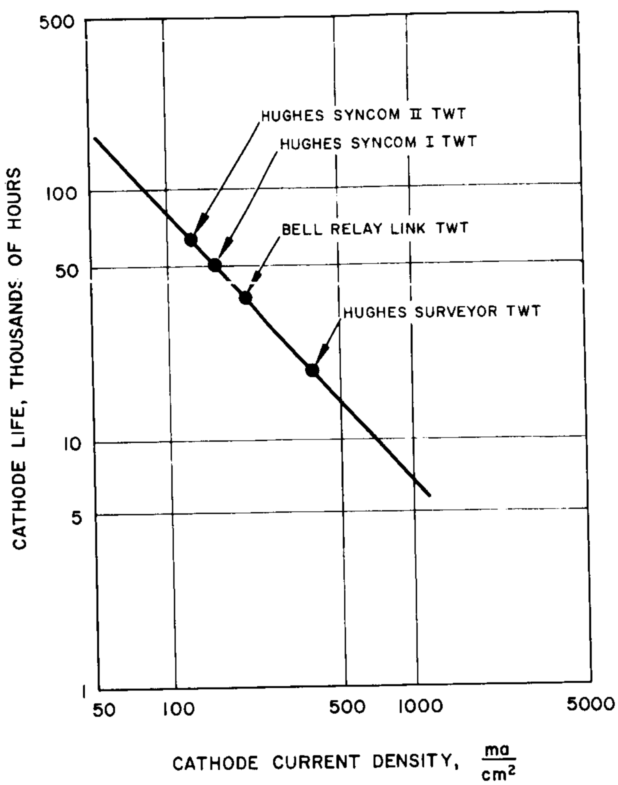

FIGURE 6-35. RELATION BETWEEN EXPECTED CATHODE LIFE AND CATHODE CURRENT DENSITY

long life requirement, additional calculations were made. For background of this investigation a more complete discussion follows.

An oxide cathode consists of a nickel pellet coated with a mixture of barium-strontium oxide (Ba Sr)0, usually abbreviated as BaO. The cathode must be heated to 650 to 800°C to act as a useful emitter. Pure BaO itself is a poor emitter; however, introduction of free barium atoms into the BaO coating produces an active thermionic emitter. During emission, the BaO coating acts as an n-type, excess-impurity semiconductor, with Ba as the impurity donor. Thus an adequate level of Ba donors must be maintained if emission is to be preserved. This level is believed to be that required to saturate the BaO coating, probably less than 0.01 percent (by weight) of free barium. Unfortunately, the Ba atoms are continuously being depleted through evaporation and through chemical reaction with residual gas molecules and ions. (Even at a vacuum as good as 10^{-9} millimeter of mercury, there remain many billions of gas molecules in just the electron gun portion of the tube.)

If emission is to be maintained, these lost Ba atoms must be continuously replaced at a rate equal to, or greater than, the sum of the evaporation rate plus the gas "poisoning" rate. The required replacement Ba atoms are produced by chemical reduction of the BaO coating molecules to produce free Ba plus an oxide of the reducing agent. The reducing agent consists of an impurity element which is purposely introduced into the nickel base metal raw material before the cathode pellet is fabricated. When the cathode is heated during operation, this additive diffuses continuously through the nickel pellet to the BaO coating where it chemically reduces the coating to produce the required Ba atoms.

Based on this model of the oxide cathode, it is clear that end of life will occur when the rate of production of new Ba atoms falls below the rate of poisoning, and evaporation loss of Ba atoms. According to the diffusion dependency hypothesis (see, for example, H. E. Kern, "Research on Oxide Cathodes," Bell Laboratories Record, December 1960), the rate of BaO reduction to free Ba is determined by the rate at which the base metal additive arrives at the BaO-nickel interface, and thus, the Ba production rate is controlled by the diffusion rate of the additive through the base nickel. As the additive is used up during life, this diffusion rate slowly decreases, until finally, when the additive concentration in the base metal has dropped to 50 or 60 percent of its original value, the diffusion rate begins to drop quite rapidly. End of life occurs when the additive diffusion rate is too low to provide free barium at a rate which will overcome barium losses. Thus, to calculate the cathode life, two important facts must be known: 1) the diffusion of base metal additive as a function of time throughout life, and 2) the Ba atom loss rate (so-called "poisoning" rate) in the tube late in life. Unfortunately, only the first of these can be calculated; the second must be inferred from actual life tests which have been run to completion.

The diffusion rates for the 384H cathode have been calculated and are shown in Figure 6-36 as a function of cathode operating temperature.

The expected operating temperature is somewhere between the two extremes shown. The calculations are based on the use of zirconium as the base metal addi-

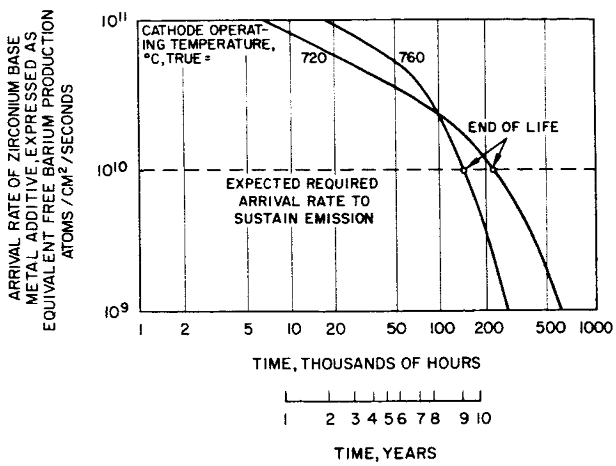

FIGURE 6-36. COMPUTED BASE METAL IMPURITY DIFFUSION RATE

tive element. This additive has been used for all Hughes space TWTs to-date, as well as the BTL Telstar TWT. This choice is based on extensive experimental studies using various impurities which indicate the Zr produces the highest activity for the longest period of time. (H. E. Kern and E. T. Graney, "Thermionic Emission and Diffusion Studies on Zirconium-Doped Nickel Cathodes," Report on Twenty-Second Annual Conference, Physical Electronics, March 1962.) For convenience, the rate at which Zr arrives at the BaO coating has been plotted in terms of the rate of Ba atom production which would result from the availability of this arrived Zr. To estimate end of life, a required minimum arrival rate must be assumed equal to the rate at which Ba atoms are expected to be lost. Based on various accelerated life studies, a conservative value is judged to be 10^{10} atoms/cm^2/sec (see references noted above). Thus, the calculated life of the 384H cathode is 140,000 to 220,000 hours, depending on cathode operating temperature.

It is seen that the life is much more strongly influenced by the arrival rate assumed to be required to maintain emission in the presence of Ba loss, than by the exact cathode temperature used. Thus a variation of 40 or 50°C in cathode temperature is not critical. However, the popular emphasis on measuring the exact minimum temperature at which full emission can be obtained in a given tube type, is of some importance, because this temperature is believed to be an indication of the poisoning atmosphere in the tube, and thus indirectly indicates the relative values of arrival rate required to sustain emission. Thus, the minimum temperature at which full emission can be achieved is probably an important yardstick, but it is not necessary that the tube actually be operated at that temperature. The strong dependence of life on the value of assumed required arrival rate emphasizes the extreme importance of the special precautions taken to minimize the poisoning atmosphere in long-life tubes. The arrival rate of 10^{10} atoms/cm^2/sec used in Figure 6-36 assumes that all these precautions have been strictly enforced. Note that a factor of 10 increase in poisoning level decreases the life from well over 100,000 hours to about 10,000 hours.

For applying the diffusion-dependent life theory, one must be certain that the amount of BaO coating available is sufficient, so that the BaO supply itself will not be depleted ahead of depletion of the zirconium. Calculations made for the presently used coating density and thickness indicate that more than adequate coating is available, thus, this is not a limiting factor in 5-year life.

The diffusion-dependency model of end of life has not been completely verified on cathodes designed for 5-year life as the time involved is so extended. However, accelerated life test data obtained, at other laboratories, by purposely designing cathodes with thinner base metal or with faster-acting additives, have tended to verify the life predicted by the theory. There exists some doubt about the failure mechanism itself, since, in one test the expected reduction in additive was not observed. However, since this theory at present most closely predicts the measured data it must suffice until additional information is available.

It is applicable to mention the effect of cathode current density on life. The life theory described, the most commonly accepted, does not, in fact, indicate any dependence at all on current density. Despite this the initial estimates mentioned previously show life as a direct function of current density. Like most general rules it is not clear on what rule this is based since the detailed accelerated life studies made to date did not include dc cathode current density as an adjustable parameter.

However, there is some indication that accelerated tests performed with tube types which happened to have lower current densities indicated a more favorable required arrival rate at end of life. Also, there are various theories relating to a possible dependence of life on cathode current density which have to do with the electrical conductivity of the coating. (Some of these are reviewed in the introduction of a report by Hollister — "Some Effects of Ion Bombardment on the Emitting Properties of Oxide-Coating Cathodes," Cornell University Research Report, EE 482.) Thus, there is some justification for this generalization but little data on which to base the exact *magnitude or slope* of the curve.

The present cathode composition, whether using the rule-of-thumb or the more sophisticated theory, has a theoretical wearout, or depletion life, in excess of 5 years. The critical factors in life dependency then involve failure due to other causes. For example, it is required that the tube processing, cathode base material heat treatment and cleaning procedures, and the cathode activation schedule be such that full use can be made of the available cathode coating and base material activating agent. Also, it is required that no element of the tube under any natural circumstance emit sufficient gas to seriously poison the cathode. To fully assure that these failure mechanisms are not present requires further work. However, a thorough review of processing, heat treatment, and cathode activation has been accomplished. As a result, some changes are being instituted; for example, humidity control of the clean room is being incorporated and a minor change in activation schedule is being evaluated. Other changes which might be considered, such as changes in heat treatment of the base material and a greater change in the activation schedule, changes in cleaning procedures, or changes in raw materials, are too drastic to incorporate into the tube without a complete experimental evaluation. The life results obtained on the 314H and other space tubes are applicable to the present tube if significant changes in processing, activation, or materials are made.

Encapsulation

The encapsulating, or potting material, serves two functions. First, the material must provide shock mounting, a function which is primarily important during launch. However, the flexibility required for shock mounting must be, at least partially, retained during the 5-year life to absorb different thermal expansion stresses between the tube and package, as the tube is temperature-cycled during times of eclipse. The second function is to conduct heat from the tube to the external package and heat sink. If the thermal conductivity changes with material degradation, the tube temperature will rise, which could accelerate degradation and cause a runaway situation. A direct thermal path from the collector to the heat sink, independent of the potting material, has been incorporated in the 384H package design to prevent a runaway condition, but for greatest reliability and life it is still important that the potting material does not deteriorate.

To evaluate the material, six structures were made, which simulate the collector region of the tube and its external heat sink. The temperature of the collector and the external heat sink are controlled by Cal-rod heaters and measured by thermocouples. For the evaluation, a test which closely duplicates actual flight conditions has been established: constant power into collector, constant temperature of spacecraft frame and high vacuum. The simulated collectors are placed in a vacuum chamber which is evacuated to 10^{-6} torr. The heat sink is maintained at a constant temperature by continual adjustment of the Cal-rod power; the collector temperature is initially set at the expected operating value and the power input to its heater is thereafter held constant through the test. Parameters recorded are: initial and final potting compound weight, temperatures, and heater power to the collector and the heat sink as a function of time. The tests are to continue until some significant change in parameters occurs. To-date, three devices have been in test for several weeks, and no significant changes in parameters have occurred. Two of the simulated collectors are operating at the maximum expected temperatures: 210°F at the collector and 176°F at the heat sink. The other device is at a slightly lower temperature. Three other devices which incorporate a slightly different thermal path from the collector to the heat sink will be tested soon. Subsequently, other materials will be tested and compared with the presently used encapsulant.

Traveling-Wave Tube Power Amplifier

POWER SUPPLY

Two Syncom II traveling-wave tube power supplies have been fabricated. One is a development breadboard currently being utilized to test circuit modifications. The other is the demonstration model power supply in a Syncom I package. The high-voltage sections of both supplies were identical. The same type of high-voltage transformer as Syncom I was employed, with the turns ratios increased to accommodate the Syncom II TWT. Several types of filament outputs have been tested in the breadboard supply, whereas the demonstration model contained the same constant current filament supply used in Syncom I.

Concentrated circuit design and development effort was applied on a filament supply which approximates a constant "power" output in the normal operation region and limits the cold filament inrush current to 140 percent of normal. This supply does not sense and control power directly. Actually, the voltage is the regulated quantity. However, the volt-ampere characteristic is shaped so that load resistance variations of $\pm$ 20 percent about the nominal hot filament value result in approximately $\pm$ 1 percent changes in filament power. This assumes a constant input voltage. A $\pm$ 1 percent change in input voltage will increase the power variations an additional $\pm$ 1 percent.

The constant power filament supply consists of a saturable core square wave oscillator with a choke in series with the output (Figure 6-37). The input is $-$ 24 $\pm$ 1 percent volts, from a Syncom I type voltage regulator. The output is a square wave voltage approximately 50 percent higher than desired at the filament. The choke serves to deliberately cause "poor" voltage regulation due to load resistance changes. Load resistance changes result in approximately equal, but opposite, voltage and current changes. For $\pm$ 20 percent resistance variations, the product of rms voltage and current remains constant within $\pm$ 1 percent. The inductor causes a triangular-shaped waveform at the load, as opposed to the square wave of the Syncom I filament supply.

In comparing the constant power filament supply with the Syncom I constant current supply, the former has fewer parts, higher efficiency, and quicker warmup time. A quantitative comparison appears in Table 6-3. The lower parts count will improve the overall reliability of the unit. A higher efficiency results from employing a reactor in the ac portion of the circuit for current limiting, instead of resistors and transistors in the dc section as is done in the constant current supply. A quicker warmup results from allowing more current to the cold filament. As stated, this inrush current is limited to avoid the extreme thermal shock a more conventional constant voltage supply would cause. The ratio of hot filament resistance to cold filament resistance is approximately 7.5:1. This investigation was intended as a feasibility study only. No decision has been made to change from the constant current supply of Syncom I. However, the advantages of the constant power filament supply are being considered in detail.

TABLE 6-3. POWER SUPPLY COMPARISON

Supply	Constant Current	Constant Power
Total parts	22	13
Efficiency, percent	64	84
Warmup time, seconds*	46	28

*Time required to reach 90 percent of hot filament value.

PHASED-ARRAY TRANSMITTING ANTENNA

The phased-array transmitting antenna design retains the original concepts of using 16 antenna elements and ferrite phase shifters. The basic elements of the antenna system are shown in Figure 6-38 and are described below.

1) *Power splitter:* This unit divides the transmitter signal into eight equal-amplitude equal-phase parts.
2) *Phase shifters:*
   a) Input couplers. Eight of these are required to couple the outputs of the power splitter to the ferrite sections.
   b) Ferrite sections. These units consist of a tube of ferrite in a circular waveguide inside of a four-pole, two-phase motor stator. There are eight of these units.
   c) Output couplers. Eight of these couplers are used to convert the RF output of the ferrite sections into two equal amplitude signals with different phase shifts.
3) *Antennas:* Sixteen antennas are used, spaced equally around a circle of one wavelength radius.
4) *Control circuits:* These provide the proper voltages for the motor windings in the ferrite section. They are described elsewhere in this report.

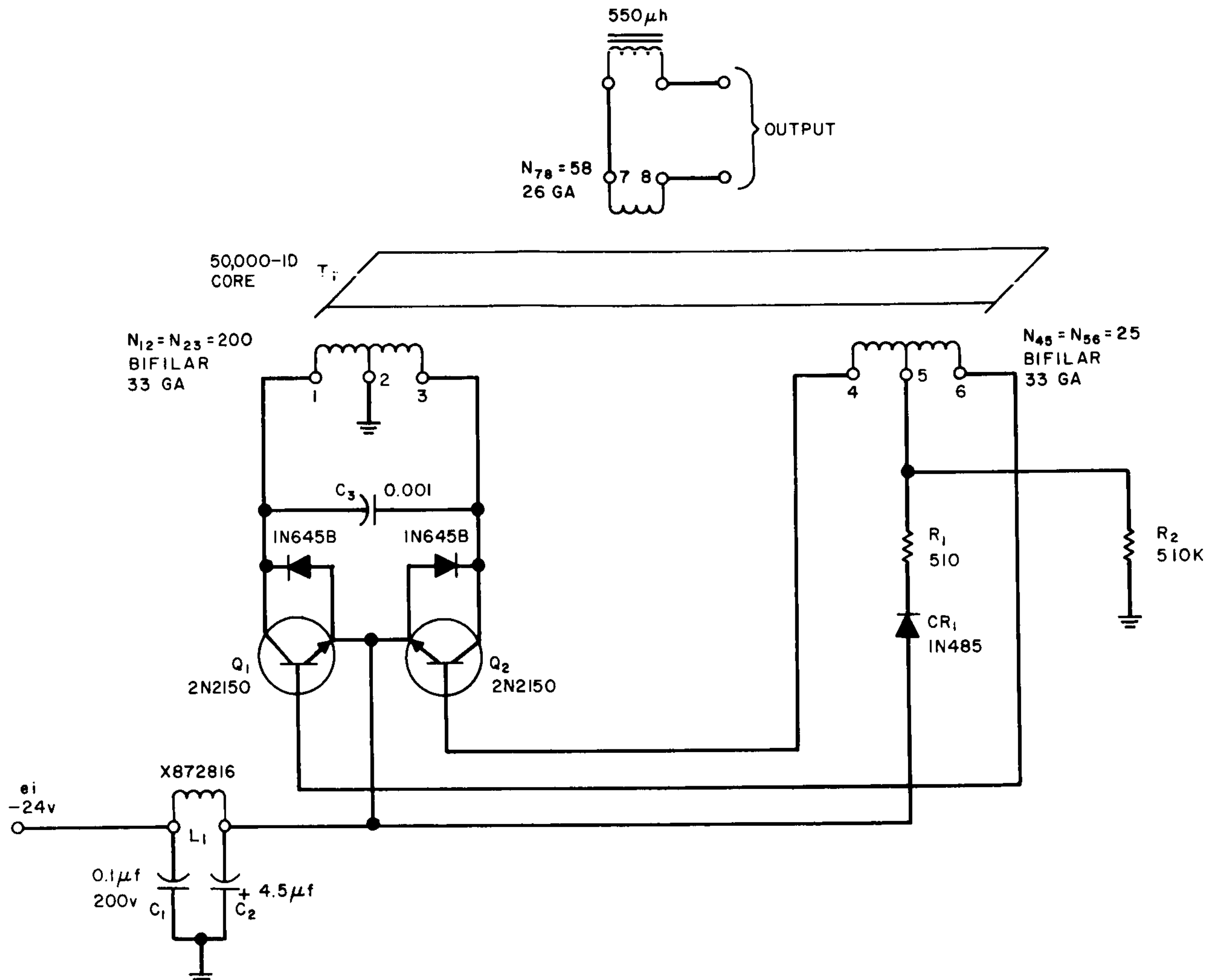

FIGURE 6-37. TRAVELING-WAVE TUBE CONSTANT POWER FILAMENT SUPPLY

An experimental model of the phased-array system had been constructed prior to initiation of this program, and was described in the Initial Project Development Plan (see Figure 6-60). This version operated at 8.8 kmc and the antenna elements were simple quarter-wave monopoles.

In the initial design at 4 kmc, the primary intent was to complete a working model of the antenna system. Design center frequency was 4080 mc and no specific attempt was made to obtain broad-band RF operation. Similarly, since this unit is in the nature of a breadboard, weight and size were not particularly restricted.

The completed assembly of the 4-kmc system is shown in Figure 6-39. The input power splitter was made in stripline with TNC connectors. The input coupler is a transition from coax, via a TNC connector, to circular waveguide. The ferrite section is located inside the motor winding. The output coupler has two TNC coax-to-waveguide transitions. Cables were used to connect the output couplers to the antennas.

An advanced version under design will use stripline-to-waveguide couplers for both the input and output couplers, and stripline rather than cables to feed the antenna elements.

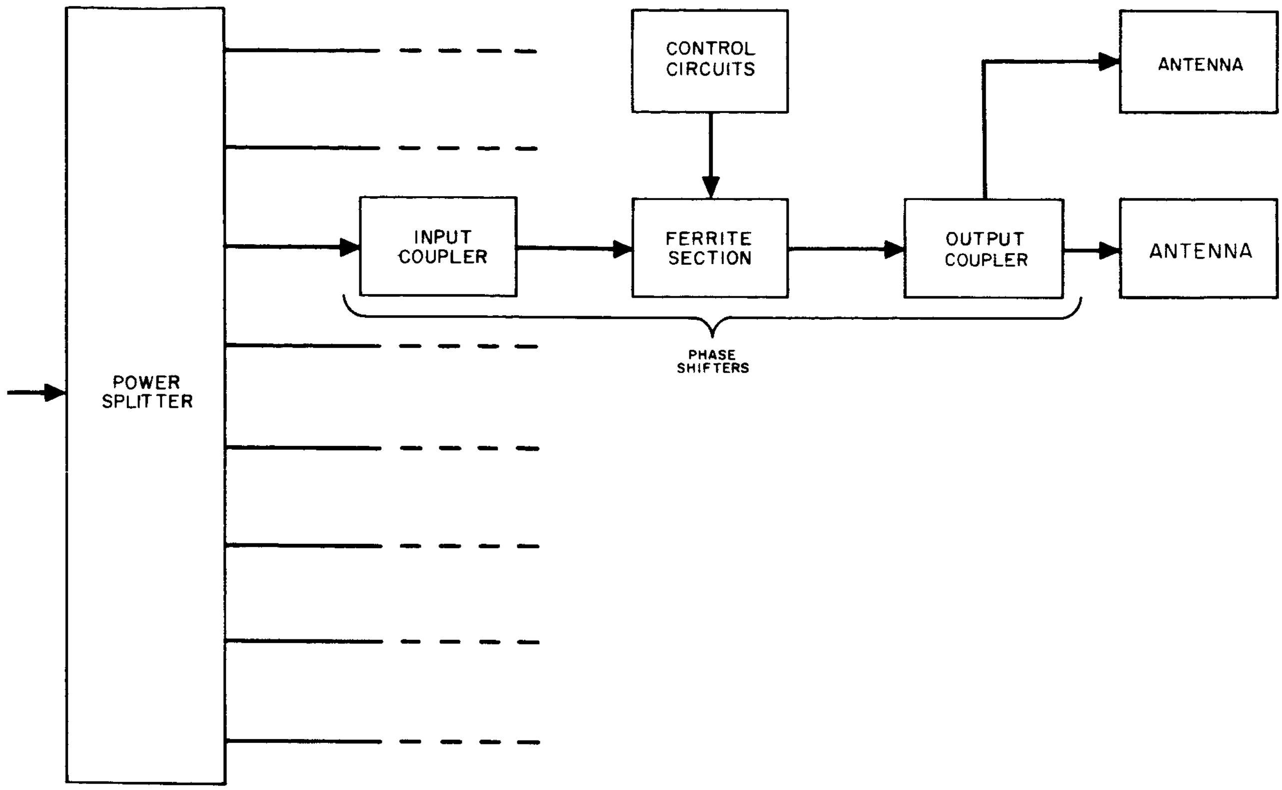

FIGURE 6-38. PHASED-ARRAY ANTENNA SYSTEM BLOCK DIAGRAM

Theory of Operation

The 16 antennas are spaced equally around a circle (see Figure 6-40). For a beam in the direction shown, a reference plane perpendicular to this direction passing through the center of the circle is used. A typical element, N, inherently has a phase shift, ϕ_n, with respect to the reference plane in the direction of the beam described by

$$\phi_n = \frac{2\pi}{\lambda} R \cos \theta_n$$

where λ is the transmitted wavelength.

For all the antenna elements to radiate in equal phase in the beam direction (which is the mechanism by which the beam is formed) this space phase shift must be cancelled out in the drive to the antenna. The result is similar to having all the elements located along the reference plane.

As the antenna rotates, the angles θ_n vary and hence the required phase shifts vary. It should be noted that diametrically opposite elements have opposite polarity phase shifts. (They are not of opposite phase in the usual sense, i.e., 180 degrees apart.)

For an electrical radius, R, equal to one wavelength, the resultant phase shift versus time is

$$\phi_n = -\phi_{n \pm 8} = 2\pi \cos(\omega t + n \cdot 22.5 \text{ degrees})$$

where ω is the rotation rate of the antenna and 22.5 degrees is the angular separation of the antenna elements (equal to 360 degrees/16).

The ferrite phase shifters are designed to produce this required phase shift and provide the two opposite polarity phase-shifted signals. It is based on the adjustable phase changer originally described in the article entitled "Adjustable Waveguide Phase Changer," by A. Gardner Fox, published in the December 1947 issue of the Proceedings of the IRE. Its operation is illustrated in Figure 6-41. The phase shift is made in circular waveguide, with the input coupler exciting a TE_{11} mode in the guide. This is essentially plane polarized in the plane of the input probe. The ferrite section, with magnetic field applied transversely by

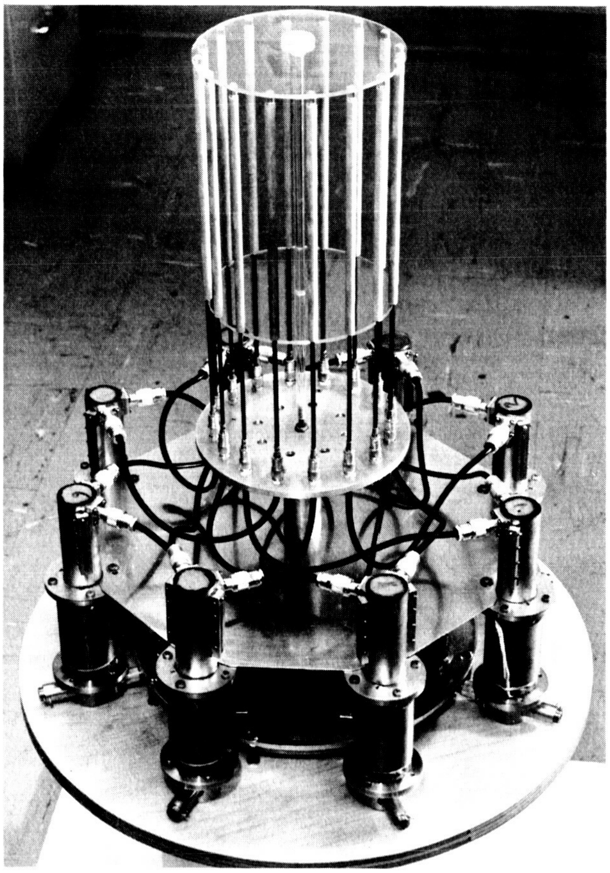

FIGURE 6-39. PHASED-ARRAY ANTENNA COMPLETED BREADBOARD SHOWING PHASE SHIFTERS
Circumference arranged around 16-element Syncom II antenna

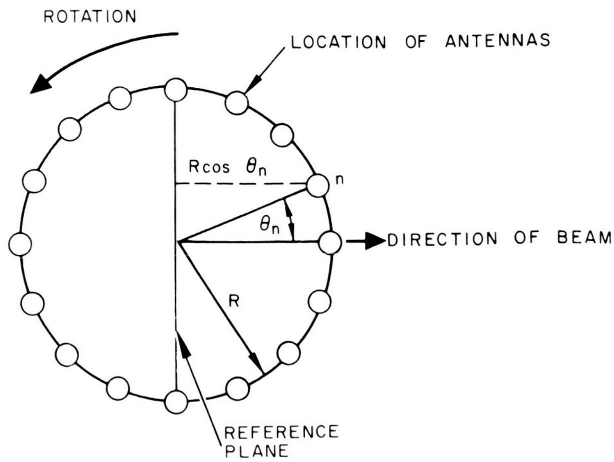

FIGURE 6-40. ANTENNA GEOMETRY

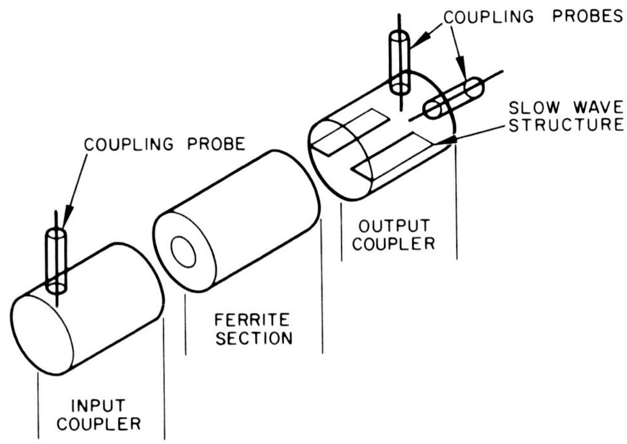

FIGURE 6-41. PHASE SHIFTERS

means of the external motor winding, acts like a "half-wave plate" which has the effect of rotating the plane of polarization, the angle of polarization rotation being equal to twice the angle of field rotation. Thus, unlimited phase shift can be achieved with no moving parts.

The output coupler consists of a slow wave structure in one plane, acting like a "quarter-wave plate" followed by two orthogonal coupling probes. The output coupler converts circular polarization to linear polarization. The plane-polarized wave from the ferrite section can be thought of as two counter-rotating circularly polarized waves. After passing through the slow wave structure, these components are converted to orthogonal plane-polarized signals which couple to the two output probes. The net effect is that rotation of the polarization in the ferrite section is equivalent to opposite polarity phase shifts of the two counter-rotating circular components and hence to opposite polarity phase shifts at the two output probes. Thus, rotation of the applied magnetic field results in phase shifts of the RF outputs. The use of the two-phase motor counteracts the factor of two between field rotation and polarization, so that output phase shift corresponds direcly to the "rotation" of the voltages applied to the motor.

For a phase shift ϕ_n, the required voltages applied to the motor winding are:

$$En_1 = E_o \cos \phi_n$$

and

$$En_2 = E_o \sin \phi_n$$

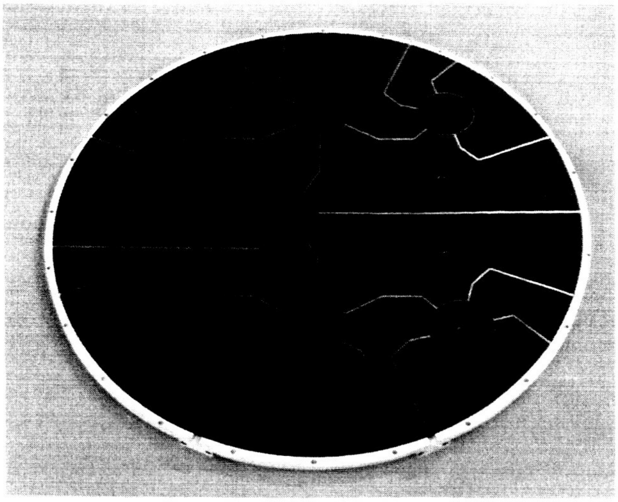

FIGURE 6-42. STRIPLINE PHOTO-ETCHED CIRCUIT PATTERN OF PHASED-ARRAY ANTENNA POWER DIVIDER

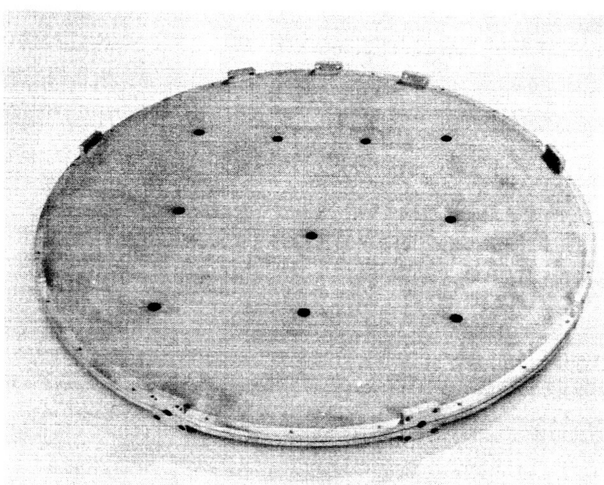

FIGURE 6-43. STRIPLINE POWER DIVIDER FOR PHASED-ARRAY ANTENNA SYSTEM
Complete unit

Using the expression for ϕ_n previously described these voltages are:

$$En_1 = E_o \cos [2\pi \cos (\omega t + n \cdot 22.5 \text{ degrees})]$$

and $$En_2 = E_o \sin [2\pi \cos (\omega t + n \cdot 22.5 \text{ degrees})]$$

The value of E_o depends on the characteristics of the motor winding and the ferrite. The generation of these waveforms is described in the section following these discussions.

Component Design

POWER SPLITTER

The completed breadboard eight-way power splitter is shown in Figures 6-42 and 6-43. It is fabricated in stripline and consists of seven identical hybrid rings. Each ring is similar to a waveguide ring or "rat-race" and is illustrated in Figure 6-43. Assuming all arms "see" matched loads, an input signal at arm 2 (or 3) splits into two equal-amplitude, in-phase signals at arms 1 and 3 (or 2 and 4) with nothing appearing at arm 4 (or 1). On the other hand, an input to arm 1 (or 4) produces equal-amplitude, out-of-phase signals at arms 2 and 4 (or 1 and 3) with nothing appearing at arm 3 (or 2). To ensure equal phase shifts to all eight outputs of the power splitter, the symmetrical connection (input to arms 2 or 3) is used and the hybrids are cascaded so that each of the eight signals traverses the same path length from input to output. The unused arms of the hybrids are terminated in resistance loads to absorb any power which may be reflected back into that arm.

The dimensions were scaled from previously built hybrid rings, and no exhaustive attempt was made to optimize the dimensions.

Data taken on the power split of the device from input to each of the eight outputs is shown in Figures 6-44 and 6-45, over a band of frequencies. The power split would be 9 db if there were no losses in the system. Since it is felt that the hybrids should be broad-band, it is not known at present why the insertion loss varied as much as it did. In any case, the eight outputs should follow each other identically. Hence it is probable that some of the line lengths were unequal or that the output TNC connectors were mismatched in various degrees. Effort is now proceeding on a more systematic approach to the device, beginning with construction and optimizing of an individual hybrid.

PHASE SHIFTERS

Ferrite Section. The dimensions of the ferrite section are the determining factor in the size of the phase shifters and will therefore be discussed first. From previous work in this field, it was known that the ferrite would be in the form of a tube, in which configuration the magnetic field is applied as in Figure 6-46.

Discussions with the ferrite manufacturer, Trans-Tech, Inc., led to their making a number of batches of ferrite which they felt would work at 4 kmc. These were then tested in various configurations of inner and outer diameter and checked for loss over the band and polarization rotation sensitivity. Although the ferrite was not completely matched into the adjacent waveguide, it was clear that some samples were not satisfactory since the passband cutoff at too high a frequency, or the loss at 4 kmc, was excessive. Figures 6-47 and 6-48 show the test configuration. Eventually, a configuration was evolved in which the ferrite was 2.5 inches long, with an outer diameter of 1.15 inch and an inner diameter of 0.625 inch. The inner tube was filled with teflon which helped to reduce the low cutoff frequency. With this diameter, the waveguide is cut off in air at 4 kmc and requires a dielectric constant of about 3 or more to transmit. The ferrite section had less than 1 db loss in the test fixture.

The motor stators used to provide the magnetic field were purchased from the Skurka Langdon Manufactur-

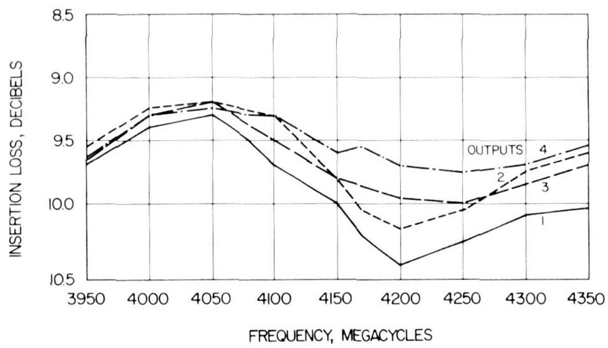

FIGURE 6-44. INSERTION LOSS OF POWER SPLITTER WITH OUTPUTS 1 TO 4

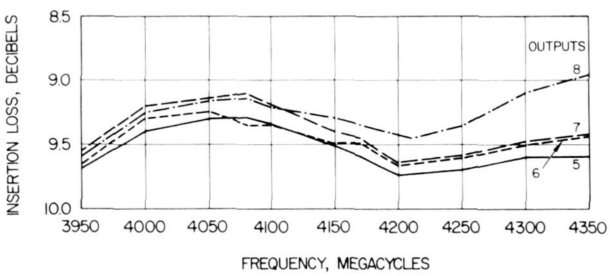

FIGURE 6-45. INSERTION LOSS OF POWER SPLITTER WITH OUTPUTS 5 TO 8

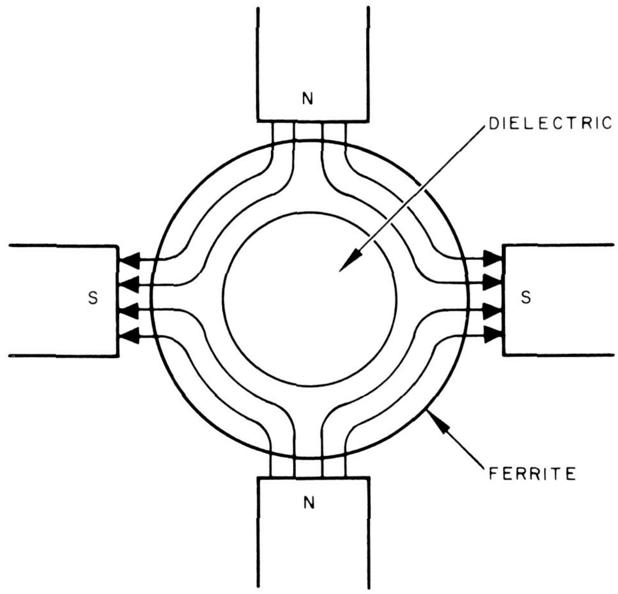

FIGURE 6-46. FIELD CONFIGURATION IN FERRITE TUBE (CROSS SECTION)

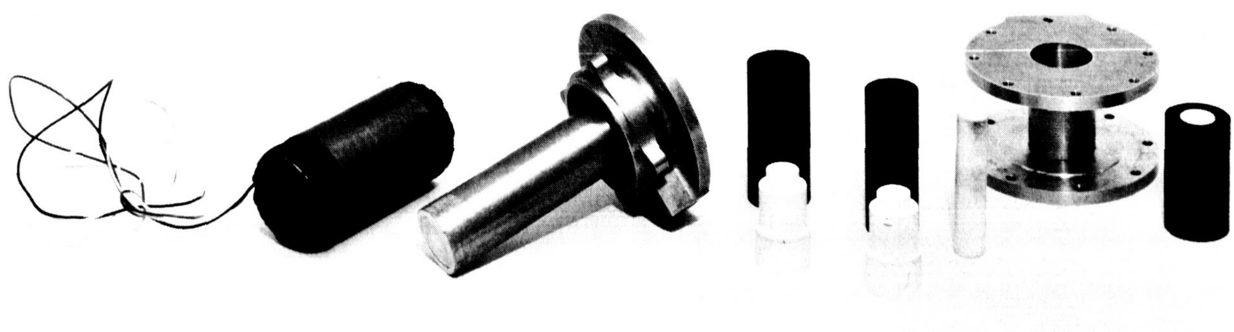

FIGURE 6-47. TEST FIXTURE FOR EVALUATION OF FERRITES FOR PHASE SHIFTERS

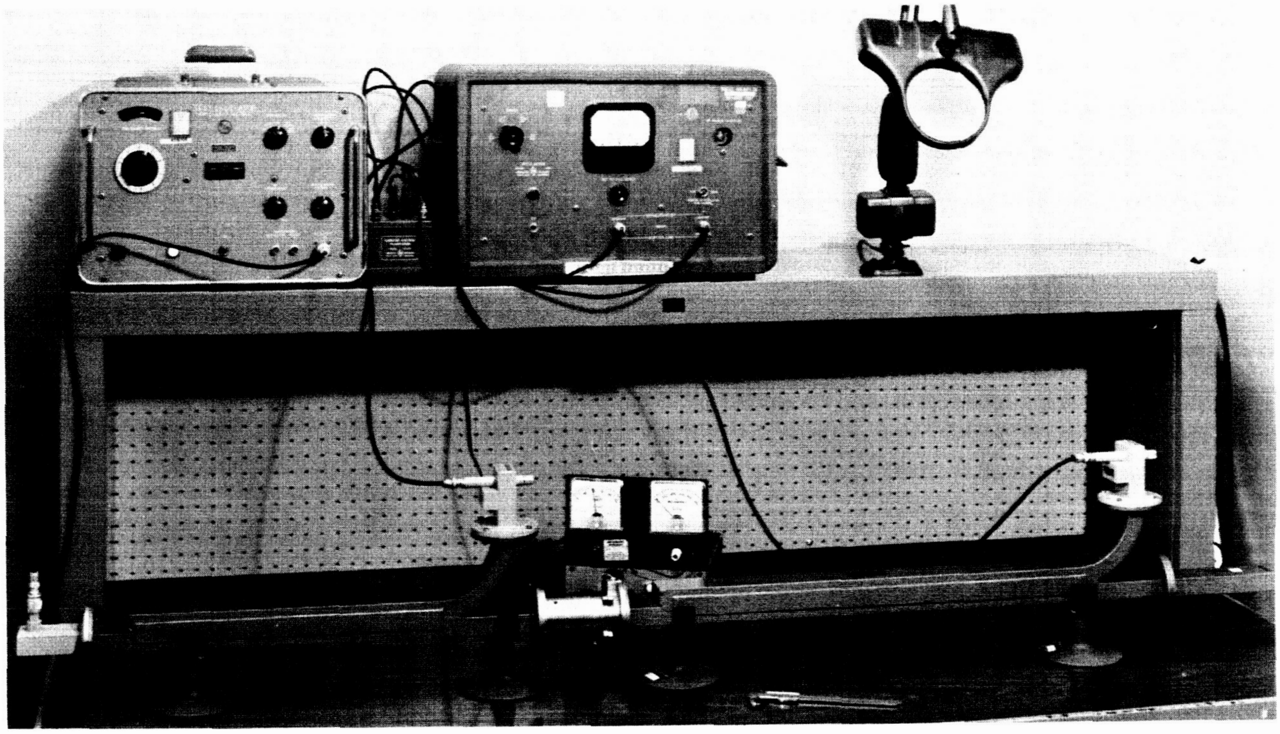

FIGURE 6-48. COMPLETE TEST SETUP USED IN EVALUATING PHASE SHIFT FERRITES

ing Company. Initially, these required about 100 ma at 6 volts to provide the 180-degree differential phase shift in the ferrite necessary to make it a pure polarization rotator. To design the control circuitry in a more efficient manner the motor was redesigned with more turns of finer wire resulting in a requirement of about 40 ma at 20 volts.

The ferrite was then matched into waveguides filled with a dielectric of K3 by using matching sections of K6 and K8 at each end. The reflection coefficient was less than 10 percent from 3950 to 4300 mc. Dimensions of the final configuration are shown in Figure 6-49, while Figure 6-50 shows the finished parts. The motor winding weighs approximately 14 ounces, while the ferrite and matching sections weigh about 6 ounces.

Input Coupler. The input coupler is shown in Figures 6-51 and 6-52 and consists of a probe coupler from coax into the waveguide filled with K3 dielectric. A TNC connector is used. An opposite probe was used to suppress unwanted modes and to improve the match. Reflected energy, which is cross-polarized in the guide, was absorbed by means of a resistive card made of Filmohm Mica placed in the guide perpendicular to the probes. Eight of these couplers were fabricated. The input VSWR was less than 1.1 over a 5-percent band.

Output Coupler. The output coupler is shown on the left side of Figure 6-50. It consists of a section of dielectric filled waveguide in which two diametrically opposed metal vanes are inserted to give a differential phase shift of 90 degrees for two orthogonal input polarizations. This results in the conversion of circular

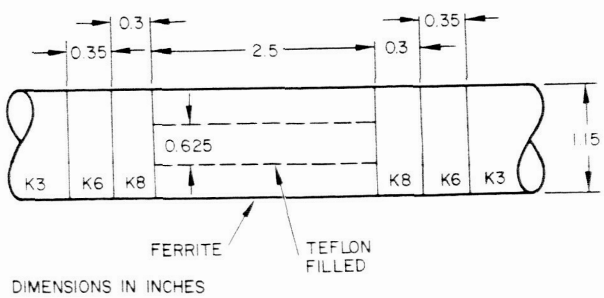

FIGURE 6-49. FINAL FERRITE CONFIGURATION

polarization to linear polarization. Two output probes, 90 degrees apart, are located past the vanes and oriented at 45 degrees to the vanes as shown in Figure 6-52. In this orientation, one output probe couples to a right-hand circular input polarization while the other couples to left-hand circular polarization. Eight of these couplers were fabricated. Typical insertion loss was 0.5 db with 0.1 db variation as a function of input polarization.

The output coupler is rotated so that the output probes are symmetrical about the input coupler probe. In this way, the two outputs have zero phase difference when the polarization is not rotated. This allows an omnidirectional antenna pattern to be formed about

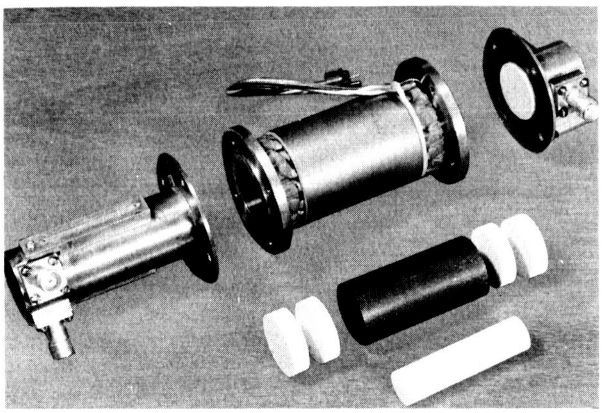

FIGURE 6-50. EXPLODED VIEW OF BREADBOARD FERRITE PHASE SHIFTER USED IN PHASED-ARRAY ANTENNA SYSTEM

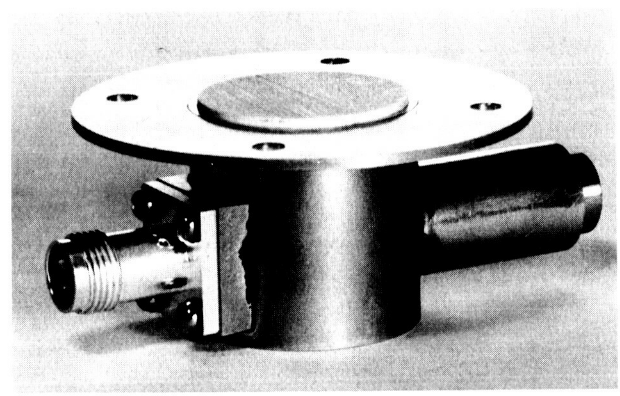

FIGURE 6-51. FERRITE PHASE SHIFTER INPUT COUPLER

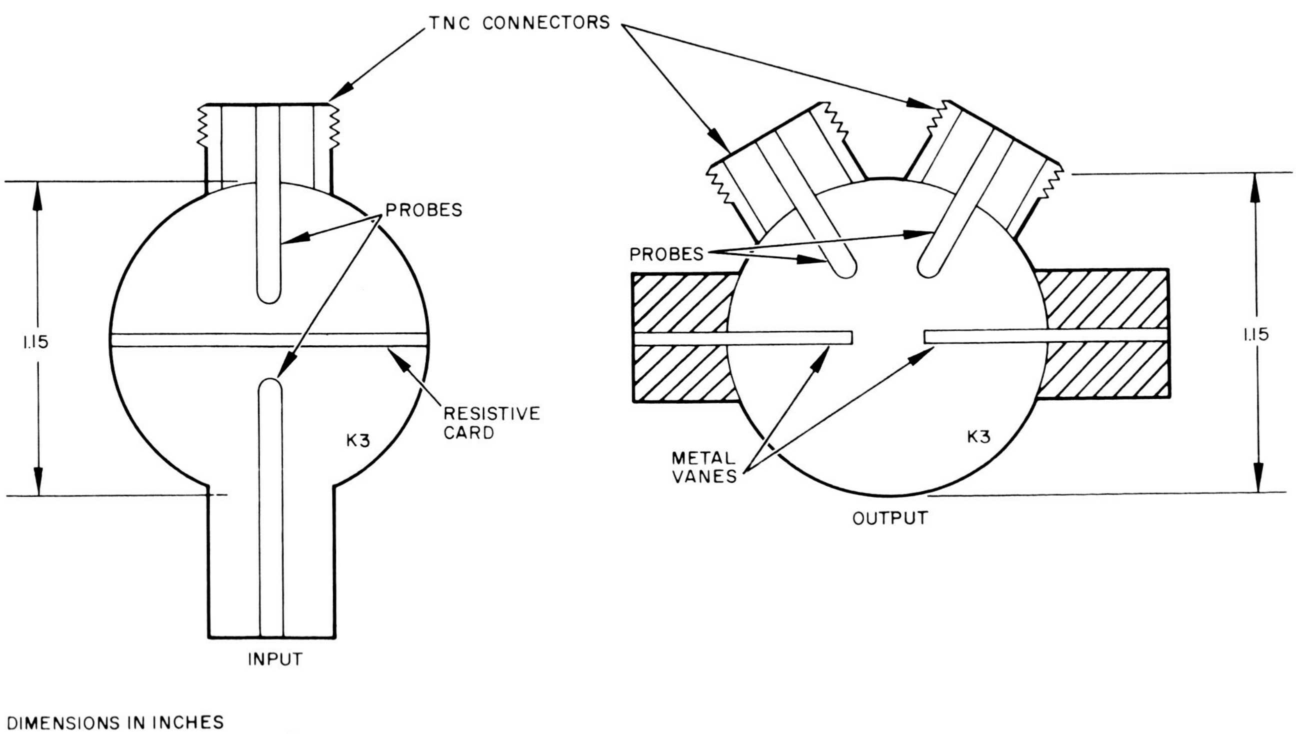

FIGURE 6-52. COUPLER CONFIGURATIONS (CROSS SECTIONS)

the axis of symmetry of the array when the voltages are removed from the phase shifter field coils. The array gain then reduces to the gain of a single element.

ANTENNAS

The antennas used in testing the phased-array system were vertically (longitudinally) polarized, and were scaled from the transmitting antenna used in Syncom I. Figures 6-53 and 6-54 show the various parts of the antenna. The antenna is covered with a fiberglass sleeve of 0.015 inch thickness for mechanical rigidity. The antennas were matched at center frequency with a simple quarter-wave section. No broad-banding was attempted initially.

The antennas were assembled on a test fixture using two eight-way power splitters following a 3-db power splitter, as shown in Figure 6-55. The coaxial cables were cut to different lengths to provide the proper phase shifts. Figure 6-56 shows a laboratory test setup for checking the antenna pattern while Figure 6-57 shows the measured (static) antenna pattern compared with the theoretical pattern.

The antenna was then tested on the Hughes antenna range with the same test fixture. Figure 6-58 shows both the vertical and horizontal patterns taken at a number of frequencies. The measured gain at 4080 mc was 15 db; with allowance for loss through the test fixture, the actual gain was estimated at 17 db.

To establish the mutual coupling between elements, two elements were mounted parallel to each other so that the spacing could be varied. The input VSWR of the driven element and the coupling to the other element were measured. The results are shown in

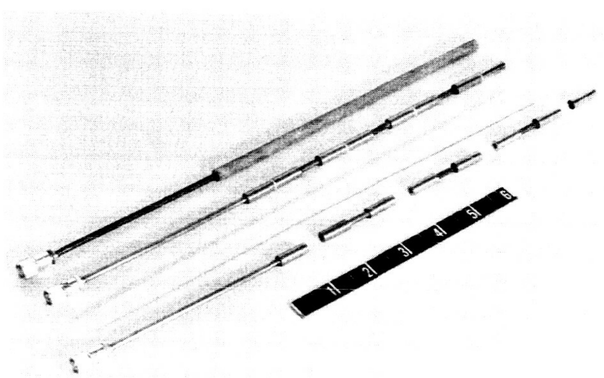

FIGURE 6-53. ONE ELEMENT OF 16-ELEMENT VERTICALLY POLARIZED 4-KMC ANTENNA ARRAY

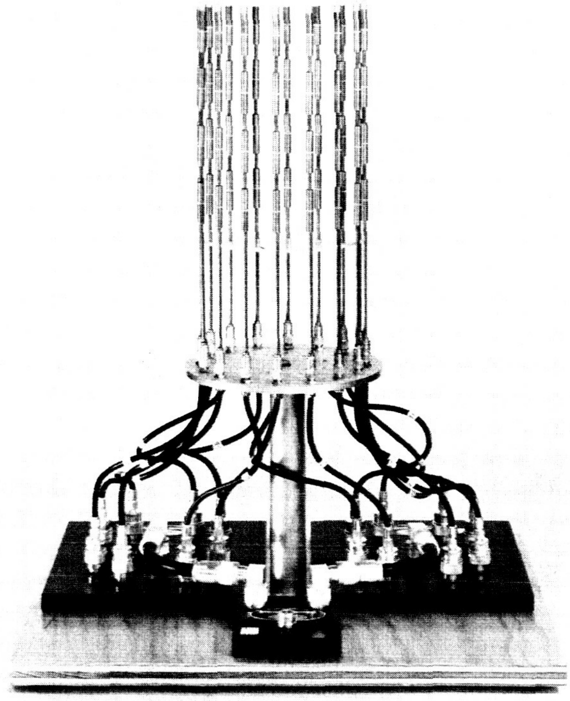

FIGURE 6-55. 4-KMC PHASED-ARRAY ANTENNA IN TEST FIXTURE FOR MEASURING STATIC BEAM PATTERNS

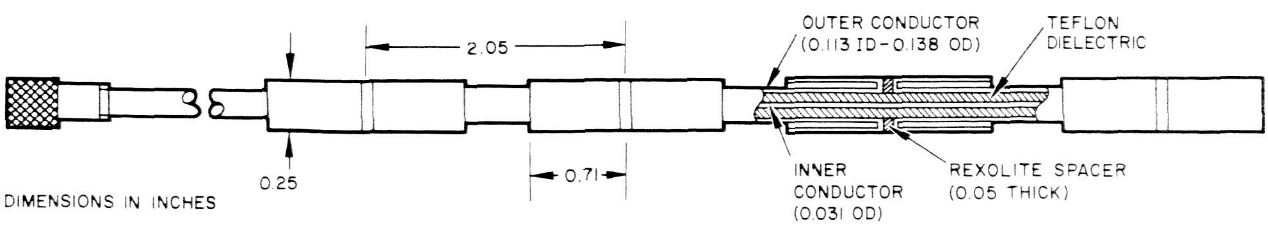

FIGURE 6-54. VERTICALLY POLARIZED ANTENNA

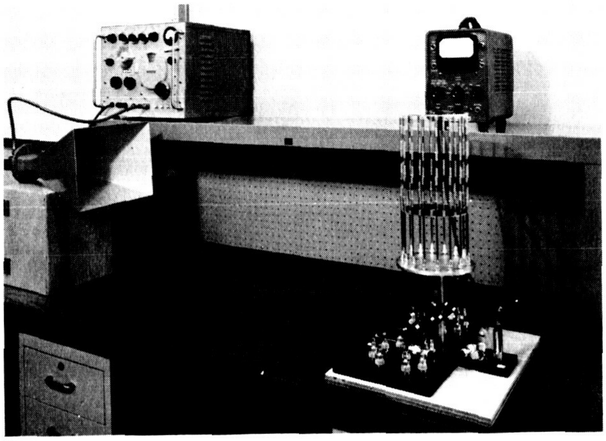

FIGURE 6-56. TEST SETUP FOR MEASURING STATIC BEAM PATTERN OF 4-KMC PHASED-ARRAY ANTENNA

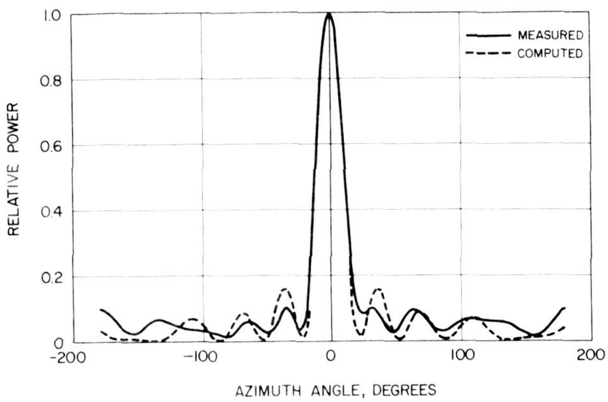

FIGURE 6-57. 4-KMC PHASED-ARRAY ANTENNA PATTERN

Figure 6-59. For the driven element alone, the input VSWR was 1.32. The resultant shape of the input VSWR curve depends on the phasing of this reflection and the mutual coupling. In the phased-array system, the closest antennas are about 1.2 inches apart in which case the power transferred to the other antenna is down about 12 db. However, since the elements are all phased to produce a beam, it is conceivable that the elements across which the beam passes could intercept more power. Attempts to measure this mutual coupling were difficult, since the antenna mismatch reflections were of the same order as the intercepted power.

A new version of this vertically polarized antenna was fabricated using larger diameter tubing (0.187 inch inside diameter) and center conductor (0.057 inch outside diameter). This eases the tolerances and assembly. The initial attempt at broad-band matching the antenna resulted in a VSWR of less than 1.5 over a 200-mc band. A complete set of 16 elements is now being fabricated.

System Tests

The complete phased-array system was assembled in the configuration shown in Figure 6-39. The phase shifts through the cables and phase shifters were checked and matched up to minimize the variations in phase lengths. Preliminary tests of the directional pattern were made by puting dc voltage on the field coils and mechanically rotating the coils to give the proper phase shifts.

To obtain an estimation of the contributions of the various elements, the patterns due to 1, 2, 4, 8, and 16 elements symmetrically placed were measured. The relative gains measured along the No. 1 element were approximately as follows:

No. of Elements	*Gain, db*
1	0
2	3
4	6
8	8
16	8

As expected, the gain varied considerably as the phase shifters were adjusted to give a beam between elements. Thus, the fact that both 8 and 16 elements gave the same gain in the No. 1 direction is misleading since the eight elements alone gave some "spin" modulation while 16 elements did not. The data does show that there is a mutual coupling loss.

Since all elements alone did not radiate equally, the 0 db reference for the single element was dependent on which element was used. Further checks of the omnidirectional pattern (with no current in the field coils) showed that the 16 elements gave a much more uniform pattern, and that 8 or less had more peaks and nulls. Thus the increase from 8 to 16 assists considerably.

It should be noted that this test setup varies considerably from the theoretical pattern discussion of the Initial Project Development Plan wherein the element spacing was varied with the number of elements.

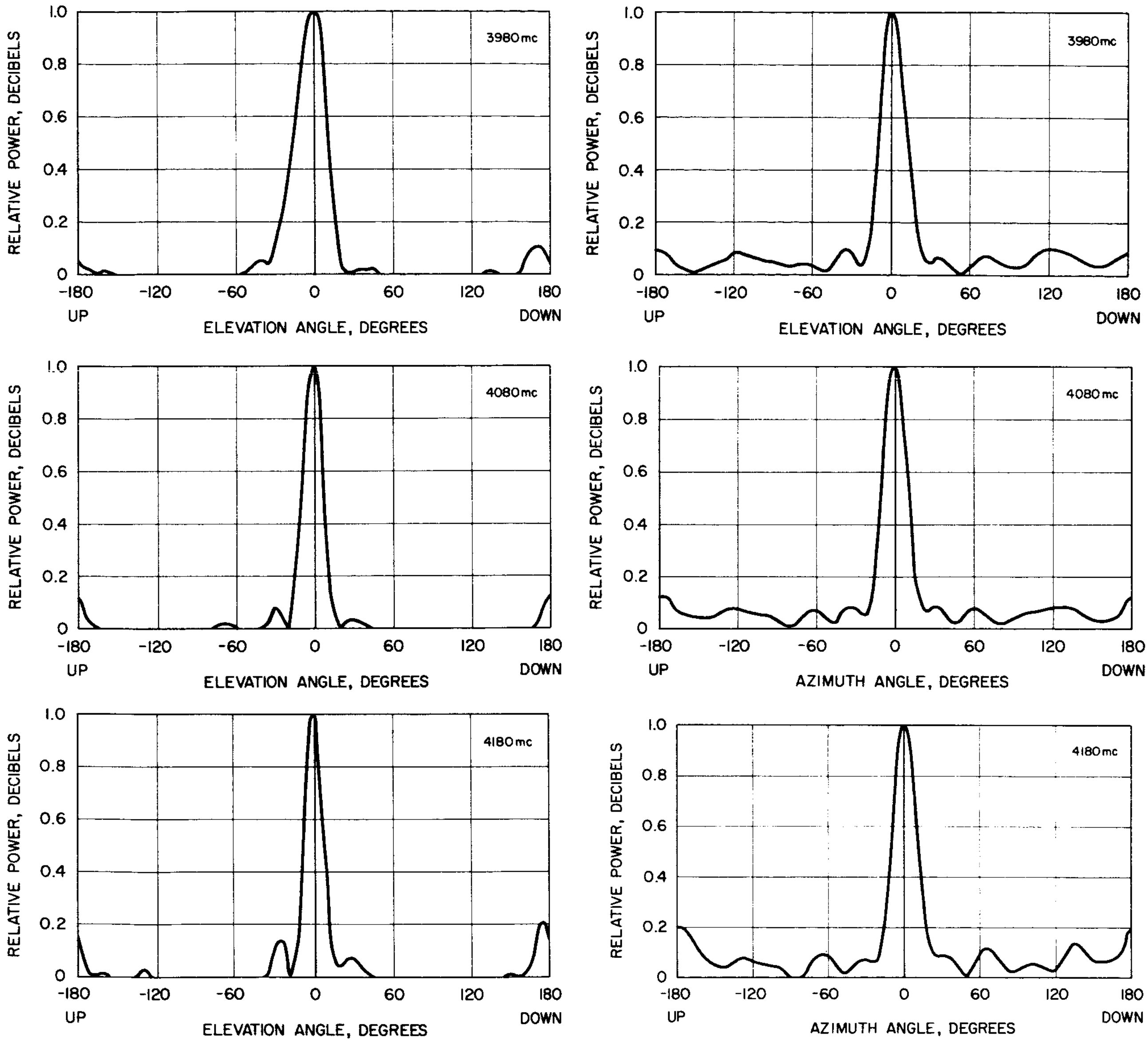

a) Vertical plane

b) Horizontal plane

FIGURE 6-58. ANTENNA PATTERNS OF 4-KMC PHASED-ARRAY ANTENNA

A plot of the antenna beam, made in the laboratory, with dc on the coils which were positioned mechanically, is shown in Figure 6-61. By integrating the area under the curve, the so-called "pattern gain" was calculated at 9.8 db. This compared favorably with the calculated value and showed that the pattern was being properly formed. Compared to the previous data, the mutual coupling loss is seen to be about 1.8 db.

The antenna was then connected to the digital and analog control circuits and the beam was caused to rotate. The output of a horn, some distance away, was recorded, for different physical rotations of the antenna. The results are shown in Figure 6-62 for rotations of 11.25 degrees. The last picture shows a rough calibration in 1-db steps. The largest variation in gain from the average was about 0.4 db.

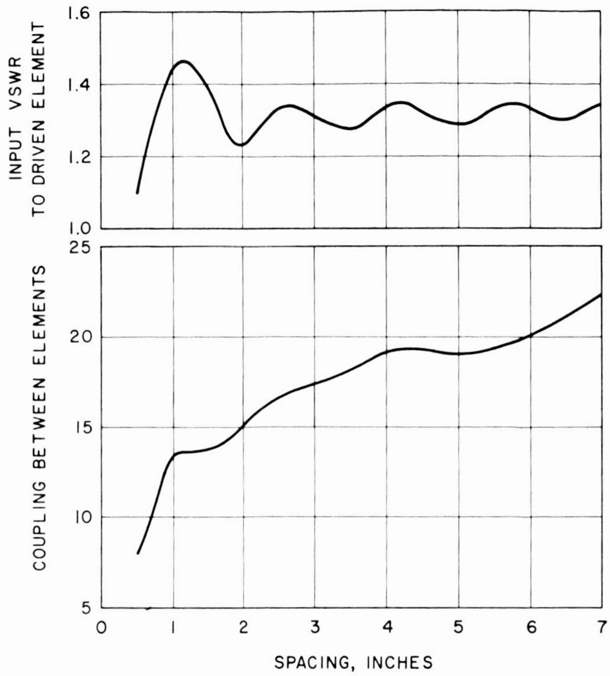

FIGURE 6-59. COUPLING BETWEEN ELEMENTS (4080 MC)

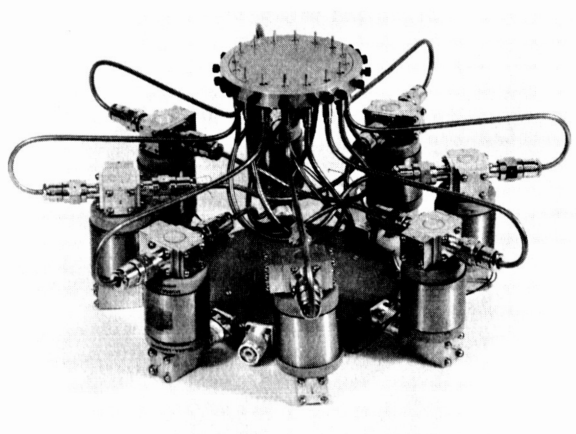

FIGURE 6-60. 8.8 KMC PHASED-ARRAY

When the antenna was placed in the spacecraft for demonstration purposes, the gain variation was again checked. This was done statically by rotating the spacecraft position and then commanding the control system to form a beam in the direction of a receiving horn. The result is shown in Figure 6-63. The variation in gain from the average was less than 0.5 db.

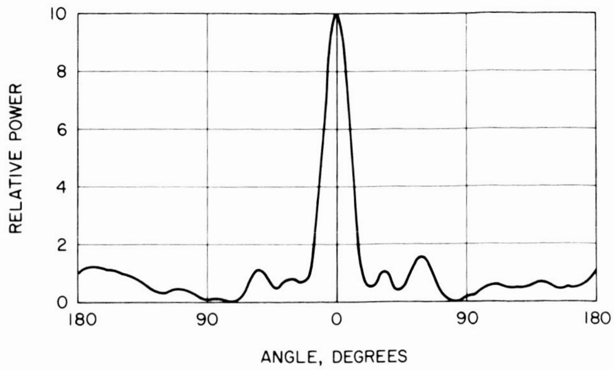

FIGURE 6-61. ANTENNA PATTERN AT 4080 MC
Pattern gain = 9.8

The main-beam pattern for small angles was checked by holding the spacecraft still and commanding the beam to move in small (1.4-degree) steps. The result is shown in Figure 6-64. The 3-db beamwidth measured about 20.2 degrees.

Stripline Circuits

A stripline version of the phased-array system is under development. It will have the advantages of fewer connectors, better coupling to and from the ferrite phase shifter, better control of line lengths, and lower loss.

The power splitter, which is already in stripline, will be combined with the input couplers through a direct stripline-probe to wave-guide transition. The output coupler is replaced by a four-probe coupler (or "turnstile"), a balun for coupling opposite probes 180 degrees apart and a square 3-db 90-degree hybrid shown in Figure 6-65. The feed lines to the antennas will also be in stripline. Due to the geometry involved, there are a number of points where two striplines cross over. The circuits will therefore be made in two planes with vertical transitions connecting them where necessary. The dielectric used is Duroid of $\frac{1}{32}$ inch thickness, while the ground plane spacing is 0.147 inch. Line widths are chosen to give a characteristic impedance of 50 ohms.

Special test fixtures were fabricated to optimize the vertical stripline-to-stripline transition, the vertical TM-to-stripline transition, the square 90-degree hybrid, and the four-probe coupler. The 90-degree hybrid is of special design with the input arms at 45 degrees (Figure 6-66).

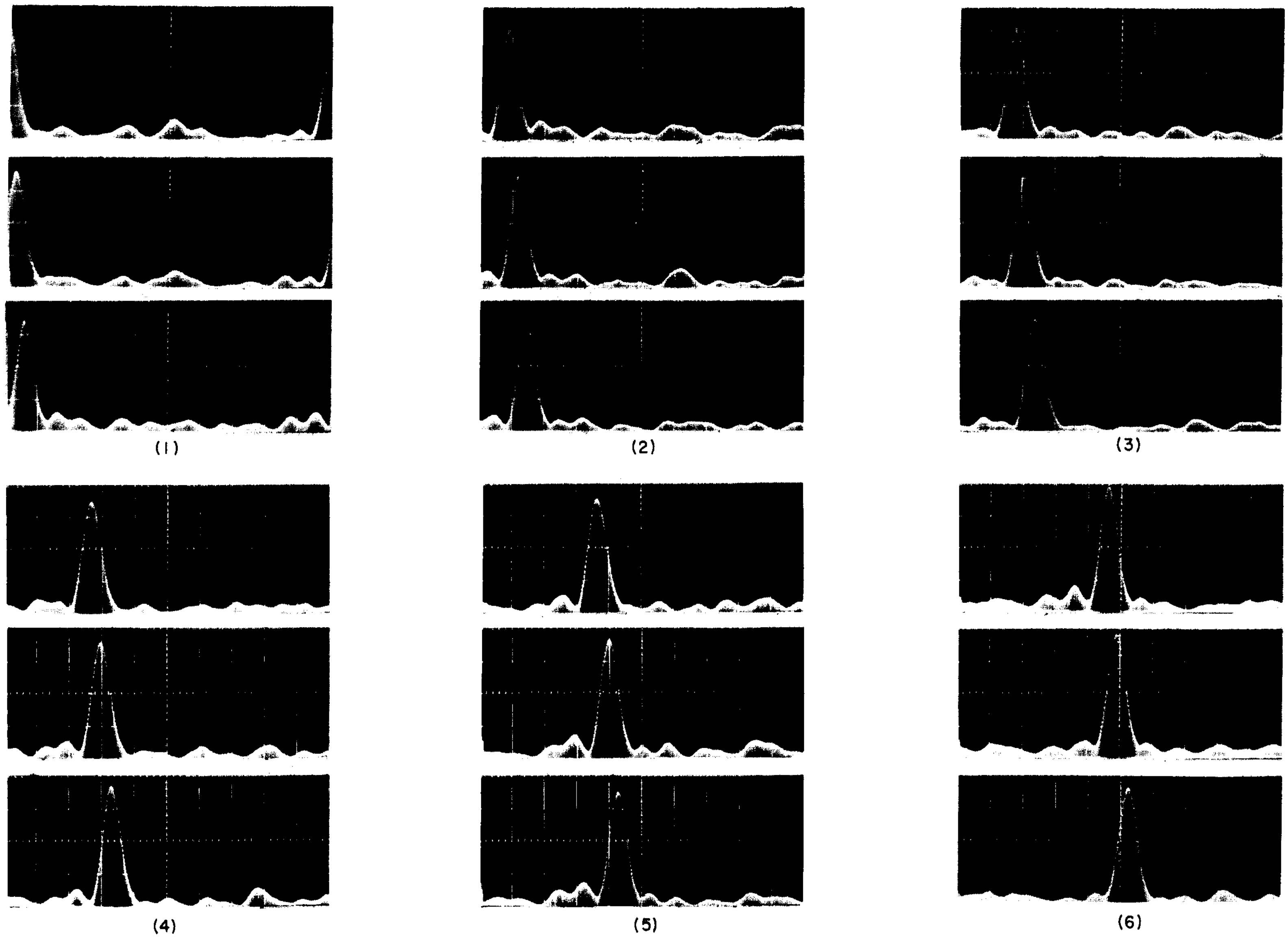

FIGURE 6-62. ROTATING BEAM PATTERNS OF PHASED-ARRAY ANTENNA
11.25-degree steps

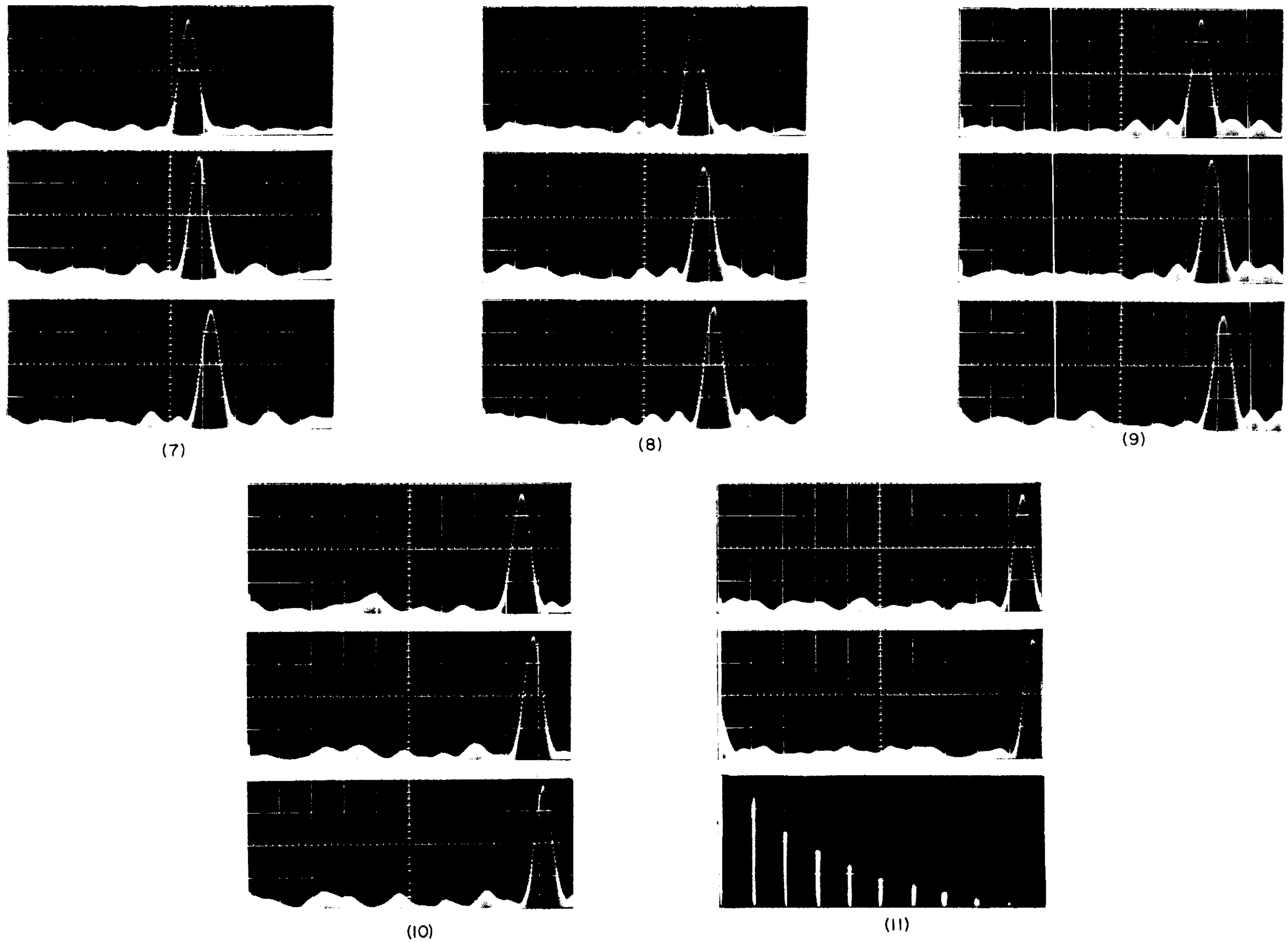

FIGURE 6-62. (CONTINUED) ROTATING BEAM PATTERNS OF PHASED-ARRAY ANTENNA

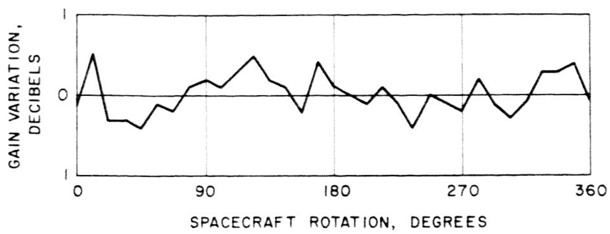

FIGURE 6-63. FLUCTUATIONS OF MAIN BEAM MEASURED IN SPACECRAFT (4080 beacon signal)

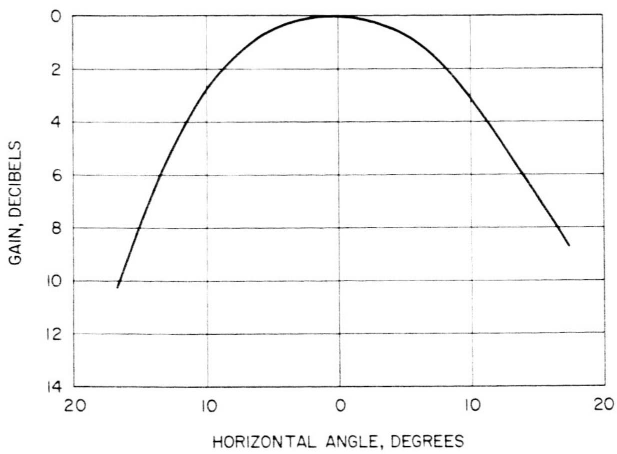

FIGURE 6-64. MAIN BEAM AT 4080 MC ANTENNA MOUNTED ON SPACECRAFT

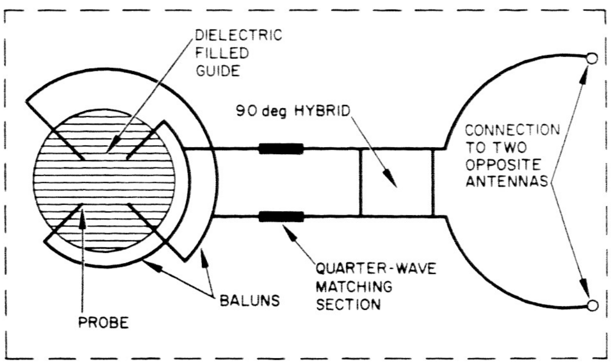

FIGURE 6-65. STRIPLINE OUTPUT COUPLER FOR PHASED-ARRAY PHASE SHIFTER

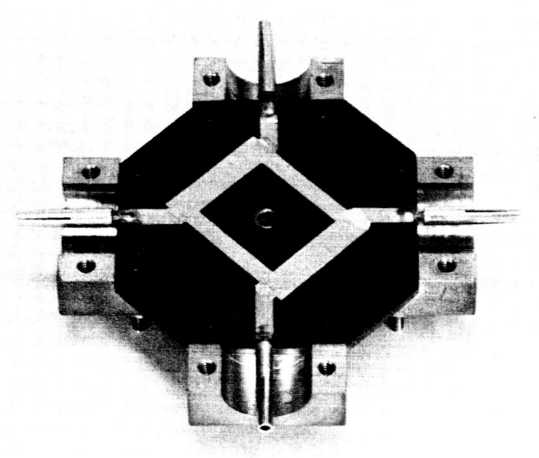

FIGURE 6-66. 4-KMC 3-DB HYBRID COUPLER

The 90-degree hybrid has the property that an input signal divides equally into two outputs which are 90 degrees apart. Hence, when such a hybrid is connected to the turnstile junction, and an input signal is applied to the hybrid, a circularly polarized signal is set up in the waveguide. If the signal is applied to the other arm of the hybrid, a circularly polarized signal of opposite sense is set up. Since the operation is reciprocal, circularly polarized signals of opposite sense in the waveguide will couple separately to the two hybrid output terminals.

An interim model of this output coupler was fabricated to facilitate early testing of the system. A diagram of this model is shown in Figure 6-67 while the completed model is shown in Figure 6-68.

The drawings of the complete output coupler stripline circuits are shown in Figure 6-69. Particular attention had to be paid to the line lengths from probe to antenna, to spacing between lines, and to corners.

An artist's conception of the completed transmitting phased-array system and receiving antenna is shown in Figure 6-70.

It is expected that losses using the stripline system will be approximately as follows:

Power splitters, input couplers	0.5 db
Ferrite section	0.75 db
Output couplers	0.5 db
Antenna	0.75 db
TOTAL	2.5 db

Particularly, the losses in the output couplers and the antennas will be reduced from the breadboard model providing an estimated improvement of a little over 1 db.

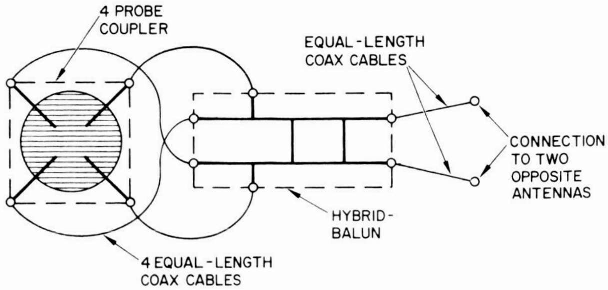

FIGURE 6-67. INTERIM MODEL OF STRIPLINE COUPLER

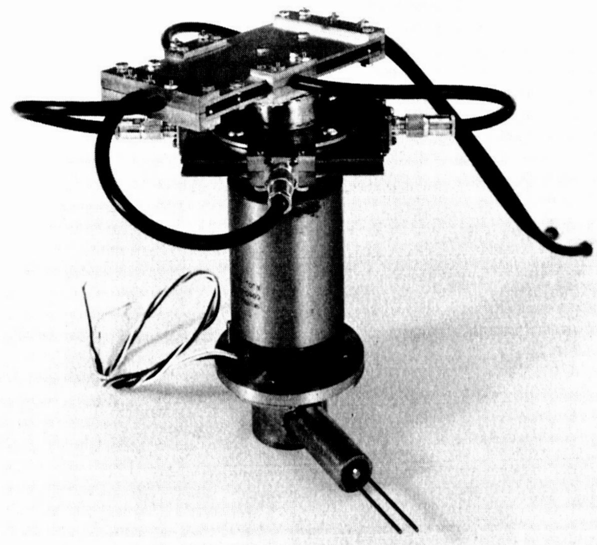

FIGURE 6-68. INTERIM MODEL OF STRIPLINE COUPLER AND FERRITE PHASE SHIFTER

Transversely Polarized Slotted Coaxial Antenna Elements

Transversely polarized element arrays would have the advantage of reducing reflections from neighboring elements and the coaxial feed for the receiving array to a minimum. The theoretical gain of a uniformly illuminated element array with 18 slots (three rows of six slots each) is 7.9 db. Due to losses in the coaxial feed and manufacturing tolerances, the realizable element gain will probably be about 7.3 db.

A coaxial antenna element consisting of slots parallel to the axis will radiate the desired transverse polarization, provided a means of exciting the slots is realized. Since excitation of a slot so oriented is difficult, a number of different approaches were investigated.

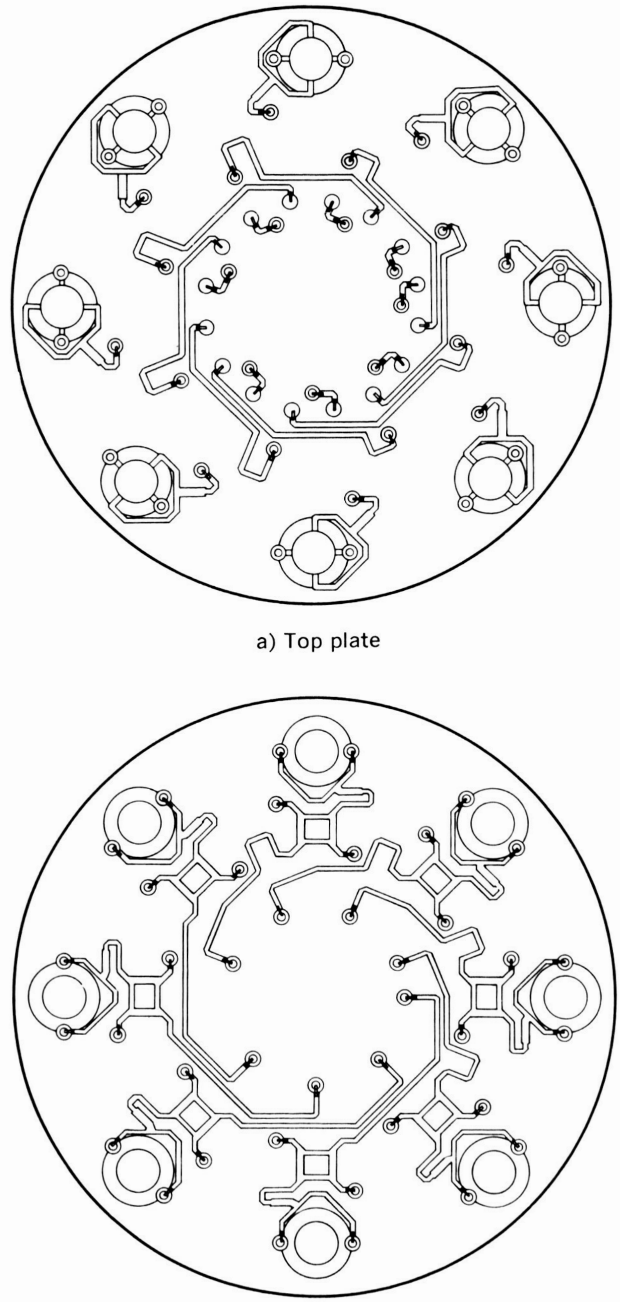

a) Top plate

b) Bottom plate

FIGURE 6-69. PHASED-ARRAY OUTPUT COUPLER CIRCUITS

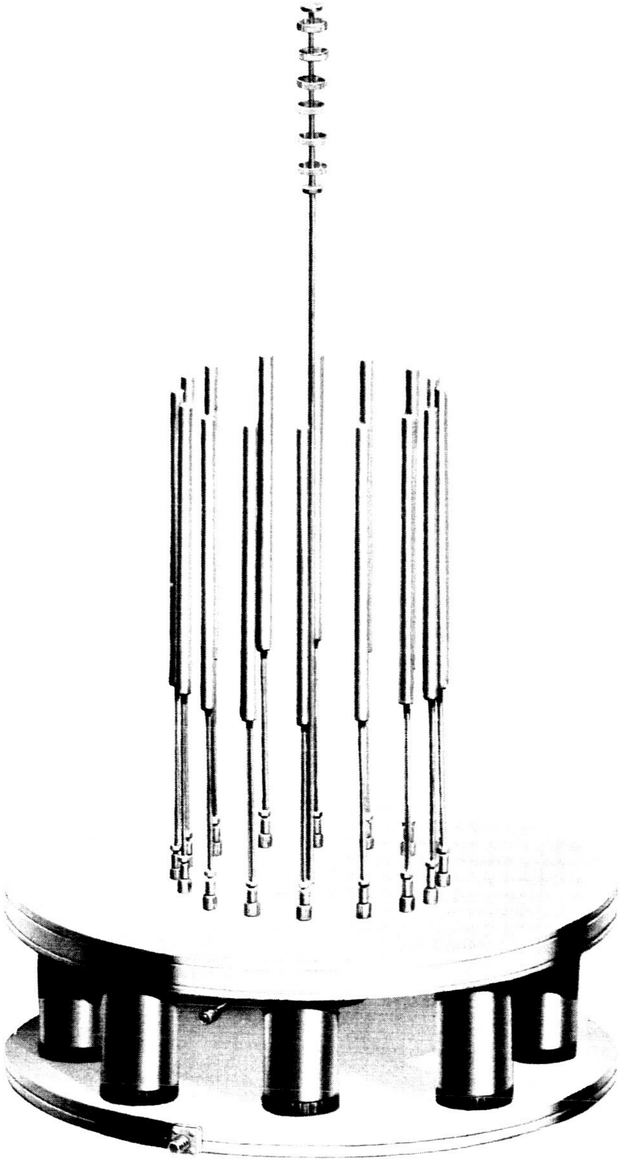

FIGURE 6-70. PHASED-ARRAY ANTENNA

Most of the approaches fall into three categories:

1) Post-fed slots
2) Low-impedance coaxial radiators
3) 50-ohm coaxial lines with complex slot radiators.

Only minor effort is being expended on the post-fed slot at this time. The greater portion of the hardware development effort was devoted to the second approach because the necessary complex slot configurations for the third approach were conceived only recently. The low-impedance technique has shown some encouraging results. The 50-ohm coaxial technique is encouraging regarding coupling and impedance matching.

POST-FED SLOTS

Of the several possible methods of exciting the slots in the coaxial arrays, capacitive probes placed by the side of each slot are most frequently used for this purpose. The capacitive probes, however, require extremely close tolerances on the positioning of the center conductor of the coaxial line. Furthermore, arrays of these probe-fed slots exhibit a high VSWR and narrow-band characteristics unless additional matching probes are placed approximately a quarter-wavelength away from each probe feeding a slot. One advantage of longitudinal slots (fed by either probes or posts) is that an interelement spacing of $\lambda/2$ can be used on an unloaded coaxial line. The required 180-degree phase reversal is obtained by placing the probes on opposite sides of alternate slots in the array. The center conductor of a probe-fed array would be unsupported except at the ends, and several dielectric beads would probably have to be used along its length for additional support.

To avoid some of the problems of the probe-fed slot, the characteristics of post-fed slots have been investigated. The post, being connected to the center conductor, has the advantages of avoiding the critical spacing, which is difficult to hold, and it supports the center conductor. Three such post-fed slots, symmetrically spaced about a point on the coaxial line, yielded no resonance at all. It was concluded that the posts were introducing an excessive amount of inductive susceptance, particularly when used in groups of three, and measurements were made which verified this observation.

Effort was then concentrated on finding a method of matching out this susceptance. One method was the use of a capacitive iris about the center conductor in the immediate vicinity of the posts. Another method was use of a combination of two capacitive probes and one inductive post to excite the three slots. The capacitive probes were placed on the opposite side of the slot from the position normally occupied by a post in an effort to keep radiation from all three slots in the proper phase relationship. This method produced an admittance curve that was resonant at approximately 4.13 kmc and was reasonably constant in conductance value over a range of 200 mc; however, a satisfactory omnidirectional pattern could not be obtained from this arrangement.

LOW-IMPEDANCE TECHNIQUES

To use a low-impedance coaxial radiator it is necessary to use a bandpass transformer. Tchebyscheff-type transformers were designed to match the 50-ohm coaxial line to the 13-ohm coaxial radiating section used. Both two- and three-section transformers were designed and tested. Each type was found to be satisfactory.

The center conductor (which has shown the most promising results to date) has a spiral tripled ridged configuration. This conductor is comprised of one-half wavelength long sections. The pitch of the ridges is reversed from section to section to accommodate the reversal of current each half wavelength along the conductor. The spiraled ridges cause the E-field to follow their spiraled path when energy is propagated along the coaxial line. In turn the surface currents have a spiraled path causing them to cross the slots in the outer conductor. In this manner the slots are excited, causing energy to be radiated. The amount of energy radiated by a slot is proportional to (a/b) sin θ, where a is the length of the slot, b is the length of one revolution of the spiral, and θ is the angle between the slot and the ridge. One-half wavelength and three wavelength slots are being investigated. In both cases slots parallel to the axis and slots inclined to the axis are being evaluated. The inclined slots are reverse pitch to the ridges exciting them in order to increase the angle θ. In the case of the long slots this necessitates reversing the pitch of the slot every one-half wavelength. The inclined slots radiate more energy; however, they introduce a cross-polarization component.

50-OHM COAXIAL RADIATORS

A complex slot in a 50-ohm coaxial line with a standard center conductor was constructed. Preliminary tests of this element revealed good coupling characteristics. The VSWR was satisfactory also. The slot is made up of nine sections. The first section is parallel to the coaxial axis and is less than a quarter-wavelength long. The next section spans 120 degrees around the coaxial line. The third section is parallel to the axis and is almost one-half wavelength long. The fourth section spans 120 degrees around the outer conductor back in line with the first section. This pattern is continued to a total slot length of two wavelengths. The VSWR of a 50-ohm element is less than 1.5 to 1 over the desired frequency band. However, there is considerable energy in the cross-polarized pattern. A method of eliminating this cross-polarization will have to be developed. Figure 6-71 is the radiation pattern of the element having short inclined slots.

Figures 6-72 through 6-75 show the details of some of the experimental elements. Figure 6-72 is of two of the elements assembled.

Transversely Polarized Cloverleaf Element Development

An UHF cloverleaf antenna array (Proceedings of IRE, December 1947, pp. 1556-1563) was scaled to obtain the desired omnidirectional pattern with horizontal polarization. A single cloverleaf test section was used in the development (Figure 6-76). The major considerations in scaling were 1) obtaining the correct resonant frequency, 2) obtaining the desired coupling

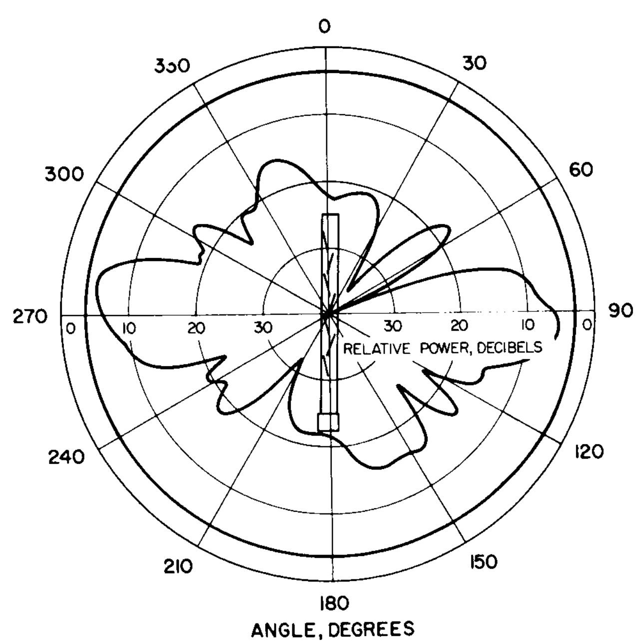

FIGURE 6-71. PATTERNS OF ARRAY OF SHORT INCLINED SLOTS ON COAXIAL LINE

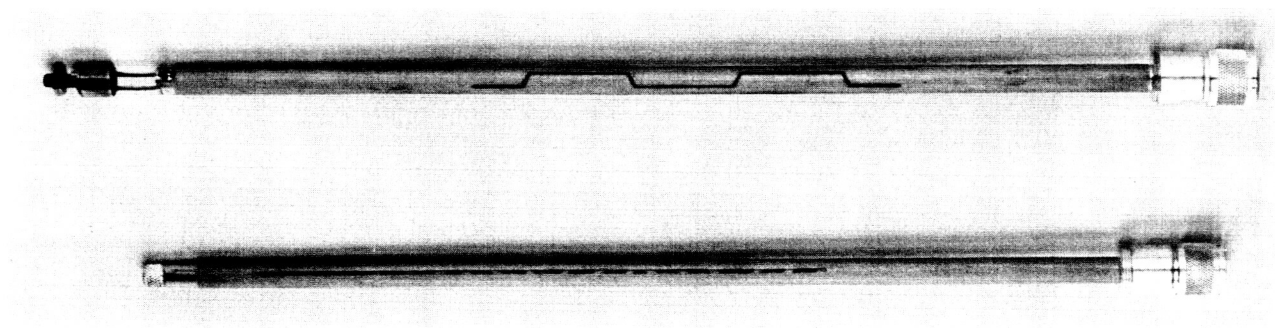

FIGURE 6-72. TRANSVERSELY ASSEMBLED POLARIZED COAXIAL SLOT RADIATORS

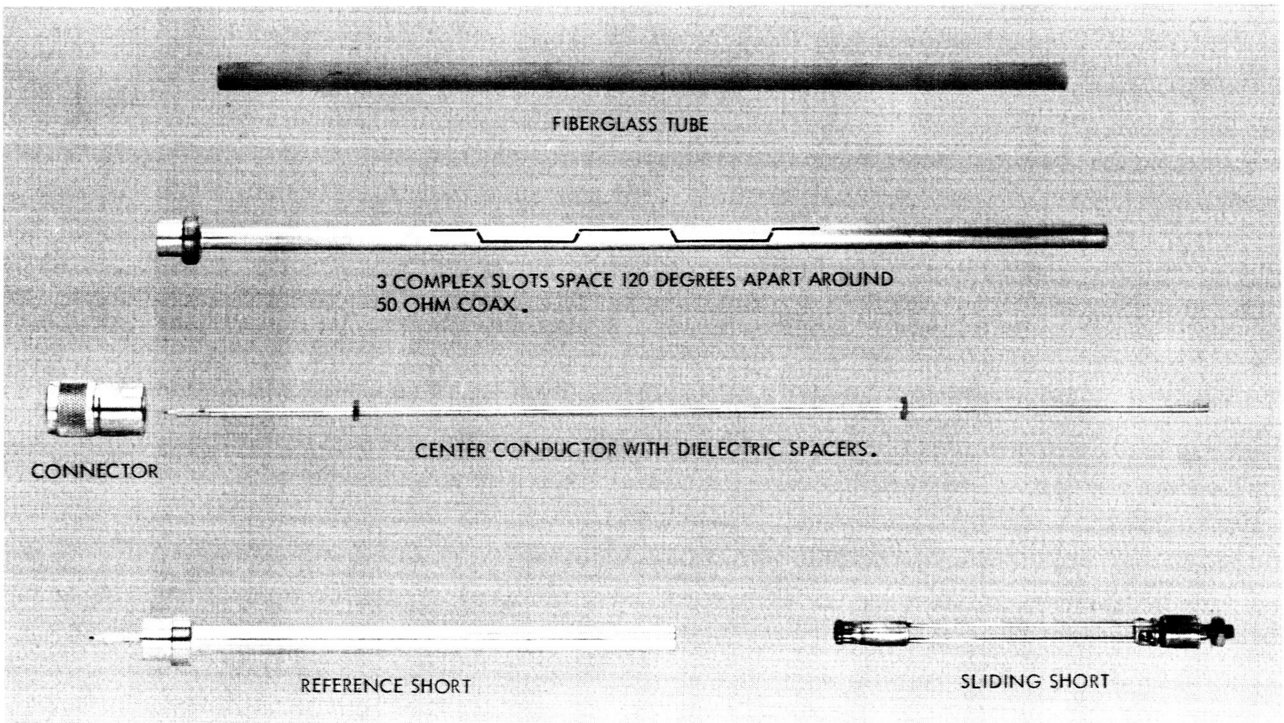

FIGURE 6-73. DETAIL OF COMPLEX SLOT RADIATOR

from the single cloverleaf, and 3) eliminating the stray currents flowing along the outside of the coaxial line which give rise to end-fire beams of approximately the same amplitude as the desired broadside beam. Tentatively, the design problems were solved as follows:

1) The resonant frequency problem was solved first by decreasing the diameter of the four loops constituting the cloverleaf. However, this resulted in lower coupling.

2) The coupling from the cloverleaf was increased to the desired amount by attaching a strip of metal to the outer edges of the loops of the cloverleaf (Figure 6-77)

3) The stray currents flowing on the outside of the coaxial line were eliminated by attaching suppressor wires to the loops of the cloverleaf at a point near where they emerge from the coaxial line, and shorting these suppressor wires to the

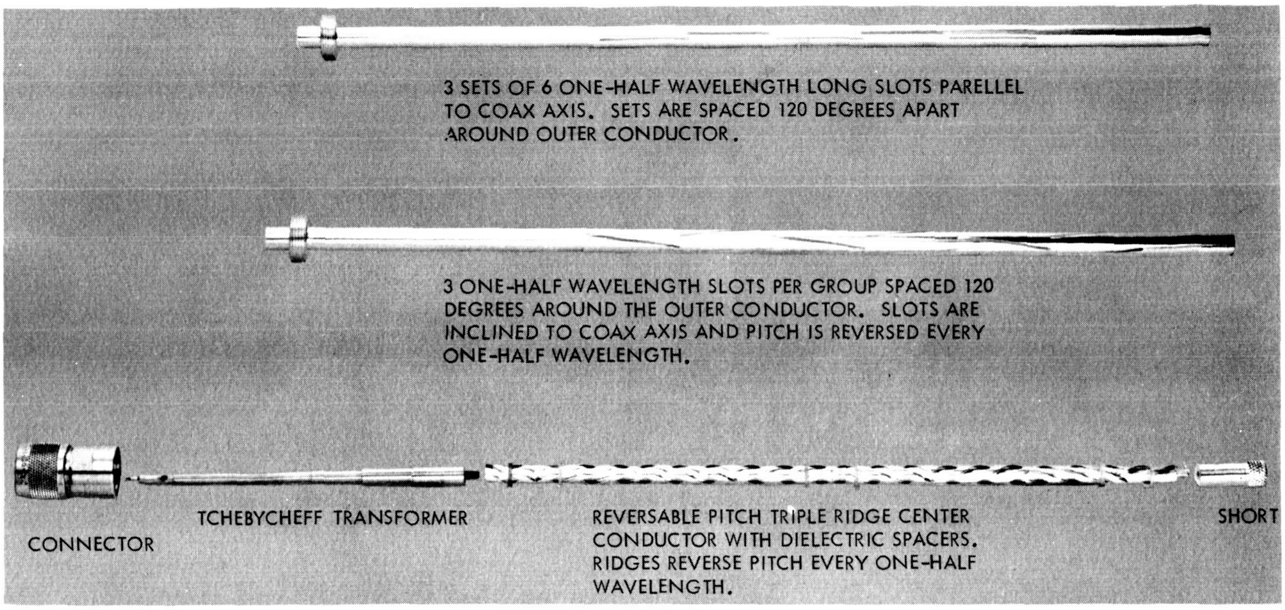

FIGURE 6-74. DETAIL OF SPIRAL CENTER CONDUCTOR ELEMENT ARRAY USING RESONANT SLOTS

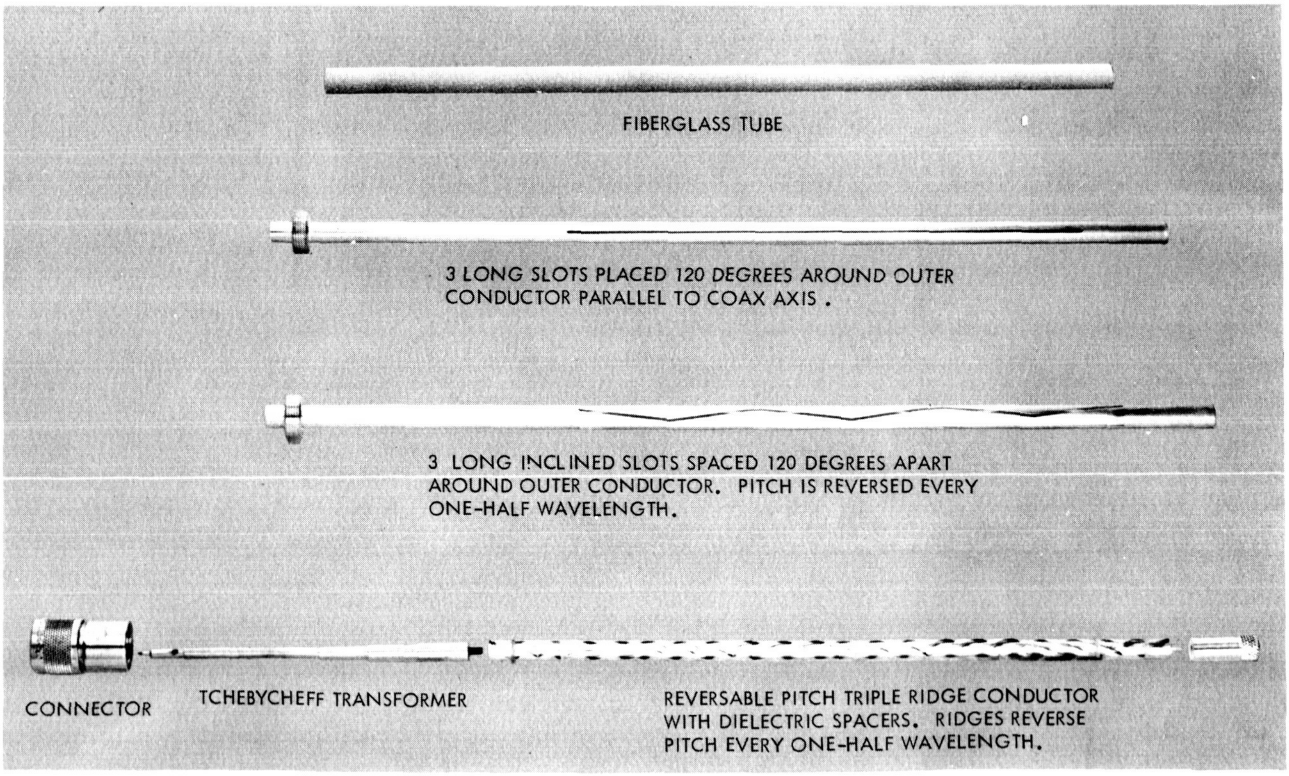

FIGURE 6-75. DETAIL OF SPIRAL CENTER CONDUCTOR ELEMENT ARRAY

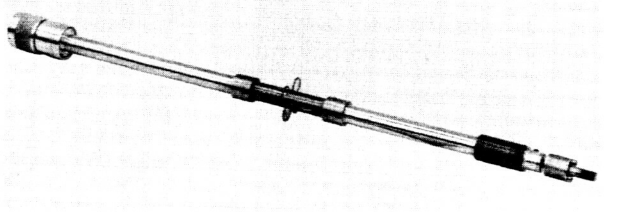

FIGURE 6-76. CLOVERLEAF RADIATING ELEMENT

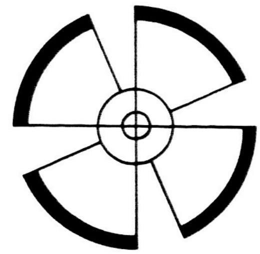

FIGURE 6-77. OUTER EDGES OF UHF CLOVERLEAF ANTENNA ARRAY

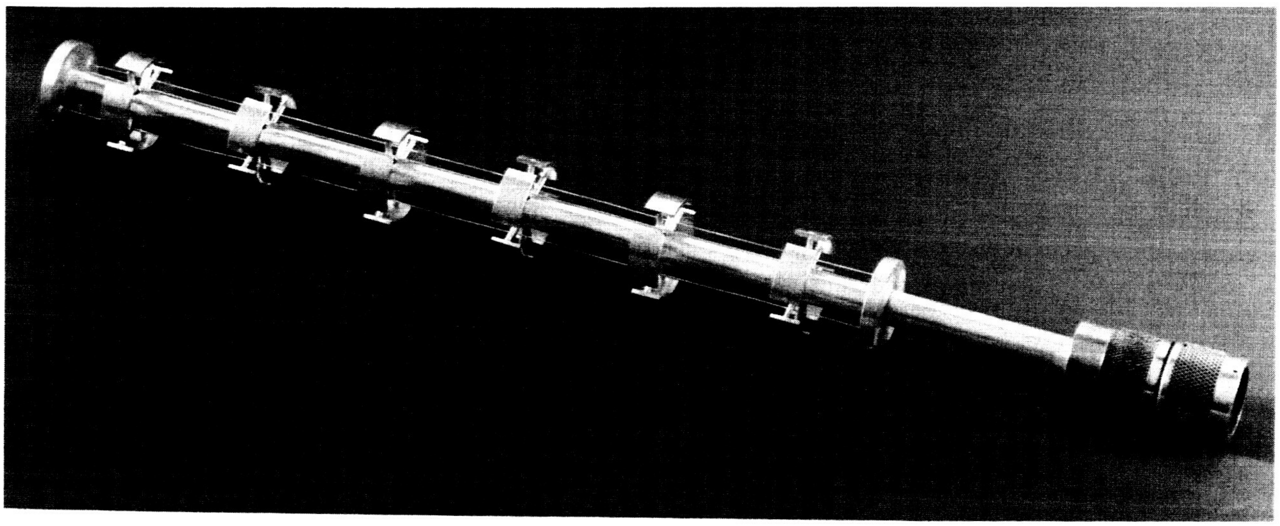

FIGURE 6-78. SIX-ELEMENT CLOVERLEAF ARRAY

outer surface of the coaxial line $\lambda/4$ down the line in each direction from the cloverleaf. An additional feature of the suppressor wire is that it acts as a vernier control on the frequency. This control is accomplished by varying the distance from the coaxial line to where the suppressor wire is connected to the loop. A symmetrical test section radiating element was tested, with results indicating an omnidirectionality of less than 2 db. The final dimensions of the cloverleaf element were established, thus completing the cloverleaf element development.

A six-element cloverleaf array was fabricated and tested (Figure 6-78). The elements were additive as shunt elements as expected; however, due to several changes in the cloverleaf parameters to ease fabrication, the array was resonant at a frequency of 3830 mc instead of at the design frequency of 4080 mc. Figures 6-79 and 6-80 show E-plane and H-plane patterns at these two frequencies. The major characteristics of this array are shown as:*

Characteristic	*3830 mc*
VSWR	1.19:1
Omni-directionality	0.3 db
Beamwidth	18.6 degrees
Sidelobe level	—9.7 db
Gain	7.6 db (maximum)

*E-plane and H-plane were made at frequencies above and below 3830 mc. The H-plane pattern deteriorated at frequencies above and below 3830 mc indicating that best operation of the cloverleaf array is obtained at 3830 mc.

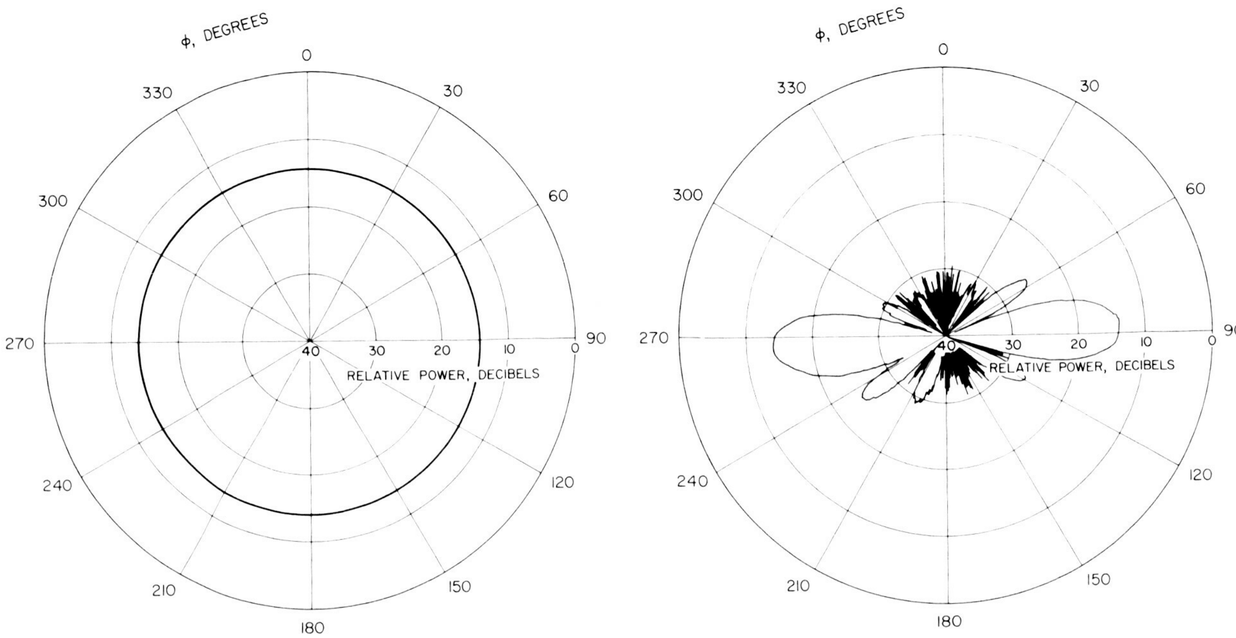

a) E-plane

b) H-plane

FIGURE 6-79. 3830-MC, SIX-ELEMENT CLOVERLEAF ARRAY

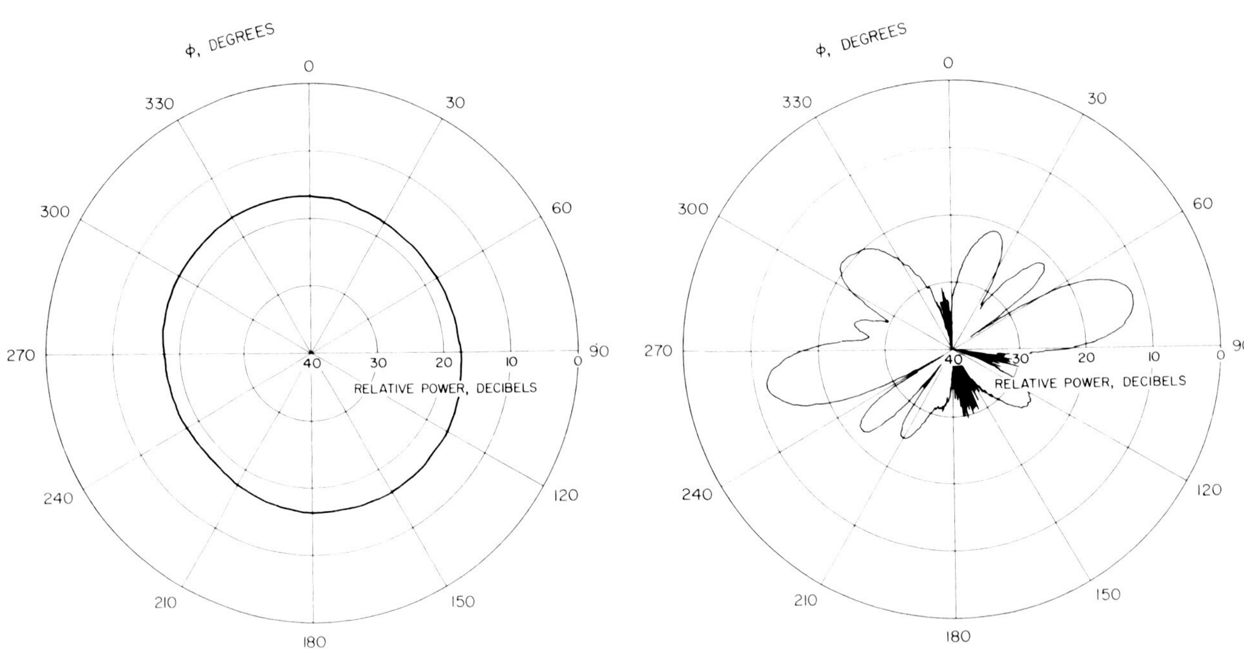

a) E-plane

b) H-plane

FIGURE 6-80. 4080-MC, SIX-ELEMENT CLOVERLEAF ARRAY

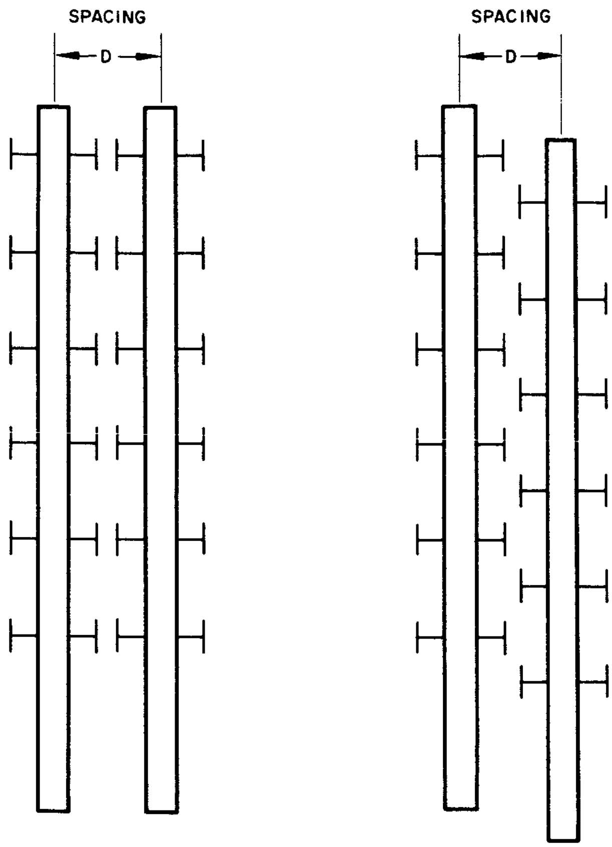

FIGURE 6-81. MUTUAL COUPLING CONFIGURATION

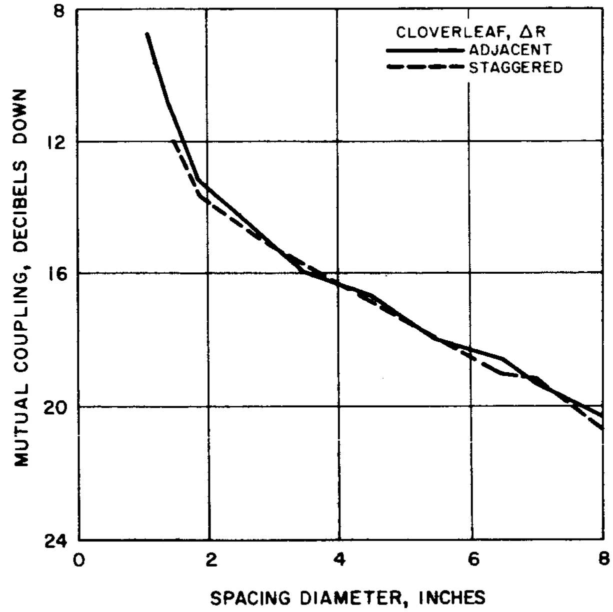

FIGURE 6-82. MUTUAL IMPEDANCE MEASUREMENTS

A second six-element cloverleaf array was fabricated for operation at 3830 mc. The impedance of this array is almost identical to the first array fabricated. The two 3830-mc cloverleaf arrays were used in a mutual coupling measurement. This measurement was made under two conditions: 1) with the cloverleaf sections adjacent, and 2) with the cloverleaf sections staggered (see Figure 6-81). The results of the mutual coupling measurement are shown in Figures 6-82 and 6-83.

PHASED-ARRAY CONTROL ELECTRONICS (PACE)

Introduction

The gain of the phased-array antenna is achieved through 16 collinear array elements located symmetrically about the spin axis of the spin-stabilized vehicle. The excitation to each of the elements is phased so that the fields radiated from the elements are reinforced in the direction of the earth. The phasing of the elements must vary in accordance with the rate of rotation of the vehicle. The processing of the signals to be transmitted is accomplished by a combination of RF and electronic circuits. The control electronics, which generate the phasing signals are discussed below.

Since some of the control signals generated define the angular position of a point on the vehicle periphery during a spacecraft revolution, they can be utilized to reference firing of the satellite control jets. The auxiliary circuits required to perform this function are also discussed.

The explanation covers some circuits which are no longer planned for spacecraft use. They are discussed for two reasons:

1) Their inclusion documents the system in the engineering model.
2) The explanation shows the evolution of system concepts during the Advanced Technical Development program.

System Description

A block diagram of a recent configuration of the phased-array control electronics (PACE) is shown in

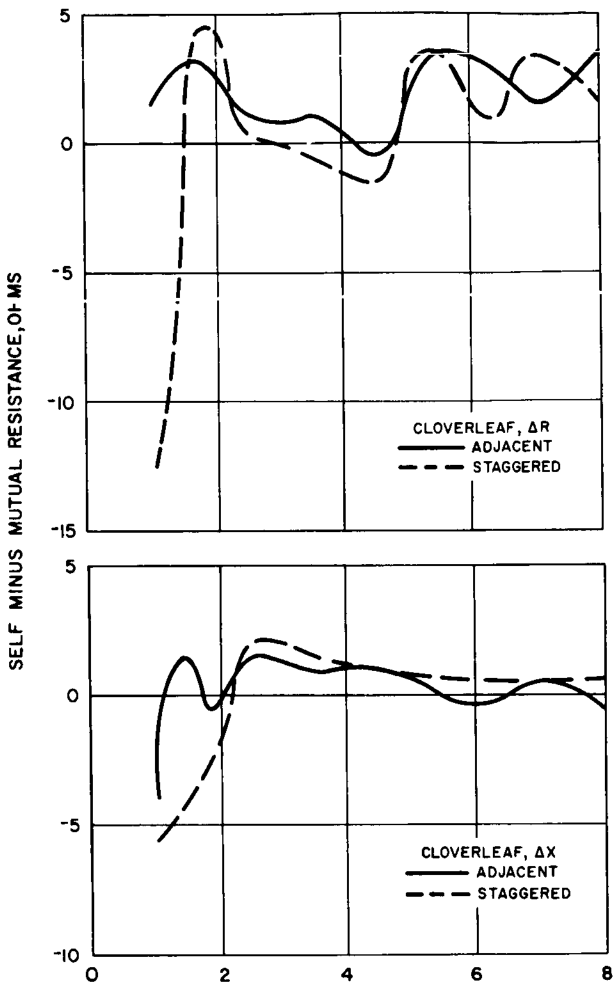

FIGURE 6-83. MUTUAL IMPEDANCE MEASUREMENTS

Figure 6-84. Because of the way this circuitry evolved, the equipment design was conducted in areas designated as the digital unit and the analog unit. These sections are divided by the dotted line on the block diagram.

Referring to the block diagram, the phase lock loop (PLL) subassembly, acting as a sampled data servo, adjusts itself such that 512 output pulses are generated for every solar input pulse. The solar pulses are generated by photovoltaic cell which responds to direct sunlight, with associated optical directivity hardware, located on the vehicle periphery. Thus, one such pulse is generated every revolution of the satellite. Part of the circuitry which forms the servo loop is a counter which, when the loop is locked, counts from zero to 512 during a revolution. The contents of this counter, at any instant, are proportional to the spacecraft spin angle since the last solar pulse. If N represents the decimal equivalent of this count, then, at any instant of time, the angle since the last solar pulse is

$$\text{Angle} = \frac{N}{512} \times 360 \text{ degrees}$$

By commanding an angle to the vehicle, and then detecting coincidence with the counter, any desired jet pulse start angle can be programmed. This coincidence detection is performed in the fire angle generator (FAG) subassembly. The FAG also provides the timing envelope for the control jet pulse. Strictly speaking, the FAG is not a part of the antenna electronics, but part of the control system. It is included here because of its association with the antenna electronics and the fact that it shares circuitry with it.

The source which drives the PLL counter drives a second counter in the variable phase control (VPC) subassembly. This counter is thus frequency locked to the PLL counter, but phase variable. Phase adjustment of this counter is performed in two ways: phase additions and subtractions can be made from the ground, via the command system, for initial alignment and station keeping; phase additions are made continually by a real-time clock to compensate for the fact that the solar reference has relative motion with respect to the spacecraft.

The VPC counter feeds a digital-to-analog converter in the sine wave generator (SWG) subassembly. This converter first generates triangular waves from the counter and then shapes these into sine waves with diode function generators. The equipment is designed such that one cycle of the sine wave occurs for each 512 inputs to the VPC counter. Thus, the sine waves have the same frequency as the spacecraft spin cycle. Two sine waves are generated, one in phase with the VPC counter (0 degree phase) and one advanced 90 degrees in phase. A third wave is generated from the 0 degree phase wave by an inverting amplifier.

The three SWG outputs drive a phase splitter which vectorially adds the inputs to produce eight sine waves of the same frequency as the inputs, all separated 22.5 degrees in phase. If the inputs are designated sin $(Wt + \theta)$, cos $(Wt + \theta)$, and $-\sin(Wt + \theta)$, then the outputs are

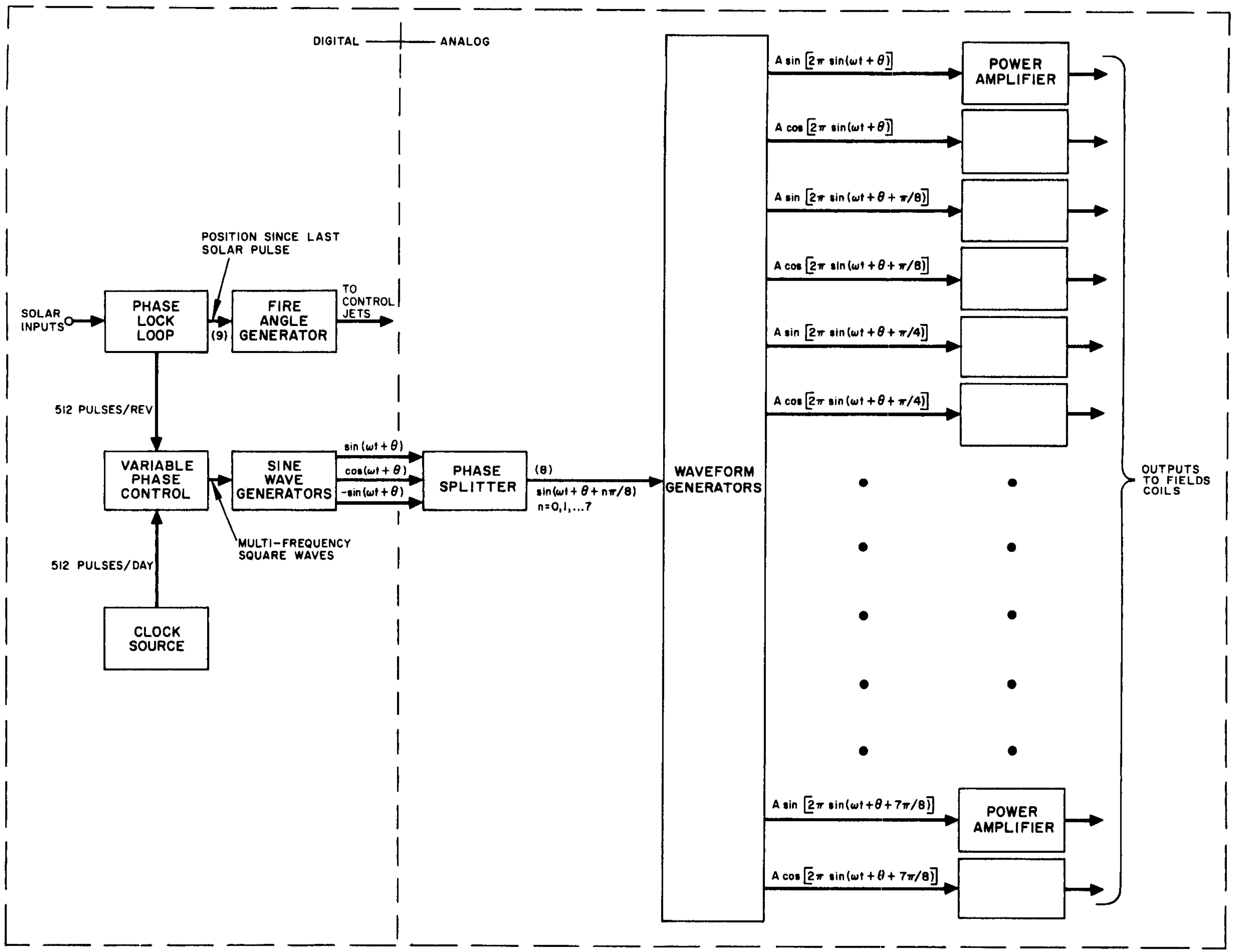

FIGURE 6-84. PHASED-ARRAY CONTROL ELECTRONICS (PACE) BLOCK DIAGRAM

$$\text{Outputs} = \sin\left(\mathrm{Wt} + \theta + \frac{N\pi}{8}\right) \quad N = 0, 1, \ldots, 7$$

Each of these waves drives two waveform generators, one of which produces the voltage sine of the input, the other the voltage cosine of the input. The 16 outputs of the generator are thus,

$$20 \sin\left[2\pi \sin\left(\mathrm{Wt} + \theta + \frac{N\pi}{8}\right)\right] \quad N = 0, 1, \ldots, 7$$

and

$$20 \cos\left[2\pi \sin\left(\mathrm{Wt} + \theta + \frac{N\pi}{8}\right)\right]$$

These are the required output signals, and, after a power gain stage, are used to drive the coils of the field generating devices.

Phase Lock Loop Subassembly

The phase lock loop is, as the name implies, a closed-loop system. The only signal input to the loop comes from a photodiode sun sensor mounted on the exterior of the satellite which provides a pulse (ψ) for each satellite revolution. A later revision of these circuits is discussed subsequently in the section entitled 'Frequency Lock Loop.'

The phase lock loop generates digital signals which ultmately are used to generate control signals to orient a transmitting antenna beam which must be pointed at the earth.

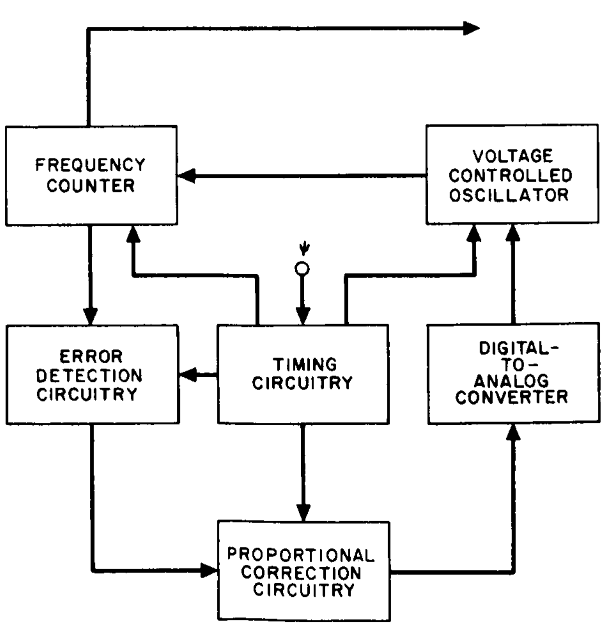

FIGURE 6-85. PHASE-LOCK LOOP SIMPLIFIED BLOCK DIAGRAM

The loop can be divided into six parts:

1) Timing circuits
2) Error detection logic circuits
3) Proportional correction circuits
4) Voltage-controlled oscillator (VCO)
5) Frequency counter

A simplified block diagram is shown in Figure 6-85.

Normally, the VCO runs at a frequency which is 1024 times the ψ input frequency, and the loop is said to be in lock. Under this condition, the error detection circuitry, which samples the frequency counter, detects no error, and the VCO frequency does not change.

In the event that the satellite spin speed changes, the VCO frequency will cease to be 1024 times the ψ frequency and the error detection circuitry will detect an error in the frequency count of the frequency counter. The error detection logic will then cause signals to be sent to the proportional correction circuitry.

The proportional correction circuitry consists of a digital accumulator with 2048 discrete states, which is capable of maintaining a constant output configuration for an infinite period of time. When the proportional correction circuitry receives signals from the error detection logic, the output configuration changes; and, as a result, the input to the digital-to-analog converter is changed.

The digital-to-analog converter supplies a constant voltage which depends on the configuration of the proportional correction circuitry. When the output configuration of the proportional correction circuitry changes, the voltage output of the converter changes also. Since there are 2048 discrete configurations possible in the proportional correction accumulator, there are also 2048 discrete voltage levels possible at the output of the converter.

The proportional correction circuitry will produce a proportional change in the output of the converter which depends on the error detected by the logic circuits, and the frequency of the VCO will be changed until it is 1024 times the spin frequency of the satellite, bringing the loop back into lock.

DETAILED DESCRIPTION OF OPERATION

Referring to Figure 6-86, the ψ signal is amplified and shaped by the ψ amplifier pulse shaper (denoted

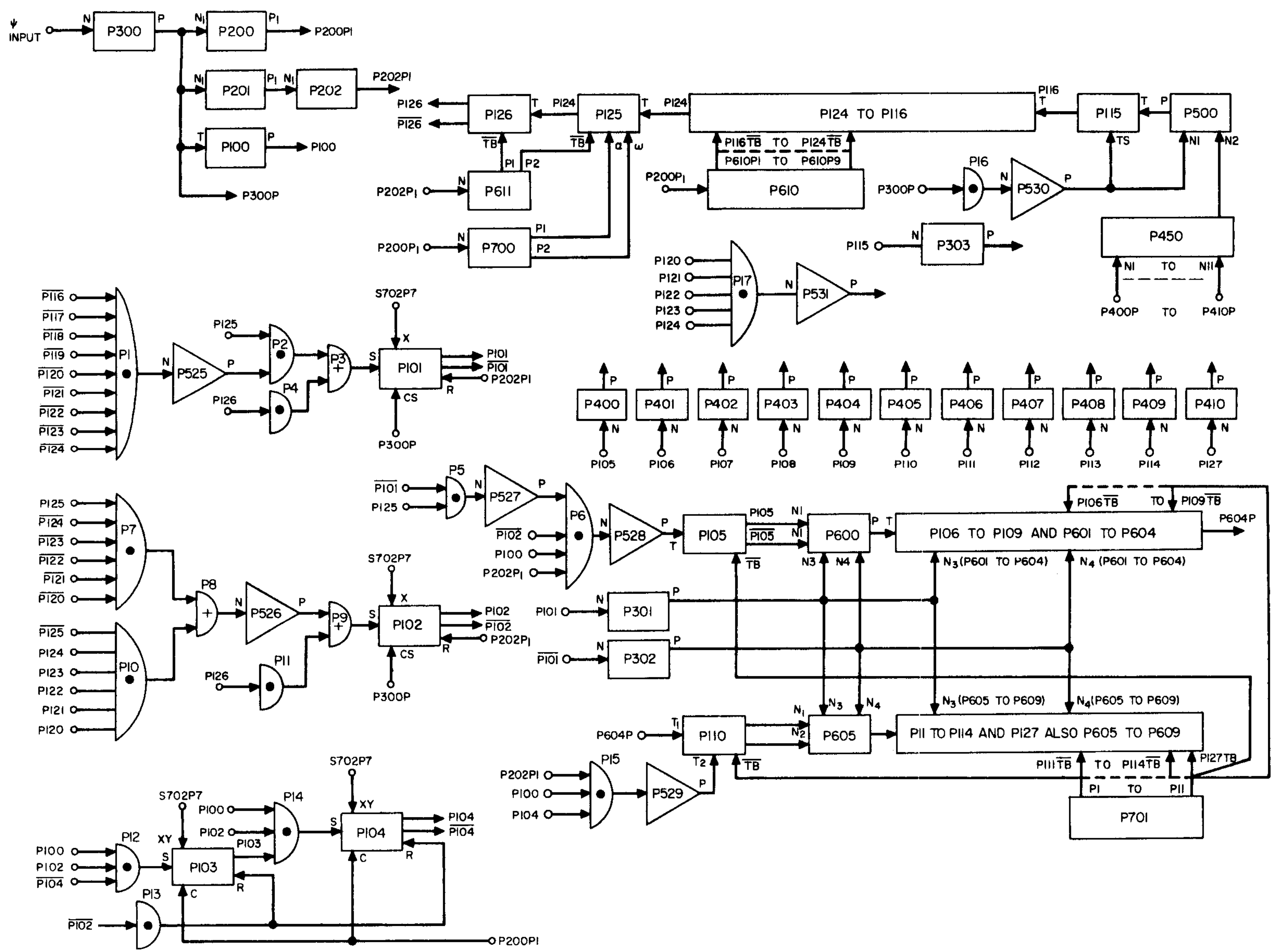

FIGURE 6-86. PHASE-LOCK LOOP BLOCK DIAGRAM

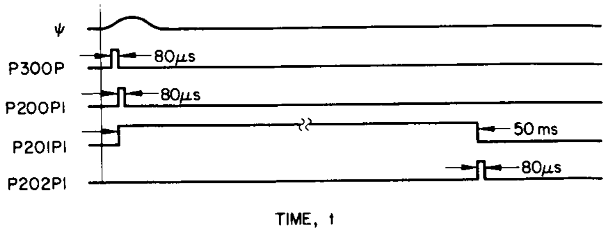

FIGURE 6-87. PHASE-LOCK LOOP TIMING WAVEFORMS

logically by P300). The output of this amplifier is a square pulse of about 60 microseconds duration which serves as the fundamental clock source of the phase lock loop. The ψ signal also generates, through the use of three monostable multivibrators (denoted by P200, P201, and P202) other timing signals. The time relationships between these signals are shown in Figure 6-87.

The phase lock loop can be in two basic modes. The first of these modes is termed the "in-lock" mode, and the second is the "out-of-lock" mode. The in-lock mode exists when the frequency source to ψ input frequency ratio is 1024 and the phase lock loop is in a stable state, i.e., there are no changes taking place in the loop which would cause a change in the source frequency. The out-of-lock mode exists when the ratio is greater or less than 1024. The state of the loop in this mode is constantly changing in such a manner as to correct the frequency ratio and thus bring the loop into the in-lock mode.

The mode of the loop is determined electronically by using logic circuits to sample the state of the frequency counter at some time during a revolution of the satellite. The time chosen for this purpose is the time of occurrence of the ψ input.

The frequency counter consists of 11 flip-flops (denoted logically by P116 through P126). The first ten of these flip-flops count during each revolution, the frequency of flip-flop P115, which is running at one half the frequency of the source, P500. Because both the frequency source and P115 are synchronized into the high state, each cycle by the ψ amplifier, and the first nine flip-flops of the frequency counter are reset just after they are sampled and before P115 has time to change, the frequency counter starts a new count during each cycle of the satellite. If flip-flop P125 is high, and flip-flops P116 to P124 are low at the pulse time of the ψ amplifier, the count will be correct, and the loop will be in-lock.

If the loop is not in-lock, it is, of course, out-of-lock, and it can be in one of two states. The first of these states exists if the frequency of the source is too low; then the flip-flop P125 will be low, and flip-flops P116 through P123 might be in any configuration. This state is termed the addition state since increments in frequency must be added to the source frequency to bring it up to the correct value.

The second possible out-of-lock state is termed the subtraction state. This state occurs when the frequency of the source is too high. Then flip-flop P125 will be high and flip-flops P116 through P124 might be in any configuration except the case where they are all low. This state is called subtraction state since increments in frequency must be subtracted from the source frequency.

The purpose of flip-flop P126 is to prevent the loop from "locking in" on integral multiples of the desired frequency ratio. If the frequency source is operating at a frequency such that the ratio is 2048 instead of 1024, the other flip-flops would register a count which would be interpreted as the proper count if P126 were not present. Flip-flop P126 is a set-reset flip-flop which will always be high when the source frequency is too high.

At this point in the description, it will be advantageous to look at the means by which the input voltage to the frequency source (voltage-controlled oscillator) is controlled.

The input to the frequency source comes from a resistive ladder which has 11 inputs. Each input to the ladder can be one of two voltage levels, +8 or −8 volts. The voltage output of the resistive ladder depends on the input voltage levels at each of the 11 inputs. The design of the ladder is such that the incremental change in voltage at the output depends on the input terminal at which the voltage is changed, and a change at one end of the ladder causes a much greater change in the output voltage than a change at the other end of the ladder. Thus one end of the ladder can be termed the most significant end, and the other end the least significant.

The inputs to the ladder come from switches which are controlled by the digital outputs of an 11 flip-flop register. The output of each switch is either +8 or −8 volts, as stated above. It is +8 volts if the input corresponds to a logical "1," and —8 volts if the input is a logical "0". The frequency of the frequency source is dependent on the state of a register, called the backward-forward counter (denoted by P105 through P127).

The backward-forward counter has the ability, as the name implies, to count both forward and backward. The implementation of this characteristic is accomplished by placing a special type of gate between each state of the counter. The gate uses signals which come from another part of the loop to determine whether the counter will count up or down. These signals are called the add and subtract signals, respectively. When the counter is counting up (i.e., adding), flip-flop (N + 1) is triggered by the negative edge of flip-flop (N). When the counter is counting down, flip-flop (N + 1) is triggered by the negative edge of the complementary signal of flip-flop (N).

There are two inputs to the backward-forward counter in addition to the signals which control addition or subtraction. These inputs actually cause the counter to change state, whereas the add and subtract signals do not cause changes in state, but they determine the direction in which the state change will occur.

The inputs which strobe the counter are placed, respectively: one at the input to the least significant flip-flop in the counter, P105, and the second at the input to flip-flop P110. Flip-flop P110 has two inputs, one from an interstage gate which precedes it, and the other as mentioned above. The two inputs comprise an ac "OR" function such that flip-flop P110 can be strobed by flip-flop P109, or by what has been called the second input to the counter.

The significance of the two inputs to the counters is that using the input at the least significant flip-flop, small changes can be caused to occur in the frequency of the source, and using the input to flip-flop P110, one can cause large changes to occur in the frequency of the source. The latter effect is due to the fact that flip-flop P110 is much more significant than P105, and causes a greater change in the output voltage of the ladder (i.e., the input voltage to the voltage-controlled oscillator).

With the understanding of the function of the means by which the frequency of the frequency source is controlled, it is necessary to comprehend the means by which the input signals to the backward-forward counter are derived. There are four of these signals: the add and subtract signals, and the two strobe signals.

The add and subtract signals come directly from the add and subtract amplifiers. These circuits are digital ramp circuits, which have long run-down times. The purpose of the long run-down is to prevent their output signals from acting as strobes.

The inputs to the add and subtract amplifiers come from flip-flop P101, called the subtract flip-flop. The input to the add amplifier is FF, and the input to the subtract amplifier is FF. The subtract flip-flop is high only when it is set high by the ψ amplifier during sample time. The subtract flip-flop will be set high only when the frequency ratio is too high and it is necessary to subtract. When it is necessary to add, flip-flop P101 will not change state. Figure 6-88 shows the time relationship between timing signals and the add and subtract control signals.

The strobe signals come from two entirely different sources. The strobe, which is the input to the least significant flip-flop of the backward-forward counter, is termed the fine correction strobe. The other strobe, which is one of the inputs to flip-flop P110 of the counter, is termed the coarse correction strobe.

The origin of the fine correction strobe is an inverter which is controlled by a number of logical functions. These functions allow the strobe to occur only when:

1) There is no coarse correction strobe.
2) The clock is present, which in this case is monostable multivibrator P202.
3) There is an error in the frequency ratio.

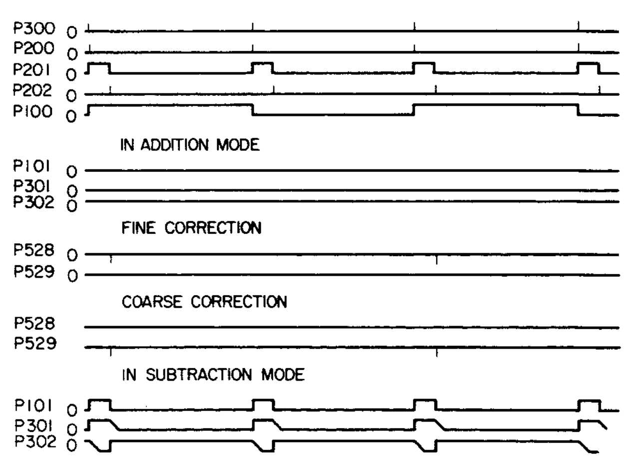

FIGURE 6-88. TIMING WAVEFORMS AND ASSOCIATED WAVEFORMS FOR PHASE-LOCK LOOP OVER SEVERAL PERIODS OF ψ

4) Flip-flop P100, which is called the count flip-flop, is high.

The purpose of flip-flop P100, which is triggered by the amplifier, is to allow a correction only during *every other* revolution of the satellite. Thus, the loop has time to stabilize between corrections.

It should be obvious, then, that a strobe will occur every other time an error is detected, and the add-subtract signals will never change if the counter is adding.

The coarse correct strobe is generated by different logical functions than the fine correct strobe. If any of the seven most significant flip-flops of the frequency counter are in error, flip-flop P102 will be set during sample time by the ψ amplifier. This will occur regardless of the condition of the error, that is, whether it is an over-count or an under-count.

The first time a coarse error is detected while the count flip-flop, P100, is high, flip-flop 103 (the first of the lock control flip-flops P103 and P103) will be set high. The second time a coarse error occurs during the time the count flip-flop is high, flip-flop P104 will be set high. Both P103 and P104 will remain in the high state until the six most significant flip-flops of the frequency counter are no longer in error.

During the time that flip-flop P104 is high, the coarse correction strobe will occur provided, of course, that the count flip-flop is high. The purpose of the lock control is to prevent a coarse correction from occurring should a noise voltage at the input to the ψ amplifier cause the frequency counter to be sampled while it was counting. Thus, a coarse error must be detected twice before any coarse correction will be made in the backward-forward counter.

The only unaccounted for parts of the phase lock loop are the slow voltage turn on (denoted P107) and the antinoise buffer (denoted P700).

The antinoise bias buffer is present because flip-flop P125 of the frequency counter has been reset. The buffer isolates flip-flop P125 from any changes that might occur in flip-flop P124, which could cause P125 to change state.

The purpose of the slow voltage turn-on is to set the backward-forward counter in a given state when the power is initially turned on. Setting up the counter initially decreases the amount of time which it would take in the worst case for the loop to get in lock if the counter came on randomly.

Fire Angle Generator Subassembly

The primary function of the fire angle generator subassembly (FAG) is to provide a control signal to start and terminate the firing of the position-correcting jets. A later, simplified version of this subassembly is described subsequently in the section entitled "Advanced jet control."

Its secondary function is to provide, upon command, a variable time interval for use in the variable phase control subassembly (VPC).

The command structure, shown below, outlines the effect of each command bit on the control of the FAG. The function of bit C116 is to indicate if the FAG is to be used.

$$\left.\begin{array}{l}\text{C101}\\\text{C102}\\\text{C103}\end{array}\right\}\ \begin{array}{l}\text{Number of Corrections in}\\\text{Fine-Correct Mode}\end{array}$$

C104—Correction Mode Control

$$\left.\begin{array}{l}\text{C105}\\\text{C106}\\\text{C107}\\\text{C108}\\\text{C109}\\\text{C110}\\\text{C111}\\\text{C112}\\\text{C113}\end{array}\right\}\ \text{Start Angle}$$

$$\left.\begin{array}{l}\text{C114}\\\text{C115}\end{array}\right\}\ \text{Select Jet}$$

C116—Operate FAG

CX —Command Execute

Two modes of correction exist within the FAG primary function. Mode control is accomplished with the use of C104. When C104 is high, the mode is coarse-correct, and a control signal is generated once every spacecraft revolution for as long as the command execute signal is present. When C104 is low, the mode is fine-correct, and only a programmed number (seven maximum) of control signals will be generated during a command execute time interval.

With the use of bits C105 through C113, the angle between the sun position and the start jet fire position can be varied. These nine bits are compared with the nine bits of the phase lock loop frequency counter;

when coincidence occurs, the N1 through N9 inputs to the multiple set gate (MSG) rise to an enable state (see Figure 6-89). If, simultaneously, inputs N10 through N13 are in their enable state, control flip-flop F100 will be set to its high state and the counter, composed of F101 through F104, will be set to a non-zero state. The setting of F100 and the non-zero counter state is implemented by the MSG outputs P1 through P5, which are connected to special set terminals of F100 through F104. The negative voltage transition which occurs at these outputs will effect a flip-flop change of state if the flip-flop output is in its low state. All of the MSG outputs P1 through P4 are not connected to the special set terminals of F101 through F104. Which terminals are connected is determined by the desired angle through which the correction jet is to be fired.

When the F100 signal is in its high state, the jet fire amplifier F300 activates a solenoid which releases the jet gas and the FAG counter input is enabled. Two counter input channels, gates F3 and F4, are provided to maintain a constant jet fire time interval.

It was mentioned that the FAG counter is set to a non-zero state. This non-zero state is necessary to fix the angle through which the jets are activated. The counter is capable of counting 16 P118 or $\overline{\text{P118}}$ pulses. Since each P118 or $\overline{\text{P118}}$ pulse represents nominally 5.6 degrees, the jet would fire for 90 degrees if the counter were reset to zero. If the non-zero state is denoted by N_I, the jet fire angle is

$$\text{Angle} = \left[15 + \frac{3}{4} - N_I \pm \frac{3}{16}\right] 5.624 \text{ degrees}$$

At the instant the FAG counter changes from a binary count of 15 to a binary count of zero, the control flip-flop F100 will be reset and the solenoid coil will be deactivated. Resetting F100 is accomplished by using the F104 signal as a clock pulse for the F100 flip-flop reset gate.

To operate the FAG's secondary function, the N10 input to the MSG must be in its low state.

Input N14 (V201P1) to the MSG is a signal positive pulse generated within the variable phase control subassembly. The rising edge of this pulse will effect negative pulses at MSG outputs P1 through P4 which will reset the FAG counter to zero. The outputs P1 through P4 are connected to $\overline{\text{TB}}$ of F101 through $\overline{\text{TB}}$ of 104, respectively.

The signal V201P1 is also coneected to the N1 inputs of the four initial condition gates, F609 through F612. Signals C105, C106, C107, and C108 are connected to the N2 inputs of F609, F610, F611, and F612, respectively. When the signal, V201P1, falls to near ground potential, the one's complement of the C105 – C108 binary number will be shifted into the FAG counter. This shift occurs because when C105, for example, is in its high state, no output will occur at point F609P to set F101. Therefore, the F101 signal will remain at its low state voltage which corresponds to the one's complement of the C105 signal. If C105 is in its low state when the V201P1 signal experiences its negative transition, an output at point F609P will occur and state F101 will be set to its high-voltage output state.

At the same time the initial conditions are set into the FAG counter, the V119 signal into gate F6 rises to its high state. The signal P303P is a square wave, and it is used to advance the FAG counter. The first trigger will occur no less than 300 microseconds after signal V119 rises.

When the FAG counter has an output count of 15, gate F7 will rise; this causes flip-flop V119 to be reset approximately 390 microseconds later.

Figure 6-90 illustrates the time sequence of operations when the FAG is performing its secondary function. Times t_1 throu t_6 are defined as follows:

t_1 – FAG Counter Reset to Zero

t_2 – One's Complement to C105 through C108 Shifted into FAG Counter and V119 is set

t^3 – First FAG Counter Trigger Pulse

t_4 – Second FAG Counter Trigger Pulse

t_5 – Count of 15 is Achieved

t_6 — V119 Reset

Letting N_I represent the decimal equivalent of the C105 through C108 binary number, the number of P303P cycles, Nc, that will be counted by the FAG counter is:

$$N_c = N_I - 1$$

Variable Phase Control

The variable phase control provides the necessary signals to the sine wave generator so that it may gener-

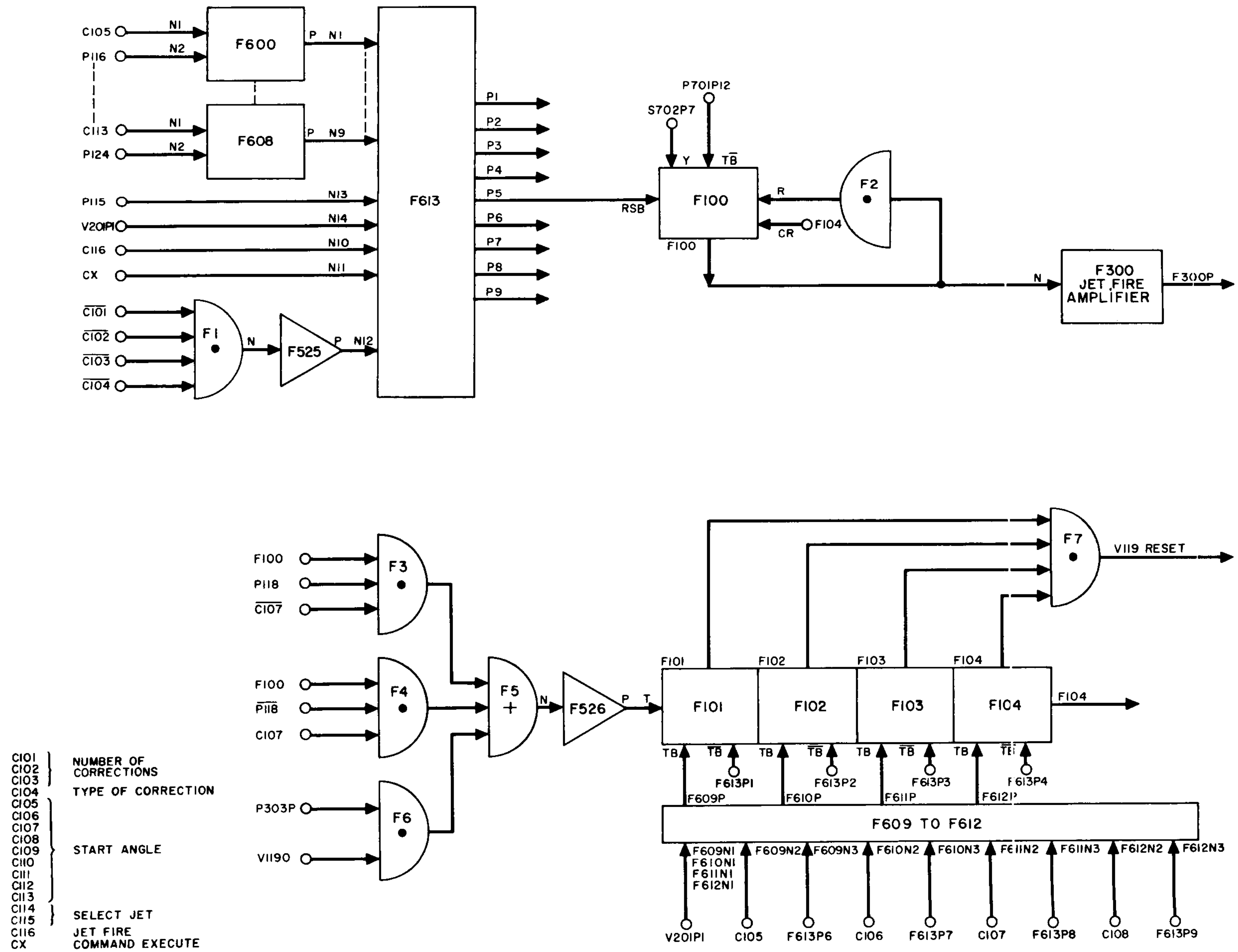

FIGURE 6-89. FIRE ANGLE GENERATOR

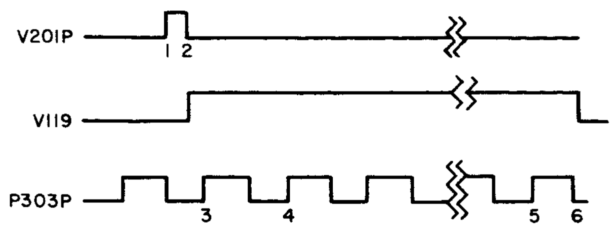

FIGURE 6-90. FIRE ANGLE GENERATOR TIMING WAVEFORMS

ate the required sine and cosine functions.

The main signals available from the variable phase control are the outputs of a nine-stage binary counter (V-120-V128). The contents of this counter contain a binary number which progresses from zero to its full-scale value of 511 in a ramp-like fashion as a function of time. The register increases one count for every cycle of the phase lock loop flip-flop P115; therefore, the register will complete its cycle (zero to zero) every 512 cycles of P115. It has been previously shown that this output (P115) has 512 cycles per spacecraft revolution when the phase lock loop is in lock. Consequently, the variable phase control counter will also complete one cycle per spacecraft revolution.

Although the variable phase control counter is frequently locked with the phase lock loop counter, it should be noted that the *phase* between the two counters is generally not zero, but instead, some constant. That is, the variable phase control register contents will be some constant binary number between 0 and 511 every ψ time, whereas the contents of the phase lock loop register is always zero at ψ time. As long as no counts are subtracted from, or additional counts are added to, the variable phase control counter, the phase between the two counters will remain constant. This will cause the highly directional phased-array antenna beam to be pointed in a given direction in space referenced to the sun. This direction may be changed by advancing or retarding the phase between the two counters. The phase may be changed by modifying the contents of the variable phase control register to increase or decrease the binary number in the register at ψ time. One method of changing this binary number is to add or subtract from one to fifteen relative counts per command execution under ground control. This capability enables the ground control to "walk" the antenna beam from any position to center the beam on the earth. The other method available for changing the phase is the automatic addition of one count every 2.812 minutes which causes 512 additions per day. Since the sun, which references the PACE *appears* to revolve around the spacecraft once per day, the phase must be continually adjusted to keep the antenna beam trained on the earth. This automatic addition of 512 counts causes the phase to be changed in a compensating direction, 360 degrees per day.

The variable phase control block diagram is given in Figure 6-91, and the waveforms in Figure 6-92. Normally, V200 and V6 are low, so that V5 is the controlling input to inverter V528 which drives the binary counter V120 through V128. This condition is shown in Figure 6-92a. Since $\overline{\text{V119}}$ is true, V528 will complement the input P303 P thus adding a count to register on every negative going edge of V528 which directly follows P115. Figure 6-92b shows how an extra "time of day" count is added. The fork oscillator V500 provides a 1553.446 cps frequency source which is counted down by the time of day counter V100 through V117 to provide an output frequency of 512 cycles per day. Inverter V301 provides a buffering action to set flip-flop V118 whenever V117 goes from its zero state to its one state. Flip-flop V118 provides a memory function which is "anded" with the timing signal P115. The output of the voltage-controlled oscillator P500, which drives P115, is buffered and inverted by V304. The negative going edge of V304 provides a trigger to the monostable multi-vibrator V200 when gate V1 is true. V200 is used to reset V118 so that only one V200 output pulse is furnished per negative transition of V301, i.e., 512 pulses per day. V200 is timed to occur when P303 is low so as to add an extra pulse on the V528 output without any crossover problems.

Command outputs C114′, C115, and C116′ are true when a ground control addition or subtraction of pulses is desired. When these are true and a command execute is sent (CX), V2 charges up the input of the monostable multi-vibrator V201. The next negative going edge of P303 then initiates the output pulses V201 P1 and V201 P2 as shown in Figure 6-92c. V201 P2 goes low driving inverter V527 to its high state, thus causing V3 to inhibit P201 P2 from returning to its normal position, i.e., its "one" state. V2 goes low due to V201 P2 and remains there as long as CX and V3 are true. When CX returns to its zero state, V2 continues to remain low but V201 P2 is allowed to return to its "one" state, thus enabling the system to act upon the

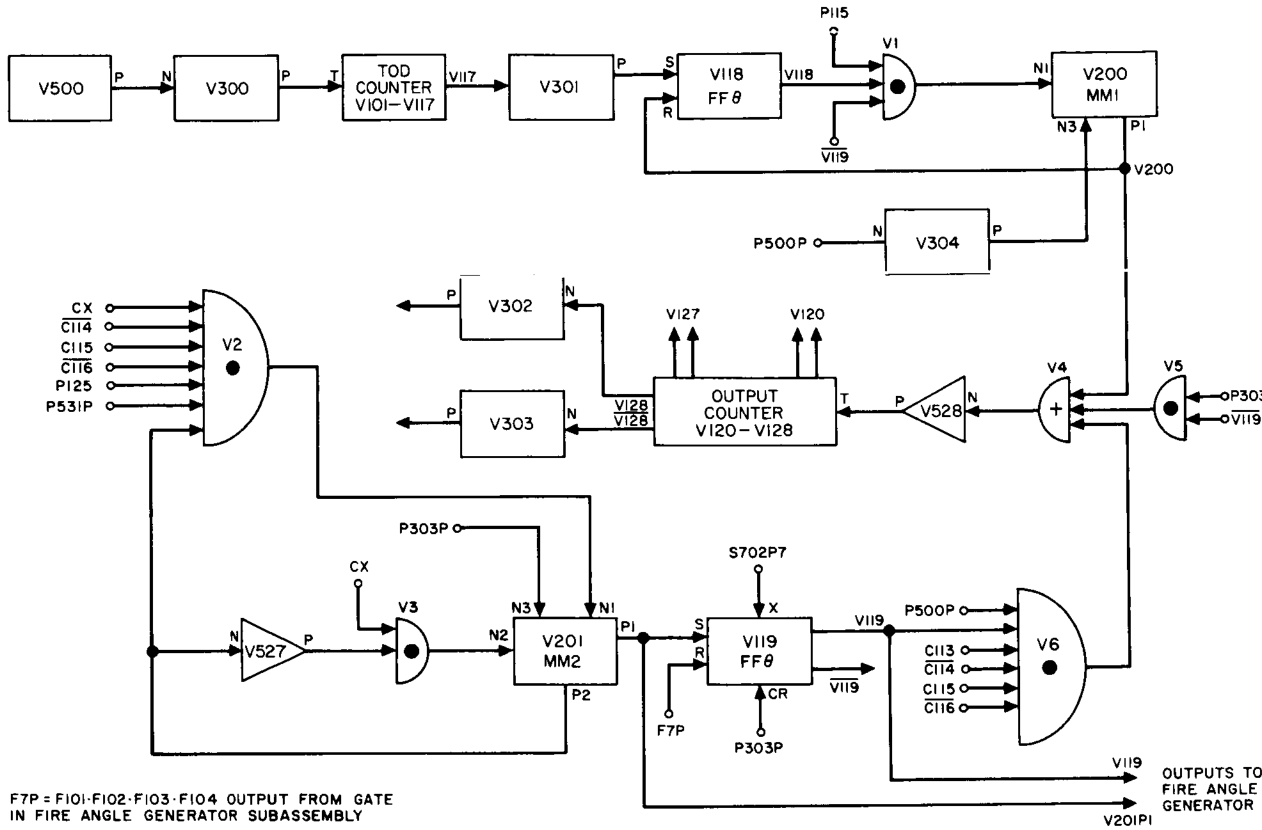

FIGURE 6-91. VARIABLE PHASE CONTROL

next command execute. This "loop" enables V201 to supply only one pulse per command execute.

V201 P1 supplies an 80-microsecond pulse to set the memory flip-flop V119, during the time P303 and P500 are low, thus preventing any crossover problems on the input to inverter V528. If C113 is true, then the double frequency input P500 will drive V528 while the P303 and the V200 inputs are disabled by $\overline{\text{V119}}$ going low. V201 P1 also provides a "clock" to set the FAG counter to the complement of the number of pulses desired to be added or subtracted in the variable phase control as determined by command inputs C105, C106, C107, and C108. V119 enables this four-stage FAG counter to count P115 negative going edges. When the FAG counter reaches full scale, a signal, F7, is provided to reset flip-flop V119 on the next negative going edge of P303. This occurs at a time when all AND gate inputs to V528 are low, which prevents any crossover problems. Thus, a double frequency input is provided to the counter during the time V119 is true; the duration of this time is controlled by the conditions set within the FAG counter. From one to fifteen counts per command execution (CX) may be added. If counts are to be subtracted from the counter, then C113 remains low and no input, other than the double frequency input to the counter, is provided during the duration of V119.

P531 P and P125′ inputs to V2 must also be true to initiate a V201 pulse which starts the entire process. These inputs are true except at ψ time and for 15 P115 negative going edges prior to ψ time so that the addition or subtraction of counts to the variable phase control is not occurring when the ψ pulse occurs. Both flip-flop P115, and the voltage-controlled oscillator, are set to their "one" state at ψ time. This might cause plus or minus one extra count to be added or subtracted to the variable phase control counter if P531 P and P125′ were not included in V2 to inhibit such a condition. However, this provision requires that the

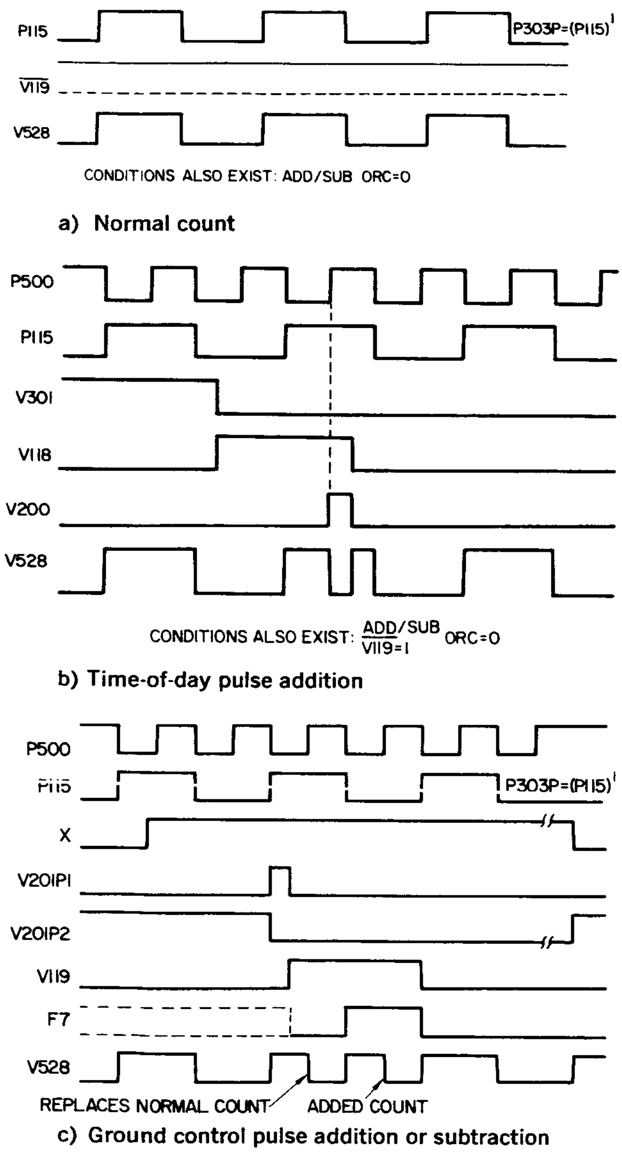

FIGURE 6-92. VARIABLE PHASE CONTROL WAVEFORMS

command execute (CX) be greater than 60 ms to assure that action is taken after the inhibited period.

Sine Wave Generator Subassembly

The sine wave generators produce approximately sin (OC $\times$ $2\pi/512 + \alpha$), sin OC $\times$ $2\pi/512 + \alpha + \pi$), and cos (OC $\times$ $2\pi/512 + \alpha$), where OC is the contents of the output counter in the VPC subassembly and α is a constant. The OC flip-flops drive 16 binary voltage weighter (BVW) switches, eight for the sine wave and eight for the cosine wave; the sin (OC $\times$ $2\pi/512 + \alpha + \pi$) signal is obtained by inverting the zero-phase sine wave.

Each set of eight BVW switches drives a resistor ladder network. Each switch output is +8 volts for a logical one input, or —8 volts for a logical zero input. The output of the unloaded ladder network is $\sum_{i=1}^{8} 2^{9-i}\, V^i$ where V^i is the i^{th} input to the ladder (input No. 1 is the least significant). The unloaded output waveform plotted versus OC is a staircase triangular wave with period 512, peak amplitudes of approximately ± 8 volts, and with resolution of 16 volts/2^8 = 16 volts/256 = 62.5 millivolts. The logic and waveforms for generating the sine and cosine waves are presented in Table 6-4 and Figure 6-93.

The sine/cosine wave amplifiers produce current gain at unity voltage gain for the sine and cosine waves, respectively. The sine wave inverter has a voltage gain of minus one plus current gain to produce the sin (OC $\times$ $2\pi/512 + \alpha + \pi$) output signal.

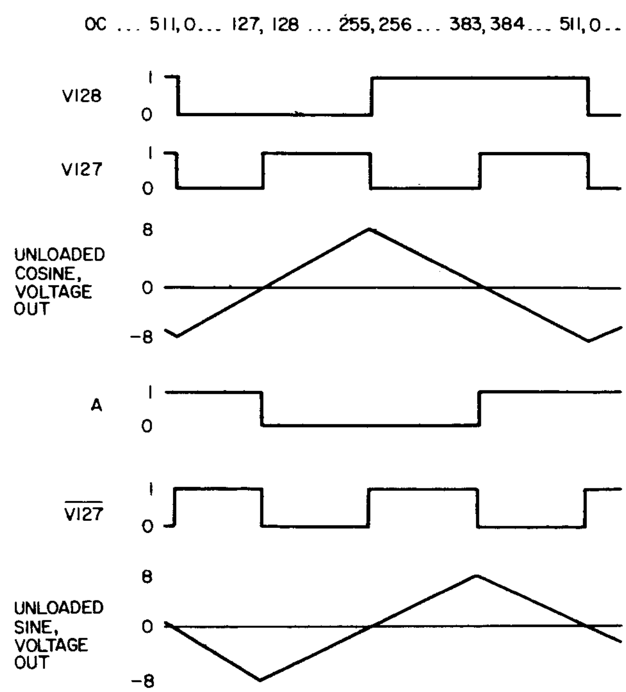

FIGURE 6-93. WAVEFORMS IN SINE WAVE GENERATORS

TABLE 6-4. LOGIC EQUATIONS FOR GENERATING SINE AND COSINE WAVES

SW 1 = $\overline{(V128)}$ (V120) + (V128) $\overline{(V120)}$	SW 1 = $\overline{(A)}$ (V120) + (A) $\overline{(V120)}$
SW 2 = $\overline{(V128)}$ (V121) + (V128) $\overline{(V121)}$	SW 2 = $\overline{(A)}$ (V121) + (A) $\overline{(V121)}$
SW 3 = $\overline{(V128)}$ (V122) + (V128) $\overline{(V122)}$	SW 3 = $\overline{(A)}$ (V122) + (A) $\overline{(V122)}$
SW 4 = $\overline{(V128)}$ (V123) + (V128) $\overline{(V123)}$	SW 4 = $\overline{(A)}$ (V123) + (A) $\overline{(V123)}$
SW 5 = $\overline{(V128)}$ (V124) + (V128) $\overline{(V124)}$	SW 5 = $\overline{(A)}$ (V124) + (A) $\overline{(V124)}$
SW 6 = $\overline{(V128)}$ (V125) + (V128) $\overline{(V125)}$	SW 6 = $\overline{(A)}$ (V125) + (A) $\overline{(V125)}$
SW 7 = $\overline{(V128)}$ (V126) + (V128) $\overline{(V126)}$	SW 7 = $\overline{(A)}$ (V126) + (A) $\overline{(V126)}$
SW 8 = $\overline{(V128)}$ (V127) + (V128) $\overline{(V127)}$	SW 8 = $\overline{(A)}$ $\overline{(V127)}$ + (A) (V127)

Waveform Generators and Amplifiers

DESCRIPTION

This portion of the Syncom II equipment is used for generating, and amplifying, the low-frequency currents that control the phase angles of the radio-frequency currents in the antenna elements. A simplified version of these circuits is discussed under the section entitled "Modified Waveform Generators." Without allowing for any redundancy, the minimum quantity of apparatus required for this function consists of one adding network as represented in Figure 6-94, 16 waveform generators as represented in Figure 6-95 and 16 power amplifiers with drivers as represented in Figure 6-96. The output currents of the power amplifiers are transmitted through the 16 field coils of the eight ferrite phase shifters associated with the antenna array (see Figure 6-97 for block diagram).

INPUT AND OUTPUT REQUIREMENTS

The adding network requires three input signal voltages as follows:

$$e_a = A \sin 2\pi \text{ feet}$$

$$e_b = A \cos 2\pi \text{ feet}$$

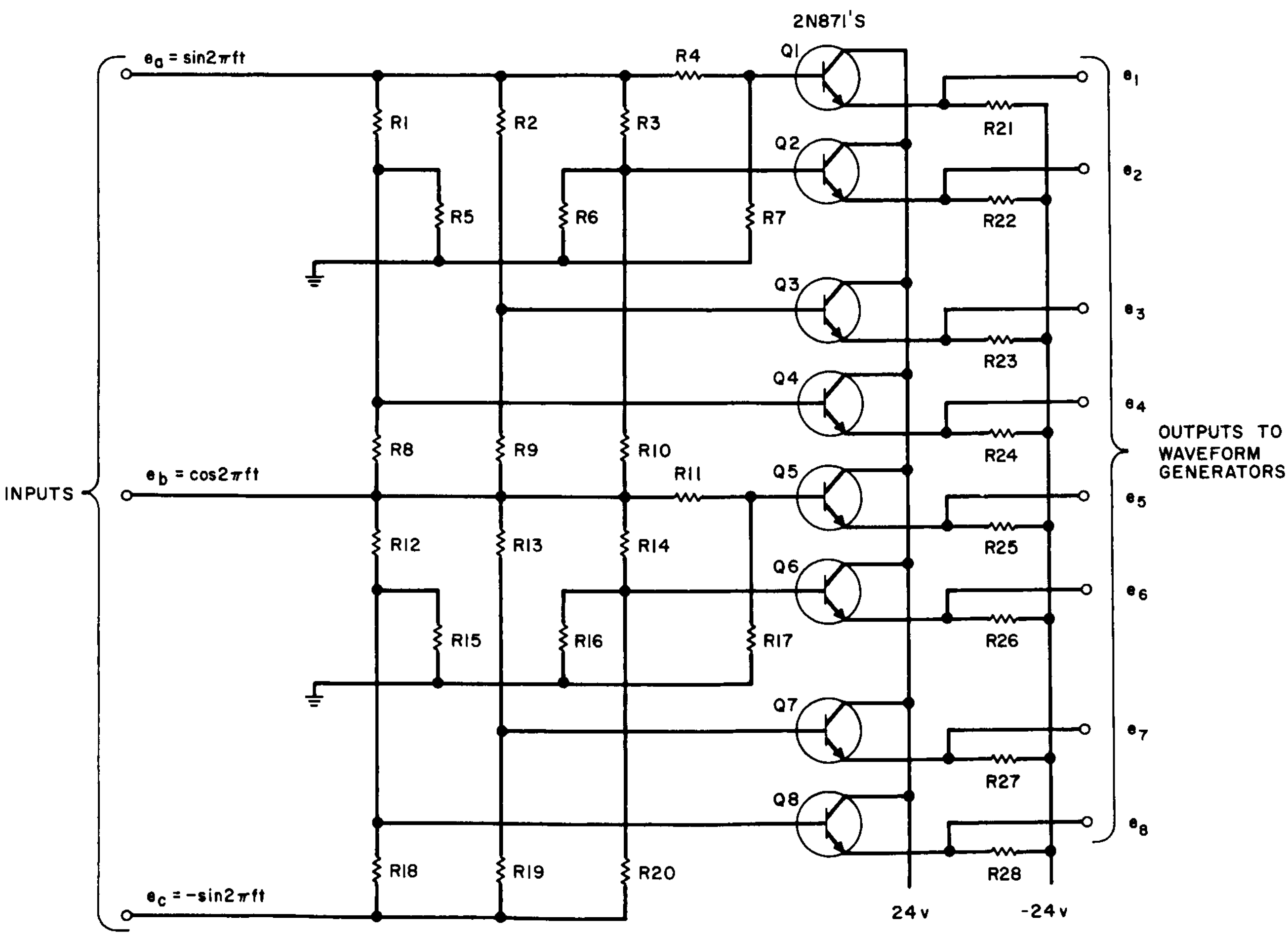

FIGURE 6-94. ADDING NETWORK

$$e_c = -A \sin 2\pi \text{ feet}$$

where the amplitude A is approximately 4.5 volts, and the frequency f is approximately 1.67 cps.

The adding network is required to produce eight sine-wave output voltages, as follows:

$$e_1 = E \sin (2\pi \text{ feet})$$

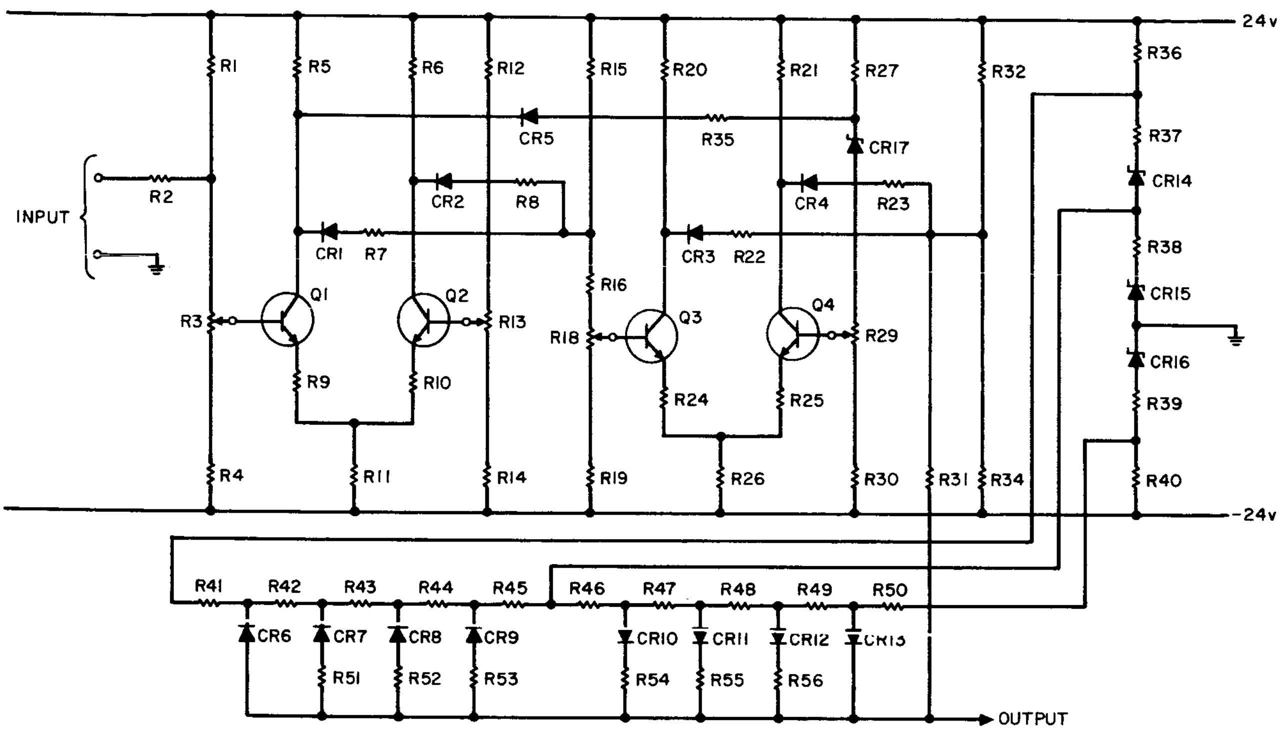

FIGURE 6-95. WAVEFORM GENERATOR

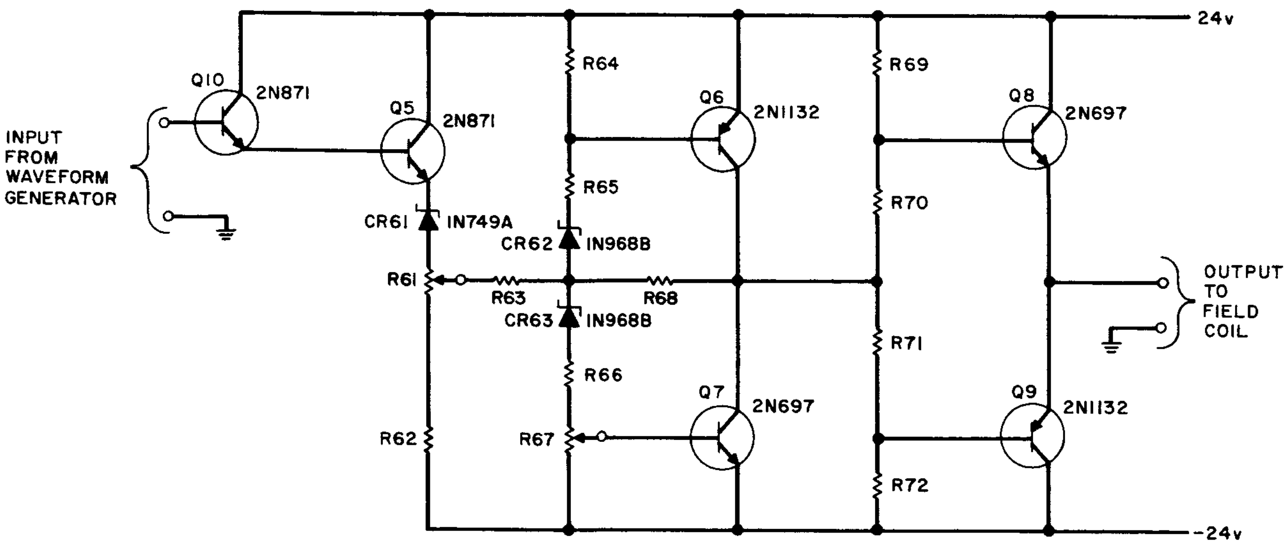

FIGURE 6-96. POWER AMPLIFIER WITH DRIVER

$$e_2 = E \sin (2\pi \text{ feet} + 22.5 \text{ degrees})$$

$$e_3 = E \sin (2\pi \text{ feet} + 45.0 \text{ degrees})$$

$$e_4 = E \sin (2\pi \text{ feet} + 67.5 \text{ degrees})$$

$$e_5 = E \sin (2\pi \text{ feet} + 90.0 \text{ degrees})$$

$$e_6 = E \sin (2\pi \text{ feet} + 112.5 \text{ degrees})$$

$$e_7 = E \sin (2\pi \text{ feet} + 135.0 \text{ degrees})$$

$$e_8 = E \sin (2\pi \text{ feet} + 157.5 \text{ degrees})$$

where the amplitude E is approximately 3.2 volts, and the frequency f is approximately 1.67 cps. The phase angles of these eight voltages differ from each other by integral multiples of 22.5 degrees, which is 360 degrees/16. Each of these voltages is applied to the input circuits of 2 of the 16 waveform generators.

The 16 waveform generators, with their associated amplifiers, are required to deliver, to the field coils, the following 16 currents:

$$i_1 = I \cos 2\pi \, [\sin (2\pi \text{ feet})]$$

$$i_2 = I \sin 2\pi \, [\sin (2\pi \text{ feet})]$$

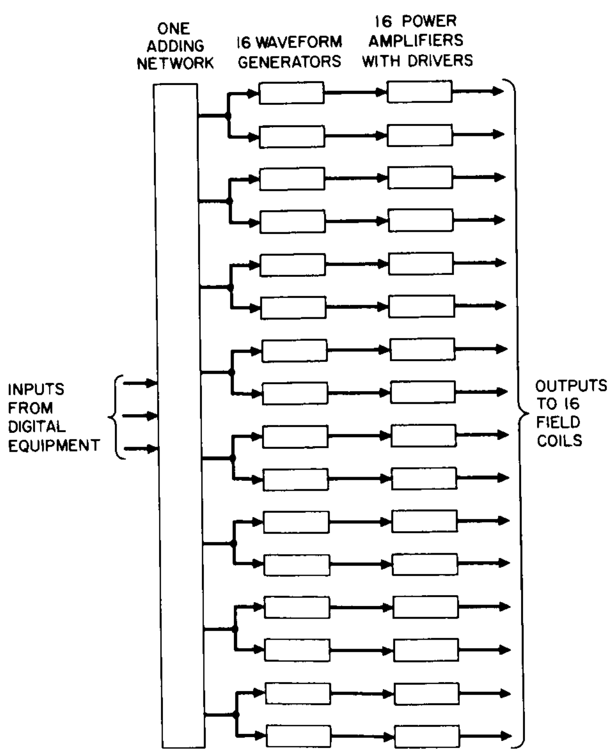

FIGURE 6-97. ANALOG ELECTRONICS BLOCK DIAGRAM

$$i_3 = I \cos 2\pi \, [\sin (2\pi \text{ feet} + 22.5 \text{ degrees})]$$

$$i_4 = I \sin 2\pi \, [\sin (2\pi \text{ feet} + 22.5 \text{ degrees})]$$

$$i_5 = I \cos 2\pi \, [\sin (2\pi \text{ feet} + 45 \text{ degrees})]$$

$$i_6 = I \sin 2\pi \, [\sin (2\pi \text{ feet} + 45 \text{ degrees})]$$

$$i_7 = I \cos 2\pi \, [\sin (2\pi \text{ feet} + 67.5 \text{ degrees}]$$

$$i_8 = I \sin 2\pi \, [\sin (2\pi \text{ feet} + 67.5 \text{ degrees})]$$

$$i_9 = I \cos 2\pi \, [\sin (2\pi \text{ feet} + 90.0 \text{ degrees})]$$

$$i_{10} = I \sin 2\pi \, [\sin (2\pi \text{ feet} + 90.0 \text{ degrees})]$$

$$i_{11} = I \cos 2\pi \, [\sin (2\pi \text{ feet} + 112.5 \text{ degrees})]$$

$$i_{12} = I \sin 2\pi \, [\sin (2\pi \text{ feet} + 112.5 \text{ degrees})]$$

$$i_{13} = I \cos 2\pi \, [\sin (2\pi \text{ feet} + 135.0 \text{ degrees})]$$

$$i_{14} = I \sin 2\pi \, [\sin (2\pi \text{ feet} + 135.0 \text{ degrees})]$$

$$i_{15} = I \cos 2\pi \, [\sin (2\pi \text{ feet} + 157.5 \text{ degrees})]$$

$$i_{16} = I \sin 2\pi \, [\sin (2\pi \text{ feet} + 157.5 \text{ degrees})]$$

The amplitude I is approximately 37 milliamperes.

EXPLANATION OF OPERATION

In the adding network (Figure 6-94) the output voltage e_1 is obtained by transmitting voltage e_a straight through the network without changing the phase angle. A similar statement applies to output voltage e_5, which is obtained directly from voltage e_b. Each of the six other output voltages is obtained by combining two of the input voltages, after attenuating them to obtain the proper ratio of amplitudes.

The circuit is a simple mechanization of the trigonometric relation

$$A \sin wt + B \cos wt = \sqrt{A^2 + B^2} \sin \left(wt + \tan^{-1} \frac{B}{A} \right)$$

The 22.5-degree component thus requires that $B/A = \tan 22.5\text{-degrees} = 0.414$, or $B = 0.414A$. This weighting is accomplished by proper selection of the resistance values. To understand why there is an attenuation, consider the 45-degree signal. The resistors from sin wt and cos wt must obviously be equal to give the correct phase. Consideration of the Thevenin equivalent of the two sources shows that each generator appears as one-half of its actual amplitude.

The transistors are impedance buffers which ensure that the waveform generators will not load the vector summing network.

Figure 6-95 shows the circuits of one complete waveform generator. The 1.67-cycle sine-wave input voltage is applied to the base circuit of transistor Q1 through resistors R2 and R3.

Transistors Q1 and Q2 are employed in a push-pull, Class A, linear amplifier circuit, in which the push-pull operation is obtained by means of resistor R11, which is common to the two emitter circuits. Figure 6-98a represents the input signal voltage of transistor Q1 as a function of time. Figure 6-98b and c represent the output signal voltages across load resistors R5 and R6, respectively. The collector circuits of Q1 and Q2 are connected to a full-wave rectifier comprising diodes CR1 and CR2. By means of resistors R15, R16, R18, and R19, this fullwave rectifier is dc biased in such a manner that diode CR1 passes current during the negative half-cycle of the signal voltage at the collector of Q1, and diode CR2 passes current during the negative half-cycle of signal voltage at the collector of Q2. The resultant output voltage of the full-wave rectifier consists of a succession of identical half sine waves, in which one half-wave is received from Q1, and the next half-wave from Q2.

Figure 6-99a shows the output voltage of diodes CR1 and CR2 as a function of voltage, rather than time. The independent variable is the input signal voltage applied to the base circuit of transistor Q1. The output voltage of the full-wave rectifier is a linear function of the input voltage, except that the slope of the curve is positive for negative values of input voltage, and negative for positive values. This output voltage is applied to the base circuit of transistor Q3.

Transistors Q3 and Q4 are used in a push-pull, Class A, linear amplifier, similar to that which comprises Q1 and Q2. The signal voltages across R20 and R21 have the same form as the voltage shown in Figure 6-99a, except that the signal voltage across R20 is reversed in polarity with respect to the signal voltage across R21, due to the push-pull action of the amplifier.

The collectors of Q3 and Q4 are connected to a full-wave rectifier comprising diodes CR3 and CR4. This rectifier is dc biased, by means of resistors R32 and R34, at a voltage level that is halfway between the positive peak signal voltage and the negative peak signal voltage. Relative to this bias voltage, the signal voltage shown in Figure 6-99a may be thought of as constituting one full cycle of a triangular ac wave, in which the signal voltage is positive with respect to this bias voltage part of the time, and negative part of the time. The action of the full-wave rectifier causes

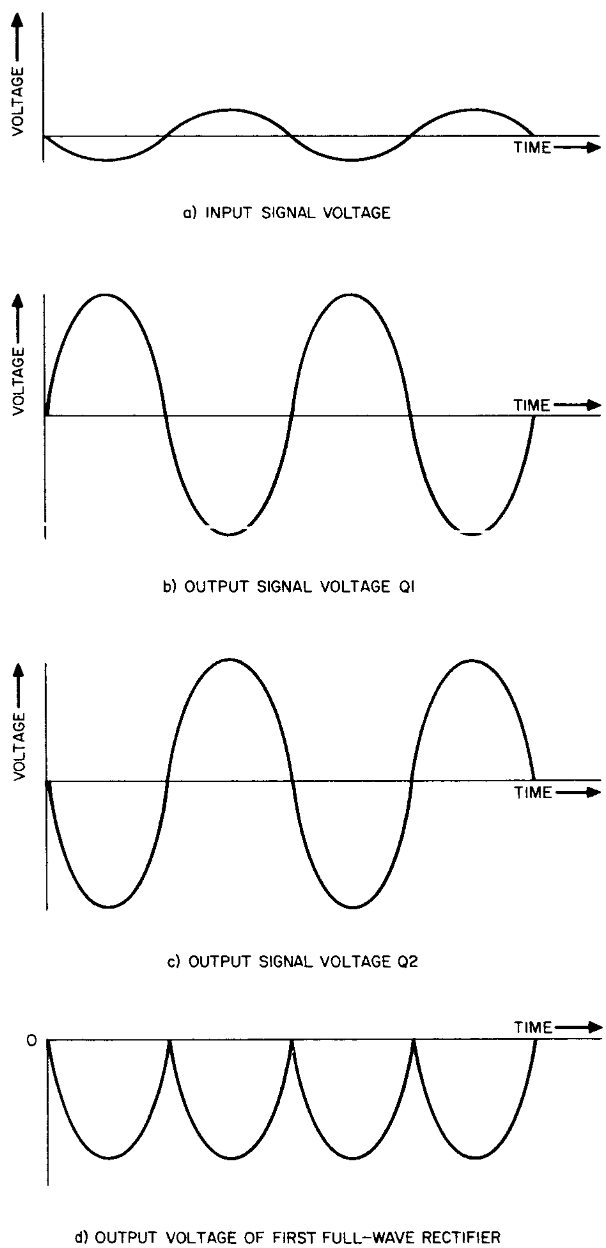

FIGURE 6-98. ANALOG WAVEFORMS VERSUS TIME

the positive part of the voltage to be reversed in polarity, so that the output voltage of the full-wave rectifier has the form shown in Figure 6-99b.

The output voltage shown in Figure 6-99b is modified in shape by means of a network consisting of diodes CR6 to CR13 inclusive, and resistors R41 to R56 inclusive. These diodes are biased by dc voltages in such a manner that they start drawing current at

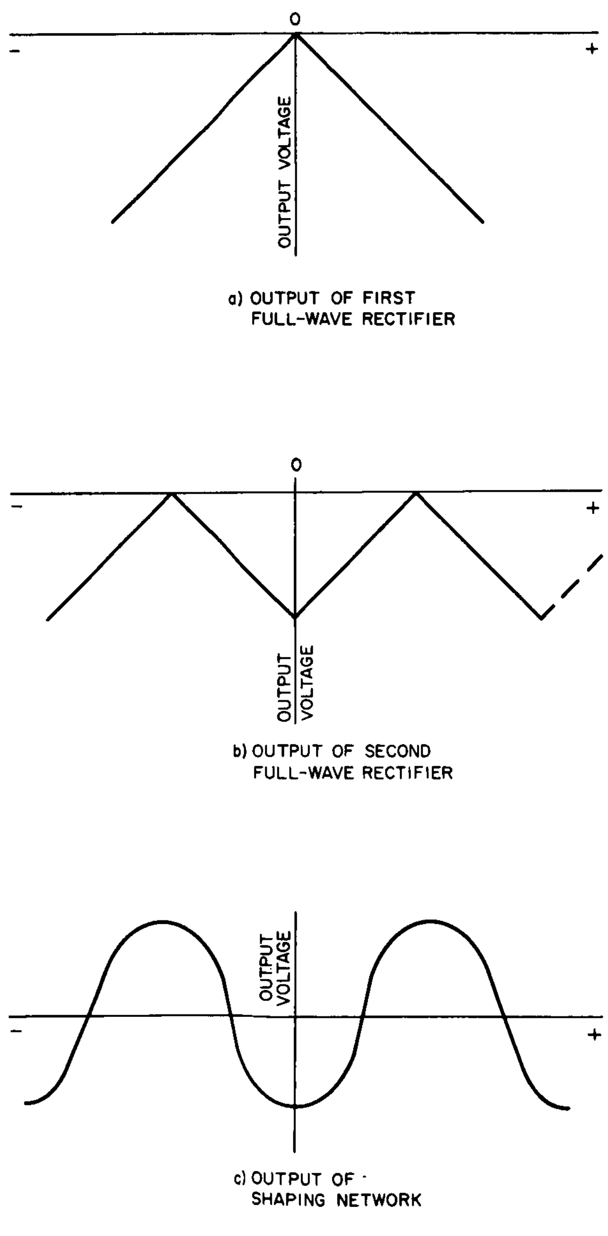

FIGURE 6-99. ANALOG WAVEFORMS VERSUS VOLTAGE

various voltage levels, causing the output circuit of the full-wave rectifier to be loaded with more and more shunt resistors as the output voltage increases. This causes the output voltage to rise less and less rapidly, with the result shown in Figure 6-99c, in which the output voltage has become approximately a cosine function of the input voltage of transistor Q1. Since this input voltage has the form $e_1 = \sin\ (2\pi \text{ feet})$, the output voltage has the form, $e_{11} = \cos 2\pi\ [\sin (2\pi \text{ feet})]$. This is the form required for supplying current to the associated field coil.

In addition to the voltage e_{11} described above, it is necessary to generate another voltage, $e_{12} = \sin 2\pi \sin\ (2\pi \text{ feet})$. Since the sine function is the same as the cosine function except for a 90-degree phase difference, the voltage curves pertaining to the generation of e_{12} may be derived from those shown in Figure 6-99, by shifting all of these curves to the left through a distance corresponding to one quarter cycle of Figure 6-99b. This shift can be obtained by adding a small constant to the independent variable. This constant is added by adjusting the dc bias voltage in the base circuit of transistor Q1 in the waveform generator that is used for generating e_{12}.

To make the waveform generator function over a wide enough range of input voltage for generating e_{12}, it is necessary to provide an additional bend in the curve of Figure 6-99b. This is indicated by means of the broken line at the extreme right of Figure 6-99b. The additional bend is obtained by means of elements CR5 and R35, shown in Figure 6-95. When the signal voltage across R5 varies in a negative direction beyond a certain level, current flows through diode CR5 and resistor R35, causing a voltage to be applied to the base circuit of transistor Q4. This voltage causes the upward bend indicated by the broken line at the right-hand end of the curve in Figure 6-99b.

In the power amplifier and driver, shown in Figure 6-96, the signal passes through two cascaded emitter-followers, Q10 and Q5, which are necessary because the source impedance of the waveform generator is much higher than the input impedance of the driver of the power amplifier.

Transistors Q6 and Q7 are used in a push-pull, Class A, common-emitter, linear amplifier, which employs the complementary symmetry principle. This amplifier has inverse feedback, which is obtained by means of a voltage divider consisting of resistors R63 and R68. This inverse feedback is used for controlling the gain of the amplifier, and for preventing drift of the dc bias voltage.

The output voltage of Q6 and Q7 is applied to the base circuits of the final amplifier stage, which uses transistors Q8 and Q9 in a Class AB, common-collector, linear amplifier, employing the complementary symmetry principle. This amplifier amplifies the signal current to a high enough level for the corresponding field coil of the ferrite phase shifter.

The system described above was the subject of a design review held 3 January 1963. The following conclusions were reached:

1) Because of the large number of components, each subsystem should be subjected to critical scrutiny to find means of reducing the number of components.
2) The phase lock loop had severe stability requirements, which increased its complexity significantly, imposed by the method in which the phase of the output counter of the variable phase control was controlled.
3) The fire angle generator did not need the capability to initiate pulses at any angle; actual requirements are only that it provide timing signals centered about either +90 or —90 degrees from the spacecraft-earth center line.
4) Means should be provided for telemetering the actual beam center position to earth.
5) The analog PACE consumed far too much power.
6) The waveform generators and the power amplifier of the analog PACE would have difficulty with temperature.
7) The power amplifier could use feedback to advantage.

Conclusion No. 4 was implemented in the engineering model by the technique shown in Figure 6-100. An additional register, the angle encoder register (AER), was added, and the contents of the VPC output counter were shifted into the AER at ψ time. The contents of the AER were then encoded for transmission to earth.

Conclusion No. 2 was arrived at by the following reasoning: if the PLL did not provide precisely 512 counts to the VPC in one spacecraft revolution, the

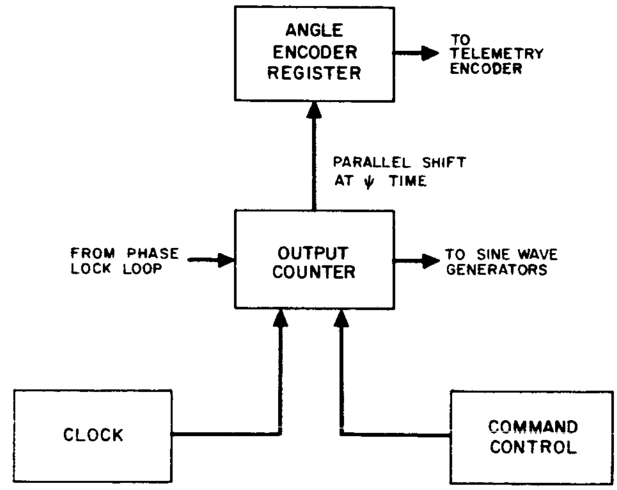

FIGURE 6-100. ORIGINAL VARIABLE PHASE CONTROL SUBSYSTEM

error in counts, ΔC_1, became a phase error $\Delta \phi_1$ in the beam position. If, during a later revolution, another error in counts, ΔC_2, having the same algebraic sign as ΔC_1, occurred, a second phase error $\Delta \phi_2$ was created. In the original VPC these two phase errors, $\Delta \phi_1$ and $\Delta \phi_2$, added. Hence, if the PLL put out the sequence of counts shown in the second column of Table 6-5, the rest of the columns would follow. It can be seen from the table that the beam has moved almost halfway off the desired position in 20 revolutions. Even with the complex PLL, if there were a small instability in spin period, the condition of Table 6-5 could occur.

The solution to this problem is shown in Figure 6-101. Corrections to beam phase, both for time of day and stationkeeping, are made into the AER. Every ψ time, the contents of the AER are parallel shifted into the output counter. Using this technique, the first four columns of Table 6-5 apply, but the error in beam position never is greater than 0.7 degree. This change was also incorporated into the engineering model, because there was uncertainty as to the spin stability of the spin fixture.

The system described above was fabricated and checked out. To facilitate checkout, some test equipment was designed and built. This equipment consists of:

1) Analog card tester
2) Digital card tester
3) Subsystem tester

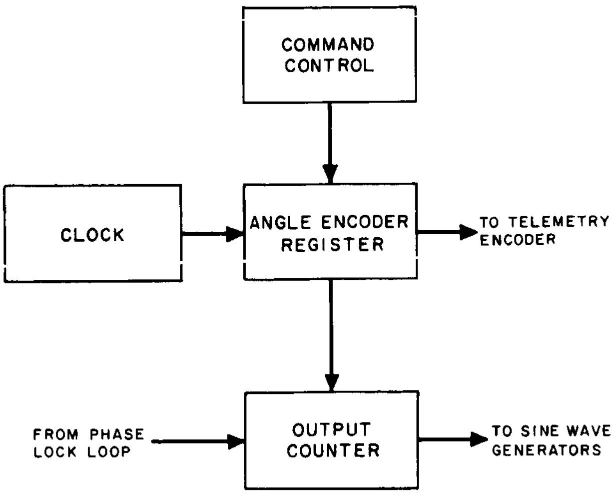

FIGURE 6-101. PRESENT VARIABLE PHASE CONTROL SUBSYSTEM

TABLE 6-5. EXAMPLE OF PHASE PROBLEM

Revolution Number	Counts per PLL Revolution	ΔC Counts	$\Delta\phi$, degrees	Error in Beam Position, degrees
1	512			
2	513	+1	0.7	0.7
3	512			0.7
4	513	+1	0.7	1.4
5	512			1.4
6	513	+1	0.7	2.1
7	512			2.1
8	513	+1	0.7	2.8
9	512			2.8
10	513	+1	0.7	3.5
11	512			3.5
12	513	+1	0.7	4.2
13	512			4.2
14	513	+1	0.7	4.9
15	512			4.9
16	513	+1	0.7	5.6
17	512			5.6
18	513	+1	0.7	6.3
19	512			6.3
20	513	+1	0.7	7.2

The card testers are used for initial checkout and electrical adjustment of the cards. They consist of signal generators, switches, and loads which can be connected to the cards by patch cords.

The subsystem tester can be used for checkout of the digital unit, the analog unit, the telemetry and command unit (digital portion), or the complete PACE system. The complete PACE system can be tested on the bench or in the spacecraft, with or without the interconnections with the RF portion of the telemetry link. Separate cables are used for each of the above tests. This eliminates any chance of inadvertent sending of improper signals from the tester, such as supplying power to the PACE system from the tester at the same time that power is being supplied by the PACE regulators.

The subsystem tester consists of the following:

1) Power supplied to supply power to the tester and to the PACE equipment.
2) A pulse simulator.
3) Circuitry for feeding digital information into the command register.
4) Circuitry for feeding commands directly into the digital system (bypassing the telemetry and command)
5) Circuitry to simulate the digital unit outputs to the analog unit.
6) Circuitry to readout on lamps the contents of output counter at ψ time.
7) Circuitry to turn on "lock" indicator lamp when the phase lock loop is "in lock."
8) Circuitry to readout on lamps the contents of the command register.
9) Lamp indication of the status of the power regulators.
10) A lamp which illuminates when the jet fire signal is given.
11) Loads for the analog outputs.
12) Numerous test points.

The PACE electronics were then checked out, spinning, in the engineering model structure. To do this, an RF command and telemetry link with the spacecraft was required. To minimize cost and schedule time, a modified Syncom I telemetry and command system was used. A block diagram of the demonstration telemetry and command system is shown in Figure 6-102. Modifications to Syncom I operation are the following:

1) Antenna beam position and command verification are the only intelligence telemetered.
2) The command system was modified so that either enable tone could operate both of the counters. This, in effect, extended the command bit length to ten bits.

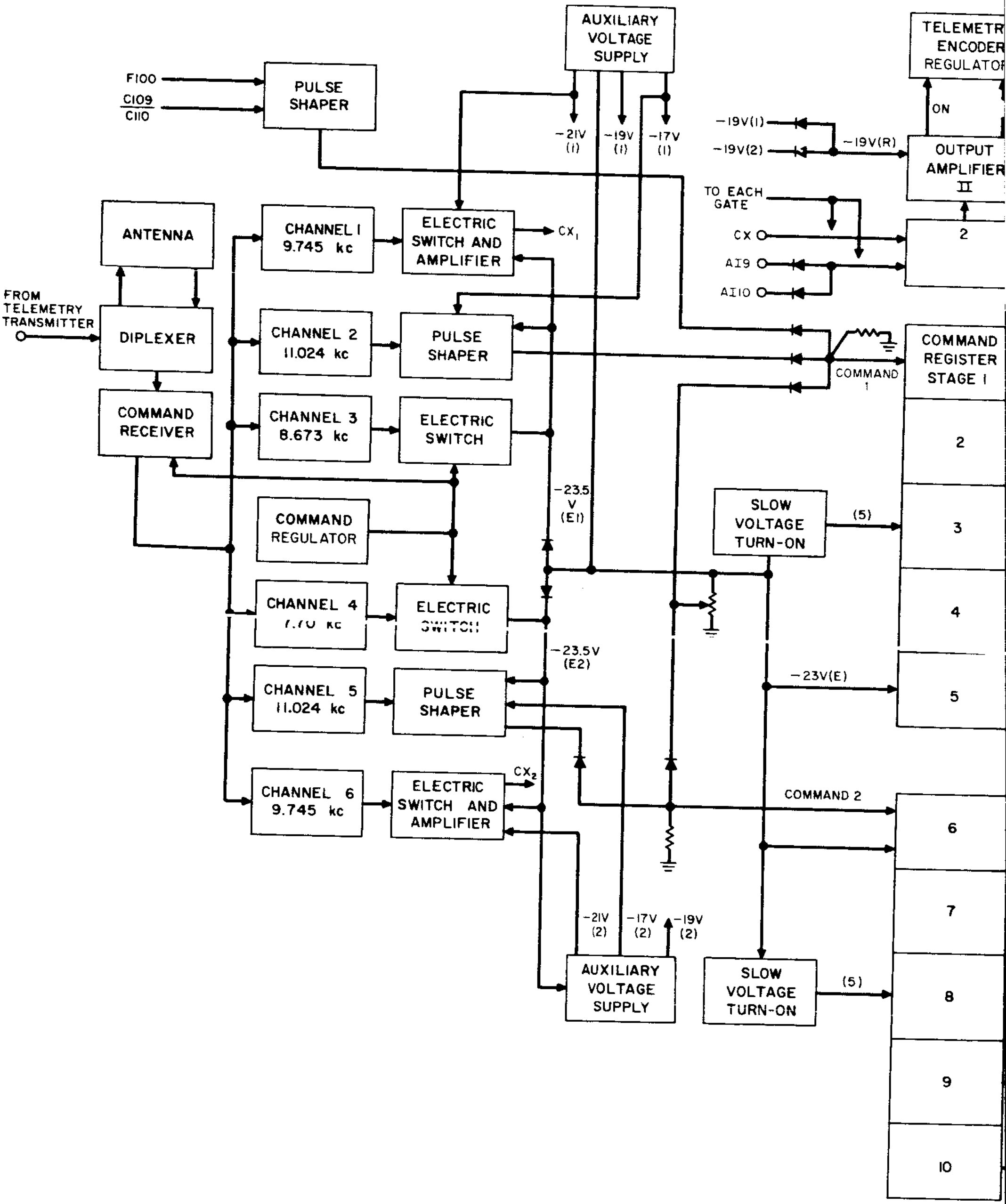

FIGURE 6-102. TELEMETRY AND COMMAND SUBSYSTEMS DEMONSTRATI

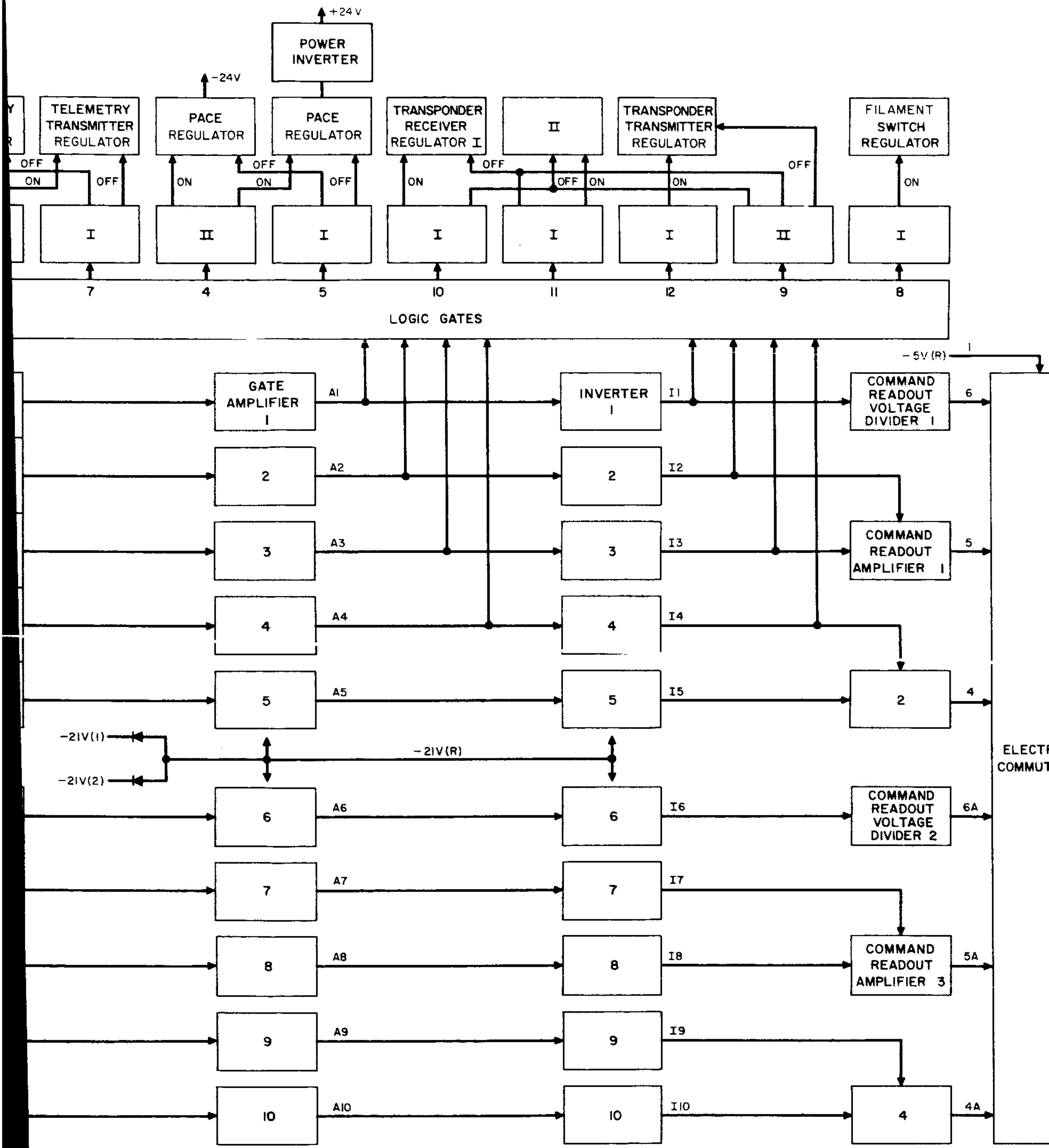
+24 V
POWER INVERTER
-24V
TELEMETRY TRANSMITTER REGULATOR
PACE REGULATOR
PACE REGULATOR
TRANSPONDER RECEIVER REGULATOR I
II
TRANSPONDER TRANSMITTER REGULATOR
FILAMENT SWITCH REGULATOR
OFF
ON
LOGIC GATES
-5V (R)
GATE AMPLIFIER 1
INVERTER 1
COMMAND READOUT VOLTAGE DIVIDER 1
COMMAND READOUT AMPLIFIER 1
COMMAND READOUT VOLTAGE DIVIDER 2
COMMAND READOUT AMPLIFIER 3
-21V(1)
-21V(2)
-21V(R)
A1
A2
A3
A4
A5
A6
A7
A8
A9
A10
I1
I2
I3
I4
I5
I6
I7
I8
I9
I10
6
5
4
6A
5A
4A
ELECT
COMMUT

ON MODEL

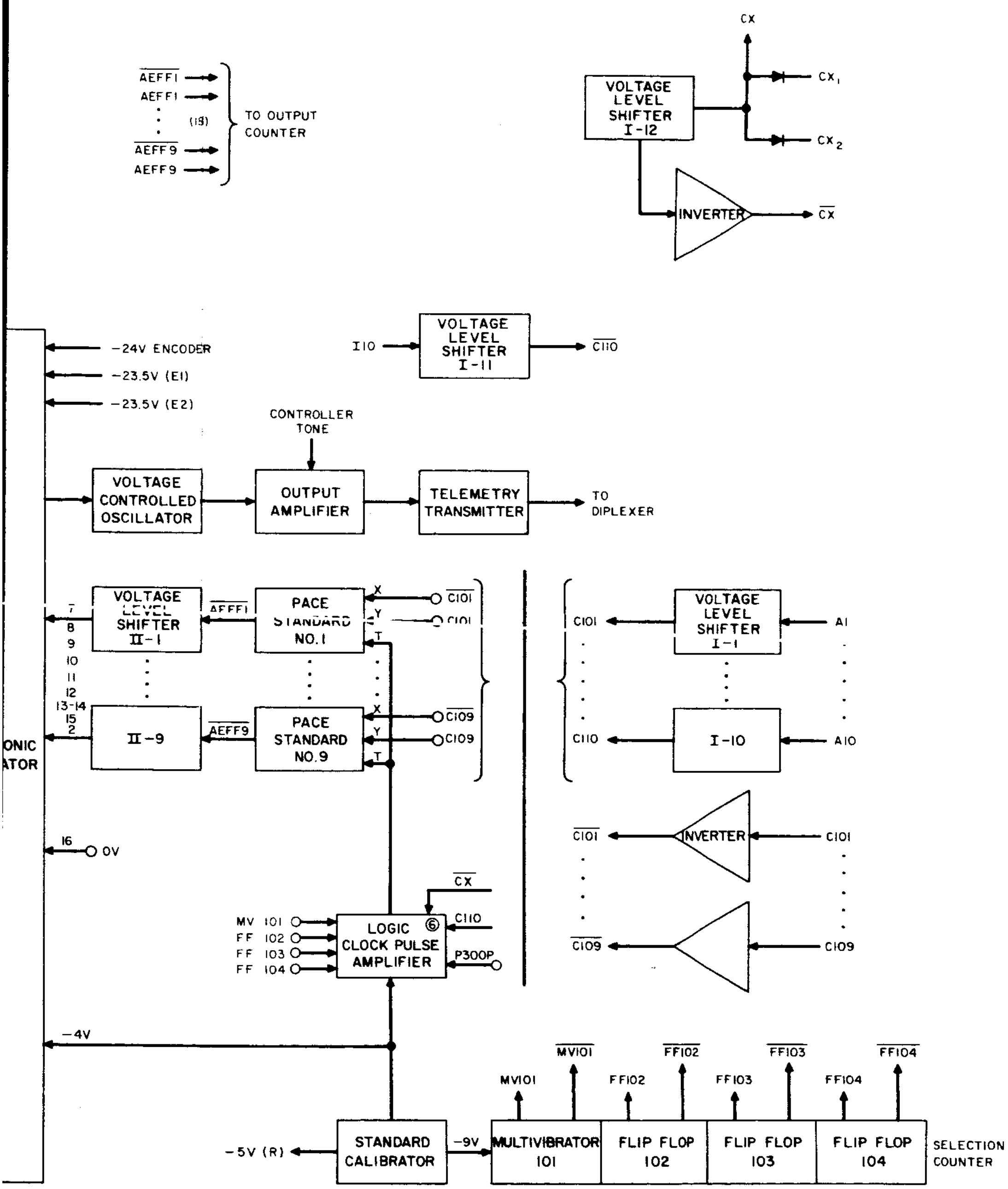
AEFF1
AEFF1
(18)
AEFF9
AEFF9
TO OUTPUT COUNTER
CX
VOLTAGE LEVEL SHIFTER I-12
CX1
CX2
INVERTER
CX
ONIC
ATOR
-24V ENCODER
-23.5V (E1)
-23.5V (E2)
I10
VOLTAGE LEVEL SHIFTER I-11
C110
CONTROLLER TONE
VOLTAGE CONTROLLED OSCILLATOR
OUTPUT AMPLIFIER
TELEMETRY TRANSMITTER
TO DIPLEXER
VOLTAGE LEVEL SHIFTER II-1
AEFF1
PACE STANDARD NO. 1
C101
C101
II-9
AEFF9
PACE STANDARD NO. 9
C109
C109
C101
VOLTAGE LEVEL SHIFTER I-1
A1
C110
I-10
A10
C101
INVERTER
C101
C109
C109
16
0V
CX
C110
MV 101
FF 102
FF 103
FF 104
LOGIC CLOCK PULSE AMPLIFIER
P300P
-4V
MV101
MV101
FF102
FF102
FF103
FF103
FF104
FF104
-5V (R)
STANDARD CALIBRATOR
-9V
MULTIVIBRATOR 101
FLIP FLOP 102
FLIP FLOP 103
FLIP FLOP 104
SELECTION COUNTER

3

3) The buffer circuits between the command system and the PACE were designed so the beam position could be adjusted upon command.

Tables 6-6 through 6-8 give the command structure for adjusting the beam and for firing the jet control electronics.

TABLE 6-6. COARSE ANTENNA ADJUST (DEMONSTRATION)

Desired Beam Position	Enable No. 1	Enable No. 2
To 0	0	16
To 22.5	0	15
To 45	0	14
To 67.5	0	13
To 90	0	12
To 112.5	0	11
To 135	0	10
To 157.5	0	9
To 180	0	8
To 202.5	0	7
To 225	0	6
To 247.5	0	5
To 270	0	4
To 292.5	0	3
To 315	0	2
To 337.5	0	1

The readout of the telemetered beam position data was accomplished by the use of the "sample and hold" circuits of Syncom I ground equipment telemetry panel. Timing signals were used to allow parallel readout of the sample and hold circuits. The data is displayed on lights for operator convenience, and by a dial which illustrates the beam position with respect to the simulated sun. Figure 6-103 is a block diagram of the display circuitry.

Frequency Lock Loop

The frequency lock loop (FLL), previously designated the phase lock loop, generates the reference timing signals for the PACE. The FLL output is a square wave, the frequency of which is 512 times the spin frequency f_s. An auxiliary output is a digital signal which indicates when the FLL is in lock, that

TABLE 6-7. FINE ANTENNA ADJUST (DEMONSTRATION)

Enable No. 1 Counts	Command Counter No. 1 States					Beam Position Increments, degrees
	1	2	3	4	5	
0	0	0	0	0	0	0
1	1	1	1	1	1	21.8
2	0	1	1	1	1	21.0
3	1	0	1	1	1	20.3
4	0	0	1	1	1	19.6
5	1	1	0	1	1	18.9
6	0	1	0	1	1	18.2
7	1	0	0	1	1	17.5
8	0	0	0	1	1	16.8
9	1	1	1	0	1	16.1
10	0	1	1	0	1	15.4
11	1	0	1	0	1	14.7
12	0	0	1	0	1	14.0
13	1	1	0	0	1	13.3
14	0	1	0	0	1	12.6
15	1	0	0	0	1	11.9
16	0	0	0	0	1	11.2
17	1	1	1	1	0	10.5
18	0	1	1	1	0	9.8
19	1	0	1	1	0	9.1
20	0	0	1	1	0	8.4
21	1	1	0	1	0	7.7
22	0	1	0	1	0	7.0
23	1	0	0	1	0	6.3
24	0	0	0	1	0	5.6
25	1	1	1	0	0	4.9
26	0	1	1	0	0	4.2
27	1	0	1	0	0	3.5
28	0	0	1	0	0	2.8
29	1	1	0	0	0	2.1
30	0	1	0	0	0	1.4
31	1	0	0	0	0	.7

TABLE 6-8. JET CONTROL COMMANDS (DEMONSTRATION)

Enable	0	21	13	5	Coarse
No. 1	25	17	9	1	Fine—3 pulses
En-	26	18	10	2	Fine—2 pulses
able No. 2	27	19	11	3	Fine—1 pulse
24	0	41.2	22.5	33.7	Start angle of jet pulse
23	45	56.2	67.5	78.7	
22	90	101.2	112.5	123.7	
21	135	146.2	157.5	168.7	
20	180	191.2	202.5	213.7	
19	225	236.2	247.5	258.7	
18	270	281.2	292.5	303.7	
17	315	326.2	337.5	348.7	

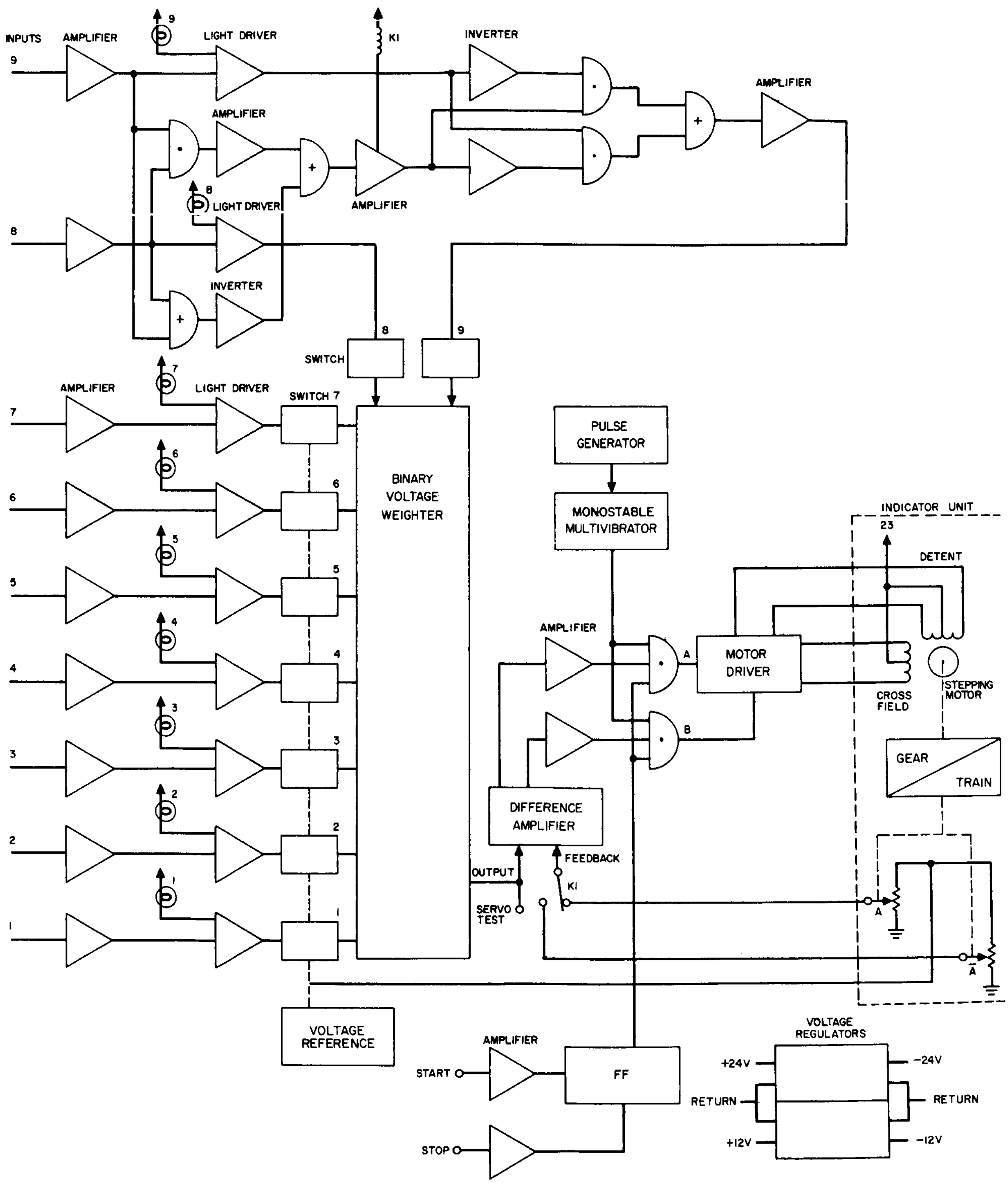

FIGURE 6-103. SYNCOM DISPLAY SYSTEM BLOCK DIAGRAM

is, when count = $(512 \pm 1)\ f_s$. The FLL has been considerably simplified from the version presently in the Syncom II engineering model. The simplification was made possible by the change in the beam positioner subsystem which eliminates the requirement for a driftless FLL.

The FLL block diagram is shown in Figure 6-104. The ψ amplifier-shaper generates a large, narrow pulse each time the low-level pulse occurs. The amplified ψ pulse triggers flip-flop 0, causing it to change state with each pulse. Negative-going transients of flip-flop 0 trigger the reset amplifier, causing the voltage-controlled oscillator (VCO) and the flip-flops in the frequency counter (FC) to be reset.

The FC is a conventional binary counter, with the exception that flip-flop 10 is only set by flip-flop 9; the resetting of flip-flop 10 is accomplished only by the reset amplifier.

The error pulse gate (EPG) is a tristable circuit. The truth table for the EPG is given below in Table 6-9.

TABLE 6-9. ERROR PULSE GATE TRUTH TABLE

Error Pulse Gate Inputs		Truth Table Outputs
FF 0	FF 10	
0	0	0
0	1	+V
1	0	−V
1	1	0

When the FLL is in lock, flip-flop 10 is in phase with flip-flop 0, and the EPG output is at zero volts. When the VCO oscillates at greater than 512 f_s, flip-flop 10 is set before flip-flop 0; the EPG output then goes to a positive voltage +V until flip-flop 0 is set, at which time the EPG output returns to zero. The positive error pulse is applied to the integrator; it causes a negative change in the integrator ouput voltage and hence a decrease in VCO frequency. When the VCO oscillates too slowly, negative error pulses are generated in a similar manner. Since the duration of the error pulse is proportional to the difference between the spin period

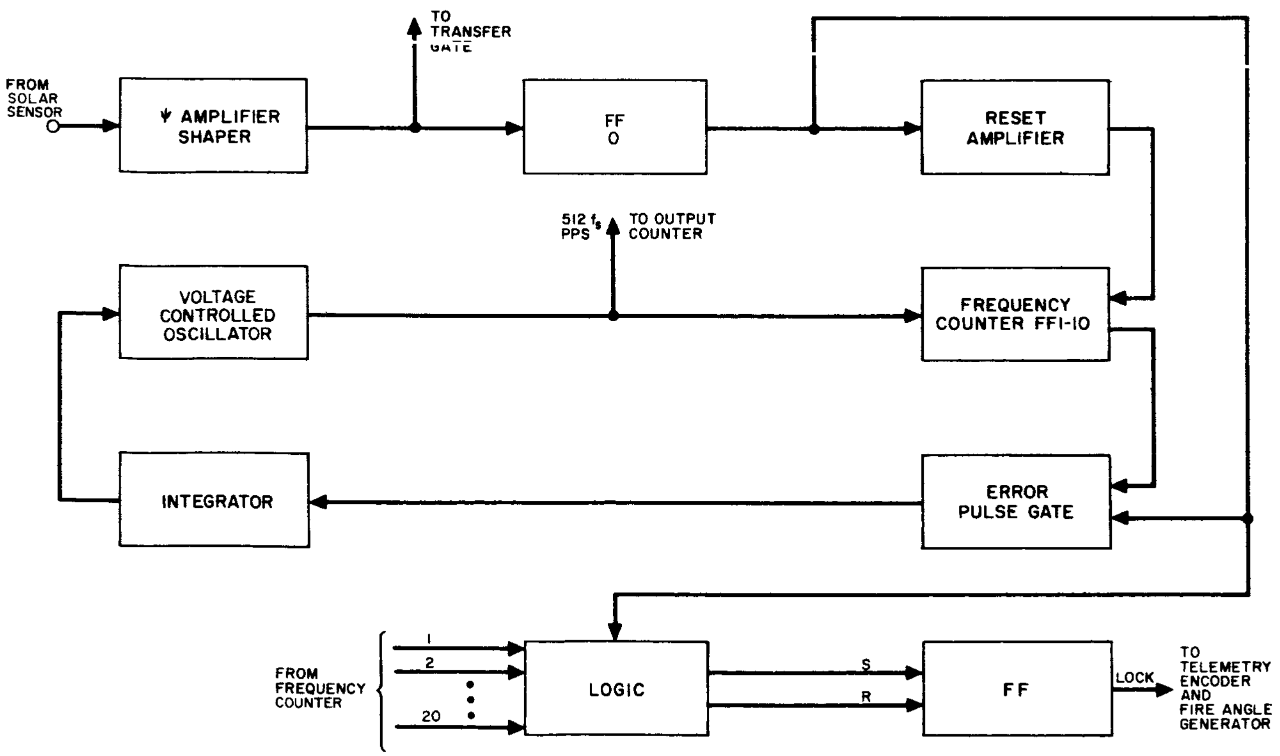

FIGURE 6-104. FREQUENCY LOCK LOOP

and the period of flip-flop 10, the slowing time of the FLL is only a matter of a few seconds. Subsequent reports will present more detailed information on the FLL dynamics.

The contents of the FC are sampled when flip-flop 0 goes high; if the FC count is 512 ± 1, the lock flip-flop is set, indicating the FLL is in lock; if the FC count is not 512 ± 1, the lock flip-flop is reset, indicating the FLL is out of lock.

The function of the jet control subsystem is to provide the controls for activating the bipropellant position-correction jets.

The original subsystem included the capability of initiating a jet pulse envelope after an angular displacement of 0.7 degree n $(n = 0_1, 0.511)$ from the sun-spacecraft line. Also, a fine correct mode made possible the commanding of a finite number of consecutive jet pulses, regardless of the command execute tone interval.

This subsystem was fabricated for the Advanced Technological Development engineering model. The subsystem was tested and demonstrated successfully.

Advanced Jet Control

As a result of the design review mentioned above, the functional requirements of the jet control electronics was changed.

The advanced jet control subsystem will be designed to provide a 45-degree pulse envelope such that the average thrust direction will be displaced ±90 degrees from the earth-spacecraft line by sequential timing and a continuous pulse envelope in real time. The sequential timing portion of the advanced subsystem will enable pulsing of both radial or both axial jets in such

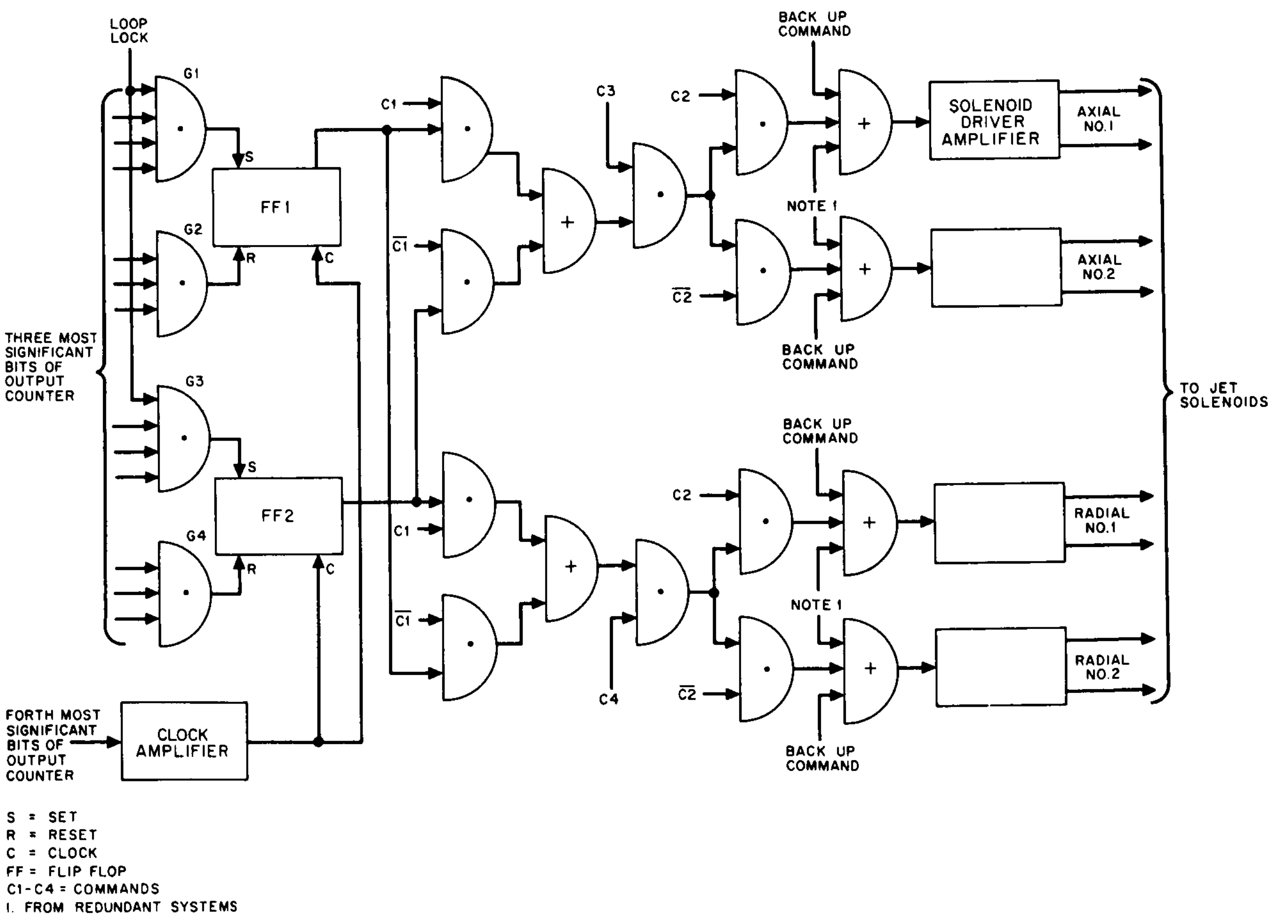

FIGURE 6-105. JET CONTROL ELECTRONICS

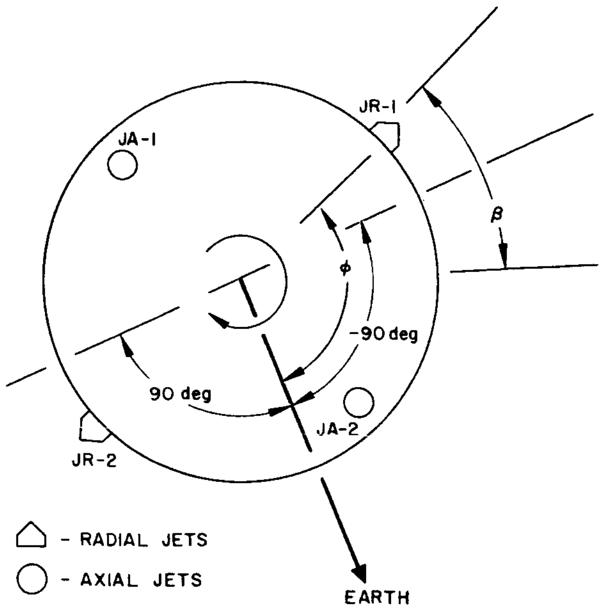

TOP VIEW

β = 45 deg ANGLE THROUGH WHICH JET IS ACTIVATED

φ = FIXED-ANGLE BETWEEN REFERENCE FERRITE PHASE SHIFTER AND JR-1

JR = RADIAL JET

JA = AXIAL JET

FIGURE 6-106. SPACECRAFT CONFIGURATION

a manner that the pulse envelope per revolution of one jet is displaced 180 degrees relative to the pulse envelope per revolution of the other, or that only one jet is activated with its pulse envelope occurring once every spacecraft revolution.

The block diagram of the advanced jet control subsystem is shown in Figure 6-105, and a simplified spacecraft configuration illustrating the jet positions is shown in Figure 6-106.

The characteristics of the variable phase control output counter is such that the counter has a count of zero when the reference (zero phase shift) ferrite phase shifter element is coincident with the spacecraft-earth line.

Thus, to obtain a jet pulse envelope with a midpoint normal to the spacecraft-earth line, it is necessary to detect the counts.

$$N_1 = (\ 67.5 \text{ degrees} + \phi)\frac{512}{360}$$

$$N_2 = (112.5 \text{ degrees} + \phi)\frac{512}{360}$$

$$N_3 = (247.5 \text{ degrees} + \phi)\frac{512}{360}$$

$$N_4 = (292.5 \text{ degrees} + \phi)\frac{512}{360}$$

where ϕ is the known angular displacement of radial jet No. 1 from the reference ferrite phase shifter element and is a multiple of 22.5 degrees.

Since ϕ is a multiple of 22.5 degrees, the binary numbers N_1 through N_4 can be detected by monitoring the four most significant bits (MSB) of the output counter. The three MSBs are inputs to an AND gate and the fourth MSB is used to clock the flip-flop on its positive voltage transition.

The numbers N_1 and N_2 are used to set and reset No. 1; and N_3 and N_4 are used to set and reset No. 2. Thus, the No. 1 pulse envelope begins when JR-1 is 67.5 degrees from the earth line and terminates ⅛ revolution later. The No. 2 pulse envelope begins when JR-1 is 247.5 degrees from the earth line and terminates ⅛ revolution later.

The logic table for controlling each solenoid is shown in Table 6-10, where the notations in parentheses correspond to the command bits as outlined in Table 6-11.

From the logic table, the following logic equations are derived.

$$\text{JR-1} = (\text{No. } 1 \cdot \overline{\text{C1}} + \text{No. } 2 \cdot \text{C1})\text{C3} \cdot \text{C2}$$

$$\text{JR-2} = (\text{No. } 2 \cdot \overline{\text{C1}} + \text{No. } 1 \cdot \text{C1})\text{C4} \cdot \text{C2}$$

$$\text{JA-1} = (\text{No. } 1 \cdot \overline{\text{C1}} + \text{No. } 2 \cdot \text{C1})\text{C3} \cdot \text{C2}$$

$$\text{JA-2} = (\text{No. } 2 \cdot \overline{\text{C1}} + \text{No. } 1 \cdot \text{C1})\text{C4} \cdot \text{C2}$$

The above logic equations represent the control signals from each of the four jet control subsystems. The last OR gate combines all four signals and the backup command.

The backup mode provides the capability of pulsing the jets in real time if the sequential timing circuits fail. Also, the backup mode can be used to operate a jet continuously.

Because the angle ϕ is measured to the reference radial jet and the axial jets are displaced ±90 degrees to the radial jet, the use of the No. 1 and No. 2 pulse envelopes will result in pulsing an axial jet in-

TABLE 6-10. LOGIC TABLE FOR CONTROLLING EACH SOLENOID

Average Thrust Direction with Respect to Earth Line	JA $\overline{(C2)}$-1 (C3) JR (C2)-1 (C3)	JA $\overline{(C2)}$-2 (C4) JR (C2)-2 (C4)
+90 (CI)	No. 1	No. 2
−90 (CI)	No. 2	No. 1

TABLE 6-11. JET CONTROL COMMANDS

COMMANDS C7 C6 C5	C4	C3	C2	C1	FUNCTION	
	0	1	0	0	Axial +90°	Jet No. 1
Function of	0	1	0	1	Axial −90°	
C7, C6, C5	0	1	1	0	Radial +90°	
AND with	0	1	1	1	Radial −90°	
C1 ⟶ C4	1	0	0	0	Axial +90°	Jet No. 2
	1	0	0	1	Axial −90°	
	1	0	1	0	Radial +90°	
	1	0	1	1	Radial −90°	
	1	1	0	0	Axial +90°	Jet No. 1 and Jet No. 2
	1	1	0	1	Axial −90°	
	1	1	1	0	Radial +90°	
	1	1	1	1	Radial −90°	
	0	0	0	0	Backup commands	
	0	0	0	1		
	0	0	1	0		
	0	0	1	1		

phase and 180 degrees out of phase with the spacecraft-earth line. If this is undesirable, the antenna beam must be rotated through an arc which will position the average jet thrust in the desired direction. If the antenna beam is rotated $+\theta$ degrees, where plus rotation is taken or in the spin direction, then the average thrust direction of axial jet No. 1 will be $+\theta$ degrees and axial jet No. 2, θ degrees — 180 degrees. In the special case where $\theta = 90$ degrees, the axial jets will be pulsed ± 90 degrees with respect to the spacecraft-earth line as outlined in Table 6-7.

The solenoid coil amplifiers will be designed with series output transistors and each driven by a separate preamplifier. Each preamplifier can be controlled by the input signal. By utilizing the series redundant configuration, the probability of a solenoid coil being continuously activated without a command is decreased, since to close the coil circuit requires that both output transistors fail.

Modified Waveform Generators and Amplifiers

The waveform generators and amplifiers as reported in the December 1962 Monthly Progress Report have been modified to achieve simplicity of design, reduction of part count, and reduction of power dissipation. The new circuit configurations are shown in Figures 6-107 and 6-108. These configurations result in a part count savings of approximately 34 percent and 50 percent less power dissipation.

The adding network is identical to the previous adder with the exception that eight more circuits are added. These additions are necessary to obtain the complements of the waveforms obtained by the previous eight waveform adders. The inputs to the adder network are:

$$e_a = A \sin 2\pi \text{ feet}$$

$$e_b = A \sin 2\pi \text{ feet}$$

$$e_c = —A \sin 2\pi \text{ feet}$$

$$e_d = —A \cos 2\pi \text{ feet}$$

The 16 outputs are of the form

$$e_{an} = \frac{A}{\sqrt{2}} \sin\left(2\pi \text{ feet} + \frac{\eta\pi}{8}\right) \quad \eta = 0.1.2, \ldots 15$$

The ferrite phase shifters require 16 signals of the form:

$$\left.\begin{aligned} e_{cm} &= B \cos 2\pi\left(\sin\left(2\pi ft + \frac{m\pi}{8}\right)\right) \\ e_{sm} &= B \sin 2\pi\left(\sin\left(2\pi ft + \frac{m\pi}{8}\right)\right) \end{aligned}\right\} m = 0,1,2, \ldots 7$$

where the zero-to-peak magnitude, B, is 20 volts.

The cos [2π sin wt] generator, Figure 6-107, produces a close approximation to the e_{cm} signals and the sin [2π sin wt] generator, Figure 6-108, produces a close approximation to the e_{sm} signals.

Both waveform generators are implemented with the use of a combination of "greater" and "lesser" gates. Zener diodes are used to shift the signal's dc bias where necessary as the signal passes through the circuit.

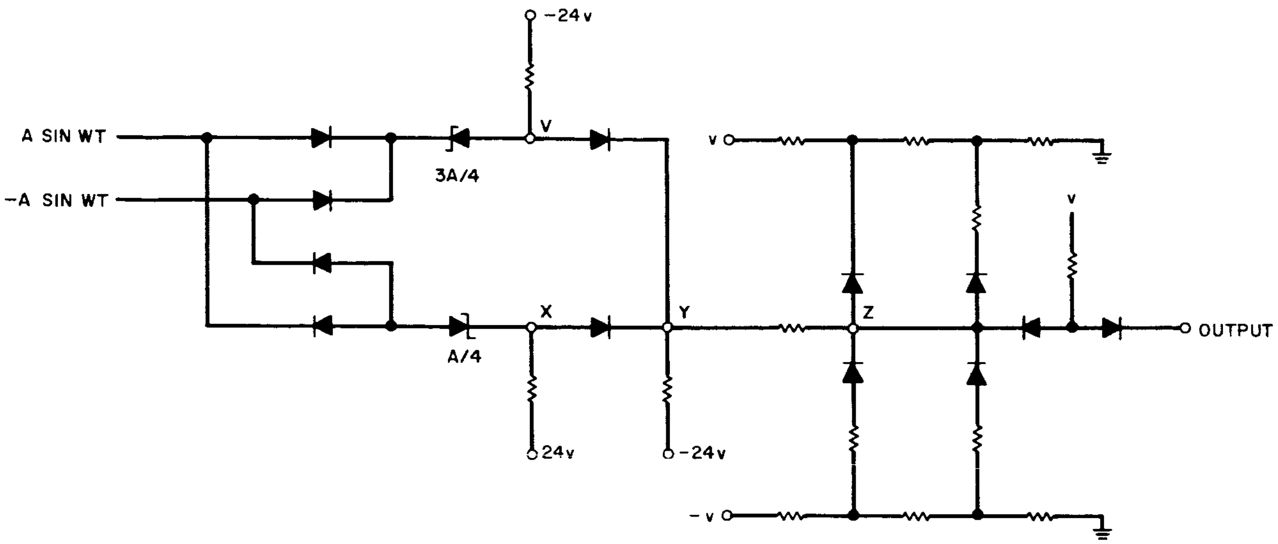

FIGURE 6-107. COS (2π SIN ωT) GENERATOR

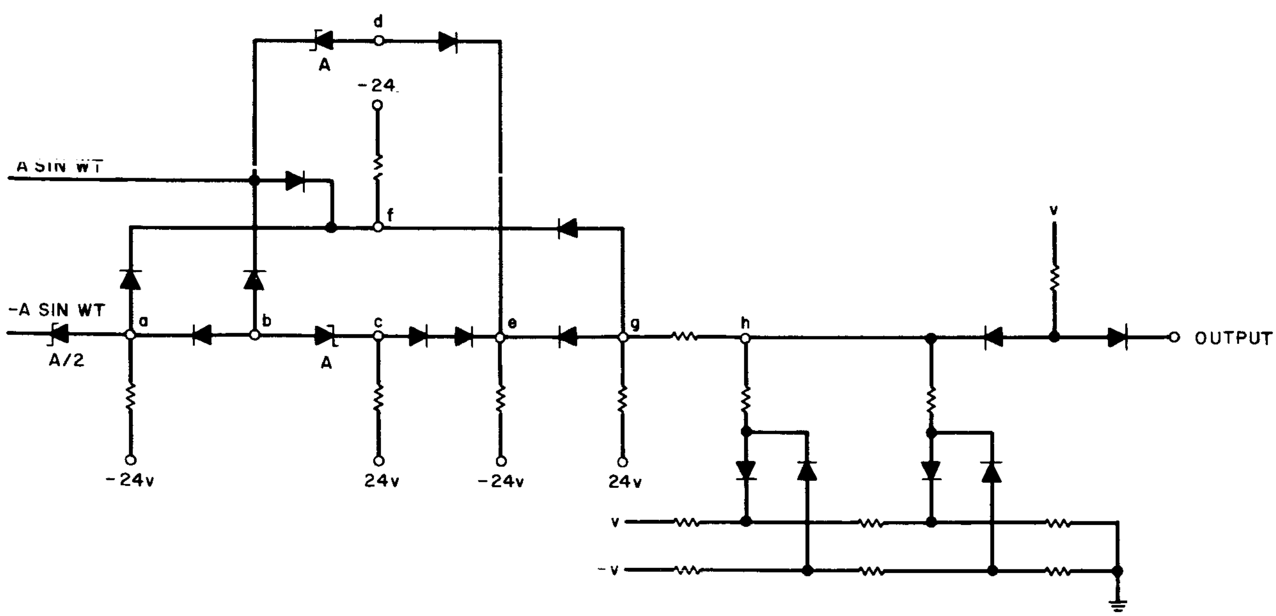

FIGURE 6-108. SIN (2π SIN ωT) GENERATOR

The inputs to Figure 6-107 are ϵ_{an} and $\epsilon_{a(n+8)}$, or A sin wt and — A sin wt, respectively. The diodes CR1 and CR2 form a greater gate. The 3A/4 zener diode drops the dc bias — 3A/4 volts. Thus, the signal at point V, shown in Figure 6-109a, is a positive full-wave rectified sinusoid between + A/4 and — 3A/4. The gate passes first the positive half cycle of ϵ_{an}, and then passes the positive half cycle of $\epsilon_{a(n+8)}$; the zener diode then drops the dc level by 3A/4 volts. Similarly the diodes CR3 and CR4 form a lesser gate and the A/4 zener diode raises the dc bias to give the waveform at point X, shown in Figure 6-109b.

The diodes CR5 and CR6 form another greater gate which gives the waveform at point Y, shown in Figure

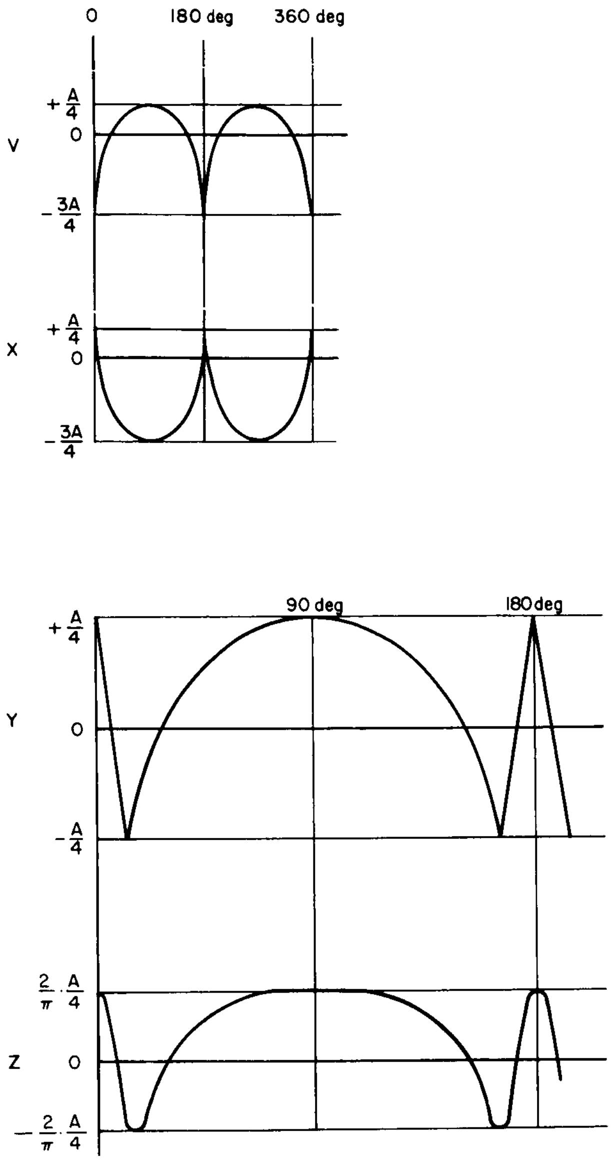

FIGURE 6-109. COS (2π SIN ωT) WAVEFORM

6-109c. The next 14 components shape the waveform at point Y into the waveform at point Z (Figure 6-109d). This waveform closely approximates the cosine of the input or:

$$\text{Output} = B \cos\left[2\pi A \sin\left(wt + \frac{M\pi}{8}\right)\right]$$

The signal is then fed into the power amplifier. The last three components allow the outputs of redundant waveform generators to be noded together. The + V is reversed to — V on all but the selected generator.

To obtain the ϵ_{SM} signal, which is in phase with the ϵ_{CM} signal just described, the same inputs are applied to the sin $[2\pi \sin wt]$ generator (Figure 6-108). The A/2 zener diode shifts the dc bias of the — A sin wt signal down by — A/2 volts at point a, Figure 6-110a.

The lesser gate gives the waveform at point b shown in Figure 6-110b. This wave is shifted negative in dc bias by the A-volts zener diode CR1 to the waveform at c, Figure 6-110c. The A-volts zener diode CR2 shifts the incoming waveform negative by A volts at point d, Figure 6-110d.

The waveforms at c and d then go through a greater gate to give the waveform at e, Figure 6-110e. The A sin wt signal and the waveform at a go through a greater gate to give the waveform at f, Figure 6-110f. The waveform at 3 and f then go through a lesser gate to give the waveform at g, Figure 6-110g.

The next 13 components shape the waveform at g into the waveform at h, Figure 6-110h. This waveform closely approximates the sine of the input or:

$$\text{Output} = B \sin\left[2\pi A \sin\left(wt + \frac{M\pi}{8}\right)\right]$$

The last three components form the noding function described previously in this section. The output then feeds into a power amplifier.

The accuracy of the waveform generators depends upon the amplitudes of the input signals and the voltage drops across the zener diodes. The input signals are generated with precise amplitudes, and accurate, low-current zener diodes are available for this application. The two waveform generator circuits have been breadboarded and the approach has been demonstrated to be practical.

Output Power Amplifier

This amplifier, which is shown in Figure 6-108, is a high-gain dc amplifier employing resistive feedback for stable operation and complementary emitter followers in the output stages for low output impedance. Transistors Q1 and Q2 are a closely matched pair, packaged in one standard TO-5 transistor case, operating as a differential amplifier. Since the circuit open-

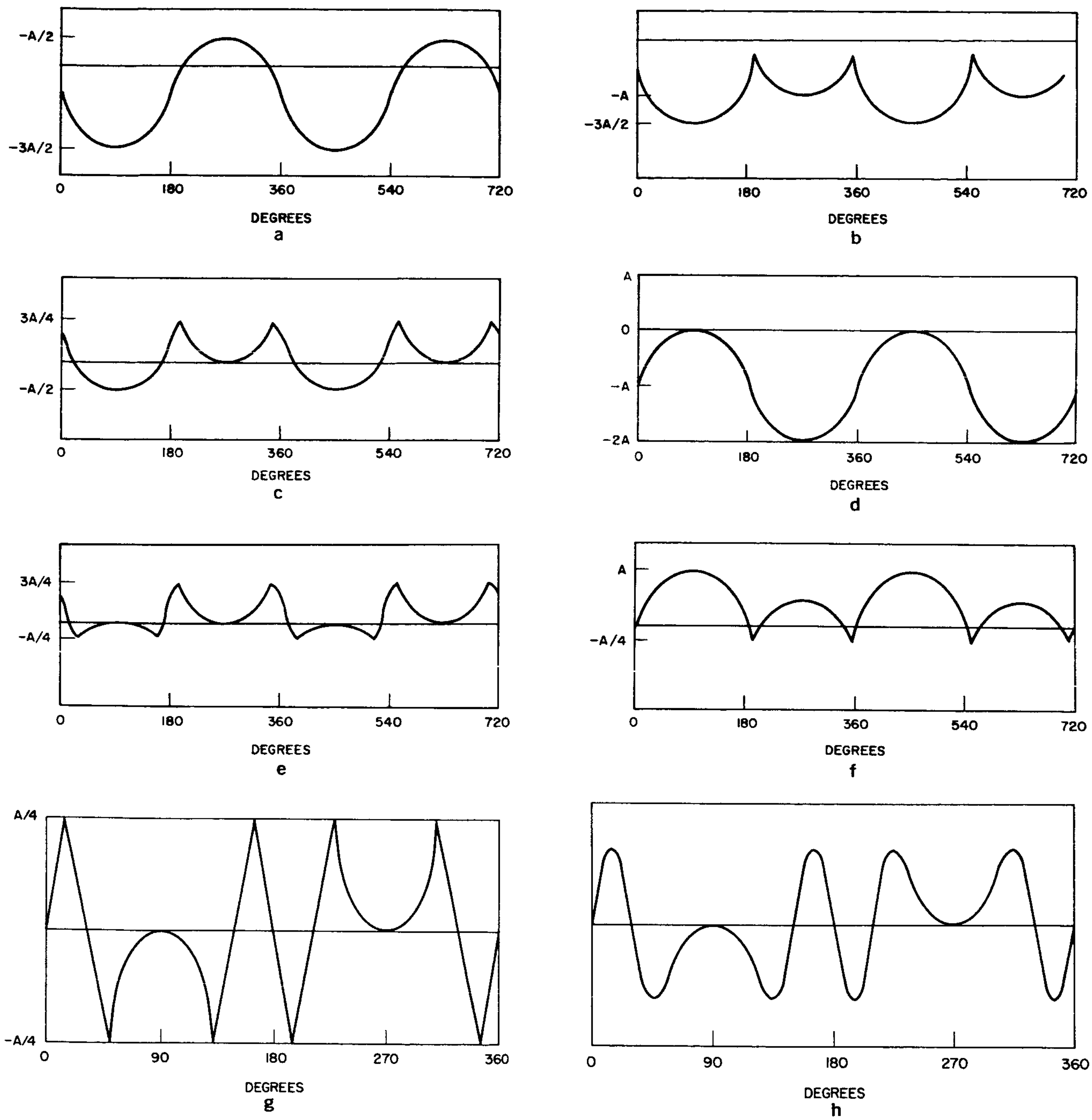

FIGURE 6-110. SIN (2π SIN ωT) WAVEFORMS

loop gain is much larger than unity, the closed-loop voltage gain is nearly $R7 + R8/R8$ with no phase reversal.

Figure 6-111 is a block diagram of the phased-array control electronics and jet control electronics subsystem. This diagram incorporates the revised subassemblies described above, plus the ψ_2 counter which counts and stores the number of cycles of the FLP-VCO between the ψ and ψ_2 pulses. The contents of the counter are telemetered as digital information, providing the $\psi - \psi_2$ angle to an accuracy of ± 0.35 degree. The variable phase control subassembly is now called the beam positioner subassembly.

Collinear-Array Receiving Antenna

The receiver system does not require a high-gain steerable antenna. Therefore, the receiving antenna consists of a four-element collinear array, similar to the Syncom I transmitting antenna. The increased bandwidth of the Syncom II dictated a broader-band element than the skirted dipole used in Syncom I.

To perform system engineering tests two scaled model antennas were fabricated. One model was a four-element array scaled from Syncom I and was matched at only one frequency. The other model was scaled from the six-element transversely polarized cloverleaf transmitting array. Without impedance matching, the cloverleaf array had a VSWR under 2.0 over the 200-mc band. Typical patterns are shown in Figure 6-112. Impedance measurements indicate that this array is resonant at approximately 6320 mc. The VSWR of the array as a function of frequency for the 200-mc bandwidth is shown in Figure 6-113. The VSWR at 6300 mc is 1.23:1, which is suitable for system tests; therefore, this array will be used for system tests without any additional impedance matching. E-plane and H-plane antenna patterns have been made across the 200-mc frequency band.

The major characteristics of this array are tabulated below:

Frequency, mc	Omni-directionality, db	Beam-width, degrees	Sidelobe Level, db
6200	0.75	19.1	11.2
6225	0.65	19.2	12.3
6250	0.75	19.3	12.1
6275	0.75	18.9	12.0
6300	0.70	18.4	11.7
6325	0.65	18.4	11.5
6350	0.70	18.1	11.4
6375	0.65	18.9	11.7
6400	0.50	19.0	11.8

Theoretical studies of the patterns and gain of an array of four skirted dipoles were made by means of a computer program which included the element pattern of an infinitely thin dipole. These studies showed that with a 0.9λ interelement spacing and a 0.45, 1, 1, 0.45 amplitude distribution for the feeding coefficients, a theoretical gain of 8.0 db was possible for the required 17.3-degree beamwidth. A more general discussion of the relationship between aperture distribution functions and gain is given in Section 9.

It was also determined that the beam of a standing-wave array tends to scan somewhat with changes in frequency before the more commonly known phenomenon of beam splitting is observed. The computer runs indicated that this tendency for the beam to scan was most noted when the sum of the series impedances of the elements was considerably larger or smaller than the characteristics impedance of the coaxial feed line. The beam scanning effect was minimum when the sum of these series impedances exactly equaled the impedance of the feed line at the center frequency. The impedance measurements described above show that coupling of the radiating elements can be controlled by means of the annular slot width; hence the perfect match desired without the use of matching devices should be attainable at the center frequency. An increase in impedance bandwidth was achieved by flaring the skirts of the dipole. This configuration is known as a biconical dipole. An extensive experimental study of the impedance of this dipole was conducted to determine its optimum size with respect to impedance bandwidth.

A complete array with interchangeable dipole sizes was made in order to optimize the contribution of the biconical dipole element pattern to total radiation pattern. An approximate 0.9λ interelement spacing was achieved by using an air-filled coaxial line with bead supports in the region of the dipoles. Suppression of the end-fire lobes at this large spacing was to be effected by the element pattern. Therefore, the tested array had uniform distribution in order to clearly discern the effects of dipole changes on these lobes. Unfortunately, no biconical dipole size was found which materially reduced these lobes. This array is shown in Figure 6-114. As was expected, the uniform distribution produces a narrow beam equal to a minimum of 12.5 degrees over the band. Typical patterns are shown in Figure 6-115.

To reduce the end-fire lobes, the interelement spacing must be decreased or a more directive element

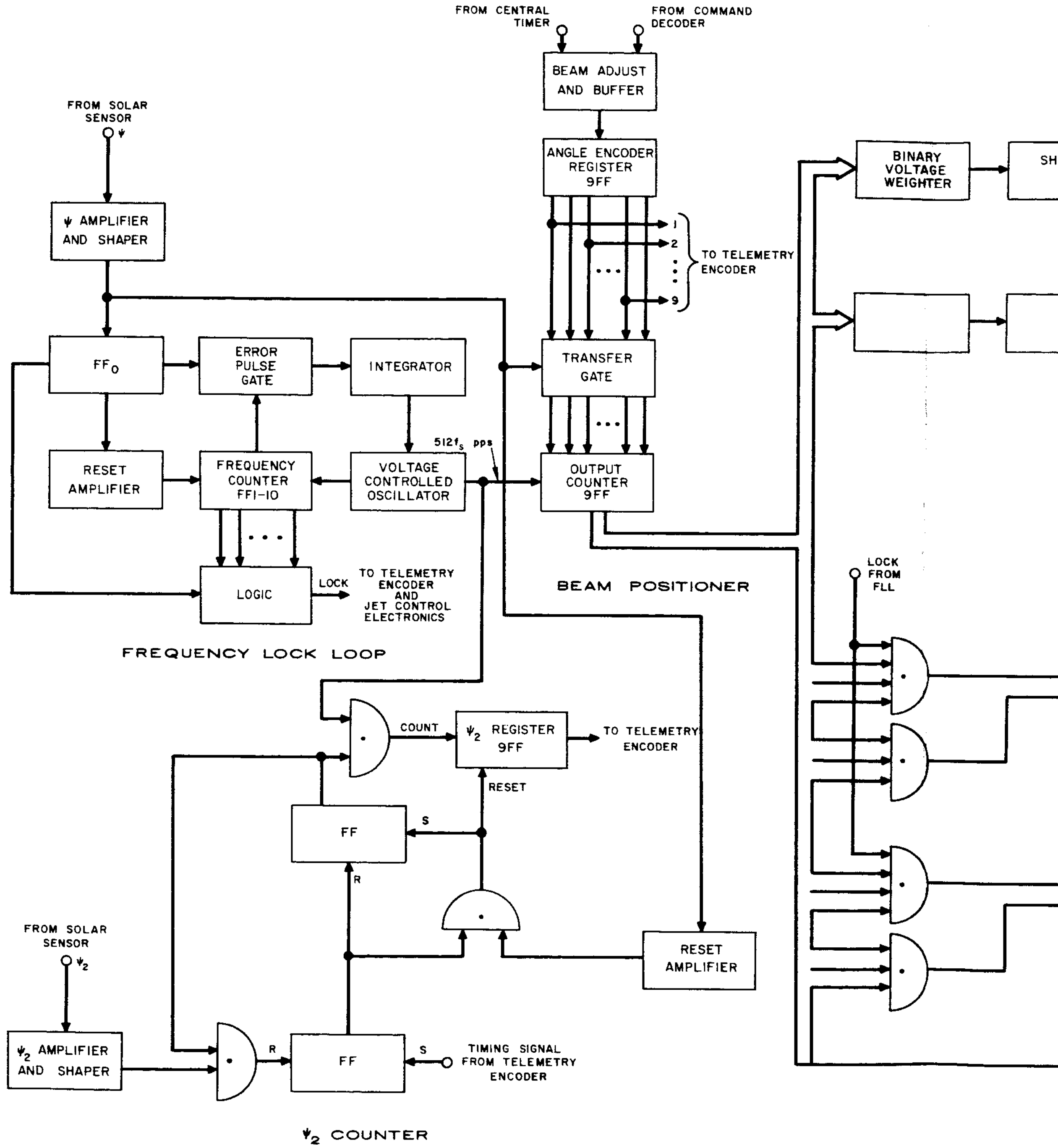

FIGURE 6-111. PHASED-ARRAY AND PULSE JET CONTROL ELECTRONICS

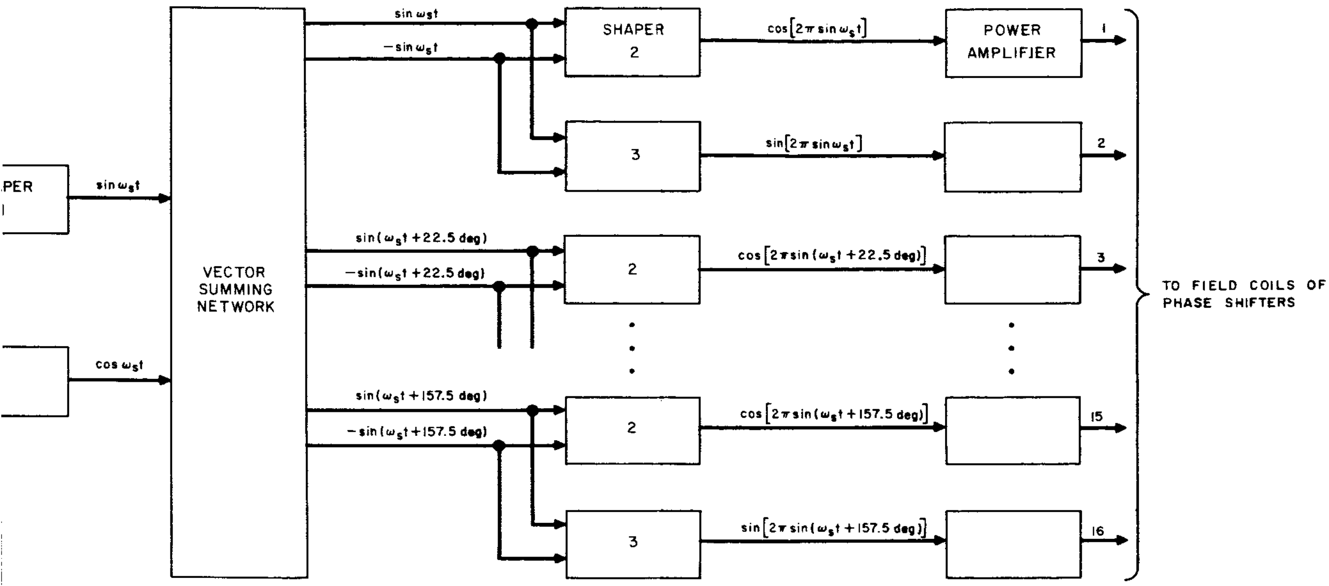

WAVE FORM GENERATOR

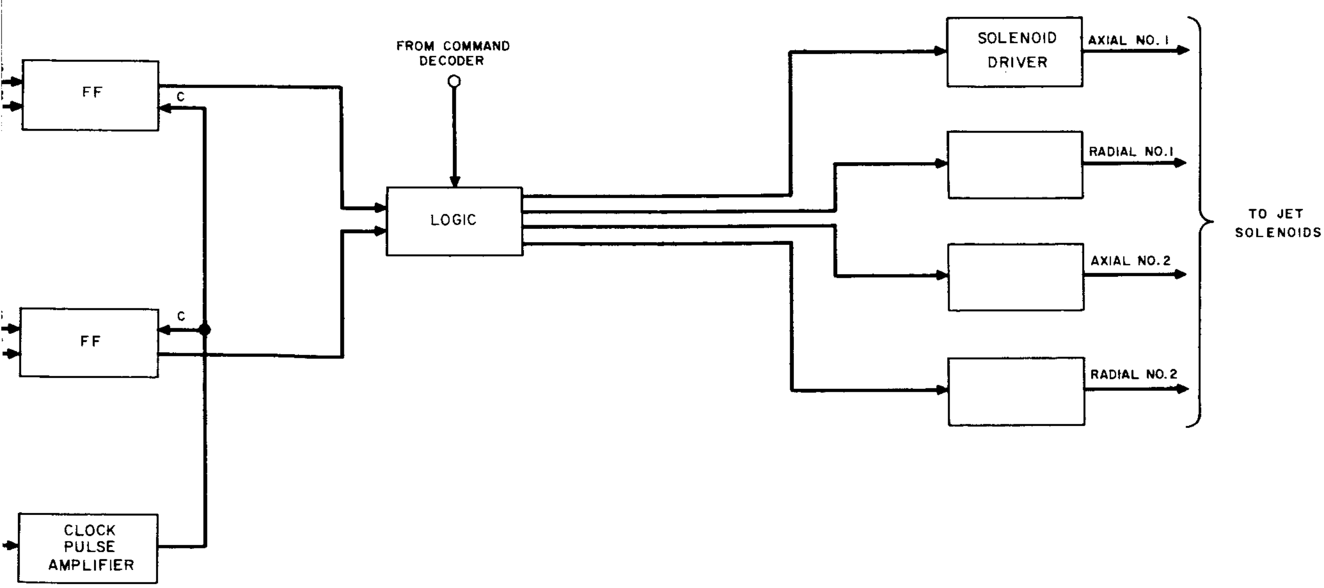

JET CONTROL ELECTRONICS

must be used. Such an element would be larger and its size and weight would represent serious problems. It would be more desirable to solve the problem by reducing the interelement spacing by the use of a dielectric filled coaxial feed line. Teflon dielectric will reduce the spacing to 0.69λ which should be adequate. It is possible that the distribution will also have to be tapered to obtain a beam of the desired width. A unit such as this is being fabricated. Test results will be included in a Summary Report Supplement. For the productized antenna serious consideration will be given to foamed ceramics for the dielectric material. Ceramics would have the advantage of no mass loss (hence no change in dielectric constant) from exposure to the hard vacuum of outer space for a period of 3 to 5 years.

CENTRAL TIMING ELECTRONICS

Figure 6-116 is a block diagram of the proposed central timer. It would provide selectable outputs for the redundant phased-array control electronics (PACE) units at 2.81 minutes per pulse in addition to providing a highly reliable means of firing the apogee engine.

The precision oscillator employs a tuning fork resonator with a frequency stability of 0.01 percent over the expected Syncom temperature range. Frequency scaling is performed by a combination of flip-flops and incremental saturating magnetic cores. The output logic is such that if two or more of the timers are activated, the apogee engine will fire. One timer failing early cannot fire the engine. The apogee engine driver would employ component redundancy to provide high reliability. To preserve quadrant symmetry and improve reliability, one timer would be packaged in each quadrant.

The proposed timer offers the following advantages:

1) The reliability of the PACE circuitry is im-

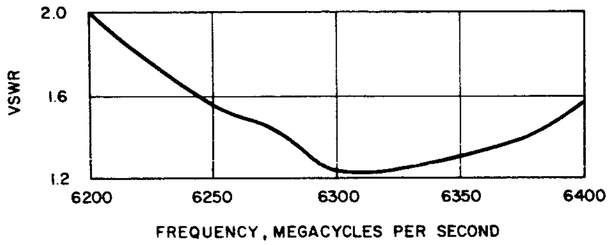

FIGURE 6-113. VSWR OF ARRAY AS FUNCTION OF FREQUENCY

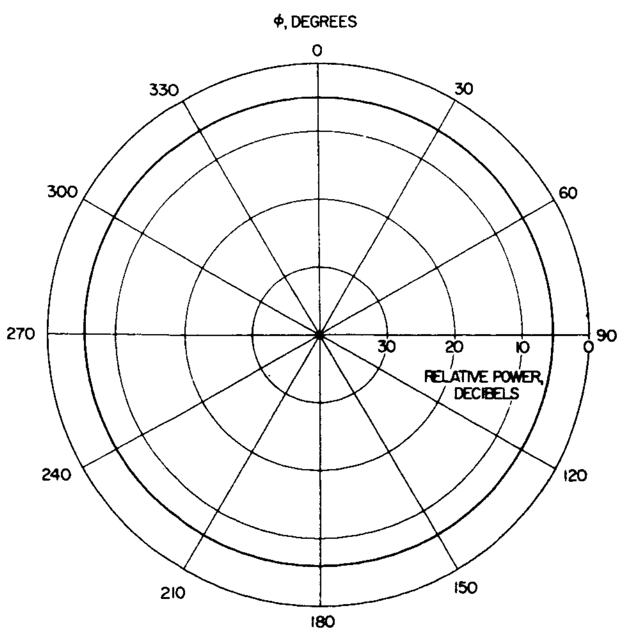

a) E-plane

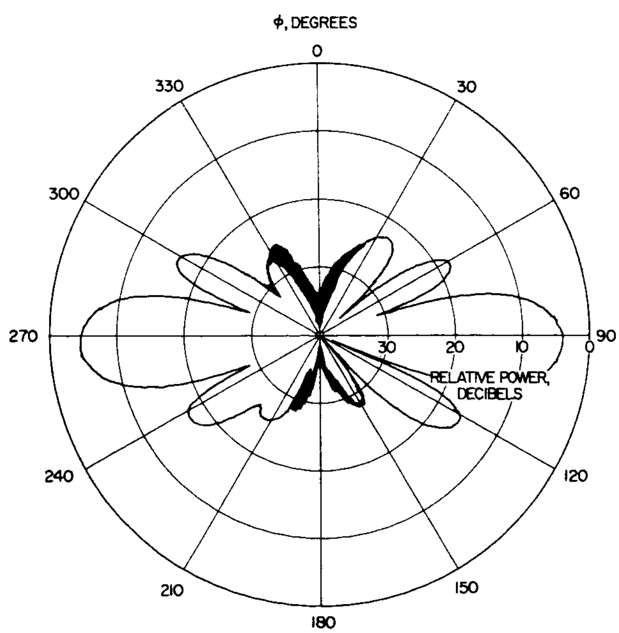

b) H-plane

FIGURE 6-112. CLOVERLEAF ARRAY ANTENNA PATTERN

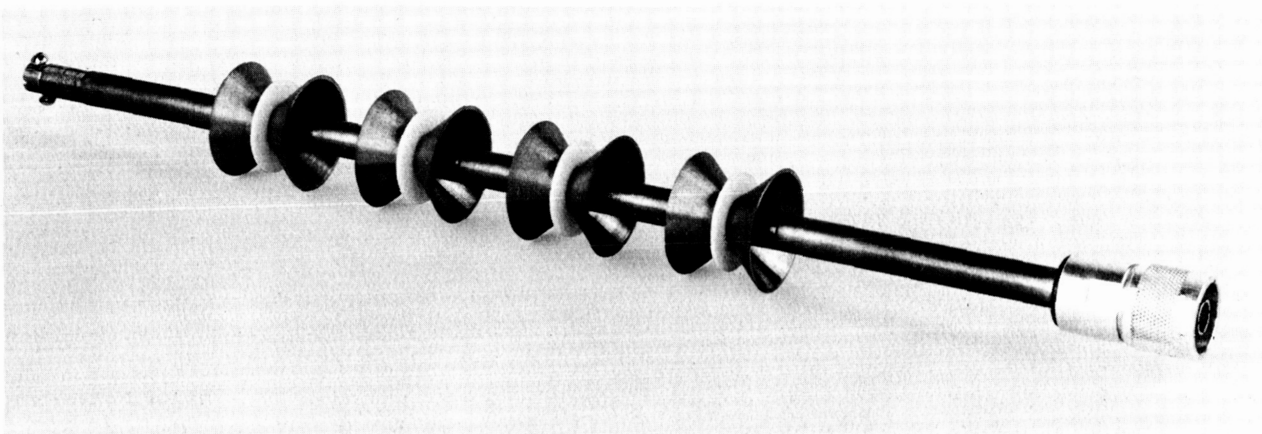

a) Assembled prototype

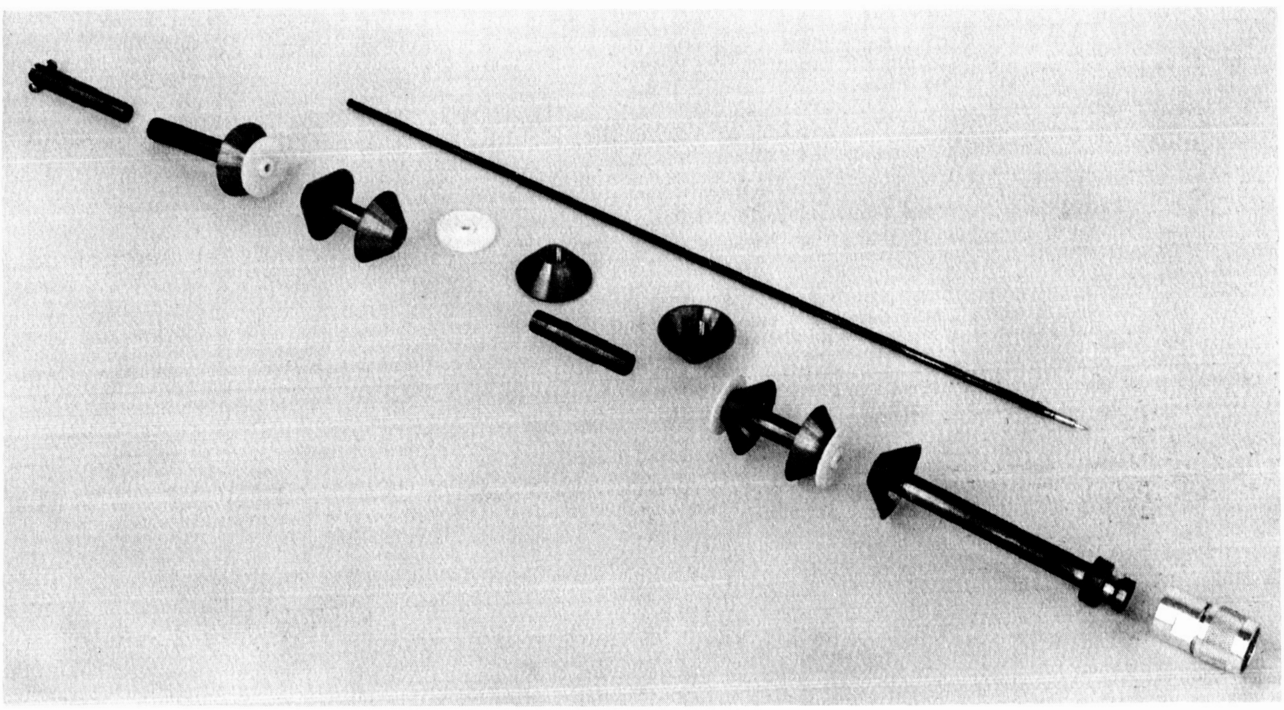

b) Exploded prototype

FIGURE 6-114. SYNCOM II FLARED DIPOLE ANTENNA

proved. The MTBF of the digital PACE is increased 1500 hours.

2) The circuit design of the oscillator and initial countdown stages and the determination of the electrical specifications for the tuning fork have already been accomplished for the PACE.

3) Since an output with a 2.81-minute period is required by the PACE circuitry, the additional equipment required to provide a source at 315 minutes is quite small. Packaged weight should be less than one ounce.

4) The proposed timer has the advantage over

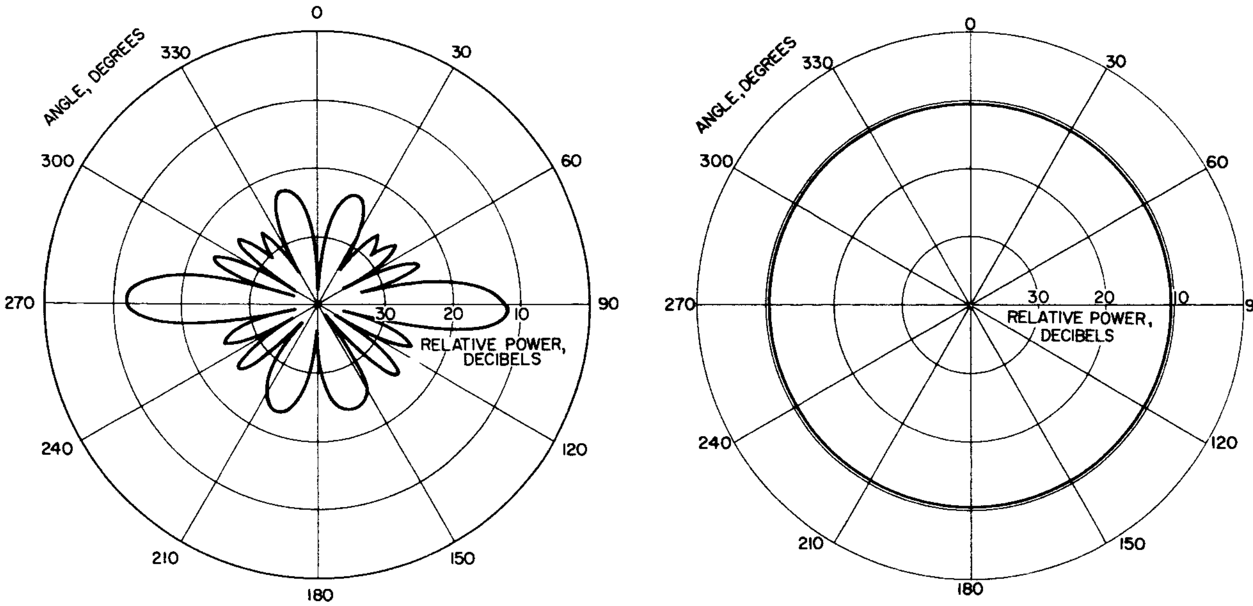

a) E-plane b) H-plane

FIGURE 6-115. MEASURED RADIATION PATTERN OF RECEIVING ANTENNA CONSISTING OF BICONICAL DIPOLES $f = 6300$ mc

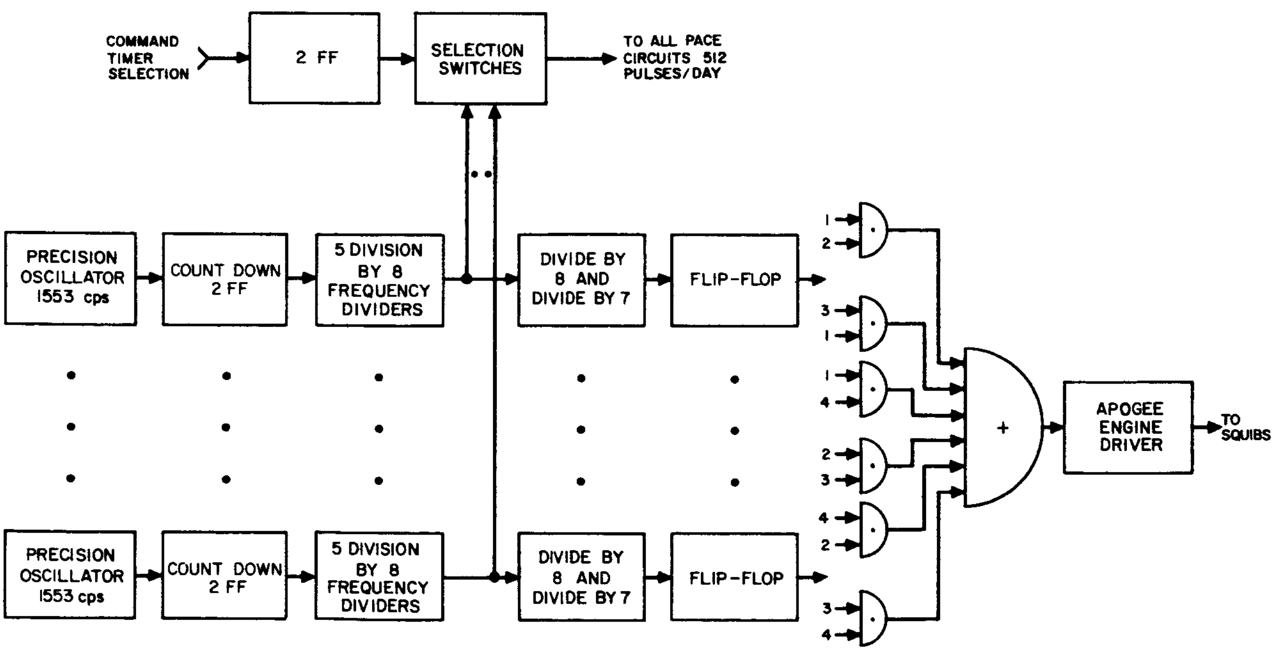

FIGURE 6-116. SYNCOM II CENTRAL TIMER

mechanical types in that no moving parts are required and that the system could be designed so the fire time is selectable.

5) This timer can be designed to work reliably even in the event of a momentary power failure, which is an advantage over other electronic types.

6) Using this timer will allow Hughes to make use of the experience gained on the Syncom I timer.

An analysis of design considerations for incremental core counters has been conducted. The analysis indicates that relibable scale-of-8 counters can readily be developed to meet the Syncom environmental conditions. Specifically, preliminary investigation indicates that temperature stability of the timer will meet all requirements.

Cores have been procured. A laboratory model pulse shaper stage has been designed and is operating satisfactorily. Design of counter stages will be initiated. Preliminary circuit design is also being accomplished for the timer quadrant selection switches, the selection flip-flops, and the apogee engine timer output buffer.

VELOCITY AND ORIENTATION CONTROL

Mission Requirements and System Description

The satellite control operations to be performed after initial orbit injection (i.e. after apogee motor burnout) include:

1) Elimination of orbit injection errors to achieve the desired stationarity and adjustment of the longitude.
2) Alignment of the spin axis with the earth's polar axis.
3) Station keeping throughout the active life of the satellite to correct for errors from such external disturbances as the sun and moon gravitational influence on the orbit inclination (about 1 degree per year), and the effect of triaxiality of the earth's gravitational field on longitude (about 0.3 fps per week).

The control system is designed to perform these functions in accordance with the accuracies indicated in Table 6-12.

TABLE 6-12. BASIC PERFORMANCE CHARACTERISTICS

Stationarity	± 0.05 degree
Spin axis orientation	± 2.0 degree
Spin rate variation	± 25 percent

GENERAL CONFIGURATION

The system for performing these operations involves both satellite and ground station components, as shown in the functional block diagram of Figure 6-117. A discussion of these components, as they relate to the functions of the control system, is given later.

The Syncom II control system is similar to that of Syncom I. The principal exceptions are: 1) The ground-based synchronous controller for providing properly phased signal pulses to the jets, is employed as a back-up to a synchronous counter and logic circuitry on board the spacecraft. 2) The two independent reaction jet subsystem units employ bipropellants (MMH and N_2O_4) instead of two separate systems using hydrogen peroxide and cold gas. Two independent and completely identical propellant and engine units are provided, each of which has the capacity to perform all station-keeping operations throughout the service life. 3) Active spin rate control is provided to maintain the spin rate in the range of 100 ± 25 rpm. This is accomplished by means of a centrifugally actuated gimbaled jet with its axis of rotation at 45 degrees to a spacecraft radius. Movement of the thrust vector through a small angle produces a tangential component of thrust of appropriate polarity and magnitude whenever spin rate deviates from the design rpm.

Syncom II employs four sets of ψ and ψ_2 sun sensors in the same configuration as in Syncom I. These sensors perform the same functions as the single set of sensors in Syncom I, that of providing information for determining the spin orientation, and for a timing reference to fire the jets in the pulsed mode.

In performing the orientation maneuver, the known initial spin axis orientation at apogee motor burnout is used in computing the phase delay and the total precession angle required to align the spin axis to the earth's polar axis. Errors in the initial orientation are, in general, small, and the resulting error at the completion of the maneuver will be correspondingly small. Measurement of the polarization angle of the energy recived from the linearly polarized transmissions of the phased-array antenna provides the information for making final correction in spin axis orientation. In the event that large orientation errors exist so that the antenna beam is not detected at the completion of the maneuver, the antenna elctronic control circuits may be deactivated, causing the conical beam to revert to

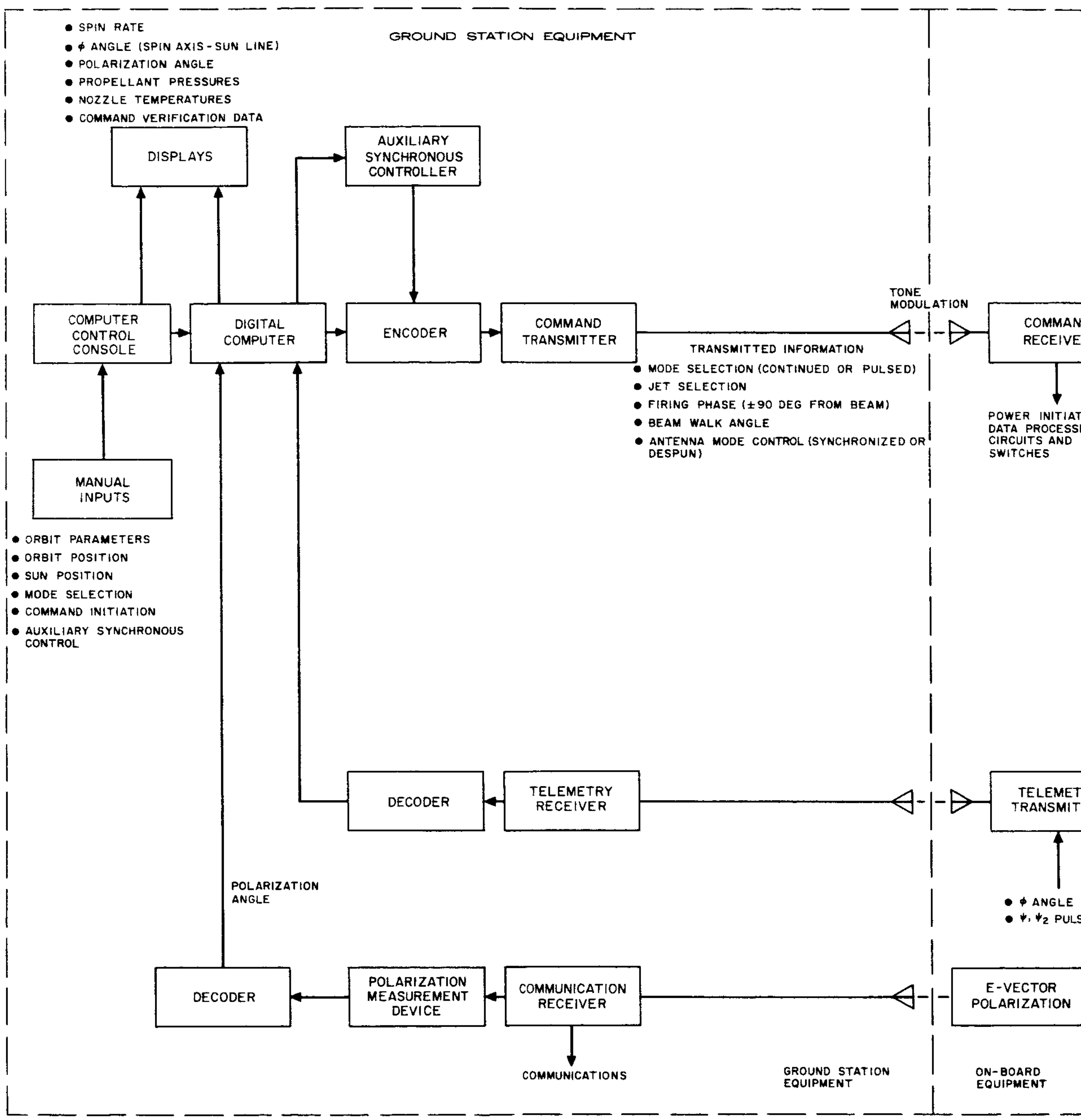

ALL ELECTRONIC CIRCUITS AND SUN SENSORS ARE QUADRUPLY REDUNDANT

PROPELLANT SYSTEMS AND JETS ARE DOUBLY REDUNDANT

FIGURE 6-117. SYNCOM II CONTROL SYSTEM

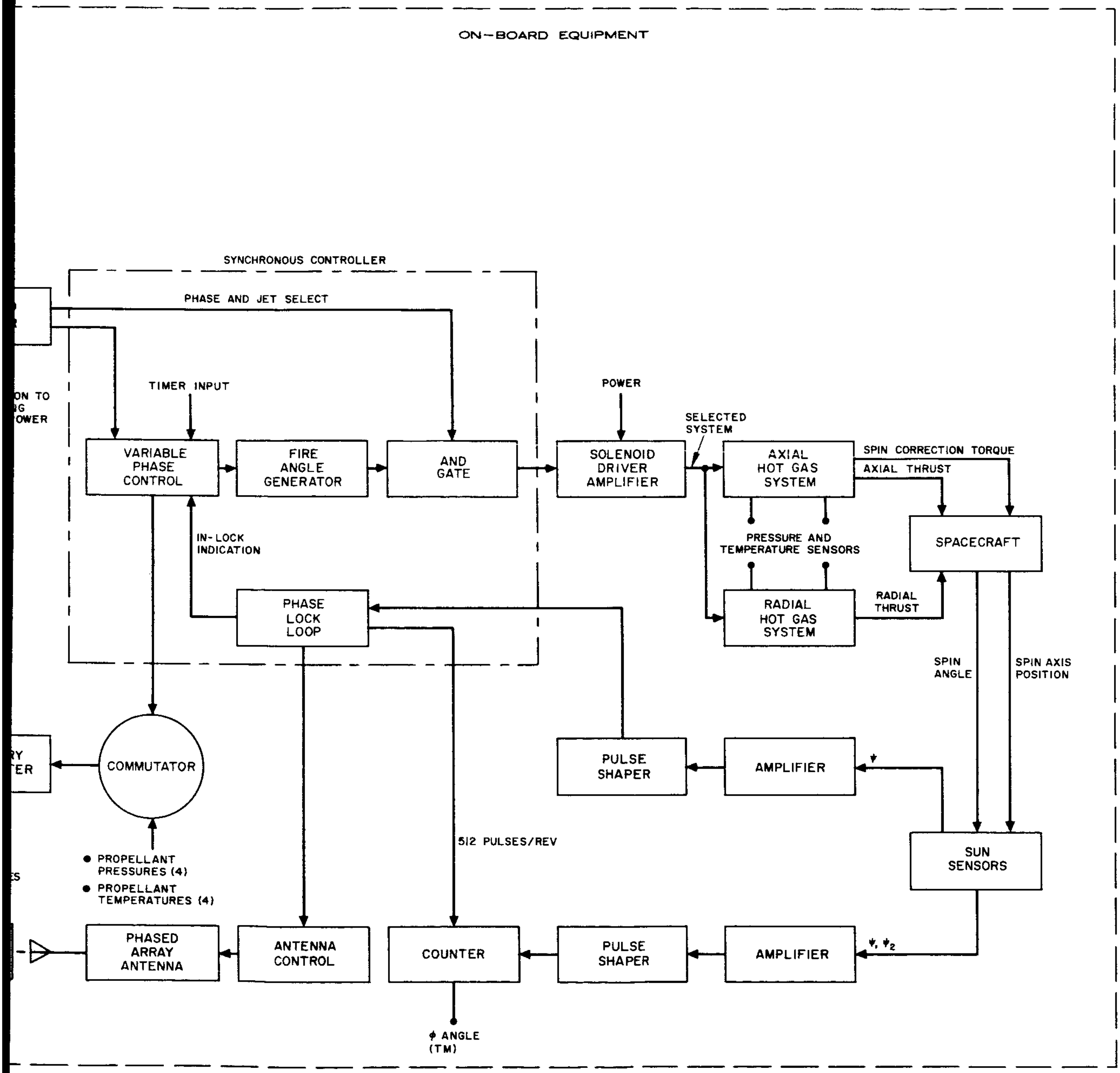
ON-BOARD EQUIPMENT
SYNCHRONOUS CONTROLLER
PHASE AND JET SELECT
TIMER INPUT
VARIABLE PHASE CONTROL
FIRE ANGLE GENERATOR
AND GATE
POWER
SOLENOID DRIVER AMPLIFIER
SELECTED SYSTEM
AXIAL HOT GAS SYSTEM
SPIN CORRECTION TORQUE
AXIAL THRUST
SPACECRAFT
PRESSURE AND TEMPERATURE SENSORS
IN-LOCK INDICATION
PHASE LOCK LOOP
RADIAL HOT GAS SYSTEM
RADIAL THRUST
SPIN ANGLE
SPIN AXIS POSITION
COMMUTATOR
PULSE SHAPER
AMPLIFIER
512 PULSES/REV
SUN SENSORS
PROPELLANT PRESSURES (4)
PROPELLANT TEMPERATURES (4)
PHASED ARRAY ANTENNA
ANTENNA CONTROL
COUNTER
PULSE SHAPER
AMPLIFIER
ϕ ANGLE (TM)

a pattern similar to the Syncom I antenna pattern. The included angle of the beam will then intersect the earth and will be detectable as an RF signal. Measurement of the polarization angle together with the sun sensor information, will provide sufficient data to determine the orientation of the spin axis.

The physical arrangement of the reaction control jets is similar to that of Syncom I. The redundant radial jets are located on opposite sides of the spacecraft with thrust vectors pointing through the center of gravity. The axial jets are also 180 degrees apart with thrust axes parallel to the spin axis and at a radius of about 26 inches from the spacecraft spin axis.

The control jets are used in either a continuous mode or a synchronous pulsed mode depending on the operation to be performed. Table 6-13 presents a list of the operations and the manner in which the jets are used. Also included in the table is the maximum total impulse required in each operation, expressed in units of equivalent velocity increment imparted to the payload.

FUNCTIONAL DESCRIPTION

The block diagram of Figure 6-117 identifies the functional elements of the control system and their interrelationships. The basic functions performed by this system are 1) to produce a thrust vector in the appropriate direction in space for the required velocity correction, and 2) to produce a moment about the appropriate axis in space to precess the spin axis in the required direction. A secondary function is to maintain the spin rate within a prescribed range.

TABLE 6-13. MAXIMUM TOTAL IMPULSE REQUIRED

Function	Jet Used	Mode	Equivalent Δv
Spin axis orientation	Axial	Pulsed	~18 fps
Orbit period and eccentricity correction	Radial	Pulsed	120 fps
Orbit inclination correction	Axial	Continuous	112 fps
Station keeping, E-W errors	Radial	Pulsed	<7 fps/year
Station keeping, N-S errors	Axial	Continuous	<180 fps/year

Velocity correction may be performed with either the axial jet in a continuous mode or the radial jet in a pulsed mode. Selection of the mode depends on the particular type of orbit correction required. The spin axis, in general, will not be reoriented once the initial alignment has been established. However, when required, precession of the spin axis is accomplished by use of the axial jet in a synchronously pulsed mode.

The direction of either the velocity maneuver (when using the radial jet) or the precession maneuver is dependent on intelligence computed on the ground and transmitted in digital code to a register in the satellite. The magnitude of the maneuver is controlled by the duration of the execute signal from the ground station. Thus, with the exception of spin rate control, which is performed entirely by on-board sensing and control, the ground station is an integral part of the velocity and orientation control system.

The basic information required for synchronous pulse jet control is the spin axis orientation and a timing signal to indicate the relative position of the jets with respect to a space coordinate system. The latter signal is provided by the ψ sensor while the orientation is established by the combined ψ and ψ_2 sensor signals, both of which are transmitted in real time to the ground station via the telemetry link.

Orbit corrections based on satellite tracking data are determined at the ground station by a digital orbital correction command computer.

An auxiliary synchronous controller at the ground station, as shown in Figure 6-117, provides the capability of controlling the jets in the synchronous pulse mode in a manner similarly functionally to the synchronous controller used in Syncom I. However, it is an all-electronic device comprised of circuits essentially identical to those used in the on-board synchronous control. Jet on-off commands are transmitted directly from the ground via the execute signal. The on-board register must be set for continuous mode when the auxiliary controller is used.

Design Requirements

ERROR ANALYSIS

Orientation. The orientation of the satellite is accomplished by pulsing the axial jets. The angle between the solar sensor maximum output and the thrust center of the pulse (ψ) is maintained constant. The resultant

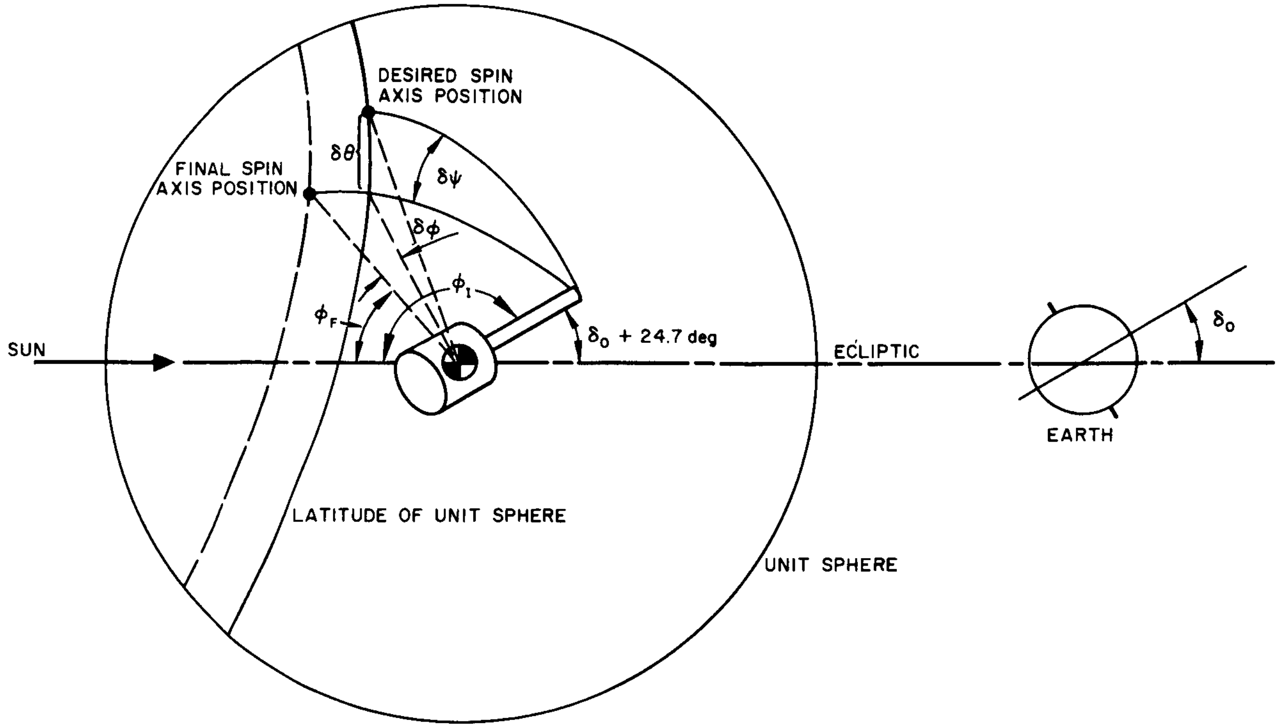

FIGURE 6-118. ANGULAR ERRORS INVOLVED IN ORIENTATION MANEUVER

motion of the satellite is such as to cause the spin axis to trace out a rhumb line over a unit sphere with the satellite at the center and the polar axis defined by the sunline. The precession continues until the angle ϕ between the sunline an dspin axis, calculated by using satellite coordinates and almanac data, equals that angle derived from the measured ψ and ψ_2 sun sensor signals.

The final position of the spin axis should be parallel to the earth's polar axis within 2 degrees to ensure adequate communications coverage. Errors in the final position are $\delta\theta$, a longitude error on the unit sphere, and $\delta\phi$, an error in the spin axis — sunline angle (refer to Figure 6-118. The errors affecting spin axis alignment are: inexact knowledge of the spin axis position at apogee engine burnout; errors in the angle ψ; and, errors in the angle ϕ.

If the final spin axis — sunline angle ϕ_F is not outside the communications beam width, any attitude error ϕ_e will become evident by using polarization measurements of the elctrical vector of the communications beam. Corrections will then be made with the axial jets to null this error. If the ψ angle is grossly in error, convergence to ϕ_F could be along a shallow rhumb line with an ensuing large number of traversals around the unit sphere and a consequent fuel wastage. Gross errors in either ϕ or ψ are not anticipated, as evidenced from estimates of the component errors in the following pages.

Errors occurring during ascent will limit the accuracy of the determination of the initial position of the spin axis in a plane containing it and the sunline (ϕ_I) to within 2 degrees. In a plane normal to this, the error may also be 2 degrees. The former error $\delta\theta_I$ will affect the final attitude by an amount $\delta\theta = [\sin \phi_F/\sin \phi_I \tan \psi]\ \delta\phi_I$. The maximum value the bracketed term may take for reasonable orientation times is 1.43. The attitude error is then 2.86 degrees. The latter error ($\delta\theta_I$) affects the final attitude error, $\delta\theta$, by an amount of $\delta\theta_I \sin \phi_F$. The maximum value of ϕ_F is 68 degrees; thus the attitude error is 1.85 degrees.

Errors in measurement of ϕ are associated solely with sun sensor characteristics. Equation 5.3 of Reference 6-1 yields the angle ϕ_I,

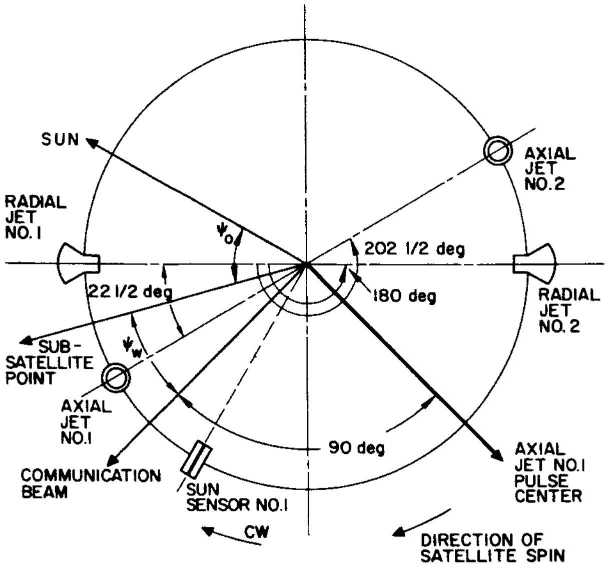

FIGURE 6-119. ANGLES INVOLVED IN DETERMINING ψ

$$\cot \phi = \sin \Psi_2 \cot I$$

where ψ_2 is the angle of rotation of the satellite about its spin axis between the maximum outputs of the ψ and ψ_2 sun sensors, and is determined from the relationship $(\tau/T)360$. τ is the observed time interval between the two sensor maximum outputs and T is the period of one revolution of the satellite. I is the angle between the ψ and ψ_2 solar cells and is nominally 35 degrees. The alignment of the two sensors can be held within ± 0.5 degree. The present requirement for the 3-db beam width of a sun sensor is 0.8 ± 0.1 degree. Inspection of data taken thus far indicates the outputs of the sun sensors are reasonably symmetrical and deviation of the peak power point from a position half way between the 3-db points is less than 0.05 degree. An rms error in ψ_2 is then 0.07 degree. The largest error in the final ϕ can be obtained from the previous equation by letting ψ_2 be its minimum, i.e., $\psi = I = 35$ degrees. For this worst case the maximum error in ϕ is then 0.566 degree.

Errors involved in the angle ψ arise from a number of sources: the ψ sun sensor, the synchronous controller, the axial jets, and alignment of the jets and sun sensors on the spacecraft. Figure 6-119 indicates the various angles involved in determining ψ by the synchronous controller.

For reasons of simplicity in command structure the antenna beam position is used as the reference for the jets. The jets are fired such that the pulse centroids occur at ± 90 degrees from the beam. One radial jet is selected as a reference from which all other jet positions are determined. For the orientation maneuver, it is necessary to conduct the operation at the time in the day when the phased array beam is at a position 90 degrees from where the selected jet pulse center is desired. In firing an axial jet in the pulsed mode, the synchronous controller requires the following angular information: the sunline, angles ψ_ω and ψ_o, the angle between the reference radial jet and the sun sensor, and the angle between the reference jet and the selected axial jet. The sunline is detected by the ψ sun sensor. A pulse shaper will be triggered at a voltage of approximately 100 mv. Tolerances in the sensor voltage and trigger circuit stability will hold the angular error to approximately 0.2 degree.

The angles ψ_ω and ψ_o are calculated based on satellite position and almanac data. Both ψ_o and ψ_ω are entered into registers in the variable phase control portions of the phased array control circuits. Since the registers are limited to 9 bits, each angle can be represented only to an accuracy of 360/512 or 0.7 degree.

Expected accuracies in aligning the sun sensors and jets relative to the reference radial jet will exceed 0.25 degree. Deviations in the centroidal pulse center of the jet from the design center may be ± 1 ms. At 100 rpm this corresponds to 0.6 degree.

The rms error of all the ψ errors is 1.33 degrees. This is a negligible perturbation from the desired rhumb line. From page 38 of Reference 1 an error in ψ of amount ψ_e causes a final attitude error, $\delta\phi = [\sin \phi_F \, \Delta\theta / \sin \psi \cos \psi] \, \delta\psi$, where $\Delta\theta$ is the total attitude correction required. The value of these angles depends on which time of year and hour of day orientation takes place. Of the acceptable orientation times the largest value for the bracketed term is 2.88. This results in an error in θ of 3.83 degrees.

In summation, the total errors attributable to the spacecraft control system and its components are: $\delta\phi = 0.566$ degrees, $\delta\psi = 1.33$ degrees, and $\delta\theta = 3.83$ degrees. The $\delta\theta$ error is readily compensated for by using information derived from the communications system — signal strength or electrical vector polarization. The errors indicate that the desired rhumb line precession is nearly achieved.

Initial Orbit Corrections and Station Keeping. Errors incurred subsequent to completion of orientation will not cause gross undesirable spacecraft motions; they are important only in that they cause a slight increase in fuel usage. Errors in spin axis inclination from the earth's polar axis are measurable to the accuracies of the sun sensors or 0.566 degree. The satellite's location is measured from earth and is thus known to the accuracy of the instruments used.

The initial inclination correction is made by continuous operation of the axial jets. The only error incurred here is an undesirable precession due to the jet being turned off at an angle different from that at which it was turned on. The maximum angular error would be 180 degrees. The precession over a 67½ degree angle, calculated in the section on functional requirements, is approximately 0.10 degree/pulse. The ratio of the effective torque of a 180 degree pulse to a 67½ degree pulse is 2:1. Therefore, the maximum precession cannot exceed 0.2 degree.

The initial eccentricity corrections and subsequent east-west stationkeeping corrections are performed by pulsing the radial jets either 90 or 270 degrees from the beam. The ψ error involved is assumed to be the same as it was for the axial jet, 1.33 degree. The total fuel expended due to this ψ error is 156 (sec 1.33° —1) = 0.045 fps.

Infinite resolution in either the precession angle or the velocity increments are possible by pulsing a jet twice in two directions. The vector summation is then the resultant thrust. This is not necessary, however, since the resolution obtainable by pulsing in one direction only is considerably less than that due the disturbances acting on the spacecraft. The resolution is the correction possible with one-half of a pulse. For precession then, this resolution is 0.05 degree, and for velocity control it is 0.0074 fps.

Spin-Speed Control. This error analysis determines the need of spin-speed control for the satellite. As a result of various misalignment errors, pulsing of the control jets produces moments on the spacecraft. Some of these are in a sense to alter the spin-speed from its nominal 100 rpm. Figure 6-120 illustrates the pertinent misalignments. The torque resulting from the radial jet is $F\delta_1$ and from the axial jet is FR sin ϵ. For a total assumed misalignment angle of 2 degrees, or its equivalent moment arm of 1 inch, the misalignment torque

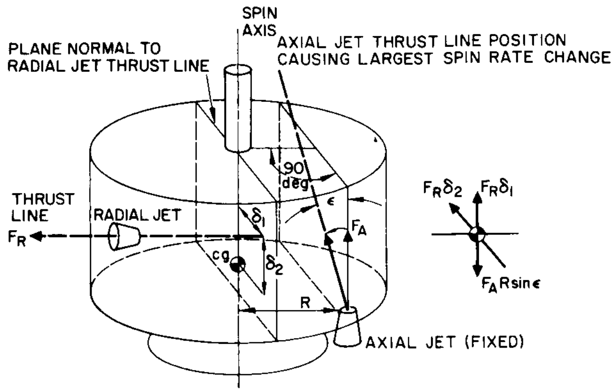

FIGURE 6-120. VARIOUS MISALIGNMENT TORQUES ASSOCIATED WITH CONTROL JETS

for each jet is 5.0 in-lb. This misalignment was apportioned as follows:

1) Control jet thrust misalignment
   Angular — ±0.50 degree
   Translational — ±0.05 inch
2) Alignment of jet to spacecraft — ±0.25 degree
3) Spacecraft radial center-of-gravity inaccuracy — ±0.25 inch
4) Spacecraft axial center-of-gravity inaccuracy — ±0.50 inch
5) Spacecraft deformation due to spin-up acceleration — unknown (assumed small)

The equations needed for the analysis are

$$I_z \Delta w = F\delta t$$

and

$$m\Delta V = Ft$$

where I_z is the spacecraft moment of inertia about the spin axis, m is the mass of the spacecraft, Δw and ΔV are respectively the changes in spacecraft spin rate and velocity, δ is the thrust misalignment moment arm, F is the jet thrust, and t is total thrusting time. These equations yield one simple expression for the change in spin rate,

$$\Delta w = \frac{m\Delta V\delta}{I_z}$$

The maximum velocity increment required for the spacecraft for 5 years is approximately 1190 fps, exclusive of spin-speed requirements. The total maximum spin rate change is then

$$\Delta W = \frac{(766)\ (1190)\ (1)}{(32.2)\ (12)\ (71)} = 33.3 \text{ rad/sec}$$

$$= 320 \text{ rpm}$$

Additional fuel requirements necessitated by spin-speed control are discussed below.

Functional and Interface Requirements

The following are functional and interface requirements for the control system components and subsystems needed to ensure adequate spacecraft control.

HOT GAS REACTION JET CONTROL SUBSYSTEM

Motor Requirements

1) *Duty cycle:*
   a) Continuous operation.
   The jets shall be capable of operating continuously at least once, up to 7 minutes, and thereafter continuously for 1-minute durations every 15 days.
   b) Pulsed operation.
   The jets shall be capable of operating once for 1½ hours with an on-time of 80 milliseconds and an off-time of 400 milliseconds. Thereafter, pulsed operation for the previously defined duty cycle shall occur every 4 days for 10-second periods.
2) *Thrust response time:* The time for the thrust to reach 95 percent of the maximum after application of a steady-state voltage of 24 volts across the valve coil, and the time for the thrust to decay to 5 percent of the maximum after voltage removal, shall be less than 12 milliseconds.
   The output impedance of the electronic switch which will drive the valve has not yet been determined. Figure 6-121 is a circuit diagram of the type of switch to be used.
3) *Repeatability:* The magnitude of the centroidal pulse center measured relative to an input into the circuit of part (2), for a 100-millisecond pulse, will be defined by the vendor. The actual centroidal pulse center shall be within ±5 milliseconds for any individual pulse.
   The variation in average centroidal pulse center from the design center shall be less than ±1 millisecond for any sequence of pulses exceeding 50.
4) *Thrust level:* With the tanks charged to the proper operating pressure, the steady-state thrust shall be 5 pounds ±5 percent at the specified operational temperatures, with an ambient pressure not exceeding 10^{-4} mm Hg. With one-half the operating pressure, the thrust shall be greater 3.0 pounds.
5) *Voltage susceptibility:* The preceding specifications shall be met when the 24-volt supply is varied ±5 volts.
6) *Effect of spin rate:* The jet system shall satisfy all system requirements when operated with spin rates from 50 to 150 rpm. The nominal spin rate will be 100 rpm.
7) *Thrust vector alignment:* The angular alignment of the center of the thrust vector to a line perpendicular to the jet mounting base shall be less than 0.5 degree. The geometric center of the jet shall be indicated on the mounting base. Translation of the center of the thrust vector from the geometric center shall be less than 0.05 inch.

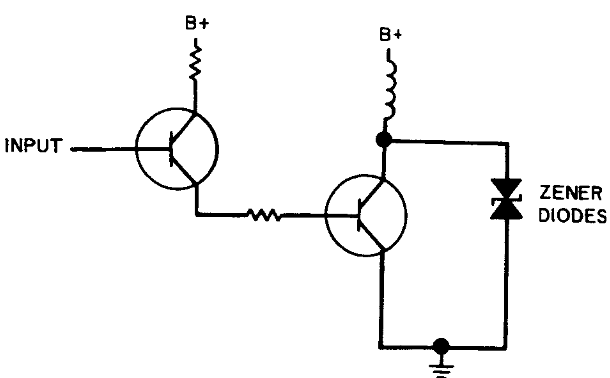

FIGURE 6-121. EQUIVALENT CIRCUIT-ELECTRONIC SWITCH

Fuel Requirements. The fuel requirements for the spacecraft are based on a weight of 766 pounds, moment of inertia about the spin axis of 71 slug-ft², a 67½ degree jet firing angle, and a precession angle of 65.6 degrees.

1) Initial orientation and orbit corrections:

Function	*Jet*	*Mode*	*Equivalent* ΔV*, fps*
Spin axis orientation	Axial	Pulsed	18

Orbit period and eccentricity corrections	Radial	Pulsed	120
Orbit inclination correction	Axial	Continuous	112

2) Disturbances external to spacecraft:

Disturbance	*Jet*	*Mode*	*Equivalent* ΔV, *fps/year*
Triaxiality (E-W)	Radial	Pulsed	7
Sun-moon gravitation (N-S)	Axial	Continuous	180
Solar pressure (precesses spin axis ¾ degree per year)	Axial	Pulsed	0.11

3) Spin axis position correction required due to radial jet thrust misalignment: As a result of alignment errors and axial center-of-gravity shift, the thrust lines of the radial jets miss passing through the c.g. of the satellite by a distance δ_2. (Figure 6-120.) Pulsing of the radial jets then causes a precession of the spin axis, necessitating corrections by the axial jets. The errors forming δ_2 are:

a) Jet thrust misalignment (refer to motor requirements above).
   Translational — 0.05 inch at base of combustion chamber
   Angular — 0.50 degree

b) Alignment of the jet to the spacecraft — 0.25 degree.

c) The total axial c.g. travel is approximately 1.5 inches due to apogee engine burn. The final position of the c.g. will be known within ± 0.5 inch.
   At the spacecraft radius of 26 inches, the angular errors result in a translation of 0.34 inch. The rms of these yields $\delta_2 = 0.56$ inch.

The precession angle resulting from one radial jet pulse is $P = (T/H)\tau$

$$T = F\,\delta_2 = (5)(0.56) = 2.80 \text{ in-lb}$$

$$H = I\,\omega_s = (71)(12)(10) = 8.520 \frac{\text{lb-sec}^2}{\text{in}}$$

$$P = \left(\frac{2.80}{8{,}520}\right)(57.3)\left(\frac{67\tfrac{1}{2}}{360}\right)(0.6)$$

$$= 0.00212 \text{ degree/pulse}$$

The total number of pulses required from the radial jets over the 5-year life is equal to the total velocity increment provided divided by the velocity increment per pulse. The velocity increment provided per pulse is $F_R\tau/M$. since the useful thrust F_R varies as the cosine of the angle between the instantaneous thrust, F, and the center of the thrust.

$$F_R = \frac{1}{\gamma}\int_{\frac{-\gamma}{2}}^{\frac{\gamma}{2}} F\cos\gamma\, d\gamma = \frac{F}{\gamma}\sin\gamma \int_{\frac{-\gamma}{2}}^{\frac{\gamma}{2}} = \frac{2F\sin\gamma}{\gamma}$$

γ will be either 45 or $67\tfrac{1}{2}$ degrees, assume $67\tfrac{1}{2}$ degrees to allow conservative calculations.

$$F_R = 0.940\ F = 4.7 \text{ pounds}$$

The pulse period, $\tau = 45/360\ (0.6) = 0.075$ second.

The velocity increment per pulse for a 766-pound vehicle is, (Reference 6-2)

$$\frac{(4.7)(0.075)}{766}(32.2) = 0.0148 \text{ fps}$$

The total velocity increment required from the radial jets for a 5-year life is $120 + 5 \times 7 = 156$ fps. The total number of pulses required then is $156/0.0148 = 10{,}530$. The total precession angle caused by the radial jet is therefore $(10{,}530)(0.00212) = 22.3$ degrees.

The number of pulses required by the axial jet to correct for this precession is obtained as follows: The precession caused per axial pulse is

$$\frac{T}{H}\tau = \frac{(5)(26)}{(71)(12)(10)}\left(\frac{67.5}{360}\right)(0.6)$$

$$= 0.0985 \text{ degree}$$

The required number of pulses is $22.3/0.0985 = 227$.

Therefore, the velocity increment required by the axial jet to compensate for precession due to the radial jets is then $227 \times 0.0148 = 3.36$ fps.

4) Spin-speed control: The spin-speed control jet (axial jets) automatically compensates for axial

jet misalignment with no increase in fuel requirements. However, it must develop a spin moment to compensate for the radial jet misalignment and the initial spin error of the spacecraft. The initial spin error is assumed at most to be 10 rpm. The spin rate change due to the radial jets is,

$$\Delta W_s = \frac{M \Delta V \delta}{I_z}, \Delta V = 156 \text{ fps}$$

$$= \frac{(766)(156)(1)}{(32.2)(12)(71)} = 4.35 \text{ rad/sec}$$

$$\approx 42 \text{ rpm}$$

The axial jet must be deflected to develop a force component F_s in a direction to compensate for the radial jet spin rate change. The velocity increment required for spin-speed control is obtained as follows: The spin-speed change due to the force T_s is,
$\Delta W_s = F_s R \Delta t / I_z$, where R is the spacecraft radius at which the axial jet is located. The velocity change due F_s is $\Delta V = F_s \Delta t / M$.
Substituting from the first equation,

$$\Delta V = \frac{I_z \Delta w}{mR}$$

The initial spin-speed error will be included in Δw, $\Delta w = 4.35 + 10 \; (2R/60) = 5.4$ rad/sec. Thus,

$$\Delta V = \frac{(71)(5.4)(32.2)(12)}{(766)(26)}$$

$$\approx 7.4 \text{ fps}$$

This is the velocity increment required normal to the spin axis. The actual increase in velocity required for the control jets is less than this. For the "worst case" the 7.4 fps would be contributed with the axial jet inclined at its maximum angle of 8.5 degrees. The difference between the total jet thrust and the component parallel to the spin axis would be the total velocity increment required. (At the end of this 7.4 fps correction, the jet would return to its normal position.)

The velocity increment is obtained from the relationship:

$$\Delta V = 7.4 \cot 8.5° \; (\sec 8.5° - 1)$$

$$= (7.4)(6.69)(1.0111 - 1)$$

$$= 0.55 \text{ fps}$$

and ΔV_o, the total velocity increment required from the jet to develop the 7.4 fps is

$$\Delta V_o = 7.4 \csc 8.5°$$

$$= (7.4)(6.76)$$

$$= 50 \text{ fps}$$

This correction can be made at the time the initial inclination correction is made. Since the inclination maneuver allows for as much as 112 fps, the 50 fps will be encompassed by this maneuver. Therefore, essentially no additional fuel is required for spin-speed control.

SUN SENSORS

General. Four sets of four sensors will be required per spacecraft. There will be two ψ and two ψ_2 sensors per set. The signals from one pair of ψ and ψ_2 sensors will be telemetered and signals from the second set will be utilized by the on-board electronic systems. Switching shall be provided to allow use of any set.

Signal Strength. With a sun incident angle of 90 degrees, the minimum peak sensor output voltage shall be 250 mv. For incident angles of 15 and 165 degrees, the minimum peak voltage shall be 185 mv.

Bandwidth. For a sun incident angle of 90 degrees, the angular distance between the 3 db power points, obtained when the sensor is rotated about an axis parallel to its sensing plane, shall be 0.80 $\pm$0.10 degrees.

Positive Slope Reference. The sun sensor outputs will be shaped prior to usage by the electronic system. The sensor level, triggering the shaping circuit, shall be 100 mv $\pm$10 percent. The deviation in the angle at which a sensor has an output of 100 mv shall be within $\pm$0.2 degree of a design angle that will be specified by the vendor.

Alignment of ψ and ψ_2 Sensors. The ψ and ψ_2 sun sensors shall be aligned such that the angle between their sensing planes shall be 35.0 $\pm$0.5 degrees.

Reference Sensor. In the assembly of four sun sensors, the outer ψ sensor and inner ψ_2 sensor will be designated as reference for alignment to the spacecraft. These will also be utilized by the on-board electronics.

SYNCHRONOUS CONTROLLER

General. The function of the on-board synchronous controller is to control the firing of the reaction control jets. It forms a part of the electronic system associated with the phased-array antenna. The portions of the phased-array electronics utilized for this function are the low frequency multiplier, variable phase control, and fire angle generator. The low frequency multiplier utilizes the ψ sensor output to provide 512 counts per spacecraft revolution between ψ pulses. Ground command inputs are inserted into the variable-phase control circuits to provide a jet firing position relative to the sunline. The fire angle generator receives inputs from the phase-locked loop and variable phase control, as well as initiating firing and jet selection commands from the ground to activate a power switch which operates the jet control valves.

Commands. The following ground commands will be required by the synchronous controller.

1) Communications beam "walk" angle for firing the jets at other than 90 or 270 degrees from the beam.
2) Firing phase – 90 or 270 degrees.
3) Mode select — continuous or pulsed.
4) Jet selection — four jets.
5) Antenna mode control — either synchronized or omnidirectional. This allows antenna information to be used to aid in the orientation maneuver, if needed.

Sun Sensor Amplifier and Pulse Shaper. With a ramp input into the sensor amplifier of 10 volts/second, the shaping circuit shall operate between 90 and 110 mw. The time lag between sensing of the proper activation signal and maximum output voltage from the shaping circuit; shall be less than 100 microseconds.

Angular Resolution. All angular references and commands utilized by the fire-angle generator in determining the jet firing angle, shall have a resolution of at least 0.70 degree.

In-sync Interlock. An in-sync condition, defined by the phase-lock loop operating at 512 ± 1 counts per revolution, shall be required to exist coincidently with the initiated command to cause actuation of the jet control valve.

Operating time. The jet pulse controller must be capable of operating continuously once for at least 1.5 hours.

ALIGNMENT OF COMPONENTS ON SPACECRAFT

Reaction Control Jets. Two axial and two radial jets are required per spacecraft. The axial jets will be placed diametrically opposite one another, as will the radial jets. The radial and axial grouping of jets will be 90 degrees apart.

One radial jet will be designated as a reference. Alignment of the other jets will be 22.5 and 202.5 degrees ± 0.25 degrees from the reference jet. The alignment point on each jet will be the geometrical center of the jet nozzle.

The geometrical centerline through the jet nozzle shall be perpendicular to the spin axis of the spacecraft, and intersect it at a position defined as the c.g. position for the condition of a burned-out apogee motor, within an angle of ± 0.25 degree.

The axial jets provide spin-speed control, as well as precession torques. The jet rotates under the influence of centrifugal force about an axis nominally 45 degrees to a spacecraft radius. Scribed lines on the base of the jet, indicating the center of the rotational axis, should be aligned 45 ± 0.5 degrees to a spacecraft radius. The base should be within 0.50 degree of being perpendicular to the spacecraft spin axis.

Sun Sensors. Four sets of four sun sensor assemblies are mounted around the periphery of the spacecraft. They will nominally be 90 degrees apart.

The sun sensor assemblies will be placed around the circumference of the spacecraft at 45, 135, 225, and 315 degrees ± 0.25 degree, relative to the reference radial jet. The outer ψ sensor in the assembly of four sensors will be used for aligning.

The sensing plane and leading edge of the reference ψ sun sensor shall be parallel to the spin axis within ± 0.50 degree. The sensing plane shall lie within ± 0.25 degree of a radial line of the spacecraft.

Dynamics Analysis: Spacecraft, Spin Rate Control Interaction

An analysis was performed to determine both the effects of movements of the spin-speed control mechanism on spacecraft stability, and the effects of spacecraft motions on the stability of the spin control mechanism. The coordinate system used in the analysis is illustrated in Figure 6-122.

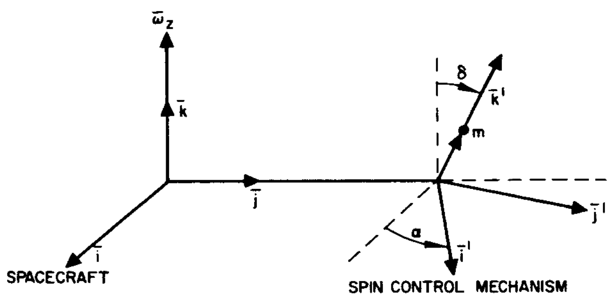

FIGURE 6-122. COORDINATE SYSTEMS INTERACTION STUDY

DEFINITION OF VARIABLES

i, j, k	Unit vectors of spacecraft coordinate system; vector k lies along positive spin axis.
i′, j′, k′	Unit vectors along principal axes of spin-speed control mechanism; vector k lies in plane of symmetry through axial jet thrust axis; vector i is rotational axis of mechanism.
ℓ	Distance between spacecraft and spin control mechanism centers of gravity.
ρ	Distance from mechanism rotational axis to center of gravity of mechanism.
δ	Angle between k and h′.
α	Angle of rotation of mechanism rotational axis relative to normal line drawn from spacecraft radial line (in Figure 6-122) α is measured from vector i).
I, I_z	Principal moments of inertia of the spacecraft $I = I_x = I_y$.
I, I_z'	Principal moments of inertia of the spin control mechanism, $I = I_x' = I_y'$.
m	Jet mass.
T	Jet thrust.
—	Bar over letter signifies that it represents a vector.
H	Angular momentum.

SYSTEM EQUATIONS

Under the assumption that the spacecraft angular velocity component in the i, j plane is negligible compared to the spin velocity w_z, the i′ component of the angular momentum derivative for the spin control mechanism, for small δ, is,

$$-(I + m\alpha^2 + m\alpha\ell\cos\alpha)\ \delta - m\rho\ell\cos\alpha\delta^2$$
$$-[w_z^2(I_z' - I) - m\rho^2 w_z^2]\ \delta$$
$$+ m\rho\ell(-w_z\sin\alpha + w_z^2\cos\alpha) = H \cdot i' \qquad (6\text{-}1)$$

The restoring torques are due to a spring and viscous damper,

$$H \cdot i' = K(\delta - \delta_B) + D\delta \qquad (6\text{-}2)$$

where δ_B is the bias, or zero torque, position of the spring. Then, the dynamic response of the mechanism is of the form

$$-(I + m\rho^2 + m\rho\ell\delta\cos\alpha)\ \delta - (D + m\rho\ell\delta\cos\alpha)\ \delta$$
$$-[K + w_z^2(I_{z'} - I) - m\rho^2 w_z^2]\ \delta + K\,\delta_B$$
$$+ m\rho\ell(-w_z\sin\alpha + w_z^2\cos\alpha) = 0 \qquad (6\text{-}3)$$

The roll torque exerted by the axial jet on the vehicle is

$$L_{roll} = -T\ell\sin\alpha\,\delta \qquad (6\text{-}4)$$

Under ideal steady-state conditions, the roll torque output of the axial jet is zero when the vehicle spin speed w_z is at its design value w_z. Thus from Equation 6-3,

$$\alpha_B = -\frac{m\rho\ell w_z^2\cos\alpha}{K} \qquad (6\text{-}5)$$

is derived as the desired bias position of the spring.

Since the center-of-gravity displacements and moments of inertia of the spacecraft are negligibly affected by δ, the spacecraft roll equation of motion is simply,

$$I_z w_z = L_D + L_{roll} = L_D - T\ell\cos\alpha\,\delta \qquad (6\text{-}6)$$

where L_D represents the disturbance torques arising from thrust misalignment of the axial and radial jets.

The roll-rate control system stability near steady state is studied by considering Equations 6-3 and 6-6. The following definitions and assumptions are required:

$$w_z = w_z + r;\ w_z = r$$
$$w_z^2 = w_z^2 + 2r\,w_z$$
$$m\rho\,\ell\cos\alpha\delta << I + m\rho^2$$
$$p\,\delta < \ell c\alpha$$

where r is the perturbed roll rate.

Equation 3-3 becomes

$$(I + m\rho^2)\ \ddot{\delta} + D\dot{\delta}$$
$$+ [K + w_z^2\ (I_{z'} - I)\ - m\rho^2\ w_z^2]\ \delta$$
$$+ m\rho\ell \sin\alpha\, \ddot{r}\ - m\rho\ell w_z \cos\alpha\, \dot{r} = 0 \qquad (6\text{-}7)$$

The thrust of the axial jet is either at the constant value T or zero. When the trust is non-zero, from Equation 3-6

$$\delta = \frac{L_D - I_z\dot{r}}{T\ell \sin\alpha} \qquad (6\text{-}8)$$

and from Equation 6-7

$$(I + m\rho^2)\ I_z\dddot{r} + DI_z\ddot{r}$$
$$+ \{I_z\ [k + w_z^2\ (I_z' - I)\ - m\rho^2 w_z^2]$$
$$- m\rho\ell^2 T \sin^2\alpha\}\ \dot{r} + 2m\rho\ell^2 T w_z \cos\alpha \sin\alpha\ r$$
$$= L_D\ [K + w_z^2\ (I_z' - I)\ - m\rho^2 w_z^2] \qquad (6\text{-}9)$$

Thus, during thrusting periods the small perturbations from steady state are characterized by a third-order constant coefficient equation. Using Rouths' criterion for analyzing the stability of the equation it is found that spacecraft stability is ensured if

1) $K > m\rho^2 w_z^2$

2) $D\ (K - m\rho^2 w_z^2) > \dfrac{2m^2\rho^3\ell^2\ T w_z \cos\alpha \sin\alpha}{I_z}$

Design values for the parameters indicate an extremely wide stability margin. For condition 1, the margin is about 23:1. Condition 2 requires that the damping force D be only greater than 2.32×10^{-6} ft-lb sec. This corresponds to a damping coefficient ζ of 8×10^{-6}.

A disturbance torque forces the steady-state solution,

$$\delta = \frac{L_D}{T\ell \sin\alpha} \qquad (6\text{-}10)$$

$$r = \frac{L_D\ [K + w_z^2\ (I_z' - I)\ - m\rho^2 w_z^2]}{2m\rho\ell^2\ T w_z \cos\alpha \sin\alpha} \qquad (6\text{-}11)$$

Clearly, the former must be within the unrestricted range of operation of δ, whereas the latter must be a permissible value of steady-state roll error.

When $T = 0$,

$$\dot{r} = \frac{L_D}{I_z} \qquad (6\text{-}12)$$

where L_D is the roll disturbance torque of the radial jet. The solution takes the form

$$r(t) = r(0) + \frac{1}{I_z}\int_0^t$$
$$\left[L_D(t) - T(t)\ell \sin\alpha\, \delta(t)\right] dt = f(t)$$

and

$$-m\rho\ell \sin\alpha\, \ddot{r} + 2m\rho\ell w_z \cos\alpha\, \dot{r} = g(t)$$

may be regarded as a function of time. The perturbed roll system dynamical equation takes the form

$$(I + m\rho^2)\ \ddot{\delta} + D\,\dot{\delta}$$
$$+ [K + w_z^2\ (I_z' - I)\ - m\rho^2 w_z^2]\ \delta = g(t) \qquad (6\text{-}13)$$

The stability of this second-order equation is assured if the signs of the coefficients of the characteristic equation are all positive and $D \neq 0$.

This requires that

$$k > m\rho^2 w_z^2$$

The term $w_z^2\ (I_z' - I)$ is small and can be neglected. This is one of the criteria for the spacecraft stability consideration and, as indicated, the stability margin is quite high, about 23:1. When $L_D = 0$, the steady-state solution is

$$\delta = \frac{2m\rho\ell w_z \cos\alpha\, \dot{r}}{K + w_z^2\ (I_z' - I)\ - m\rho^2 w_z^2}$$

Orientation Maneuver Analysis

An IBM 7090 simulation of the vehicle attitude performance during the orientation maneuver is currently in progress. The simulation includes the spin rate control mechanism and nutation damper.

With reference to Figure 6-123, the equations of motion of the satellite are as follows:

$$\ell T(t)\ \cos\delta - T(t)\, d \sin\delta \cos 45^\circ$$
$$+ mgw_z z\ (1 - I_3/I) = I\dot{w}_x + (I_z - I)\ (w_y w_z$$
$$(6\text{-}14)$$

$$T(t)\, d \sin\delta \cos 45^\circ = I\dot{w}_y + (I - I_z)\ w_x w_y$$
$$(6\text{-}15)$$

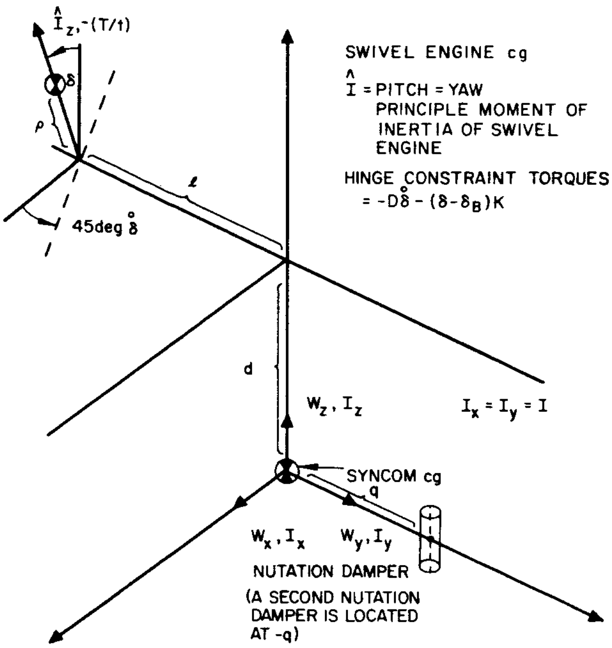

FIGURE 6-123. VARIABLES AND PARAMETERS OF SYNCOM DYNAMICS STUDY

$$T(t)\ell \sin\delta \cos 45^\circ = I w_z \tag{6-16}$$

$$z - (I - I_z/I) w_z z = w_x q - w_z w_y q \tag{6-17}$$

$$(I + m\rho^2)\,\delta + D\delta + [k + (I_z - I - m\rho^2) w_z^2]\,\delta + m\rho\ell w_z \cos\delta \cos 45^\circ - m\ell w_z^2 \rho \cos 45^\circ = k\delta_B \tag{6-18}$$

These equations have been written under the following approximations:

1) For the short-period motions of interest, the satellite center of gravity moves with constant velocity.
2) The motion of the swivel jet does not displace the satellite center of gravity.
3) The satellite and the swivel jet are both figures of revolution.

Equation 6-17, plus the coupling term mq $w_z z$ $(I - I_z/I)$ of Equation 6-15, is the model of the nutation damper. It has been derived from experimental results. Equation 6-18 is approximate, in that the effects of body nutation on the spin control mechanism have not been included. Equation 6-18 is written above to indicate the form of the more complete equation used in the simulation. The spring constant, K, of Equation 6-17, has been made nonlinear to represent the effects

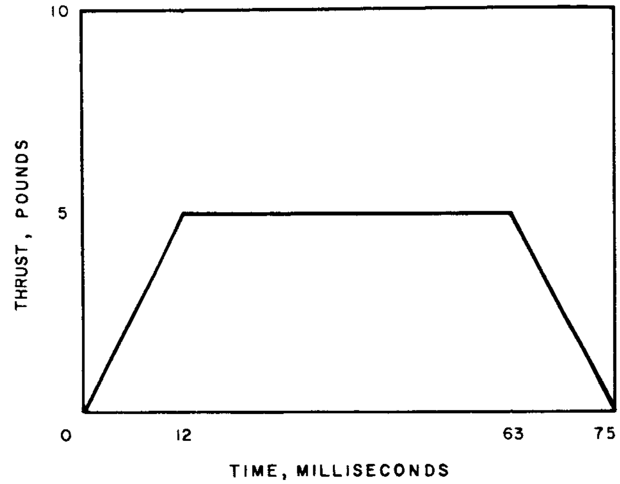

FIGURE 6-124. ENGINE THRUST PULSE

of the spin rate control mechanism stops. The thrust pulse $T(\epsilon)$ used in the simulation is shown in Figure 6-124, and is a straight-line approximation to that actually present.

Dynamic performance, fuel consumption, and attitude trajectory accuracy are the principal simulation outputs.

Bipropellant Reaction Control System

Following a competition among seven bidders for development of the reaction control system, the subcontract was awarded to the Marquardt Corporation. A unit of the bipropellant system under development by Marquardt is shown in Figure 6-125. The propulsion system consists of two identical units. Each unit has two oxidizer tanks, two fuel tanks, two thrust chambers, and associated valves and plumbing.

The propulsion system will provide a velocity increment of 2300 fps to a 575-pound spacecraft for velocity correction and orientation plus an additional impulse of 600 lb-sec for spin rate control. After orientation of the spacecraft and correction of injection errors, either of the two propulsion units is capable of meeting the spacecraft station-keeping and spin control requirements for a period of 5 years.

Each propulsion unit incorporates two thrust chambers, one of which has a thrust axis parallel to the spin axis of the spacecraft, and the other in a radial direction perpendicular to the spin axis. Spin control is accomplished by gimbaling the axial engine as a centrifugally actuated control! The line of thrust of the axial engine then depends on the rotational speed of the spacecraft. The axial engine can either increase or decrease spacecraft spin rate. The radial engines are buried in the spacecraft shell, and require a heat shield to prevent overheating of adjacent components. The two thrust chambers are identical in configuration and performance requirements.

Marquardt proposes monomethyl hydrazine as a fuel and nitrogen tetroxide with 15 percent nitric oxide as an oxidizer. The propellants are placed in pressurized tanks and are positioned by the centrifugal force of the rotating spacecraft. In this blowdown system the thrust chamber pressure will decay from 100 to 65 psi because of the drop in tank pressure (from 300 to 149 psi). The corresponding thrust reduction will be from 5 to $3\frac{1}{2}$ pounds.

The reaction control system will be made entirely of stainless steel from the thrust chamber injector head to the tanks to avoid dissimilar metals problems. The thrust chambers will be constructed from molybdenum which will withstand an expected chamber temperature of 2600°F. The chambers will be coated with molybdenum disilicide to prevent high-temperature oxidation.

Marquardt is currently funded to complete a unit of work which is to include:

1) Fabrication and testing of a breadboard propulsion unit.

2) A feasibility test demonstration.

3) Delivery of an engineering model (one unit).

This effort is scheduled for completion on 6 May 1963. Marquardt has made preliminary tests on the thrust chamber. Approximately 45 tests of 3-to-4 seconds duration were completed by 15 March 1963. The purpose of the tests has been primarily to check out instrumentation. Performance data have been invalidated by measurement errors. The response of the instrumentation used for monitoring pressure thrust and propellant flow rate will have to be improved, particularly before tests in the pulse mode are begun.

Marquardt is proceeding with a fabrication procurement test of components for the breadboard unit and engineering model. A description of the major components of the system follows.

Each of the two thrust chambers provided in each control unit will be both functionally and dimensionally identical. The radial engine, shown in Figure 6-126, requires a heat shield to prevent overheating of spacecraft components. The rocket engine consists of a thrust chamber, injector head, and two propellant control solenoid valves. The thrust chamber will be made of molybdenum and will be coated with molybdenum disilicide to prevent high-temperature oxidation. The thrust chambers will produce 5 pounds vacuum thrust at a chamber pressure of 100 psi and an expansion ratio of 40:1.

The injector head provides the mounting surface for the thrust chamber, solenoid valves, heat shield (radial engine only), and assembly mounting to the spacecraft. The injector configuration is a single doublet with a fixed orifice design. The injector head, and all upstream components, are made of stainless steel to minimize potential galvanic corrosion problems, during the expected 5-year life of the system. The joint between the thrust chamber and the injector head is made pressure-tight with a stainless steel "K" seal. Cooling of the injector head is provided by circulation of propellants through annuli close to the "K" seal joint.

Each rocket engine will incorporate two propellant control solenoid valves (Figure 6-127), one for oxidizer injection control and one for fuel injection control. The two propellant valves, which are identical, are of a poppet type with a conical seat of teflon and metal. The design of this type of seat has been proven in Apollo and Advent programs at Marquardt. The propellant valves contain a 5-micron filter and also a flow calibration orifice, which is used to compensate for variations in manufacturing tolerances.

The eight propellant tanks of the system will employ either a trunnion or spherical cap mount design, which permits expansion of the tank under pressurization loads. The tank design is shown in Figure 6-128. The tank material is to be 17-7 PH. An ultimate tensile strength of 160,000 psi minimum with a burst factor of two was used in the design.

Stainless steel lines will be used throughout the system for propellant supply and pressurant charging. Fill and drain valves (Figure 6-129), will be provided at the bottom of each tank. The same valve design will be used for both the fill and vent valves. Fitting sizes are selected for noninterchangeability between the fuel

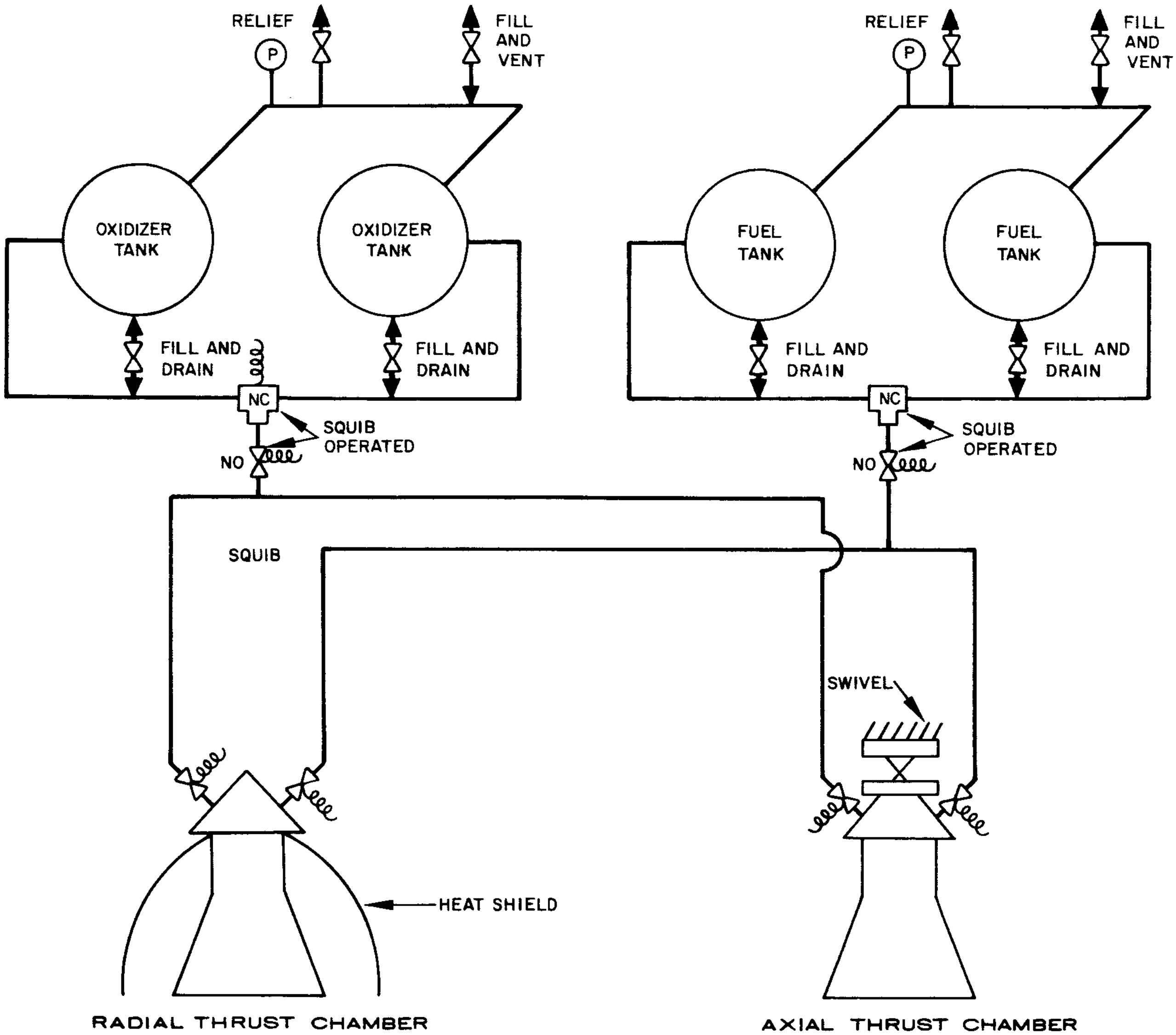

FIGURE 6-125. SYNCOM II REACTION CONTROL UNIT
Two units per vehicle

and oxidizer legs of the system. The basic valve design employs redundant sealing at both the GSE and valve opening exits.

A combination burst diaphragm and relief valve (Figure 6-130) will be used in each propulsion unit to provide protection against catastrophic failure due to system over-pressurization. The relief valve is used to prevent total loss of pressurization, when the burst diaphragm fails. The burst diaphragm will have a burst pressure range of 350-385 psig. The relief valve will have a cracking pressure of 350 psig for a rated flow of 0.10 lb/sec of nitrogen and a reseat pressure of 325 psig. The burst diaphragm is welded in place to assure zero leakage. A filter, located between the burst diaphragm and the relief valve, will trap burst diaphragm fragments which might contribute to relief valve leakage or malfunction.

Explosive valves are shown in Figures 6-131a and 6-131b. The dual-bridge squib incorporates two independent electrical circuits, either of which is sufficient

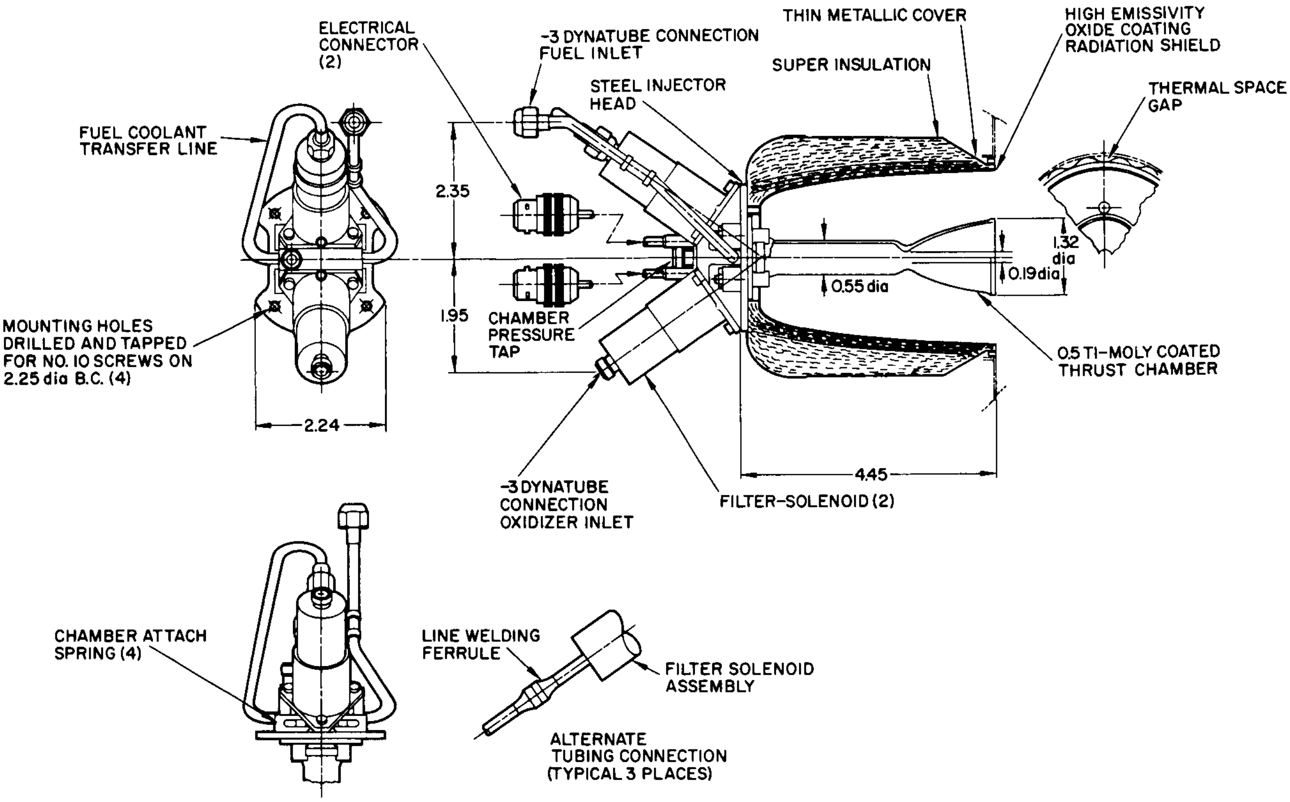

FIGURE 6-126. RADIAL THRUST CHAMBER

to ignite the primer charge. Detonation of the primer charge releases high-pressure combustion gases to accelerate the ram. On the normally closed valve (Figure 6-130, this energy is sufficient to sever the two hemispherical diaphragms on the propellant tank inlets and to form a leak-tight seal at the tapered portion of the ram. The severed pieces of the diaphragms are trapped below the cutter, out of the propellant flow path. On the normally open valve, the tapered ram is similarly driven home, producing a leak-tight seal across the valve. In system operation (see Figure 6-124) the normally closed valve will not be activated until just before the reaction control unit is required for service. The normally open valve is then used to shut off the system should leakage occur at the propellant valves.

MARQUARDT AXIAL ENGINE SWIVAL MECHANISM

The Marquardt Corporation is designing a swival mechanism, illustrated in Figure 6-132 for the axial engine. The Hughes and Marquardt designs are fundamentally similar in that both are spring-biased, flexure-pivoted, viscous-damped, and pinned (during launch). Present planning calls for testing of both configurations with a selection of either based on test results.

The torsion bar type of spring is lightweight and requires less space than does the coil-type spring. In addition, this method allows for transmittal of propellant through the bars without the tendancy of stress loading the line at the solenoid and spacecraft interfaces. One end of each torsion bar (one oxidizer, one fuel) is fixed relative to the rotating portion of the mechanism while the other end of each bar is fixed relative to the base plate (hence, the spacecraft).

The rotating portion of the mechanism is supported by two tubes each of which is bent in a single plane. This method of support is characteristically lightweight, rigid, and easily welded. The explosive pin-pullers (two are used for greater rigidity during launch

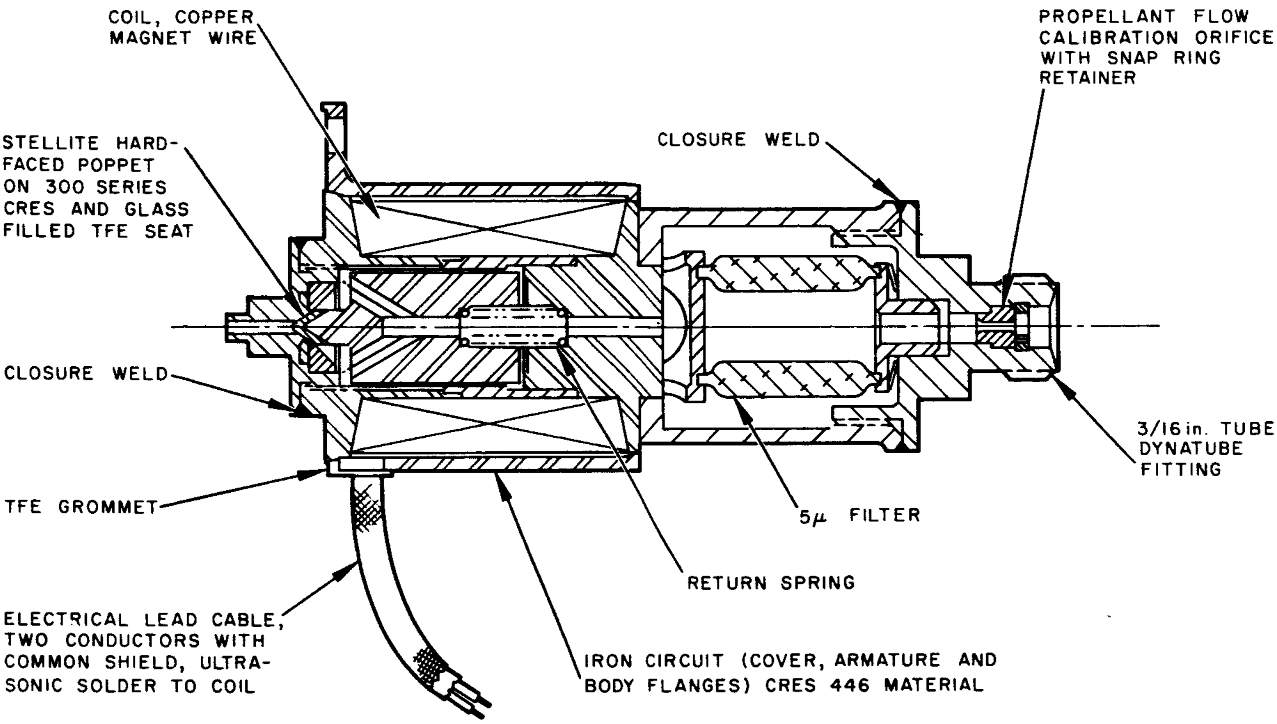

FIGURE 6-127. PROPELLANT VALVE

and spinup) are supported by two stationary rib-type structures. These structures provide the stops for the rotating portion.

Standard Bendix flexure pivots are used. The flexure springs are either welded or brazed in a sectioned, hollow cylindrical housing, the appropriate sections of which are pinned to the rotating and stationary portions of the mechanism.

Marquardt Corporation is considering either a hydraulic or a pneumatic viscous damper consisting of two bellows interconnected by an orifice plate. The pneumatic design offers the advantage of an absolute fluid state in the bellows while the hydraulic fluid design may become contaminated with gas bubbles during fabrication and loading. The hydraulic design, however, offers less severe sealing problems.

Spin Rate Control

Possible variations in the Syncom II Spacecraft spin rate, due largely to jet misalignment torques, have established the requirement for spin rate control. In response to this requirement, three alternative methods of producing corrective torques on the spacecraft were considered, all involving control of jet thrust vector to produce a tangential impulse. The three methods are: are:

1) Fixed jet plus jet vanes (Figure 6-133)
2) Dual fixed jets (Figure 6-134)
3) Gimbaled jet (Figure 6-135)

The gimbaled jet method of spin rate control was selected for Syncom II. This control provides a tangential thrust component proportional to spin rate variation from nominal in a manner analogous to that of a centrifugal governor. Mechanization of the concept involves flexure pivots, torsion spring, motion damper, boost phase locking device, and a propellant transfer method.

Studies of the gimbaled jet motion relative to the spacecraft showed the importance of damping for stable operation. Three dampers were evaluated:

1) Eddy current
2) Dry friction
3) Viscous friction

with a viscous friction type being selected.

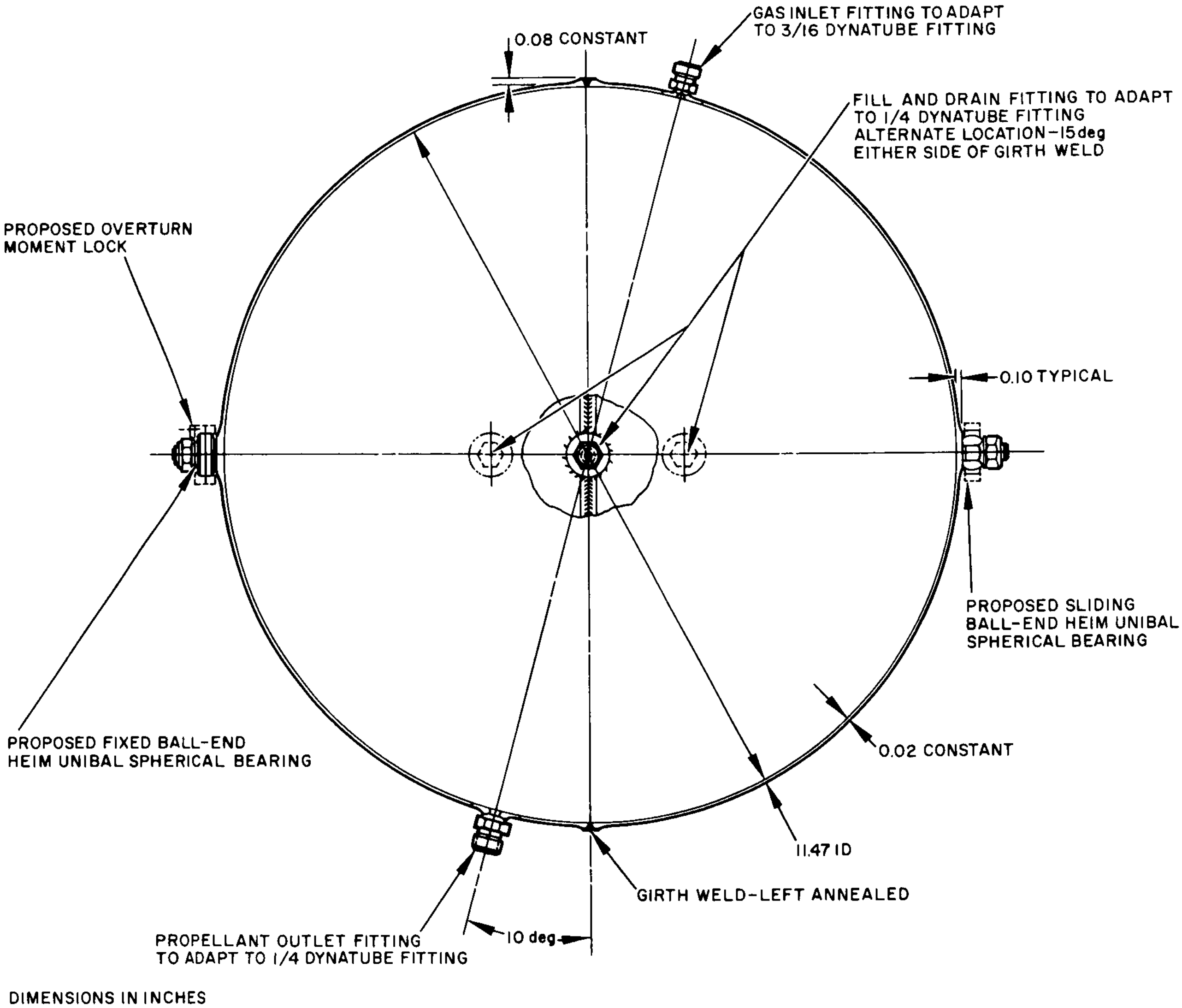

FIGURE 6-128. PROPELLANT TANK

To further analyze gimbaled jet development problems in terms of a feasible mechanism, an engineering model was designed and fabricated (Figure 6-133 and 6-136). The test program for this model, including transient performance, centrifuge, and vibration tests (both mounted on T-1 and directly on a shaker) is in progress, with partial results reported here, and further results will appear in a Summary Report Supplement.

CONCEPT EVALUATION

Fixed Jet plus Jet Vanes. The characteristic feature of the fixed jet plus jet vanes method of spin rate control method is centrifugally operated jet vanes. In Figure 6-133, an end view of the control, one of the vane mechanisms, is shown in both the extended and retracted positions. By proper selection of the spring gradient a hysteretic drive is possible (Figure 6-137), which allows the vane to be retracted fully from the vicinity of the jet plume for more than half the operating time of the jet. This, with the slicing action of the vane into the jet plume, tends to keep vane vibration to a minimum. As in the gimbaled jet mechanism, described below, rotating bearings are replaced by

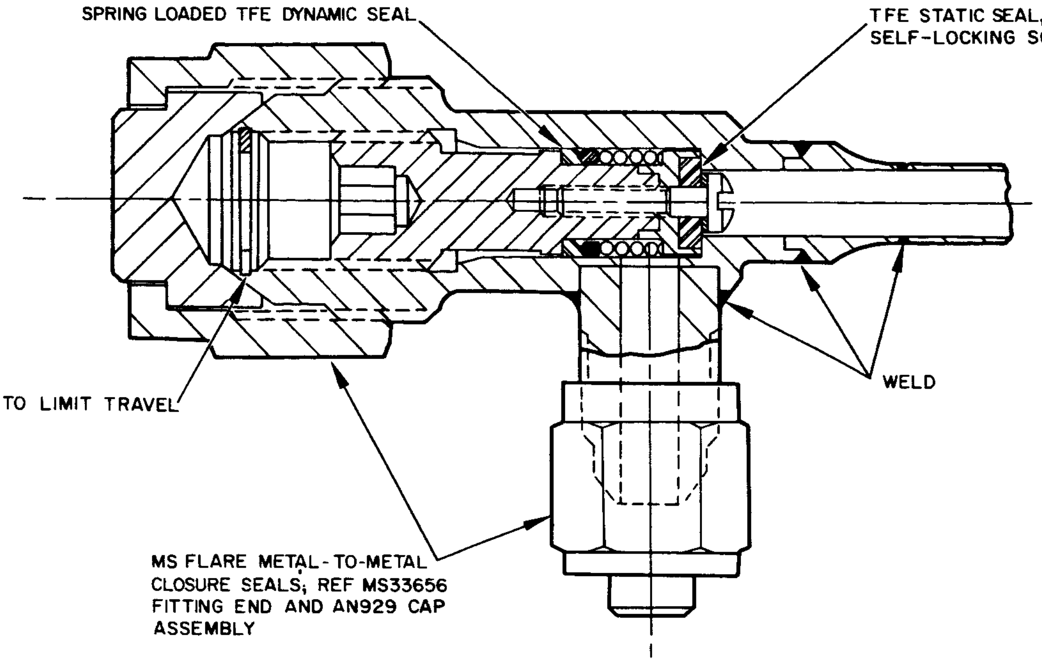

FIGURE 6-129. FILL AND DRAIN AND FILL AND PURGE VALVES

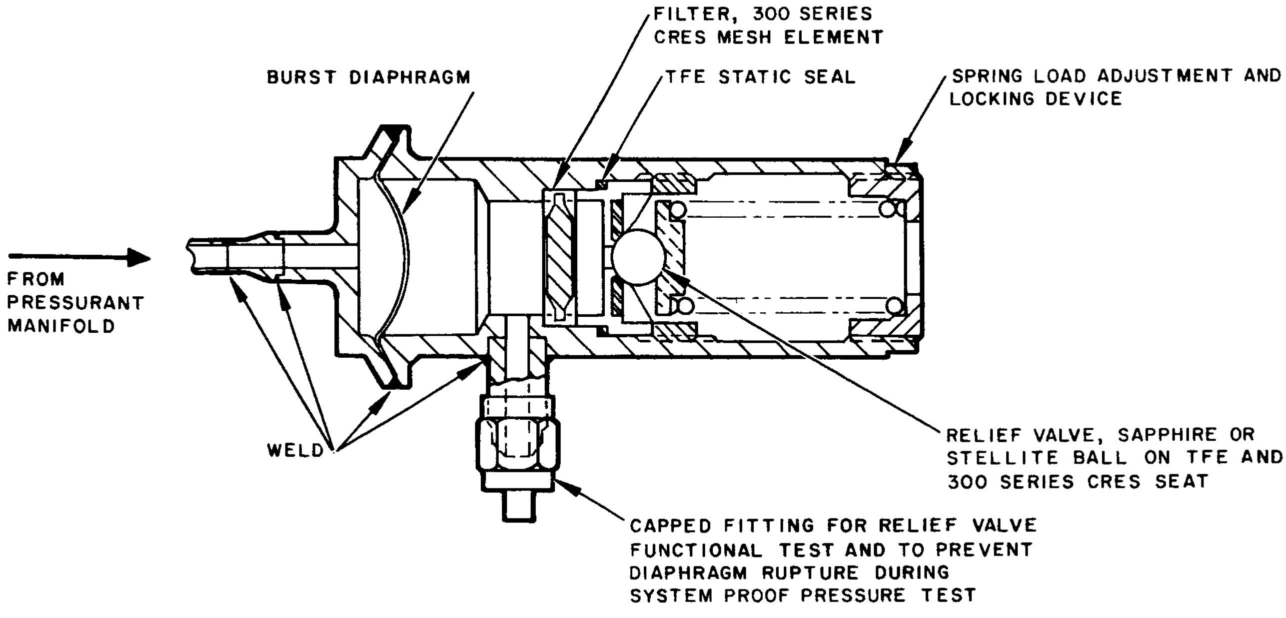

FIGURE 6-130. RELIEF VALVE

flexure pivots to eliminate the possibility of cold welding in a vacuum.

Dual Fixed Jets. The dual fixed jet method of spin rate control is shown schematically in Figure 6-134. The jets are placed in fixed angular positions such that one jet provides an accelerating torque and the other a retarding torque. For bipropellant jets, two sets of propellant valves (oxidizer and fuel) are

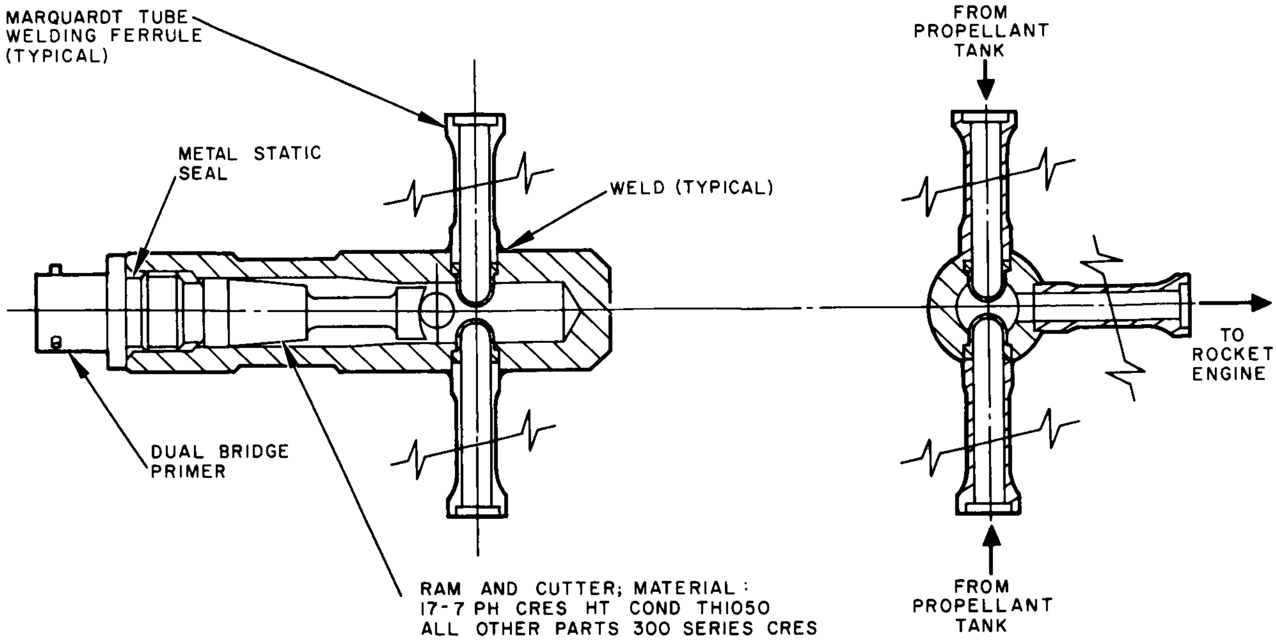

a) Normally closed

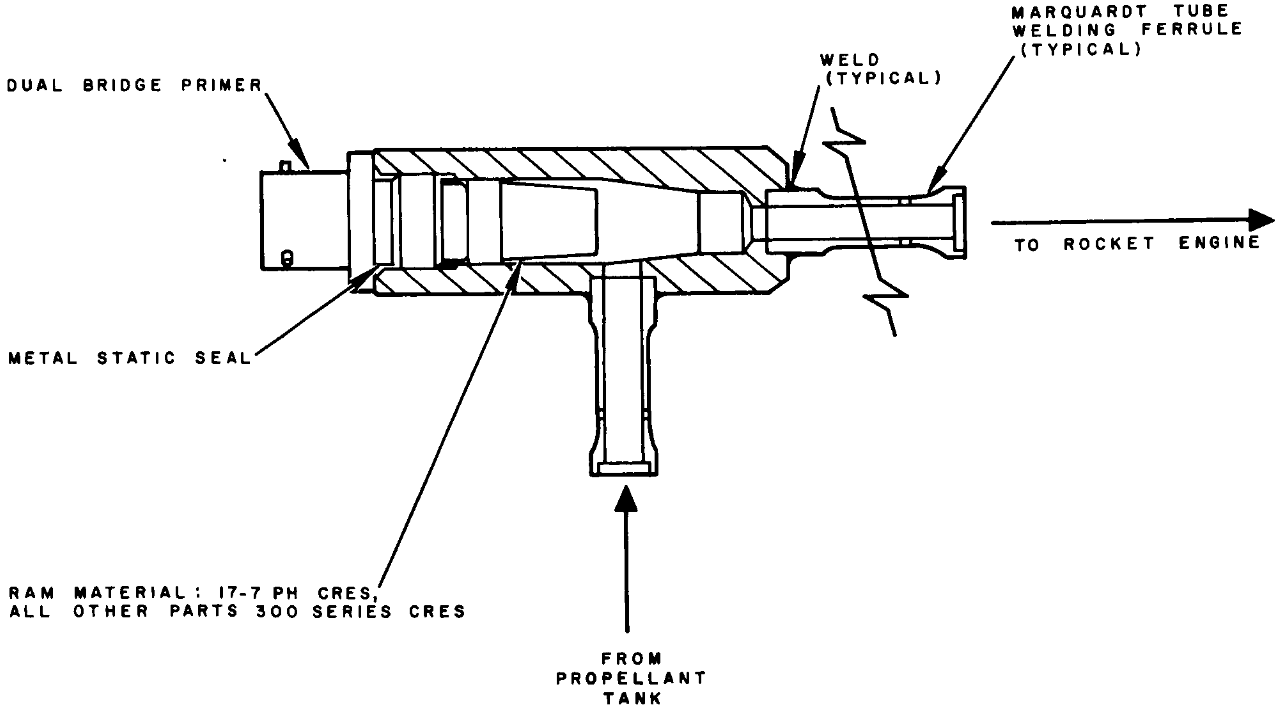

b) Normally opened

FIGURE 6-131. EXPLOSIVE VALVE

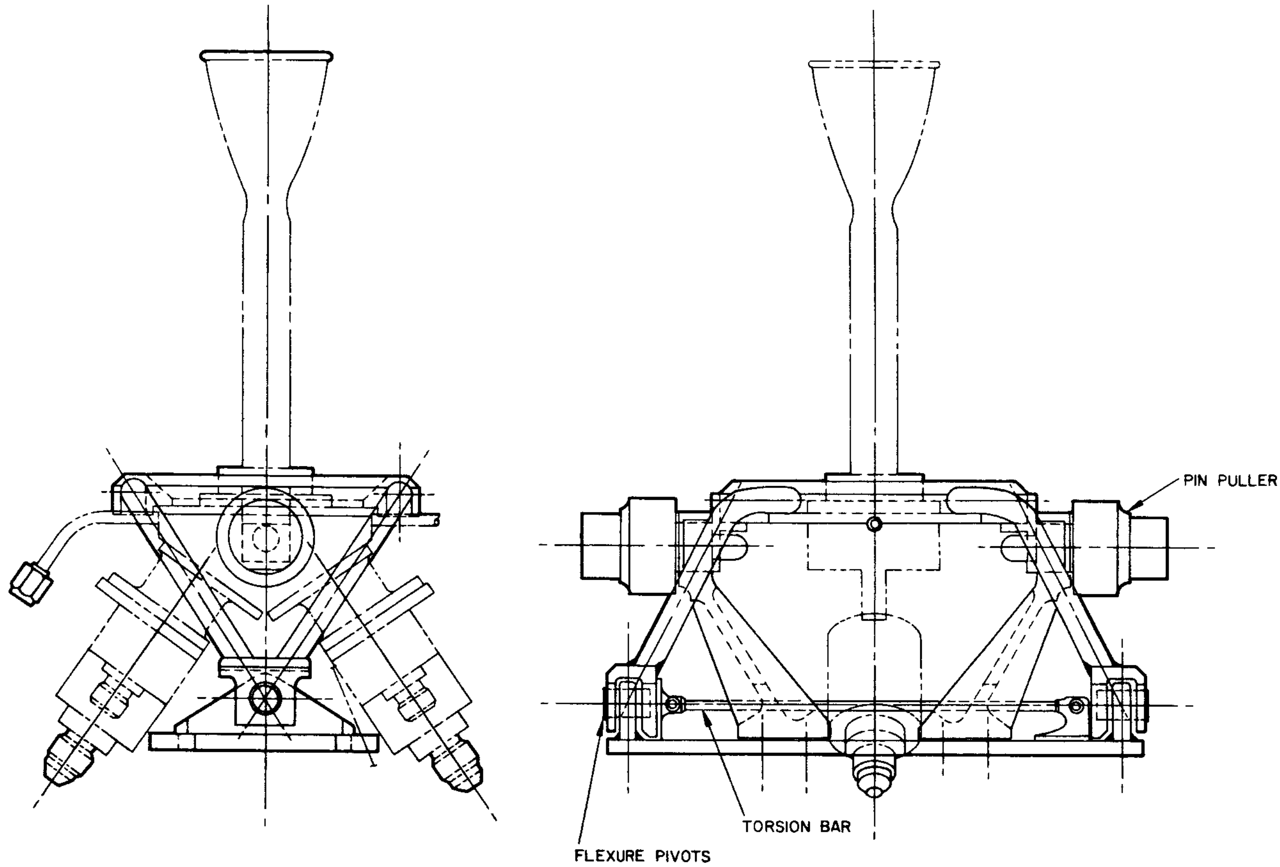

FIGURE 6-132. TORSION BAR SWIVEL MECHANISM

required. In operation the jets would be actuated by a "g" switch or similar scheme.

Gimbaled Jet. The gimbaled jet spin rate control utilizes flexure pivot mounts, flexible propellant lines, torsion spring, and motion damper (Figures 6-135 and 6-136). In operation, a corrective torque proportional to spin rate error is produced, up to a maximum limit equivalent to 10 percent of jet thrust.

Two features of the gimbaled jet of particular interest are: 1) The centrifugal force available to position the jet, and the desired corrective thrust direction are 90 degrees out of phase, and 2) jet thrust misalignment relative to the gimbal axis produces a disturbing torque to the mechanism each time the jet is fired.

As the centrifugal force and desired jet rotation are 90 degrees out of phase, a method of converting radial force to tangential force is needed. A mass and linkage arrangement could be used, or the jet gimbal axis could be canted at an appropriate angle to a spacecraft radius. The latter method was chosen as providing an inherently simpler, lighter, and more reliable device.

The main effect of canting the gimbal axis is to increase the impulse requirement for spin rate control. If it were feasible to place the gimbal axis collinear with a spacecraft radius, a rotation of ±5.7 degrees would provide the desired 10 percent tangential thrust. In this case, the additional impulse to provide spin rate correction would amount to 0.5 percent of the total control impulse required over the service life of the spacecraft (i.e., of the total orientation and velocity control requirements). A 45-degree cant angle requires that the jet be rotated ±8.1 degrees. An additional 1.0 percent impulse is required. Considering both the desire for maximum utilization of the available centrifugal force and minimization of the impulse required, the 45-degree cant angle appears optimum (see

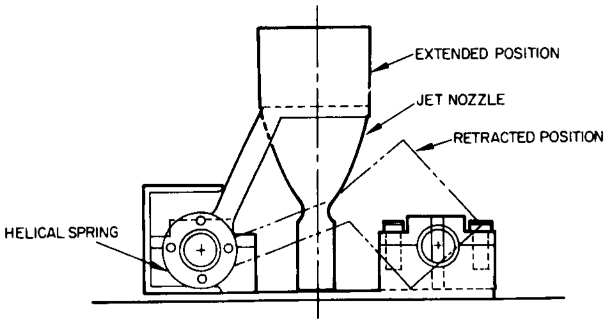

FIGURE 6-133. FIXED JET PLUS JET VANES

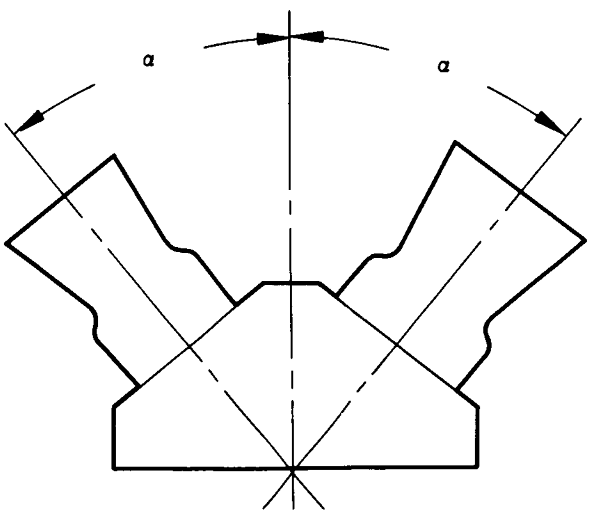

FIGURE 6-134. DUAL FIXED JETS

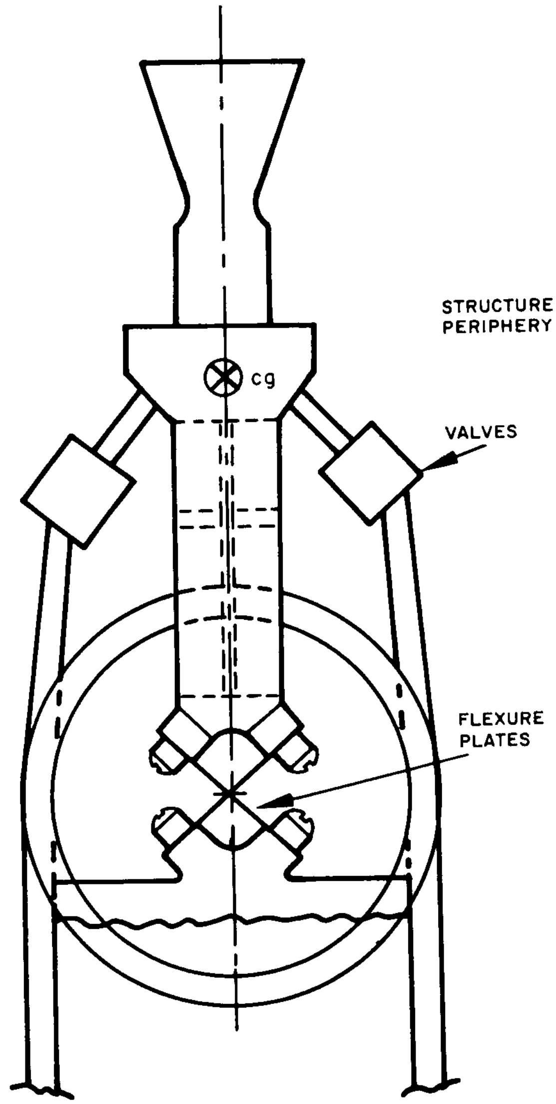

FIGURE 6-135. GIMBALED JET

subsequent discussions for analysis of this point). Figure 6-138 illustrates the effect of cant angle on the additional impulse required for spin rate correction and on the thrust component parallel to the jet axis.

Unavoidable jet thrust misalignment of the gimbaled jet is an important feature of this mechanism since the motion damping inherent in the flexure pivot is small and a definite possibility of resonance excitation exists. This problem generates the requirement for a motion damper attached to the mechanism.

More detailed analysis of jet oscillations shows that a series of pulses, properly phased, can produce corrective torques other than those corresponding to the mean position of the oscillating mechanism, thus potentially increasing the impulse required for spin rate control. Since this effect increases with amplitude, it was assumed in the design that an oscillation amplitude due to misalignment torques would be kept to within 1 degree.

SPIN RATE CONTROL SELECTION

In addition to the features of the three candidate spin rate controls discussed above, the factors in Table 6-14 were considered in making a concept selection

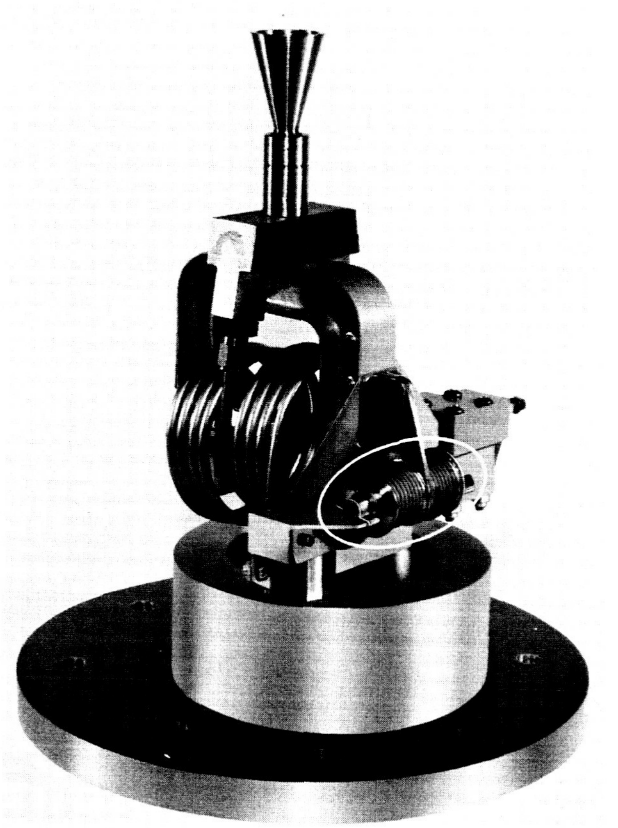

FIGURE 6-136. MODEL OF GIMBALED JET ASSEMBLY

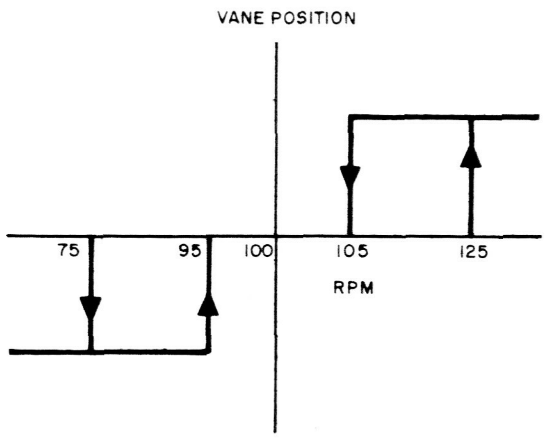

FIGURE 6-137. JET VANE SPIN RATE CONTROL CHARACTERISTICS

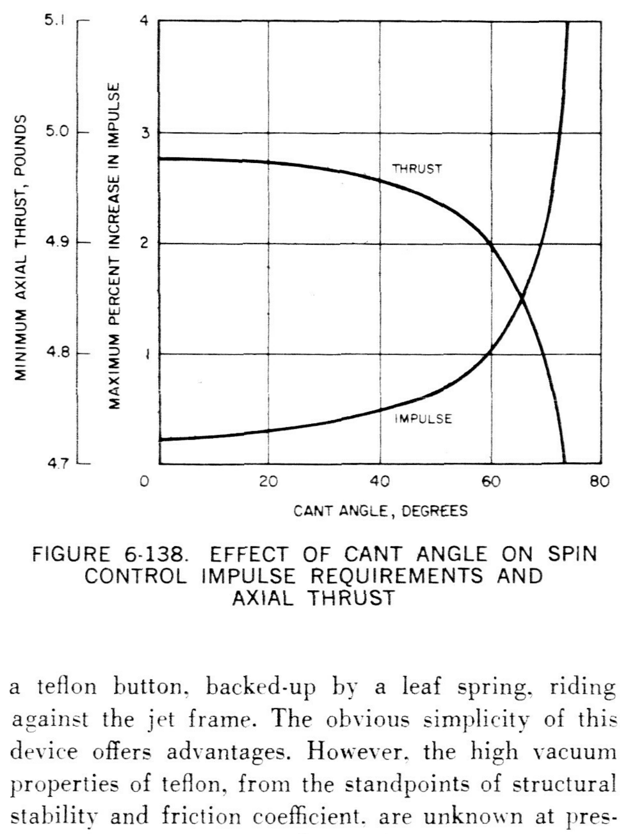

FIGURE 6-138. EFFECT OF CANT ANGLE ON SPIN CONTROL IMPULSE REQUIREMENTS AND AXIAL THRUST

for detailed feasibility studies. (Those factors in the table not rated were assumed generally equivalent for the three controls.) A summary of the ratings (assuming unity weight for the factors) shows the jet pulse vanes and gimbaled jet to be more desirable concepts than the dual jets.

The final selection of the gimbaled jet was based on a combination of the above analysis and an evaluation of certain immeasurable factors (such the equality of applicability of simply stated factors to each of several relatively complicated systems).

DAMPER SELECTION

Three damper concepts were evaluated: 1) eddy current, 2) dry friction, and 3) viscous friction. The evaluation of these candidates is summarized in Table 6-15.

Specific mechanizations were worked out for the two friction dampers. The dry friction design features a teflon button, backed-up by a leaf spring, riding against the jet frame. The obvious simplicity of this device offers advantages. However, the high vacuum properties of teflon, from the standpoints of structural stability and friction coefficient, are unknown at present. Since teflon is the subject of many space experiments, further consideration can be given to this type of damper when additional data is available.

A viscous damper with a bellows configuration appears to offer the most direct solution as it combines the required damping with reliability and low weight.

TABLE 6-14. EVALUATION—SPIN RATE CONTROL CONCEPTS*

Factors	Jet plus Vanes	Dual Jets	Gimbaled Jet
Weight	1	3	2
Sliding contact	3	1	2
Flexible propellant lines required	1	1	2
Complexity of test program	2	1	1
Applicable experience	3	2	1
Dynamical stability	1	1	2
Reliability	1	2	1
Positive actuation	2	3	1
Failure mode	1	2	3
Complexity	1	3	2
Vibration	2	1	2
ΔV required	2	3	1
Size			
Materials			
Heat transfer			
Critical tolerances			
Summary	20	23	20

*In the above ratings, 1 is high and 3 is low.

TABLE 6-15. EVALUATION—DAMPER CONCEPTS*

Factors	Eddy Current	Dry Friction	Viscous Friction	Notes
Size	(0)	(+)	(+)	
Weight	(0)	(+)	(+)	
Materials	(+)	(0)	(+)	
Sliding contact	(+)	(0)	(+)	
Complexity	(2)	(1)	(3)	
Reliability	(1)	(3)	(2)	
Critical design	(2)	(1)	(2)	
Basic data	(+)	(0)	(+)	Teflon Performance in space environments
Applicable experience	(2)	(3)	(1)	

*Some items are rated (+) satisfactory or (0) unsatisfactory; and some are rated in order of desirability (1, 2, or 3 — with high rating = 1).

Table 6-15 summarizes considerations of the above three damper configurations. The device, shown schematically in Figure 6-139, consists of two bellows mounted on the spacecraft structure and joined by a plate attached to the frame of the gimbaled jet. Motion of the jet forces fluid (silicone) through an orifice in the plate from one bellows to the other.

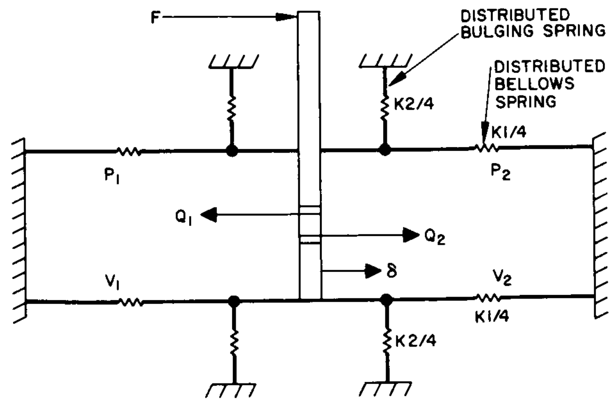

FIGURE 6-139. SCHEMATIC OF VISCOUS DAMPER

GIMBALED JET DETAILED DESIGN

Cant Angle Optimization. Since the actuating centrifugal force and the desired tangential thrust are 90 degrees apart, it is necessary to cant the gimbal axis with respect to a radial line. By equating the tangential thrust component to centrifugal force as a function of cant angle, it is shown that the optimum cant angle is 45 degrees.

Consider Figure 6-140:

$$K\theta = (F \sin \alpha)\,\ell \text{ or } \theta = \frac{F\ell}{K} \sin \alpha$$

$$\text{For } \alpha = 0^\circ \quad P_T = P \sin \theta$$

$$\text{For other } \alpha \quad P_T = P \sin \theta \cos \alpha$$

$$\text{For small } \theta \quad \sin \theta \approx \theta$$

$$\text{So } P_T = P\theta \cos \alpha \text{ or } \theta = \frac{P_T}{P \cos \alpha}$$

Equating the two expressions for θ:

$$P_T = \frac{PF\ell}{K} \sin \alpha \cos \alpha = \frac{PF\ell}{2K} \sin 2\alpha$$

Differentiating and setting the derivative = 0:

$$\frac{dP_T}{d\alpha} = \frac{PF\ell}{K} \cos 2\alpha = 0$$

Whence $\alpha = 45$ degrees for best relationship between tangential thrust production and centrifugal action on jet. Having determined the required cant angle and noting that the maximum tangential thrust to be allowed is 10 percent of the jet axial thrust, the limit angle of travel is readily established as $\theta_{max} = 8$ degrees, 8 minutes, that is,

$$\frac{(P_T)_{max}}{P} = \theta_{max} \cos \alpha = 0.1$$

so that $\theta_{max} = 8$ degrees, 8 minutes.

JET MISALIGNMENT DYNAMICS

Since the gimbaled jet will behave nominally with second-order dynamics, the possibility of resonance excitation was considered. If the natural frequency of the mechanism is close to a multiple or submultiple of the spin speed, the inherent small jet misalignment torque could excite an amplitude oscillation of the jet by causing enforcement of the oscillation with each jet pulse. This would result in a loss of spin-rate control as well as the possibility of incurring damage to the jet by forceful contact with the ±8 degrees travel stop.

One optimum method of avoiding this oscillation buildup with the rotating jet is to tune the response of the mechanism in such a way that each disturbance torque causes an oscillation in a reverse phase to the previous disturbance oscillation, thus causing exact cancellation of the oscillation every second jet pulse. This optimum relationship between the nominal spin rate period, T_s, and the desired period of the mechanism, Tm, is

$$\frac{Tm}{T_s} = \frac{1}{n + \frac{1}{2}}$$

where n is any integer 0, 1, 2. . . . A reasonable size for the mechanism restricts n to about 3. Thus, for a nominal spin rate period of 0.6 second the period of the mechanism is 0.171 second, or the natural frequency is 5.83 cps. A change in n to 2.5 or 3.5 would cause phase re-enforcement of the oscillation and instability of the mechanism. This corresponds to a change in the frequency ratio of only 14 percent. Investigation of tolerances in machining the propellant tubing (which comprises the restraining spring for the mechanism) and deviation in the spin rate from nominal (caused primarily by biasing of the jet from a position parallel to the spin axis and initial Agena spin-up error) indicates that the variation in the frequency ratio from the ideal could be as much as 14 percent. Therefore, design of the rotating jet was made assuming that the worst case of amplitude re-enforcement prevails.

The effect of jet oscillations less than maximum travel is to cause a bias for the spin correction torque.

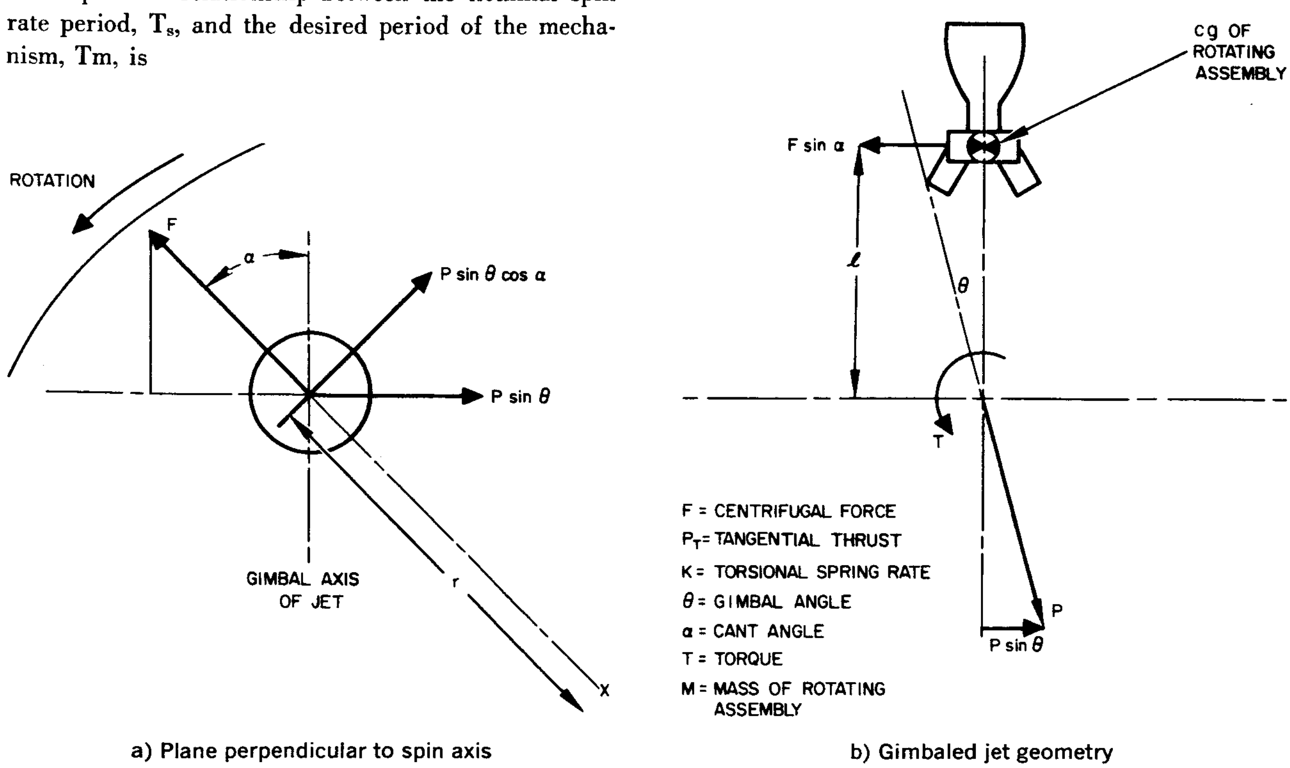

FIGURE 6-140. GIMBALED JET PARAMETERS—CANT ANGLE DETERMINATION

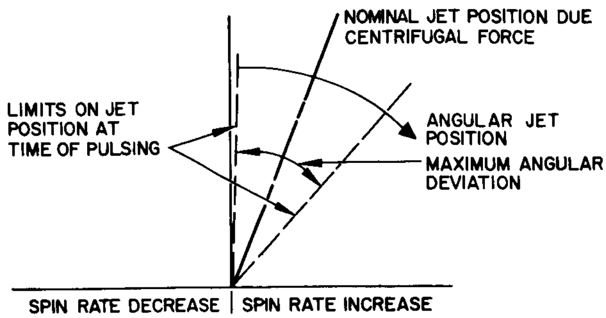

FIGURE 6-141. EFFECT OF JET OSCILLATIONS OF BIAS

The largest bias would result for the case of oscillation re-enforcement when the jet on-time corresponds to the width of one-half period of the jet oscillation (see Figure 6-141). For $n = 3$ this relationship almost exactly prevails. The average value of one-half a sine wave is 0.636 of the maximum. For an amplitude oscillation of ± 1 degree, the largest bias from the nominal jet position would then be 0.636 degree. Full jet travel is 8.1 degrees; therefore, the oscillation causes a bias of $0.636/8.1. \times 100 = 7.85$ percent of the spin-speed control range. For a ± 25 rpm control range the bias corresponds to about ± 2 rpm. The bias is reduced proportionally with the reduction in the maximum permissible oscillation amplitude.

A brief analog computer study was performed to determine the nature of the jet oscillation and the damping required to restrict the maximum amplitude to 1 degree for the maximum expected misalignment torque. Figure 6-142 is the response of the undamped jet to a step input. Figure 6-142b is the jet response for the case of oscillation cancelling (mechanism frequency = 3.5 times spin rate) by consecutive thrust pulses. Figure 6-142c is the jet response for oscillation re-enforcement (mechanism frequency = 3.0 times spin rate). For the latter case, addition of damping equivalent to 0.1 of critical limits the amplitude to 1 degree, as seen in Figure 6-142d. A check was made of this conclusion with a Fourier analysis of the disturbing torque and the response of a second-order system to the pertinent harmonics, which were 1.67, 3.34, and 5.01 cps.

TORSION SPRING DESIGN

The necessity for flexible propellant line connections, plus a torsion spring, led to the proposal for use of the propellant tubing formed into coils to serve both needs at once. (Surveyor experience shows this to be effective for flexible propellant transfer ducts.)

Referring to Figure 6-140 and formulating torque equations:

$$T = (F \sin \alpha)\ (\ell \cos \theta)$$

$$= [M(r + \ell \sin \theta \sin \alpha)\omega^2] \sin \alpha\ (\ell \cos \theta)$$

If 2θ can be assumed small, then replace $\sin 2\theta$ by 2θ and

$$T = Mr\,\omega^2 \ell \sin \alpha\ (\cos \theta + \frac{\ell\theta}{r} \sin \alpha)$$

or since

$$\cos \theta + \frac{\ell\theta}{r} \sin \alpha \approx 1$$

$$T = Mr\,\omega^2 \ell \sin \alpha = \text{centrifugal torque.}$$

This torque is equal to the spring torque, which is

$$K\theta + T_o \quad \text{so that}$$

$$K\theta + T_o = Mr\,\omega^2 \ell \sin \alpha$$

$$T_o = Mr\,\omega^2{}_o\, \ell \sin \alpha = \text{spring preload,}$$

$$\theta = 0, \omega_o = 100 \text{ rpm}$$

K (spring rate) is determined from the simultaneous requirements:

$$\theta_{max} = \pm 8°8' \text{ and}$$

$$\omega_{max} = 125 \text{ rpm}$$

$$\omega_{min} = 75 \text{ rpm}$$

Because there is a wide permissible speed range, 75 to 125 rpm, it is not necessary to provide a fine adjustment for the preload value T_o or spring rate K, thus simplifying the device.

Minimum speed can be expected to range from 75 to 85 rpm and maximum speed from 111 to 125 rpm including the effects of tolerances.

The torsional spring was mechanized by coiling the propellant tubing about a center coincident with the gimbal axis (Figure 6-143). For stress analysis purposes the coiled tubing may be assumed to be a long beam loaded by end moments. This is an efficient device from the standpoint of stress since the stress is constant with length.

Considering strain energy:

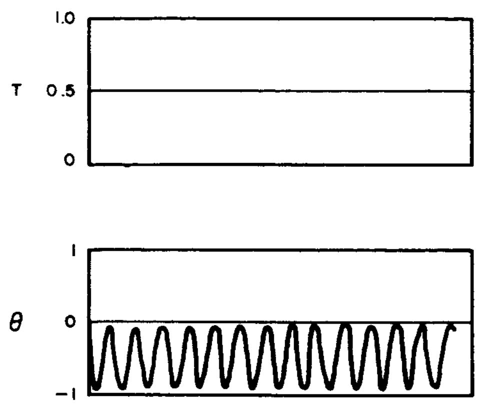

a) Step response to undamped system

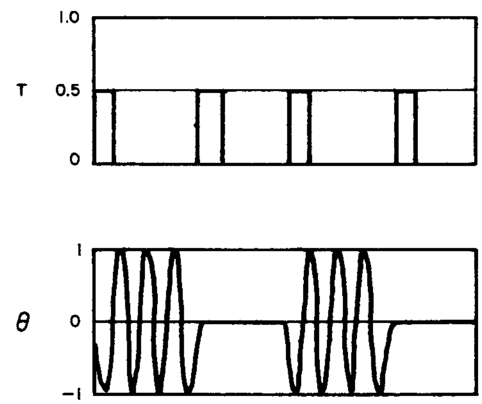

b) Pulse response of undamped system for frequency 3.5 x spin rate

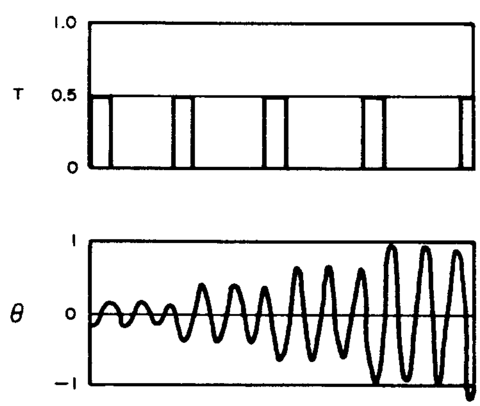

c) Pulse response of undamped system for frequency 3.0 x spin rate

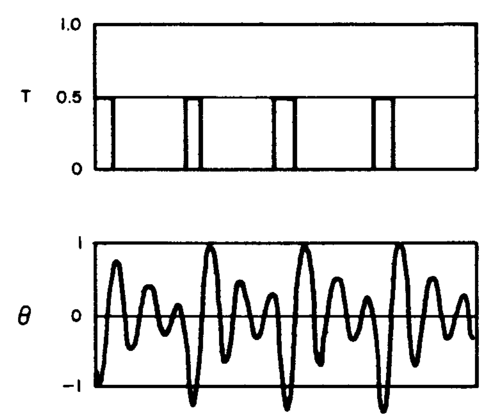

d) Same as c) with exception that damping is 0.10 of critical

T = DISTURBANCE TORQUE APPLIED TO JET, INCHES—POUNDS
θ = ANGULAR POSITION OF JET FROM NOMINAL

FIGURE 6-142. ANALOG COMPUTER RESULTS

$$U = \frac{T\phi}{2} = \frac{T^2}{2K} = \frac{T^2\ell}{2EI} = \frac{\ell I}{C^2}\,\frac{S^2}{2E} = \frac{1}{AC^2}\,V\,\frac{S^2}{2E}$$

U = strain energy
T = torque
θ = angle of bend
K = spring rate
ℓ = tube length

E = modulus of elasticity
I = moment of inertia of cross section
C = distance from the neutral axis to the outer fibre
A = cross-sectional area of metal
V = total volume of metal in tube length
d = outer diameter of tube
d_i = inner diameter of tube
S = stress

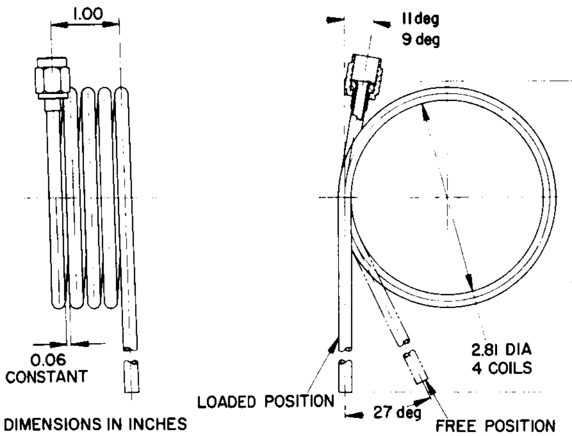

FIGURE 6-143. COILED TUBING SPRING

For the tubing cross section

$$\frac{I}{AC^2} = \frac{1}{4}\frac{\left[1-\left(\frac{d_i}{d}\right)^4\right]}{\left[1-\left(\frac{d_i}{d}\right)^2\right]}$$

Assuming

$$\frac{d_i}{d} = 0.75$$

$\frac{I}{AC^2} = 0.39$, so

$$U = 0.39\ V\frac{S^2}{2E}$$

Note that the factor 0.39 is, in effect, an efficiency factor for the shape. It is, for example, unity for a simple tension member and 0.333 for a rectangular bar loaded in the same manner as the tube.

Since the strain energy needed is fixed, the volume of the tube and therefore the weight depends on the square of the allowable stress. In selecting a tubing configuration, the cross section is based on the stress and the length is based on the spring rate desired. In this study d = 0.188 inch, with a wall thickness of 0.016 inch. The maximum bending stress selected is 50,000 psi. The material is 304 stainless steel with a minimum yield point of 60,000 psi.

Note the specific use of stainless steel. It has been assumed that all structural materials will be made compatible with the jet propellants (MMH and N_2O_4).

Since the tubing will operate under internal pressure, both the added stress due to pressure (300 psig) and the bourdon effect on bending stiffness were considered and found to have small effects on the design.

FLEXURE PIVOT DESIGN

The requirement for avoiding metal-to-metal contact under high-vacuum conditions to prevent the possibility of cold welding plus the desirable properties of rotation about a fixed center, low spring rate, while providing restraint in all directions, facilitated selection of the flexure pivot as a bearing substitute. In addition to the above desirable properties, the flexure pivot also has no play and no friction. Each pivot (see Figure 6-144) consists of a pair of spring steel bands. The two pivots are widely separated to provide moment resistance in the plane of the yoke. Note that the greatest loading occurs from moment in this plane (43 in-lb from centrifugal force and 262 in-lb from 50 g vibration).

The individual bands have a maximum column loading of 65 pounds and are calculated to withstand a critical load of 103 pounds. When bent to the maximum angle, the maximum stress is 53,000 psi, including bending and axial loading from centrifugal force. Material: Heat-treated 17-7 PH.

DAMPER DESIGN

The viscous damper design chosen consists of a hydraulic orifice plate attached to the rotating frame of the gimbaled jet which works against small quantities of silicone hydraulic oil confined by bellows (Figures 6-144 and 6-145) grounded to the fixed base of the spin rate control, forcing the oil through the orifice and hence dissipating energy.

This configuration combines the required damping with reliability and low weight.

Design problems with the damper are due primarily to temperature effects and bulging of the bellows along its diameter. Expansion of the fluid can be accommodated by insertion of a small bellows at a position exactly between the two main bellows. This bellows will not affect the response or operation of the main bellows since the pressure at the midpoint is constant.

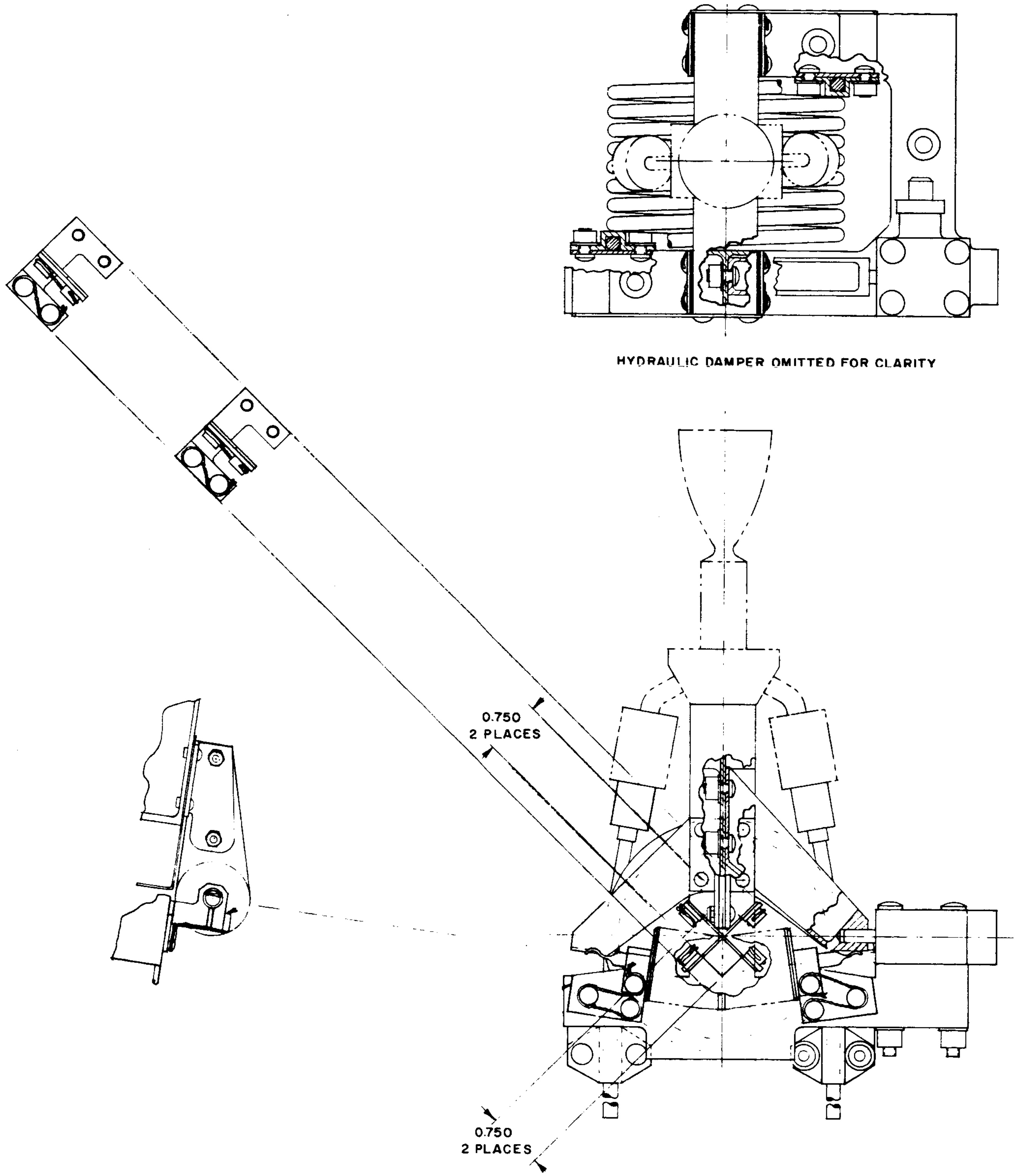

FIGURE 6-144. FLEXURE PIVOT DETAIL

Thus, it will serve only to accept the increased volume of fluid resulting from the temperature increase. The temperature environment of the damper will be from 0 to 135° F. The upper temperature is the result of a heat transfer analysis based on a conservative estimate of the maximum temperature existing at the base of the jet injection chamber (less than 200° F). The basic damping effect depends on the viscosity of the oil. Thus, the damping effect approximately doubles as the temperature varies from 135° F to 0° F.

The bulging of the bellows at the sides, an undesirable expansion, was found to affect the dynamic response of the bellows primarily in the same manner as an oil-spring. From preliminary tests, in which a single bellows was filled with water and subjected to compression, it was concluded that the effect of bulging was to contribute a spring gradient considerably weaker than the actual oil-spring gradient of the silicon fluid. The design must therefore compensate for this effect.

The following brief analysis indicates the nature of the effect of the bellows bulge (Figure 6-139). Spring K_1 is the normal spring gradient associated with the bellows. It is shown distributed as four springs for reasons of symmetry. K_2 is the spring associated with the bulging of the bellows and is also shown distributed.

The mass of the fluid in bellows 1 is

$$m_1 = \rho V_1$$

where ρ is the density of the fluid and V is the volume.

Differentiating,

$$m_1 = \rho V_1 + V_1 \rho$$

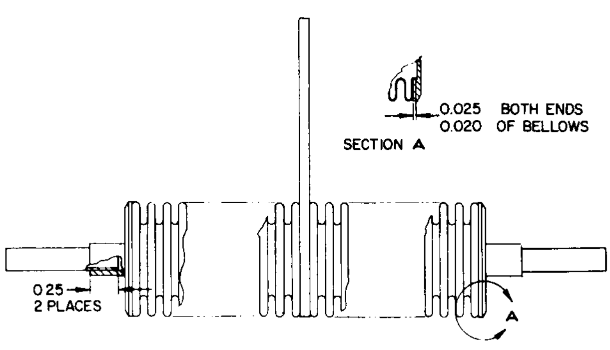

FIGURE 6-145. VISCOUS DAMPER DESIGN

The flow, $Q_1 = \frac{m_1}{\rho} = V_1 + \frac{V_1}{\rho}\rho$

The bulk modulus, $N = -V\frac{dP}{dv}\Big|_{m=\text{const.}} = \rho\frac{dP}{d\rho}$

Substituting the above into the flow equation,

$$Q_1 = V_1 + \frac{V_1}{N}P_1$$

and similarly,

$$Q_2 = V_2 + \frac{V_2}{N}P_2$$

Since there is no leakage and the bulk modulus is constant, it is possible to write

$$P_1 = \frac{V_2}{V_1 + V_2}P_L \text{ and } P_2 = \frac{V_1}{V_1 + V_2}P_L$$

where $P_L = P_2 - P_1$.

Substituting into the flow equation,

$$Q = V - \frac{V_e}{N}P_L \text{ where } V_e = \frac{V_1 V_2}{V_1 + V_2}$$

The orifice will be designed to produce laminar flow, i.e.,

$$Q = C\,P_L$$

where C is the orifice coefficient.

Equating the equations for Q and recognizing that $V = a\delta$, where a is the area of the plate between the bellows and δ the velocity of the plate, P_L can be related to the displacement δ in LaPlace transform notation as,

$$\frac{P_L}{\delta} = \frac{a/C\,S}{\frac{V_e}{NC}S + 1}$$

The forces acting in the bellows plate are

$$F = aP_L + K_1\delta$$

Substituting for P_L, the transfer function of the damper is,

$$-\frac{F}{\delta} = \frac{\frac{a^2}{C}S}{\frac{a^2}{CK_2}S + 1} + K_1$$

K_2 is the oil-spring of the fluid due to its compressibility and can be shown to equal a^2N/V_e. The spring associated with the bulging of the bellows acts in exactly the same manner; i.e., in the case in which the orifice is blocked, the center plate is able to move when a force is applied, due to either oil compression or bellows bulging or both. The oil-spring is considerably stiffer than that associated with bulging; therefore, K_2 will be considered to be the "bulging" spring. The term a^2/C in the equation is the damping evident when K_1 is zero and K_2 is infinite.

The effect of the lag term is to cause the damper to act like a spring for frequencies above the lag breakpoint (this is analogous to the idea that at high frequencies the damper behaves as if the orifice were plugged). To ensure that damping is provided near the natural frequency of the spin control mechanism, the lag break frequency should be ≥ 3 times the natural frequency. Thus,

$$a^2/CK_2 \leq \frac{1}{3\omega_n}$$

This gives a method of estimating the lower acceptable limit on K_2, assuming that a^2/C, the damping coefficient for linear motion of the orifice plate, is given. If the damping ratio for damper design purposes is taken as 0.3, then $K_2 \geq 470$ lb/in.

The bellows spring K_1 should be small relative to the primary spring of the spin control mechanism (the bipropellant tubes). Knowing K_1 and the desired minimum damping, it is necessary to choose a bellows so that K_2, the "bulging" spring, is large enough to meet the lag breakpoint requirement.

LOCKING MECHANISM

Provision has been made in the spin rate control design for the addition of a locking mechanism to hold the control jet in its center position during the severe dynamic environment of launch and boost. It serves the purpose of preventing severe hammering of the control against its stops, and of holding the flexures in their straight position while subjected to high loads. The lock is released by a squib-operated pinpuller identical to that used on Surveyor.

It is possible that further damper development will create deletion of the squib-operated lock feasible.

HEAT TRANSFER ANALYSIS

The operation of the spin rate control jet necessarily causes heating of the gimbaled assembly. An initial concern, due to the high heat flow resistance of the flexure pivots, was for the overheating of the propellants. The major danger of the propellant overheating occurs just after jet shut-off when the nozzle is at high temperature and the cooling effect of propellant flows ceases.

The mass of metal in an injector required to prevent the bulk temperature from rising above 270° F was estimated based on the model of Figure 6-146. Radiation loss occurs principally from the expansion section of the nozzle, but accounts for only about 10 percent of the heat flow in the 90 seconds from shut-down. Since the throat section of the nozzle is an effective heat conduction restriction, the major portion of the heat flow to the injector during the first 10 seconds is contributed by the combustion section of the nozzle; and, it is during this period when the highest percentage of radiation from the expansion sections occurs (approximately 2 percent).

For conservative assumptions (e.g., no radiation loss, no transfer to stagnant propellants, etc.) the injector mass is approximately 0.16 pound. Further observations based on the analysis were: Raising or lowering the emissivity 0.1 would change the block weight by only 0.005 pound; halving gasket conductivity would increase block weight by 9 percent; and doubling the mean temperature would raise block weight 40 percent.

In view of the above estimates, it has been assumed that heat transfer to the propellants can be controlled without major design effort. However, a review of the Marquardt design is planned in this regard.

MODEL SPIN RATE CONTROL TEST PLANS

The test plans for the model spin rate control mechanism are designed to provide operational data on a

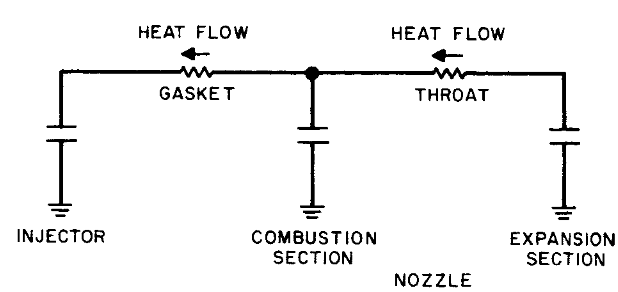

FIGURE 6-146. EQUIVALENT CIRCUIT-HEAT TRANSFER ANALYSIS

specific mechanism embodying the design features previously described. A series of tests have been planned and are described below.

Static Test. This test involves measurement of the combined and individual spring rates of the torsion springs, flexures, and bellows.

Transient Decay Test. This test will be performed to measure the effective damping ratio both with and without the damper, and for a range of oil viscosities and initial conditions on amplitude. (The variation in oil viscosity will simulate the effect of temperature on damping. Amplitude effects will provide a check on linearity.)

Centrifuge Test. By testing the control in a centrifugal field, confirmation of the design regarding performance and structural integrity(at overspeed) are expected. Gimbaled jet position will be measured during these tests.

Vibration Test. This test is in two parts: shake table tests of the control individually, and as part of the T-1 engineering model of the Syncom II spacecraft. For the individual shake tests the vibration environment will be according to the reaction control system specifications, following low-level testing to measure vibration modes. Shake tests of the unlocked jet employing the damper for vibration control will be performed.

Miscellaneous Tests. A check on damper frequency response alone is planned. Endurance tests of the bellows are to be performed by cycling the gimbaled jet unit with the bellows in place and operating.

TEST RESULTS

The following test results have been measured and analyzed:

Static Test. Measurements were made with a bellows mockup (final design uses twice as many convolutions) on the gimbaled jet model. Bellows spring rate is essentially constant and cannot be assumed negligible in any refinement of design. Further measurements are needed for analysis of centrifuge test results.

Transient Decay Test. Preliminary results, based on accelerometer measurements for one oil viscosity and one orifice configuration, showed a damping ratio of approximately 0.26 as compared with approximately 0.001 for the undamped device.

Centrifuge Test. Instrumentation and other test setup preparations are in process.

Vibration Test. Both the T-1 vibration test and the individual shake test of the gimbaled jet are programmed following Advanced Technological Development.

Miscellaneous Tests. A frequency response test of a bellows damper model was performed using the apparatus shown in Figure 6-147. The frequency range covered was 1 to 16 cps. The force amplitude versus frequency characteristics (Figure 6-148) shows the proper slope sign at lower frequencies. However, the variation of the slope from the theoretical 20 db/decade requires further investigation. Endurance tests are programmed following Advanced Technological Development.

SUMMARY — ENGINEERING MODEL, SPIN RATE CONTROL

With the exception of the bellows damper shown, the two units delivered for installation on the T-1 spacecraft are shown in Figure 6-136. A third unit has been retained for feasibility testing.

The features of the fabricated model are summarized below.

Mounting plate: The interface between the spin rate control and the spacecraft. Specifications call for scribe lines on this plate indicating the gimbal axis and a line bisecting the gimbal axis (between the flexures) and at a 45-degree angle to the gimbal axis to aid assembly to the spacecraft. The coiled tubing springs are clamped to the mounting plate such that the tubing is crushed lightly.

The pin-holder and puller is mounted directly to the plate. Machined surfaces at 45 degrees to the surface of the plate form one side of the flexure pivot. The mounting plate material is anodized aluminum.

Yoke subassembly: The frame for mounting the jet assembly; the yoke stop (pin receptacle); and the yoke spring stops (dynamical stops). The yoke is assembled to the mounting plate by means of the flexures. Yoke material: anodized aluminum, milled cross section.

Pin puller, cartridge actuated: Has been simulated for the purposes of this test series. The unit proposed for service has already been qualified on the Surveyor program. The pin-puller pin functions to prevent damage to the gimbaled assembly and/or the flexures during the relatively high accelerations during boost. The metal-to-metal contact presents a development

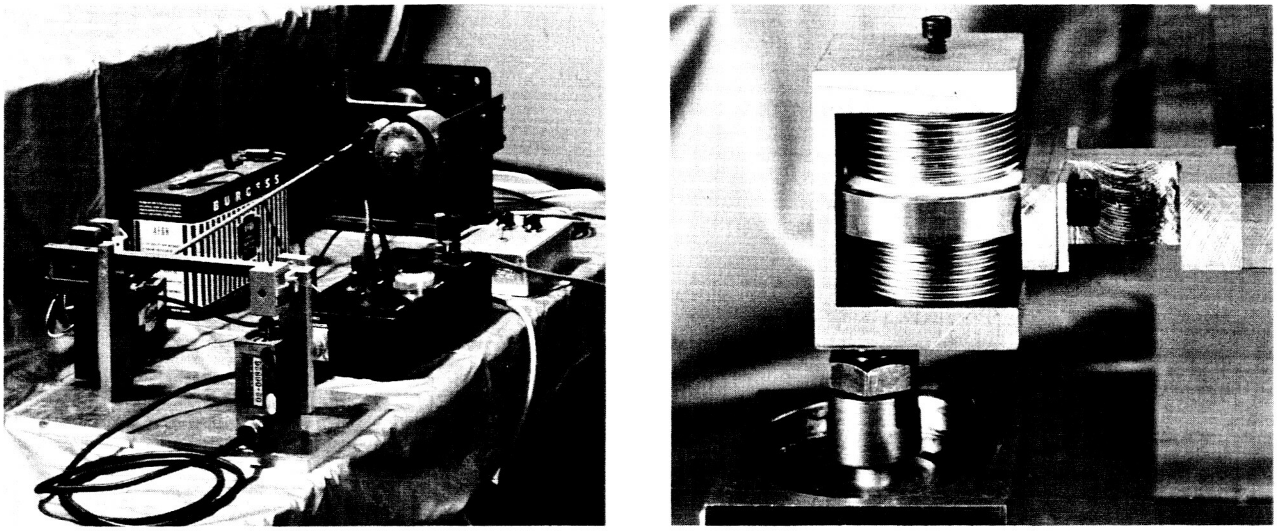

a) Test setup b) Closeup

FIGURE 6-147. VISCOUS DAMPER DESIGN

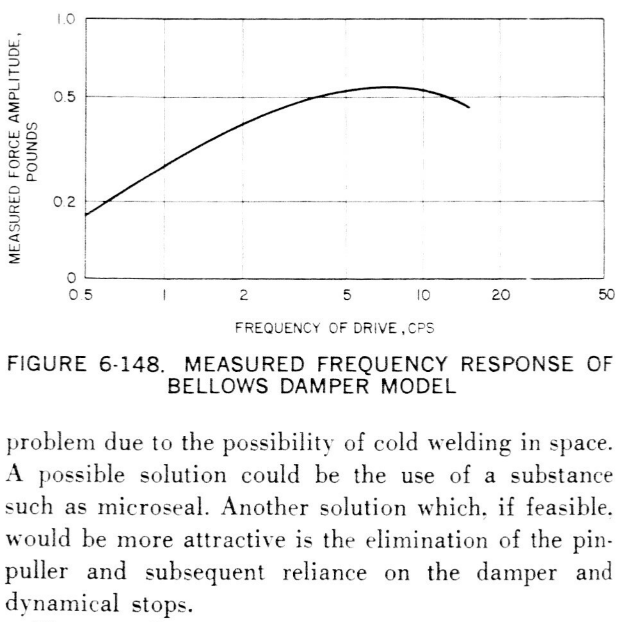

FIGURE 6-148. MEASURED FREQUENCY RESPONSE OF BELLOWS DAMPER MODEL

problem due to the possibility of cold welding in space. A possible solution could be the use of a substance such as microseal. Another solution which, if feasible, would be more attractive is the elimination of the pin-puller and subsequent reliance on the damper and dynamical stops.

Flexures: Equivalent to bearings, they perform the function of essentially frictionless bearings, while eliminating metal-to-metal contact between moving parts. Figure 6-149 shows the installation. Material: 17-7 PA stainless steel, heat treated.

Torsion coils: To provide the major spring action for the mechanism while also serving as flexible propellant feed lines. The coils fabricated for the test series are 321 stainless steel. However, an operational unit may require heat treated springs. Another area of concern is the connection of the tubing to the propellant valves. The present model uses flared fittings, whereas operationally, a welded joint would be preferable.

Viscous damper: To control through hydraulic dissipation of input energy, the tendency of the spin rate control toward undue oscillations. The features of this subunit are indicated in Figure 6-150. The end-caps are tilted at 8.5 degrees to the vertical such that the orifice plate (yoke-mounted vertical member in Figure 6-150) is parallel to an end-cap at maximum travel. The gimbal axis is in the vicinity of a tangent to the circumference of the bellows convolutions. This combination of geometry is designed to minimize the distortion of the bellows.

The bellows are compressed on assembly so that they are continuously in compression during the duty cycle.

Pinch tubes (321 stainless) permit leak-checking the bellows assembly after welding, and filling the assembly with 750 centistoke silicone hydraulic oil (under a vacuum). After filling, the pinch tubes are pinched closed and tinned with soft solder. To protect the soldered end from accidental contact with the propellants, a tight-fitting teflon boot will be used.

Hydroformed bellows of 17-7 PH are initially specified for development. A welded plate bellows is considered as a backup item.

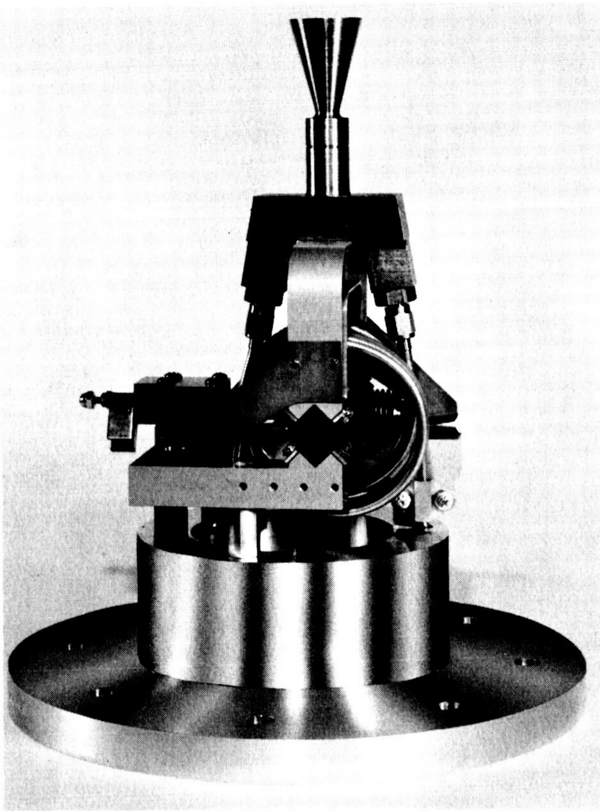

FIGURE 6-149. SPIN RATE CONTROL MODEL
Flexure pivot view

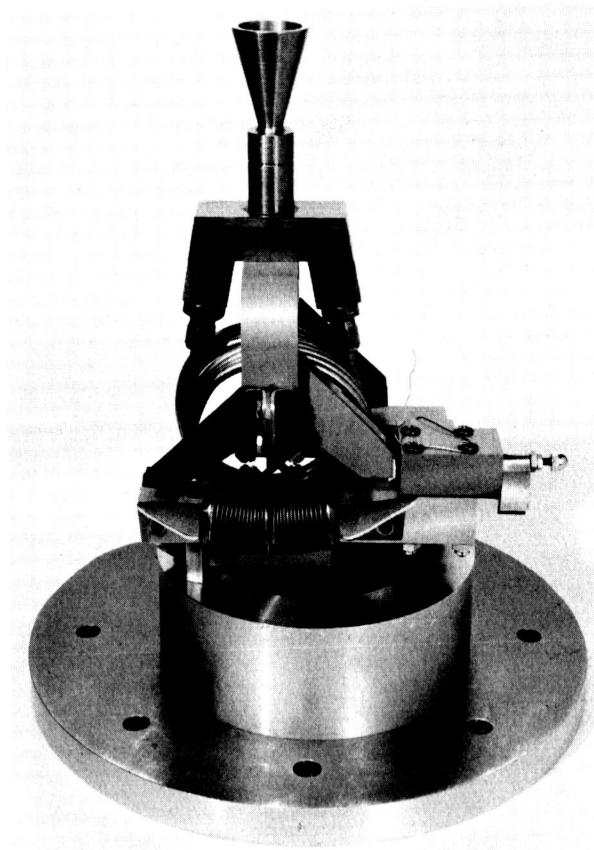

FIGURE 6-150. SPIN RATE CONTROL MODEL
Bellows damper view

Note that (Figure 6-136) the simulated jet subassembly is bolted to the top flange of the yoke. For vibration testing, spacers will be mounted between the flanges, allowing the mounting bolts to pass through both flanges for greater rigidity.

Sun Sensors

Two sun angle indications are required to provide spacecraft attitude information. The ψ sun sensor has the plane of its sensing beam parallel to the spin axis. The time between sensor outputs gives a direct measure of spin rate. A ψ_2 sensor is mounted adjacent to the ψ sensor such that the plane of its beam intersects the ψ beam at 35 degrees. The intersection of the two beams is perpendicular to the spin axis. The time interval between outputs of the two sensors provides a measure of the sunline – spin axis angle ϕ.

Two ψ and two ψ_2 sensors will form one sun sensor set. One pair of ψ, ψ_2 sensors will provide inputs to the on-board control electronics and the other pair will have their outputs telemetered. The ψ signal is used in the low frequency multiplier loop of the control electronics to provide the basic angular reference. The ψ_2 signal is used in conjunction with the pulse output from the low frequency multiplier loop to form the ψ_2 angle directly. Four such sets of sun sensors will be positioned around the periphery of the spacecraft. The outputs will be switched into the electronic and telemetry circuits by ground command.

The Syncom I sun sensors (Figure 6-151) have been evaluated for Syncom II application. They have been found acceptable but might be improved with some minor changes. These changes include possible use of a narrower silicon cell (0.25 x 2 cm rather than 0.50 x 2 cm). Since only approximately 8 percent of a cell is illuminated, the reduced cell width will not affect the output voltage characteristics.

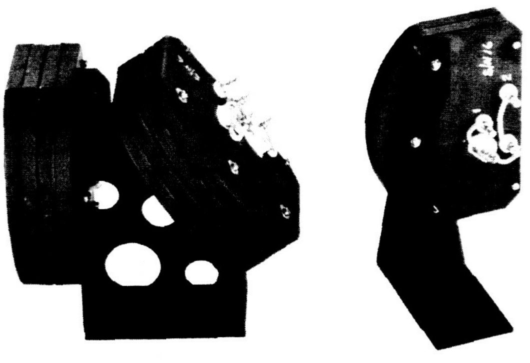

FIGURE 6-151. SYNCOM I SINGLE AND MULTIPLE SUN SENSOR ASSEMBLY

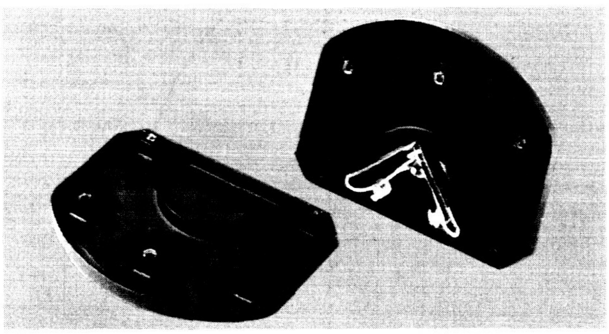

FIGURE 6-152. "EXPLODED" VIEW OF SYNCOM I SUN SENSOR

The illuminated portion is believed to load down the cell. A narrower cell will then increase the output voltage and cause more uniformity between the performance of cells.

The Syncom I sensor performance is summarized below.

General description: The sun sensor is a device utilizing two photovoltaic cells and associated shadow masks to provide an output signal when the sun is within its defined field of view. The field of view is defined by two narrow slits formed by two precisely spaced cup-shaped, metal sensor "halves" (see Figure 6-152). When the sunline and the plane formed by the two slits coincide, the photovoltaic cells are illuminated and an output signal is produced.

Beamwidth: The nominal beam shape of the sun sensors is 0.8 by 150 degrees (Figure 6-153). The 3-db beamwidth of the sun sensor is 0.8 $\pm$0.1 degree for sunline angles (ϕ_s) between 45 and 135 degrees, and less than 1.25 degrees for sunline angles (ϕ_s) between 15 and 45 degrees and 135 and 165 degrees.

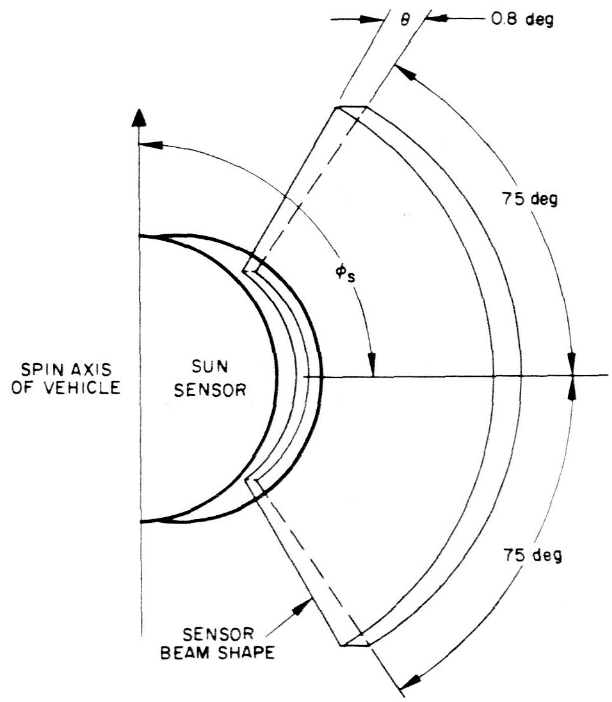

FIGURE 6-153. SYNCOM I SUN SENSOR FIELD OF VIEW

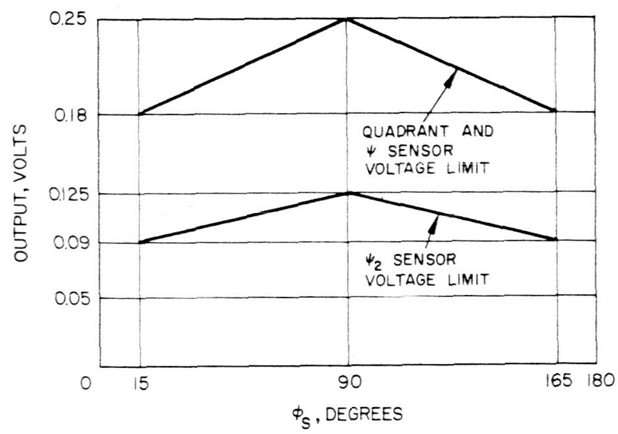

FIGURE 6-154. SENSOR OUTPUT SIGNALS

Output voltage: The sensor output voltage across a 1000-ohm resistive load is greater than the limits shown in Figure 6-154 when the sunline lies in the sensor field of view.

Weight: The sun sensor weighs less than 0.035 pound.

Installation: The central plane of the sensor beam is parallel to the sensor mounting surface within 0.1 degree.

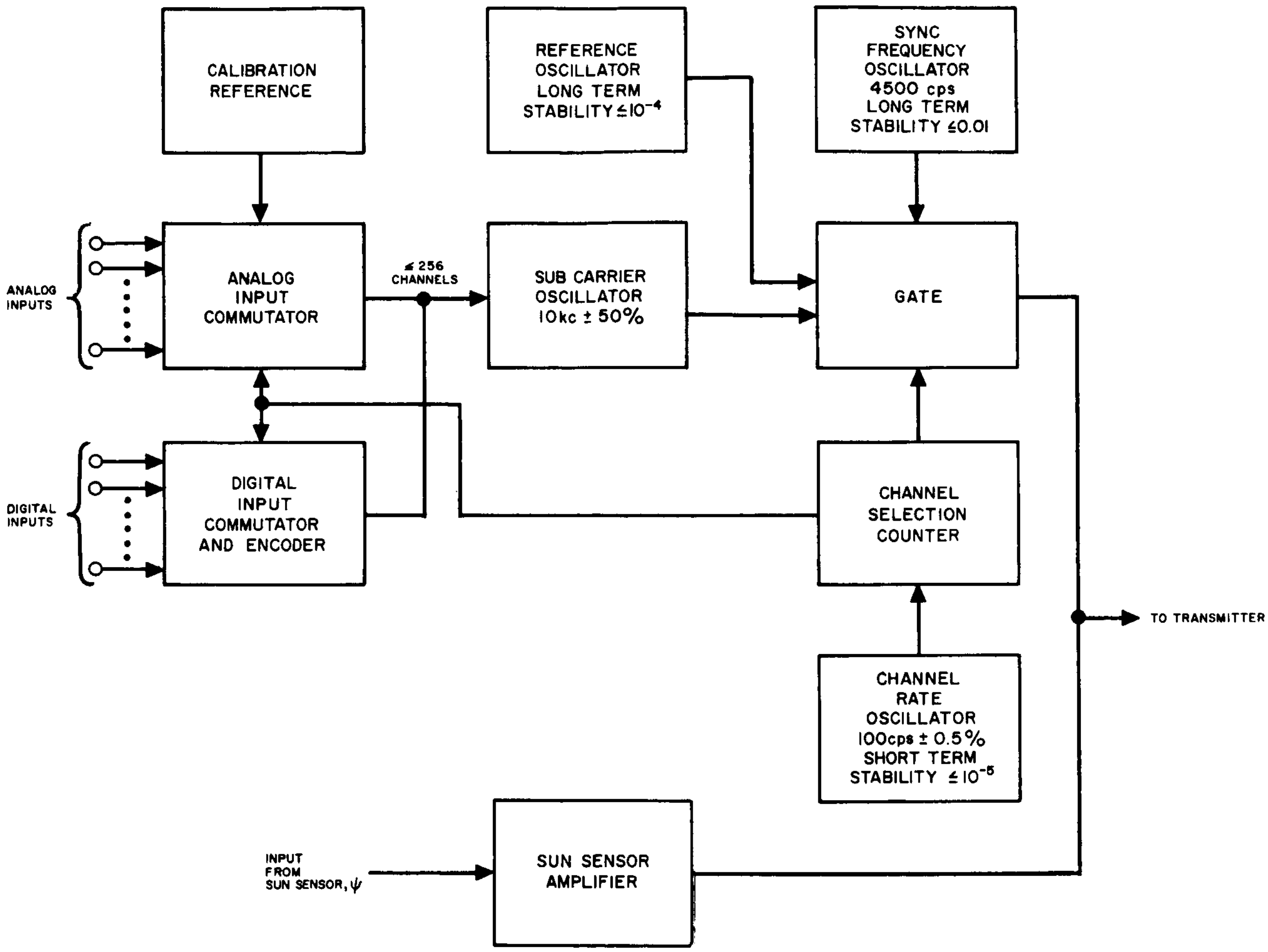

FIGURE 6-155. SYNCOM II TELEMETRY ENCODER GODDARD PFM STANDARD

RF Electronics

The RF equipment for telemetery and command is, for the most part, adapted directly from the Syncom I spacecraft. The command receiver will be identical in function and packaging. The telemetery transmitter will be identical in function, but will be packaged to include the bias unit. A diplexer similar to Syncom I can be used to separate the command and telemetry signals at each subsystem. The Syncom I approach of utilizing hybrid baluns to channel the signals among subsystems will be employed.

Four telemetry transmitters and four command receivers will be utilized in the Advanced Syncom spacecraft. Each command receiver will connect only to its own decoder. However, the output of each decoder can command any quadrant. The telemetry system will be similar, in that each encoder is connected to a particular transmitter, and all signals will be available to each encoder.

Telemetry Encoder

In the initial phases of the program, the telemetry format described in the NASA-Goddard Space Flight Center document, "Preliminary Standard for Spacecraft Pulse Frequency Modulation," was considered for Syncom II. Figure 6-155 is a block diagram of the telemetry encoder envisioned for implementing the format of the document referenced above. The encoder parameters are:

Data subcarrier frequency	10 kcps, ±50
Sync frequency (f_o)	4500 cps
Reference frequency (f_r)	To be specified
Data rate	50 data bursts per second
Number of data frames	To be determined (16 maximum)

The channel rate oscillator is a 200-cps tuning fork oscillator which serves as a trigger for the channel selection counter. The channel selection counter consists of N flip-flops, where N is the smallest integer equal to or greater than $(6 + \log_{2n})$, and n is the number of data frames; there are 15 data channels per frame.

The reference frequency is obtained from either a tuning fork or crystal oscillator.

The analog input commutator selects the analog signal to be telemetered, as determined by the state of the channel selection counter, and switches the selected signal to the voltage-controlled oscillator. The digital input commutator selects the digital binary signals to be telemetered in groups of up to three bits at a time, and applies the selected signals to the digital input encoder. The digital inputs to be selected are determined by the state of the channel selection counter. The digital input encoder converts the three (or fewer) digital signals into a voltage which may assume one of eight discrete levels corresponding to the eight possible states of the inputs. This voltage is then applied to the voltage-controlled oscillator.

The stepped frame synchronization bursts are obtained by applying the outputs of the appropriate flip-flops of the channel selection counter to the digital input commutator.

The frame synchronization and reference frequencies are gated to the telemetry transmitter at the appropriate times as determined by the lesser significant bits of the channel selection counter.

The calibration reference provides an accurate known voltage which is applied as one of the analog inputs; ground potential is applied as another analog input, providing two-point calibration of the subcarrier oscillator.

The sun sensor pulses are amplified and directly phase-modulate the telemetry carrier.

With relaxation of the requirement to conform to the Goddard Space Flight Center PFM Telemetry Standard, the Syncom II telemetry format was changed to the Syncom I type. Figure 6-156 is a revised block diagram of the telemetry encoder.

The inputs are time-division multiplexed by the commutator and applied to the subcarrier oscillator which has a frequency of 14.5 ±7.5 percent. There are at present 64 channels. Table 6-16 presents a preliminary allocation of the telemetry channels. The commutation rate is eight channels per second, resulting in a telemetry format time of 8 seconds.

When the command execute tone is received by the spacecraft, it is applied to the telemetry encoder output amplifier. The command execute tone gates off the subcarrier oscillator signal and replaces it as the input to the telemetry transmitter.

When the command being executed is the operation of a bipropellant solenoid, the command execute tone is amplitude-modulated to indicate that the control signal actually is applied to the solenoid coil.

The sun sensor pulses ψ and ψ_2 are amplified and directly phase modulate the telemetry carrier.

The synchronization pulse is transmitted once every 8 seconds; the sync voltage is out of the data range, and is a precise voltage used for calibration.

Means for telemetering vibration and acceleration data are being investigated.

TABLE 6-16. SYNCOM II TELEMETRY ENCODER PRELIMINARY CHANNEL ALLOCATION

Subsystem	Information	Type	No. of Channels	
Power	Unregulated bus voltages	Analog	2	
	Battery Voltages	Analog	2	
	Solar Panel Temperature	Analog	1	5
PACE	Beam Angle	Digital	3	
	Lock and Timer Selection	Digital	1	4
Command	Command Verification	Digital	3	3
Control	ψ_2 Angle	Digital	3	
	Propellant Tank Pressures	Analog	4	
	RCS Temperatures	Analog	2	9
Transponder	Transmitter Power	Analog	4	
	Receiver Signal Strength	Analog	4	
	Mode and TWT Selection	Digital	1	9
Miscellaneous	Spacecraft Identification	Digital	1	
	Telemetry Identification	Digital	1	
	Synchronization Calibration	Analog	2	
	Telemetry Radiated Power	Analog	1	
	Temperatures	Analog	2	
	Radiation Experiment	Analog	5	12
	Spares			22
	Total Channels			64

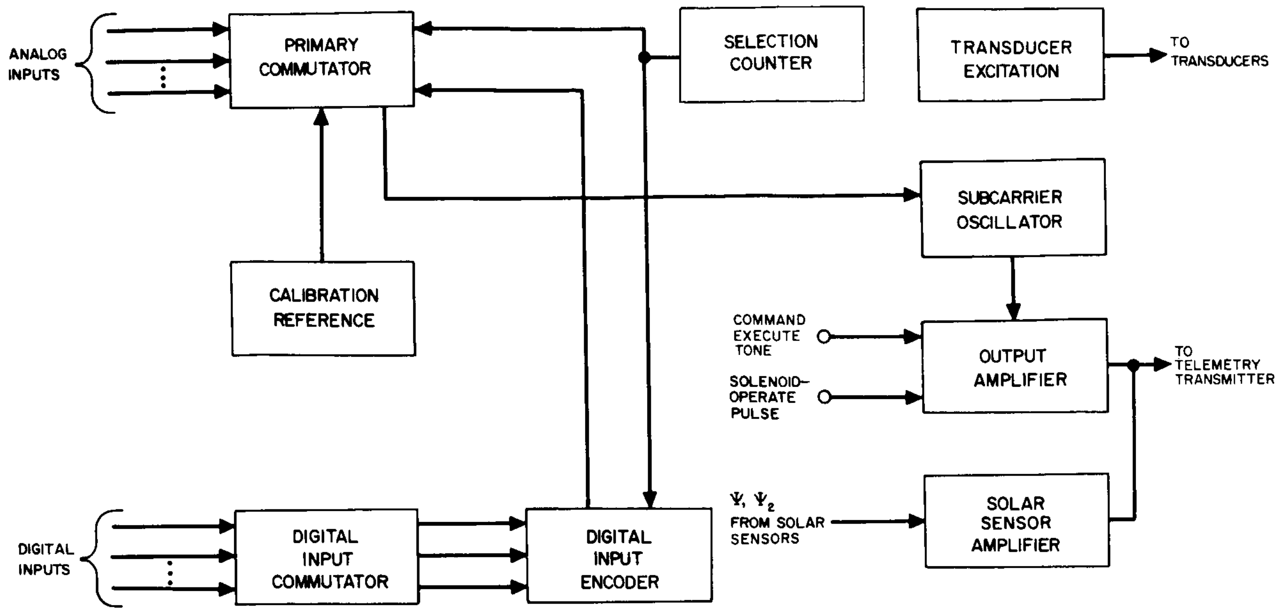

FIGURE 6-156. TELEMETRY ENCODER

COMMAND DECODER

Description of Operation

PRIMARY MODE

The primary decoder mode operates from a non-return to zero (NRZ) format, frequency-shift-keyed digital wave train with inherent bit sync information. The bit synchronization information is contained in a sine wave whose alternate zero crossings are at the time center of the data bits. This sine wave amplitude modulates either the "zeros" tone or the "ones" tone, whichever is being transmitted.

Figure 6-157 is a block diagram of the command decoder. Prior to command initiation the zeros tone with the bit synchronization wave is transmitted to the vehicle. This tone passes through tone filter No. 2 and hence to the audio detector. After a few cycles of the bit sync wave, the audio detector begins reproducing the bit sync sine wave. The sine wave is shaped into a square wave by the clock amplifier. The clock amplifier then provides bit shift signals to the command register, which, in primary mode, is connected as a shift register.

After an interval sufficient to allow the buildup of clock pulses in the satellite, the command is transmitted. The order structure is as follows:

Bits 1 — 7 word sync and address

Bits 8 — 14 data or command bits

Each of the redundant decoders has a separate digital address. When this address is detected, a latching enable switch is closed, which connects command power to the rest of the decoder. The command is then shifted into the command register. The block diagram is drawn assuming neither a one or zero tone is transmitted after the last data bit. Since the clock stops with neither frequency present, the shifting stops after the last data bit is received.

As in Syncom I, the commands are verified via telemetry prior to execution. After verification, execution is accomplished by transmitting a tone separate from either the ones or zeroes tone. Execution commences with receipt of this tone and lasts as long as the tone is present. When the tone is removed, execution ceases and the trailing edge resets the enable switch, thus turning off decoder power. This execution technique permits execution in real time, a vital requirement for Syncom. This type of execution is not available in presently planned standard equipment, but from preliminary reading of standard equipment specifications, its inclusion would require a very simple modification.

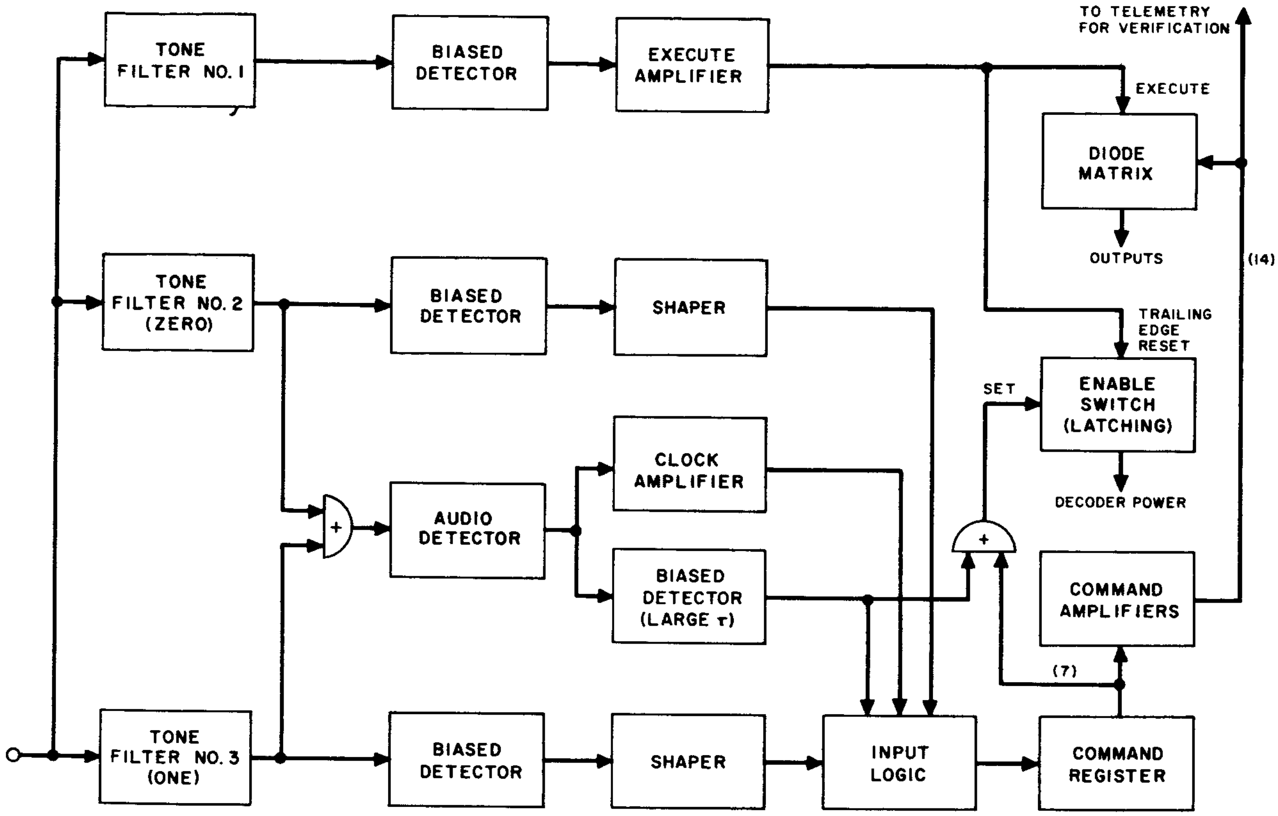

FIGURE 6-157. DUAL-MODE COMMAND SYSTEM

BACKUP MODE

The audio detector which generates the bit shift clock in the satellite is used to drive a biased detector with a large time constant. If the bit sync wave on either tone is left on for a long time (say, 5 seconds), this biased detector changes state. This state change turns on the enable switch and changes the command register operation to count rather than shift. The commands can then be entered into the register by counting either the ones tone or the zeros tone as in Syncom I. Execution and verification are accomplished as in the primary mode.

ELECTRICAL POWER

System Design

The power system selected uses radiation resistant, moderately high efficiency, N on P silicon solar cells as the primary energy source. Satellite operation during eclipse periods is maintained with electrical power from hermetically sealed nickel cadmium storage batteries. The use of proven and tested components assures high confidence of satisfactory power system operation for 5 years in orbit.

The major characteristics of the electrical power system are summarized in Table 6-17. The power system shown in Figure 6-158 consists of the following:

1) A solar array composed of flat-mounted N on P solar cells on fiberglass-faced, aluminum honeycomb substrate panels. Sixteen panels are used to form the outer cylindrical surface of the spacecraft. Parallel interconnections at the cell level enhance solar array reliability. The physical wiring of the individual cell groups (see Figure 6-159) has been segregated by connecting alternate cell groups to provide maximum system flexibility. This interconnection method allows as many as four separate and isolated solar array

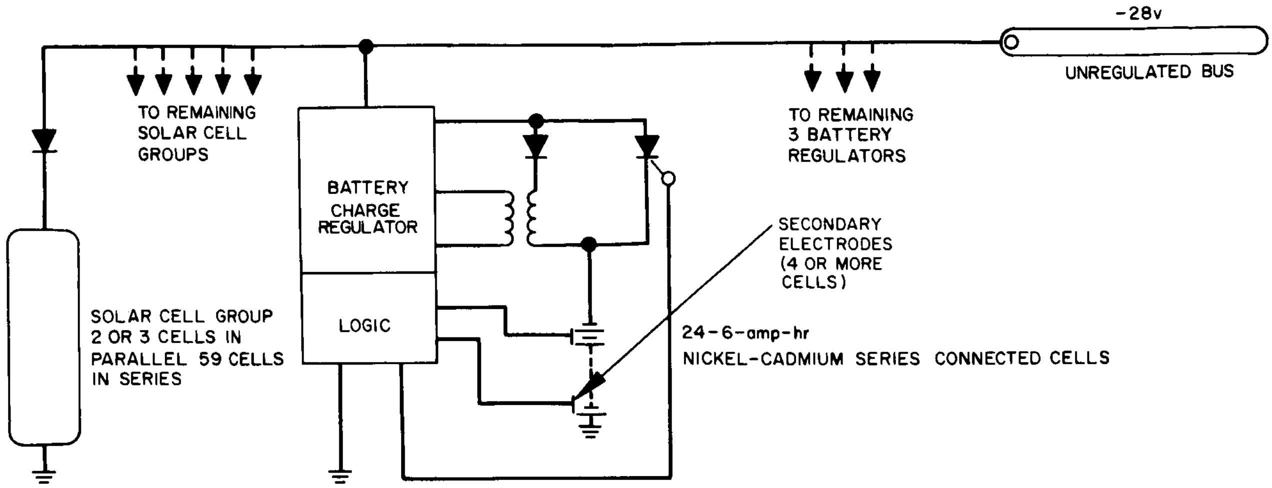

FIGURE 6-158. ELECTRICAL POWER SYSTEM SCHEMATIC

outputs to be utilized. Changes from one to four distinct buses can be accomplished by only a spacecraft harness change with no redesign or rework to the solar array.

2) Energy storage for normal operation of the spacecraft while in complete eclipse. The storage system consists of four 24-cell nickel-cadmium batteries, each connected to the spacecraft bus through separate charge regulators and discharge logic devices. These batteries, in addition to supplying spacecraft power during boost and eclipse periods, also provide energy for pulse loads, such as control system valve solenoids and the apogee motor igniter.

3) Disconnects that prevent inadvertent battery discharging by the command receivers.

4) A charge regulator in series with each battery that maintains the battery in a fully charged state with a minimum number of series-connected solar cells in the solar array.

5) A separate voltage regulator or voltage regulator-switch combination for each major electronic unit. The nominal voltage at the equipment will be maintained at —24 volts. Each regulator unit input circuitry will be current-limiting to protect the unregulated voltage supply bus from excessive current requirements.

6) Separate, regulated high-voltage dc-dc converter and filament power supplies for each traveling-wave tube.

TABLE 6-17. ELECTRICAL POWER SYSTEM CHARACTERISTICS

Solar cell	
Silicon N-P type	
Air mass zero sunlight efficiency at 140 mw/cm² and 77°F with 0.006 covers installed	9 percent
Cell active area	1.8 cm²
Total number of cells	22,420
Total number of series strings	380
Array	See Figure 6-160
Battery	
Type	Nickel-cadmium
Number of batteries	4
Number of cells per battery	24
Nominal cell rating	6 amp-hr
Maximum depth of discharge	20 percent
Average depth of discharge	12.7 percent

Design Criteria and Assumptions

Table 6-18 is a summary of power demands for the spacecraft. To evaluate the 5-year operational capability of the Advanced Syncom, the following criteria and assumptions were considered:

1) The orbit achieved will be a nominal 24-hour stationary synchronous orbit with a maximum eclipse time of 1.15 hours (see Figure 6-161).

2) Maximum battery depth of discharge will be limited to 20 percent of nominal battery capacity.

3) Leakage current of subsystem regulators will be 3.5 milliamperes when on and neglible when off.

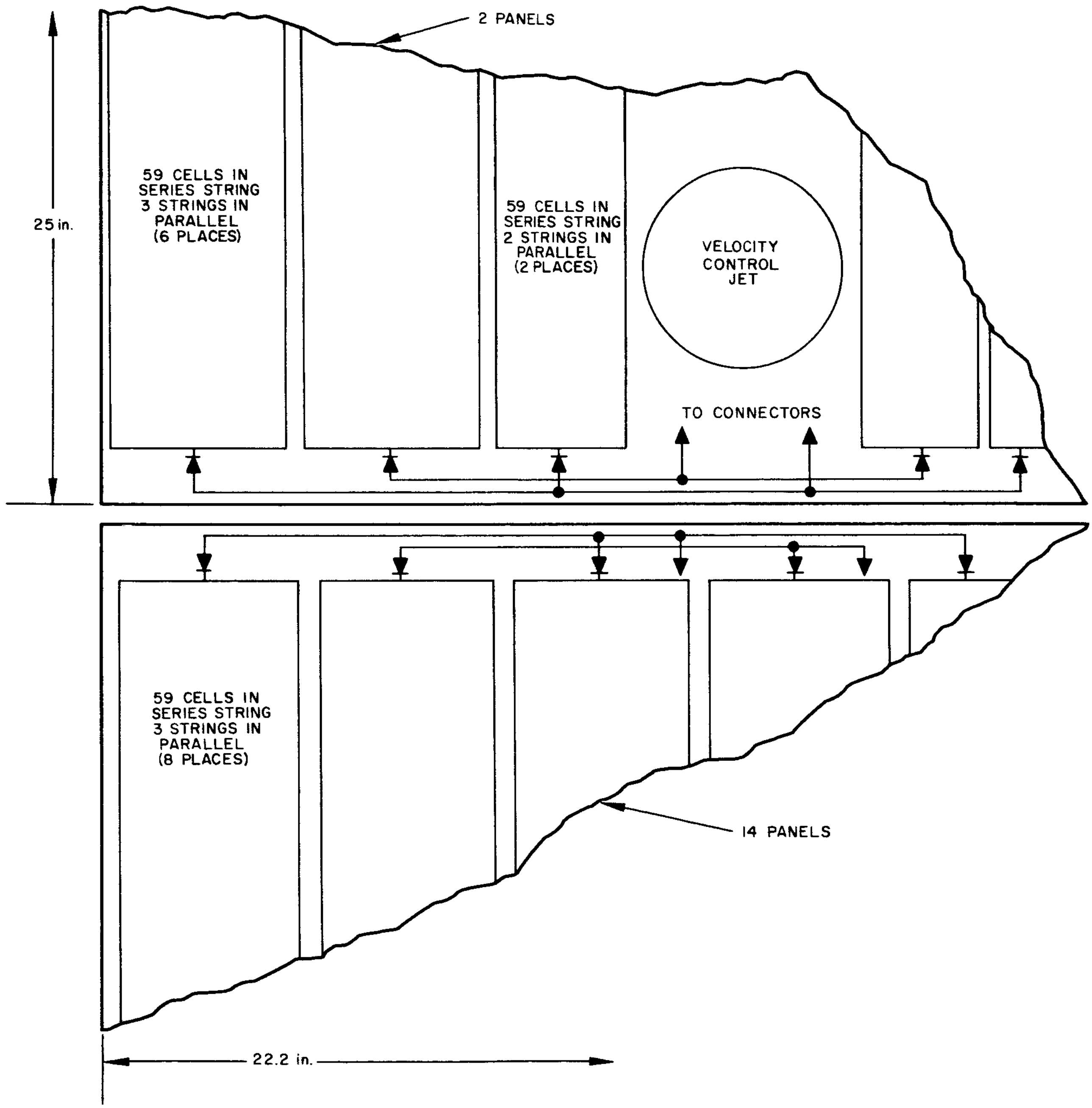

FIGURE 6-159. SOLAR CELL PANEL LAYOUT

4) Traveling-wave tube efficiency will be 30 percent dc-RF, traveling-wave tube filament, 1.3 watts at 24 volts, and traveling-wave tube converter efficiency (high voltage and filament) 90 percent.

5) Battery maximum charging rate and charging efficiency are based on two batteries capable of supplying the complete spacecraft electrical load during eclipse. Available battery charging time

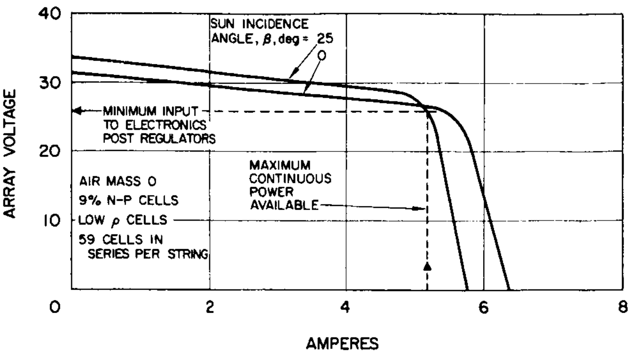

FIGURE 6-160. SOLAR ARRAY CHARACTERISTICS

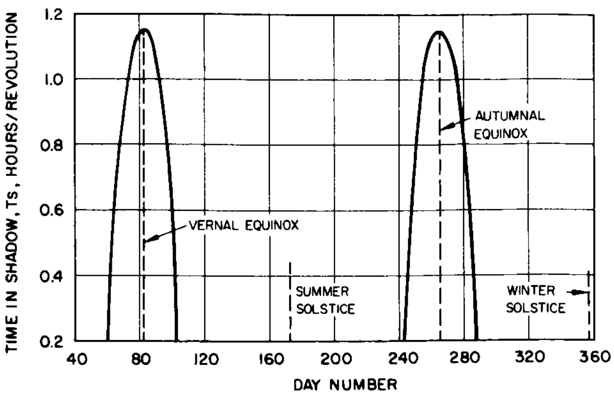

FIGURE 6-161. SHADOW TIME FOR SATELLITE IN 24-HOUR EQUATORIAL ORBIT

will be 22.85 hours per orbit minimum. Battery discharging time will be 1.15 hours per orbit maximum.

6) One ohm-cm N-on-P silicon solar cells will be used.
7) Bus voltage is greater than —26 volts at the input to the subsequent regulators.
8) Solar panel temperatures will be:

Normal incidence $\beta = 0$ $\quad 75 {}^{+5}_{-10}$ °F

Oblique incidence $\beta = 25$ degrees $\quad 60 {}^{+5}_{-10}$ °F

9) Battery temperature will range 40 to 100° F.

Solar Array

The solar array is composed of 22,240, 1-by-2-cm N-P silicon solar cells connected in 128 series-parallel groups as shown in Figures 6-159 and 6-162. Each series-parallel group is connected to the spacecraft electrical bus with a blocking diode. Series-parallel solar cell interconnections have been used to increase electrical power system reliability.

Within the physical constraints of the spacecraft envelope the solar cells can be installed on each panel in such a manner as to provide the designed 28-volt output with a single row of solar cells extending from the top to the bottom of each panel. By developing the entire bus voltage in this manner it is possible to provide sufficient paralleling of cells to enhance system reliability. Array electrical characteristics are shown in Figure 6-160.

N-P low resistivity cells are approximately ten times more resistant to radiation damage than P-N cells. Although high resistivity N-P cells have even greater radiation resistance than low resistivity types, their output voltage is significantly lower and their use would necessitate a 10 percent increase in spacecraft length to accomplish the desired series-paralleling connection of cells.

TABLE 6-18. AVERAGE ELECTRICAL POWER REQUIREMENTS

Subsystem	Number of Units per Quadrant	Total Number of Units Operating	Milliamperes per Unit	Milliamperes per Bus Load
Telemetry	1	1	245	245
Command receivers	1	4	27	108
Encoder	1	1	27	27
Antenna electronics	1	1	650	650
Communications receivers	2	4	75	300
Traveling-wave tubes (4-watt)	2	4	693	2772
Battery charging	4	4		620
Total bus load				4722

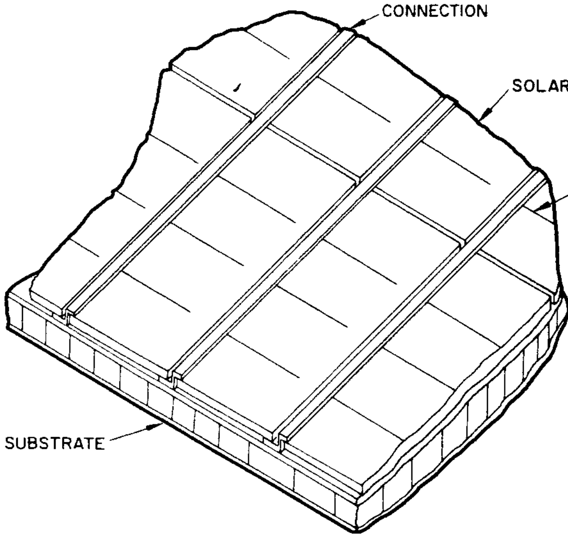

FIGURE 6-162. SOLAR CELL MOUNTING

The solar cells are bonded to 16 lightweight, fiberglass-faced, aluminum honeycomb panels. Each panel is approximately 22.2 by 25 inches and subtends an arc of 0.79 radian. Two of the 16 panels used have a slightly different cell layout to accommodate protrusion of the velocity control jet through the panel (see Figure 6-159).

The quantity of series-connected solar cells is determined by the individual cell characteristics and the output voltage requirements.

SOLAR ARRAY OUTPUT

The power output of the solar panels is based on zero air mass, temperature of 77° F, and solar intensity of 140 mw/cm^2 and may be summarized as follows:

Total cells per string	59
Total cells per group	177
Total groups per panel	8
Total cells per panel	1416 (on 14 panels)
	1298 (on 2 panels)
Total panels per spacecraft	16
Total cells per spacecraft	22,420
Sun incidence angle, β	25 degrees
Effective area of illuminated cylinder	0.636
Effective groups illuminated, $0.636 \times 64 \times \cos \beta$	36.83
Power output per group at normal incidence, $177 \times 22.7 \times 10^{-3}$ watts	4.02 watts
Total power output with 8 percent degradation, $\beta = 25$ degrees	136.2 watts
Output voltage 0.46×59	27.0 volts
Blocking diode voltage	0.7 volts
Net array voltage	26.3 volts
Total array current	5.14 amperes

CELL PARALLELING REQUIREMENTS

The number of parallel cells to be used in each cell grouping is a function of reliability and ease of manufacture. The Reliability section of this report contains detailed calculations that show a solar array reliability of 0.998 for a 1-year period, which is greater than that required for successful operation of the spacecraft for the 5-year operational period.

Figure 6-163 plots the number of parallel solar cells versus power loss in the event of a single-cell failure. Only a small theoretical gain is possible if more than three cells are operated in parallel. The power loss at the end of 5 years is as follows:

Three parallel cells	8.5 percent
Seven parallel cells	6.1 percent

The parallel interconnection of cells on a cylindrical surface becomes more difficult as the number of cells in parallel increases. Three to four cells are the maximum number that can be efficiently installed with a minimum of breakage within the constraints of the existing shroud envelope.

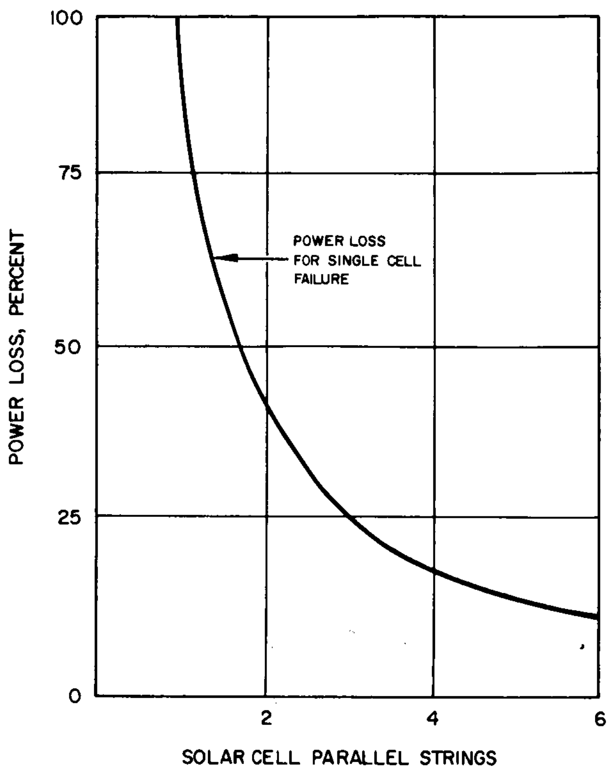

FIGURE 6-163. POWER LOSS VERSUS PARALLEL STRINGS

Radiation Effects

Two radiation sources may exist in the Syncom II orbit which could result in reduction of the solar array output: solar flare activity and Van Allen radiation. With the 6-mil glass covers similar to those used on Syncom I, the Van Allen radiation will cause less than 0.2 percent per year solar cell output degradation. Solar flare activity (with the assumptions described below) will result in a predicted 8 percent degradation in the last 2 years of the predicted 5-year functional life of the spacecraft.

Micrometeorites are not considered to degrade the basic array output since a typical collision will result only in a small nonshorting cell puncture, which will be so small compared to the total area that the overall effect will be negligible.

ENVIRONMENT

Nuclear range-energy relations yield the result that the 0.006-inch glass covers will stop protons of energies less than 3 mev and electrons of energies less than 220 kev from penetrating the solar cells. Therefore, only particles with energies greater than these threshold energies will be considered further.

Electron fluxes have been measured by the State University of Iowa (References 6-5 and 6-6). The resulting data indicate that at an altitude of 22,700 nautical miles the number of electrons with energies greater than 40 kev is 10^7 to 10^8/cm^2-sec and greater than 1.6 mev is 10^3/cm^2-sec. Therefore, a reasonable number to choose for N (greater than 220 kev) is 5×10^5 electrons/cm^2-sec. For a 5-year period (about 1.5×10^7 seconds), this gives a total integrated electron flux of 2×10^{12} electrons/cm^2.

Proton fluxes have been measured by a group at the Goddard Space Flight Center (Reference 6-7). At the desired altitude, data for proton energies greater than 3 mev are sparse. It is suspected that the flux of protons with energies between 3 and 20 mev is negligible, the flux above 20 mev is less than 10 to 100 protons/cm^2-sec., and the flux above 100 mev is at cosmic radiation levels; i.e., about 0.2 proton/cm^2-sec. This gives a total integrated flux for 5 years of 10^8 to 10^9 protons/cm^2 with energies greater than 20 mev.

CALCULATIONS

An empirical formula has been derived (Reference 6-8) for the expected solar cell degradation in space based on laboratory experiments at RCA, Bell Telephone Laboratories, Space Technology Laboratories, Lockheed Missile and Space Company, Transitron, General Electric Company, and MSVD.

$$f = 1 - \left[\frac{7}{9}\left(\frac{\phi}{<\phi_{25}>}\right)^{1/2} + 1\right]^{0.5}$$

where

f = fraction of degradation in cell efficiency

ϕ = particle flux in orbit

$<\phi_{25}>$ = average value of particle flux which causes 25 percent degradation I_{sc}.

Values of $<\phi_{25}>$ that represent efficiency degradation in space have recently become available (Reference 6-9). Replacement of efficiency data for I_{sc} data introduces an error in flux values by at most a factor of 3 – much less than the errors in the known values of

Van Allen particle fluxes. From Explorer XII, $<\phi_{25}> = 1.5 \times 10^{10}$ protons/cm^2 for E greater than 120 kev and 1.9×10^{10} for E greater than 2 mev on cells with 0.003-inch covers. From Midas III, $<\phi_{25}> = 6.7 \times 10^{10}$ protons/cm^2 for E greater than 20 mev on cells with 0.006-inch covers. From TRAAC, $<\phi_{25}> = 3.3 \times 10^{11}$ protons/cm^2 for E greater than 4 mev on "blue" cells with 0.006-inch covers. From terrestrial laboratory data, $<\phi_{25}> = 2.5 \times 10^{14}$ electrons /cm^2 for E greater than 220 kev on cells with 0.006-inch covers.

Efficiency degradation from Van Allen particles is found to be less than 0.2 percent per year with 6-mil cover glasses, using the following parameter values:

$<\phi_{25}> = 6.7 \times 10^{10}$ protons/cm^2 for E greater than 20 mev

$<\phi_{25}> = 2.5 \times 10^{14}$ electrons/cm^2 for E greater than 200 kev

Proton flux: 10^8/cm^2 with energies greater than 20 mev; electron flux: 2×10^{12}/cm^2 with energies greater than 220 kev.

SOLAR FLARE ACTIVITY

The solar flare cycle is now passing through a minimum and will increase to a maximum in 1968. The previous maximum flare activity occurred in 1957. On the basis that no better long-range prediction method exists, it is assumed that the next flare cycle will be similar to the last one. The notation of Dessler (Reference 6-8) is followed for large and small solar flare proton events. Naugle's estimates for typical events are also used (Reference 6-9). Hence, the large flare will yield in the vicinity of the earth typically 1.4×10^9 protons/cm^2 and the small flare, 7×10^7 protons/cm^2. It is assumed most of the solar protons have energies above 20 mev. The number of flares during each year is assumed as follows:

	Small	Large
1964	0	0
1965	0	0
1966	1	0
1967	2	2
1968	4	9

A large relativistic flare could occur during the satellite's lifetime. These flares occur nonperiodically, but have averaged one every 4 years. The last were in November 1949, February 1956, and May 1960. These flares have fluxes of 10^9 to 10^{13} protons/cm^2.

The total proton flux above 20 mev will then be approximately 1.6×10^{10} protons/cm^2 without the relativistic flare, or possibly 10^{11}/cm^2 including it. The degradation from the regular flares will be about 8 percent, occurring during 1967 and 1968. This observation is based on J. E. Naugle's estimates of the particle fluxes produced by solar flares and an extrapolation of the known degradations of solar cells on Midas III, based on the assumption that the solar flare protons have an energy spectrum similar to the protons in the inner Van Allen zone.

Energy Storage System

Energy storage is provided by four separate nickel-cadmium batteries of 24 cells each. The cells, rated at 6 amp-hr each, are hermetically sealed and use sintered plate construction. Four or more of the 24 cells in each battery will have a sensory electrode whose output is proportional to the state of charge of the cell. The sensory electrode current is proportional to the cell state of charge and is used to terminate battery charging. Other specifications for the battery cell are given in Table 6-19.

The cell utilizes flat-plate construction with both the input and output terminals electrically insulated from the cell case. Electrical insulation of the terminals from the case allows direct thermal conduction to the spacecraft structure resulting in more uniform battery cell temperatures, hence potentially increased system reliability.

SELECTION OF THE NICKEL-CADMIUM CELL

The three basic types of battery cells presently available for energy storage use in space systems have the following approximate storage efficiencies, energy densities, and cycle lives at 75°F and 25 percent depth of discharge.

Cell	*Watt-Hour Recharge Efficiency*	*Watt-Hours Per Pound*	*Cycle Life*
Nickel-cadmium	0.65 to 70	10	9500
Silver-cadmium	0.70 to 80	13	100 to 1500 (est)
Silver-zinc	0.80 to 90	50	200

Although improvements in silver-cadmium cells (particularly in prevention of silver migration) will improve their cycle life considerably, the nickel-cadmium cell is the most reliable to date. In addition, it has been used successfully in a majority of the satellites in orbit. The 5-year life required of the spacecraft makes obvious the choice of the nickel-cadmium cell at a moderate decrease in energy density and storage efficiency.

BATTERY DESIGN

The design of the battery depends on the bus voltage desired, dark-time power load, depth of discharge, solar array recharging rate, time available for recharge, and reliability requirements. Twenty-two series-connected cells would be required to furnish the minimum voltage (26 volts) to the electronics subsystems. However, two additional cells have been added to each battery to accommodate a two-cell failure (shorted).

The electrical loads for eclipse operation are itemized in Table 6-18. The total load of 4.1 amperes, shared by the four batteries, results in an ampere-hour discharge for the longest eclipse period of 4.1/4 amperes $\times$ 1.15 hour, approximately equal to 1.2 amp-hr per battery. Limiting the depth of discharge to 20 percent requires a 6.0 amp-hr cell. At this depth of discharge the end-of-discharge voltage will remain above 28.8 volts (1.2 volts per cell). At a discharge rate twice as high as this for the cell size tested, and to a 25 percent depth of discharge, Cook Electric Company has reported end-of-discharge voltages for a group of test cells of 1.15 volts at the end of 4000 cycles. At the 20 percent depth-of-discharge point in these tests, the cell voltage was 1.20 volts.* However, to allow for errors in predicting spacecraft temperatures and the possibility of a cell failure, this conservatism is employed.

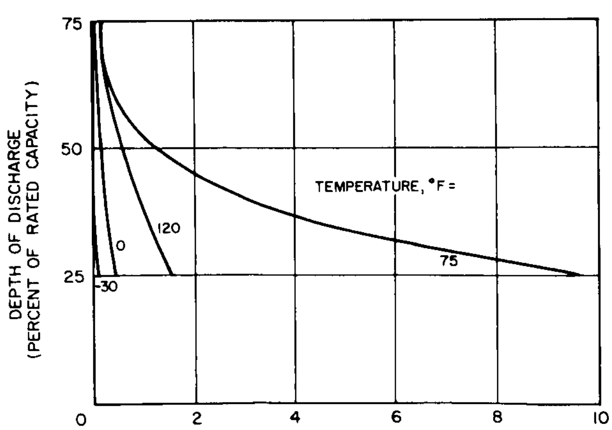

FIGURE 6-164. CYCLE LIFE OF 12-AH SEALED NICKEL-CADMIUM CELLS

TABLE 6-19. DESIGN SPECIFICATIONS FOR A NICKEL-CADMIUM BATTERY CELL

Type	Sealed sintered pate
Weight	Less than 0.62 pound
Terminals	Ceramic bushing suitable for 5-year use
Capacity	6.0 amp-hr @ 75°F @ 1.2 amperes 4.8 amp-hr @ 100°F @ 1.2 amperes 4.8 amp-hr @ 30°F @ 1.2 amperes
Maximum Charge Rate (with cut-off control)	5 amperes
Overcharge Capability	0.6 ampere continuous
Maximum Charge Voltage	1.48 volts
Cycle Life	10,000 minimum @ 25 percent depth
Environment	30 to 100°F sustained operation Space vacuum Operation in any orientation Vibration, shock, and acceleration typical of spacecraft launchings

BATTERY CHARGING

Battery charging is performed at the maximum rate of 300 milliamperes, as limited by the charge regulators. Maximum current available for battery charging with the electronics loads shown in Table 6-18 is 1.0 ampere. Recharging each of the four batteries at 250 milliamperes will take approximately 1.2 amp-hr/0.25 $\times$ 1.33 = 6.4 hours.

The charge will be terminated upon reaching a fully charged condition by battery regulator charge logic. Specially constructed cells containing sensory elements in the series string will provide the logic input. The cells with sensory elements will have a slightly lower ampere-hour capacity than the other cells in the string. The device to sense a fully charged condition is an auxiliary electrode in the cell; cells with such an electrode are presently available from the General Electric Company. The sensory electrode is an oxygen electrode similar to those used in fuel cells. The output

*W. W. Clark, W. G. Ingling, I. F. Luke, "Alkaline Battery Evaluation," ASD-TDR-62-553, June 1962.

current of the electrode is proportional to the buildup of the partial pressure of oxygen in the cell as a fully charged state is reached. This current is used to limit the charging current into a fully charged battery to a "low trickle" charge of less than 20 milliamperes.

Limiting the overcharge of the battery with the use of an auxiliary (sensory) electrode has several important advantages: 1) solar array power is not wasted by continuous overcharging of the battery. 2) battery reliability is increased by not dissipating heat into the cells from continuous overcharging. 3) terminal seal life is increased by not allowing a buildup of cell internal pressure and 4) the charging apparatus can be designed more simply and reliably.

BATTERY RELIABILITY

Recently reported results of the most extensive life cycling tests ever conducted on nickel-cadmium cells indicate that: 1) cell cycle-life with shallow discharges is considerably longer than cycle-life at deep discharges and 2) cycle-life is reduced by high and low ambient temperatures. A summary of the test results is shown in Figure 6-164. These data show that for long life, depths of discharge should be kept below 25 percent and battery temperatures should be maintained near 75°F. Syncom II batteries will be maintained near this temperature by proper thermal design. At a 20 percent depth of discharge, the 500 charge-discharge cycles will be achieved with a high degree of reliability.

The major deterrent to greater reliability and longer life of the nickel-cadmium battery cell is the failure of present-day insulating and sealing techniques of the cell terminals. The 6-amp-hr cell size selected for Syncom II minimizes the mechanical construction problems in the manufacture of a suitable seal. However, containment of the potassium-hydroxide electrolyte at the insulating interface is still a problem when long cell life is required.

Hughes intends to conduct a joint development program with General Electric Company to develop an improved seal. General Electric has devoted considerable effort to seal development during the development of cells for the ADVENT program. Ceramic bushings with a molymanganese interface, and later a titanium-hydride ceramic-to-metal bushing, were developed. The latter has been on test for approximately 1½ years under continuous cycling conditions (approximately five cycles per day) and has shown no evidence of leakage. Accelerated tests, however, indicate that this seal may leak at 3 years. The following is an outline of the program that is to be conducted; it will have two phases and take an estimated 6 months.

Phase I. Search for exact location and cause of leaks in hermetically sealed terminals. The first part of this phase will be a survey of existing terminal seals and their mode of failure to classify the various types of seals presently used, or being designated for use, in aerospace cells. (Samples of both seals and cells will be obtained.) The physical design and bonding method of the seals will be cycled, and any leaks that occur will be examined for cause and location of defect. During the cycling program, cells will be withdrawn for terminal seal examination. This will continue throughout the program.

The second part, the experimental study, involves the detailed investigation of the location and causes of terminal leaks and will include the following areas:

1) Material study (chemical analysis)
    a) Ceramic insulator
    b) Metal-to-ceramic interface
    c) Braze alloy
2) Design problems
    a) Internal stresses
    b) Imposed stresses during operation
3) Process variables — The use of vapor metalizing techniques will be used to obtain fewer and consistent metal layers. These will be compared to the equivalent layers on existing seals to ascertain if fabrication techniques are the cause for leaks.
4) Environmental defects
    a) Chemical corrosion
    b) Galvanic corrosion
    c) Stress corrosion
    d) Microcrack development due to cycling

Phase II. Improvement of battery seals. The purpose of this phase is to obtain an improved terminal seal. To accomplish this, the following areas will be investigated in detail:

1) Choice of material
2) Establishment of suitable processes
3) Proper design of cells with the improved seal

It is planned that improved seals obtained from this program will be fully tested on cells in extended cycling programs.

BATTERY CHARGE REGULATOR

Battery charge regulators for Syncom II will be of a boost type. The 24-cell batteries used require charge battery terminal voltages in excess of 36 volts. The use of a boost type of charging regulator permits battery charging continuously from the solar panel, and at the same time minimizes the total number of series solar cells required, because solar panel design can be based on the minimum voltage input to the electronics subsystems (−26 volts), rather than the high battery charge voltages required.

The use of this boost regulator results in a higher overall efficiency of the regulator, since only a fraction of the battery charging power must be transformed. The regulator senses the battery state of charge and regulates the current into the series battery string. Several battery sensory electrodes are connected to the regulator charge control circuitry with "or" gates to sense the highest cell charge and prevent battery overcharge.

STRUCTURE

Structural Design

The outline and major dimensions of the spacecraft are shown in Figure 6-165. The structure, fabricated of aluminum and magnesium, separates into three subassemblies, as shown in Figure 6-166, for ease in assembly operations.

The aft section is composed of a 30-inch diameter central thrust tube, fabricated of aluminum, and surrounded by 12 radial magnesium ribs. The thrust tube is shown in Figure 6-167, mounted on the assembly tool. Across the front of the ribs is a sheet aluminum bulkhead to provide shear stiffness. A spun aluminum ring is wrapped around the periphery of the ribs. The thrust tube is stiffened in the longitudinal direction by 12 internal stringers, installed adjacent to the ribs; the aft end of the thrust tube forms one-half of a V-band clamp flange, for attachment to the Agena interstage structure. Figure 6-168 shows the aft structure.

The central subassembly consists of an inner and an outer sheet magnesium tube, separated by 12 radial aluminum panels spaced to fall in line with the ribs of the aft section. The outer tube is split into eight segments to allow access to component bays with a minimum of structural disassembly.

Figure 6-169 shows the center section during assembly, and Figure 6-170 shows the aft and center sections assembled together. The forward structure consists of another sheet aluminum bulkhead, almost a duplicate of the aft bulkhead, upon which are mounted eight A-frame trusses welded up from ½-inch aluminum tubing. On the aft face of the bulkhead are 12 T-shaped bars to which the midsection panels will be bolted. Figure 6-171 is a view of the completely as-

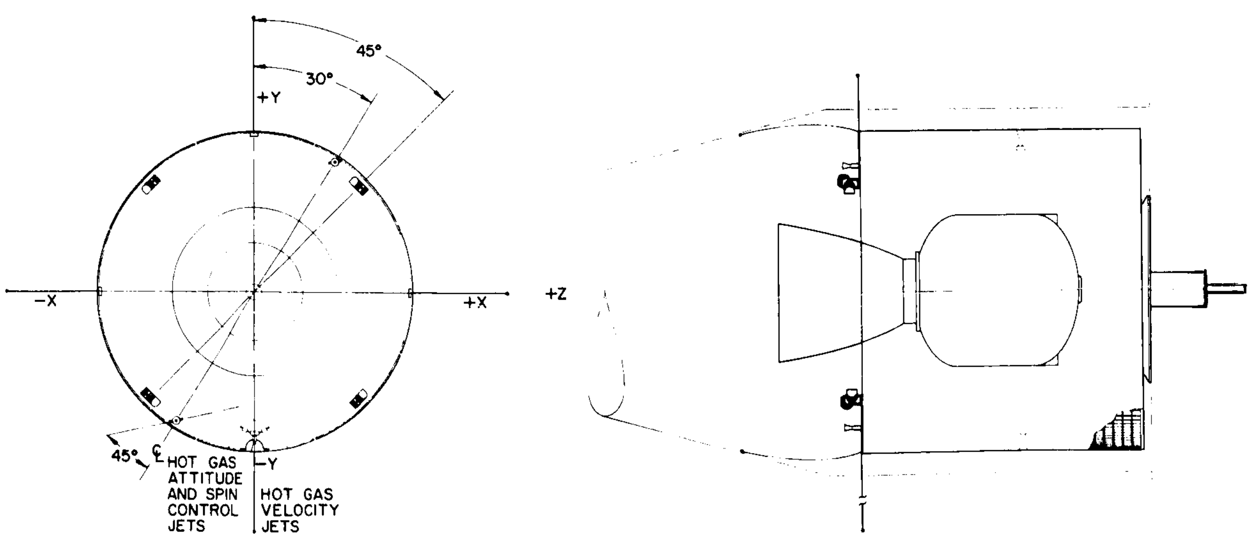

FIGURE 6-165. SYNCOM MARK II OUTLINE DRAWING

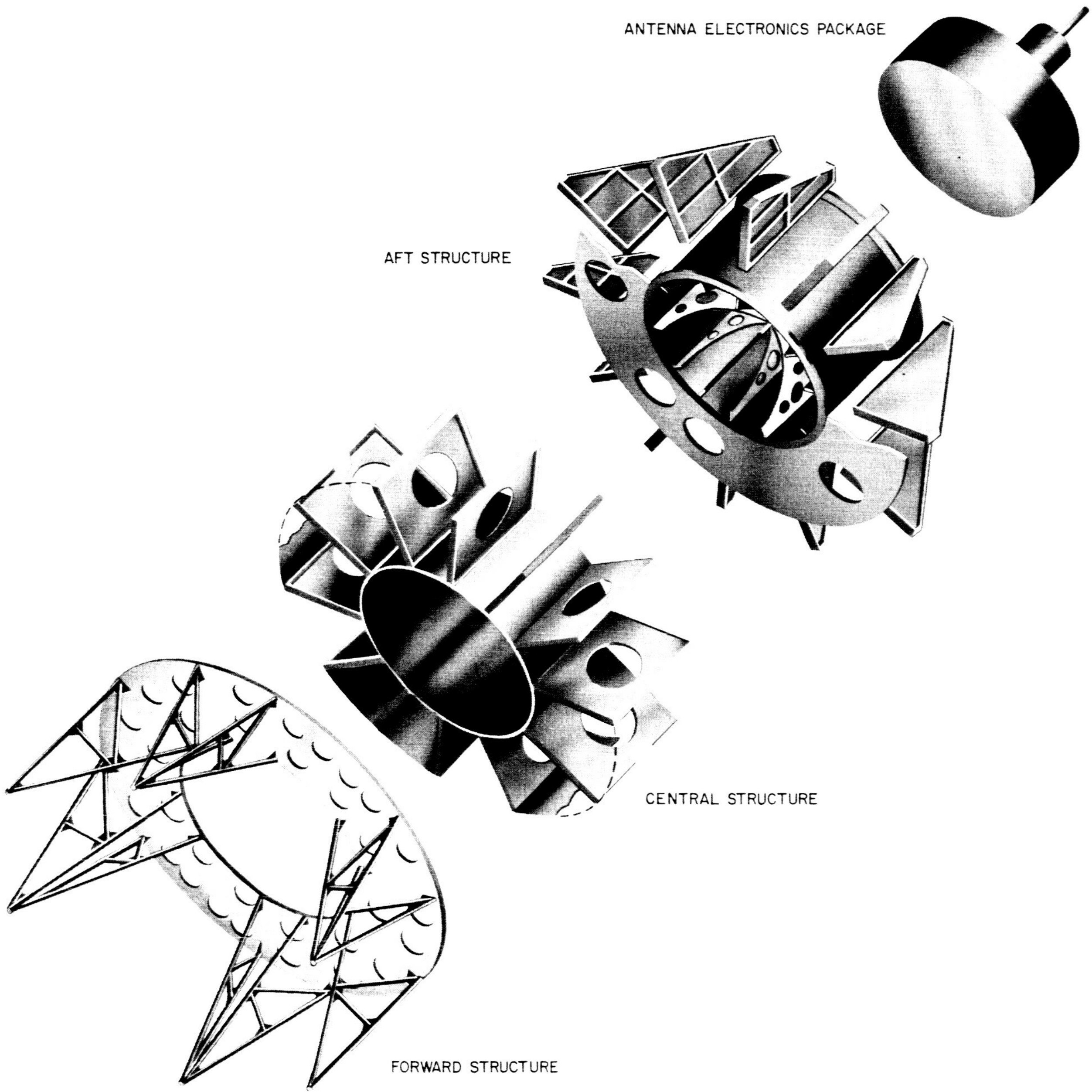

FIGURE 6-166. STRUCTURAL ARRANGEMENT

sembled spacecraft structure and shows the forward trusses.

General Arrangement

The center subassembly with its 12 panels and inner and outer cylinders, together with the forward and aft bulkheads, forms 12 bays or compartments (which structurally act as torque boxes) for the installation of units. The eight reaction control system fuel and oxydizer tanks occupy eight compartments, and the transponder quadrant packages occupy the remaining four bays (one of which is seen in Figure 6-170).

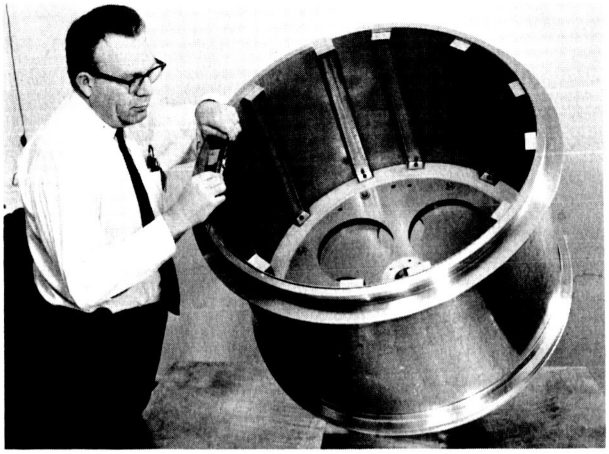

FIGURE 6-167. THRUST TUBE ASSEMBLY

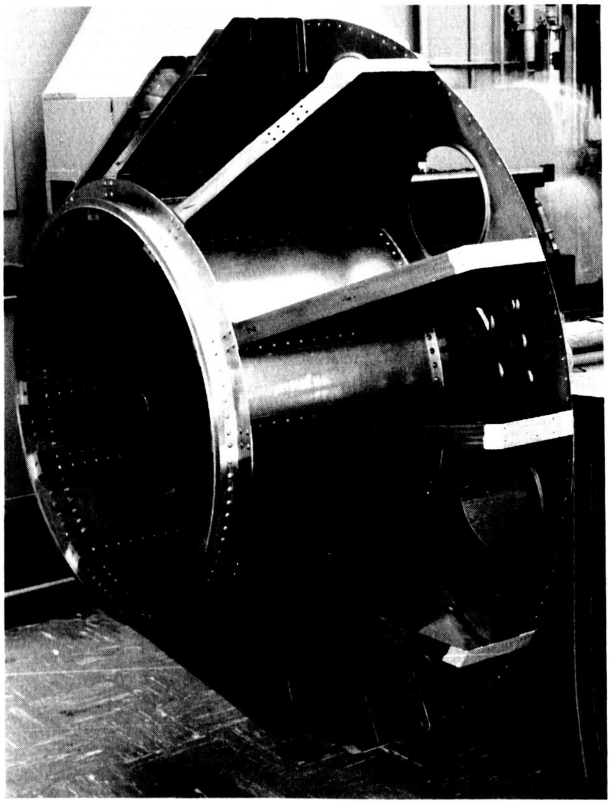

FIGURE 6-168. AFT SUBASSEMBLY COMPLETED

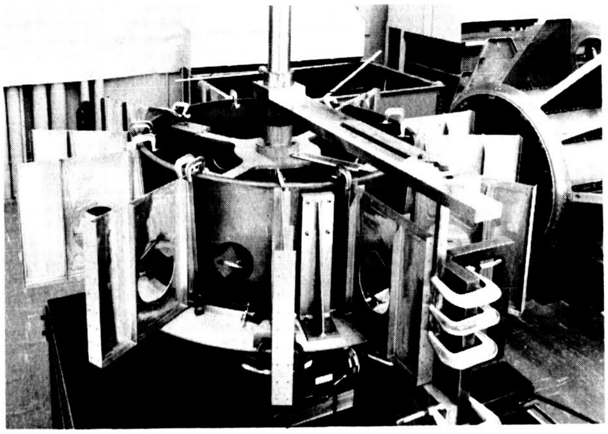

FIGURE 6-169. CENTER SECTION COMMENCING ASSEMBLY

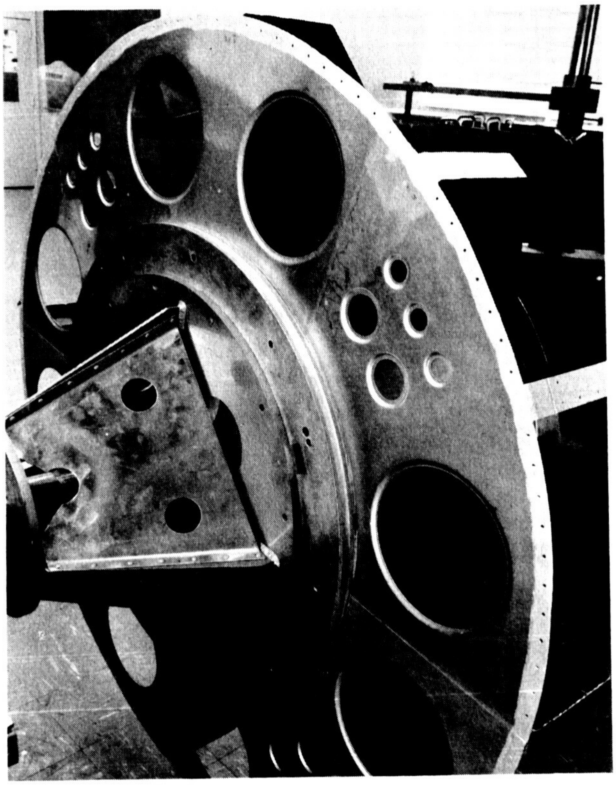

FIGURE 6-170. AFT SUBASSEMBLY DURING FABRICATION (AFT VIEW)

The tanks are mounted to their adjacent panels, while the quadrant packages are supported by machined rails attached to the forward and aft bulkheads and to the flanges of the panels. The two velocity control rockets are attached to two opposite panels, and two nutation dampers are supported within the assembly.

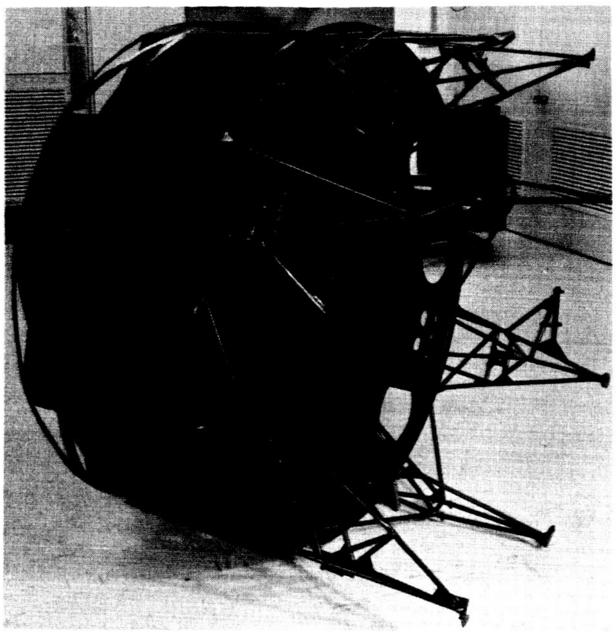

FIGURE 6-171. SPACECRAFT STRUCTURE FORWARD QUARTER VIEW

The communications antenna electronics package, attached to the internal stringers, is suspended within the aft end of the thrust tube. The 12 radial ribs are used as mounting surfaces for units with high heat outputs, such as traveling-wave tubes (TWT), TWT power supplies, and telemetry transmitters. To simplify the wiring, additional units such as the RF switches and some filters will also be carried on the ribs. Brackets spanning the inter-rib bays will carry the storage batteries and are of a design which allows considerable flexibility of installation, enabling the battery cells to be used as static and dynamic ballast. A thermal radiation barrier will enclose the aft end of the spacecraft.

The four telemetry-command antennas will be attached to the tops of four A-frame trusses. The other four trusses will support the sun sensor assemblies and two of them will also mount the attitude-spin control rockets. Battery brackets, similar to those at the aft end, will carry the remaining batteries and will also permit last-minute variations in placement for balancing purposes.

The apogee injection motor, of a short cylindrical configuration approximately $28\frac{1}{4}$ inches in diameter, is nested into a mounting seat consisting of 12 brackets attached within the thrust tube stringers. On eight of these brackets, a step forms a locating seat for the motor ring, while all 12 carry the thrust and radial loads through pairs of quarter-inch bolts. This design ensures that the thrust vector of the motor will be properly aligned without any positioning adjustments, yet without demanding strenuous efforts for precision machining. A thermal radiation barrier will be attached to the throat ring of the motor and, on its outer periphery, to the trusses.

The cylindrical outer surface of the spacecraft, 57 inches in diameter and 50 inches long, consists of 16 panels of quarter-inch honeycomb, constructed of fiberglass cloth skins over an aluminum core. The outer surfaces of these panels will be covered with silicon solar cells. Each panel is attached by a four-screw central insert to the spacecraft structure. This arrangement ensures that the solar panel can never carry any structural loads.

The spacecraft assembly drawing, Figure 6-172, shows the installations of the dummy units into the structure. Ready accessibility to all units has been provided as much as possible within the weight and size limitations. The communications antennas are easily removed as a single package. Removal of the aft thermal radiation barrier exposes all the rib-mounted units and the aft batteries. By taking off two solar panels and a segment of the outer structural shell, a quadrant package is exposed. It may then be removed by taking out the mounting screws which penetrate the bulkheads. Electrical test plugs are provided on the outside of the spacecraft at the forward end for normally needed test points.

Booster-Spacecraft Interface

As shown in Figure 6-173, a conical interstage structure (government-furnished equipment — (GFE)) is attached to the forward end of the Agena, and carries a ball-bearing spin table approximately 30 inches in diameter. The spin table (also GFE) is spun up to 100 rpm (nominal) by a set of small solid propellant rocket motors or gas jets just prior to staging. The payload attach fitting, a ring forming the forward face of the spin table, is one-half of a V-clamp flange, the other half being the aft flange of the spacecraft thrust tube. A V-band clamp, held tight by three double-squib redundant explosive bolts, releases the spacecraft after spinup. The Agena is backed off by means of cold gas reaction nozzles, thus imparting no disturbing impulses to the spacecraft.

The aerodynamic fairing, attached to the forward shoulder of the Agena, is expected to be a Lockheed Nimbus-type shroud, shortened to reduce weight as permitted by the requirements of the payload length.

The only electrical interfaces required are: 1) a battery-charging umbilical, and 2) a timer pulse to initiate spacecraft separation after spinup. It is probable that the timing pulse will be carried as a breakaway plug or frangible wires across the spin table interface (part of the GFE spin table), and the battery umbilical will possibly be a breakaway plug and cable attached to the aerodynamic fairing.

Dummy Spacecraft

As an aid in determining a realistic configuration, a full-scale plastic and wood dummy spacecraft was constructed, as shown in Figure 6-174. This has been a definitive assistance for visualizing such problems as clearances, accessibility, and load paths.

Weight and Balance Analysis

The results of the weight studies and measurements conducted are summarized below. Included are weight summaries for the planned launch configuration spacecraft and the structural engineering model spaceframe constructed during this program.

The measurements and analyses conducted indicate that the spacecraft can meet the design mission requirements within the capabilities of the Atlas-Agena D launch vehicle, and that the planned general internal arrangement provides roll to pitch moment-of-inertia ratios greater than 1.2 for all launch and orbit conditions. Further, the anticipated accuracies of measurement of weight, center of gravity, and moment of inertia are within the performance specification requirements for these measurements.

During the studies, detailed analyses were made of the designs, design layouts, and manufacturing drawings to assess the elemental weights. An IBM 7090 computer was utilized in the performance of computations and for the preparation of detailed reports.

Tables 6-20 and 6-21 provide summaries of the weight status for the planned launch configuration spacecraft, and for the structural engineering model spacecraft, HSX 302 T-1. The structural weight estimates of Table 6-20 are based on measured values for similar portions of HSX 302 T-1. Ballast is provided to bring the spacecraft weight to 1518 pounds.

Final values of weights and center of gravity for the engineering model (T-1) will be obtained when installation of dummy units is completed prior to vibration testing. These results will be submitted in a supplementary report.

TABLE 6-20. SYNCOM II ESTIMATED WEIGHT STATUS

Solid-Propellant Configuraion

Subsystem	Weight, pounds	ϕ*	θ**
Electronics	134.7	0.216	0.089
Wire harness	19.9	0.032	0.013
Power supply	105.5	0.169	0.069
Controls, inert	48.2	0.077	0.032
Propulsion, inert	122.2	0.196	0.081
Structure	138.3	0.222	0.091
Miscellaneous	55.4	0.089	0.036

Items	Weight, pounds	z-z	I_{z-z}	I_{x-x}	R/P
Final orbit condition	624.2	23.5	55.9	44.74	1.25
N_2 pressurization	3.0				
N_2H_3 — CH_3 fuel	53.5				
N_2O_4 oxidizer	85.0				
Total at apogee burnout	765.7	23.5	69.8	51.7	1.35
Apogee motor propellant	752.3				
Total payload at separation	1518.0	24.7	84.5	66.6	1.27

*Ratio of subsystem weight to final orbit condition weight.
**Ratio of subsystem weight to total payload at separation.

Structural Analysis

STRUCTURAL DYNAMICS

The dynamic loads employed in the design of the engineering model structure (T-1) are contained in Table 6-22. These loads are based on the specified sinusoidal qualification test environment and the maximum expected structural transmissibilities. The anticipated variations in transmissibility over the frequency band 5 to 2000 cps were utilized in providing qualification test specifications for major components.

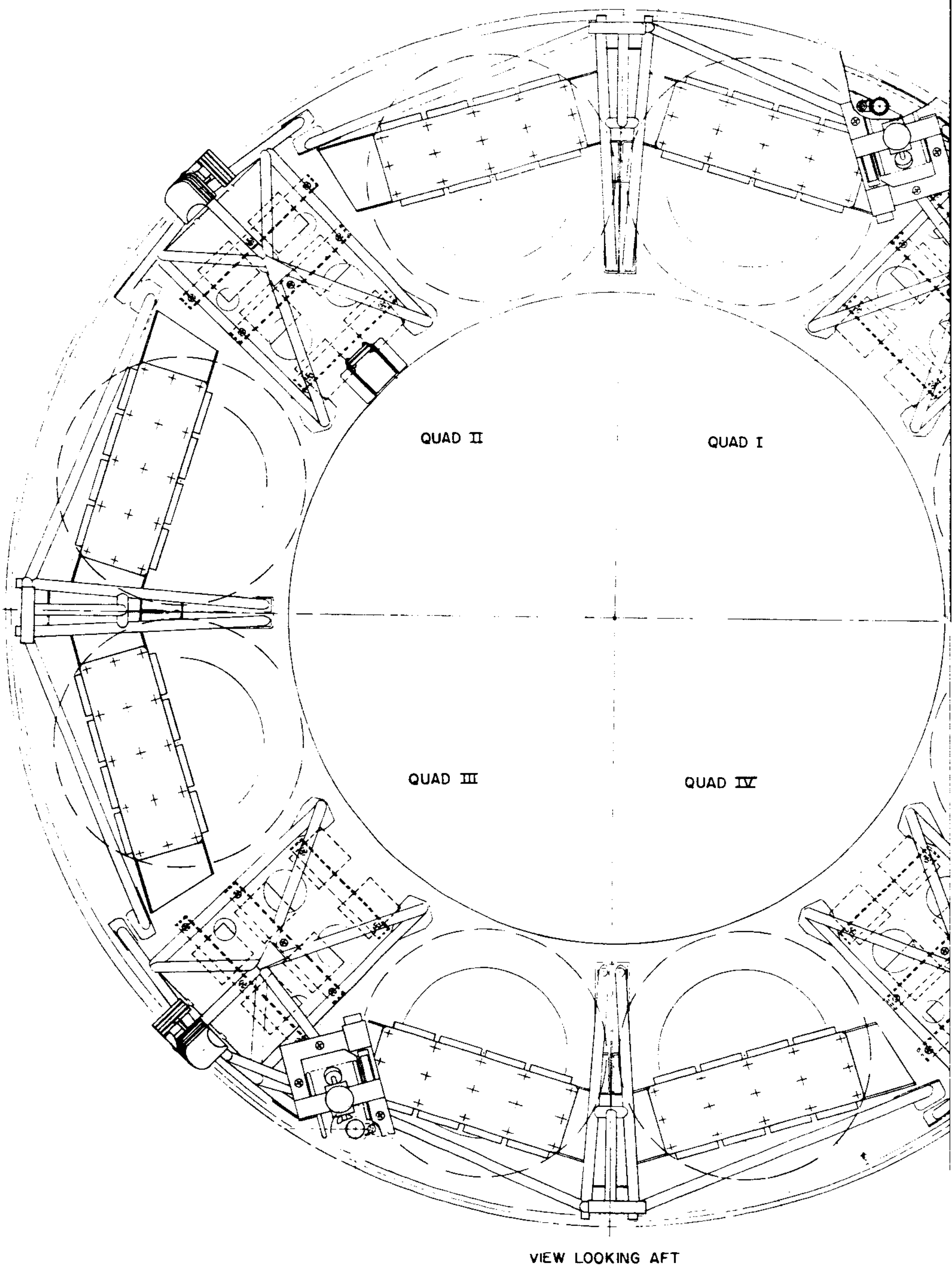

FIGURE 6-172. SYNCOM II GENERAL ARRANGEMENT

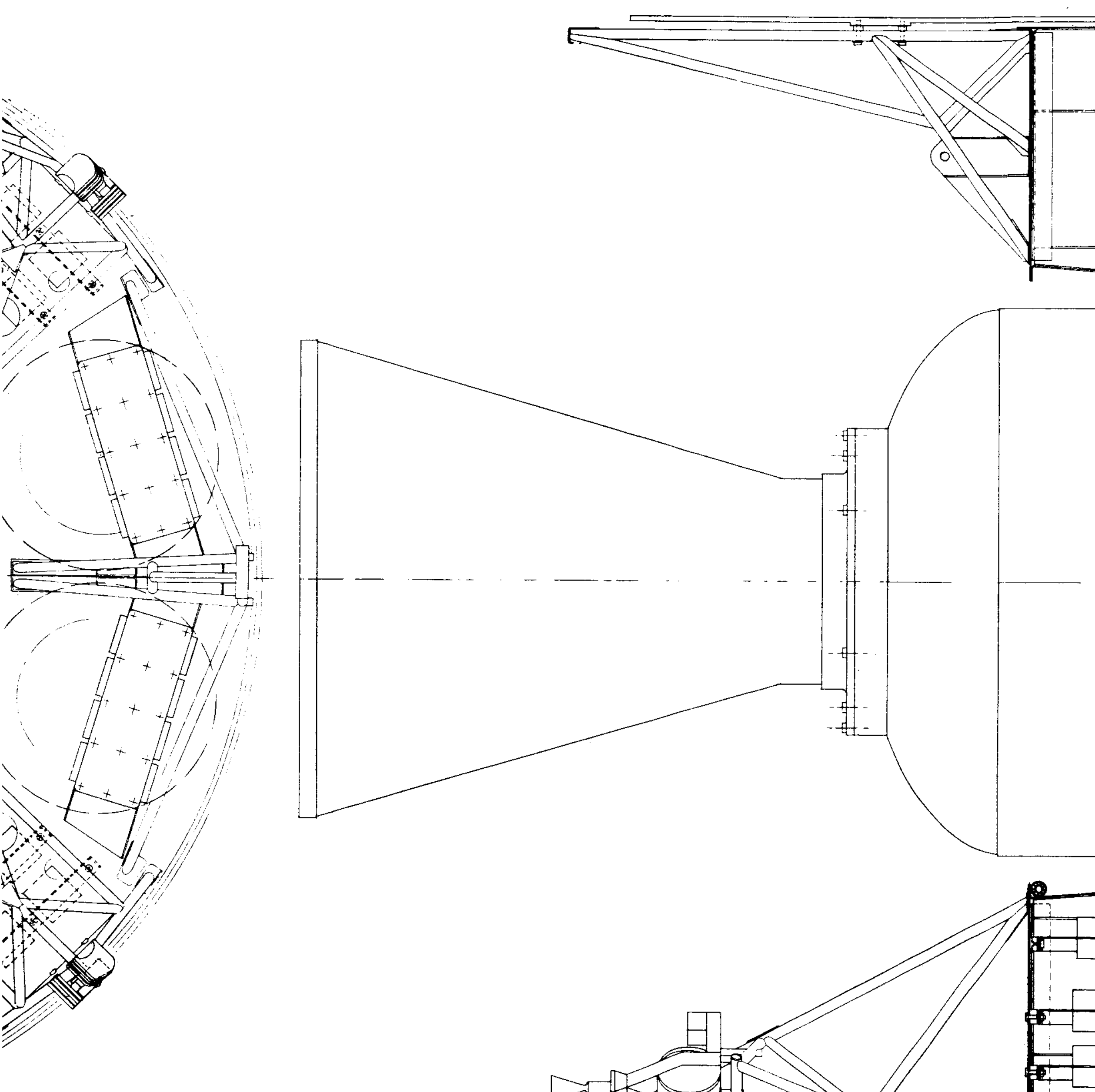

COMPONE

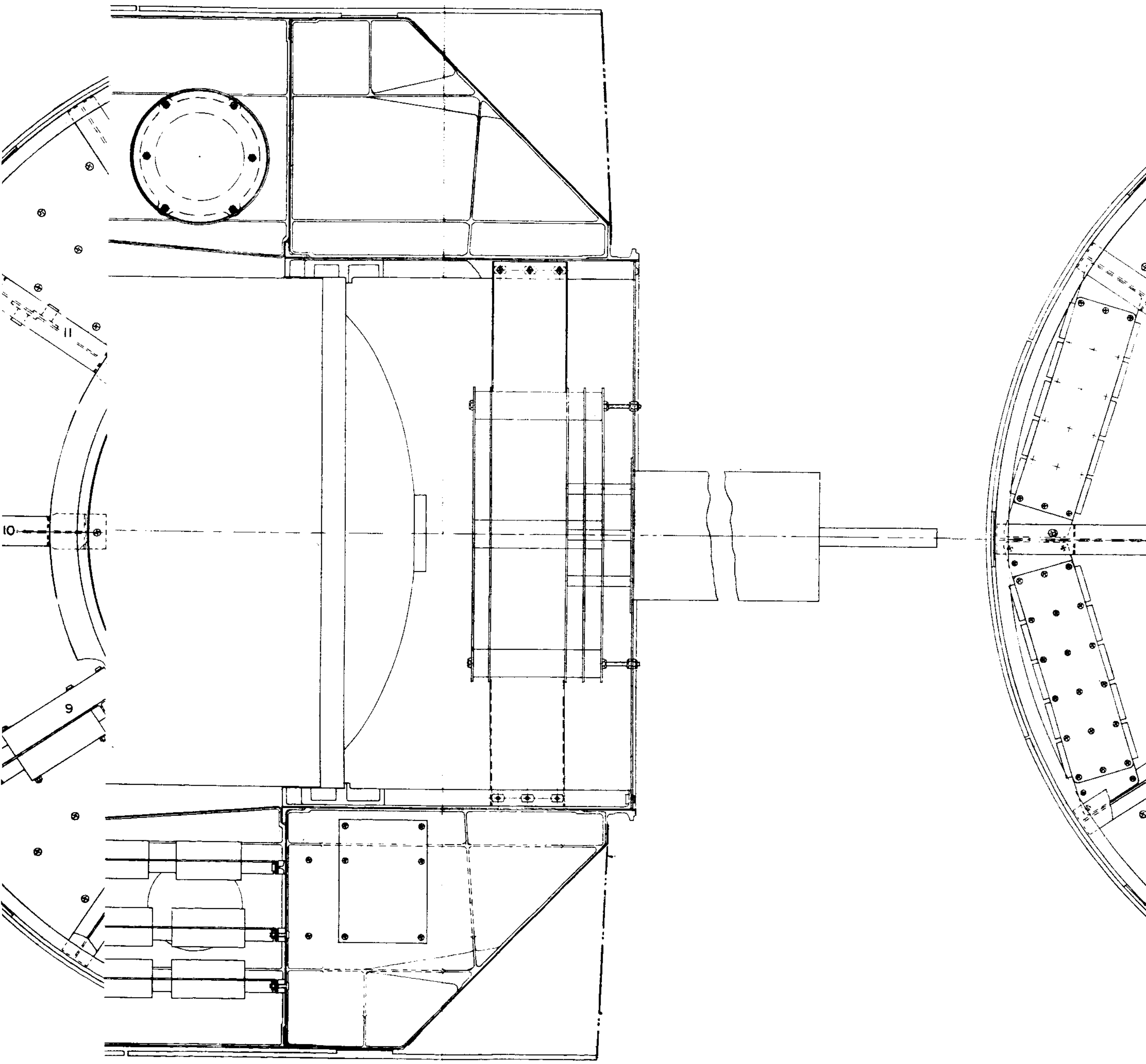

NTS ROTATED FOR CLARITY

3

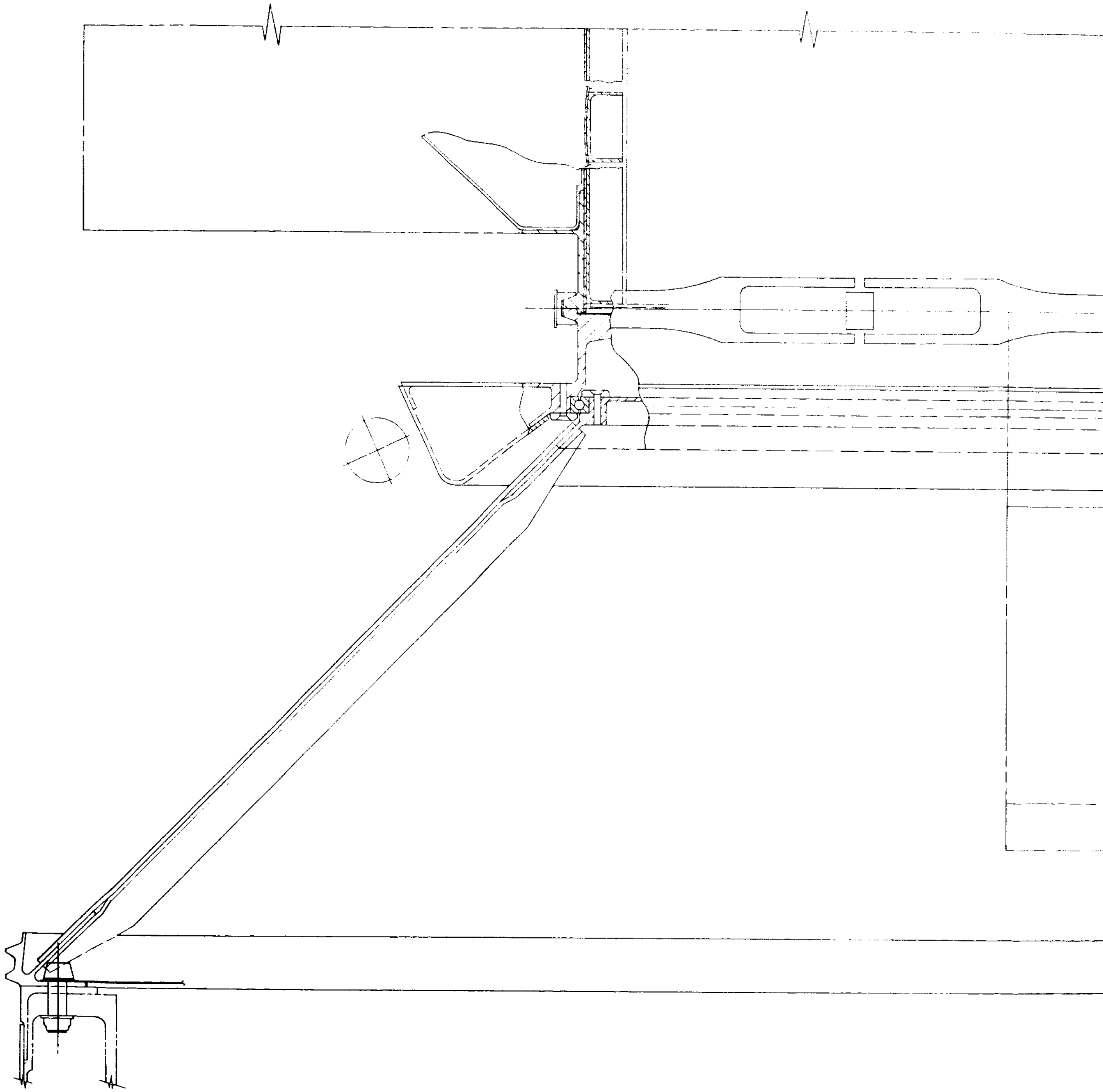

FIGURE 6-173. PROPOSED INTERFACE, SYNCOM MARK II — AGENA D

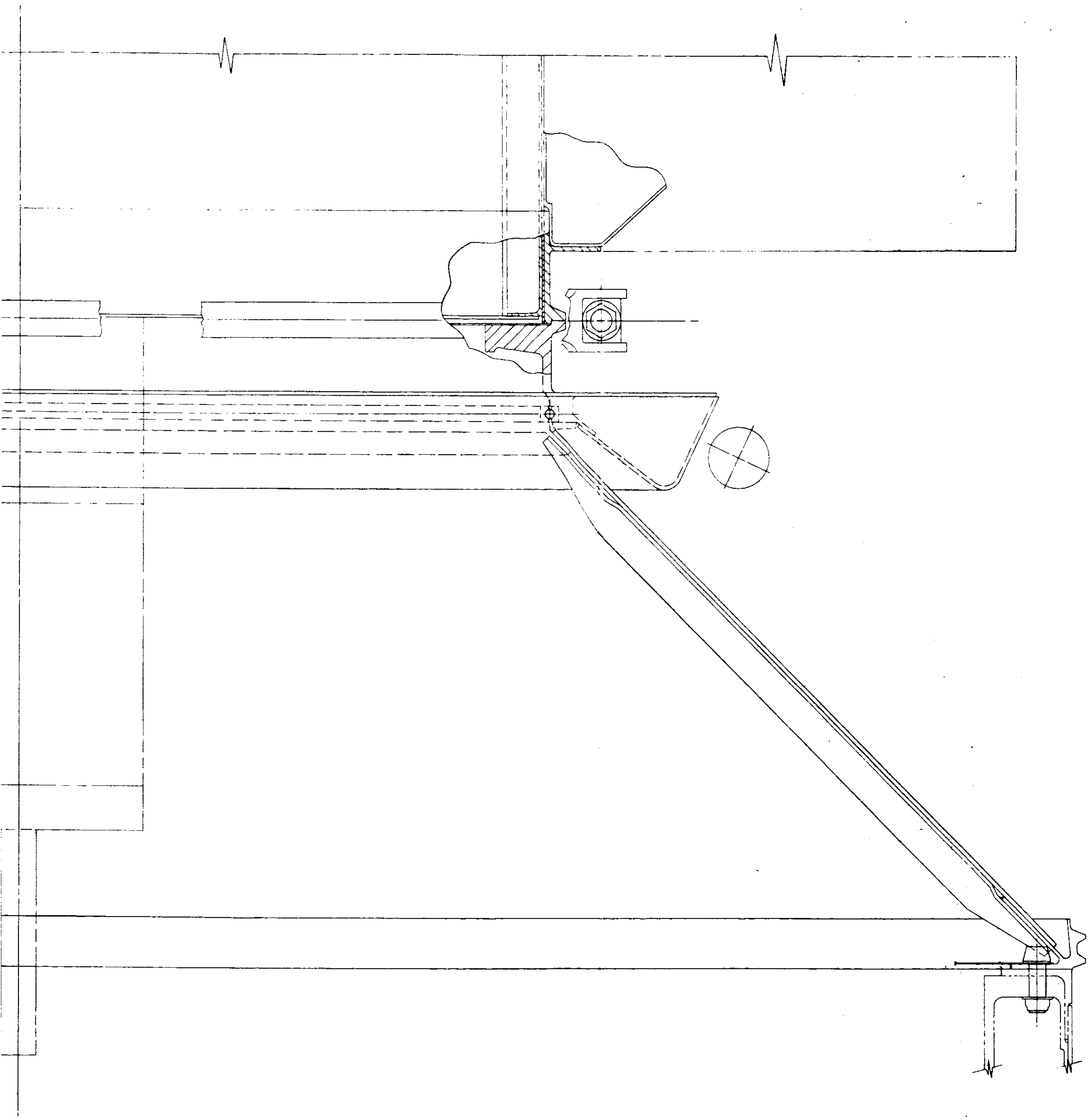

v

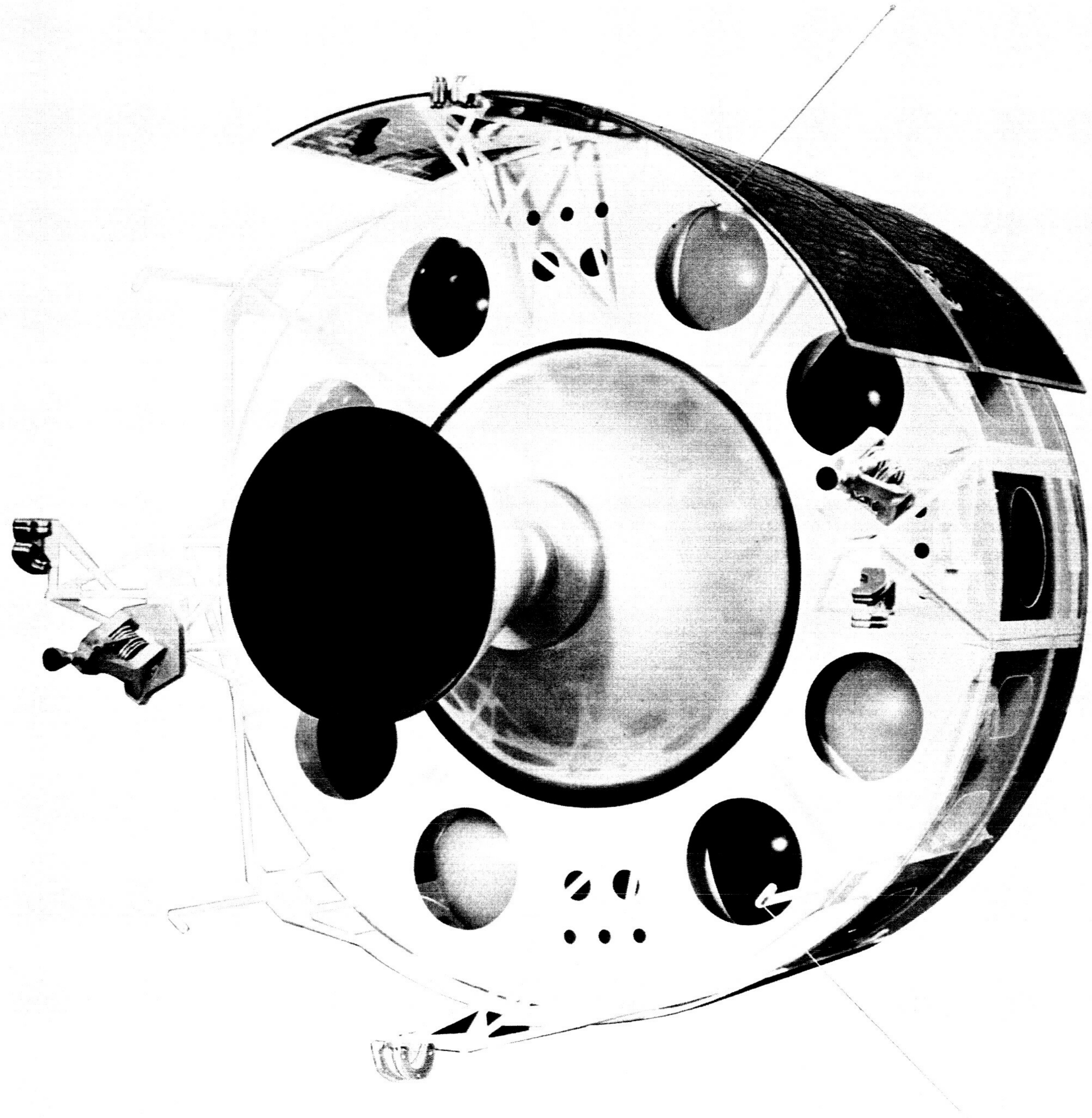

FIGURE 6-174. SYNCOM II SPACECRAFT MOCKUP STRUCTURE

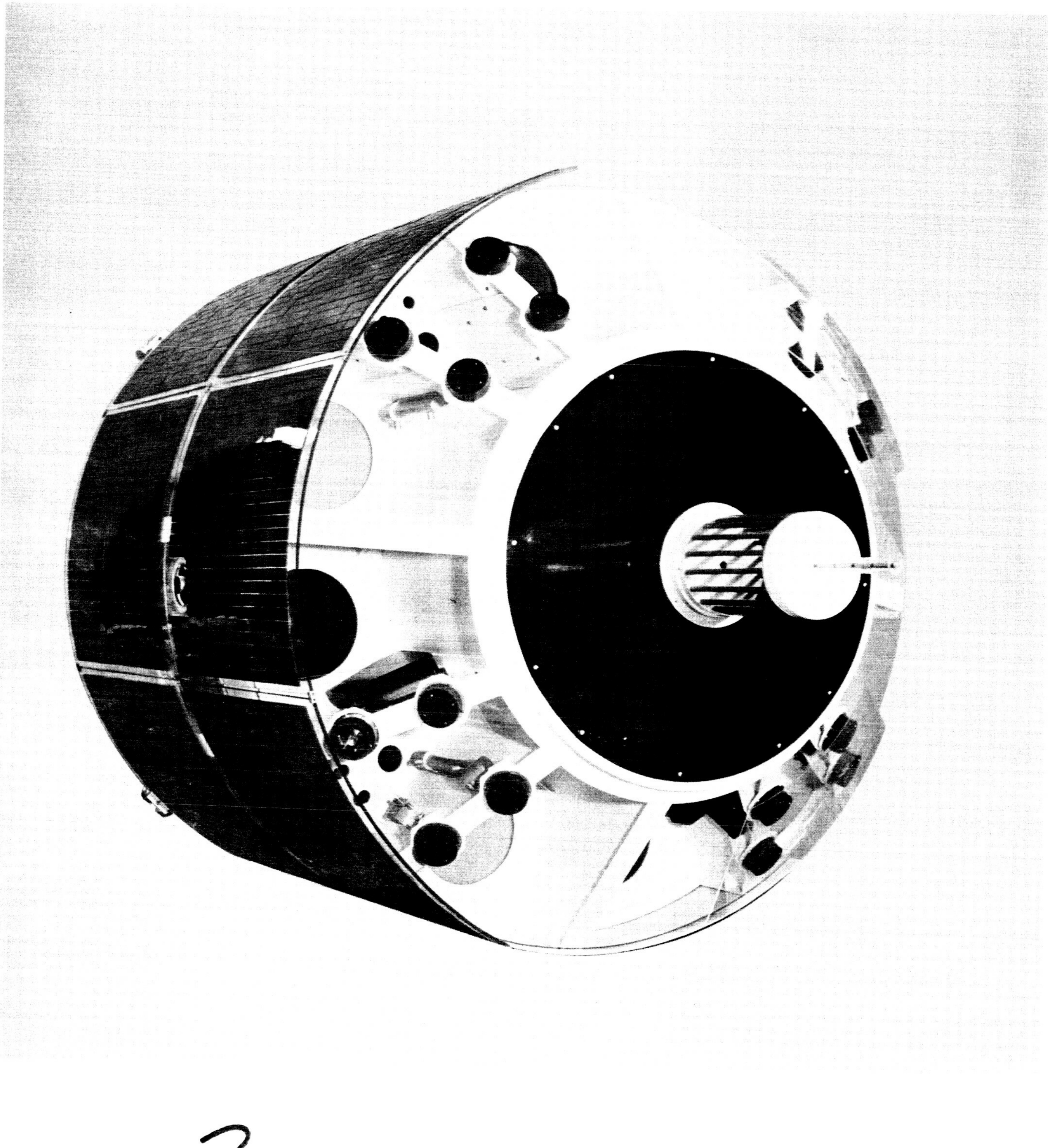

3

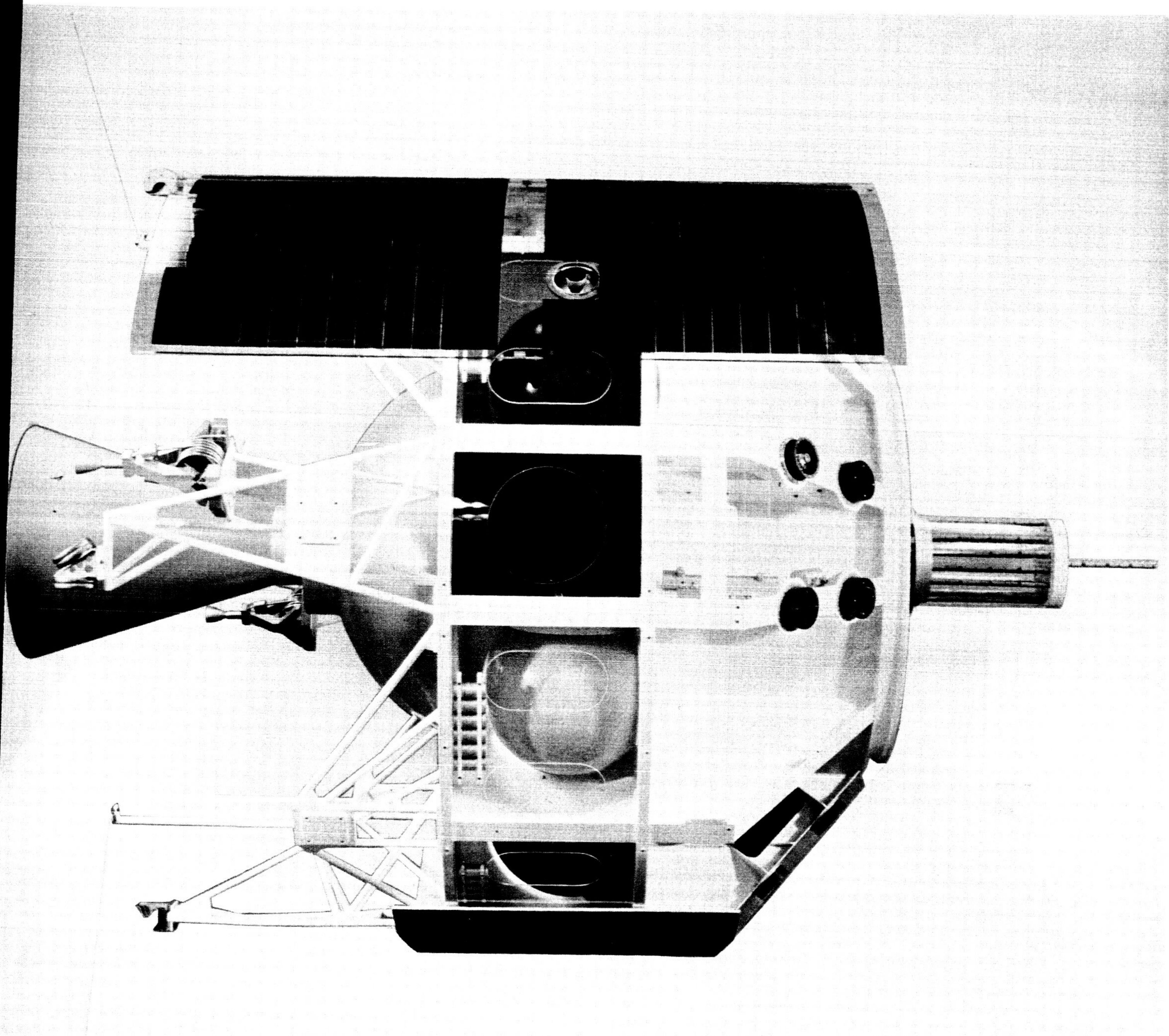

2

TABLE 6-21. SYNCOM II ESTIMATED WEIGHT STATUS
Engineering Model (HSX 302 T-1)

Subsystem	Weight, pounds
Electronics	134.7
Wire harness (ballast)	19.9
Power supply	103.3
Controls, inert	32.5
Propulsion, inert	122.2
Structure	142.1
Miscellaneous	60.1

Item	Weight, pounds	z-z	I_{z-z}	I_{x-x}	R/P
T-1: no motor, no fuel	508.2	21.3	54.2	37.4	1.45
$N_2H_3-CH_3$ fuel plus N_2	51.7				
N_2O_4 oxidizer plus N_2	83.2				
T-1: no motor	643.1	21.8	67.3	44.1	1.53
Apogee motor dummy plus installation	874.9				
T-1 fully loaded	1518.0	24.7	84.5	66.9	1.26

The development of a dynamically similar mathematical model of the T-1 spacecraft has constituted one of the major analytical efforts. The 1518-pound injected weight Syncom II is simulated. The model has been completed and will be used extensively during vibration testing of the T-1 spacecraft. The model will be utilized to anticipate the variations in response resulting from proposed reductions in the structural weight of T-1. In this function the model has the important advantage of reversibility, in that a structural modification which produces an undesirable response can be withdrawn. Modifications to structure which show good analytical results will then be applied to the T-1 spacecraft and investigated by vibration test. An additional use of the model will be that of predicting the change in resonant frequencies resulting from different boundary conditions. The resonances of the structure in the "free-free" condition (such as during apogee motor burning) or when mounted on the Agena vehicle will, in both cases, differ from the frequencies measured during vibration tests.

The analytical model is shown schematically in Figure 6-175. The longitudinal and lateral responses of the spacecraft are separately represented by seven degrees of freedom. Selection of the degrees of freedom was

TABLE 6-22. DYNAMIC LOADS EMPLOYED IN THE DESIGN OF THE ENGINEERING MODEL STRUCTURE

Environments

Sinusoidal Excitation (all three axes, log sweep at two octaves per minute, 4.6 minutes duration):

5-15 cps	0.25-inch double amplitude
15-250 cps	3 g peak
250-400 cps	5 g peak
400-3000 cps	7.5 g peak

Random Excitation (6 minutes along each of three axes):

20-80 cps	0.04 g^2/cps
80-1280 cps	Increasing from 0.4 g^2/cps at 1.22 db/octave
1280-5000 cps	0.07 g^2/cps

Shock Excitation (applied only to components, three shocks in each direction):

Longitudinal: 30 g sawtooth pulse of 0.015 second duration.
Lateral: 15 g sawtooth pulse of 0.015 second duration.

Responses	Maximum Longitudinal Response, g 0-Peak, approximately 80 cps	Maximum Lateral Response, g 0-Peak, approximately 40 cps
Antenna electronics	30	30
Traveling-wave tubes	30	30
Electronics packages	30	30
MMH and N_2 tanks	30	30
Telemetry transimtter	18	30
Converter	18	30
Solar panel	30	30
Battery pack	30	30
Thermal switch	18	30
Nutation damper	30	30

The general transmissibility envelope for components is given in Table 6-23.

TABLE 6-23. COMPONENT TRANSMISSIBILITY ENVELOPE

Frequency, cps	Longitudinal Amplification	Lateral Amplification
5-20	5	5
20-60	5	10
60-100	10	5
100-300	5	5
300-500	2	2
500-2000	1	1

based on symmetry of the spacecraft about the thrust axis and on individual component analyses. Detailed studies were performed on the bipropellant tanks and apogee motor to establish the best simulation for these elements in the complete model. A bipropellant tank study is described later in this section.

The equations of motion of the model are given in a later section and are based on the following assumptions:

1) In the axial modes the thrust tube remains circular with a diameter that varies linearly with length of the tube.
2) In the axial modes the radial component of apogee motor propellent displacement is negligible.
3) In the lateral modes the bending stiffness of the thrust tube-rib network is represented by a uniform beam. Bending contributes less than 30 percent of the total stiffness.
4) In the lateral modes the propellant stiffness is negligible.
5) In the lateral modes the bending stiffness of the apogee motor case and skirt are negligible.
6) Radial displacements of the forward and aft bulkheads are negligible.
7) The bending stiffnesses of the rib and tank mounting panel webs are negligible.
8) The normal force per unit length exerted by the rib on the thrust tube varies linearly along the length of the thrust tube.
9) Each quadrant electronics package may be represented by one mass.
10) Each pair of bipropellant tanks may be represented by a rigid mass at the composite center of gravity.

Development vibration testing during this period has been limited to solar panels. Vibration testing of the engineering model spacecraft was delayed to permit additional engineering acceptance testing of the communications system.

The solar panel development program has included qualification tests of six panels to date. A group of five panels was first tested without solar cells, diodes, or wiring to establish the best structural configuration. The difference in response characteristics between these panels and one having cells, diodes, and wiring was recognized and accepted to minimize development time. The second test phase consisted of qualification testing the best of the first five panels with solar cell covers, wiring and diodes installed. Solar cell covers slightly heavier than the flight version were installed to compensate for the unavailable solar cells.

All of the panels were of honeycomb construction; a 5052 aluminum honeycomb core was set between No. 112 fiberglass fabric face sheets. The face sheets were oriented with fibers running parallel to the panel edges and were 0.003 inch thick. Face sheets were bonded to the core using a wet layup technique and aromatic amine cured epoxy resin. All panel edges were filled with RE 1-19-1 epoxy syntactic foam. The characteristics of individual panels are given in Table 6-24.

The panels were attached to the shaker at the insert through a rigid fixture. A typical installation is shown

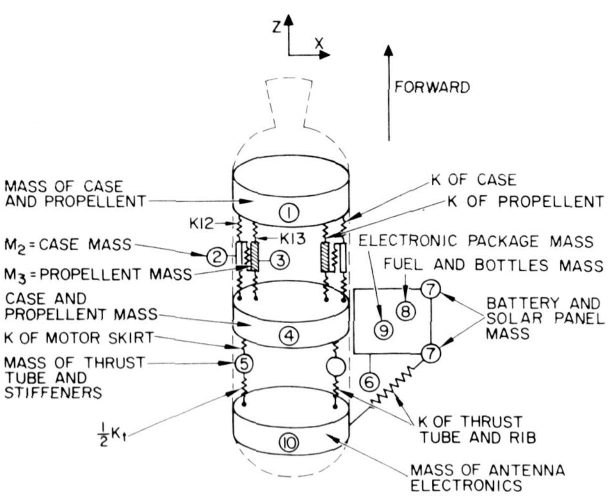

FIGURE 6-175. MATHEMATICAL MODEL SCHEMATIC

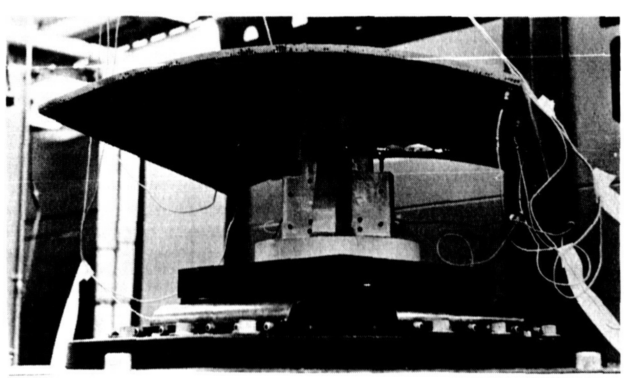

FIGURE 6-176. SOLAR PANEL VIBRATION TEST SETUP

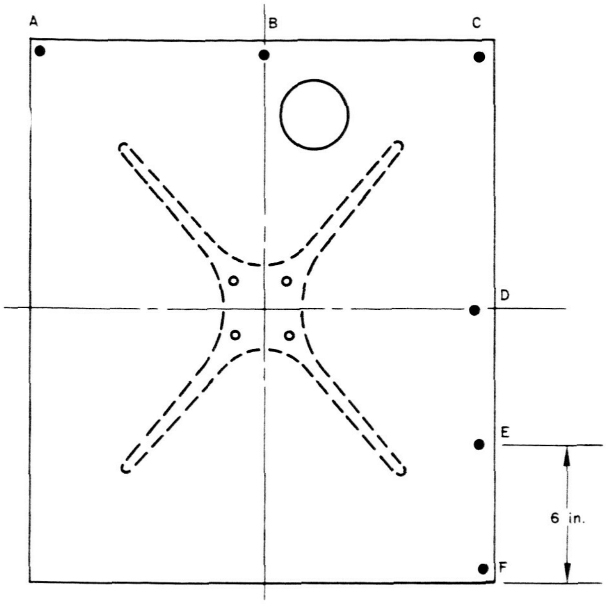

FIGURE 6-177. PANEL ACCELEROMETER LOCATIONS

in Figure 6-176. Resonant frequencies and mode shapes were obtained for lateral (perpendicular to panel) inputs during slow frequency sweeps from 5 to 2000 cps at 1 g input. The panels were then subjected to lateral sinusoidal qualification inputs as follows:

Frequency Range, cps	*Input*
2000-400	7.5 g peak
400-250	10 g peak
250-60	15 g peak
60-25	30 g peak
25-15	1 inch double amplitude
15-5	1/4 inch double amplitude

Frequency sweeps at qualification levels were run in the 2000 to 5 cps direction. The 60 to 25 cps band was entered first at 15 g and 22 g input, prior to attempting 30 g. None of the panels was tested beyond the 60 to 25 cps band at 22 g. All sweeps were performed at two octaves per minute.

The panel instrumentation consisted of seven accelerometers distributed as shown in Figure 6-177. Three additional accelerometers were attached at the top of the fixture to measure input along three orthogonal axes. Permanent recordings of accelerometer outputs were obtained with an oscillograph.

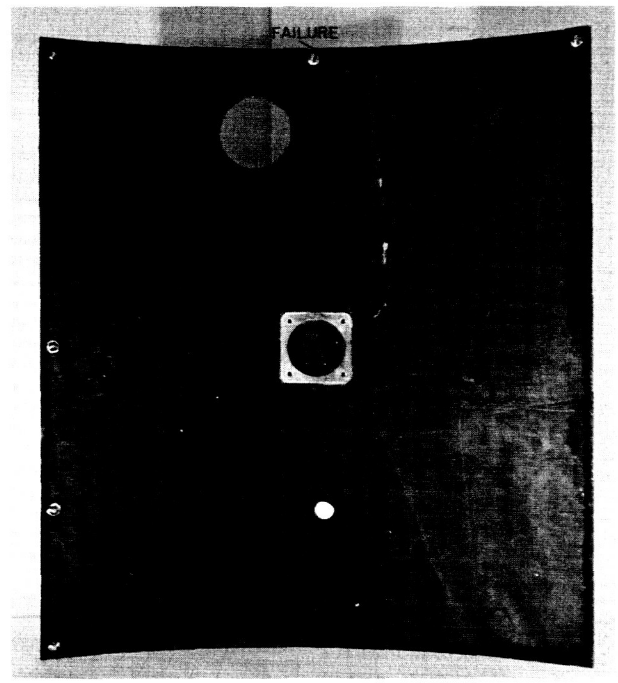

FIGURE 6-178. SOLAR PANEL CONFIGURATION "A" AT FAILURE

The results of the panel tests are summarized in Table 6-25 and Figures 6-178 through 6-182. All of the failures occurred in the second or higher panel mode. It was concluded that panel C would require excessive structural weight and development time to be acceptable, and this configuration was dropped from the program. The failure of panel C involved large relative deflections at the panel edge and complete fractures of the panel or cracks near three of the four stiffener legs. Panels A and B were modified to A1 and B1 and retested with the results shown in Table 6-25. The modification of panel B amounted to repair of the local face sheet separations. It was concluded from the results of testing A1 and B1 that a modified version of B1 would be the better configuration. This conclusion was drawn from the following observations:

1) The failures of panels A and A1 were in both cases at a lower input level than the failure of panel B1.
2) The failures of panels A and A1 were in both cases more severe than the failures of panels B

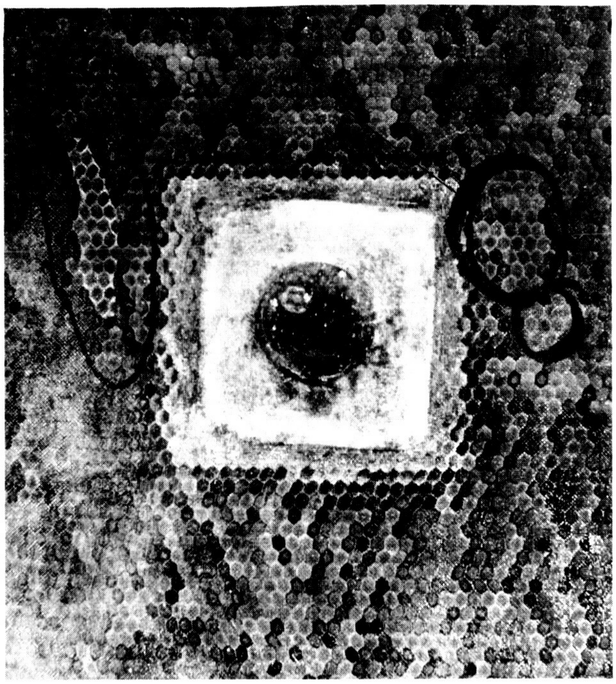

FIGURE 6-179. SOLAR PANEL CONFIGURATION "B" AT FAILURE

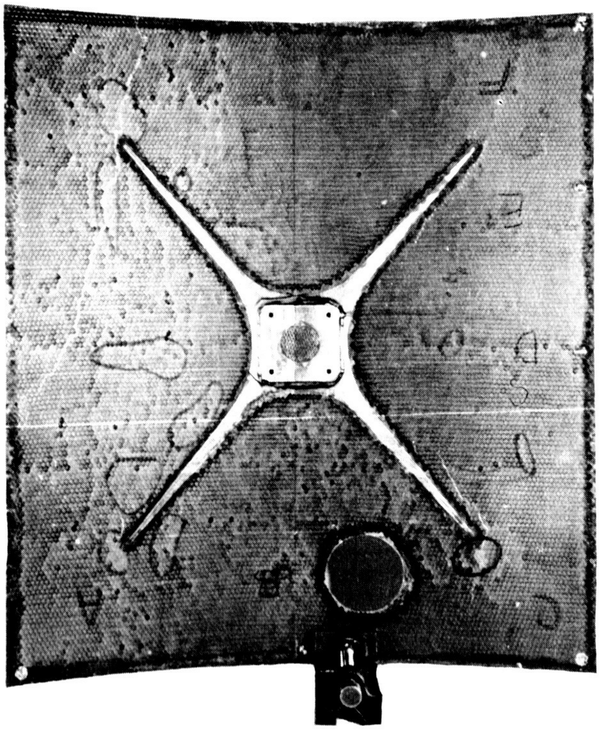

FIGURE 6-180. SOLAR PANEL CONFIGURATION "C" AT FAILURE

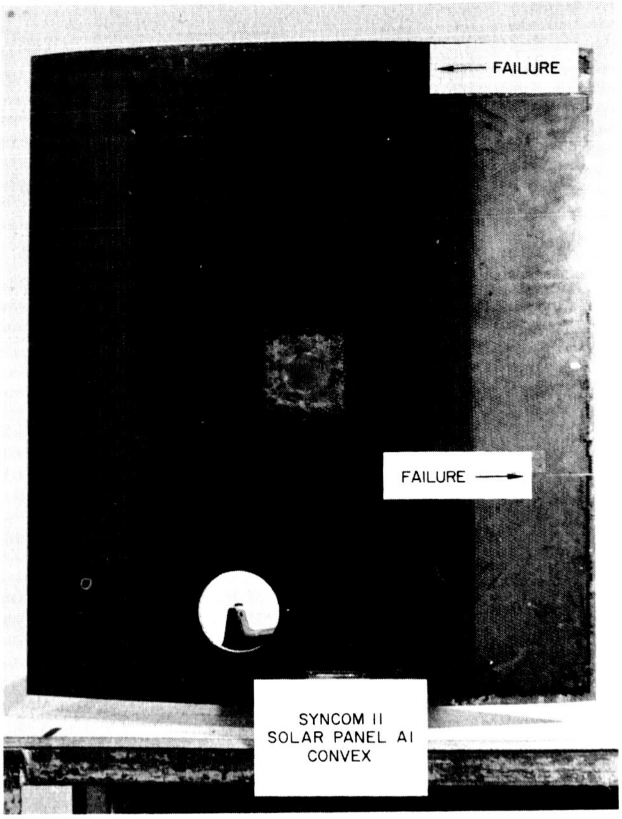

FIGURE 6-181. SOLAR PANEL CONFIGURATION "A" AT FAILURE

and B1. The type of failure which occurred on panel B was eliminated by improved bonding techniques.

3) Panel B1 would have weighed 1.09 pounds without the repair material. This was the lightest configuration to successfully qualify at 15 g input in the frequency band 25 to 60 cps.

Following the B1 test the panel was modified as shown in Table 6-24 and retested as configuration B2, with solar cell covers, diodes, and wiring. This failure of panel B2 is shown in Table 6-25 and Figure 6-182. This failure was significantly different from those of previous panels in that the failure line was in a lateral plane of the spacecraft, and bisecting the panel insert. As a result of this failure, the development program will be extended further, with approximately six configurations under study. In addition, it is anticipated that the solar panels which are mounted on the engineering model will be restrained during vibration test-

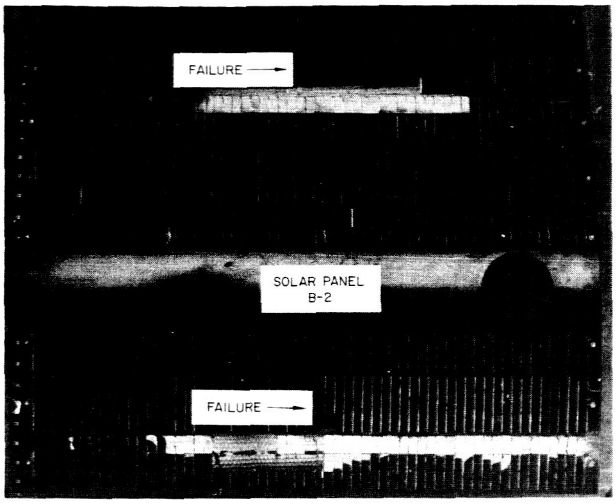

FIGURE 6-182. SOLAR PANEL CONFIGURATION "B-2" AT FAILURE

ing. This restraint will also provide a necessary thermal barrier against heat transmission between panels.

The stress analysis is given at the end of this section.

AXI-SYMMETRIC VIBRATIONS OF THIN PRESSURIZED SHELL FILLED WITH COMPRESSIBLE FLUID

This discussion is concerned with the axi-symmetric vibration of a thin spherical container filled with a compressible fluid under internal pressure. By axi-symmetric vibration, it is meant that the deflection pattern is symmetric with respect to a diameter so that planes taken normal to this diameter will always cut the sphere in a circular cross section. This is the type of vibration which will be encountered if the system is excited axially along a diameter.

The general approach to the solution of this problem is first to obtain the equations of motion for both the spherical shell under internal pressure, and for the compressible fluid. To account for the effect of internal pressure, the former required the consideration of second-order terms in the strain displacement relations. Upon solving the two sets of equations and imposing the continuity conditions of equal pressure and radial displacement at their common boundary, the frequency equation for the shell-fluid system is obtained.

Since this analysis was carried out for a compressible fluid, it is also applicable to a gas-filled spherical container as well. In addition, should the requirement occur, the analysis may be used to estimate the natural frequency of a spherical solid-propellant motor by using some reduced density to compensate for the mass of propellant that is vacated by the bore. Even though the analysis of a solid-propellant motor would require the satisfaction of additional continuity conditions which were not needed in this case, it should nevertheless give a good approximation for the frequency. The reason is that Young's modulus for the propellant is so small in comparison to the modulus for the shell; the additional stiffness resulting from the satisfaction of these additional boundary conditions is small.

Equations of Motion

The equations of motion for a spherical shell under internal pressure were derived by means of Hamilton's principle. This procedure requires the expression for both the kinetic and potential energy of the system. The kinetic energy of the system is given entirely by the vibrating shell. The potential energy of the system is composed of the membrane strain energy and the bending strain energy of the shell, and the potential energy of the fluctuating pressure which represents the interaction between the shell and fluid during vibration. In order to take into account the effect of internal pressure, it was necessary to consider second-order terms in the strain displacement relations.

If T is the kinetic energy of the system and U its potential energy, then according to Hamiliton's principle the equations of motion may be obtained by taking the time integral of the Lagrangian L, where $L = T\text{-}U$, stationary, i.e.,

$$\delta \int L dt = 0$$

The characteristic equation which ensures a stationary value for $\int L dt$ is

$$\frac{\partial L}{\partial q_i} - \frac{d}{dt}\left(\frac{\partial L}{\partial q_i}\right) - \frac{d}{dx}\left(\frac{\partial L}{\partial q_i'}\right) + \frac{d^2}{dx^2}\left(\frac{\partial L}{\partial q_i''}\right) - \cdots = 0$$

when the Lagrangian is a function of only one spatial coordinate x, which is the case for the sphere under axi-symmetric vibrations. In the above equation q_i is a displacement component, and the primes denote differentiation with respect to x. Application of this characteristic equation to the sphere gave the following two equations of motion

$$(1+k)\left(\frac{\partial^2 v}{\partial \phi^2}+\cot\phi\,\frac{\partial v}{\partial \phi}-v\cot^2\phi\right)-\nu v$$

$$+\frac{1}{12}\left(\frac{h}{a}\right)^2\left(\frac{\partial^3 w}{\partial \phi^3}+\cot\phi\,\frac{\partial^2 w}{\partial \phi^2}-\cot^2\phi\,\frac{\partial w}{\partial \phi}\right)$$

$$-(1+\nu+k)\frac{\partial w}{\partial \phi}-\frac{\rho a^2(1-\nu^2)}{E}\frac{\partial^2 v}{\partial t^2}=0 \qquad (6\text{-}19)$$

$$(1+\nu+k)\left(\frac{\partial v}{\partial \phi}+v\cot\phi-2w\right)$$

$$+k\left(\frac{\partial^2 w}{\partial \phi^2}+\cot\phi\,\frac{\partial w}{\partial \phi}\right)-\frac{1}{12}\left(\frac{h}{a}\right)^2$$

$$\left[\frac{\partial^3}{\partial \phi^3}+2\cot\phi\,\frac{\partial^2}{\partial \phi^2}-(\nu+\csc^2\phi)\frac{\partial}{\partial \phi}\right.$$

$$\left.+\cot\phi\,(1-\nu+\csc^2\phi)\right]\left(v+\frac{\partial w}{\partial \phi}\right)$$

$$+\frac{qa^2(1-\nu^2)}{Eh}-\frac{\rho a^2(1-\nu^2)}{E}\frac{\partial^2 w}{\partial t^2}=0 \qquad (6\text{-}20)$$

In these equations, v is the displacement component tangent to a meridian measured in the ϕ direction, w is the radial component of displacement normal to the shell surface, p is the density of the shell material, E is Young's modulus, "a" is the radius of the sphere, and h is the constant wall thickness of the shell. The fluctuating pressure q is the quantity which couples the oscillating spherical shell and the oscillating sphere of fluid. The factor k is dependent upon the internal pressure P_o and is defined by

$$k=\frac{P_o\,a\,(1-\nu^2)}{4\,Eh}$$

Determination of q

An expression for the fluctuating pressure q was obtained from the solution of a set of four linearized differential equations which governs the motion of a compressible inviscid fluid. Two of the equations were Euler's equations of motion, the third stated the conservation of mass, and the fourth was an equation of state which brought the physical properties of the fluid into the picture. These four equations were combined to yield the following differential equation, expressed in spherical coordinates, for q.

$$\frac{1}{C_o^2}\frac{\partial^2 q}{\partial t^2}=\frac{\partial^2 q}{\partial r^2}+\frac{2}{r}\frac{\partial q}{\partial r}+\frac{\cot\phi}{r^2}\frac{\partial q}{\partial \phi}+\frac{1}{r^2}\frac{\partial^2 q}{\partial \phi^2}$$

The subscript "o" refers to some reference state. (Note that by letting the velocity of sound c_o become infinite, the above equation will reduce to the case for an incompressible fluid.)

The above differential equation has the solution

$$q=Ar^{-1/2}\,J_{n+1/2}\left(\frac{\omega_n}{c_o}r\right)P_n(\cos\phi)\sin\omega_n t$$

where A is a constant of integration and ω_n is the natural frequency of the n^{th} mode. $J_{n+1/2}$ and P_n are the Bessel function of half order and the Legendre polynomial, respectively.

TABLE 6-24. SYNCOM II SOLAR PANEL CONSTRUCTION

Panel	Case Depth, inches	Insert Geometry, inches	Panel Weight, pounds	Convex Face Sheets	Concave Face Sheets
A	0.365	3 x 3 x 5/16 aluminum	1.35	2 full ply	2 full ply
B	0.245	3 x 3 x 1/8 aluminum	1.09	3 full ply	1 full ply, 4 ply staggered with widths of 17, 14, 11, and 8 inches
C	0.245	4 armed-1/8 aluminum	1.22	1 full ply	1 full ply
A1	0.365	3 x 3 x 5/16 aluminum	1.34	1 full ply, 2 ply staggered with widths of 13 and 11 inches	1 full ply, 2 ply staggered with widths of 13 and 11 inches
B1*	0.245	3 x 3 x 1/8 aluminum	1.38	3 full ply	1 full ply, 4 ply staggered with widths of 17, 14, 11, and 8 inches
B2	0.245	3 x 3 x 1/8 aluminum	2.54	1 full ply, 4 ply staggered with widths of 18, 14, 10 and 6 inches	1 full ply, 4 ply staggered with widths of 18, 14, 10, and 6 inches

*Configuration B1 is the same as configuration B. The increase in weight is due to the additional material used locally to repair the face sheet separations.

TABLE 6-25. SOLAR PANEL VIBRATION TEST RESULTS

Panel	Failure Frequency, cps	Resonant Frequency, cps	Double Amplitude Displacement at Failure, inches						
			Input	A	B	C	D	E	F
A	63	62	−0.075	+1.2	—	+1.4	+1.2	+1.1	+1.3
B	56	56	−0.085	+1.5	+0.1	+1.6	+1.2	+0.9	+1.1
C	48	41	−0.18	+1.3	−1.8	+1.5	+1.5	+1.0	+1.5
A1	70	70	90°, 0.06	+1.2	+0.4	+1.7	+1.0	+1.2	+1.2
B1	54	54	90°, 0.14	+2.1	90°, 1.2	+2.2	+2.2	+1.7	+2.3

Panel	Input at Failure, g	Failure Description
A	14.5	Concave face sheet separated from core, top to bottom of the panel (along Syncom thrust axis), and approximately ½ inch wide. (See Figure 4.)
B	13.1	Three local concave face sheet separations, the largest being 2½ inches long by ½ inch wide. (See Figure 5.)
C	21.1	Complete panel fractures or cracks near three stiffener legs. (See Figure 6.)
A1	15.0	Complete panel fracture extending in from top and side of panel. (See Figure 7.)
B1	20.2	Convex face sheet crack along insert.
B2	15.0	Panel fracture extending from one vertical edge of the panel to the other, approximately bisecting the panel. (See Figure 8.)

By means of the equation of motion for the fluid in the radial direction, it was possible to eliminate the constant A and express q in terms of the radial acceleration. When the resulting expression is evaluated at $r = a$, the q obtained is exactly the quantity which is to be substituted in Equation (A-1b). This value of q can be written in the form

$$q(a) = -m_f \left.\frac{\partial^2 w}{\partial t^2}\right]_{r=a} \qquad (6\text{-}21)$$

where m_f may be thought of as the apparent mass of fluid which is acting with each unit area of shell surface during vibration. It is defined by the relation

$$m_f = \frac{2\rho_o\, a\, J_{n+\frac{1}{2}}\left(\frac{\omega_n}{c_o}a\right)}{\left(\frac{\omega_n}{c_o}a\right)\left[J_{n-\frac{1}{2}}\left(\frac{\omega_n}{c_o}a\right) - J_{n+\frac{3}{2}}\left(\frac{\omega_n}{c_o}a\right)\right] - J_{n+\frac{1}{2}}\left(\frac{\omega_n}{c_o}a\right)} \qquad (6\text{-}22)$$

where ρ_o is the density of the fluid at some reference state.

Frequency Equation

The spatial part of the displacement components v and w have solutions in the form of Legendre and associated Legendre polynomials, respectively. Their substitution into the differential equation reduces them to algebraic ones from which the following frequency equation was obtained.

$$1 + \frac{m_f}{\rho h} = \frac{1}{\Omega_n^2\left[(1+k)(n^2+n-1) + \nu - \Omega_n^2\right]}$$
$$\Bigg\{(1+\nu+k)(1-\nu+k)\left[n(n+1)-2\right] + \frac{1}{12}\left(\frac{h}{a}\right)^2 n(n+1)\left[n(n+1) - (1-\nu)\right]\left[(1+k)(n^2+n-1)+\nu\right]$$
$$-\left[2(1+\nu+k) + \frac{1}{12}\left(\frac{h}{a}\right)^2 n(n+1)\left[n(n+1)-(1-\nu)\right]\right]\Omega_n^2\Bigg\}$$

The frequency parameter is defined by

$$\Omega_n^2 = \frac{\rho a^2 (1 - v^2)}{E} \omega_n^2$$

Numerical Example

Using the following tank parameters, which are representative for one version of the Advanced Syncom,

$a = 6$ inches

$h = 0.013$ inch

$E = 30 \times 10^6$ psi

$v = 0.3$

$$\rho = \frac{0.283}{386} \quad \frac{\text{lb-sec}^2}{\text{in}^4}$$

it was found that the fundamental frequency for the spherical shell alone was 3940 cps. This suggests that for all practical purposes this particular spherical shell may be considered as a rigid body. Hence, when the tank is only partially full, the frequency of the system will be governed by the sloshing frequencies of the fluid. It is interesting to note that an internal pressure of 400 psi (design pressure based on 184,000 psi ultimate and factor of safety of 2) produced only a 1.5 percent increase in frequency. On the other hand, the inertia of the fluid was found to have a considerable effect on the frequency. For an incompressible fluid with a specific gravity of 0.786, the unpressurized shell-fluid system had a fundamental frequency of 945 cps. If compressibility of the fluid is considered, this frequency will be further reduced by an estimated 5 percent.

Axial Vibration Model

The governing equations for the axial vibration case within the framework of assumptions set forth previously is given by

$$m_1\ddot{Z}_1 + C_{12}(\dot{Z}_1 - \dot{Z}_2) - C_{13}(Z_3 - Z_1) + K_{12}(Z_1 - Z_2) - K_{13}(Z_3 - Z_1) = 0$$

$$m_2\ddot{Z}_2 + C_{12}\{(\dot{Z}_2 - \dot{Z}_4) - (\dot{Z}_1 - \dot{Z}_2)\} - C_{23}(\dot{Z}_3 - \dot{Z}_2) + K_{12}\{(Z_2 - Z_4) - (Z_1 - Z_2)\} - K_{23}(Z_3 - {}_2) = 0$$

$$m_3\ddot{Z}_3 + C_{13}\{(\dot{Z}_3 - \dot{Z}_1) + (\dot{Z}_3 - \dot{Z}_4)\} + C_{23}(\dot{Z}_3 - \dot{Z}_2) + K_{13}\{(Z_3 - Z_1) + (Z_3 - Z_4)\} + K_{23}(Z_3 - Z_2) = 0$$

$$m_4\ddot{Z}_4 + C_{45}(\dot{Z}_4 - \dot{Z}_5) - C_{12}(\dot{Z}_2 - \dot{Z}_4) - C_{13}(\dot{Z}_3 - \dot{Z}_4) + K_{45}(Z_4 - Z_5) - K_{12}(Z_2 - Z_4) - K_{13}(Z_3 - Z_4) = 0$$

$$(m_5 + m_6 a_6^2 + m_8 a_8^2 + m_9 a_0^2) Z_5 + (m_6 a_6 b_6 + m_8 a_8 b_8 + m_9 a_9 b_9) Z_7 - C_{45}(Z_4 - Z_5) + C_t(Z_5 - Z_{10}) - C(Z_7 - Z_5) - K_{45}(Z_4 - Z_5) + K_t(Z_5 - Z_{10}) - K(Z_9 - Z_5) = 0$$

$$(m_7 + m_6 b_6^2 + m_8 b_8^2 + m_9 b_9^2) Z_7 + (m_6 a_6 b_6 + m_8 a_8 b_8 + m_9 a_9 b_9) Z_5 + \bar{C}(\dot{Z}_7 - \dot{Z}_5) + \bar{K}(Z_7 - Z_5) = 0$$

$$m_{10}\ddot{Z}_{10} - C_t(\dot{Z}_5 - \dot{Z}_{10}) - K_t(Z_5 - Z_{10}) = F(t)$$

where

m_1 = mass of aft section of motor, including propellant

m_2 = mass of center section of motor case

m_3 = mass of propellant in center section

m_4 = mass of forward section of motor, including propellant

m_5 = equivalent mass of thrust tube and stiffeners

m_6 = mass of ribs, thermal switches, . . .

m_7, m_7' = mass of batteries, solar panels plus distributed weight

m_8 = mass of fuel tanks plus distributed weight

m_9 = mass of quadrant electronics package plus distributed weight

m_{10} = mass of antenna electronics package

The spring constant K_{12} represents the spring located between mass m_1 and m_2. Similarly, C_{12} represents the damping between mass m_1 and m_2. This notation carries through for the other masses of the system. Where two springs have the same value because of symmetry, the prior notation introduced prevails. For example, $K_{24} = K_{12}$ but only notation K_{12} was retained.

The spring K_t is the linear spring of the tube, including the stiffeners and an effective width of the ribs. K is the equivalent spring constant for the ribs, mounting panels, and rotation of the sides of the thrust tube.

The constants a_6, b_6; a_8, b_8; and a_9, b_9 relate the displacements of masses m_6, m_8, and m_9 to the displacements on m_5 and m_7. The constants were obtained by assuming that the mounting panel experiences only shear, providing a linear relationship between Z_6, Z_8, Z_9, and Z_5, Z_7.

Lateral Vibration Model

In deriving the equations of motion for lateral excitation, it was more convenient to use influence coefficients. The equations are:

$$(X_1 - X_2) - \frac{\bar{Z}_1 - \bar{Z}_4}{\bar{Z}_2 - \bar{Z}_4}(X_2 - X_4) + g_{12}(\dot{X}_1 - \dot{X}_2) - \frac{\bar{Z}_1 - \bar{Z}_4}{\bar{Z}_2 - \bar{Z}_4} g_{24}(\dot{X}_2 - \dot{X}_4) = -\alpha_{12} m_1 \ddot{X}_1$$

$$(X_2 - X_4) - \frac{\bar{Z}_2}{\bar{Z}_4}(X_4 - X_5) + g_{24}(\dot{X}_2 - \dot{X}_4) - \frac{\bar{Z}_2}{\bar{Z}_4} g_{45}(\dot{X}_4 - \dot{X}_5) = -\alpha_{12}[m_1 \ddot{X}_1 + (m_2 + m_3)\ddot{X}_2]$$

$$(X_4 - X_5) + g_{45}(\dot{X}_4 - \dot{X}_5) = \bar{Z}_4(\alpha_{mm} \cdot m + \alpha_{mv} \cdot V) - \alpha_{45}[m_1 \ddot{X}_1 + (m_2 + m_3)\ddot{X}_2 + m_4 \ddot{X}_4]$$

$$(X_8 - X_5) + g_{58}(\dot{X}_8 - \dot{X}_5) = \bar{Z}_8(V_r - V_{m.p.}) + \bar{Z}_8(\alpha_{vm} \cdot V + \alpha_{mm} \cdot m)$$

$$(X_5 - X_{10}) + g_t(\dot{X}_5 - \dot{X}_{10}) = \alpha_{vv} \cdot V + \alpha_{vm} \cdot m$$

$$(X_5 - X_{10}) + g_t(\dot{X}_5 - \dot{X}_{10}) = (\alpha_{vv} + L\,\alpha_{mv})\, m_{10} \dot{X}_{10} - \alpha_{vv} F(t)$$

where

L = length of thrust tube

α_{12} = shear flexibility of motor case between mass m_1 and m_2.

α_{45} = shear flexibility of motor skirt

$\alpha_{vv}, \alpha_{vm}, \alpha_{mm}$ = influence coefficients for integral structure formed by bulkheads, mounting panels, ribs, and thrust tube.

V_r = shear angle of rib lying in the plane of excitation

$V_{m.p.}$ = shear angle of mounting panel lying in the plane of excitation.

The influence coefficients and shear strain are dependent upon the material constant and physical dimensions of the structural components.

The quantities V and m are the shear and moment due to the inertia force acting at a section just aft of mass m_5.

$$V = -[m_1 \ddot{X}_1 + (m_2 + m_3)\ddot{X}_2 + m_4 \ddot{X}_4 + (m_5 + m_6 + m_7 + m_7' + m_8 + m_9)\ddot{X}_5]$$

$$m = -[m_1 \ddot{X}_1 \bar{Z}_1 + (m_2 + m_3)\ddot{X}_2 \bar{Z}_2 + m_4 \ddot{X}_4 \bar{Z}_4 + m_7' \ddot{X}_7' \bar{Z}_7' + m_8 \ddot{X}_8 \bar{Z}_8 + m_9 \ddot{X}_9 \bar{Z}_9]$$

In these equations, $\bar{Z}_1$, $\bar{Z}_2$, etc., are the distances of mass m_1, m_2, etc., above the aft bulkhead measured in the Z direction.

The subscripts of the damping coefficients have the same meaning as in the axial model. However, the units in this case are different since we have displacement equations of motion instead of force equations of motion.

STRESS ANALYSIS

THRUST TUBE DRAWING NUMBERS
X209692 X209718

MATERIAL

7075-T6 aluminum alloy
QQ-A-2-87 sheet
QQ-A-2-83 plate

SECTION PROPERTIES

Assumed effective skin width = 1.13 inches

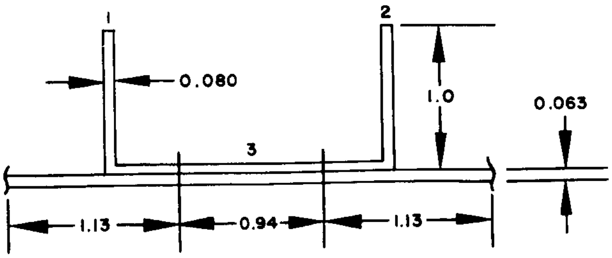

Item	A	y	Ay	Ay^2	Iox
1	0.0800	0.563	0.04500	0 02530	0.00666
2	0.0800	0.563	0.04500	0 02530	0.00666
3	0.1375	0.103	0.01417	0.00146	———
4	0.2020	0.0315	0.00636	0.00020	———
	0.4995		0.11053	0.05226	0.01332

$y = 0.221$ inch $Ay^2 = 0.0244$

$$
\begin{aligned}
I_x = {} & 0.05226 \\
& \underline{0.01332} \\
& 0.06558 \\
& \underline{0.0244} \\
& 0.04118 \text{ in}^4
\end{aligned}
$$

$$\rho = \sqrt{I/A}$$

$$= \sqrt{0.04118/0.4995}$$

$$= 0.287$$

TOTAL EFFECTIVE COMPRESSION AREA

$$A = 12 \times 0.4995 = 6.0 \text{ in}^2$$

EFFECTIVE BENDING SECTION

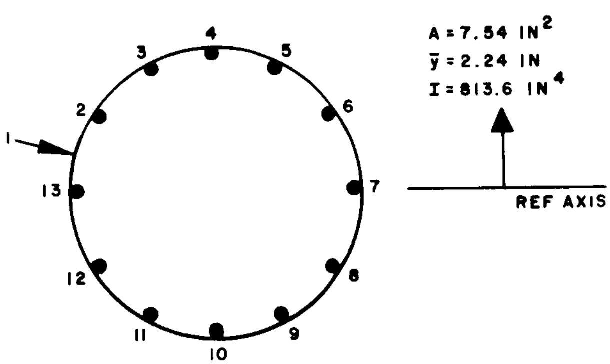

ASSUMPTIONS

1) Entire tension side is effective
   Stringer area $= 0.2975$ in^2
2) Computed compression area is effective
   area $= 0.4995$ in^2
   $y = 0.221$ in

Item		A	y	Ay	Ay^2	Iox
1	$\pi \times 15 \times .063$	2.9600	9.55	28.20	270.00	62.6
2		0.2975	8.12	2.42	19.70	
3		0.2975	12.29	3.64	44.60	
4		0.2975	14.712	4.37	64.40	
5		0.2975	12.29	3.64	44.60	
6		0.2975	8.12	2.42	19.70	
7		0.2975	0	0	0	
8		0.2975	−8.15	−4.07	33.20	
9		0.4995	−12.31	−6.15	75.60	
10		0.4995	−14.779	−7.38	109.00	
11		0.4995	−12.31	−6.15	75.60	
12		0.4995	−8.15	−4.07	33.20	
13		0.4995	0	0	0	
		7.5400		16.87	788.60	62.6

$y = 2.24$ in $\qquad Ay^2 = 37.6$

$$
\begin{aligned}
I_x = {} & 788.6 \\
& \underline{62.6} \\
& 851.2 \\
& \underline{37.6} \\
& 813.6 \text{ in}^4
\end{aligned}
$$

EFFECTIVE WIDTH COMPUTATIONS

$$F_{CRITICAL} = \frac{\pi^2 E}{(L/\rho)^2} = \frac{\pi^2 \times 10.5 \times 10^6}{(18.9/.287)^2}$$

$$= 23900 \text{ psi}$$

$$w = 0.85\, t \sqrt{E/F_c} \qquad \text{(Reference 6-11, page 374)}$$

$$= 0.85 \times 0.063 \sqrt{10.5 \times 10^6/23900} = 1.13 \text{ inches}$$

APPLIED LOADS

Axial Load and Lateral Load

$$P_c = 1518 \frac{\text{lb}}{\text{g}} \times 30.0\text{g} = 45500 \text{ lb}$$

Moment at Station 2.3 due to lateral load at c.g. of satellite: See Figure 6-183

$$M = 45500 \times (24.65 - 2.3) = 1{,}015{,}000 \text{ in-lb}$$

CALCULATED STRESSES

$$f_c = \frac{P}{A} = \frac{45500}{6.0} = 7590 \text{ psi}$$

$$f_B = \frac{Mc}{I} = \frac{1{,}015{,}000 \times 17.24}{813.6} = 21500 \text{ psi}$$

ALLOWABLE STRESS

$F_{cc} = 23600$ psi (column allowable)

MARGIN OF SAFETY

$$M.S._U = \frac{23600}{21500} - 1 = +0.10$$

THRUST TUBE RING DRAWING NUMBER X209716

MATERIAL

7075-T651 aluminum
QQ-A-283

SECTION PROPERTIES

$A = 2\pi rt$
$= 2 \times \pi \times 15 \times 0.140 = 13.2 \text{ in}^2$
$I = \pi r^3 t$
$= \pi \times 15^3 \times 0.140 = 1485 \text{ in}^4$

APPLIED LOADS

$P_C = 45500$ lb

MOMENT DUE TO AXIAL LOAD

$M = 45500 \times 24.65 = 1{,}120{,}000$ in-lb

CALCULATED STRESSES

$$f_C = \frac{P}{A} = \frac{45500}{13.2} = 3450 \text{ psi}$$

$$f_B = \frac{Mc}{I} = \frac{1{,}120{,}000 \times 15}{1485} = 11300 \text{ psi}$$

ALLOWABLE STRESSES

$$\frac{F_C}{\eta} = \frac{0.871\ E}{(R/t)^m\,(L/R)^n}$$ (Reference 6-12, page 3-32)

$$= \frac{0.871 \times 10.5 \times 10^6}{(15/0.140)^{1.245}\,(2.3/15)^{.47}} = 67000 \text{ psi}$$

(for 99 percent probability)

Assume allowable stress $= F_{CY} = 65000$ psi
(Reference 6-10, page 3.2.7.ob)

MARGIN OF SAFETY

$$M.S._U = \frac{65000}{11300} - 1 = +4.75$$

ATTACHMENTS OF THRUST TUBE TO THRUST TUBE RING

RIVETS

MS 20470 AD — 3/16 Diameter 188 Rivets
2117-T3 Aluminum (Reference 6-10, page 8.1.1.1.1c)
$F_{SU} = 0.30000$ psi
$P_S = 862$ pounds

APPLIED LOADS

Axial and Lateral Load

$P = 45500$ pounds
Moment at Station 0.00 due to lateral load at satellite c.g.
$M = 45500 \times 24.65 = 1{,}120{,}000$ in-lb

CALCULATED STRESSES

Axial Load Condition

$$P_S = \frac{45500}{188} = 242 \text{ lb/rivet (shear)}$$

Lateral Load Condition

$$P_S = \frac{2M}{nR} = \frac{2 \times 1{,}120{,}000}{188 \times 15} = 796 \text{ lb/rivet}$$

ALLOWABLE STRESSES

$P_S = 862$ pounds (Reference 6-10, page 8.1.1.1.1c)
$P_{BRU} = F_{BRU} \times D \times t$
$= 131000 \times 0.190 \times 0.140$
$= 3480$ pounds (not critical)

MARGIN OF SAFETY

$$M.S._U = \frac{862}{796} - 1 = +0.08$$

RIB, BULKHEAD STIFFENER DRAWING NUMBER X209690

MATERIAL

AZ31B — H24 magnesium
QQ-M-44

SECTION PROPERTIES (SECTION A-A)
(Aft bulkhead has not been included)

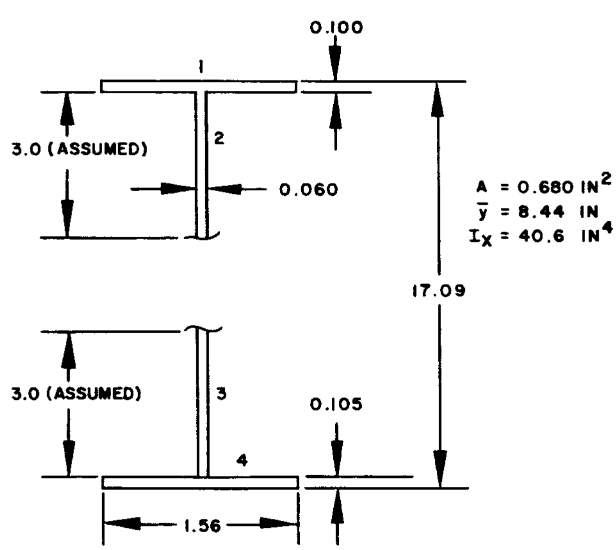

Item	A	y	Ay	Ay²	Iox
1	0.156	17.04	2.66	45.4	
2	0.180	15.49	2.78	43.0	
3	0.180	1.605	0.29	0.5	
4	0.164	0.052	—	—	
	0.680		5.73	88.9	0

$\bar{y} = 8.44$ $\quad Ay^2 = 48.3$ $\quad I_x = 88.9 - 48.3 = 40.6 \text{ in}^4$

APPLIED LOADS

Assume that 12 ribs react longitudinal load equally.

Equipment	Longitudinal	Lateral
Control system	$\frac{189.75 \times 30}{4 \times 2 \times 12} = 60 \frac{\text{lb}}{\text{in}}$	$^{*}\frac{189.75 \times 30}{4} = 1420$ lb
Batteries	$\frac{79.0 \times 30}{12} = 197$ lb	$\frac{79 \times 30}{12} = 197$ lb
Solar panels	$\frac{41.0 \times 30}{12} = 103$ lb	$\frac{41.0 \times 30}{12} = 103$ lb
Electronics	$\frac{20 \times 30}{2 \times 12} = 25 \frac{\text{lb}}{\text{in}}$	$\frac{20 \times 30}{2 \times 12} = 25 \frac{\text{lb}}{\text{in}}$
Structure	$\frac{110.65 \times 30}{12} = 277$ lb	$\frac{110.65 \times 30}{12} = 277$ lb

*Entire side load on one rib.

The critical loaded rib will be subjected to the control system loads. The electronics load is for reference only.

Longitudinal and lateral loads are applied independently.

Loads at Section A-A due to longitudinal forces:

$$60 \times 13 \times 6.5 = 5070$$
$$277 \times 6.5 = 1800$$
$$300 \times 13 = 3900$$
$$M = 10770 \text{ in-lb}$$
$$V = 60 \times 13 + 277 + 300 = 1357 \text{ lb}$$

Loads at Section A-A due to lateral forces:

$$1697 \times 15.83 = 26900$$
$$197 \times 15.56 = 3060$$
$$103 \times 18.56 = 1910$$
$$M = 31870 \text{ in-lb}$$
$$P = 1697 + 197 + 103 = 1997 \text{ lb}$$

CALCULATED STRESSES

$$f_c = \frac{Mc}{I} + \frac{P}{A}$$
$$= \frac{31870 \times 8.65}{40.6} + \frac{1997}{0.680} = 9740 \text{ psi}$$

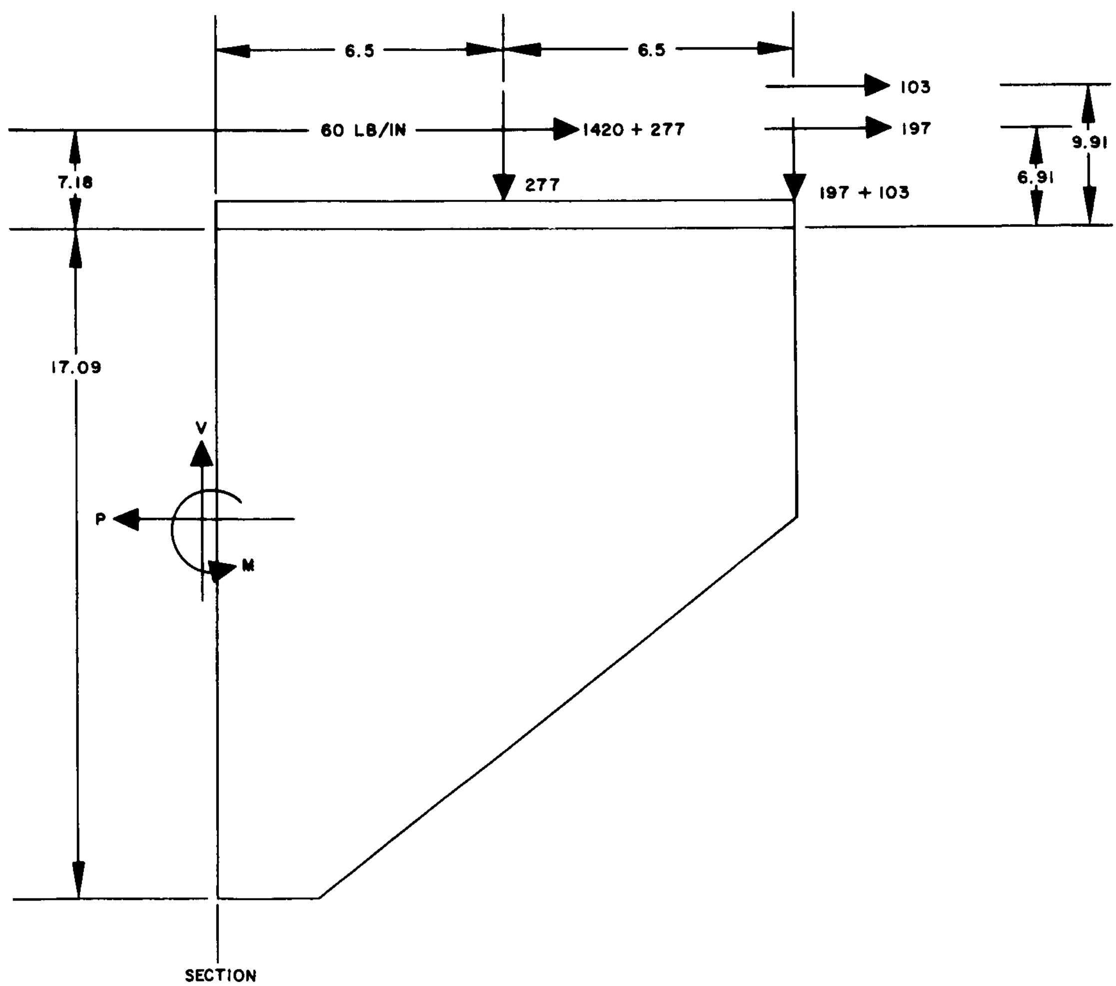

ALLOWABLE STRESS

$b/t = 0.78/0.100 = 7.8$

$$F_C = \frac{0.316\sqrt{F_{CY} \times E}}{(b/t)^{.75}} \qquad \text{(Reference 6-13, page 217)}$$

$$= \frac{0.316\sqrt{10000 \times 6.5 \times 10^6}}{(7.8)^{.75}} > F_{cy}$$

$F_C = 10000$ psi

MARGIN OF SAFETY

$$M.S._U = \frac{10000}{9740} - 1 = +0.03$$

WEB SHEAR STRESS

$$f_s = \frac{V}{A} = \frac{1357}{(17.09 - 6)0.060} = 2040 \text{ psi}$$

ALLOWABLE STRESS

$a/b = 11.09/6.76 = 1.64 \qquad K_S = 6.0$

$F_{SCR} = KE(t/b)^2$ (Reference 2, page 394)

$$= 6.0 \times 6.5 \times 10^6 \left(\frac{0.060}{6.76}\right)^2 = 3070 \text{ psi}$$

MARGIN OF SAFETY

$$M.S._U = \frac{3070}{2040} - 1 = +0.50$$

LOCAL FLANGE BENDING, DUE TO
SOLAR PANEL ATTACHMENTS

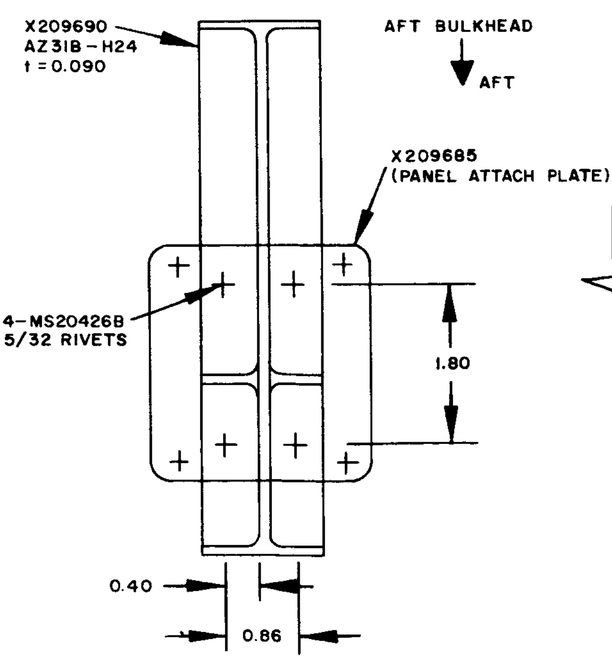

APPLIED LOADS

This attachment supports one solar panel

$$P = \frac{41.0 \times 30}{16} = 76.9 \text{ lb/panel}$$

Torque applied to rib due to lateral load condition:

$$T = 38.45 \times \frac{22}{2} = 424 \text{ in-lb}$$

LOAD/RIB ATTACHMENT

$$P = \frac{424}{2 \times 0.86} = 246 \text{ pounds}$$

MOMENT AT 0.090 RIB FLANGE

$M = 246 \times 0.40 = 98.5$ in-lb

CALCULATED STRESS

$$f = \frac{6\,M}{b\,d^2} = \frac{6 \times 98.5}{{}^*2 \times 0.090^2} = 36500 \text{ psi}$$

*Assumed effective bending section

ALLOWABLE STRESS

$F_{BU} = 1.25 \times F_{TU}$
$= 1.25 \times 34000 = 42500$ psi

MARGIN OF SAFETY

$$M.S._U = \frac{42500}{36500} - 1 = +0.16$$

ATTACHMENTS, RIB BULKHEAD STIFFENER TO THRUST TUBE

RIVETS

MS 20470B — 3/16 diameter
5056 aluminum (Reference 6-10, page 8.1.1.1.1c)
$F_{SU} = 28000$ psi
$P_S = 802$ pounds

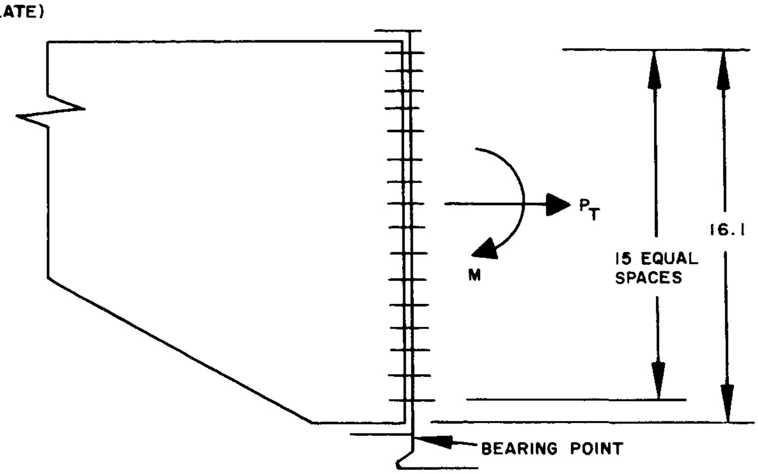

By assuming on Mc/I stress distribution in the fastener pattern, the fastener tension load can be expressed as

$$P_N = \frac{M \ell_N}{m \Sigma \ell_i^2}$$

M = moment on fastener pattern

ℓ_N = distance from fastener to bearing point

$\Sigma \ell_i^2$ = summation of distances squared from all fasteners to bearing point

m = number of rows of fasteners

$\ell_N = 16.1$

$m = 2$

$$\ell_i^2 = 16.1^2 + 15.07^2 + 14.04^2 + 13.01^2 + 11.98^2 + 10.95^2 + 9.92^2 + 8.89^2 + 7.86^2 + 6.83^2 + 5.80^2 + 4.77^2 + 3.74^2 + 2.71^2 + 1.68^2 + .65^2 = 1481$$

APPLIED LOADS

$M = 31870$ in-lb

$P_T = 1997$ pounds

CALCULATED FASTENER LOAD

$$P_N = \frac{31870 \times 16.1}{2 \times 1481} + \frac{1997}{32} = 236 \text{ pounds}$$

ALLOWABLE FASTENER LOAD

$P_T = 401$ pounds
(assumed to be 50 percent of shear value)

MARGIN OF SAFETY

$$M.S._U = \frac{401}{236} - 1 = +0.70$$

PANEL, MOUNTING DRAWING NUMBER X209678

MATERIAL

7075-T651 aluminum
QQ-A-283

SECTION PROPERTIES

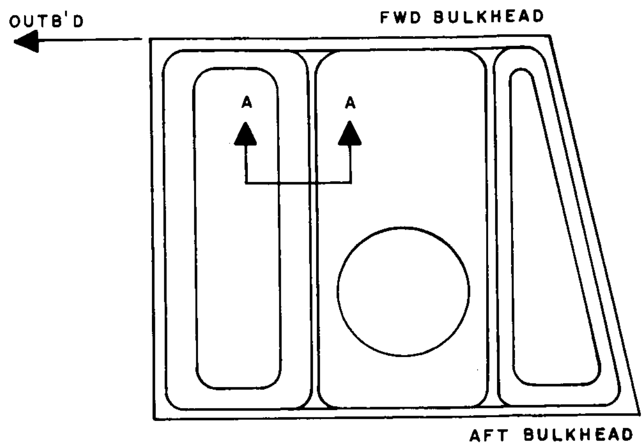

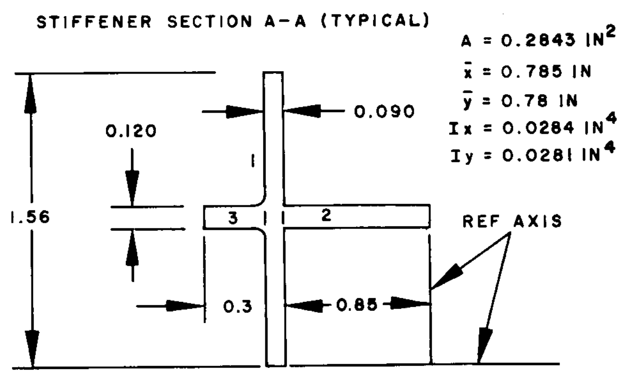

$x = 0.785 \quad Ax^2 = 0.175 \qquad I_y = 0.1831 + 0.020 - 0.175 = 0.0281$

$y = 0.78 \quad Ay^2 = 0.73 \qquad I_x = 0.1730 + 0.0284 - 0.173 = 0.0284$

APPLIED LOADS

Lateral Load (normal to panel or inboard-outboard direction)

$$*P = \frac{189.75 \times 30}{4} = 1420 \text{ pounds}$$

*Entire side load on one panel.
Each stiffener must be capable of resisting 710 pounds.

LOADS ON STIFFENER

REACTION AT AFT BULKHEAD

$$R = \frac{355\ (6.15 + 9.78)}{12.72} = 444 \text{ pounds}$$

Item	A	x	y	Ax	Ax^2	Ioy	Ay	Ay^2	Iox
1	0.1403	0.895	0.78	0.1258	0.1125	—	0.1095	0.0854	0.0284
2	0.1020	0.425	0.78	0.0433	0.0184	0.020	0.0795	0.0620	—
3	0.0420	1.115	0.78	0.0468	0.0522		0.0328	0.0256	—
	0.2843			0.2159	0.1831	0.020	0.2218	0.1730	0.0284

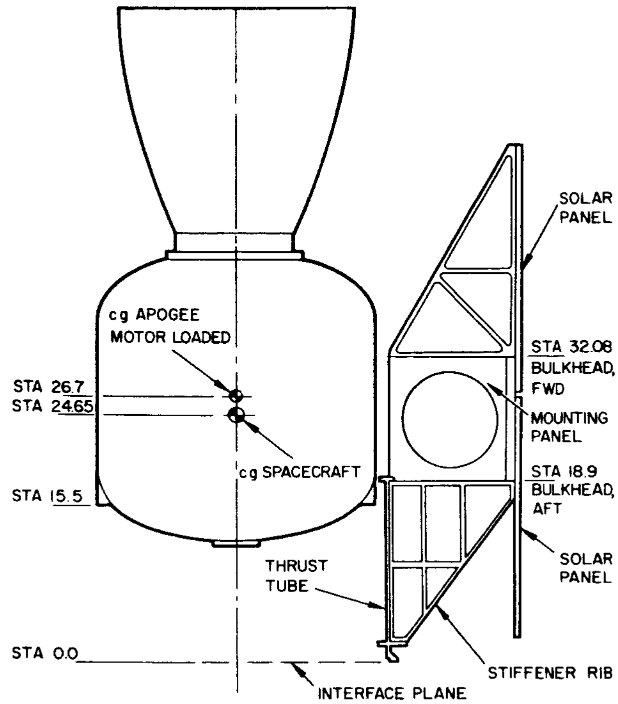

FIGURE 6-183. VIEW SHOWING PRIMARY STRUCTURAL DETAILS OF THRUST TUBE, STIFFENER RIB, AND BULKHEADS

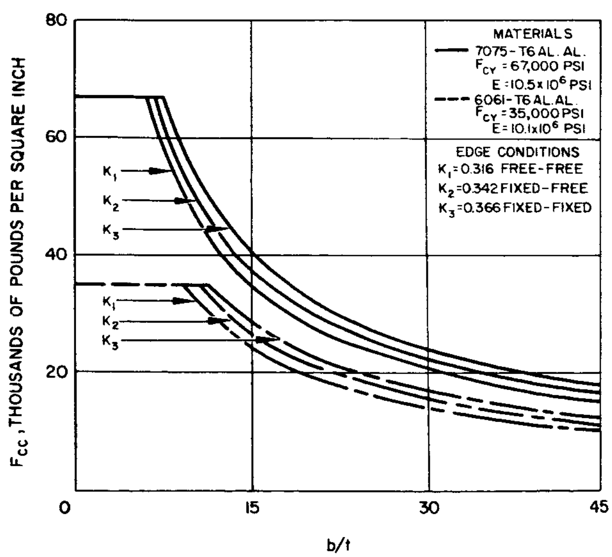

FIGURE 6-184. ALLOWABLE CRIPPLING STRESS VERSUS b/t

$$F_{cc} = \frac{K}{(b/t)\ 0.75} F_{cy}\,E$$

REACTION AT FORWARD BULKHEAD

$R = 710 - 444 = 266$ pounds

MAXIMUM BENDING MOMENT

$M = 266 \times 6.15 = 1640$ in-lb

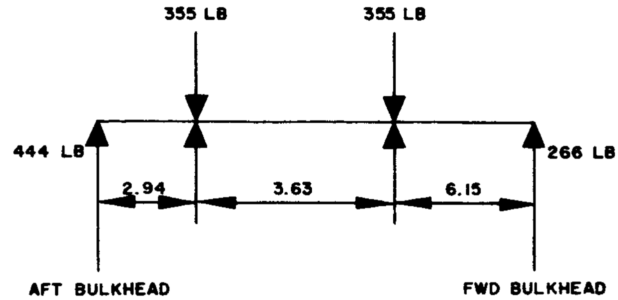

CALCULATED STRESSES

$$f_B = \frac{Mc}{I} = \frac{1640 \times 0.78}{0.0284} = \frac{45100 \text{ psi}}{\text{(normal to panel)}}$$

$$f_B = \frac{Mc}{I} = \frac{1640 \times .785}{0.0281} = \frac{45900 \text{ psi}}{\text{(inboard-outboard)}}$$

ALLOWABLE STRESS

$b/t = 0.78/0.090 = 8.65$ $\quad F_{cc} = 52000$ psi

(Refer to Figure 6-184)

$b/t = 0.85/0.120 = 7.1$ $\quad F_{cc} = 67000$ psi

MARGIN OF SAFETY

$$M.S._u = \frac{52000}{45100} - 1 = +0.15$$

AFT BULKHEAD DRAWING NUMBER X209689

MATERIAL

0.050 2024-T3 aluminum sheet
QQ-A-355

APPLIED LOADS

Assume the stiffener loads of the mounting panel shear into the aft bulkhead and are resisted at the inner ring segment and the outer ring segments. The stiffener load at the aft bulkhead is 444 pounds.

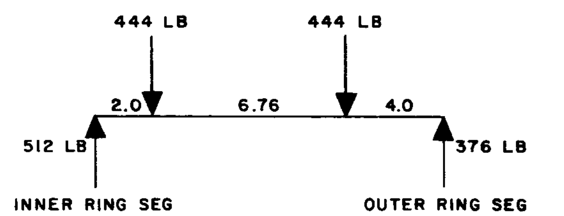

REACTION AT INNER RING SEGMENT

$$R = \frac{444\,(10.76 + 4.0)}{12.76} = 512 \text{ pounds}$$

REACTION AT OUTER RING SEGMENT

$R = 888 - 512 = 376$ pounds

Bulkhead shear load is 512 pounds

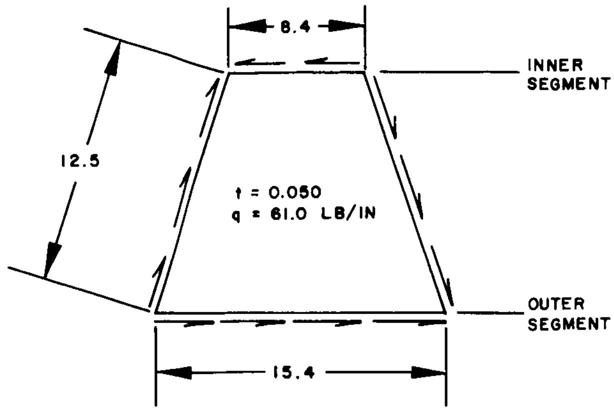

$$\text{Shear flow } (q) = \frac{512}{8.4} = 61.0 \, \frac{\text{lb}}{\text{in}}$$

CALCULATED STRESS

$$f_s = \frac{q}{t} = \frac{61.0}{0.050} = 1220 \text{ psi}$$

ALLOWABLE STRESS

$a/b = 12.5/11.9^* = 1.05$ $\qquad k_s = 7.2$

*Average of 8.4 and 15.4.

$F_{S_{CR}} = KE\,(t/b)^2$ $\qquad$ (Reference 2, page 394)

$$= 7.2 \times 10.5 \times 10^6 \left(\frac{0.050}{11.9}\right)^2 = 1330 \text{ psi}$$

MARGIN OF SAFETY

$$M.S._u = \frac{1330}{1220} - 1 = +0.09$$

RING SEGMENT, INNER DRAWING NUMBER X209676

MATERIAL

0.050 AZ 31D-H24 magnesium sheet
QQ-M-44

APPLIED LOADS

Assume the stiffener loads of the mounting panel shear into the forward bulkhead and are resisted at the inner and outer ring segments. The stiffener load at the forward bulkhead is 266 pounds.

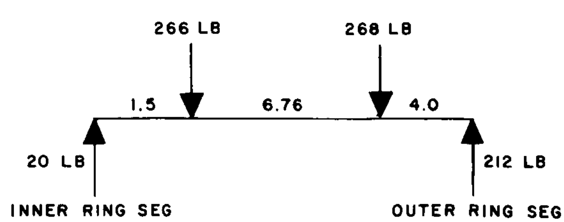

REACTION AT INNER RING SEGMENT

$$R = \frac{266\,(10.76 + 4.0)}{12.26} = 320 \text{ pounds}$$

REACTION AT OUTER RING SEGMENT

$$R = 532 - 320 = 212 \text{ pounds}$$

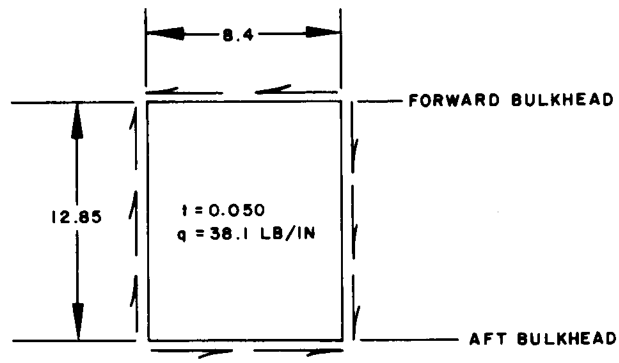

Inner segment shear load is 320 pounds

$$\text{Shear flow } (q) = \frac{320}{8.4} = 38.1 \, \frac{\text{lb}}{\text{in}}$$

CALCULATED STRESS

$$f_s = \frac{q}{t} = \frac{38.1}{0.050} = 760 \text{ psi}$$

ALLOWABLE STRESS

$a/b = 12.85/8.4 = 1.53$ $\qquad K_s = 6.0$

$F_{S_{CR}} = KE\,(t/b)^2$ $\qquad$ (Reference 6-11, page 394)

$$= 6.0 \times 6.5 \times 10^6 \left(\frac{0.050}{8.4}\right)^2 = 1380 \text{ psi}$$

MARGIN OF SAFETY

$$M.S._U = \frac{1380}{760} - 1 = +0.81$$

BATTERY SUPPORT, AFT

MATERIAL

Supports
6061-T6 aluminum alloy $t = 0.050$ inch
QQ-A-327

Cover plates
7075-T6 aluminum alloy $t = 0.063$ inch
QQ-A-287

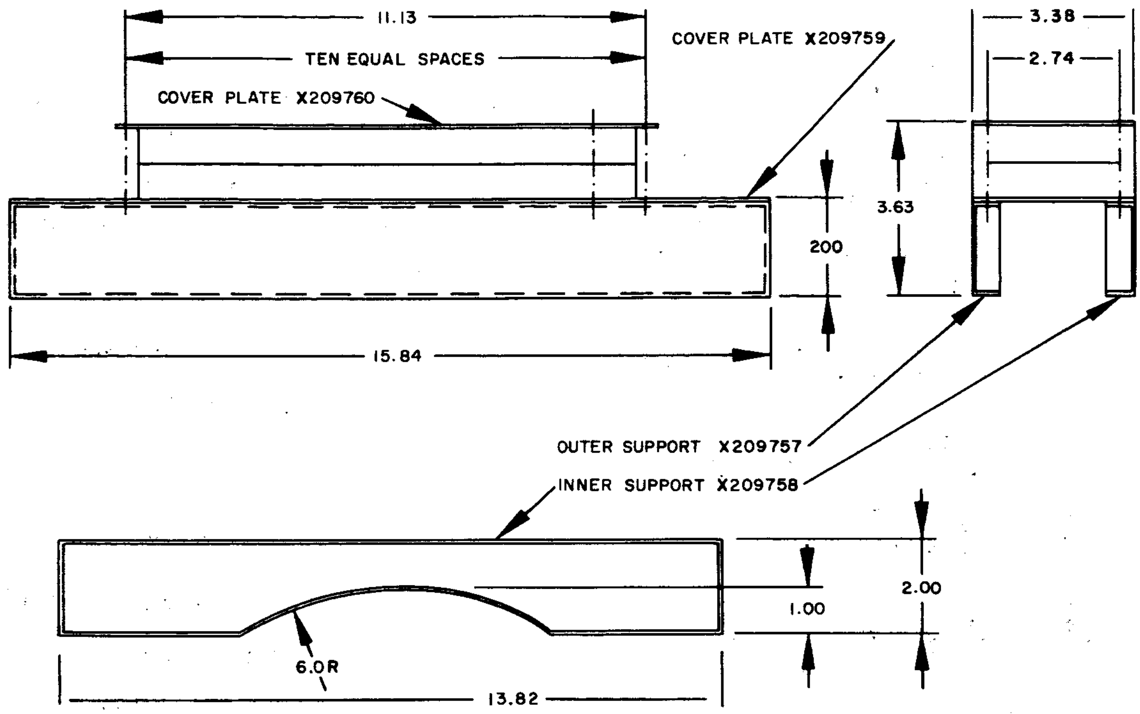

BATTERY SUPPORT, AFT

	A	X	AX	AX^2	I_{OY}	Y	AY	AY^2	I_{OX}
1	0.0300	0.300	0.00900	0.0027	0.0009	0.025	0.00075	0.00002	—
2	0.0450	0.025	0.00113	0.00003	—	0.500	0.02250	0.01125	0.00416
3	0.0300	0.300	0.00900	0.0027	0.0009	0.975	0.02930	0.01860	—
	0.1050		0.01913	0.00543	0.0018		0.05255	0.03987	0.00416

$$X_1 = \frac{0.01913}{0.105} = 0.1825 \text{ inch}$$

$$I_{Y_1} = 0.00723 - 0.00349 = 0.00374 \text{ in}^4$$

$$Y_1 = 0.500 \text{ inch}$$

$$I_{X_1} = 0.04403 - 0.02625 = 0.01778 \text{ in}^4$$

	A	X	AX	AX^2	I_{OY}	Y	AY	AY^2	I_{OX}
1	0.1050	0.1825	0.01913	0.003495	0.00374	0.50	0.0525	0.02625	0.01778
2	0.0630	0.500	0.03150	0.015250	0.00525	1.032	0.0651	0.06725	—
	0.1680		0.05063	0.018745	0.00899		0.1176	0.09350	0.01778

$$X = \frac{0.05063}{0.1680} = 0.301 \text{ inch}$$

$$I_Y = 0.0277 - 0.01525 = 0.0124 \text{ in}^4$$

$$Y = \frac{0.0935}{0.1680} = 0.556 \text{ inch}$$

$$I_X = 0.1113 - 0.0520 = 0.0610 \text{ in}^4$$

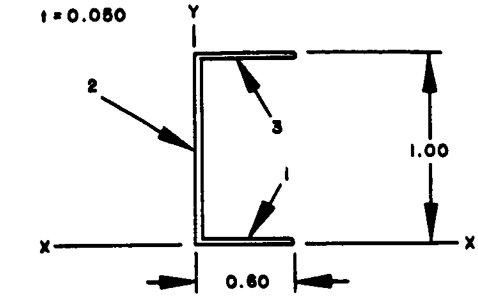

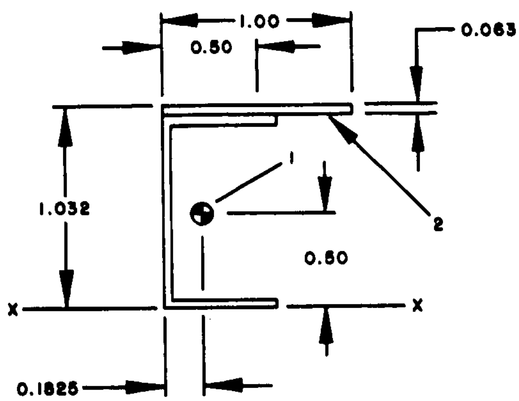

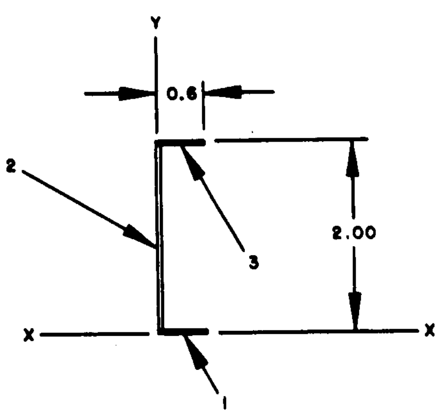

APPLIED LOADS

$n_X = n_X = 30$

$W = 6.0$ pounds $\quad nW = 180$ pounds each axis loaded separately

CALCULATED STRESSES

Assume the inner support is a uniform beam of 1.0 inch depth.

Outer Support

Vertical Load Case

$$W_1 = W_2 = \frac{W}{2} = 90 \text{ pounds}$$

$$R_1 = R_2 = 45 \text{ pounds}$$

$$M_{max} = \frac{Wd}{\ell}\left(a + \frac{Cd}{2\ell}\right) \text{ at midspan}$$

(Case 14, art. 32, reference 5)

$$M_{max} = \frac{90.0 \times 7.92}{15.84}\left(2.295 + \frac{11.25 \times 7.92}{31.68}\right)$$

$$= 45.0 \times 5.08 = 229 \text{ in-lb}$$

$$f = \frac{M\overline{Y}}{I_X} = \frac{229 \times 1.0}{0.0903} = 2530 \text{ psi}$$

Outer support

Lateral Load Case

Assume couple forces act at shear centers with magnitude as shown below, and lateral loads act along centerline of each beam.

$$C = 1.813 \times 180 = 326 \text{ in-lb}$$

$$F_C = \frac{\text{couple}}{\text{bolt spacing}} = \frac{326}{2.74} = 119 \text{ pounds}$$

$$W_3 = W_4 = 90 \text{ pounds}$$

$$M_Y = 229 \text{ lb-in}$$

$$M_X = 229 \times \frac{119}{90} = 303 \text{ in-lb}$$

	A	X	AX	AX^2	I_{OY}	Y	AY	AY^2	I_{OX}
1	0.0300	0.300	0.00900	0.0027	0.0009	0.025	0.00075	0.00002	—
2	0.0975	0.025	0.00244	0.0001	—	1.000	0.09750	0.09750	0.0333
3	0.0300	0.300	0.00900	0.0027	0.0009	1.975	0.05920	0.11700	—
	0.1575		0.02044	0.0055	0.0018		0.15745	0.21452	0.0333

$\overline{Y} = 1.0$ inch

$I_{X_3} = 0.2478 - 0.1575 = 0.0903 \text{ in}^4$

$$\overline{X} = \frac{0.02044}{0.1575} = 0.130 \text{ inch}$$

$I_{Y_3} = 0.00730 - 0.00266 = 0.00464 \text{ in}^4$

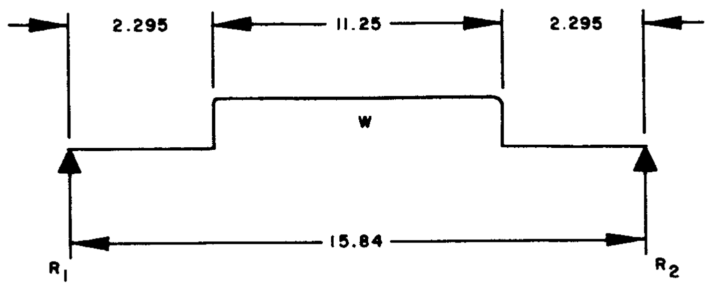

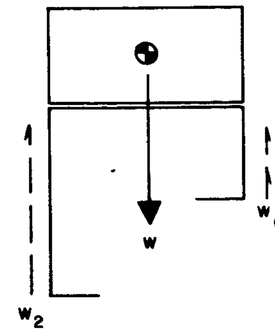

VERTICAL LOAD SYSTEM

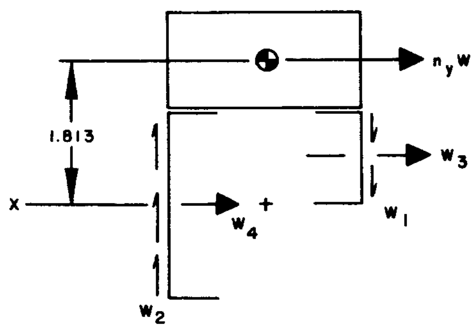

LATERAL LOAD SYSTEM

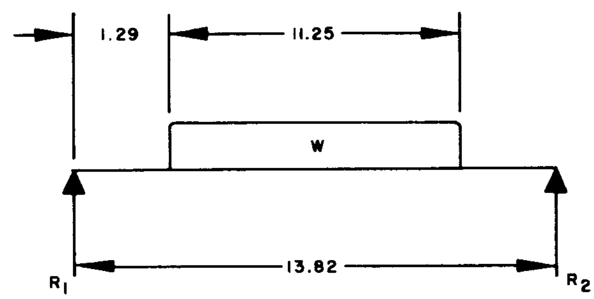

BEAM GEOMETRY

$$f_1 = \frac{M_X Y}{I_X} = \frac{303 \times 1.0}{0.0903} = 3360 \text{ psi}$$

$$f_2 = \frac{M_Y X}{I_Y} = \frac{229 \times (0.600 - 0.128)}{0.00464} = 23{,}300 \text{ psi}$$

$$\Sigma f = f_1 + f_2 = 3360 + 23{,}300 = 26{,}660 \text{ psi}$$

ALLOWABLE STRESSES

$$\left(\frac{b}{t}\right)_{\text{FLANGE}} = \frac{0.60}{0.050} = 12 \text{ for } K = K_2$$

$F_{CC} = 31{,}600$ psi: (See Figure 6-184).

MARGIN OF SAFETY

$$\text{M.S.} = \frac{31.6}{2.53} - 1 = \text{large}$$

$$\text{M.S.} = \frac{31.6}{26.7} - 1 = 0.18$$

Inner Support

Vertical Load Case

$W = 90$ pounds

$R_1 = R_2 = 45$ pounds

$$M_X = \frac{90 \times 6.91}{13.82}\left(1.29 + \frac{11.25 \times 6.91}{27.64}\right)$$

$$= 44.9 \times 4.11 = 184.5 \text{ in-lb}$$

$$f = \frac{M_X Y}{I_X} = \frac{184.5 \times 0.50}{0.01778} = 5190 \text{ psi}$$

ALLOWABLE STRESSES

$$\frac{b}{t} = 12$$

$F_{CC} = 31{,}600$ psi: (See Figure 6-184).

MARGIN OF SAFETY

$$\text{M.S.} = \frac{31.6}{5.19} - 1 = 5.09$$

Inner Support

Lateral Load Case

$M_Y = 184.5$ in-lb

$$M_X = 184.5 \times \frac{119.0}{90.0} = 244 \text{ in-lb}$$

$$f_3 = \frac{244.0 \times 0.556}{0.0610} = 2230 \text{ psi}$$

$$f_4 = \frac{184.5 \times 0.301}{0.0124} = 4470 \text{ psi}$$

$f = f_3 + f_4$

$= 2230 + 4470$

$f = 6700$ psi

ALLOWABLE STRESSES

$$\frac{b}{t} = \frac{0.60}{0.05} = 12 \qquad \text{6061-T6} \qquad K = K_2$$

$F_{CC} = 31{,}600$ psi (See Figure 6-184).

$$\frac{b}{t} = \frac{1.00}{0.05} = 20 \qquad 7075\text{-T6} \qquad K = K_1$$

$F_{cc} = 32{,}500$ psi (See Figure 6-184).

MARGIN OF SAFETY

$$M.S. = \frac{31.6}{6.7} - 1 = 3.72$$

THERMAL CONTROL

Thermal Control System Objectives

The temperature control system for the spacecraft will be designed to maintain the average temperature of the mounting surfaces of the subsystem equipment within the range of 50 to 80°F during all operating conditions. The localized mounting surface temperatures will remain as close to the average as possible, and will not exceed the range of 40 to 100°F, except for the traveling-wave tube, which can operate over a much wider range without performance degradation. Only the external structure of the spacecraft and the solar cell panels will be allowed to operate outside these temperature limits.

Checkout, Prelaunch, and Exit Phase Thermal Control

During checkout in the spin balance and assembly buildings, the temperature of the spacecraft will be maintained within limits by the ambient air temperature of these buildings.

When the spacecraft is mounted on the launch vehicle prior to launch, temperature-conditioned air will maintain the temperature of all spacecraft subsystems within limits.

Since the nose fairing of the launch vehicle will protect the spacecraft from execessive aerodynamic heating, the heat capacity of the spacecraft and its subsystem equipment is sufficient to maintain the temperatures of the equipment within the limits during the exit phase. After the shroud cover is removed, the temperature control system will control the equipment temperatures.

Orbital Phase Thermal Control

When the spacecraft is in synchronous orbit the principal modes of heat transfer between the spacecraft and its environment are direct solar and infrared radiation to space. The secondary modes of heat transfer to the spacecraft will be solar-reflected and infrared radiation from the earth and its atmosphere. Following orientation, the spin axis of the spacecraft will be approximately aligned with the spin axis of the earth. Therefore, the angle between the sun's rays and the forward spin axis of the spacecraft will vary approximately between 65 and 115 degrees during the year.

The subsystem equipment and the fuel and oxidizer tanks are thermally coupled to the back of the solar panels by thermal radiation. Since the power dissipation in the subsystem equipment is low, its temperature and that of the tanks will be approximately equal to the solar panel temperature. The heat losses from the forward end of the spacecraft will be minimized by a thermal radiation barrier. There will be some heat transfer between the tanks, subsystem equipment, and the aft end of the spacecraft by conduction in the support structure and also by thermal radiation. This heat transfer is desirable because it serves to minimize the temperature difference in the spacecraft.

The high heat dissipation equipment such as the TWTs, the dc-to-dc converters, and telemetering equipment will be mounted on the support ribs. The heat loss from this equipment will be controlled by the surface properties of the thermal radiation barrier or ground plane on this end of the spacecraft.

This thermal control concept for the Syncom II is quite similar to the one used in the Syncom I design. The principal difference is that the II temperature control system may be augmented with an active temperature control device located on the support ribs.

Solar Panel Temperatures

Temperatures of the solar panels are expected to vary from 50 to 70°F, depending on the solar incidence angle. These temperatures were computed using a solar absorptance of 0.84 and infrared emittance of 0.83 for the solar cells and exposed support structure. The minimum temperature resulting from eclipses is not expected to go below —155°F, the predicted minimum solar panel temperature for Syncom I.

Vernier Control Rockets Thermal Consideration

There are two principal thermal considerations associated with the vernier control rockets: measures must be included to prevent the overheating of the spacecraft structure and critical portions of the vernier system during and immediately after operation, and provisions must be made for an adequate temperature environment for the system when it is not in use.

The control system utilizes a bipropellant combination consisting of monomethyl hydrazine as the fuel and 85 percent nitrogen tetroxide, 15 percent nitric oxide as the oxidizer. The lower temperature limits for the fuel and the oxidizer are 62.5 and —20°F, respectively.

With the exception of the rocket nozzle, all of the vernier control rocket system will be contained within the spacecraft where the temperatures will be maintained above the lower limit of the oxidizer and fuel. During solar illumination the temperatures of the nozzles can be maintained above the freezing point by proper selection of thermal surface coatings. During eclipses, the nozzles will lose heat, but the control valves can be protected from freezing by keeping the thermal resistance of the fuel and oxidizer lines high and by allowing sufficient heat flow into the valves from the interior structure of the spacecraft.

Based on an average specific heat ratio between the combustion chamber and the nozzle exit plane of 1.27 and an 8-degree nozzle exit half-angle, the turning angle of the exhaust plume will not exceed 90 degrees. For this turning angle, adverse effects on the solar panels and spacecraft structure should be small. The control rockets will have a thermal radiation shield between the nozzle and the spacecraft structure. After the control rocket is turned off, this thermal radiation shield will also be used to heat-sink some of the heat from the nozzle. Thermal barriers between the combustion chamber and the valves will reduce the soakback of heat from the combustion chamber to the valves and propellant after firing.

APOGEE INJECTION ROCKET MOTOR

The Syncom II apogee engine, shown in Figure 6-185, is similar to the Syncom I apogee engine developed by JPL with respect to: 1) configuration, 2) materials, and 3) propellant formulation. Maximum utilization of Syncom I technology has been incorporated into the design. The engine, weighing 874.5 pounds, will provide a velocity increment of 6100 feet per second for an injected spacecraft weight of 1518 pounds. In addition to providing a propellant offloading capability commensurate with a spacecraft weight of 1300 pounds, the following improvements have been incorporated to the design:

1) The nozzle is bolted to the case providing increased control of initial thrust alignment.
2) The initiator can be installed after the engine is mounted in the spacecraft.
3) The redesigned attachments minimize engine weight.

The engine case assembly, fabricated from 410 stainless steel, is of preformed and welded construction. The elliptical ends are drawn, welded to the cylindrical section, and machined prior to heat treatment of the case assembly.

The submerged nozzle assembly contains: 1) the molded carbon phenolic exit cone reinforced with glass rovings, 2) a ZTA graphite nozzle throat for minimum erosion, and 3) a stainless steel nozzle closure. The completed nozzle assembly has an expansion ratio of 35 to 1. Potential improvements in rocket engine performance through incorporation of a contoured nozzle will be evaluated during the development program.

The propellant, JPL 540, is a polyurethane type containing 16 percent aluminum. Precise control of propellant specific impulse has been demonstrated during tests of the Syncom I engine at simulated altitude conditions. The cylindrical propellant gain is bonded directly to the nitrate-base rubber insulation which protects the interior of the case from the propellant flame temperature.

The pyrotechnic-type ignition system contains dual bridge squibs for redundancy. The squibs meet the one ampere — one watt safety requirement of the Atlantic Missile Range.

A pyrogen type ignition system will be evaluated during the initial development phase to minimize the characteristics ignition shock of the pyrotechnic type igniter.

Program Plan

The program consists of three phases:

1) Subscale tests using Syncom I components to evaluate performance of a contoured nozzle.
2) An engine development program consisting of six heavy-wall and 10 flight weight engine tests. Testing will include exposure to the expected flight environment and operation at simulated altitude conditions.
3) A quality assurance test phase consisting of eight engines fired under-simulated-altitude conditions after exposure to combined environmental conditions.

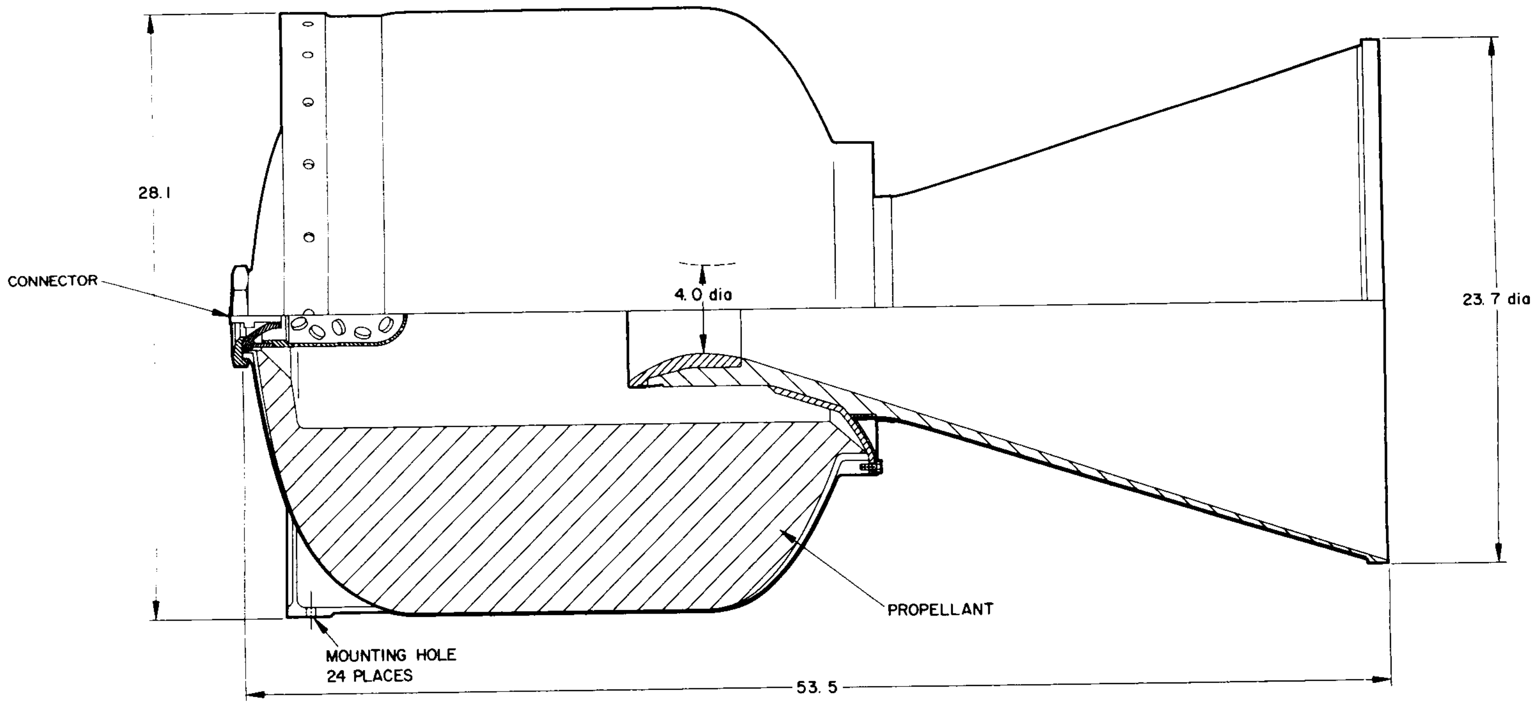

FIGURE 6-185. SYNCOM II APOGEE ENGINE

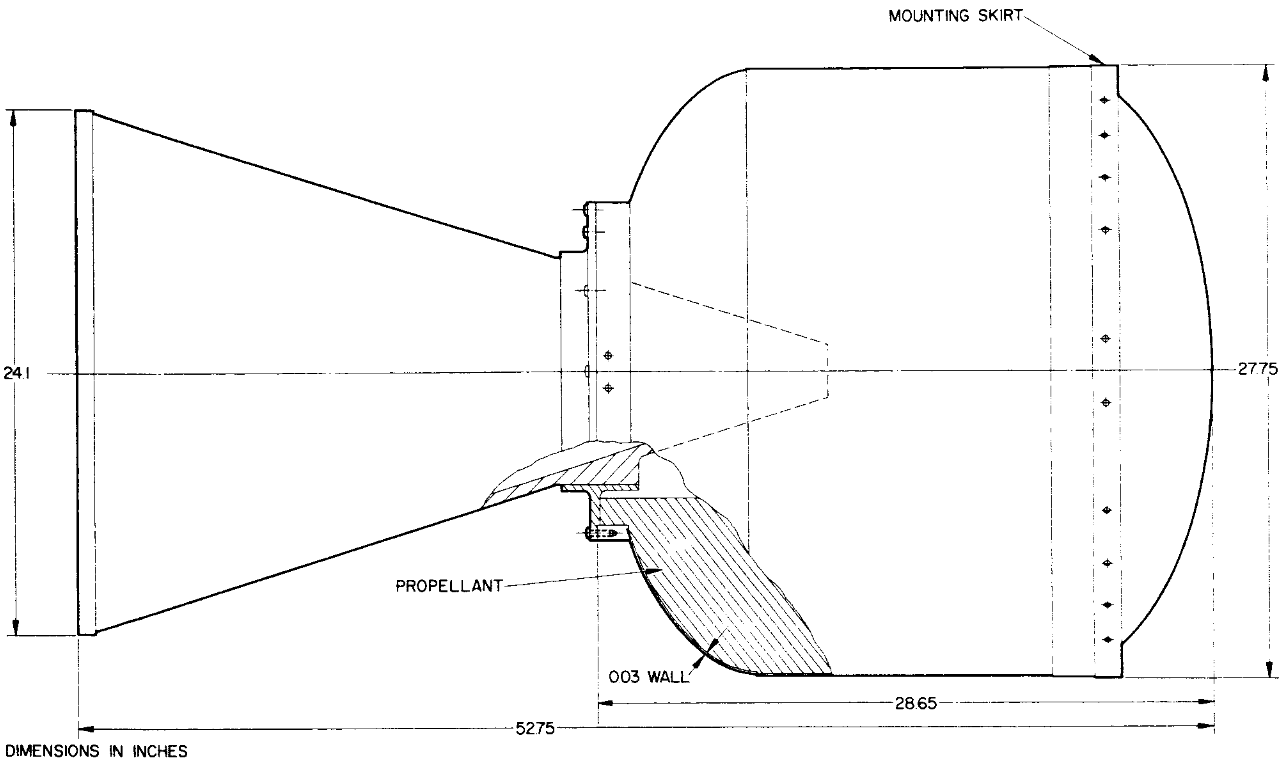

FIGURE 6-186. DUMMY APOGEE ENGINE

The subscale phase will be completed by June 1963, developmental testing completed by January 1964, and quality assurance testing completed by May 1964.

Dummy Engine

To permit early evaluation of the spacecraft structural design, a dummy engine was fabricated by Hughes and loaded with inert propellant by JPL. The inert formulation has physical properties similar to the line propellant. The dummy engine, shown in Figure 6-186, duplicates the total weight and moment of inertia of the flight configuration; however, a redistribution of component and propellant weight was allowed for ease of fabrication. The dummy unit will be suitable for the intended test.

To permit evaluation of the spacecraft structural been finalized through joint action of Hughes, JPL and NASA-Goddard representatives with a few exceptions, primarily weight and postfiring balance. Minimum weight and imbalance have been established as design objectives commensurate with program costs and schedules.

REFERENCES

6-1. Williams, D.D., "Dynamic Analysis and Design of the Synchronous Communications Satellite," Hughes TM-649, May, 1960.
6-2. Lotta, J.G., "Syncom II Weight Status," 2243.11/284, 7 March 1963.
6-3. Advanced Syncom Monthly Progress Reports.
6-4. Advanced Syncom Initial Project Development Plan, Vol. I (Technical Plan).
6-5. O'Brien, B.J., et al., "Absolute Electron Intensities in the Heart of the Earth's Outer Radiation Zone," *J. Geoph. Res.* 67, 397, January, 1962.
6-6. Rosser, W.V., et al., "Electrons in the Earth's Outer Radiation Zone," Presented at 1962 Annual Meeting of Am. Geoph. Union.
6-7. MacDonald, F.B., et al., "Summary of Early Results from Explorer XII Transactions," Am. Geoph. Union 43, 211, June 1962.
6-8. Friedlander, S.A., "Parametric Study of Proton and Electron Damage to Solar Cells," Hughes IDC 22-44.3/192.
6-9. Naugle, J.E., Nucleonics 19, 89, April 1961.
6-10. Armed Forces Supply Support Center, "Strength of Metal Aircraft Elements" MIL-HDBK-5, Washington 25, D.C., March 1961.
6-11. Peery, D.J., *Aircraft Structures*, McGraw Hill Book Company, New York, New York, 1949.
6-12. "Strength, Efficiency, and Design Data for Beryllium Structures," U.S. Department of Commerce PB 181324, Washington 25, D.C.
6-13. Journal of the Aeronautical Sciences, "The Ultimate Strength of Aluminum Alloy Formed Structural Shapes in Compression," Robert A. Needham, April 1954.
6-14. Roark, R.J., *Formulas for Stress and Strain*, McGraw-Hill Book Company, New York, New York, Third Edition 1954.

7. SPACECRAFT RELIABILITY

SYSTEM RELIABILITY STUDIES

Introduction

The reliability of the Syncom II spacecraft is one of the most important design parameters contributing to economic feasibility of the systems employing satellites. Although current state-of-the-art lifetime predictions are subject to uncertainty, the techniques for optimization of the configuration exist and have been utilized during the Advanced Technological Development program. The Syncom spacecraft utilizes a configuration in which redundancy exists at both the unit and quadrant levels.

System Reliability Requirements

The Advanced Syncom reliability objective was established at three years useful lifetime in orbit. The present reliability goal, based on a 100 percent duty cycle, is based on a 50 percent probability of survival for 3 years of one quadrant, voice channels or TV. It is possible to express these characteristics in terms of mean time between failures (MTBF), but due to the stepwise degradation, a probability description is more realistic. In a highly redundant device, the 50 percent probability life is nearly the same as the mean life of the equipment.

Orbital reliability is defined for each element as the probability that it will survive for 1 year, provided it was operable at the beginning of orbital life. In addition to orbital reliability, the boost and orientation reliability must be considered. This is defined as the probablity that all elements are functioning at the beginning of orbital life so that the full life expectancy may be realized.

Communications and telemetry, each with separate reliability characteristics, form the two mission functions utilized for reliability analysis. The reliability requirements for each mission function are outlined in Table 7-1 and include the probability of survival of boost and synchronization-orientation. The table indicates that the transponder may operate in either a multiple access mode or frequency translation mode during the communications phase. The multiple access mode of operation is considered primary to communications success since this mode performs the voice channel mission functions.

Reliability Analyses and Requirements Studies

During the Advanced Technological Development Program, mathematical models were developed for reliability to assess proposed equipment configurations, and for those specialized tradeoff and requirements studies presented later in this section. The system reliability model has been continuously upgraded and periodic predictions performed. Present effort is being concentrated on detailed analyses of parts counts, stress derating, and operating environments for the equipments designed during this program phase.

Reliability has been apportioned among the units and subsystems in accordance with preliminary estimates presented in the Initial Project Development Plan. These estimates, shown in Table 7-2, form re-

TABLE 7-1. SPACECRAFT RELIABILITY OBJECTIVES

Phase of Operation	Boost Reliability	50 Percent Lifetime, years
Communications		
Multiple access mode		
Four quadrants	0.96	1.0
Three quadrants	0.99	2.0
Two quadrants	0.99	2.5
One quadrant	0.99	3.0
Frequency translation mode		
Four quadrants	0.96	0.5
Three quadrants	0.99	1.0
Two quadrants	0.99	1.5
One quadrant	0.99	2.5
Telemetry		
Four quadrants	0.98	2.0
Three quadrants	0.99	3.0
Two quadrants	0.99	4.0
One quadrant	0.99	5.0

liability goals or objectives for each equipment consistent with the Syncom mission objectives.

TABLE 7-2. SYNCOM MARK II ONE YEAR RELIABILITY OBJECTIVES

Subsystem And Unit	Reliability Objective
Transponder subsystem	
Transmitter	
TWT and electronics	0.615
Antenna and diplexer	0.970
Receiver	
Frequency translation mode	0.762
Multiple-access mode	0.762
Antenna and diplexer	0.958
Antenna control electronics subsystem	0.842
Command subsystem	
Receiver and diplexer	0.950
Decoder A and B	0.962
Antenna and hybrid	0.988
Telemetry subsystem	
Transmitter and diplexer	0.886
Encoder	0.748
Power supply subsystem	
Battery and charging circuitry	0.896
Solar panel	0.998
Reaction control subsystem	
Solar sensors	0.998
Apogee motor	0.999
Structure	0.999

TABLE 7-3. SYNCOM MARK II — FAILURE RATES PERCENT PER 1000 HOURS

Equipment	Derating* to 0.10	Derating* to 0.50
Antenna	0.0200	
Capacitors		
Ceramic	0.0010	
Ceramic, varible	0.0010	
Electrolytic	0.1400	
Glass	0.0030	
Mica	0.0010	
Mica, button	0.0010	
Mica, dipped	0.0010	
Paper	0.0010	
Tantalum	0.0100	
Tantalum, foil	0.0150	
Tantalum, slug	0.0010	
Crystals	0.0200	0.0300
Coaxial connectors	0.0200	
Coaxial relay	0.0250	
Coupler, direction	0.0100	
Diodes	0.0100	
Switching	0.0020	
Varacter	0.0210	
Zener	0.0150	
Filters	0.0160	
Ferrite phase shifter	0.0200	
Junction Box	0.0010	
Inductors	0.0020	0.0200
Mixers	0.0300	
Resistors		
Composition	0.0020	
Film	0.0290	
Film, power	0.1080	0.1520
Wire wound	0.0170	0.0790
Wire wound, power	0.1060 .016	0.0680
RFC	0.0010	
Transformers**	0.0500	
Transistors	0.0200	0.0500
Traveling wave tube	5.0	

*Ambient temperature, 55 c. maximum.
**Derated for maximum reliability.

The failure rates data shown in Table 7-3 have been used throughout these studies in determining design tradeoffs and in estimating unit, subsystem, and system reliability. For high population parts these failure rates are based upon data from MIL Handbook 217* assuming a maximum temperature environment of 55°C and a stress derating of 90 percent. The failure rates of low population parts not available in MIL Handbook 217 were derived as a compromise between Hughes data and data found in Martin, AVCO, Bell Tel, and RCA publications. The list of failure rates at 50 percent derating was intended as a permissible deviation for components which must be stressed at higher levels because of design considerations.

It is expected that the failure rates of certain components will be redesignated relevant to a high reliability parts program and other data which becomes available. In addition, the preliminary list as presented will be revised to include delineation of specific component applications within each class of components (i.e., signal transformers will be distinguished from power transformers; RF inductors will be distinguished from tuning inductors; digital and signal transistor applications will be delineated, etc.).

Such a revised listing will be implemented by a detailed analyses of Syncom drawing releases with cooperation of each design area. Whereas reliability predictions have been used primarily for design tradeoffs, the revised listing will serve to provide a more

*MIL Handbook 217 "Reliability Stress Analysis for Electronic Equipment."

accurate indication of progress toward spacecraft subsystem and system reliability achievement.

Resistors, capacitors, transistors and diodes are to be applied in the spacecraft design with maximum derating since these comprise a substantial portion of the electronics and thus the failure rate of any unit or subsystem. Inductors, transformers, crystals, and other low population elements are to be high-reliability components with particular attention applied to circuit applications to minimize each component stress level. A high reliability parts program is currently in the implementation process for the Syncom II program. This program, coupled with design practices utilizing maximum derating, proven parts application, redundancy, and fail safe techniques will enhance an optimum approach to the attainment of the 3- to 5-year spacecraft mission objective.

COMMUNICATIONS MISSION RELIABILITY

The Initial Project Development Plan (IPDP) presented lifetime curves for total communications. This analysis assumed that both communications receivers operate simultaneously at 100-percent duty cycle (a conservative estimate) and that the survival of one frequency translation receiver would be adequate for successful communication. Since each receiver or mode may not operate simultaneously, an analysis has been performed to determine the reliability of each communications mode during the orbital mission, again assuming a 100-percent duty cycle (worst case analysis) for each. The results yield lifetime curves and data expressing the probability of successful multiple access (Figure 7-1a) and frequency translation (Figure 7-1b) communications for at least one, two, three, or four effective quadrants surviving a discrete mission period. These lifetime curves, when superimposed, form envelopes for each quadrant plot which, in turn, determines minimum and maximum reliability limits for the spacecraft communication system operating 100-percent of the time. This may be better visualized by a plot of 50-percent probability of survival intercepts for each mode, Figure 7-2. This figure further illustrates a sequence of steps from full performance in terms of channel capacity, which results because of the four-quadrant binomial nature of the spacecraft transponder subsystem, and occurs if there is no catastrophic failure mechanism due to design inadequacy. Further definition and allocation

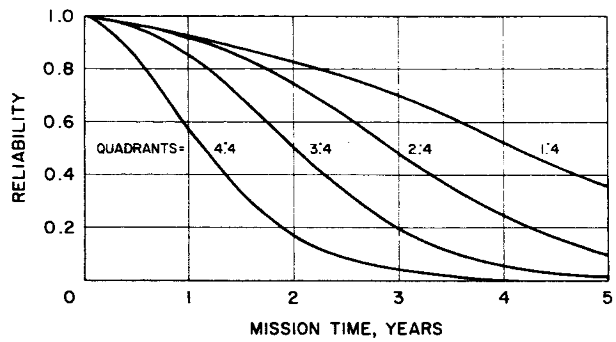

a) Single sideband mode

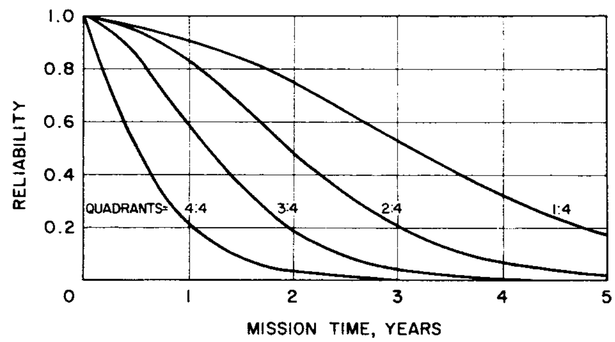

b) Frequency translation mode

FIGURE 7-1. PROBABILITY OF SUCCESSFUL COMMUNCIATIONS

of each transponder mode utilization factor will provide a composite lifetime estimate for total communications, which would fall between the limits similar to those presented.

The mathematical model representing the orbital configuration during either communications mode may be expressed by the following equations for reliability. The symbols are further defined in the mathematical mode section.

Multiple Access Communication Mode

$$R_{SSC} = (R_B R_{SO}) \Bigg[\sum_{r=1,2,3,4}^{4} \frac{4!}{(4-r)!r!} \left[R_{CX}(1 + P_s\lambda_{cx}t)\, R_{MA}(1 + P_s\lambda_{ma}t)\right]^{r} \left[1 - R_{CX}(1 + P_s\lambda_{cx}t)\, R_{MA}(1 + P_s\lambda_{ma}t)\right]^{4-r} \Bigg]$$

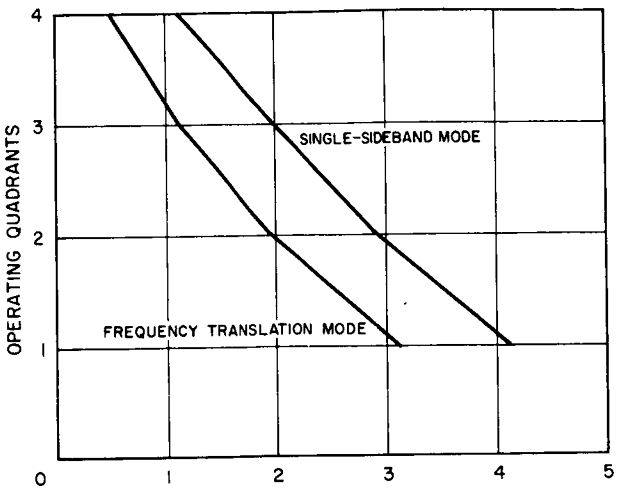

FIGURE 7-2. 50 PERCENT PROBABILITY OF QUADRANT SURVIVAL

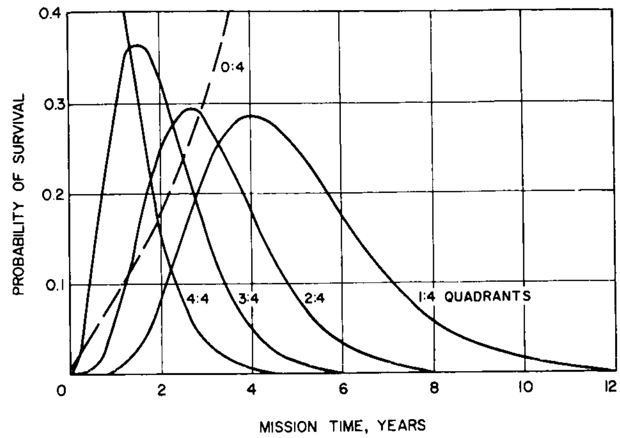

FIGURE 7-3. PROBABILITY OF SURVIVAL FOR EXACTLY ONE OR TWO OR THREE OR FOUR OF FOUR QUADRANTS MULTIPLE ACCESS COMMUNICATION MODE

$$R_{FAG}\, R_{DC}\, R_{AC}\left[1+P_s\lambda_a t+\frac{P_s^2(\lambda_a t)^2}{2!}+\frac{P_s^3(\lambda_a t)^3}{3!}\right]$$

$$[1-(1-R_{DAB}\, R_{RC})^4]\;[1-(1-R_{ss})^4]$$

$$(R_{CXA}\, R_{CRA}\, R_{TA})\; R_{CR}\;(1+P_s\,\lambda_{cr}\,t)\; R_{PS}\, R_{AM}\, R_S$$

Frequency Translation Communication Mode

$$R_{FTC}=(R_B\, R_{SO})\left[\sum_{r=1,2,3,4}^{4}\frac{4!}{(4-r)!r!}\right.$$

$$[R_{CX}(1+P_s\lambda_{cx}t)\;\; R_{FT}]^r$$

$$\left.[1-P_{CX}(1+P_s\lambda_{cx}t)\; R_{FT}]^{4-r}\right]\;[1-(1-R_{ss})^4$$

$$[1-(1-R_{DAB}\, R_{RC})^4]\; R_{AC}\;\; R_{FAG}\, R_{DC}$$

$$\left[1+P_s\,\lambda_a\,t+\frac{P_s^2(\lambda_a t)^2}{2!}+\frac{P_s^3(\lambda_a t)^3}{3!}\right]$$

$$(R_{CXA}\, R_{CRA}\, R_{TA})\; R_{CR}\;(1+P_s\,\lambda_{cr}\,t)\; R_{PS}\, R_{AM}\, R_S\, R_{CT}$$

Figure 7-3 presents the probability of survival for multiple access communications for one of four, two of four, three of four, and four of four effective quadrants surviving a discrete orbital mission period. These curves present relative probabilities which become valuable to the establishment of the spacecraft replacement design criteria. The predictions are based upon preliminary unit complexities and parts count estimates and will be upgraded to incorporate both the exact parts count obtained from detailed circuit drawings and accurate stress and derating factors for each component. This information, along with catastrophic failure mode and effects analyses, will be assessed as an integral part of the Syncom II design review program.

Telemetry and Command Configuration Analysis

The operation of the telemetry link is a necessary function during the boost-synchronization and orientation phases of the mission. During the communications phase, however, this equipment is desirable but not necessarily essential. When a communications failure occurs during orbital operation, the telemetry link functions to determine the availability of a redundant substitute. The redundant element is then switched by a ground station command to replace the failed unit or quadrant subsystem. If the telemetry is not functioning at that time, a predetermined operations sequence at the ground command station is initiated to switch redundant units and quadrant subsystems until communications are restored.

The telemetry and command subsystems reliability models presented in the Initial Project Development Plan, dated 15 August 1962 (Figure 6-69), have been examined to determine the amount of degradation in telemetry mission success when a nonredundant configuration is employed in each spacecraft quadrant.

The results are shown in Figure 7-4, curves (a), (b), and (c) show the predicted probabilities of telemetry mission success as a function of time for configurations (a), (b), and (c) respectively. These predictions indicate that interquadrant redundancy is adequate and that the removal of one of the two telemetry transmitters and encoders and one of the two command receivers and decoders in each quadrant will not substantially change the telemetry mission reliability during the 3- to 5-year spacecraft mission time.

Since the command subsystem is also required for the multiple access and frequency translation com-

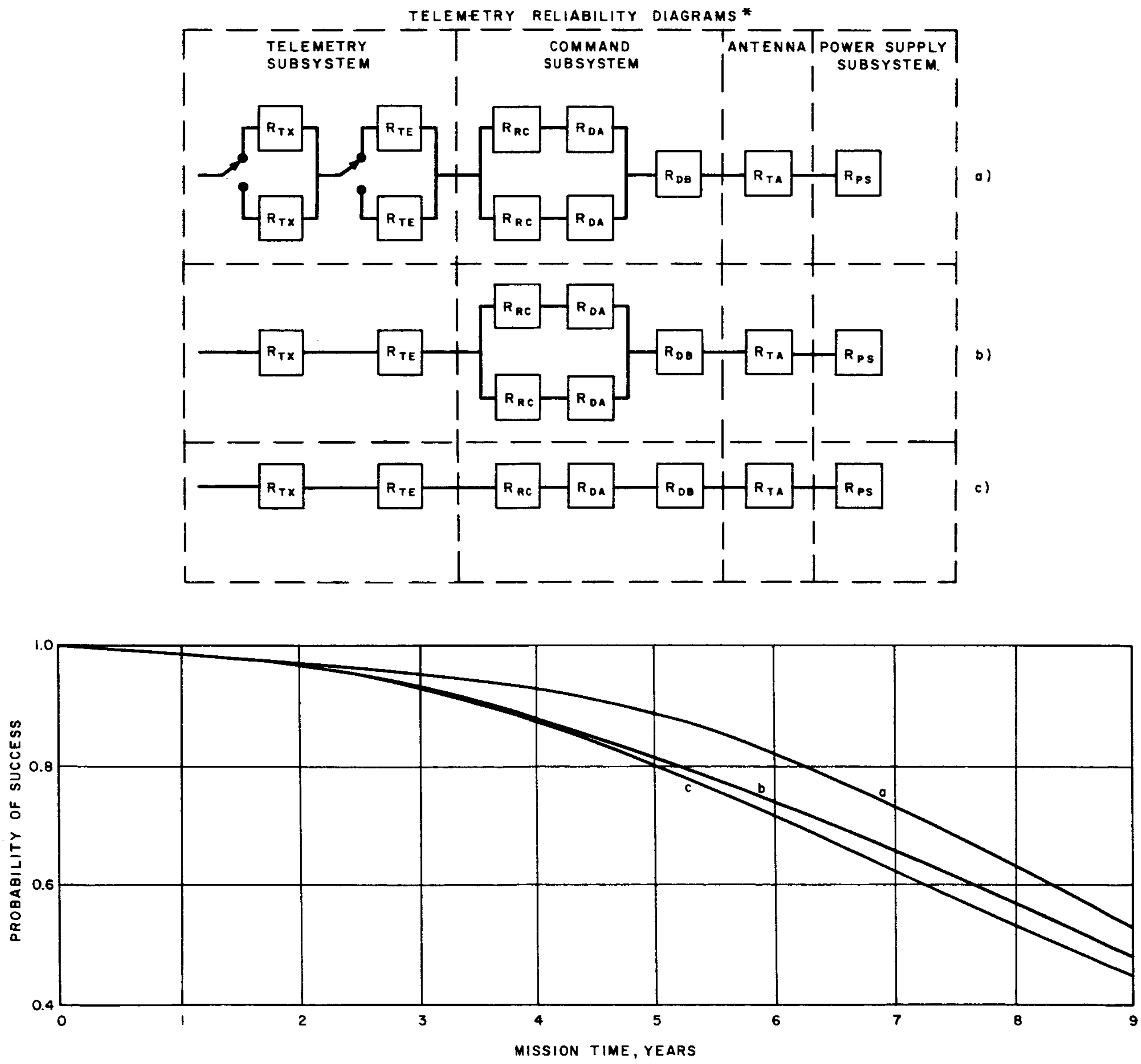

* ONLY ONE QUADRANT OF THE TELEMETRY AND COMMAND SUBSYSTEMS IS SHOWN

FIGURE 7-4. PROBABILITY OF TELEMETRY MISSION SUCCESS munication modes of operation, the effect of the nonredundant quadrant command configuration upon communications mission success has been evaluated and yields no significant variation in the data presented. A comparison of predicted reliability for the redundant and nonredundant configurations, a and c respectively, may be made by comparing data presented in Tables 7-4 and 7-5 for the multiple access communications mode and Tables 7-6 and 7-7 for the frequency translation mode.

The nonredundant configuration presented by Figure 7-4, diagram (c), was recommended for incorporation as the Syncom II spacecraft design. This configuration will yield a high probability of obtaining telemetry data during the lifetime of the spacecraft; it will not result in a degradation in the communications mission but will simplify interconnections and switching, enhancing reliability, and will result in an overall reduction in cost and weight of the spacecraft.

The curves presented in Figure 7-4 include the effect of the telemetry subsystem, command subsystem, power supply subsystem, and antenna which are each required for successful completion of the telemetry mission. The analyses and recommendations presented assume that any quadrant of the telemetry subsystem will sample and transmit the required spacecraft data.

TABLE 7-4. SYNCOM II RELIABILITY ANALYSIS 30 MULTIPLE ACCESS MODE COMMUNICATIONS WITH REDUNDANT COMMAND QUADRANT CONFIGURATION

Time	R (Total) for Four Binomial Terms			
hours	4:4	3:4	2:4	1:4
720.00	0.988362	0.992491	0.992497	0.992497
1440.00	0.969105	0.984953	0.985050	0.985050
2160.00	0.943173	0.977196	0.977657	0.977659
2880.00	0.911556	0.968954	0.970310	0.970324
3600.00	0.875250	0.959921	0.962993	0.963042
4320.00	0.835230	0.949788	0.955680	0.955815
5040.00	0.792426	0.938265	0.948330	0.948638
5760.00	0.747704	0.925104	0.940888	0.941512
6480.00	0.701855	0.910112	0.933285	0.934431
7200.00	0.655586	0.893156	0.925440	0.927390
7920.00	0.609515	0.874171	0.917264	0.920382
8640.00	0.564173	0.853152	0.908659	0.913398
12960.00	0.326786	0.690798	0.842853	0.871082
17280.00	0.168386	0.499688	0.744130	0.824288
21600.00	0.079111	0.326380	0.616206	0.767186
25920.00	0.034483	0.195460	0.477269	0.696531
30240.00	0.014123	0.108871	0.347232	0.613745
34560.00	0.005488	0.057084	0.238994	0.524036
38880.00	0.002038	0.028452	0.156805	0.434014
43200.00	0.000728	0.013586	0.098763	0.349540
47520.00	0.000251	0.006255	0.060084	0.274592
51840.00	0.000084	0.002790	0.035490	0.211084
56160.00	0.000027	0.001211	0.020441	0.159252
60480.00	0.000009	0.000513	0.011522	0.118227
64800.00	0.000003	0.000213	0.006374	0.086563
69120.00	0.000001	0.000087	0.003469	0.062625
73440.00	0.000000	0.000035	0.001861	0.044837
77760.00	0.000000	0.000014	0.000986	0.031811
82080.00	0.000000	0.000005	0.000516	0.022387
86400.00	0.000000	0.000002	0.000268	0.015642
90720.00	0.000000	0.000001	0.000137	0.010858
95040.00	0.000000	0.000000	0.000070	0.007492
99360.00	0.000000	0.000000	0.000035	0.005141
103680.00	0.000000	0.000000	0.000018	0.003510

TABLE 7-5. SYNCOM II RELIABILITY ANALYSIS 37 MULTIPLE ACCESS MODE COMMUNICATIONS WITH NONREDUNDANT COMMAND QUADRANT CONFIGURATION

Time	R (Total) for Four Binomial Terms			
hours	4:4	3:4	2:4	1:4
720.00	0.988362	0.992491	0.992497	0.992497
1440.00	0.969105	0.984953	0.985050	0.985050
2160.00	0.943173	0.977196	0.977656	0.977659
2880.00	0.911555	0.968953	0.970309	0.970323
3600.00	0.875248	0.959920	0.962991	0.963041
4320.00	0.835227	0.949784	0.955676	0.955811
5040.00	0.792421	0.938258	0.948323	0.948632
5760.00	0.747695	0.925093	0.940877	0.941501
6480.00	0.701842	0.910095	0.933268	0.934414
7200.00	0.655568	0.893132	0.925416	0.927365
7920.00	0.609492	0.874137	0.917228	0.920347
8640.00	0.564143	0.853106	0.908610	0.913349
12960.00	0.326705	0.690627	0.842644	0.870866
17280.00	0.168265	0.499331	0.743599	0.823699
21600.00	0.078985	0.325862	0.615228	0.765968
25920.00	0.034379	0.194874	0.475839	0.694444
30240.00	0.014052	0.108321	0.345478	0.610645
34560.00	0.005445	0.056637	0.237119	0.519925
38880.00	0.002015	0.028126	0.155012	0.429051
43200.00	0.000716	0.013370	0.097197	0.343998
47520.00	0.000246	0.006123	0.058815	0.268792
51840.00	0.000082	0.002714	0.034524	0.205338
56160.00	0.000026	0.001170	0.019744	0.153818
60480.00	0.000008	0.000492	0.011040	0.113289
64800.00	0.000003	0.000202	0.006054	0.082226
69120.00	0.000001	0.000082	0.003264	0.058926
73440.00	0.000000	0.000032	0.001733	0.041764
77760.00	0.000000	0.000013	0.000908	0.029313
82080.00	0.000000	0.000005	0.000470	0.020398
86400.00	0.000000	0.000002	0.000241	0.014085
90720.00	0.000000	0.000001	0.000122	0.009659
95040.00	0.000000	0.000000	0.000061	0.006582
99360.00	0.000000	0.000000	0.000031	0.004459
103680.00	0.000000	0.000000	0.000015	0.003005

Thus the quadrants are assumed to operate sequentially with one required to survive for mission success. (Previous analyses of the telemetry subsystem have been based upon a binomial operation.)

As before, it is assumed that all command receivers must be energized, but that the decoders have a low duty cycle and that one quadrant of the command subsystem will provide the necessary spacecraft commands.

The analyses presented are further based upon a minimum number of encoder and decoder channels, 64 and 55 respectively. Although the spacecraft may require more channels, resulting in a degradation of the estimates discussed, the relative percentage of deviation between the curves representing each configuration should not change. The tradeoffs between redundancy, reliability, cost, and weight will be further examined if a substantial increase in the encoder and decoder complexities occurs.

Launch Sequence Reliability Analysis

The determination of mission reliability, incorporating the launch sequence reliability as well as boost and synchronization-orientation reliabilities are essential. The mathematical analysis of the probability of

TABLE 7-6. SYNCOM II RELIABILITY ANALYSIS 31 FREQUENCY TRANSLATION MODE COMMUNICATIONS WITH REDUNDANT COMMAND QUADRANT CONFIGURATION

Time	R (Total) for Four Binomial Terms			
hours	4:4	3:4	2:4	1:4
720.00	0.903815	0.989409	0.992449	0.992497
1440.00	0.811982	0.972720	0.984652	0.985046
2160.00	0.725425	0.950174	0.976285	0.977633
2880.00	0.644747	0.922239	0.967025	0.970237
3600.00	0.570281	0.889545	0.956570	0.962824
4320.00	0.502147	0.852824	0.944660	0.955349
5040.00	0.440292	0.812862	0.931087	0.947760
5760.00	0.384530	0.770455	0.915701	0.939997
6480.00	0.334583	0.726374	0.898418	0.931995
7200.00	0.290104	0.681347	0.879211	0.923686
7920.00	0.250708	0.636032	0.858115	0.915002
8640.00	0.215986	0.591016	0.835212	0.905880
12960.00	0.083398	0.349855	0.669102	0.839101
17280.00	0.029737	0.184533	0.486701	0.748855
21600.00	0.009973	0.089342	0.326212	0.640401
25920.00	0.003185	0.040529	0.204700	0.525472
30240.00	0.000978	0.017478	0.121909	0.415651
34560.00	0.000290	0.007241	0.069657	0.318748
38880.00	0.000084	0.002904	0.038510	0.238266
43200.00	0.000024	0.001134	0.020733	0.174427
47520.00	0.000007	0.000433	0.010924	0.125540
51840.00	0.000002	0.000162	0.005654	0.089109
56160.00	0.000000	0.000060	0.002884	0.062530
60480.00	0.000000	0.000022	0.001452	0.043461
64800.00	0.000000	0.000008	0.000723	0.029964
69120.00	0.000000	0.000003	0.000357	0.020515
73440.00	0.000000	0.000001	0.000175	0.013960
77760.00	0.000000	0.000000	0.000085	0.009448
82080.00	0.000000	0.000000	0.000041	0.006363
86400.00	0.000000	0.000000	0.000020	0.004266
90720.00	0.000000	0.000000	0.000009	0.002848
95040.00	0.000000	0.000000	0.000004	0.001894
99360.00	0.000000	0.000000	0.000002	0.001254
103680.00	0.000000	0.000000	0.000001	0.000828

TABLE 7-7. SYNCOM II RELIABILITY ANALYSIS NO. 40 FREQUENCY TRANSLATON MODE COMMUNICATIONS WITH NONREDUNDANT COMMAND QUADRANT CONFIGURATION

Time	R (Total) for Four Binomial Terms			
(hours)	1:4	2:4	3:4	4:4
720.00	0.903815	0.989409	0.992449	0.992497
1440.00	0.811982	0.972720	0.984652	0.985045
2160.00	0.725425	0.950173	0.976285	0.977633
2880.00	0.644746	0.922238	0.967024	0.970237
3600.00	0.570280	0.889543	0.956568	0.962822
4320.00	0.502146	0.852821	0.944657	0.955346
5040.00	0.440289	0.812857	0.931081	0.947754
5760.00	0.384526	0.770446	0.915691	0.939986
6480.00	0.334577	0.726361	0.898402	0.913978
7200.00	0.290097	0.681328	0.879188	0.923661
7920.00	0.250699	0.636008	0.858081	0.914967
8640.00	0.215975	0.590985	0.835167	0.905832
12960.00	0.083377	0.349768	0.668936	0.838893
17280.00	0.029716	0.184401	0.486354	0.748321
21600.00	0.009957	0.089200	0.325695	0.639385
25920.00	0.003176	0.040407	0.204086	0.523898
30240.00	0.000973	0.017390	0.121293	0.413551
34560.00	0.000288	0.007185	0.069111	0.316248
38880.00	0.000083	0.002871	0.038069	0.235542
43200.00	0.000023	0.001116	0.020404	0.171661
47520.00	0.000006	0.000424	0.010693	0.122888
51840.00	0.000002	0.000158	0.005500	0.086683
56160.00	0.000000	0.000058	0.002785	0.060396
60480.00	0.000000	0.000021	0.001392	0.041646
64800.00	0.000000	0.000007	0.000687	0.028463
69120.00	0.000000	0.000003	0.000336	0.019304
73440.00	0.000000	0.000001	0.000163	0.013003
77760.00	0.000000	0.000000	0.000078	0.008706
82080.00	0.000000	0.000000	0.000037	0.005797
86400.00	0.000000	0.000000	0.000018	0.003841
90720.00	0.000000	0.000000	0.000008	0.002533
95040.00	0.000000	0.000000	0.000004	0.001664
99360.00	0.000000	0.000000	0.000002	0.001088
103680.00	0.000000	0.000000	0.000001	0.000709

survival through the launch sequence and its effect upon the orbital phase reliability is more complex than might be expected. In the case of a nonredundant system, the overall mission reliability may be simply expressed by the product of the equipment survival probabilities for each mission phase sequence. However, in a highly redundant system such as the Advanced Syncom spacecraft, this technique provides an incomplete mathematical model. Similarly incorrect is the approach that the probability of survival of redundant equipment through a particular phase sequence, such as boost, be computed independently of the following phases and the result multiplied by the reliability of the following sequence. Here it must be recalled that orbital analyses have been based upon the assumption that all equipment survived the launch sequence; in essence, the launch sequence reliability was assumed equal to one. By the technique described in the IPDP, the probability of one equipment failing and the second remaining operable, considering a redundant pair, was not included in the mathematical analysis. A more correct method is to define the equations that describe all possible modes of survival for redundant equipment that undergoes multiple mission phase sequences in its lifetime, such as in the Syncom application. For parallel operation of equipment, the general equation may be written as

$$R_p = 1 - \left(1 - \prod_{i=1}^{n} R_i\right)^{m}$$

where

R_p = the reliability of the parallel combination

n = number of mission phase sequences

R_i = reliability of the equipment during the i^{th} phase sequence

m = number of redundant equipment

The general expression for reliability of equipment in a standby configuration may be written as

$$R_s = \sum_{q=1}^{s} \left[\frac{s!}{(s-q)!\,q!} \prod_{i=1}^{n-1} R_i^{q} R_n \left(1 - \prod_{i=1}^{n-1} R_i\right)^{s-q} \right.$$

$$\left. \left[P_s \lambda t + \frac{P_s^2 (\lambda t)^2}{2!} + \cdots \frac{P_s^{q-1} (\lambda t)^{q-1}}{(q-1)!} \right] \right]$$

$$+ \sum_{r}^{s} \frac{s!}{(s-r)!\,r!} \prod_{i=1}^{n-1} R_i^{q} R_n \left(1 - \prod_{i=1}^{n-1} R_i\right)^{s-r}$$

where

R_s = reliability of the standby configuration

s = number of equipment in the standby configuration

q = an integer $0 < q \leq S$

n = number of mssion phase sequences, i.e. boost, synchronization-orientation, orbit (3)

R_i = reliability of one equipment during the i^{th} phase sequence

R_n = reliability of one equipment during the final phase sequence

P_s = probability of successful operation of the switching function

λ = failure rate of one equipment during the n^{th} phase sequence

t = specified time associated with the n^{th} sequence

r = an integer $= q + 1$ $1 < c \leq s$

As noted above, the general expression for a series equipment is simply

$$R = \prod_{i=1}^{n} R_i$$

where

R = reliability of the series equipment

n = number of sequence intervals

R_i = reliability of the equipment during the i^{th} sequence interval

These equations have been developed by an examination of survival probabilities for each sequence interval and the effect of equipment failure or survival upon subsequent intervals. The formulation of a "truth table" will validate the applicability of the expressions to a reliability analysis of multiple mission phase sequences.

The computer program developed for the reliability analysis of the Advanced Syncom spacecraft configuration has been updated to include these equations and the general capability of evaluating multiple sequence reliability. A redefinition of the spacecraft mathematical model incorporating boost, synchronization-orientation, and orbital sequence reliabilities in the terms described is not required since the mathematical models which describe spacecraft reliability are accurate and include an equivalent boost (R_B) and synchronization-orientation reliability (R_{SO}). However, the derivation of the equivalent $R_B R_{SO}$ is not straightforward and the equations technique described herein has been developed for computer evaluation of the effects of these sequence intervals upon the orbital reliability.

Table 7-8 illustrates the results from the multiple sequence analysis by presenting the predicted spacecraft mission reliability for multiple access communication in tabular form. The effect of the boost and synchronization phase sequences upon the orbital mission may be determined by comparing this table with Table 7-4. It may be observed that the predicted reliabilities for boost and synchronization-orientation are high and therefore have little effect upon the orbital mission reliability.

Antenna Control Electronics Reliability Analysis

A reliability assessment of the phased-array control electronics subsystem (January, 1963 configuration) has been performed and the reliability diagram for the concept reviewed incorporated into the system reliability model (Figure 7-5). The subsystem configuration has subsequently been simplified in several significant areas and will be re-assessed. This assessment has included a compilation of parts count information for each circuit and a preliminary investigation of circuit redundancy, derating, duty cycles, and failure mode characteristics for subsystem functions.

The antenna phase control electronics were divided into two primary circuit functions: 1) the digital control circuits, which generate the antenna phase reference signals, and 2) the analog drive circuits, which receive the phase reference signals and convert them to analog form to provide excitation for the ferrite phase shifters to control the direction of the phased-array antenna beam. The digital control and analog drive circuits of the configuration reviewed consisted of approximately 2100 and 1500 electronic components respectively. The digital circuit parts count includes the parts for timing and locating the phase of control system jet pulsing.

TABLE 7-8. SYNCOM II RELIABILITY ANALYSIS 32 ANALYSIS OF MISSION RELIABILITY FOR MULTIPLE ACCESS COMMUNICATIONS INCLUDING THE PROBABILITY OF SURVIVAL THROUGH BOOST AND SYNCHRONIZATION-ORIENTATION

Boost-Synchronization-Orientation Reliability for Four Binomial Quadrants				
Time (hrs)	4:4	3:4	2:4	1:4
6.22	0.999837	0.999841	0.999841	0.999841

Orbital Mission Reliability for Four Binomial Quadrants Including Boost-Synchronization-Orientation				
Time (hrs)	4:4	3:4	2:4	1:4
720.00	0.987858	0.992332	0.992339	0.992339
1440.00	0.968296	0.984788	0.984894	0.984894
2160.00	0.942100	0.977016	0.977501	0.977504
2880.00	0.910260	0.968745	0.970155	0.970170
3600.00	0.873772	0.959671	0.962838	0.962889
4320.00	0.833610	0.949483	0.955523	0.955663
5040.00	0.790701	0.937894	0.948169	0.948488
5760.00	0.745908	0.924657	0.940720	0.941362
6480.00	0.700021	0.909582	0.933108	0.934282
7200.00	0.653740	0.892539	0.925250	0.927241
7920.00	0.607683	0.873464	0.917056	0.920234
8640.00	0.562375	0.852358	0.908430	0.913249
12960.00	0.325441	0.689605	0.842416	0.870915
17280.00	0.167571	0.498444	0.743437	0.824061
21600.00	0.078682	0.325352	0.615342	0.766862
25920.00	0.034280	0.194735	0.476381	0.696101
30240.00	0.014035	0.108418	0.346443	0.613233
34560.00	0.005452	0.056825	0.238365	0.523484
38880.00	0.002024	0.028313	0.156344	0.433469
43200.00	0.000723	0.013516	0.098447	0.349037
47520.00	0.000249	0.006221	0.059878	0.274153
51840.00	0.000083	0.002775	0.035362	0.210717
56160.00	0.000027	0.001204	0.020364	0.158956
60480.00	0.000009	0.000510	0.011477	0.117996
64800.00	0.000003	0.000212	0.006348	0.086386
69120.00	0.000001	0.000086	0.003455	0.062492
73440.00	0.000000	0.000035	0.001853	0.044740
77760.00	0.000000	0.000014	0.000982	0.031740
82080.00	0.000000	0.000005	0.000514	0.022336
86400.00	0.000000	0.000002	0.000266	0.015605
90720.00	0.000000	0.000001	0.000137	0.010832
95040.00	0.000000	0.000000	0.000070	0.007474
99360.00	0.000000	0.000000	0.000035	0.005128
103680.00	0.000000	0.000000	0.000018	0.003501

Investigation of this portion of the subsystem indicates that complex redundancy exists, and a failure of the control excitation to the phasing circuit to one or more of the 16 antenna elements will cause a degradation, in performance and not a catastrophic failure. The RF would continue to be supplied to the element. Laboratory tests are to be performed to determine the antenna system failure modes and the loss effect of antenna elements upon subsystem performance. These tests should result in criteria for incorporating degradation effects in the reliability mathematical model.

A reliability prediction based upon the early engineering model design for the phased-array control electronics subsystem has been made to indicate reliability achievement. This prediction presented in Figure 7-6 encompasses a preliminary estimate of parts stress applications, duty cycles, and unit redundancy, but does not accommodate those functions within the subsystem that result in a degradation in performance rather than a catastrophic failure mechanism.

This reliability prediction reflected the need for a more reliable design to meet the spacecraft lifetime objective of 3 to 5 years. In recognition of this need, specific recommendations were made during the Syncom II design review program to improve the reliability of the subsystem. Action has been taken to reduce, significantly, the complexity of these circuits, while improving performance. Consistency of parts types throughout the subsystem has been examined to reduce to a minimum the number of different parts in subsequent circuit modifications.

A recommendation, based on these preliminary studies, was made suggesting that interquadrant paralleling of functions within the subsystem be considered as indicated in Figure 7-5 by the dashed lines. This redundancy would be accommodated prior to sine wave generator subassembly. The solar sensor arrangement shown in Figure 7-5 is desirable so that all sensors will supply inputs to all electronics packages. These recommended configurations will be compared with the additional circuit complexity for isolation to determine if a reasonable reliability improvement in the overall subsystem can be achieved.

As a result of the conclusion that this (obsolete) design configuration was not adequate for a flight model spacecraft, the estimate presented in Figure 7-6 has not been incorporated into the system reliability estimates, but subsystem objectives will be utilized until

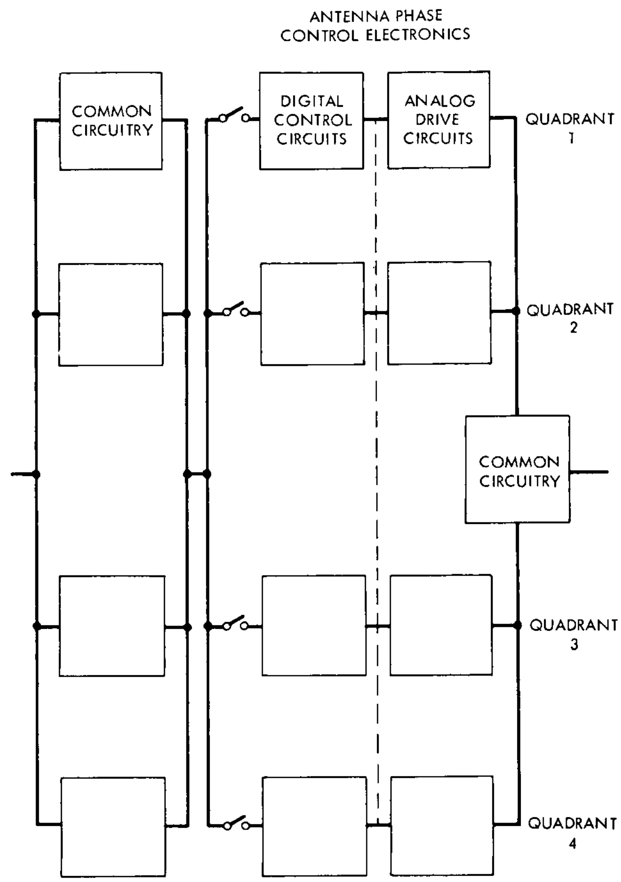

FIGURE 7-5. PHASED ARRAY ANTENNA SUBSYSTEM RELIABILITY DIAGRAM

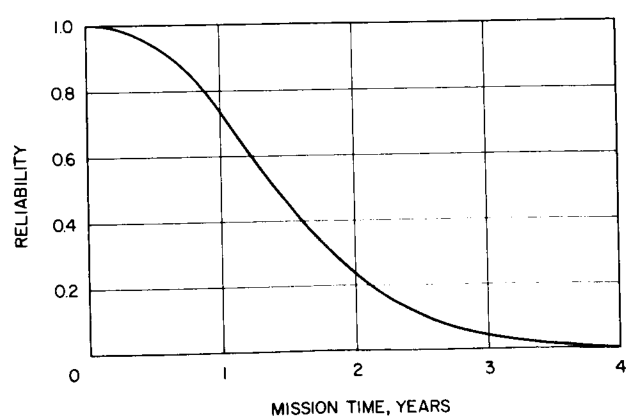

FIGURE 7-6. PHASED ARRAY CONTROL ELECTRONICS RELIABILITY ESTIMATE

further definition of the simplified circuits is completed and analyzed.

Power Supply Assessment

The solar array provides the primary power source during exposure of the spacecraft to solar light, which is nearly continuously, and a battery and charging circuitry is incorporated in the spacecraft to sustain communications throughout the brief orbital eclipse periods. Therefore, a failure of the battery or charging circuitry will cause loss of communications only during eclipses. Multiple redundancy is incorporated in the design of these units to prevent power shorts and enhance the spacecraft reliability of operation during a solar eclipse. Eclipse periods are less than 1 percent of the time in equatorial, synchronous orbits.

The system reliability studies have included analyses of several power supply configurations. This effort has been directed toward the optimization of the solar electric panel layout for maximum power output, ease of fabrication through simplification of interconnections, and enhancement of reliability through parallel redundancy of strings and minimum cost. Promising power supply configurations including both n-p and p-n solar cell types have been evaluated using the best available failure data and analysis techniques. Two examples of the results of these analyses are shown in Figures 7-7 and 7-8. These figures present the probability of survival of solar cell strings for selected mission periods based upon a binomial distribution of failures. These results may be compared to the number of acceptable solar panel string failures so that the design will ensure that adequate power will be available to the subsystems during the lifetime of the spacecraft. An analysis of the present concept for an n-p solar cell arrangement follows:

The present solar array design concept consists of 22,240 1 by 2 centimeter n-p silicon solar cells connected in 128 series-parallel groups. Each series-parallel group is assumed to be connected to the spacecraft electrical bus with two blocking or isolating diodes in parallel. It may be seen from the figures presented that the series-parallel solar cell connections provide redundancy which increases the reliability of the electrical power system. Of the 128 series-parallel string groups, 124 of them consist of three paralleled strings, each with 59 solar cells in series per string, and the other four groups consist of two paralleled strings each, also

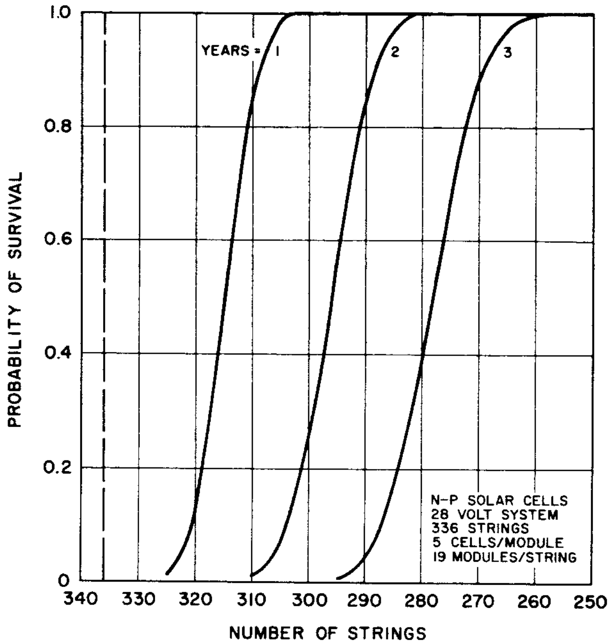

FIGURE 7-7. SOLAR ARRAY PANEL RELIABILITY ANALYSIS FOR A NONREDUNDANT 28-VOLT CONFIGURATION

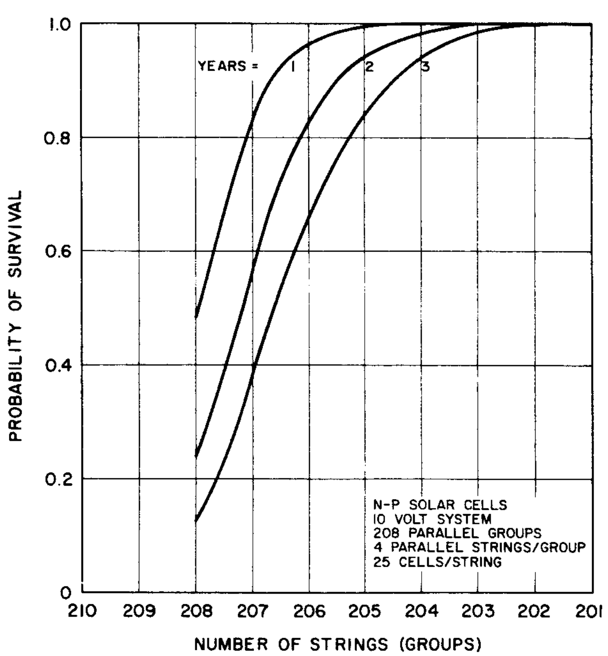

FIGURE 7-8. SOLAR ARRAY PANEL RELIABILITY ANALYSIS FOR A REDUNDANT 10-VOLT CONFIGURATION

with 59 solar cells in series per string. The mathematical model representing the reliability for this solar electric panel configuration is

$$R_{SEP} = (R_{S3}\,R_{DP})^{124}\,(R_{S2}\,R_{DP})^{4}$$

where

R_{SEP} = reliability of the solar electric panel

R_{S3} = reliability of one three-string parallel group

$= [1 - (1 - R_{Cell})^3]^{59}$

R_{DP} = reliability of the string group diode pair

$= [1 - (1 - R_{Diode})^2]$

R_{S2} = reliability of one two-string parallel group

$= [1 - (1 - R_{Cell})^2]^{59}$

This analysis represents the probability of survival for n total strings (128) based upon a purely random distribution of cell failures. For example, if R cell is exponentially distributed, i.e., $R_{Cell} = e^{-\lambda_c t}$, and $\lambda_c = 0.01 \times 10^{-5}$ failures per hour and if R_{Diode} is also exponentially distributed with $\lambda_d = .01 \times 10^{-5}$ failures per hour, a representative numerical analysis may be performed for any discrete mission period.

Utilization of these values for λ to determine solar cell and diode reliability yields a probability of survival for *all* strings of 0.990 for a 5-year mission time. It can be demonstrated, using the same cell failure characteristics, that the total number of catastrophic cell failures is equal to or less than 0.1 percent per year with a variance of approximately 20 cells per year. Even an increase in the cell failure rate by five times would result in less than 0.5 percent failures per year, insuring adequate power to the subsystems during the spacecraft lifetime.

In addition to the assumption of a random distribution of failures, a second assumption in applying this model is that the failure mode of the solar cell is an open circuit such that a cell or string failure results only in a loss of power from the individual cell or string and does not affect the performance of the remaining strings. Monte Carlo techniques to account for adjacent string failures have not been applied since these probabilities are extremely small in the redundant string configuration. These analyses show that the solar array will provide a high probability of supplying a battery charge capability and power to the subsystems during the lifetime of the spacecraft as long as no other failure mode causes a catastrophic failure of this subsystem.

A detailed analysis of the battery and charging circuitry will be performed upon the definition of circuitry and combined with this analysis to provide the probability of successful operation during periods of eclipse.

Reliability Block Diagram

The reliability block diagram representing the orbital Syncom II spacecraft logic has been continually upgraded during the Advanced Technological Development Program to reflect the latest system configuration. The reliability diagrams representing the two primary Syncom II mission functions are shown in Figure 7-9 for communications and Figure 7-10 for telemetry. The subsystems illustrated in each figure are oriented into groups of units which are redundant in each spacecraft quadrant and group of units which are common to all quadrants. A high reliability for each of the common groups is emphasized in the design approach since the catastrophic failure of one will cause a degradation in satellite performance or perhaps cause a total mission failure (i.e., failures of critical units such as the apogee rocket motor, communications antenna, power supply, etc.).

The reliability of quadrant unit groups is based on interquadrant series, and parallel and switching arrangements which represent the mission function of each subsystem. Conventional reliability expressions based upon an exponential distribution of failures apply to each unit and redundant unit group. The communications subsystem is shown in a redundant arrangement without logic paths to allow flexibility of reliability presentation. Thus the reliability of this subsystem may be expressed in terms of the probability of survival of one, two, three, or four quadrants for each mode of operation. The telemetry subsystem is treated as sequential. The four-unit power supply battery and charging circuitry configuration shown exhibits complex multiple redundancy resulting in a nonexponential binomial failure distribution requiring the survival of at least one of four during normal operation and at least two of four during the longest eclipse periods.

The various switching functions make possible the positive selection of equipments and thus alternate modes of operation for both units and quadrants. For reliability prediction, all switches are required to be

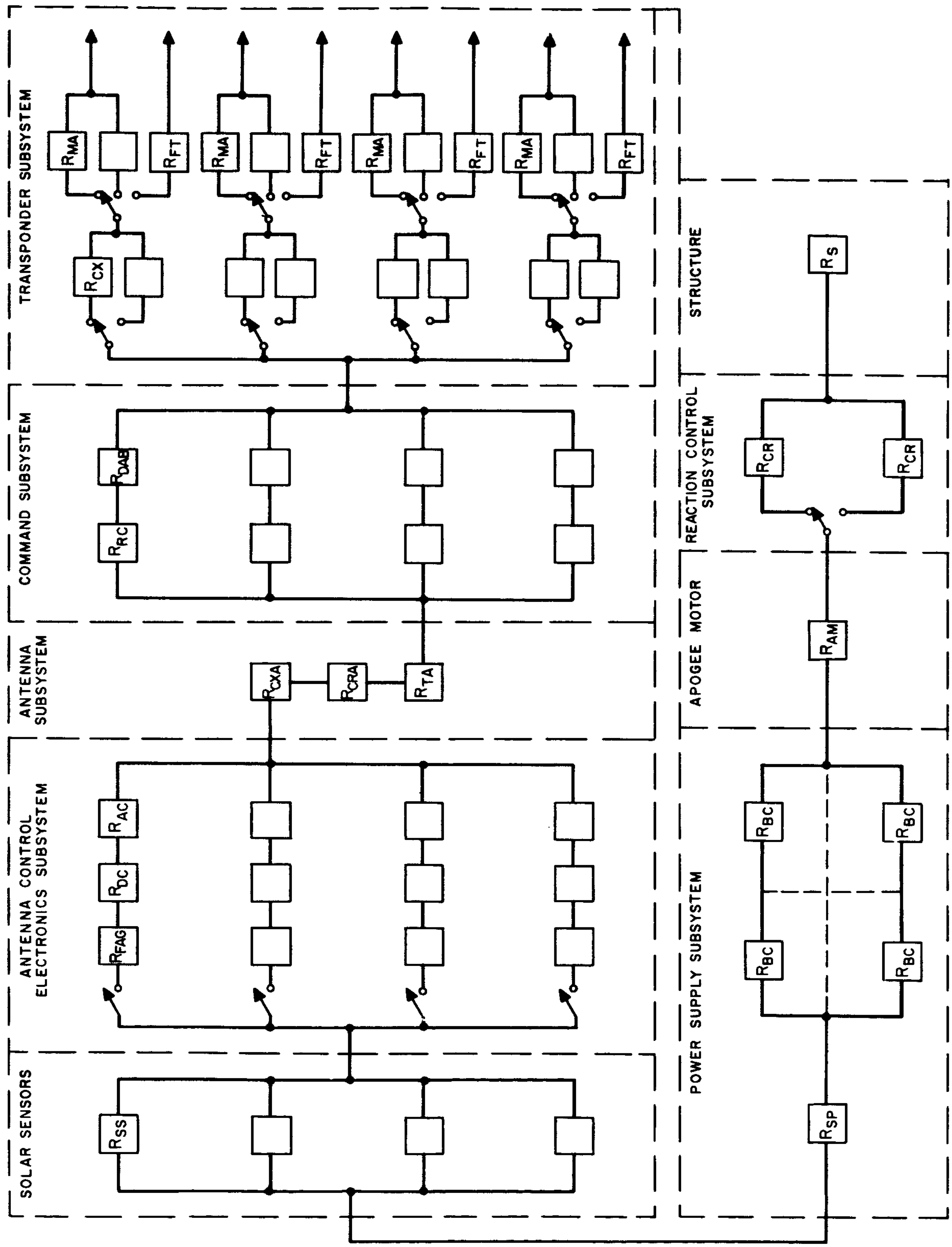

FIGURE 7-9. COMMUNICATION RELIABILITY DIAGRAM

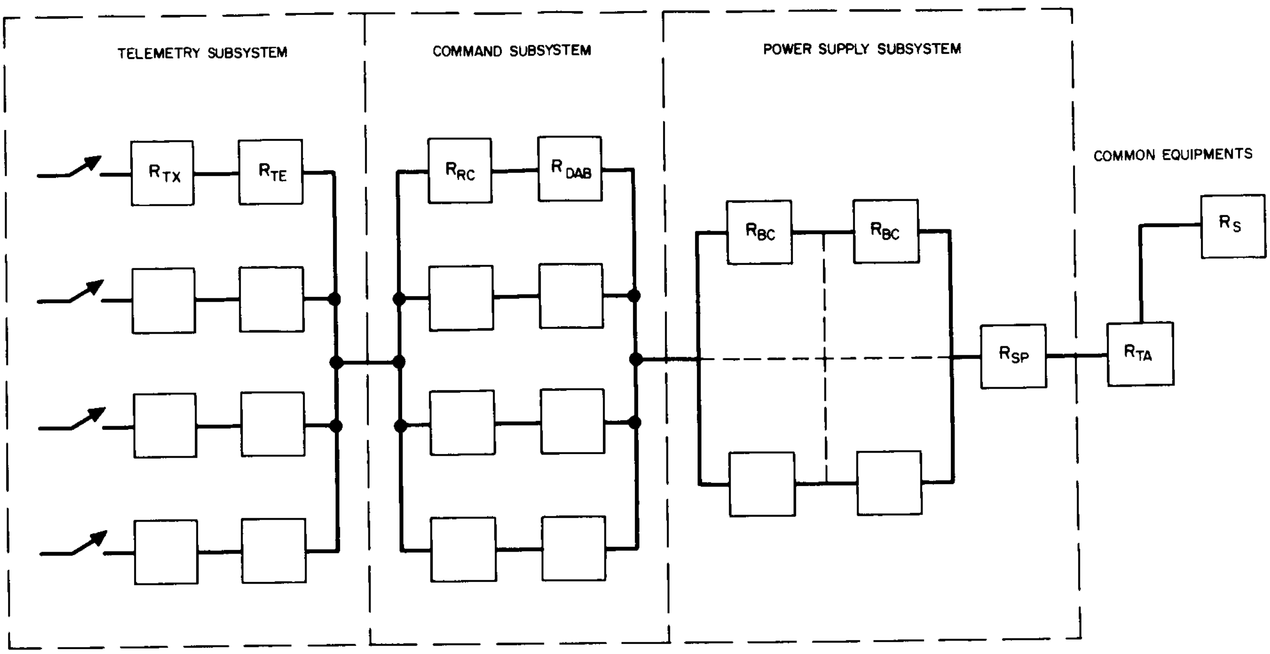

FIGURE 7-10. TELEMETRY RELIABILITY DIAGRAM

fail-safe, that is, failure of a specific switch will cause only a loss of redundancy in that function and will not in itself cause failure of the subsystem or redundant unit group.

Figures have been derived for the presently planned spacecraft configuration and are suitable for a preliminary reliability prediction to indicate the probability of mission success at this time. The further definition of the configuration and mission will necessarily require a revised reliability block diagram, mathematical model, and prediction of mission success. Definitions for the symbols used in the figures are as follows:

R_{CX} = reliability of one communications transmitter

R_{MA} = reliability of one multiple-access receiver

R_{FT} = reliability of one frequency translation receiver

R_{DAB} = reliability of one command decoder (A + B combined)

R_{RC} = reliability of one command receiver and diplexer

R_{FAG} = reliability of one fire angle generator (orientation timing)

R_{DC} = reliability of one antenna control electronics, digital circuits

R_{AC} = reliability of one antenna control electronics, analog circuits

R_{SS} = reliability of one solar sensor group

R_{CXA} = reliability of the communications transmitter antenna and diplexer

R_{CRA} = reliability of the communications receiver antenna and diplexer

R_{TA} = reliability of the command and telemetry antenna

R_{CR} = reliability of one reaction control (Hot gas system velocity and orientation jets)

R_{TX} = reliability of one telemetry transmitter and diplexer

R_{TE} = reliability of one telemetry encoder

R_{BC} = reliability of one battery set and charging circuitry

R_{SP} = reliability of the solar panel

P_s = probability of success of switching function

R_{CX} = reliability of one communications transmitter

λ_{cx} = failure rate of one communications transmitter

R_{MA} = reliability of one multiple access receiver

λ_{ma} = failure rate of one multiple access receiver

R_{CTF} = reliability of communications transponder subsystem — frequency translation mode

$$= \left[\sum_{r=1,2,3,4}^{4} \frac{4!}{(4-r)!r!} [R_{CX}(1+P_s\lambda_{cx}t)R_{FT}]^r [1-R_{CX}(1+P_s\lambda_{cx}t)R_{FT}]^{4-r} \right]$$

where

R_{FT} = reliability of one multiple access receiver

λ_{ma} = failure rate of one multiple access receiver

R_{TS} = reliability of the telemetry subsystem

$$= R_{TX}R_{TE}\left[1 + P_s\lambda_t t + \frac{(\lambda_t t)^2 P_s^2}{2!} + \frac{P_s^3(\lambda t)^3}{3!}\right]$$

where

R_{TX} = reliability of one telemetry transmitter and diplexer

R_{TE} = reliability of one telemetry encoder

λ_t = failure rate of one telemetry subsystem quadrant

R_{CS} = reliability of command subsystem

$$[1-(1-R_{DAB}R_{RC})^4]$$

and

R_{DAB} = reliability of one command decoder (A and B)

R_{RC} = reliability of one command receiver and diplexer

R_{AS} = reliability of spacecraft antenna subsystems

$$= R_{CXA}\,R_{CRA}\,R_{TA}$$

and

R_{CXA} = reliability of communications transmitter antenna and diplexer

R_{CRA} = reliability of communications receiver antenna and diplexer

R_{TA} = reliability of command and telemetry antenna

R_{ACS} = reliability of antenna control electronics subsystem

$$= R_{FAG}\,R_{AC}\,R_{DC}\left[1 + P_s\lambda_a t + \frac{P_s^2(\lambda_a t)^2}{2!} + \frac{P_s^3(\lambda_a t)^3}{3!}\right]$$

and

R_{FAG} = reliability of one fire angle generator

R_{AC} = reliability of one antenna control electronics, analog circuits

R_{DC} = reliability of one antenna control electronics, digital circuits

λ_a = failure rate of one antenna control quadrant

R_{sss} = reliability of the system solar sensors

$$= [1-(1-R_{SS})^4] \text{ and}$$

R_{SS} = reliability of one solar sensor group

R_{RCS} = reliability of the reaction control subsystem

$$= R_{CR}(1+P_s\lambda_{cr}t)$$

and

R_{CR} = reliability of one reaction control; (hot gas system, velocity and orientation jets)

λ_{cr} = failure rate of one reaction control

R_{PS} = reliability of the power supply; at least two of four batteries and charging circuitry surviving during eclipse

$$= [3R_{BC}^4 - 8R_{BC}^3 + 6R_{BC}^2]\,R_{SP}$$

where

R_{BC} = reliability of one battery set and charging circuitry

R_{SP} = reliability of the solar panel

R_{AM} = reliability of the apogee motor

R_S = reliability of the structure

The reliability of each communications mode and telemetry incorporating the redundant nature of each subsystem may now be combined and further defined for the mathematical model as:

Multiple Access Communictations

$$R_{MAC} = (R_B R_{SO}) \left[\sum_{r=1,2,3,4}^{4} \frac{4!}{(4-r)!r!} [R_{CX}(1+P_s\lambda_{cx}t)R_{MA}(1+P_s\lambda_{MA}t)]^r [1-R_{CX}(1+P_s\lambda_{cx}t)R_{MA}(1+P_s\lambda_{MA}t)]^{4-r} \right]$$

$$[1-(1-R_{SS})^4] \; [1-(1-R_{DAB}R_{RC})^4]$$

$$R_{FAG} R_{AC} R_{DC} \left[1 + P_s\lambda_a t + \frac{P_s^2(\lambda_a t)^2}{2!} + \frac{P_s^3(\lambda_a t)^3}{3!} \right]$$

$$(R_{CXA} R_{CRA} R_{TA}) \, R_{CR} \, (1 + P_s\lambda_{cr}t) \, R_{PS} \, R_{AM} \, R_S$$

Frequency Translation Communications

$$R_{NC} = (R_B R_{SO}) \left[\sum_{r=1,2,3,4}^{4} \frac{4!}{(4-r)!r!} [R_{CX}(1+P_S\lambda_{cx}t)R_{FT}]^r [1-R_{CX}(1+P_s\lambda_{cx}t)R_{FT}]^{4-r} \right]$$

$$[1-(1-R_{SS})^4] \; [1-(1-R_{DAB}R_{RC})^4]$$

$$R_{FAG} R_{AC} R_{DC} \left[1 + P_s\lambda_a t + \frac{P_s^2(\lambda_a t)^2}{2!} + \frac{P_s^3(\lambda_t t)^3}{3!} \right]$$

$$(R_{CXA} R_{CRA} R_{TA}) \, R_{CR} \, (1 + P_s\lambda_{cr}t) \, R_{PS} \, R_{AM} \, R_S$$

Telemetry

$$R_T = (R_B R_{SO}) \; [1-(1-R_{DAB}R_{RC})^4]$$

$$R_{TX} R_{TE} \left[1 + P_s\lambda_t t + \frac{P_s^2(\lambda_t t)^2}{2!} + \frac{P_s^3(\lambda_t t)^3}{3!} \right] R_{TA} R_{PS} R_S$$

These equations have resulted from reliability requirements and trade-off studies accomplished during the Advanced Technological Development Program. As the program continues, these equations will be updated further to include alternate modes of system operation in addition to new design concepts and configurations.

SYSTEM AVAILABILITY STUDIES

Introduction

An evaluation of the general reliability function, R(t), has been accomplished to yield mathematical models for the following system parameters; launch rate to establish the initial system; deployment time; replacement criteria; time availability for a single spacecraft; and time availability for a three-satellite synchronous equatorial system. Briefly, the launch rate criteria has been defined by the rate of growth of the system and the number of spacecraft (channels) which became inoperative during the deployment period. The deployment time required to initiate a system may be readily determined from this function and a knowledge of the number of spacecraft launched. Replacement criteria have been derived in accordance with two basic assumptions: 1) there is a minimum number of channels per spacecraft acceptable to complete a successful mission, and 2) there is a mathematical model which accurately represents the system reliability functions, $R_s(t)$. The time availability (or up-time ratio) is the percentage of total time that the system is expected to be in an operable state. The mathematical expression of these relationships in terms of the spacecraft reliability function is expected to yield parameters for achieving optimum communication capability in relation to cost.

The fourfold redundancy and stepwise quadrant degradation of the Syncom II spacecraft make it possible, by proper choice of replacement decision criteria, to reduce the frequency of catastrophic communication

P_s = probability of success of switching function

R_{CX} = reliability of one communications transmitter

λ_{cx} = failure rate of one communications transmitter

R_{MA} = reliability of one multiple access receiver

λ_{ma} = failure rate of one multiple access receiver

R_{CTF} = reliability of communications transponder subsystem — frequency translation mode

$$= \left[\sum_{r=1,2,3,4}^{4} \frac{4!}{(4-r)!r!} [R_{CX}(1+P_s\lambda_{cx}t)R_{FT}]^r [1-R_{CX}(1+P_s\lambda_{cx}t)R_{FT}]^{4-r} \right]$$

where

R_{FT} = reliability of one multiple access receiver

λ_{ma} = failure rate of one multiple access receiver

R_{TS} = reliability of the telemetry subsystem

$$= R_{TX}R_{TE}\left[\frac{1+P_s\lambda_t t+(\lambda_t t)^2P_s^2}{2!}+\frac{P_S^3(\lambda t)^3}{3!}\right]$$

where

R_{TX} = reliability of one telemetry transmitter and diplexer

R_{TE} = reliability of one telemetry encoder

λ_t = failure rate of one telemetry subsystem quadrant

R_{CS} = reliability of command subsystem

$$[1-(1-R_{DAB}R_{RC})^4]$$

and

λ_c = failure rate of one command quadrant

R_{DAB} = reliability of one command decoder (A and B)

R_{RC} = reliability of one command receiver and diplexer

R_{AS} = reliability of spacecraft antenna subsystems

$$= R_{CXA}R_{CRA}R_{TA}$$

and

R_{CXA} = reliability of communications transmitter antenna and diplexer

R_{CRA} = reliability of communications receiver antenna and diplexer

R_{TA} = reliability of command and telemetry antenna

R_{ACS} = reliability of antenna control electronics subsystem

$$= R_{FAG} = R_{AC}R_{DC}\left[1+P_s\lambda_a t+\frac{P_s^2(\lambda_s t)^2}{2!}+\frac{P_s^3(\lambda_s t)^3}{3!}\right]$$

and

R_{FAG} = reliability of one fire angle generator

R_{AC} = reliability of one antenna control electronics, analog circuits

R_{DC} = reliability of one antenna control electronics, digital circuits

λ_a = failure rate of one antenna control quadrant

R_{sss} = reliability of the system solar sensors

$$= [1-(1-R_{SS})^4]$$

and

R_{SS} = reliability of one solar sensor group

R_{RCS} = reliability of the reaction control subsystem

$$= [1-(1-R_{CR})^2]$$

and

R_{CR} = reliability of one reaction control; (hot gas system, velocity and orientation jets)

R_{PS} = reliability of the power supply; at least two of four batteries & charging circuitry surviving during eclipse

$$= [3R_{BC}^4 - 8R_{BC}^3 + 6R_{BC}^2]R_{SP}$$

where

R_{BC} = reliability of one battery set and charging circuitry

R_{SP} = reliability of the solar panel

R_{AM} = reliability of the apogee motor

R_S = reliability of the structure

R_{LT} = reliability of the spacecraft system control times

The reliability of each communications mode and telemetry incorporating the redundant nature of each subsystem may now be combined and further defined for the mathematical model as:

Multiple Access Communictations

$$R_{MAC} = (R_B R_{SO}) \left[\sum_{r=1,2,3,4}^{4} \frac{4!}{(4-r)!r!} \right.$$

$$[R_{CX}(1 + P_s\lambda_{cx}t) R_{MA}(1 + P_s\lambda_{MA}t)]^r$$

$$\left. [1 - R_{CX}(1 + P_s\lambda_{cx}t) R_{MA}(1 + P_s\lambda_{MA}t)]^{4-r} \right]$$

$$[1 - (1 - R_{SS})^4] \; [1 - (1 - R_{DAB} R_{CR})^4]$$

$$R_{FAG} R_{AC} R_{DC} \left[1 + P_s\lambda_a t + \frac{P_s^2(\lambda_a t)^2}{2!} + \frac{P_s^3(\lambda_s t)^3}{3!} \right]$$

$$(R_{CXA} R_{CRA} R_{TA}) \; [1 - (1 - R_{CR})^2] R_{PS} R_{AM} R_S R_{CT}$$

Frequency Translation Communications

$$R_{NC} = (R_B R_{SO}) \left[\sum_{r=1,2,3,4}^{4} \frac{4!}{(4-r)!r!} \right.$$

$$[R_{CX}(1 + P_s\lambda_{cx}t) R_{FT}]^r$$

$$\left. [1 - R_{CX}(1 + P_s\lambda_{cx}t) R_{FT}]^{4-r} \right]$$

$$[1 - (1 - R_{SS})^4] \; [1 - (1 - R_{DAB} R_{RC})^4]$$

$$R_{FAG} R_{AC} R_{DC} \left[1 + P_s\lambda_a t + \frac{P_s^2(\lambda_a t)^2}{2!} + \frac{P_s^3(\lambda_s t)^3}{3!} \right]$$

$$(R_{CXA} R_{CRA} R_{TA}) [1 - (1 - R_{CR})^2] R_{PS} R_{AM} R_S R_{CT}$$

Telemetry

$$R_T = (R_B R_{SO}) \; [1 - (1 - R_{DAB} R_{RC})^4]$$

$$R_{TX} R_{TE} \left[1 + P_s\lambda_t t + \frac{P_s^2(\lambda_t t)^2}{2!} \right.$$

$$\left. + \frac{P_s^3(\lambda_t t)^3}{3!} \right] R_{TA} R_{PS} R_S R_{CT}$$

These equations have resulted from reliability requirements and trade-off studies accomplished during the Advanced Technological Development Program. As the program continues, these equations will be updated further to include alternate modes of system operation in addition to new design concepts and configurations.

SYSTEM AVAILABILITY STUDIES

Introduction

An evaluation of the general reliability function, R(t), has been accomplished to yield mathematical models for the following system parameters; launch rate to establish the initial system deployment time; replacement criteria; time availability for a single spacecraft; and time availability for a three-satellite synchronous equatorial system. Briefly, the launch rate criteria has been defined by the rate of growth of the system and the number of spacecraft (channels) which became inoperative during the deployment period. The deployment time required to initiate a system may be readily determined from this function and a knowledge of the number of spacecraft launched. Replacement criteria have been derived in accordance with two basic assumptions: 1) there is a minimum number of channels per spacecraft acceptable to complete a successful mission, and 2) there is a mathematical model which accurately represents the system reliability functions, $R_s(t)$. The time availability (or up-time ratio) is the percentage of total time that the system is expected to be in an operable state. The mathematical expression of these relationships in terms of the spacecraft reliability function is expected to yield parameters for achieving optimum communication capability in relation to cost.

The fourfold redundancy and stepwise quadrant degradation of the Syncom II spacecraft make it possible, by proper choice of replacement decision criteria, to reduce the frequency of catastrophic communication failures. Thus, primary emphasis has been placed on a study of the availability function during the Advanced Technological Development Program for several "decision to replace" criteria to optimize availability and minimize the replacement rate. Preliminary studies have resulted in the development of mathematical models and formulas which describe the relationship between reliability predictions and spacecraft availability assuming a fixed time (old age) replacement policy. It is apparent from the probabilistic models that a significant gain will be achieved by minimizing the actual replacement time and maximizing the booster and launch sequence reliabilities. An estimation of the number of communications spacecraft required, as a function of the predicted spacecraft failure distributions for the fixed time replacement policy, has been made. Curves are presented showing plots of 1) cumulative probability of failure versus time, 2) probability of failure in 6 months after replacement versus time, 3) conditional probability of failure in the next 6 months after replacement versus time, 4) percent of nonuseful time and number of replacements per year versus time, 5) expected remaining lifetime, 6) ratio of duplicated time to total time as a function of replacement time, and 7) frequency distribution of satellite outages. The fourth figure is of primary importance since it describes availability (One minus the percent of nonuseful time) in terms of the replacement interval and the satellite launch rate required to obtain a prescribed availability.

Even though the old age replacement policy yields a high availability and low replacement rate for each satellite orbital location, (for example, 0.98 with 0.36 per year) the number of outages which limit availability may be further minimized by formulating a probabilistic model which considers the "state of health" of each spacecraft after launch and during the orbital mission. Periodic monitoring of each spacecraft would provide up-to-date information to improve the reliability prediction and therefore replacement criteria. Therefore, by computing the communication channel transition probabilities periodically during the orbital mission, the estimates of the probabilities of failure may be improved and used to reduce the probability of an unanticipated failure which would cause an outage of the full time required to prepare and launch a new spacecraft. An extension of this work would involve an analysis of techniques which might take advantage of the remaining useful life of an operable satellite that has been replaced. This would involve estimates of standby reliability in space if both satellites are not to be used simultaneously. The following sections describe the mathematical models and resulting conclusions for a fixed time replacement policy.

Probabilistic Model for Spacecraft Availability and Replacement Rate

Probabilistic models for spacecraft availability and replacement rate have been developed and in this section a summary of the steps in the mathematical development is presented.

The probability of a spacecraft failure prior to, during, and after replacement are characterized by three failure modes (Figure 7-11). Formulation of the utilization, outage, and duplication times yields equations that describe the function of useful time (up-time ratio or availability), fractions of nonuseful time (down-time ratio), and fraction of duplication time. Mathematical models for the number of satellites needed and replacement rate are presented. Numerical estimates of availability and replacement rate for one spacecraft based upon the probability of survival of at least one of four communications quadrants (Figure 7-12) illustrates the models.

SYSTEM DESCRIPTION AND DEFINITIONS

In this system, a communication satellite has a known distribution of life times given in Figure 7-11. A single satellite is in operation. Some replacement rule (to be discussed in a subsequent report) is used to establish r, the time of decision to replace the satellite. At time S later, the satellite is replaced. The replacer has definite and instantaneous knowledge of the satellite's status (live or dead).

Three failure modes can be described:

1) The satellite fails at time j, before the replacement decision is made, the replacement decision is instantly made, and replacement occurs at time S later, i.e., at time j + S.
2) The satellite lives until time r but fails between r and r + S, i.e., after the replacement decision is made, but before the replacement is completed. Failure occurs at r + k.
3) The satellite lives until time r and then until after r + S; i.e., after replacement has been com-

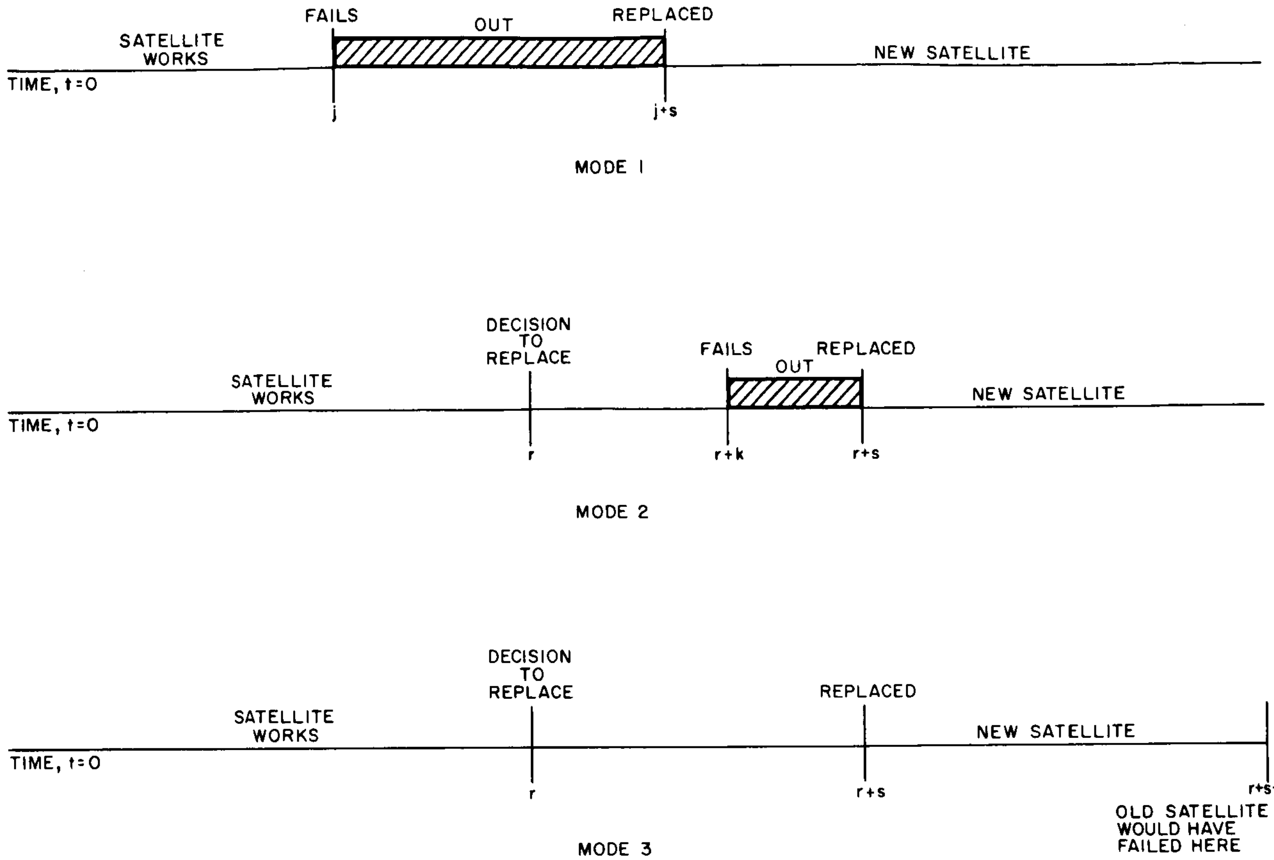

FIGURE 7-11. SPACECRAFT FAILURE MODES

pleted the original satellite is still in working order. Furthermore, the original satellite is removed, even though still usable, as soon as replacement is complete. If it were not removed, it would fail at some later time r + S + 1. Figure 7-11 illustrates the three failure modes and aids in the definition of the terms.

The probability of failure by time t will be indicated by P(t). Thus,

P(r) = probability of satellite failure between time zero and time r, which is the time of decision to replace

P(r + S) = probability of failure by time r + S, etc.

UTILIZATION, OUTAGE, AND DUPLICATION TIMES

Consider a period of time T long enough to be essentially infinite compared to any single satellite lifetime.

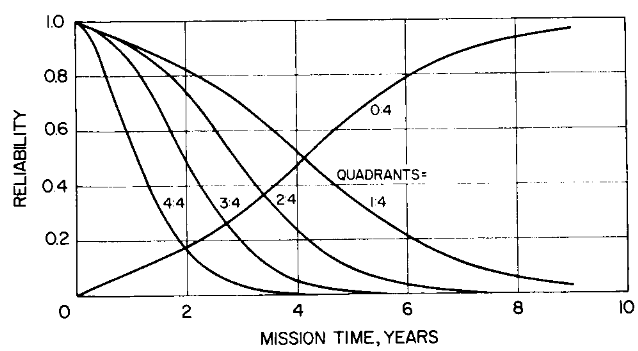

FIGURE 7-12. QUADRANT PROBABILITY OF SURVIVAL, MULTIPLE-ACCESS COMMUNICATION MODE

It will be composed of a random mixture of satellite lifetimes, each ending in one of the three failure modes.

The length of time due to each Mode 1 failure will be j + S, and of this j will be useful and S will be nonuseful. N will be the total number of satellites used in time T. The probability of failure in Mode 1 will be P(r). Therefore, the expected time spent by satellites that fail in Mode 1 will be:

$N[P(r)\ (j+S)]$	total time
$N[P(r)\ (j)]$	total useful time (live satellite)
$N[P(r)\ (S)]$	total nonuseful time (dead satellite)

The length of time due to each Mode 2 failure will be $r + S$, and of this $r + k$ will be useful and $S - k$ will be nonuseful time. The probability of failure in Mode 2 will be $P(r + S) - P(r)$, that is, the probability of failing by time $r + S$ minus the probability of failing by time r. Therefore, the expected times spent by satellites that fail in Mode 2 will be:

$$N[P(r+S) - P(r)]\ (r+S) \quad \text{total time} \tag{7-1}$$

$$N[P(r+S) - P(r)]\ (r+k) \quad \text{total useful time (live satellite)} \tag{7-2}$$

$$N[P(r+S) - P(r)]\ (S-k) \quad \text{total nonuseful time (dead satellite)} \tag{7-3}$$

The length of time due to each Mode 3 failure will be $r + S$ and will be all useful. The length of time that would be spent by the old satellite after replacement as duplication time if it were not removed at replacement is 1. The probability of failure in Mode 3 will be $1 - P(r + S)$. Therefore, the expected times spent by satellites that fail in Mode 3 will be:

$$N[1-P(r+S)]\ (r+S) \quad \text{total time} \tag{7-4}$$

$$N[1-P(r+S)]\ (r+S) \quad \text{total useful time (live satellite)} \tag{7-5}$$

$$N[1-P(r+S)]\ (1) \quad \text{total duplication time} \tag{7-6}$$

These expressions can be combined in various ways:

$$T = N\{P(r)\ (j+S) + [P(r+S)\ P(r)]\ (r+S) + [1-P(r+S)]\ (r+S)\} \tag{7-7}$$

$$= N\{(j-r)\ P(r) + (r+S)\} \tag{7-8}$$

$$T_{useful} = N\{P(r)\ (j) + [P(r+S) - P(r)]\ (r+k) + [1-P(r+S)]\ (r+S)\} \tag{7-9}$$

$$= N\{P(r)\ (j-r-k) + P(r+S)\ (k-S) + (r+S)\} \tag{7-10}$$

$$T_{nonuseful} = N\{P(r)\ (S) + [P(r+S) - P(r)]\ (S-k)\} \tag{7-11}$$

$$= N\{k\,P(r) + (S-k)\ P(r+S)\} \tag{7-12}$$

$$T_{duplication} = N[1-P(r+S)]\ (1) \tag{7-13}$$

Fraction of nonuseful time is:

$$\frac{T_{nonuseful}}{T} = \frac{k\,P(r) + (S-k)\ P(r+S)}{(j-r)\ P(r) + r + S} \tag{7-14}$$

Fraction of useful time is:

$$\frac{T_{useful}}{T} = \frac{(j-r-k)\ P(r) + (k-S)\,P(r+S) + (r+S)}{(j-r)\ P(r) + (r+S)} \tag{7-15}$$

Fraction of duplication time is:

$$\frac{T_{duplication}}{T} = \frac{(1)\ [1-P(r+S)]}{(j-r)\ P(r) + (r+S)} \tag{7-16}$$

NUMBERS OF SATELLITES NEEDED

The number of satellites needed in time T will be designated N, an $T = N\,L$, where L is the mean satellite useful life. Since there are three failure modes, this can be broken down into N_1, N_2, and N_3, with L_1, L_2, and L_3 for mean lives. Then

$$N = N_1 + N_2 + N_3 \tag{7-17}$$

$$T = T_1 + T_2 + T_3 \tag{7-18}$$

and so

$$T = N_1L_1 + N_2L_2 + N_3L_3 \tag{7-19}$$

and

$$N = \frac{T_1}{L_1} + \frac{T_2}{L_2} + \frac{T_3}{L_3} \qquad (7\text{-}20)$$

The rate of replacement of satellites is given by

$$\frac{N}{T} = \frac{1}{L} = \frac{1}{(j - r)\,P(r) + (r + S)} \qquad (7\text{-}21)$$

NUMERICAL VALUES

The lifetime characteristic for Syncom II given in Figure 7-12 enables estimation of the fraction of useful time and the expected launch rate. If a satellite is replaced on the average of every 2 years, unless a failure occurs sooner, the $r = Z$. Because of the knowledge of the satellite status, this does not mean an arbitrary replacement at 2 years, but rather a replacement based on some stated criterion that occurs on the average of every 2 years, such as having at least three channels functioning. The rest of the parameters are as follows as determined from Figure 7-12.

$$r = 2 \text{ years}$$

$$P(r) = 0.18$$

$$S = 0.2 \text{ year}^*$$

$$j = 1 \text{ year}$$

$$k = 0.1 \text{ year}^*$$

$$P(r + S) = 0.20$$

For convenient numerical evaluating

$$\frac{T_{useful}}{T} = 1 - \frac{T_{nonuseful}}{T}$$

substituting

$$\frac{T_{useful}}{T} = 1 - \frac{k(Pr) + (S - k)\,P(r + S)}{(j - r)\,P(r) + r + S}$$

$$= 0.9812$$

The number of satellites needed is evaluated from the equation that defines rate of replacement of satellites (shown under the heading of "Numbers of Satellites Needed"), using the same parameters.

*Reaction time is 0.1 year, but because of boost failures 50 percent of the time S must be increased to 0.2 year and k to 0.1 from 0.05.

$$\frac{N}{T} = \frac{1}{2.02} = 0.495 \text{ per year}$$

The replacement rate is equal to N/T divided by the boost reliability 0.5 or 0.99 per year.

These conclusions are conservative, as possible use of satellite communication channels in those satellites that had called for replacement is neglected. It is interesting to compare this result with that for a satellite with the lifetime characteristics of Syncom II, which is replaced only upon complete failure. Maintainability theory gives

$$\frac{T_{useful}}{T} = \frac{1}{1 + \frac{S}{\lambda}}$$

When S is as before the replacement time and λ is the mean life for at least one channel (4 years)

$$\frac{T_{useful}}{T} = \frac{1}{1 + \frac{0.2}{4}} = 0.952$$

Cost effectiveness considerations make use of this model appropriate to optimize the decision criteria adopted for Syncom II.

Spacecraft Launch Rate and Availability: Fixed Time Replacement Policy

Probabilistic models for spacecraft availability and replacement rate have been developed by previous discussion. An estimation of the number of communication satellites required as a function of the predicted spacecraft failure distributions is presented here. The estimate is based on a fixed time replacement policy, i.e., a discrete period of time is selected and the spacecraft is replaced at the end of that period even if it remains operable. If it fails before the fixed replacement time, it is replaced immediately (limited by the time required for launch).

At least three distinct replacement policies may be developed. The first category comprises schemes using only *a priori* information. Such an approach is developed in this discussion where predictions of failure distributions as functions of time and number of communication channels still operating are made before the flight. A replacement policy is evolved based on this information only to provide a preliminary indication of the number of spacecraft required and launch rate for a selected availability. Clearly, if more information were available, a more efficient replacement policy could conceivably be developed. It may be noted that this policy may be extended to the dynamic condition during orbital flight where telemetry data is available to upgrade the reliability model and predicted failure distributions as failures occur.

The second category of replacement policy has available the preflight failure rate distributions and in addition uses information regarding the current live-or-dead status of the four communications quadrants. Replacement policies may be developed utilizing this extra information.

The third category has available the information of the second category as well as a large amount of telemetry channel information during the flight program to determine the status of the spacecraft subsystems. This additional information enables even more efficient replacement policies to be devised. The latter replacement policies are more complex in nature and may require dynamic programming to optimize the replacement criteria for maximum availability with a minimum number of spacecraft and duplication time. These policies are currently under investigation.

FAILURE DISTRIBUTION ESTIMATES

The failure distributions used for this analysis were presented in Figure 7-12. Negative exponential distributions were assumed for components and were combined in a computer program to include the circuitry, interconnections, redundancy, and switching to obtain the estimates presented and used here. Although these distributions may vary somewhat as the details of circuits are further defined, the method described is representative of the first approximation to availability and the replacement interval.

The example considered includes only the probabilities concerned with complete communications failure — i.e., all 4 communications quadrants (channels) are dead. The data is available for the other cases — 0, 1, 2, or 3 dead — and more comprehensive analyses can be made using the same methods. The failure distribution used is shown in Table 7-9. Column 3, as the probability of at least 1 of the 4 working, and in Column 2 as the probability of none of the 4 working. Columns 4, 5, and 6 give the probabilities respectively of at least 2, 3, and 4 quadrants or channels working.

The cumulative distribution with time to complete failure (none out of four communications quadrants operable) is shown in Figure 7-13 and the density function, actually the failure rate as a function of time, in Figure 7-11. It can be seen that the system failure rate is nearly constant for $1\frac{1}{2}$ years, then rises rapidly to a maximum at 4 years before dying out at about 9 or 10 years. Figure 7-14 shows the conditional failure rate — that is, the probability that a satellite will fail in the next 6 months, if it has not yet failed at time r (the time at which the satellite is replaced).

FRACTION OF NONUSEFUL TIME

The derivation of some useful equations used here is presented in "Probabilistic Model for Spacecraft

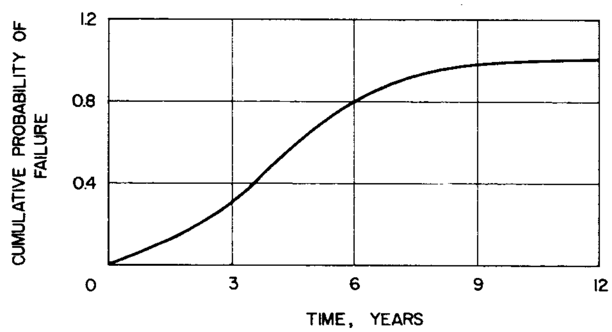

FIGURE 7-13. CUMULATIVE DISTRIBUTION OF FAILURES

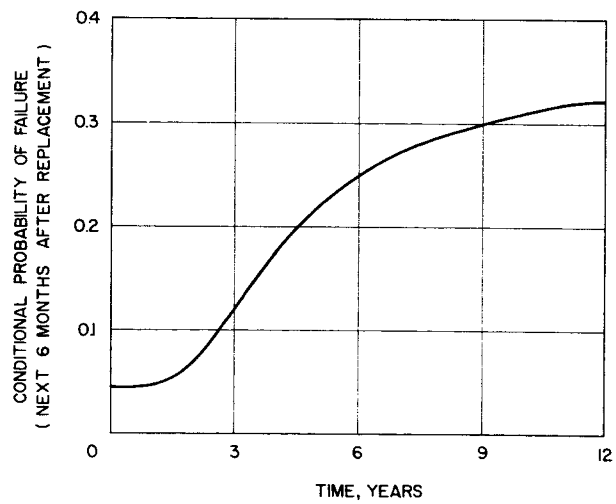

FIGURE 7-14. CONDITIONAL DISTRIBUTION OF FAILURES

TABLE 7-9. SATELLITE COMMUNICATION CHANNEL PROBABILITIES

t years (1)	1-P(t) = P (none working) (2)	1-P(t) = P (one or more working) (3)	P (two or more working) (4)	P (three or more working) (5)	P (all four working) (6)
0	0.000000	1.000000	1.000000	1.000000	1.000000
1/12	0.007503	0.992497	0.992497	0.992491	0.988362
2/12	0.014950	0.985050	0.985050	0.984953	0.969105
3/12	0.022341	0.977659	0.977657	0.977196	0.943173
4/12	0.029676	0.970324	0.970310	0.968954	0.911556
5/12	0.036958	0.963042	0.962993	0.959921	0.875250
6/12	0.044185	0.955815	0.955680	0.949788	0.835230
7/12	0.051362	0.948638	0.948330	0.938265	0.792426
8/12	0.058488	0.941512	0.940888	0.925104	0.747704
9/12	0.065569	0.934431	0.933285	0.910112	0.701855
10/12	0.072610	0.927390	0.925440	0.893156	0.655586
11/12	0.079618	0.920382	0.917264	0.874171	0.609515
1	0.086602	0.913398	0.908659	0.853152	0.564173
1.5	0.128918	0.871082	0.842853	0.690798	0.326786
2	0.175712	0.824288	0.744130	0.499688	0.168386
2.5	0.232814	0.767186	0.616206	0.326380	0.079111
3	0.303469	0.696531	0.477269	0.195460	0.034483
3.5	0.386255	0.613745	0.347232	0.108871	0.014123
4	0.475964	0.524036	0.238994	0.057084	0.005488
4.5	0.565986	0.434014	0.156805	0.028452	0.002038
5	0.650460	0.349540	0.098763	0.013586	0.000728
5.5	0.725408	0.274592	0.060084	0.006255	0.000251
6	0.788916	0.211084	0.035490	0.002790	0.000084
6.5	0.840748	0.159252	0.020441	0.001211	0.000027
7	0.881773	0.118227	0.011522	0.000513	0.000009
7.5	0.913437	0.086563	0.006374	0.000213	0.000003
8	0.937375	0.062625	0.003469	0.000087	0.000001
8.5	0.955163	0.044837	0.001861	0.000035	0
9	0.968189	0.031811	0.000986	0.000014	0
9.5	0.977613	0.022387	0.000516	0.000005	0
10	0.984358	0.015642	0.000268	0.000002	0
10.5	0.989142	0.010858	0.000137	0.000001	0
11	0.992508	0.007492	0.000070	0	0
11.5	0.994859	0.005141	0.000035	0	0
12	0.996490	0.003510	0.000018	0	0

Availability and Replacement Rate." The significant terms of those equations are redefined below:

r = time of decision to replace

$r + s$ = time of replacement

j = time of failure if failure occurs before r

$r + k$ = time of failure if failure occurs between r and $r + s$

$r + s + m$ = time of failure if failure occurs after $r + s$ (in the Report referred to above, 1 was used instead of m)

$P(t)$ = probability of failure by time t

T = period of time long compared to any single satellite life

N = number of satellites used in time T

The fraction of nonuseful time is as given under the referenced heading:

$$\frac{T_{nonuseful}}{T} = \frac{kP(r) + (S - k)P(r + s)}{(j - r)P(r) + r + s}$$

A realistic example would be the assumption that it always takes 1 month after a decision to replace is made before a launch is attempted. The probability of success of such launch attempts is assumed to be $p = \frac{1}{2}$ and in the event of a failure, another attempt is made 1 month later. The time to replace has a geometric distribution with a means of $1/p$ or, in this case, $S = 2$ months, and an average of two satellites will be launched for each one successfully put into orbit and working properly. In a 2-month period, any of the failure rate curves can be adequately approximated by a straight line. Therefore, it is assumed that $k = 1$ month, for $S = 2$ months is the average life, after r, of those failing between r and $r + s$.

The remainder of the calculation follows in a straightforward manner from the above equation and Table 7-10, and the results are plotted in Figure 7-15.

SATELLITE REPLACEMENT RATES

The equation for satellite replacement rates, N/T, is:

$$\frac{N}{T} = \frac{1}{L} \qquad \frac{1}{(j - r)P(r) + r + s}$$

These results are also plotted in Figure 7-15. They do not include the satellites assumed lost during launch but only those failing after a successful launch.

SATELLITE DUPLICATION TIME

The equation for satellite duplication time, the ratio of time the old replaced satellites still could have functioned had they been used after being replaced to total time, is

$$\frac{T_{duplication}}{T} = \frac{(1)\ [1 - P(r + s)]}{(j - r)P(r) + r + s}$$

This is a measure of waste of still-useful satellites. It is also an indication of the potential saving or gain by replacing the old satellite but using either it or the new one in standby until the other fails, or using it for extra service, peak loads, etc.

DISCUSSION OF RESULTS

Figure 7-13 shows the failure rate distribution and indicates that the median satellite life is 4.1 years and that 25 percent of all satellites will live (at least one channel still working) for 5.65 years, 10 percent for 7.25 years, and only 1 percent for as long as 10.6 years.

Figure 7-16 shows the density function of failures for any 6-month period as a function of time. The failure rate decreases slightly in the first year, then rises to a peak at 4 years and dies down to its original value by 6.5 years and to nearly zero by about 10 or 12 years. The probability of failure at 10 years is low, not because the satellite is more reliable at that time but because the chance of its living long enough to fail then is low.

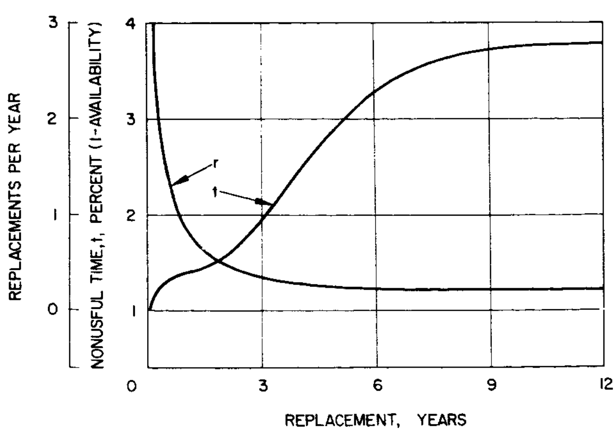

FIGURE 7-15. NONAVAILABILITY AND REPLACEMENT RATES

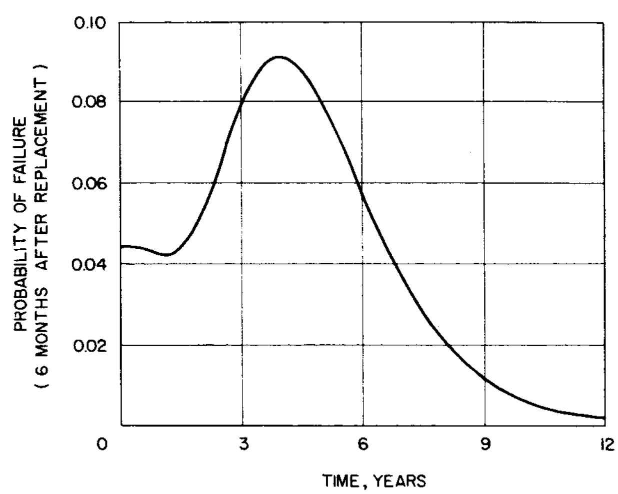

FIGURE 7-16. FAILURE RATE AS FUNCTION OF TIME

TABLE 7-10. SUMMARY OF SATELLITE LIFE DISTRIBUTION

t years (1)	$\Delta P(t)$ (2)	$\frac{\Delta P(t)}{1-P(t)}$ (3)	$\frac{T_{non}}{T}$ (4)	j (5)	$\frac{N}{T}$ (6)	m (7)	$\frac{T\ duplicate}{T}$ (8)
0	0.007503					4.50427	
1/12	0.007447		0.009961	0.04166	4.00522		
2/12	0.007391		0.011199	0.08318	3.01128		
3/12	0.007335		0.011938	0.12458	2.41624		
4/12	0.007282		0.012434	0.16588	2.02007		
5/12	0.007227		0.012787	0.20708	1.73735		
6/12	0.007177	0.044185	0.013052	0.24818	1.52546	4.18938	6.87109
7/12	0.007126		0.013259	0.28919	1.36074		
8/12	0.007081		0.013427	0.33010	1.22903		
9/12	0.007041		0.013567	0.37095	1.12131		
10/12	0.007008		0.013687	0.41174	1.03158		
11/12	0.006984		0.013799	0.45244	0.95568		
1	0.042316	0.044377	0.013902	0.49331	0.88064	3.86071	3.73123
1.5	0.046794	0.046328	0.014523	0.74169	0.63738	3.52397	2.46076
2	0.057102	0.053719	0.015492	1.01021	0.50182	3.19564	1.76839
2.5	0.070655	0.069274	0.017052	1.31429	0.41830	2.89627	0.33674
3	0.082786	0.092096	0.019183	1.64856	0.36277	2.63935	1.05069
3.5	0.089709	0.118854	0.021681	1.99180	0.32424	2.42792	0.85579
4	0.090022	0.146166	0.024292	2.32318	0.29686	2.25796	0.72076
4.5	0.084474	0.171785	0.026795	2.62965	0.27716	2.12259	0.62581
5	0.074948	0.194634	0.029047	2.90501	0.26288	2.01472	0.55799
5.5	0.063508	0.214418	0.030976	3.14729	0.25253	1.92815	0.50877
6	0.051832	0.231281	0.032568	3.35681	0.24501	1.85784	0.47241
6.5	0.041025	0.245551	0.033844	3.53518	0.23958	1.79978	0.44510
7	0.031664	0.257610	0.034841	3.68475	0.23566	1.75080	0.42414
7.5	0.023938	0.267823	0.035604	3.80834	0.23285	1.70833	0.40768
8	0.017788	0.276530	0.036179	3.90900	0.23085	1.68702	0.39436
8.5	0.013026	0.284030	0.036614	3.98984	0.22947	1.63446	0.38713
9	0.009424	0.290510	0.036920	4.05388	0.22842	1.59901	0.37334
9.5	0.006745	0.296249	0.037133	4.10397	0.22764	1.56164	0.36400
10	0.004784	0.301290	0.037296	4.14266	0.22715	1.51943	0.35472
10.5	0.003366	0.305843	0.037414	4.17220	0.22681	1.46859	0.34462
11	0.002351	0.310001	0.037493	4.19450	0.22657	1.40376	0.33274
11.5	0.001631	0.313800	0.037551	4.21118	0.22641	1.31706	0.31782
12	0.001130	0.317250	0.037591	4.22352	0.22630	1.19672	0.29805

This point is clarified by Figure 7-14, which shows the probability of failure in any 6-month interval, given that the satellite has not failed until then. It can be seen that the failure probability is low and almost constant the first year, then rises steadily to a value six or seven times as high by 7 to 10 years. If the system were of the classical Poisson failure rate type, this curve would be a constant in time. That it varies so much from a straight level line is an indication that the common Poisson or negative exponential approximations cannot be used here.

It is assumed that replacement is attempted as soon as possible after a failure and at r years if there is no previous failure, and that once a satellite is replaced, the old one is never used again even though still usable. Figure 7-15 shows the percentage of nonusable time and the number of satellites used per year (not including launch failures) as a function of r, the predetermined replacement time. If a predetermined minimum outage level is assigned, this curve can be used to determine the optimum replacement time and the satellite replacement rate required.

Example 1. In the first example, not over 2 percent outage is permitted. Satellites must be replaced after

3.15 years or when they fail, if failure occurs earlier. This requires a rate of 0.35 satellite per year, or an average of one every 2.86 years. Since a launch reliability of 0.5 is assumed, launches must be attempted at the rate of 0.70 per year, or an average of one every 1.43 years.

Example 2. In the second example, not over 3 percent outage is permitted. Satellites must be replaced after 5.25 years or when they fail, if failure occurs earlier. This requires a rate of 0.26 satellite per year, or an average of one every 3.85 years. Launches must be attempted at the rate of 0.52 per year, or an average of one every 1.92 years.

As shown in Figure 7-17, having replaced a satellite that is still usable, the old satellite still has appreciable expected life remaining. In Example 1, for the 68 percent of cases in which a still usable satellite is replaced at the end of 3.15 years, the mean remaining life of the replaced satellites is 2.57 years. Thus the replacement decision rule is rather wasteful of satellite life, and is therefore indicative of improvement. In Example 2, the remaining life is 1.97 years when replacing at age 5.25 years.

If the old satellite can continue operating, the ratio of duplicate coverage time to total time, $T_{dup/T}$, is shown in Figure 7-18. Where this fraction exceeds one, it indicates that the replacement rate is so high that several satellites are still "alive" and could be used to reduce the outage time if desired. The question of what to do with the old satellites will be further explored.

The nature of the distribution of the outage time is nearly of great interest as the average amount of outage time. For Type I failure (unexpected), the outage time will be a geometric distribution by 30-day increments and with $p = 0.5$, from the assumptions. For Type II failures (after a replacement decision but before replacement), the outage time will be uniformly distributed, since failure rates are assumed linear over short intervals. For Type III failures, there is no outage. The overall outage distribution will be a combination of the two and will be a function of the replacement time. Figure 7-19 shows the outage distributions for

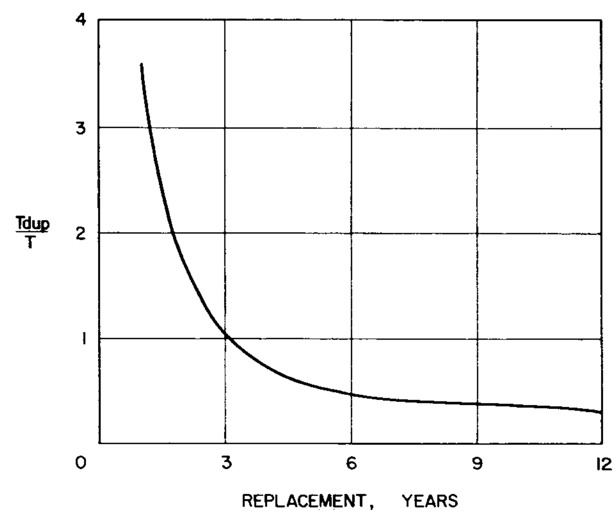

FIGURE 7-18. RATIO OF DUPLICATION TIME TO TOTAL TIME

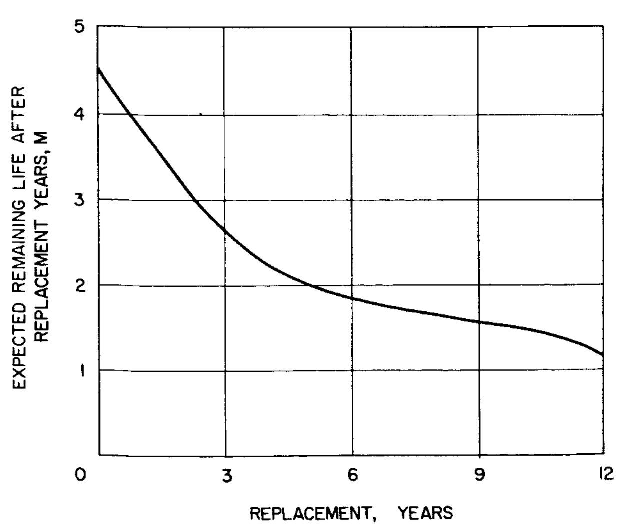

FIGURE 7-17. EXPECTED REMAINING LIFE OF SATELLITE

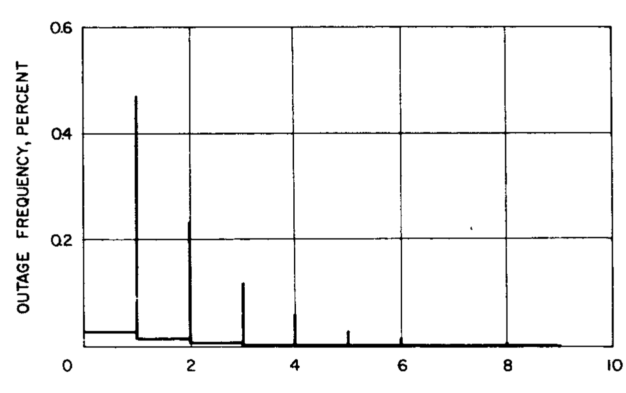

FIGURE 7-19. FREQUENCY DISTRIBUTION OF SATELLITE OUTAGES

examples 1 and 2. The discontinuous nature of the curve is a result of the rather unrealistic assumption of an exactly constant launch time, but the general trend of the curve is correct.

DERIVATION OF FIGURES

To obtain the results shown in the figures, the following formulas were used.

Figure 7-13. P(t) plotted against t and tabulated as Column 3 in Table 7-9.

Figure 7-14. $\Delta P(t) = P(t + 3 \text{ months}) - P(t - 3 \text{ months})$. This is calculated at 1-month intervals for the first year and adjusted to a 6-month basis. For $t > 1$ year it is calculated directly on a 6-month basis. (See Column 2, Table 7-10.

Figure 7-15. $\Delta P(t + 3 \text{ months})/1 - P(t)$ with modifications as for Figure 7-16 for $t \leq 1$ year. See Column 3, Table 7-10.

Figure 7-16.

$$\frac{T_{\text{nonuseful}}}{T} = \frac{kP(r) + (S - k)P(r + s)}{(j - r)P(r) + r + s}$$

(See Column 4, Table 7-10.) The time is now expressed as r instead of t, to indicate that r is the time of decision to replace satellite. To calculate j, use

$$j = \frac{\sum_{t=o}^{r} t\Delta P(t)\Delta t}{\sum_{t=o}^{r} \Delta P(t)\Delta t} = \frac{\sum_{t=o}^{r} t\Delta P(t)}{P(t)}$$

(See Column 5, Table 7-10) ; k is assumed constant and so is s.

$$\frac{N}{T} = \frac{1}{(j - r)P(r) + r + s}$$

(See Column 6, Table 7-10).

Figure 7-17. Let R = maximum possible life of a satellite, assumed in the example to be 14 years.

$$m = \frac{\sum_{t=r}^{R} (t - r)\Delta P(t)\Delta t}{\sum_{t=o}^{r} \Delta P(t)\Delta t} = \frac{\sum_{t=r}^{R} (t - r)\Delta P(t)}{1 - P(r)}$$

(See Column 7, Table 7-10.)

Figure 7-18.

$$\frac{T_{\text{duplication}}}{T} = \frac{m[1 - P(r + s)]}{(j - r)P(r) + r + s}$$

(See Column 8, Table 7-10.)

COMPONENTS AND MATERIALS

Syncom II assignments within this area during the Advanced Technological Development Program concerned two categories of effort.

The first comprised liaison with project, system, and development activities for appraisal of potential problem areas and possible solutions to these problems. The second was to study the factors that might contribute to failures of parts or materials in the expected life span. Since extensive tests have not been conducted for long periods of time in the space environment, and since it is impossible to extend the testing period to an optimum length of time, fundamental studies of degradation and failure mechanisms must be made to establish reliable means of predicting behavior over the required 3- to 5-year life span.

The study of considerations which could affect long term reliability was initiated with a rather detailed analysis of the expected environments. An analysis of the long term reliability problem and a fundamental approach to solution is being prepared. The approach is one of determining the methods by which degradation and failure occur. This is essential since long term tests cannot be conducted and valid extrapolation can only be made if the failure mechanism is understood and valid criteria for extrapolation are established.

MATERIAL AND PROCESS STUDIES

Three thermal-control paints are being exposed to ultraviolet radiation in vacuum to evaluate their potential longevity. Two paints are known to degrade badly, by different mechanisms, while one is stable. The stable paint has a ceramic pigment and was developed for Surveyor. It can be used on the exterior while one of the others, more resistant to abrasion during work, can be used on the interior. This program includes exposures to both normal and high-intensity ultraviolet, to determine the degree to which testing

Paint	Solar intensity	Temperature (degrees/F)	Exposure (hours)	Solar exposure (hours)	Alpha (before exposure)	Alpha (after exposure)
Hughes Surveyor white	1X	75	500	500	0.20	0.24
Antimony oxide	1X	100	100	100	0.29	0.37
Antimony oxide	5X	200	20	100	0.29	0.55
Antimony oxide	1X	300	50	50	0.28	0.30
Antimony oxide	5X	200	200	1000	0.29	0.56
Skyspar	5X	115	100	500	0.25	0.56
Skyspar	10X	315	50	500	0.23	0.60
Skyspar	1X	110	50	50	0.22	0.40

of such materials can be accelerated, and the degree to which the degradation is proportional to the product of time and intensity at different intensities. The total program will comprise 45 separate tests, of which eight have been completed at this time.

From the above tests it appears that the reciprocity law may not hold for the antimony oxide degradation mechanism.

An encapsulating material for the traveling-wave tube, capable of higher temperature operation than that used in the Syncom I tubes, is being tested. The Syncom II tubes, with higher power and efficiency, might operate substantially hotter than those of Syncom I. If present tests are favorable a tube will be prepared with this material for operational tests.

The possible usefulness of beryllium as a structural material is being considered, although present high cost and fabrication problems are factors.

The NASA Specification MFSC-PROC-158A for soldering favors the use of nickel-plated stranded wire. Silver-plated wire was used in Syncom I, and tests are being made to compare the behavior of the two types from standpoints of solder wicking and ease of soldering.

Most of the electronic parts used in Syncom I were procured with component specifications originally prepared for the Surveyor space program, although the temperature requirement of Syncom is more moderate and sterilization requirements are not necessary. For the long-term use of Syncom II, however, specific modifications in these basic specifications will be incorporated. An added requirement will include a period of power aging.

It is expected that about seventy types of electronic parts other than magnetics will be used in Syncom II designs. Approximately fifty of these types now have basic procurement specifications, and twenty of the fifty have been completely qualified to the requirements of the basic specifications. Other parts now having specifications have received partial testing.

Any additional testing necessary will be conducted with parts procured to specification requirements but without the aging, concurrently with the procurement of similar, but aged parts, for flight use. By this procedure, unforeseen weaknesses may be detected in time for correction in parts procured for flight use.

Magnetic parts will be designed and samples tested to prove the designs before producing flight parts.

Glass-cased, evacuated, frequency-control crystals were recommended for both the engineering model and subsequent flight use. Such crystals have successfully passed preliminary shock and vibration tests; like other parts, they will receive more complete testing as the program proceeds.

A high-frequency filter is being designed and samples fabricated.

Materials used in the phase-shifter were approved, and the phase-shifter will receive complete qualification tests for flight use.

Environments of Syncom Mark II

A study was conducted of the anticipated space environments that Syncom II would encounter during the course of its lifetime.

Environments at the expected altitude of the vehicle are almost independent of the earth's meteorological conditions, in contrast with the situation at low altitudes, but are greatly influenced by solar activities. The density and electromagnetic radiation from the quiet sun can be extrapolated, with relatively small error and uncertainty, from existing data at the top of the atmosphere. However, high-energy electromagnetic radiation, micrometeoritic environments, and corpuscular radiation, especially solar flare radiation, are almost impossible to predict with comparable accuracy, because of the meager observation data at high altitudes and the large fluctuations associated with seasons and solar activities.

To define the most probable environments, the current best values are cited from various literature references. The discussions are condensed but necessary data are presented for purposes of prediction. Ideally, the investigation of the effects of environments should be based on a knowledge of the degradation mechanisms of various critical materials. Pending the initiation of contemplated studies of the degradation mechanisms of components and materials under the environments that will be encountered by Syncom II, attention is directed to Reference 7-2, in which some ideas on the mechanisms in high vacuum and in fields of electromagnetic radiation are presented.

PRESSURE, CONSTITUENTS, AND CONCENTRATION

The transit phase of Syncom II, from the earth's surface to final orbit, will occur in a low-pressure atmosphere. Approximately 10 minutes after launch the pressure will have reached 10^{-6} Torr; within 1.5 hours after launch the vehicle will be operating in pressures of less than 10^{-12} Torr, and at its final orbital altitude the estimated pressure will be in the 10^{-15} Torr range. Of interest is the particle density at this altitude. It has been estimated to be 10^2 to 10^4 particles/cm^3 (Reference 7-3). The equation below can be used to approximate the mean free path at these densities (Reference 7-4).

$$\text{Mean free path} = \frac{1}{\sqrt{2}\pi n\sigma^2}$$

where

n = Particle concentration

σ = Particle diameter, about 10^{-8} cm for a hydrogen atom and $\sigma/2 = (1.2 - 1.5) \times 10^{-13} \times A^{1/3}$ cm for a nucleus, where A is the atomic mass (Reference 7-5)

Thus, at a density of 10^3 particles/cm^3 the mean free path is approximately 10^6 miles.

Once in orbit the satellite would encounter a space gas made up of protons (hydrogen ions). For a very short period, on the order of a few minutes, the vehicle will pass through an ozone layer. During transit to final orbit, high concentrations of NO^+, O_2^+ and O^+ will be seen (Reference 7-6).

ELECTROMAGNETIC RADIATION

Within 10 minutes after launch, the vehicle will be exposed to the full range of solar electromagnetic radiation, which extends from gamma rays up to wave lengths in the far infrared region. The total energy falling on a surface in space at one earth radius is 2 calories/cm^2/minute (Reference 7-6).

The radiation above 4000 Å will not cause any detrimental effect on the vehicle except that the amount absorbed will contribute primarily to heating the vehicle. Below 4000 Å, radiation in the ultraviolet range will also contribute to the heating effects, however, the energy density is small compared to that above 4000 Å. Figure 7-20 illustrates the solar irradiance above 2000 Å (Reference 7-1). The amounts of energy absorbed will depend directly on the absorptivity of the exposed surfaces.

The sun emits a continuum of ultraviolet radiation from 4000 Å down to about 1500 Å. Below 1500 Å, the ultraviolet radiation is in the form of line spectra; the Lyman line (1216 Å) and the He-II line (304 Å) are the most intense. Figure 7-21 shows the ultraviolet radiation emitted by the sun per second and also integrated for a total duration of 5 years.

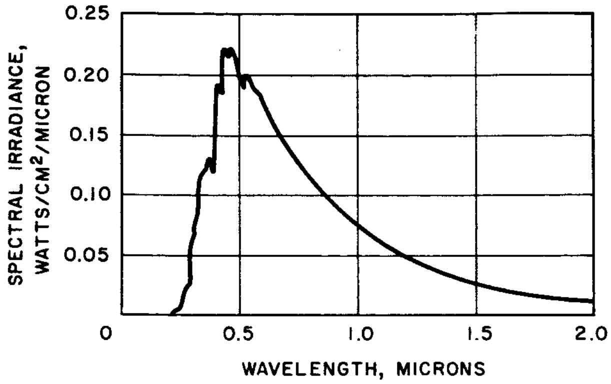

FIGURE 7-20. SOLAR SPECTRAL IRRADIANCE ABOVE EARTH'S ATMOSPHERE AT EARTH'S MEAN DISTANCE FROM SUN

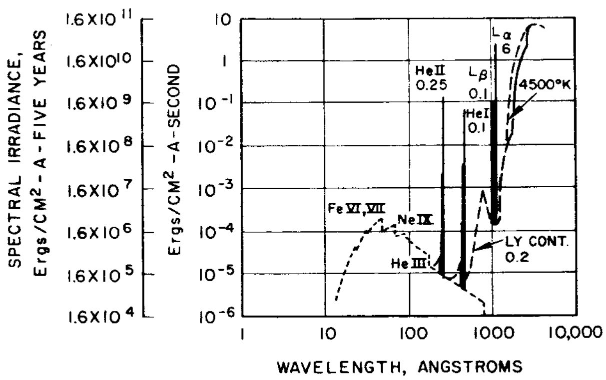

FIGURE 7-21. SOLAR SPECTRAL IRRADIANCE ABOVE EARTH'S ATMOSPHERE

The sun also emits X and gamma radiation. The irradiance in this region is dependent on the sunspot cycle in the presence of solar flares. The ultraviolet spectrum discussed previously is not dependent on solar activity to more than a few percent (Reference 7-7).

The gamma and X radiation from a quiet sun during sunspot maxima is extremely low. During flares, however, this radiation may become significant in its effects on materials. The characteristics of bursts of intense radiation associated with flares are shown in Table 7-11. Figure 7-22 shows the solar X-ray emission. Emission of energy is low, and the lower limit of the shorter wave length is approximately 8 Å. Short wave lengths are seen only during flares.

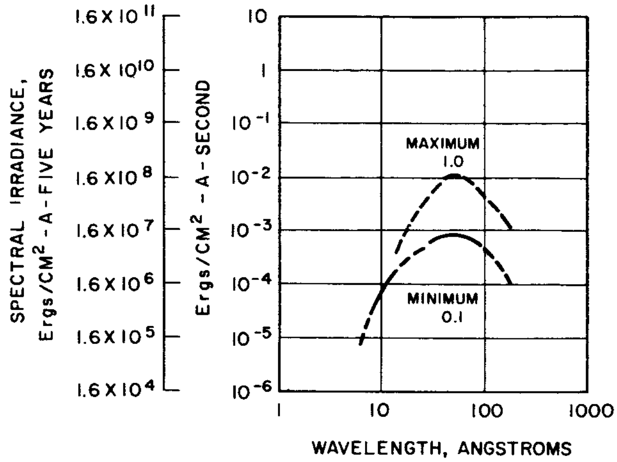

FIGURE 7-22. SOLAR SPECTRAL IRRADIANCE ABOVE EARTH'S ATMOSPHERE AT MAXIMUM AND MINIMUM SUNSPOT CYCLES

TABLE 7-11. CHARACTERISTICS OF X AND GAMMA RAYS ASSOCIATED WITH SOLAR FLARES

Energy Flux (Ergs/cm²-sec)	Photon Energy (kev)	Time Duration	Reference
2×10^{-4}		18 sec	(10)
4.5×10^{-6}	E > 20		(10)
3.2×10^{-5}		100 sec	(10)
$(1.2\text{-}2.4) \times 10^{-6}$			(10)
$10^{-2} - 10^{-5}$	5 – 80	~10 min	(11)
10^{-4}	~500	< 18 sec	(11)

THERMAL ENVIRONMENTS

Temperatures of the solar panels are expected to vary from 50° to 70°F (10° to 21°C) depending on the solar incidence angle. These temperatures were computed using a solar absorptance of 0.84 and infrared emittance of 0.83 for the solar cells and exposed support structure. The minimum temperature resulting from eclipses is not expected to go below —155°F (—104°C), which is the predicted minimum solar panel temperature for Syncom I.

CORPUSCULAR RADIATION

Cosmic-Ray (Galactic Cosmic-Ray) Radiation. Galactic cosmic rays are a highly penetrating radiation reaching the earth and which have their origin beyond the solar system. Although all the details of primary cosmic rays are not known many of the major features have been revealed in recent years.

Since cosmic rays possess high energy (some particles have energies greater than 10^{17} electron volts), they are capable of inducing extraordinary interactions with matter in the upper atmosphere. High-energy particles induce nuclear reactions known as spallation, fission, fragmentation, and the subsequent secondary processes. The products are disrupted target elements, and the mass-yield curve depends on the target element as well as on the energy of the incident particle, as shown in Figure 7-23 (Reference 7-9). Primary particles also produce protons and neutrons as well as pi-mesons. A neutral pi-meson disintegrates immediately into two photons (the mean life is approximately 10^{-14} seconds), which multiply into showers. Charged pi-mesons (positive and negative) disintegrate into mu-mesons and neutrinos (the mean life is 2.6×10^{-8} seconds). Pi-mesons interact with nuclei very strongly but mu-mesons interact very weakly. Mu-mesons lose energy primarily by ionization until they decay into electrons and neutrinos (the mean life is 2.1×10^{-6} seconds). Thus the local cosmic-ray radiation in the atmosphere contains protons, neutrons, pi-mesons, mu-mesons, electrons, photons, and strange particles.

where

$N(\geq E)$ = The flux of primary particles with energies equal to or greater than E, in units of particles per square meter per second per steradian

$[m_0c^2 + E]$ = The total energy of the particle per nucleon, in bev

C = Constant for a given particle

n = Constant that varies with energy for a given particle

Since the rest-mass energy of a nucleon, m_oc^2, is about 0.93 bev, the expression above is often written as $C/(1 + E)^n$. The constants C and n have been accumulated from various literature sources and are tabulated in Table 7-12 (References 7-10, 7-11, and 7-12). The integral energy spectrum is plotted in Figures 7-24 through 7-26 (Reference 7-10 for each type of charged particle. The differential energy spectra of albedo neutrons are plotted in Figure 7-27 (Reference 7-8 at distances of 5 and 9 earth radii from the center of the earth above the geomagnetic equator. At large dis-

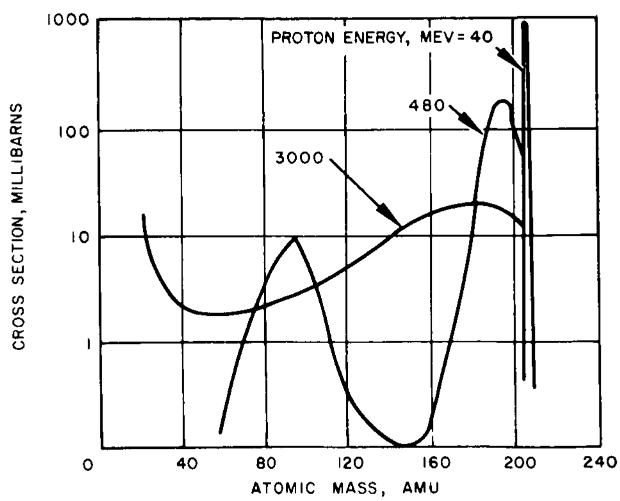

FIGURE 7-23. MASS YIELD CURVE FOR PROTON BOMBARDMENT OF BISMUTH (12)

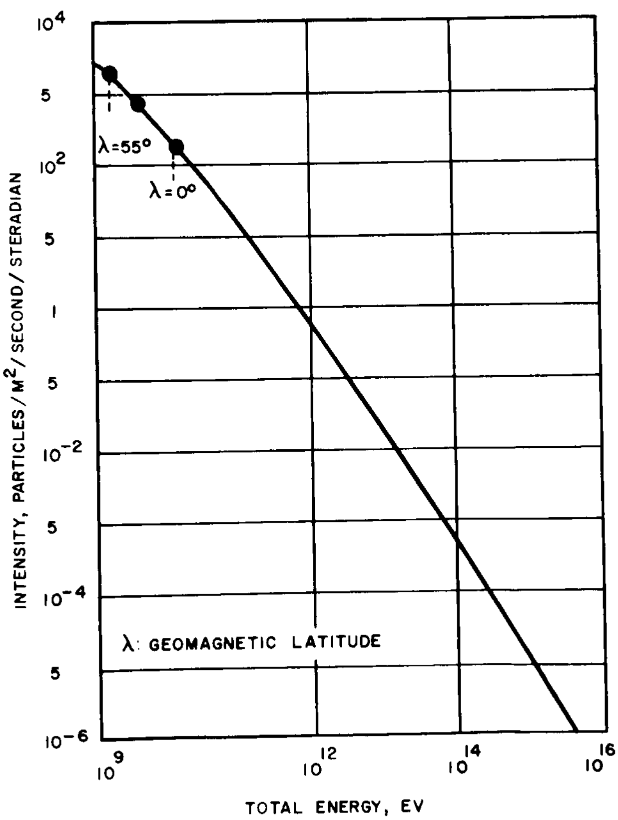

FIGURE 7-24. INTEGRAL ENERGY SPECTRUM OF PRIMARY PROTONS (14)

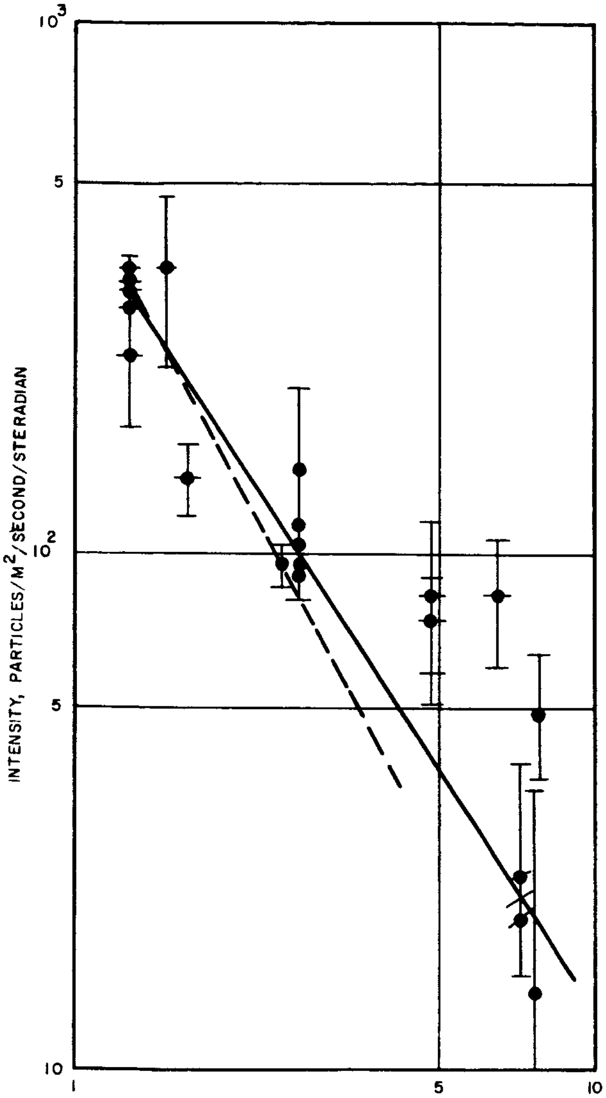

FIGURE 7-25. INTEGRAL ENERGY SPECTRUM OF PRIMARY ALPHA PARTICLES (14)

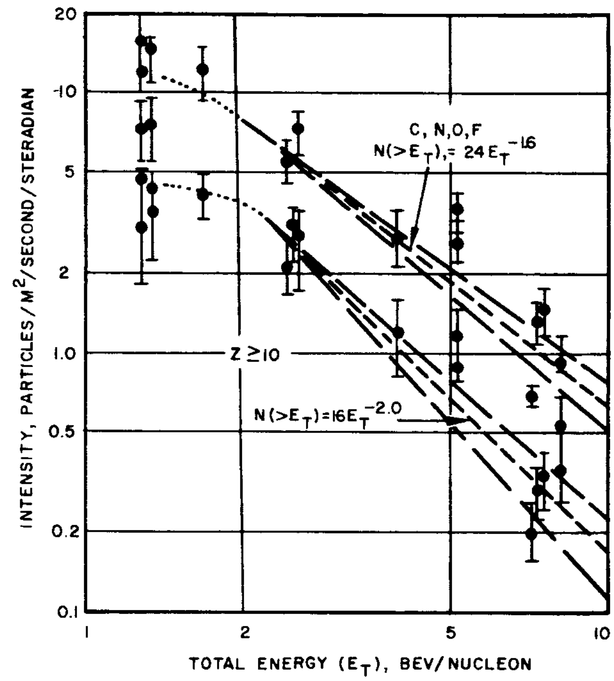

FIGURE 7-26. INTEGRAL ENERGY SPECTRA OF PRIMARY MEDIUM

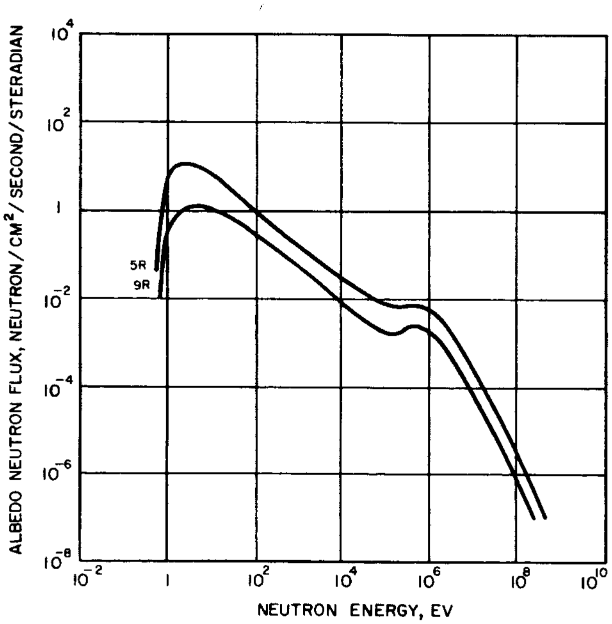

FIGURE 7-27. DIFFERENTIAL ENERGY SPECTRA OF ALBEDO NEUTRONS ABOVE GEOMAGNETIC EQUATOR

tances from the earth the flux of particles during solar maxima, as detected by the Pioneer V space probe, is about 2.5 x 10^4 particles per square meter per second (Reference 7-13).

One of the remarkable characteristics of cosmic rays is their isotropy. The average diurnal effect is very small, amounting to only 0.1 to 0.2 percent change for the meson component over long periods of time but to nearly a 1 percent change for albedo neutrons. There is some evidence that the diurnal effect is some-

TABLE 7-12. THE CONSTANTS C AND n

Z	Element	C (Constant for given particle)	n (Constant varying with energy for given particle)	Energy Range within which the Constants Are Valid (Bev/nucleon)	Ref. No.
1	Proton	3800	1.0	—	16
		4000	1.15	2-20	14
2	He	360	1.2		16
		370 ± 100	1.50 ± 0.18	1.8-3.0	15
		370 ± 100	1.49 (+ 0.23, − 0.20)	0.33-800	15
		380	1.2	0.35-10	
		460	1.6	1.5-8	14
3-5	Li, Be, B	14	1.5	—	15
6-9	C, N, O, F	21	1.5	—	15
		20	1.2	—	16
		24	1.6	3-8	14
> 2	—	—	1.2 ± 0.3	1.8-3.0	15
≥ 10	—	16	2.0	3-8	14
		10	1.5	—	15
		6	1.2	—	16

what larger for the lower-energy cosmic-ray particles than for those of higher energy, but the effect is not pronounced (Reference 7-11). No definite correlation appears to exist between the day to day variations in cosmic rays and any specific events occurring on the sun. A definite relationship does exist, however, between solar activity in general and cosmic-ray fluctuations; that is, the percentage fluctuation in cosmic rays increases when the sun is active (Reference 7-11).

"Twenty-seven day" effects on the primaries may be correlated with the rotation of the sun. Although it is difficult to decide whether the 27-day effects on the cosmic rays constitute an increase or a decrease, the changes in neutron intensity at sea level may amount to 5 to 10 percent, whereas the changes in meson intensity are about one-third as much. The most pronounced fluctuation in cosmic-ray intensity follows the 11-year solar cycle. A correlation exists between the intensity of cosmic rays and solar activity, as measured by Zurich sunspot numbers. The inverse relationship between solar activity and cosmic-ray intensity

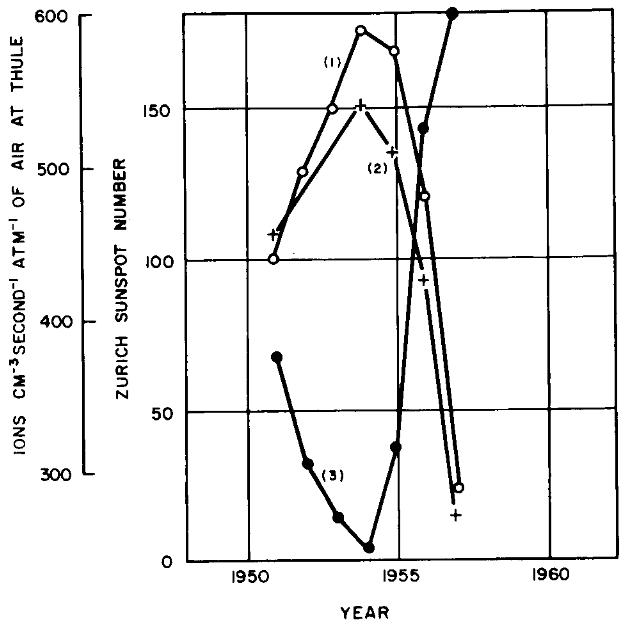

FIGURE 7-28. INVERSE RELATIONSHIP BETWEEN SOLAR ACTIVITY AND COSMIC RAY INTENSITY

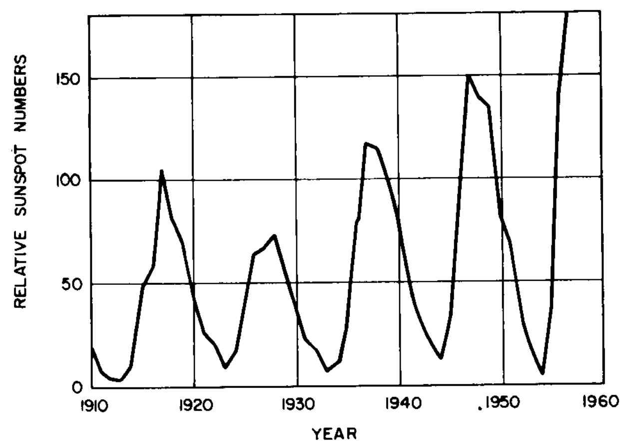

FIGURE 7-29. ELEVEN YEAR SOLAR CYCLE AS MEASURED BY ZURICH SUNSPOT NUMBERS

in shown in Figure 7-28 (Reference 7-11). The fluctuation of sunspot numbers for the last half century is plotted in Figure 7-29 (Reference 7-11).

Solar Flare (Solar Cosmic-ray) Radiation. A solar flare causes a sudden increase in intensity of the hydrogen alpha line (6563 Å). The flares occur in the neighborhood of sunspots and seldom emit white light. After its inception, the flare rapidly expands over an

5

area of a few million to a billion square miles of the solar disk, reaching a peak intensity, and gradually decays and completely disappears within several minutes to several hours, depending on the size of the flare. A classification of solar flares is shown in Table 7-13 (Reference 7-14).

Half an hour or more following the appearance of large solar flares, energetic particles, consisting mostly of protons, are detected at the earth, especially in the

TABLE 7-13. CLASSIFICATION OF SOLAR FLARES (REFERENCE 7-14)

Flare Class	Average Duration in Minutes	Range of Area in Millionths of Sun's Hemisphere*	Approximate Line-Width of Hα in A at Maximum Brightness
1-	—	100	2
1	17	100-250	2-4
2	29	250-260	4-6
3	62	600-1200	6-8
3+	180	> 1200	> 8

*1 millionth of the sun's hemisphere = 1.17×10^6 square miles = 3.04×10^6 square kilometers.

polar regions inside the auroral zones. The radiation dies away with a time constant of 1 to 3 days (Reference 7-8). The constituent particles are electrons, protons, alpha particles, and quite small amounts of medium nuclei (C, N, and O). Data on the abundance of solar electrons and protrons in the event of 4 September 1960 (over Minneapolis) is tabulated in Table 7-14 (Reference 7-15). Another event occurred on 15 November 1960, in which the abundance of electrons of rigidity greater than 0.7 bev was found to be less than 2 percent of the abundance of protons over Minneapolis (Reference 7-16). The ratios of protons to alpha particles and of protons to medium nuclei are expected to vary considerably between solar events, whereas the ratio of alpha particles to medium nuclei is expected to remain relatively constant (Reference 7-16).

The particle flux associated with solar flare radiations varies widely with time and the size of the flare. The changes in differential and integral proton spectra with time are shown in Figures 7-30 (Reference 7-15) and 7-31 (Reference 7-17), respectively. After the peak of radiation, the integral flux decays with time at a rate approximately proportional to t^{-n}, where t is time and n is a number, roughly equal to 3. The

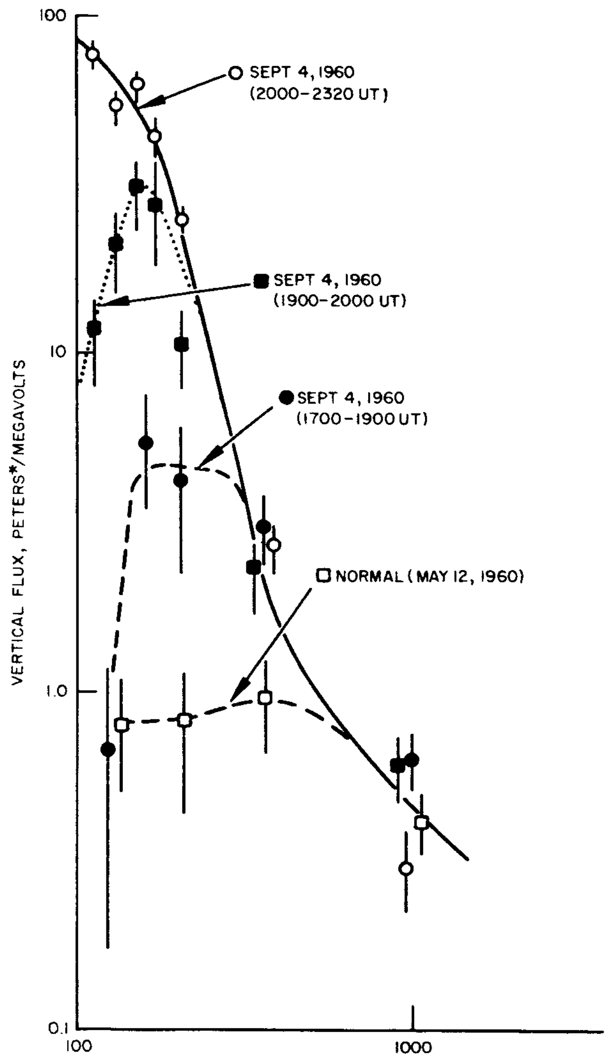

* 1 PETER = 1 PARTICLE/M^2/SECOND/STERADIAN

FIGURE 7-30. DIFFERENTIAL PROTON ENERGY SPECTRA

time variation of the integral flux is shown in Figures 7-32) (Reference 7-16) and 7-33 (Reference 7-18). In the radiation associated with the solar flare event that occurred on 15 November 1960, the maximum observed particle flux above 80 mev was 600 particles/cm^2/second/sterad and the total particle flux above 80 mev observed at the earth was about 10^8 particles/cm^2 (Reference 7-16).

A serious difficulty in evaluating solar flare radiation as an environment for a space vehicle is its irregularity.

TABLE 7-14. THE ABUNDANCE OF SOLAR PROTRONS AND ELECTRONS (REFERENCE 7-15)

Time	Proton and Electron Fluxes*	Observed Number of Particles	Flux, peters**
Period C, 2000-2320 UT, 4 Sept. 1960	All electrons	2	18 ± 13
	Solar electrons (450 < E < 800 mev)	0	< 18
	Solar protons (PC > 450 mev)	—	6900
	Solar protons (E > 450 mev) (by extrapolation of observed spectrum)	—	26
Normal time, 12 May 1960	All electrons (PC > 700 mev)	11	33 ± 10
	All protons (PC > 700 mev)	—	1100 ± 100
	Electron to Proton Ratios	electron flux / proton flux	
Period C	Solar cosmic rays (PC > 450 mev)	< 0.25%	
	Solar cosmic rays (E > 450 mev)	< 70%	
Normal	Galactic cosmic rays (PC > 700 mev)	3 ± 1%	
	Galactic cosmic rays (E > 700 mev)	4 ± 1.5%	

*E and PC refer to cutoff energies. For explanation, see Reference 21.
**1 peter = 1 particle/m²/sec/steradian.

TABLE 7-15. SOLAR FLARES OBSERVED DURING THE INTERNATIONAL GEOPHYSICAL YEAR (REFERENCE 7-14)

Month	Importance				Total
	(1⁻)	1	2	3 and 3⁺	
1957 July	28	334	39	5	406
Aug	36	320	25	2	383
Sept	50	368	53	10	481
Oct	71	436	21	2	530
Nov	35	275	18	2	330
Dec	37	298	27	0	362
1958 Jan	13	196	23	1	233
Feb	9	215	24	0	248
Mar	38	352	54	4	448
Apr	35	295	14	1	345
May	53	313	18	2	386
June	91	254	32	1	378
July	90	340	31	3	464
Aug	86	335	33	4	458
Sept	71	305	28	1	405
Oct	27	279	23	0	329
Nov	29	189	14	2	234
Dec	36	285	20	1	342
TOTAL	835	5389	497	41	6762

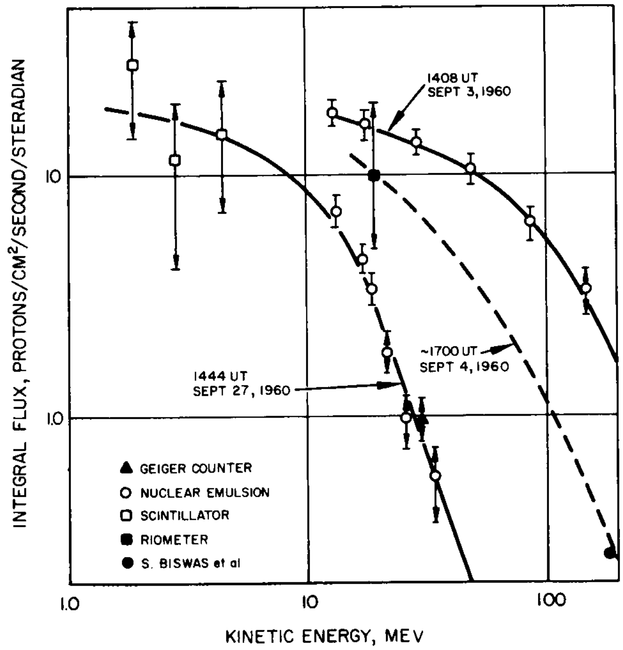

FIGURE 7-31. INTEGRAL PROTON ENERGY SPECTRA

Many flares of various sizes (a total of 6762 flares of all classes, as shown in Table 7-14 (Reference 7-14) were observed during the 18 months of the International Geophysical Year. Unfortunately the abundance of constitu ent particles, the energy ranges, the energy spectra, and the total flux vary widely with each event, depending on the size of flare. Although the fluctuation is much more severe than that of galactic cosmic rays, a few interesting phenomena are associated with the frequency of occurrence of solar-flare radiation events,

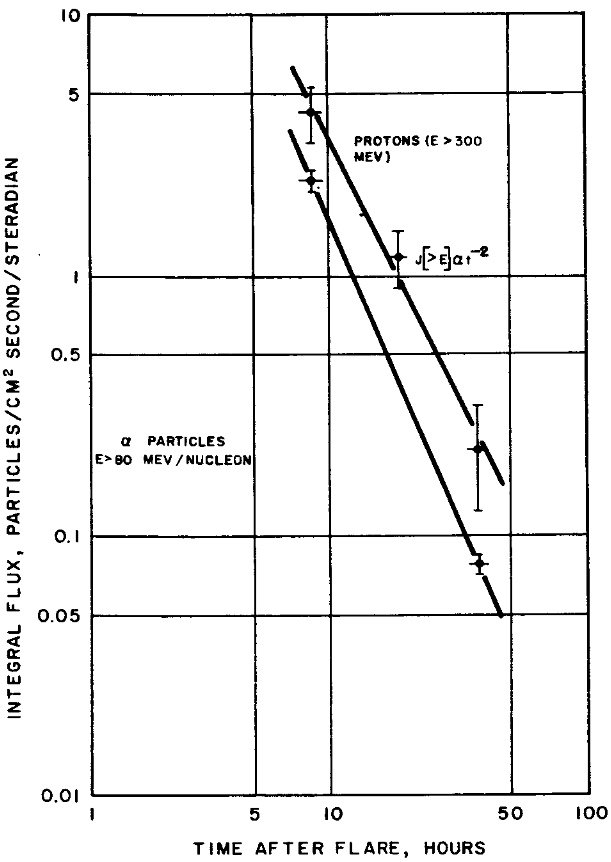

FIGURE 7-32. TIME VARIATION OF INTEGRAL FLUX

namely, a) there may be an 11-month cycle in the peak number of events, b) there is a semiannual variation which has maxima in March and September, probably near the equinoxes, c) the maximum number of events occurs on the average near the September equinox and the minimum number occurs during December or January (Reference 7-14) and d) since solar flares are associated with sunspots, the number of flares also varies with the 11-year solar cycle. Predicted and observed sunspot numbers for the present solar cycle are shown in Figure 7-34 (Reference 7-19).

METEOROIDS AND MICROMETEOROIDS

Within a few minutes after launch, the vehicle will be in a region where meteoroids may strike. Table 7-16 (Reference 7-20) gives data indicating the

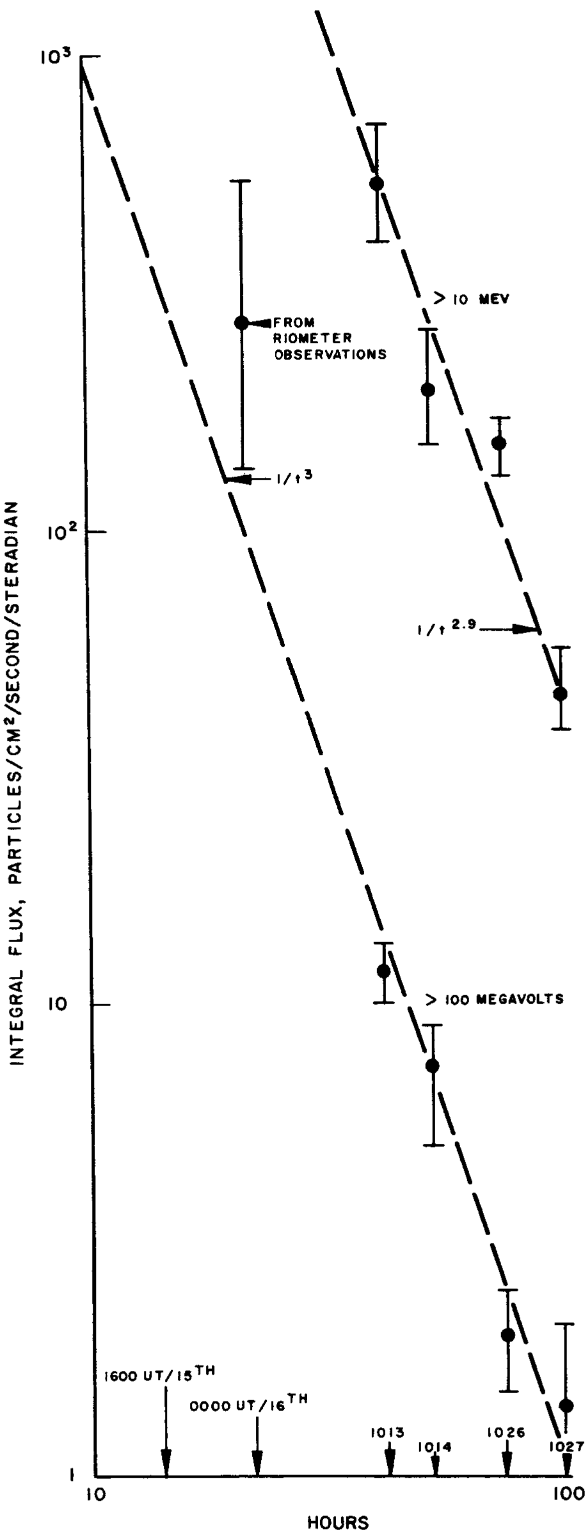

FIGURE 7-33. TIME VARIATION OF INTEGRAL FLUX

TABLE 7-16. DATA ON MICROMETEOROIDS
(REFERENCE 7-20)

Kinetic Energy, ergs	Velocity, kilometers per second	Mass, grams	Number Striking a 3-Meter Sphere		Penetration in Aluminum, centimeters
			per day	per 5 years	
2.5×10^{12}	28	0.63	0	0	6.2
1.6×10^{11}	28	4.0×10^{-2}	1.7×10^{-4}	3.1×10^{-1}	2.5
2.2×10^{10}	26	6.3×10^{-3}	1×10^{-3}	1.8×10^{0}	1.3
2.9×10^{9}	24	1×10^{-3}	6.5×10^{-3}	1.2×10^{1}	0.66
3.9×10^{8}	22	1.6×10^{-4}	4.1×10^{-2}	7.4×10^{1}	0.34
5.1×10^{7}	20	2.5×10^{-5}	2.6×10^{-1}	4.7×10^{2}	0.17
6.6×10^{6}	18	4.0×10^{-6}	1.6×10^{0}	2.9×10^{3}	0.090
8.2×10^{5}	16	6.3×10^{-7}	1×10^{1}	1.8×10^{4}	0.043
1.1×10^{5}	15	1×10^{-7}	6.5×10^{1}	1.2×10^{5}	0.022
1.8×10^{4}	15	1.6×10^{-8}	4.1×10^{2}	7.4×10^{5}	0.012

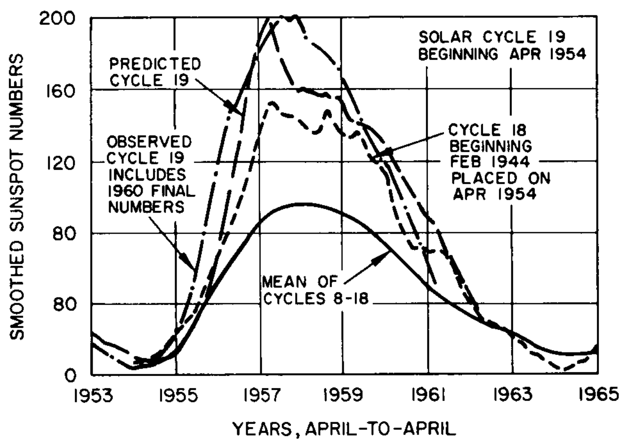

FIGURE 7-34. PREDICTED AND OBSERVED SUNSPOT NUMBERS

average number of micrometeoroids, their energy, velocity, and mass. Also number of particles striking a sphere 3 meters in diameter per day and per 5-year period is given. The last column gives the depth of penetration in aluminum by the striking meteoroids. Deviation from this flux would be encountered during passage through comet tails. However, damage due to comet debris would be quite difficult to predict.

REFERENCES

7-1. "Advanced Syncom, Initial Project Development Plan, 1," Hughes Aircraft Company, Culver City, August 1962.

7-2. Tada, H.Y., "Degradation Mechanisms of Components and Materials at an Altitude of 250 km," TM-726, Hughes Aircraft Company, Culver City, September 1962.

7-3. McCoy, T.M., "Hyperenvironment Simulation" Part I, WADD TR 60-785, January 1961.

7-4. Dushman, S., *Vacuum Techniques*, John Wiley and Sons, New York, 1949.

7-5. Evans, R.D., *The Atomic Nucleus*, McGraw-Hill, New York, 1955.

7-6. Johnson, F.S., "Structure of the Upper Atmosphere," *Satellite Environment Handbook*, edited by Johnson, F.S., p. 9, Stanford University Press, Stanford, 1961.

7-7. Kreplin, R.W., Chubb, T.A. and Friedman, H., "X-Ray and Lyman-Alpha Emission from the Sun as Measured from the NRL SR-1 Satellite," *Journal of Geophysical Research, 67*, p. 2231, June 1962.

7-8. Dessler, A.J., "Penetrating Radiation," *Satellite Environmental Handbook*, edited by Johnson, F.S., p. 47, Stanford University Press, Stanford, 1961.

7-9. Miller, J. M. and Hudis, J., "High-Energy Nuclear Reactions," *Annual Review of Nuclear Science*, edited by Segre, E. and Schiff, L.I., *9*, p. 159, Annual Reviews, Palo Alto, 1959.

7-10. Singer, S.F., "The Primary Cosmic Ray Radiation and Its Time Variations," *Progress in Elementary Particle and Cosmic Ray Physics,* edited by Wilson, J. G. and Wouthuysen, S.A., *4,* p. 205, Interscience Publishers, New York, 1958.

7-11. Neher, H. V., "The Primary Cosmic Radiation," "*Annual Review of Nuclear Science,* edited by Segrè, E., *8,* p. 217, Annual Reviews, Palo Alto, 1958.

7-12. Peters, B., "The Nature of Primary Cosmic Radiation," *Progress in Cosmic Ray Physics,* edited by Wilson, J. G., *1,* p. 193, Interscience Publishers, New York, 1957.

7-13. Vosteen, L. F., "Environmental Problems of Space Flight Structures: I," *Ionizing Radiation in Space and Its Influence on Spacecraft Design,* NASA ND-1474, Washington, October 1962.

7-14. Goedeke, A. D., "The Frequency of Occurrence of Solar Flare Radiation Events," *1961 Proceedings,* p. 325, Institute of Environmental Science, Washington (1961).

7-15. Earl, J. A., "Cloud-Chamber Observation of Solar Cosmic Rays over Minneapolis on September 4, 1960," *Journal of Geophysical Research, 67,* p. 2107, June 1962.

7-16. Ney, E.P. and Stein, W.A., "Solar Protrons, Alpha Particles, and Heavy Nuclei in November 1960," *Journal of Geophysical Research, 67,* p. 2087, June 1962.

7-17. Fichtel, C.E., Kniffen, D.A. and Ogilvie, K.W., "September 26, 1960, Solar Cosmic-Ray Event," *Journal of Geophysical Research, 67,* p. 3669, September 1962.

7-18. Davis, L.R. and Ogilvie, K. W., "Rocket Observations of Solar Protons during the November 1960 Events; 2," *Journal of Geophysical Research, 67,* p. 1711, May 1962.

7-19. IGY Bulletin, "Sunspot Numbers," *Transactions American Geophysical Union, 43,* p. 237, June 1962.

7-20. Whipple, F. L., "The Meteoritic Risk to Space Vehicles," *Vistas in Astronautics,* p. 115, 1958.

8. SPACECRAFT SUPPORT EQUIPMENT

The multiple-channel communication, telemetry, and command systems,coupled with the multiple redundancy of equipment throughout the Advanced Syncom spacecraft,requires that more automatic test equipment and readout procedures be utilized in the system support equipment than are employed in the Syncom I program. The handling fixtures must combine flexibility in usage with safety in moving and testing a 1500-pound vehicle. The weight and balance equipment must retain accuracy while supporting up to 800 pounds. The test equipment must rapidly and accurately check operation of all spacecraft functions. These criteria have established the ground rules for the studies and fabrication of support equipment accomplished during this program. The progress to date is reported in the following sections.

ADVANCED SYNCOM TEST EQUIPMENT

Most of the effort has been directed toward the design and fabrication of equipment for testing the transponder electronics developed on the Advanced Technological Development (ATD) program. This includes equipment for testing both the frequency translation and multiple-access modes of the transponder. In addition, studies of Syncom II test equipment have been initiated and a review of the possible use of equipment from the RELAY test support stations for support of Syncom II test has been started.

ATD Transponder Test Equipment

The test equipment utilized to demonstrate the Syncom II ATD transponders is shown in Figure 8-1. Demonstration of the frequency translation mode was accomplished using television as a wideband signal. A video pattern generator or the video detector output of a television receiver is used to excite a wideband modulator which drives a 6-kmc klystron amplifier. These signals are transmitted through the 6-kmc horn to the spacecraft receiving antenna. The frequency translation transponder converts the received 6-kmc signal to the 4-kmc transmitting frequency with no change in modulation index. These signals are transmitted through the phased array antenna to the 4-kmc receiving horn. The 4-kmc receiver recovers the video and drives the TV receiver. The equipment required to adequately test the multiple access mode, however, is more complex and is described in reference to Figure 8-1.

The various baseband sources are shown at the left of the block diagram. Two single-sideband transmitter-receiver units on frequencies of 1.975 and 3.850 mc are used to effect voice communication. Each operates on the upper sideband and has over 45 db of carrier suppression and lower sideband suppression. The bandwidth is 3.1 kc, which is standard for this type of service. Operation is controlled from a telephone-type headset.

The multiple signal generator provides a second baseband input derived from 55 crystal oscillators ranging from 0.1 to 5.5 mc in 0.1-mc steps. The output of these oscillators is combined in a resistive network and then sent through gain control and wideband amplifiers. This generator has the dual function of simulating multichannel loading and of checking baseband response.

A white noise test set is a third baseband input and is included for making intermodulation distortion measurements.

A pilot signal of 284 kc is inserted at the transmitter baseband input. When this pilot signal is received it is sent to a phase detector where it is compared with the pilot signal transmitter. Any difference results in a dc error voltage which is applied to a voltage controlled oscillator in the transmitter. This results in received signals being of identical frequency as those transmitted.

The baseband signals are combined with a 32.58-mc signal to produce sidebands both above and below 32.58 mc and to suppress the carrier frequency. The lower sideband is removed by passing the signals through an upper sideband filter and a tuned amplifier.

The remaining single sideband signal is then mixed with another signal to convert it to 6390 mc. This mixer is also followed by a filter to eliminate difference signals out of the mixer. These single sideband signals can now be sent to the spacecraft through a directional coupler, attenuator, and cables, or through a traveling-wave tube amplifier and horn antenna.

The return link from the Syncom transponder is a phase modulated 4170-mc signal. This path again is either via cables or through space to a horn antenna. The resulting signal at the ground station proceeds through an input mixer, an IF amplifier, and a discriminator. The baseband output amplifier then amplifies the signal.

This equipment was used in conjunction with the spacecraft for demonstration of parameters. Telephone conversation was carried on either with or without the other channels loaded with no discernible difference in quality.

Syncom II Test Equipment

The studies of Syncom II test equipment have progressed to the block diagram stage. The test equipment design is based upon the following requirements:

1) The equipment must adequately check the desired parameters. Tables 8-1 through 8-3 show a proposed set of required tests for the communication transponders. Tests of a similar level will be required for other subsystems.

2) The test equipment and the ground station equipment will be identical to the maximum extent possible. Some differences in input-output equipment will occur because of the different primary functions. However, whenever the same function is accomplished by each set of equipment, the equipment will be the same. This approach assures that all tests on the spacecraft from the first performance test to any field test can be compared on a common basis.

3) The test equipment must be semi-automatic wherever possible. Some functions of the transponders will still require visual observation of a spectrum analyzer for proof of performance. Except for these few functions, the results of all other tests will be handled through a processor which yields printouts as permanent records. The processor will include the ability to flag out-of-tolerance results, thus permitting immediate remedial action.

TABLE 8-1. FREQUENCY TRANSLATION TRANSPONDER TESTING

Parameter to be Tested	Test Equipment Required	Comments
1) Input and output frequencies and bandwidths (including IF)	Communications panel, 35 to 75 mc signal generator, transfer oscillator, electronic counter and frequency converter, TV signal generator, TV monitor, and spectrum analyzer	
2) Image rejection	Same as above	Spectrum analyzer would be used to receive and measure transponder outputs in response to image inputs.
3) Power output	RF power meter	
4) Sensitivity	Same as 1	Phase-locked loop status would be monitored as a function of signal level.
5) Signal distortion (intermodulation, phase distortion, etc.)	Same as 1	Distortion checks would be made by viewing TV patterns on TV monitor on inputs and outputs of transponder.

TABLE 8-2. SSB/PM MULTIPLE ACCESS TRANSPONDER TESTING

System Test	Test Equipment Required
Receiver sensitivity or minimum readable signal level and dynamic range	Test single-sideband generator and PM receiver (similar to ground station), spectrum analyzer, oscilloscope, power meter
Transponder bandwidth	Test single-sideband generator and PM receiver, spectrum analyzer, oscilloscope
Phase modulation index	Test single-sideband generator and PM receiver, spectrum analyzer
Power output	Test single-sideband generator and PM receiver, power meter, spectrum analyzer
Intermodulation distortion	Noise generator, narrow-band reject filter, test single-sideband generator and PM receiver, spectrum analyzer
Noise figure (if test access permits)	Noise tube and noise meter

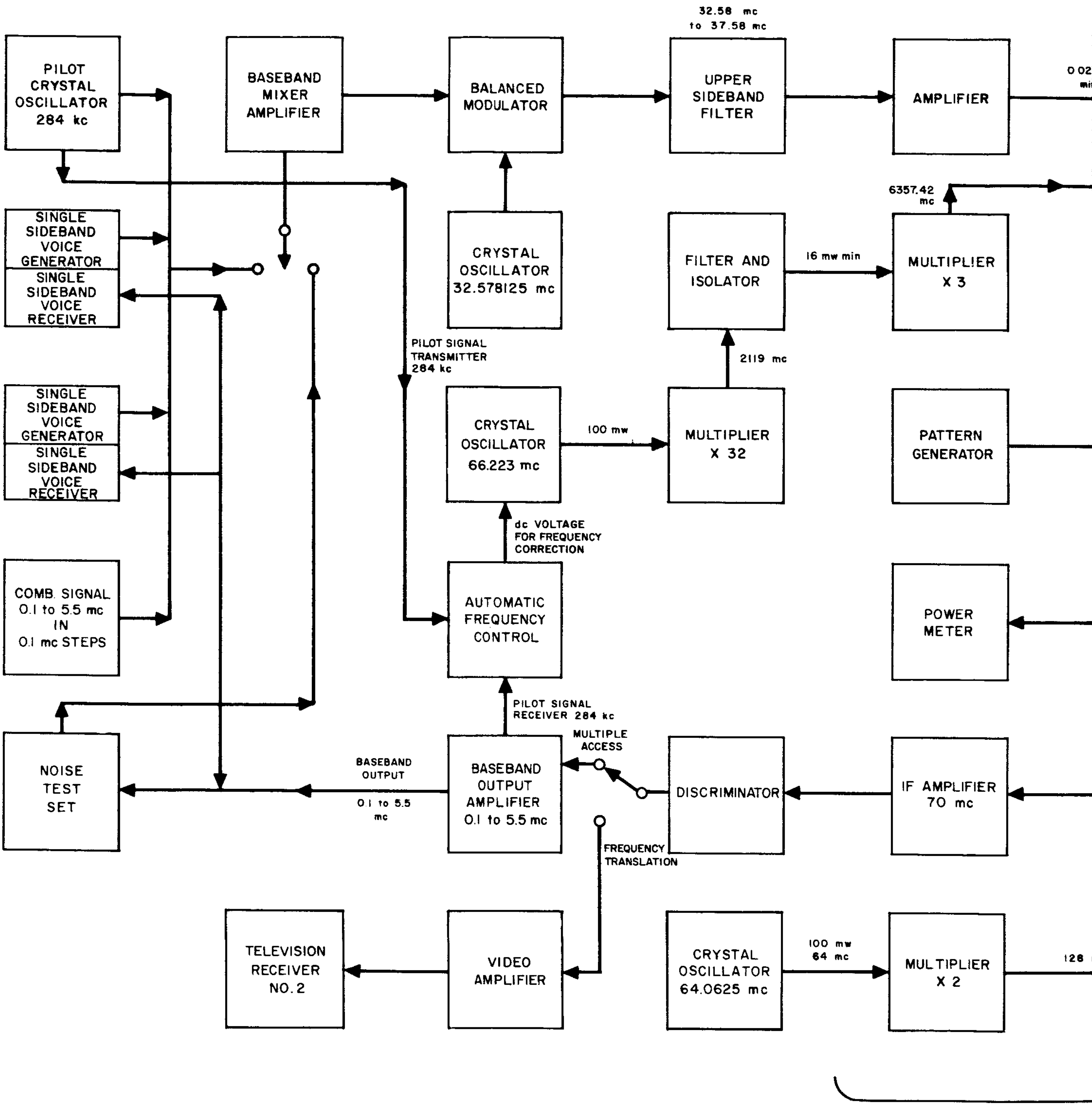

FIGURE 8-1. SYNCOM II TRANSPONDER TEST AND DEMONSTRATION PANEL

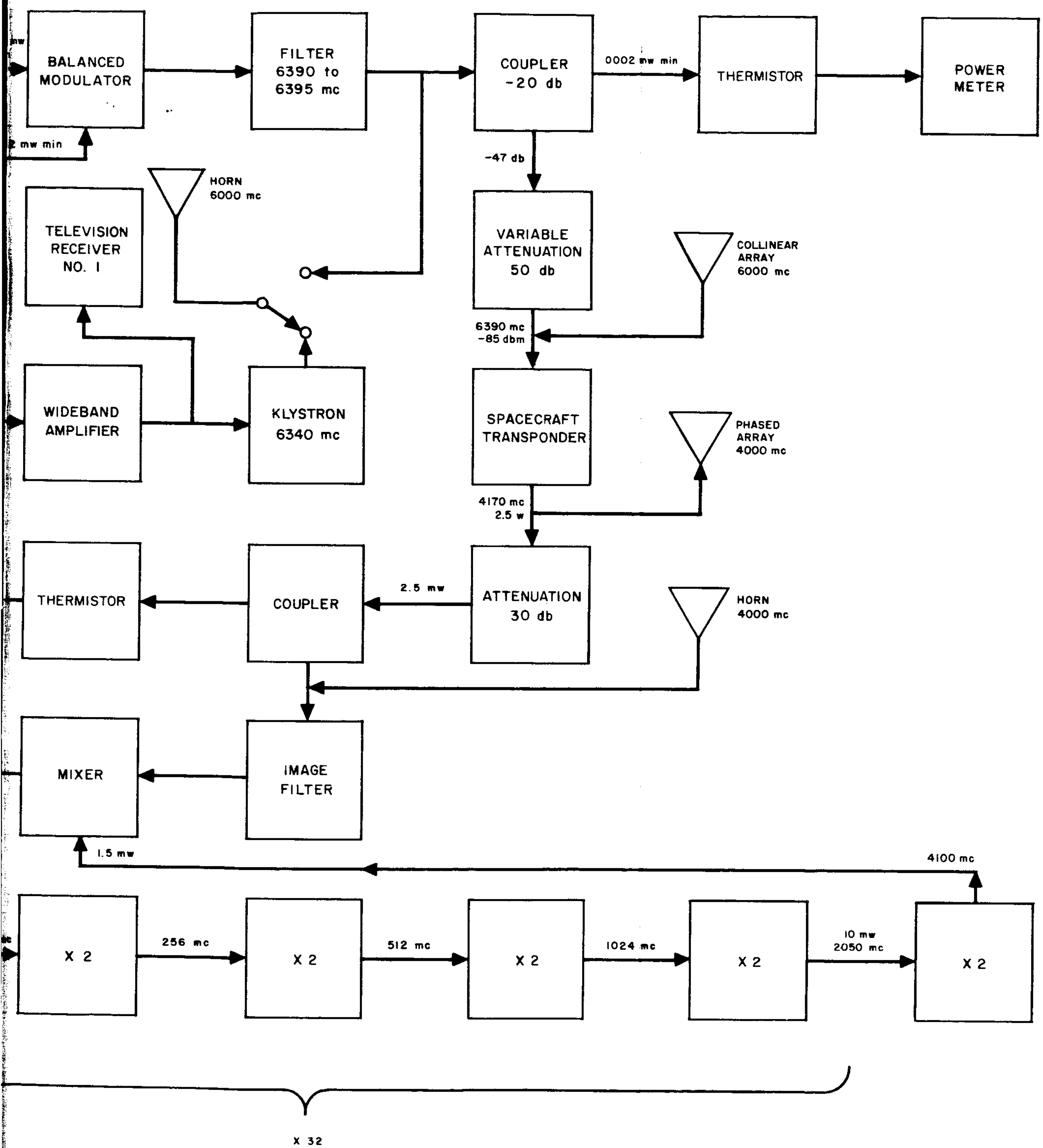

BALANCED MODULATOR
FILTER 6390 to 6395 mc
COUPLER -20 db
0002 mw min
THERMISTOR
POWER METER
mw min
-47 db
HORN 6000 mc
TELEVISION RECEIVER NO. 1
VARIABLE ATTENUATION 50 db
COLLINEAR ARRAY 6000 mc
6390 mc
-85 dbm
WIDEBAND AMPLIFIER
KLYSTRON 6340 mc
SPACECRAFT TRANSPONDER
PHASED ARRAY 4000 mc
4170 mc
2.5 w
THERMISTOR
COUPLER
2.5 mw
ATTENUATION 30 db
HORN 4000 mc
MIXER
IMAGE FILTER
1.5 mw
4100 mc
X 2
256 mc
X 2
512 mc
X 2
1024 mc
X 2
10 mw
2050 mc
X 2
X 32

4) Testing will be required when the spacecraft is in orbit. Adequate information to yield estimates of spacecraft life in orbit can best be made by continuing the measurements which preceded launch. Therefore, each ground station is equipped with all the capabilities of the system test equipment. This equipment can be used directly for telemetry and command system checks and in conjunction with the NASA-furnished communications stations for transponder checks.

Figures 8-2 through 8-5 are the block diagrams of the presently planned test equipment designed to meet the stated requirements. The equipment will generate appropriately modulated signals to exercise and test the communication transponder. The telemetry data processor will receive, decommutate, record, and display telemetry and test signals. A command generator and an electronic synchronous controller for control of the spacecraft are also included.

RELAY Trailer Review

The RELAY test stations were examined to determine the necessary additions and modifications re-

TABLE 8-3. ANTENNA CONTROL SYSTEM TESTING

System Test	Equipment
1) Stationary spacecraft	
a) Antenna radiation pattern is de-spun in synchronism with the ψ-pulse, has 24-hour angular correction, and responds to external commands.	4-gc antenna horn Antenna horn stand 4-gc crystal detector (HP 420A) Oscilloscope (TKX545)
b) Reaction jet fire signal occurs at correct angular position and with correct pulse width.	Plug-in preamplifier (TKX Type C/A) Pulse generator
2) Rotating spacecraft	
a) External commands control angular position of antenna radiation pattern.	4-gc antenna horn 4-gc crystal detector (HP 420A)
b) Antenna radiation pattern reverts to pancake shape.	Antenna horn stand Oscilloscope (TKX545)
c) Reaction jet fire signal occurs at correct angular position and with correct pulse width.	Plug-in preamplifier (TKX Type C/A) Command generator Telemetry receiver Reaction jet fire signal detector Spin table

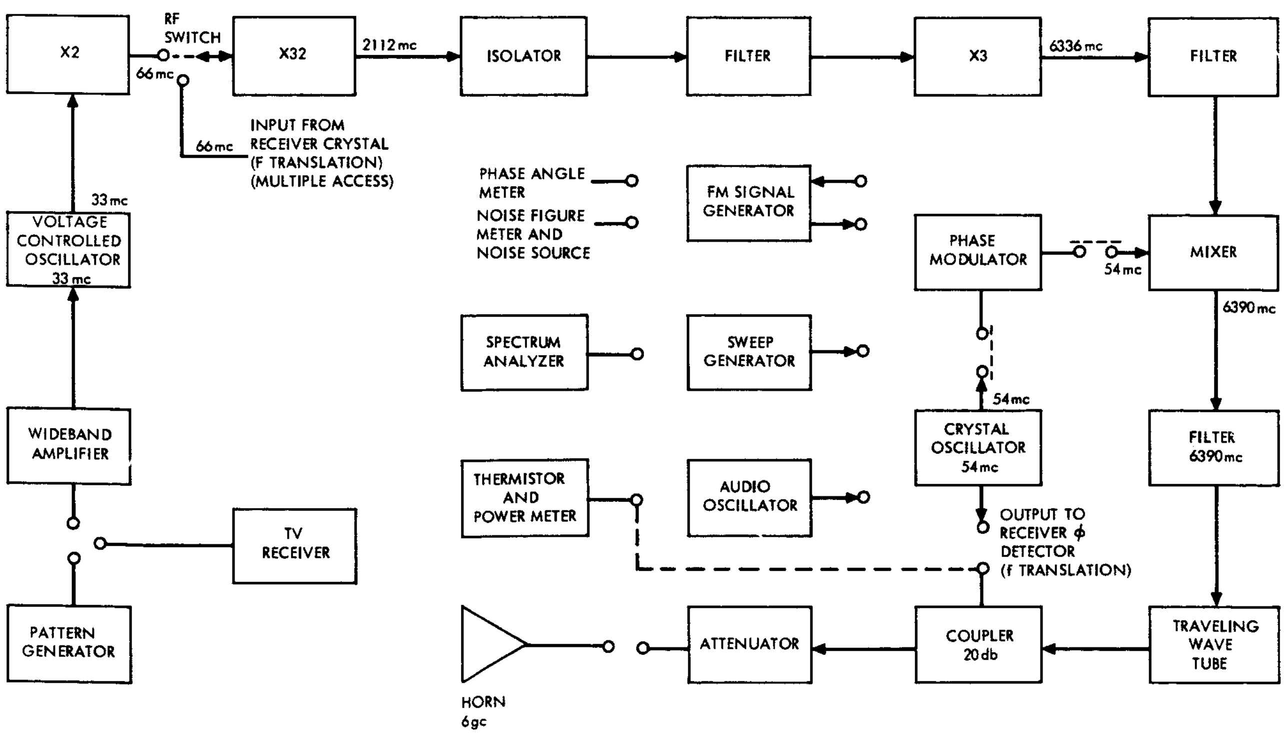

FIGURE 8-2. FREQUENCY TRANSLATION TRANSMITTER

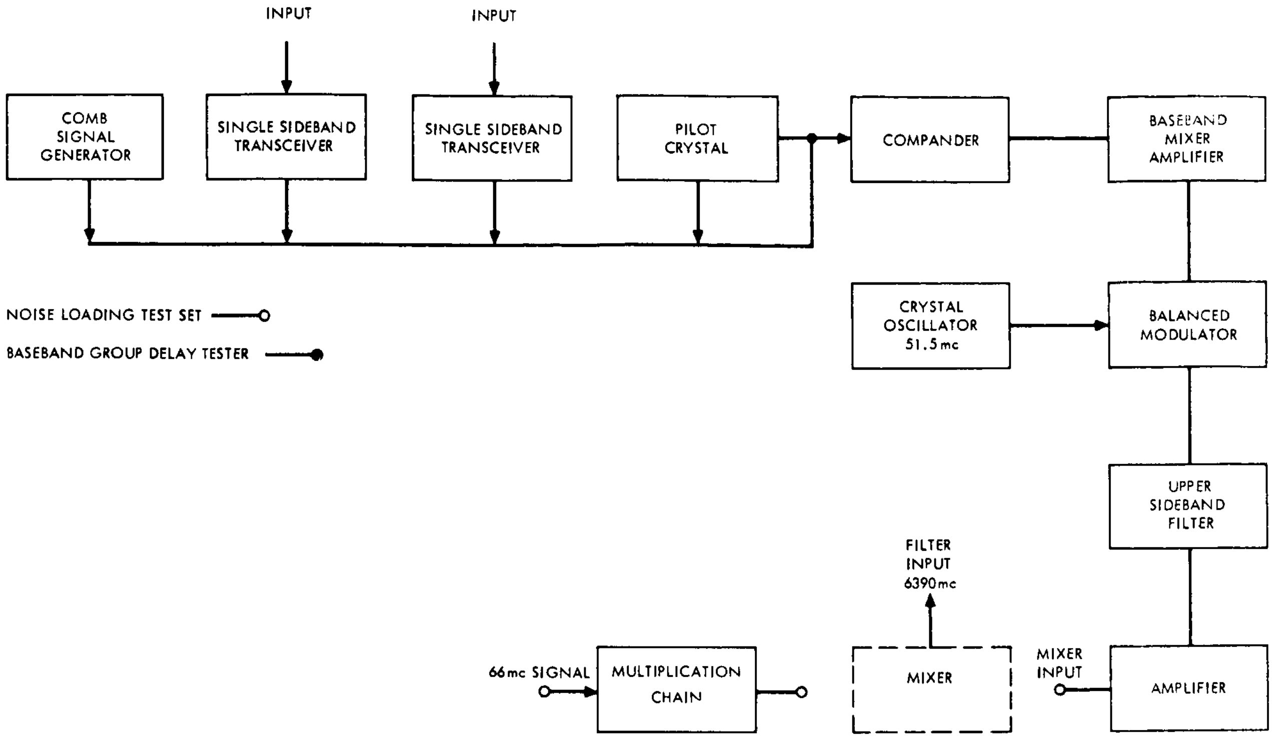

FIGURE 8-3. MULTIPLE ACCESS TRANSMITTER

quired for participation as telemetry and command stations in the Advanced Syncom program.

There are two RELAY test stations currently in operation. One is located in Nutley, New Jersey, and the other at Goldstone Dry Lake in the Mojave Desert. Both stations have command capability over the RELAY satellite, telemetry monitoring facilities, and wideband communication equipment. At the present time, the Nutley test station is exercising prime control, with the Mojave station acting as backup. The test stations will be described concurrently, with notations where differences exist.

Each test station consists of two vans designed for highway touring, which are also air, water, or rail transportable. One side of each van is removable, so that both vans can be placed side by side, thus providing one large enclosure. The vans can also be operated separately. One van, the communication van, can perform wideband communication experiments, while the other trailer independently performs the functions of tracking, telemetry, and command.

The telemetry and command control system consists of five basic subsystems:

Antenna
Transmitter
Receiver
Recording
Control

The control subsystem includes the command encoder, telemetry decoding equipment, display equipment, and time code generator.

The VHF antenna system consists of one 148-mc, cross-polarized yagi, surrounded by eight 136-mc, cross-polarized yagis, all mounted on a platform capable of rotation in azimuth and elevation. The command antenna is a seven-element yagi (148.26 mc) located in the center of the mounting with means for selecting left- or right-hand circular polarization and vertical or horizontal plane polarization. The telemetry array consists of eight cross-polarized, seven-element yagis (136.47 mc) mounted in a square perimeter around the command antenna. Line filters pass the 136-mc frequency to a dual channel preamplifier. This antenna will be usable without modification.

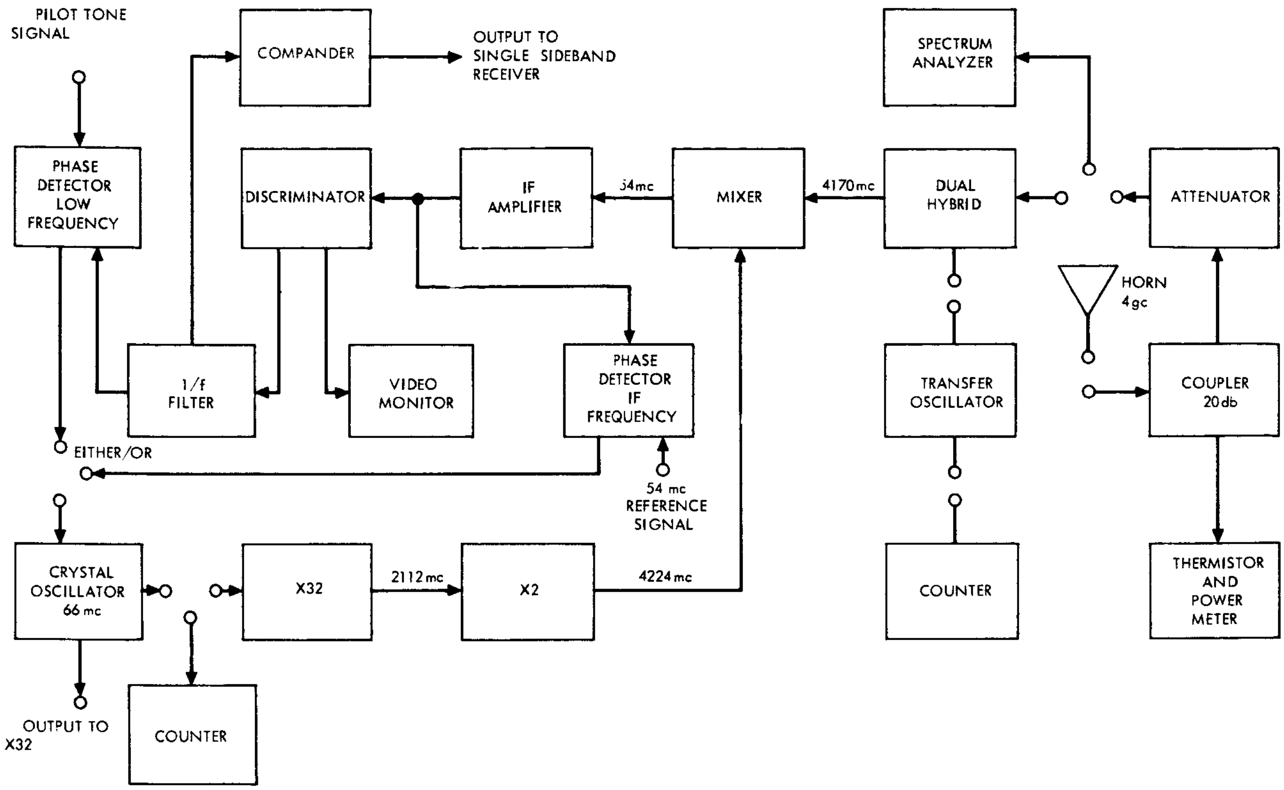

FIGURE 8-4. DUAL MODE RECEIVER

The command transmitter at the Nutley site is a Hughes 3-kilowatt transmitter operated at 148.250 mcs. It is the same unit used in the Syncom I program. The transmitter at the Mojave station is a 300-watt unit at the same frequency. The 3-kilowatt unit will be directly applicable, whereas the 300-watt unit lacks the necessary power to provide reliable control in the planned synchronous orbit.

The receiver subsystem consists of appropriate filters, VHF preamplifiers, a multicoupler, and receivers. The primary receiver at both stations is a Motorola phase lock receiver, Model 136-137 mc. The back-up receiver at Nutley is a Defense Electronics Type TMH-A6A, and at Mojave, a Nems-Clarke Model 1456 phase-lock demodulator. All of this receiving equipment is compatible with the Advanced Syncom.

The RELAY project employs a PCM telemetry system, while Syncom II will use a PFM system. Requirements in this field necessitate a new telemetry processor and new encoder. Further investigation is required to determine whether the RELAY discriminator is applicable.

The additional item in the control system for which new equipment is necessary is the electronic-synchronous ground controller. The PB-250 computer, already in the RELAY system, might have application to this function.

The instrumentation subsystem has been designed for versatility. It is supported by an extensive recording facility so that much of the system can be evaluated in actual operation. The following inventory lists the test and recording equipment, all of which is directly applicable to Advanced Syncom.

INVENTORY OF TEST EQUIPMENT
Mojave Site

Bendix, Load, Model 636NC
Bird, Thermaline, wattmeter, Model 621
Hewlett Packard, low frequency function generator, Model 202A
Hewlett Packard, signal generator, Model 616B
Hewlett Packard, VHF noise source, Model 343A
Hewlett Packard, plug in, Model 525A
Hewlett Packard, VTVM, Model 410B
Hewlett Packard, AC VTVM, Model 400H
Hewlett Packard, VTVM, Model 410B
Hewlett Packard, power meter, Model 431A

INVENTORY OF TEST EQUIPMENT

(2) Hewlett Packard, T-connector, Model 455A
(2) Hewlett Packard, N-connector, Model 458A
Hewlett Packard, signal generator, Model 608D
Hewlett Packard, thermistor mount, Model 478A
Hewlett Packard, frequency converter, Model 525A
Hewlett Packard, oscillator, Model 650A
Hickock, tube tester, Model 539B
Kay, attenuator, Model 30-0
Lambda, power supply, Type C-480M
Lavoie, spectrum analyzer, no Model No.
Lavoie, attenuator, Model LA 18M
Offner, dynograph amplifier, Model 482
Precision Instruments, bulk tape degausser, Model DG-1
Tektronix, scope, Type 310A
Textronix, cart, Model 500/53A
(2) Tektronix, scope, Model 545A
Tektronix, plug in, Type CA
Tektronix, plug in, Type H
Tektronix, plug in, Type D
Triplett, volt-ohm meter, Model 630

Nutley Site

Bendix load, Model 636NC
Bird Electronics Corporation, wattmeter, Model 612
Calrad, tape head degausser, Type TD-69
Hewlett Packard, low frequency generator, Model 202A
Hewlett Packard, VHF noise source, Model 343A
(2) Hewlett Packard, VTVM, Model 410B
Hewlett Packard, wattmeter, Model 431A

(2) Hewlett Packard, T-connector, Model 455A
(2) Hewlett Packard, N-connector, Model 458A
Hewlett Packard, amplifier, Model 466A
Hewlett Packard, thermistor mount, Model 478A
Hewlett Packard, frequency converter, Model 525A
Hewlett Packard, frequency converter, Model 525B
Hewlett Packard, oscillator, Model 650A
Hickock, tube tester, Model 539B
Kay, attenuator, Model 30-0
Lambda, power supply, Type C-480M
Lavoie, attenuator, Part No. K90700070
Precision Instruments, bulk tape degausser, Model DG-1
(2) Simpson, volt-ohm meter, Model 260
Tektronix, scope, Type 310A
Tektronix, cart, Model 600/53A
Tektronix, scope, Model 545A
Tektronix, plug in, Type H
Tektronix, plug in, Type D
Telonic, radio frequency detector, Model XD-8A
Telonic, attenuator, Model TG-975
(2) Triplett, volt-ohm meter, Model 630
Western Electric, FM terminal test set, Model J68408A
 ITI electric oscilloscope Model KS15869
Nems Clarke, special-purpose receiver, Type 1502A
Triplett, volt-ohm meter, Model 630
(2) Triplett, volt-ohm meter, Model 630NA
Western Electric, FM terminal test set, Model J68408A
 ITI electric oscilloscope, Model 1515869

WEIGHT AND BALANCE EQUIPMENT

Weight Measurement

The weight of each component will be measured by means of calibrated, simple balanced-beam gram scales. Each major subassembly will be weighed by conventional double-pendulum-type scales. The accuracy of the scales to be used is within ± 0.05 percent over the full-scale reading.

The weight of the total spacecraft less apogee motor will be measured by standard tension load cells. The spacecraft will be supported at the separation plane by a special weight, center-of-gravity, and moment-of-inertia fixture. The fixture will be suspended by two wires incorporating the load cells (Figure 8-6a. The accuracy of the load cells to be used is 0.10 percent over the full scale output.

Component Center-of-Gravity Measurement

The center of gravity will be obtained for the components using a specially designed single-pendulum device. This device has been in use at Hughes extensively and has proven its accuracy and reliability. The fixture, shown schematically in Figure 8-7, consists of a flat level work surface supported above a knife-edge fulcrum. The device is maintained in stable equilibrium by a pendulum weight suspended from the work surface. The pendulum weight is variable and is selected so the total center of gravity of the machine, including the specimen being measured, falls below the fulcrum. Attached to the table, or work surface, are balancing weights which may be moved horizontally along an accurate linear scale.

The component undergoing weight and balance determination is positioned on the table. One coordinate of the component's center of gravity is then found by determining the distance that the balance weight must be moved to re-level the table (the initial leveling having been disturbed by the placement of the component on one side of the table). By re-orienting the position of the component on the table and repeating this procedure, the precise location of the center of gravity

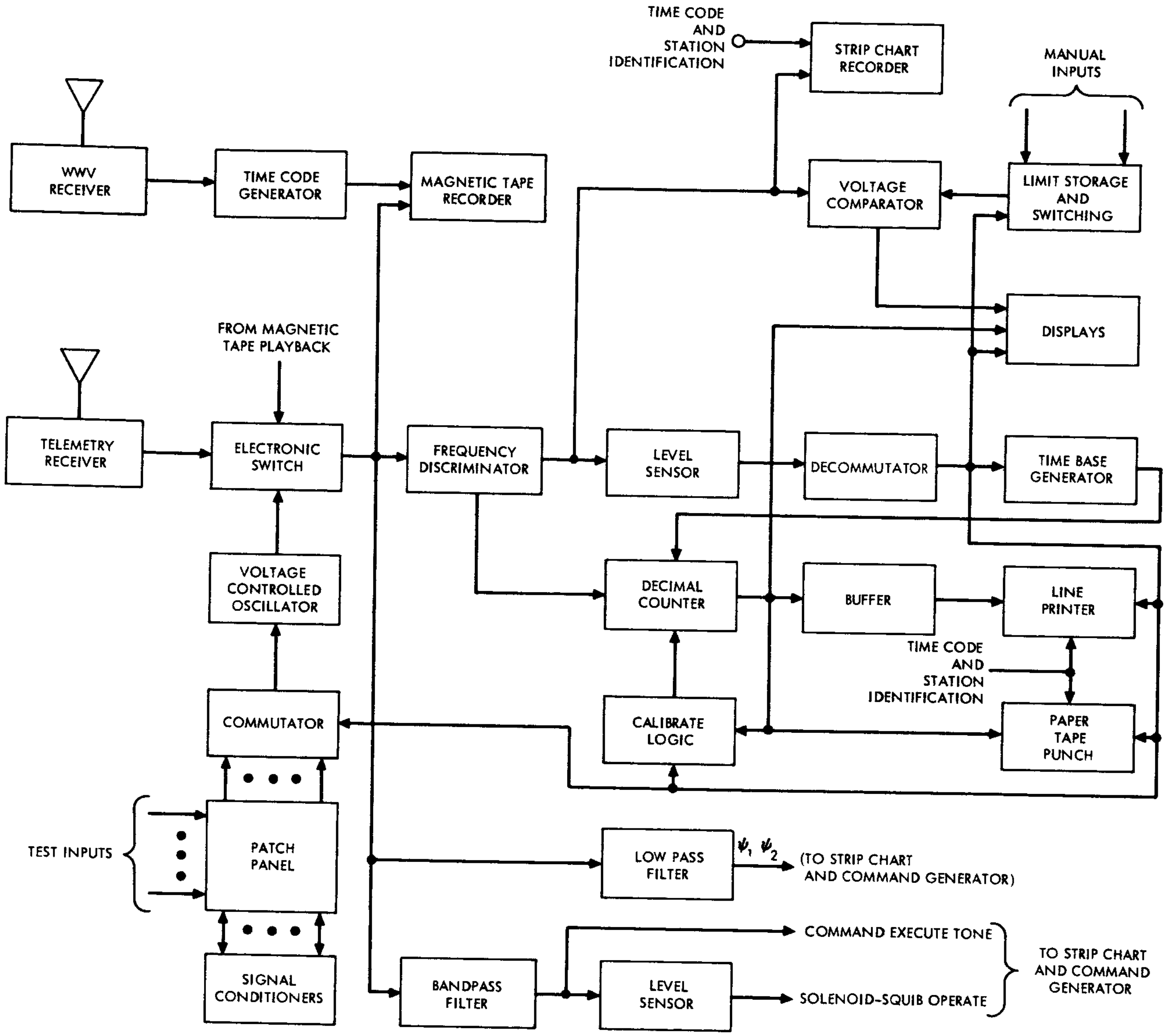

FIGURE 8-5. SYNCOM II TELEMETRY PROCESSOR AND SYSTEM TEST

is determined. Based on previous experience with this equipment, the center of gravity of the component can be located within ± 0.001 inch.

Spacecraft Longitudinal Center of Gravity Measurements

Longitudinal center of gravity of the total spacecraft will be determined with the assembly supported by the weight, center of gravity, and moment of inertia fixture. The spacecraft and fixture will be turned from the roll to the pitch position by a crane and roll-over device as shown in Figures 8-6b through 8-6d. While in the pitch position the longitudinal center of gravity location is determined from the weight of the structure and of the fixture, the reactions of the load cells, and the geometry of the fixture.

Spacecraft Moment of Inertia Measurements

The bifilar torsion pendulum method will be employed to determine the moments of inertia of the

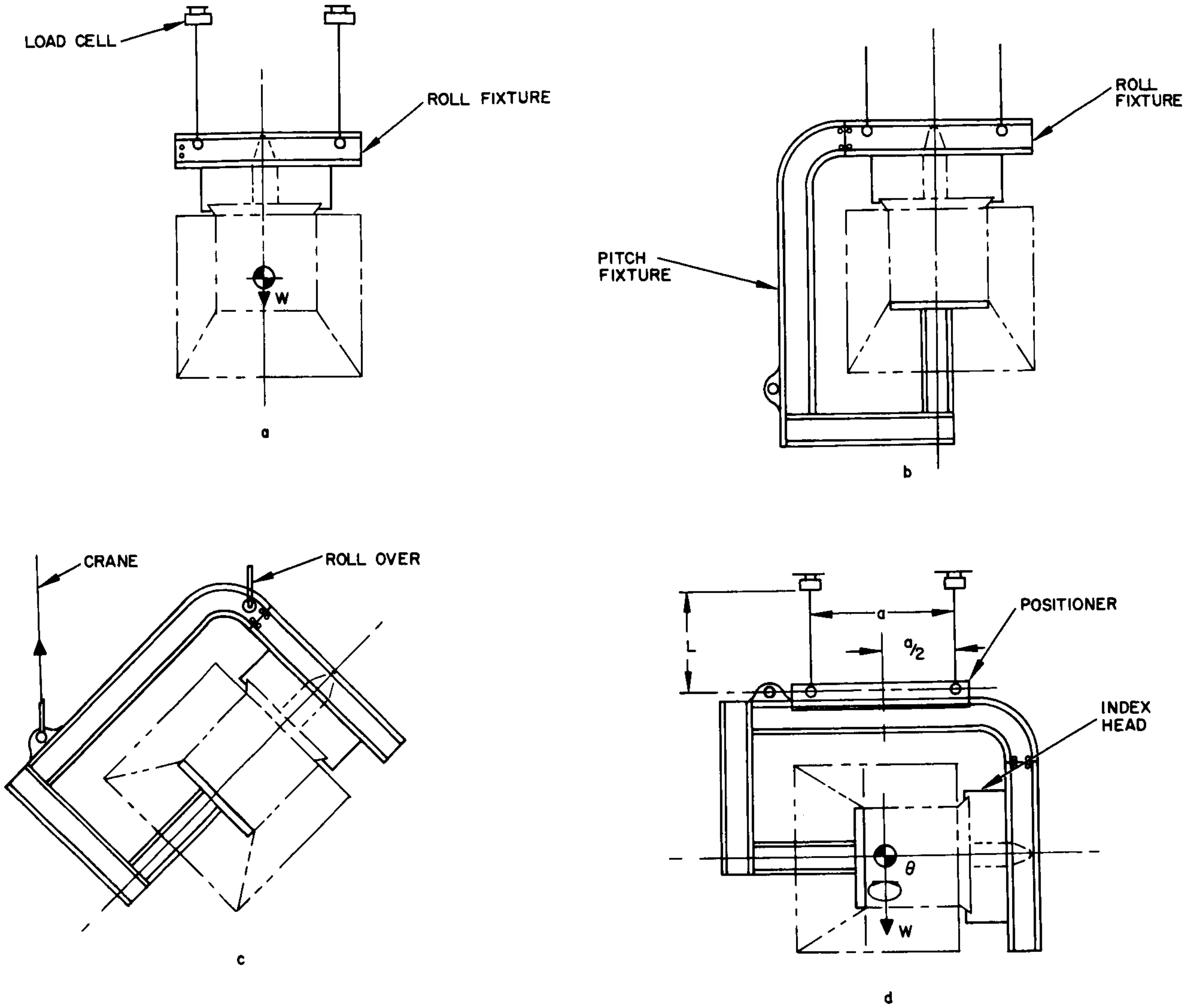

FIGURE 8-6. COMBINATION WEIGHT, CENTER OF GRAVITY, AND MOMENT OF INERTIA EQUIPMENT

spacecraft. This method has been used by Hughes on the Syncom I and on many other projects in the past. It has been found to be an economical procedure in addition to its simplicity, accuracy, and reliability.

The procedure is to support the spacecraft by two equal-length cables placed equidistant from the center of gravity and parallel to the axis about which the moment of inertia is to be determined. The spacecraft is then given a small angular displacement, released, and allowed to oscillate. From the oscillation frequency and the geometry of the system, the mass moment of inertia is determined analytically. The system is shown schematically in Figures 8-6a and 8-6d.

The derivation of the equation used to determine the moment of inertia follows. For small angles, it can be shown that

$$I\theta + \frac{Wa^2}{4L}\theta = 0$$

where

I = moment of inertia, slug-ft^2

θ = angular displacement, radians

W = spacecraft weight, pounds

a = distance between support cables, feet

L = length of support cables, feet

from which the frequency is

$$f = \frac{1}{2\pi}\sqrt{\frac{Wa^2}{4IL}}$$

which when solved for the mass moment of inertia gives

$$I = \frac{Wa^2}{16\pi^2 f^2 L}$$

It can be shown that the maximum error in the experimental determination can easily be held to minimal allowances. Aerodynamic damping, for example, has been found to be negligible because of the small amplitudes and low frequencies used.

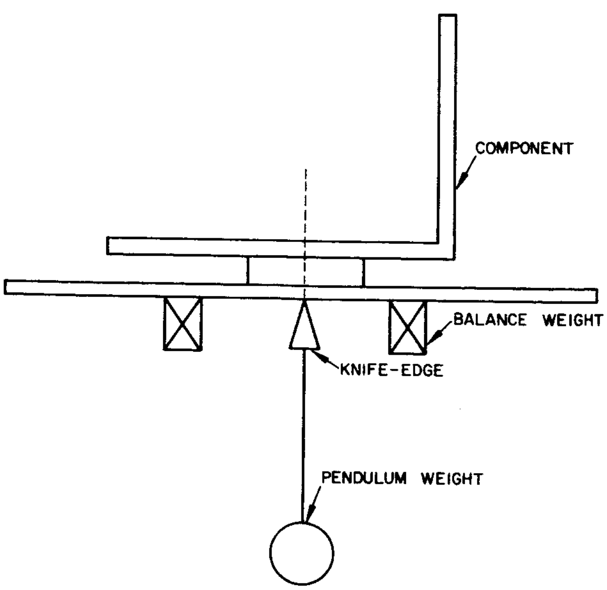

FIGURE 8-7. COMPONENT CENTER OF GRAVITY MEASUREMENT

Static and Dynamic Balancing about Spin Axis

The spacecraft is to be dynamically balanced about the spin axis so that this axis will coincide with the principal axis of inertia. This will be accomplished on a Hughes-designed vertical spin balance machine similar to that used throughout the Syncom I project, (Figure 8-8). Typical residual dynamic unbalance measurements from the Syncom Mark I tests range from 0.00006 to 0.0003 slug-ft^2. The spacecraft (less apogee motor) will be attached to the spin balance machine at the apogee motor mounting surface with its geometric axis coincident with the axis of rotation of the spin balance machine. The knife-edge supports of the spin balance machine will allow static balancing of the spacecraft by correcting any unbalances of the spacecraft about the knife edge where the line of the knife edge passes through the geometric axis and is perpendicular to it. Since the spacecraft can also be spun while supported on the

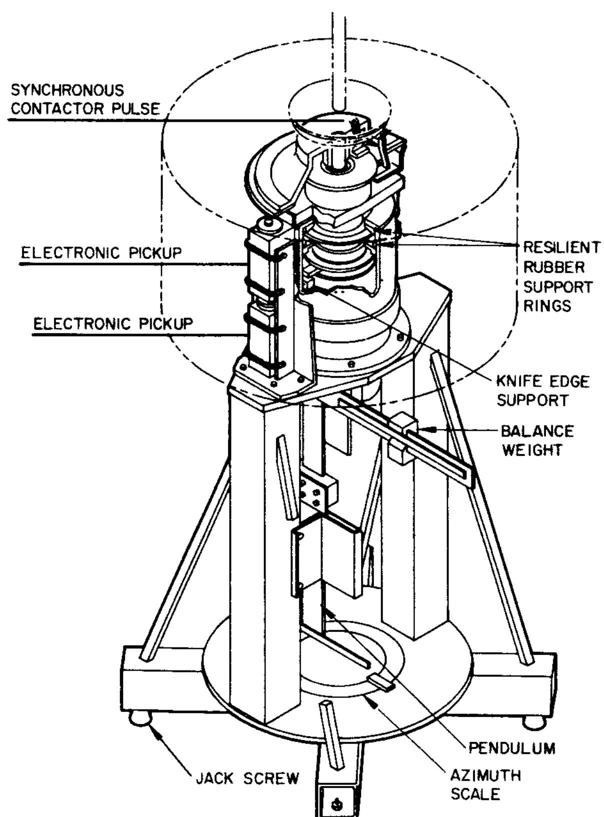

FIGURE 8-8. SYNCOM MARK I VERTICAL SPIN BALANCE MACHINE

knife edge, this permits dynamic balancing by eliminating the deflection of the attached pendulum. After dynamic balancing, operational tests may be conducted by spinning the spacecraft while supported on the knife edge.

HANDLING EQUIPMENT

Spin Test Fixture

A spin test fixture for the performance of antenna tests on a spinning spacecraft was designed and is being utilized. The base of this fixture is of welded steel construction with three legs and built-in leveling features. Power is supplied by a 1-hp motor with a V-belt drive providing the necessary reduction to 108 rpm output. At substantial savings in fabrication, two identical cast aluminum housings were utilized. One, mounted to the base, serves as the shaft housing. The other housing is mounted to the shaft and provides necessary mounting holes for attaching the spacecraft.

Mobile Assembly Fixture

A fixture to hold basic structure during all phases of assembly is available for use. This fixture is sufficient for the study, but a more versatile fixture will be designed for the production program. This fixture will also be used to hold the spacecraft during checkout operations, and at any time maintenance is being performed. The fixture is of welded tubular aluminum construction. With the spacecraft secured to a cradle by a clamping ring, it can be rotated 360 degrees about a horizontal axis. A hand wheel, which drives the cradle through a worm gear reductor, makes a one-man operation possible. In addition to the cradle being self-locking in any position, a locking pin arrangement is provided for safety. Four swivel casters are provided for mobility. Two casters are equipped with foot-operated braking devices to secure the fixture in one position.

Hoisting Sling

A combination spacecraft and apogee motor sling was designed and fabricated. A spreader bar design was chosen to ensure safe and efficient operation. The sling is capable of lifting the spacecraft from either end by four attach points, and the addition of a simple adapter converts it to an apogee motor hoisting sling. To ensure that no undue sudden shock loads due to lifting are transmitted into spacecraft structure or apogee motor casing, each of the four suspension cables are shock mounted. The cable shock absorbing springs also function as load equalizers.

Clamp

A simple ring-gland type clamp has been designed and fabricated. For ease of operation the clamp consists of four segments. This clamp is used for attaching the spacecraft to various handling, tooling, and test equipment.

Apogee Motor Charging Equipment

An accessory motor stand, dummy motor charging mandrel, and mandrel puller have been fabricated and delivered to JPL. During charging, the dummy motor will be supported in a vertical position at the motor mount holes by the accessory stand. The mandrel, which is of welded tubular aluminum construction, is then installed and positioned.

Test Fixture

Two fixtures have been designed and are available for vibration testing of the spacecraft. One fixture duplicates the clamp portion of the Agena interface geometry. The spacecraft is attached to this fixture at the thrust tube. The second fixture duplicates the JPL motor attachments.

9. NEW TECHNOLOGY

SPACECRAFT LAUNCH RATE AND AVAILABILITY: FIXED TIME REPLACEMENT POLICY

An analytical technique,considered to be unique, has been developed to determine satellite availability and replacement rate. The results of this technique as applied to the Syncom II satellite are discussed in section 7b of this report.

X3 MULTIPLIER

The X3 multiplier raises the frequency of the output of the X32 multiplier to that required for the input mixer. The input frequency to the X3 is 2112 mc and the output frequency is 6336 mc. This multiplier is a waveguide structure with a fixed line length for input tuning and self-biased diodes as varactor multipliers. Input power is 12 mw and output power is 3 mw.

OUTPUT RF POWER SWITCH

The output RF power switch selects one of two redundant traveling wave tubes in the transponder and connects it to the output multiplexer.

A three-port circulator has been adapted to this application by controlling the direction of magnetic field and hence the direction of circulation. A current is applied to the coil which sets up a magnetic field in the garnet inside the circulator. The external current can then be removed. The total loss due to mismatch and insertion loss is expected to be less than 0.2 db.

10. PROJECT REFERENCE REPORTS

- R. J. Oedy, "NASA-GSFC Engineering Design Tests for Atlas-Agena B and Thor-Agena B Payloads," IDC 2241.3/200, 26 June 1962.
- J. S. Culver and M. J. Neufeld, "Visit to NASA to Discuss Syncom II Design Requirements," IDC 2230.10/31, 5 July 1962.
- F. A. Figge and M. J. Neufeld, "Trip Report, Lockheed (LMSC) Syncom II," IDC 2230.10/32, 18 July 1962.
- J. G. Lotta, "Syncom II Weight Status," IDC 2243.11/153, 26 July 1962.
- P. E. Norsell, "Syncom II Launch Pad Air Conditioning Requirements," 23 August 1962.
- J. G. Lotta, "Syncom II Weight Status," IDC 2243.11/172, 24 August 1962.
- J. S. Culver and F. A. Figge, "Report of Trip to Lockheed, Burbank, on Mutual Syncom II Design Considerations," IDC 2241.3/253, 13 September 1962.
- Advanced Syncom, "Initial Project Development Plan," Volume I, Technical Plan, SSD2380R, 15 August 1962.
- Advanced Syncom, "Initial Project Development Plan," Volume II, Development Plan, SSD2381R, 15 August 1962.
- Syncom Project Notice No. 20, "Syncom II Communication Frequencies," 8 August 1962.
- D. T. Dupree, "Technical Documentation Requirements for Syncom II Spacecraft," IDC 2280.5/130, 13 August 1962.
- J. C. Meyer, "Vitramon Capacitors for Syncom II," IDC 2280.05/139, 23 August 1962.
- P. E. Norsell," Major Item Structure, Advanced Syncom," 5 September 1962.
- P. E. Norsell, "Major Item Descriptive Material, Advanced Syncom," 18 September 1962.
- J. G. Lotta, "Syncom II Weight Status," IDC 2243.11/183, 18 September 1962.
- R. A. Browne, "Syncom II Preliminary Unit Responses," IDC 2241.3/260, 21 September 1962.
- R. W. Clapp, "Syncom II Antenna Patterns," IDC 2230.5/82, 26 September 1962.
- Advanced Syncom, "Monthly Progress Report," SSD2473R, September 1962.
- V. H. Ho, "Trip Report" – Visit to Ball Brothers Research Corporation, Boulder, Colorado, 15 October 1962.
- D. S. Braverman and D. D. Williams, "Single-Sideband to Phase Modulation Multiple Access System Analysis," TM 721, October 1962.
- "Preliminary Performance Specification, Syncom II Apogee Rocket Motor," 17 October 1962.
- "Specification No. X-254044, Performance Specification, Syncom II Bipropellant Reaction Control System," 23 October 1962.
- Advanced Syncom, "Monthly Progress Report," SSD2537R, October 1962.
- Paul M. Blair, Jr. and Herbert Y. Tada, "Environments of Syncom,Mark II," TM 732, October 1962.
- J. G. Lotta, "Syncom II Weight Status," IDC 2243.11/214, 8 November 1962.
- J. M. Zajec, "Trip Report" – Attendance at Project Telstar Component Reliability Symposium, Murray Hill, New Jersey, 14 November 1962. Report dated 20 November 1962.
- M. J. Neufeld, "Bendix Photo-Detector for Syncom Attitude Reference," Technical Report, 27 November 1962.
- Advanced Syncom, "Monthly Progress Report," SSD2574R, November 1962.
- J. G. Lotta, "Syncom II Weight Report," ABL-248 Configuration, IDC 2243.11/20, 7 December 1962.
- D. C. Mead, "Syncom II Dual Mode Command Decoder," IDC 2941.20/69, 14 December 1962.
- Revised Preliminary Performance Specification, Syncom II Apogee Rocket Motor, 14 December 1962.
- M. J. Neufeld, "Revised Ascent Guidance Errors for Advanced Syncom" (Confidential), 19 December 1962.

- Advanced Syncom, "Monthly Progress Report," SSD3020R, December 1962.
- Browne, R. A., "Syncom II Solar Panel Vibration Test," IDC 2241.3/304, 7 January 1963.
- Lotta, J. G., "Syncom II Weight Status," IDC 2243.11/246, 8 January 1963.
- "Revised Preliminary Performance Specification, Syncom II Apogee Rocket Motor," 11 January 1963.
- Summers, R. C., "Syncom II Solar Panel Structural Dummy Development Schedule," IDC 2243.30/560, 17 January 1963.
- Syncom II Project Notice No. 5, "Syncom II Apogee Motor," 14 January 1963.
- Syncom II Project Notice 6, "Subcontracted Spacecraft Equipment," 14 January 1963 (supersedes Syncom II Project Notice No. 36, 22 October 1962).
- Syncom II Project Notice No. 7, "Syncom II Acceptance and Qualification Test Plan Approval," 14 January 1963.
- Meyer, J. C., "Pyrotechnic Devices," IDC 2280.05/254, 21 January 1963.
- Bernstein, P. W., "Minutes of Design Review of Syncom II Structure and Disposition of Design Review Comments," IDC 2241.3/314, 23 January 1963.
- Quality Control Bulletin, "Syncom II Quality Requirements for Advanced Technological Development Equipment," QCB 13-1, 23 January 1963.
- Vorndran, J. W., "Minutes and Disposition of Recommendations, Design Review of Syncom II Phased Array Control Electronics," DR File No. 2941.20/DR5, 27 January 1963.
- Advanced Syncom, "Monthly Progress Report," SSD3068R, January 1963.
- Mead, D. C., "Syncom II Central Timer," IDC 2941.20/78, 25 January 1963.
- Advanced Syncom Report, "Liquid Bipropellant Apogee Injection Rocket Studies," Approval Release, 30 January 1963.
- "Performance Specification, Syncom II Bipropellant Reaction Control System," Specification No. X-254044, 29 January 1963.
- Mason, F. D., "Estimation of Required Number of Communications Satellites as a Function of Failure Rates: Fixed Time Replacement Policy," IDC 2230.7/86, 24 January 1963.
- Master Index, Syncom II Spacecraft, Flight Model 475000-100
  Revision A, dated 5 February 1963
  Revision B, dated 7 February 1963
  Revision C, dated 21 February 1963
- Lotta, J. G., "Syncom II Weight Status," IDC 2243.11/265, 6 February 1963.
- Engineering Procedures Manual, Project Bulletin 7-17.1, "Advanced Syncom Project – Engineering Data," 4 February 1963.
- Lotta, J. G., "HSX-302 T-1 Weight Status, Syncom II," IDC 2243.11/273, February 1963.
- Brenan, R. A., "Syncom II Telemetry Reliability," IDC 2207.1/6, 15 February 1963.
- Advanced Syncom, "Performance and Test Specification," SSD3101M, 18 February 1963.
- Rubin, P. A., "Review of RELAY Test Stations," IDC, 26 February 1963.
- Culver, J. S., "Syncom II Apogee Motor Tolerances," IDC 2243.30/636, 27 February 1963.
- Meyer, J. C., "Syncom II Quality Control Information," IDC 2280.05/269, 28 February 1963.
- Letter Report, "Study of 4Gc and 6Gc Multiplexers for Syncom II," Purchase Order No. 4-753000-FF 31-1, 28 February 1963.
- Advanced Syncom, "Demonstration Plan," SSD 3114B, February 1963.
- Advanced Syncom, "Monthly Progress Report," SSD 3119R, February 1963.
- R. A. Brenan and M. L. Gazin, "Reliability – JPL Work Statement, Syncom II," 7 March 1963.
- Syncom I and Syncom II Project Notice No. 66, "Reporting of New Technology," 8 March 1963.
- Master Index, Syncom II Spacecraft, Flight Model 475000-100, Revision D, 18 March 1963.

APPENDIX A

STUDIES OF ALTERNATE CONFIGURATIONS

Several alternate apogee motor configurations were considered for Syncom II application. Use of an ABL-248 engine in a scaled-down version was one approach studied. Another approach considered all aspects of replacing the solid propellant motor with a liquid propellant motor. Weight and balance analyses, in addition to proposed structures, were considered in each case. Although none of these studies resulted in significant changes in the Syncom program, they are included here as reference material.

STUDY OF ABL-248 ENGINE

A study was conducted to evaluate the feasibility of using the Allegheny Ballistics Laboratory engine ABL-248 as an apogee engine for Syncom II. The study consisted of a weight and balance analysis and a structural layout.

The approach taken in the weight analysis was to consider a scaled-down Syncom II that could be injected into the synchronous orbit. Only two electronic quadrants are included and two telemetry transmitters. As a consequence, the control subsystem was scaled to contain only two fuel and oxidizer tanks. The weight breakdown is shown in Table A-1, and the ratio of major subsystems, in Table A-2.

The weights for the ABL-248 engine were taken from Allegheny Ballistics Laboratory reports and are to be considered typical of these engines. For purposes of the analysis, the engine was considered to be in a fully loaded condition. Although the final orbit payload weight resulting was not the optimum that could be achieved with the ABL-248 engine, the weight of 379.4 pounds provides an indication of the engine's capability.

Table A-3 illustrates weight and balance status at various times in the trajectory. The table shows that the roll-to-pitch moment of inertia at payload separation from the booster does not meet the design objective of 1.2. At apogee motor burnout, however, this value approximates the desired design objective. In the final orbit condition, after expulsion of the control system liquids, the ratio again is unacceptable.

Several methods can be employed to relieve these deficiencies. First, the amount of propellant could be reduced (which was not considered in this study, in which a fully loaded condition was used). Second, the engine could be moved aft of the location shown in Figure A-1. Third, the internal equipment could be rearranged to place more weight closer to the outer diameter.

In the post-apogee motor burnout and final orbit conditions, it is quite possible to achieve higher roll-to-pitch moment of inertia ratios. However, the condition at separation from the booster appears difficult to improve adequately.

TABLE A-1. WEIGHT BREAKDOWN OF SCALED-DOWN SYNCOM II

Item	Weight, pounds
Electronics	91.70
Wire Harness	10.00
Power Supply	94.60
Control System	19.40
Apogee Motor	42.60
Apogee Motor Hardware	1.00
Structure	105.10
Miscellaneous and Balance	15.00

TABLE A-2. RATIO OF SUBSYSTEM WEIGHTS TO FINAL ORBIT WEIGHT AND TO SEPARATION WEIGHT

Subsystem	Subsystem Weight to Final Orbit Condition Weight	Subsystem Weight to Total Payload at Separation Weight
Electronics	0.242	0.100
Wire harness	0.026	0.011
Power supply	0.249	0.103
Controls	0.051	0.021
Propulsion	0.115	0.114
Structure	0.277	0.114
Miscellaneous and balance	0.040	0.016

TABLE A-3. WEIGHT AND BALANCE STATUS FOR TWO POINTS IN TRAJECTORY

	Weight, pounds	Z-Z	I_{z-z}	I_{x-x}	R/P
Final orbit condition	379.40	22.00	35.09	36.75	0.95
N_2 pressurization	1.60				
N_2H_3-CH_3 fuel	27.80				
N_2O_4 oxidizer	46.20				
Total at apogee burnout	455.00	22.00	42.12	37.95	1.11
Apogee motor propellant plus inerts	464.40				
Payload at separation from booster	919.40	30.08	45.77	65.97	0.69

Layout of Syncom II ABL-248 Configuration

Figure A-1 illustrates a possible layout of the ABL-248 engine within a modified Syncom II vehicle. Some of the significant changes in the Syncom II were:

1) Reduction of the number of electronic quadrants from four to two.
2) Reduction of control system tanks from eight to four.
3) Scaling down of the structural subsystem.

As shown in Table A-3, this configuration has an unsatisfactory roll-to-pitch moment of inertia.

The alternate spacecraft structure utilizing the ABL-248 apogee motor consists of a conical aluminum thrust tube built up from sheet metal and machined parts. A machined ring provides the interface for the Atlas-Agena. Another machined ring mates with the ring on the ABL-248 apogee motor at the nozzle end and is fastened to the motor by means of a Marman clamp. The two rings are riveted to a cone-shaped tube of sheet metal with eight exterior tee stiffeners running fore and aft. These stiffeners provide the surfaces to which the control jet fuel tank mounting panels and quadrant electronic package mounting panels are riveted. The mounting panels are machined from magnesium plate with integral stiffening ribs and provide surfaces for mounting four control jet fuel tanks, two quadrant electronic packages, and four storage battery packages. The aft end of the apogee motor is attached to a spider-like stiffener machined from magnesium and riveted to the thrust-tube assembly.

Both the bulkhead and outer ring are fabricated from sheet magnesium employing lightening holes and beads for added stiffness. Aluminum sheet metal channels separate the mounting panels at their aftmost outer edges. The connection between the bulkhead and mounting panels is made by a magnesium tee riveted to the bulkhead and bolted to the mounting panels.

The individual truss work towers supporting the four sun sensors, single orientation jet, and four telemetry and command whip antennas are fabricated from round aluminum tubing and sheet metal gussets welded in place and attached as separate units to the bulkhead by bolts. The 16 solar cell panels are fabricated and mounted in a manner similar to that of the current solid apogee motor configuration, providing center mounting. The two quadrant electronic packages are attached to mounting panels 180 degrees apart. Each package is split and mounted on both sides of the panel. Mounting of the control jet fuel tanks and the single velocity jet is similar to that of the current configuration. Four of the six tank mounting panels are also used for mounting four storage battery packages, four traveling-wave tubes, and four dc converters. Two mounting panels each carry a telemetry transmitter.

Recommendations

The Hughes study of an ABL-248 engine for apogee boost indicated it to be unsatisfactory for the particular design parameters. Its roll-to-pitch moment of inertia did not meet Syncom design objectives. Some variation in the design could increase this ratio; the large pitch-to-roll ratio of the loaded motor itself, however, would be extremely difficult to overcome.

LIQUID APOGEE MOTOR STUDY

Use of a liquid bipropellant apogee injection rocket instead of a solid propellant motor was considered. The structural approaches, equipment complement, and ascent sequence were to remain relatively unchanged.

Two basic tankage and structural configurations were given primary consideration. The first had four spherical tanks for fuel and oxidizer, with small spherical pressurizing bottles. The second had three toroidal tanks — one each for fuel, oxidizer, and pressurization. The study was based on the following apogee motor requirements:

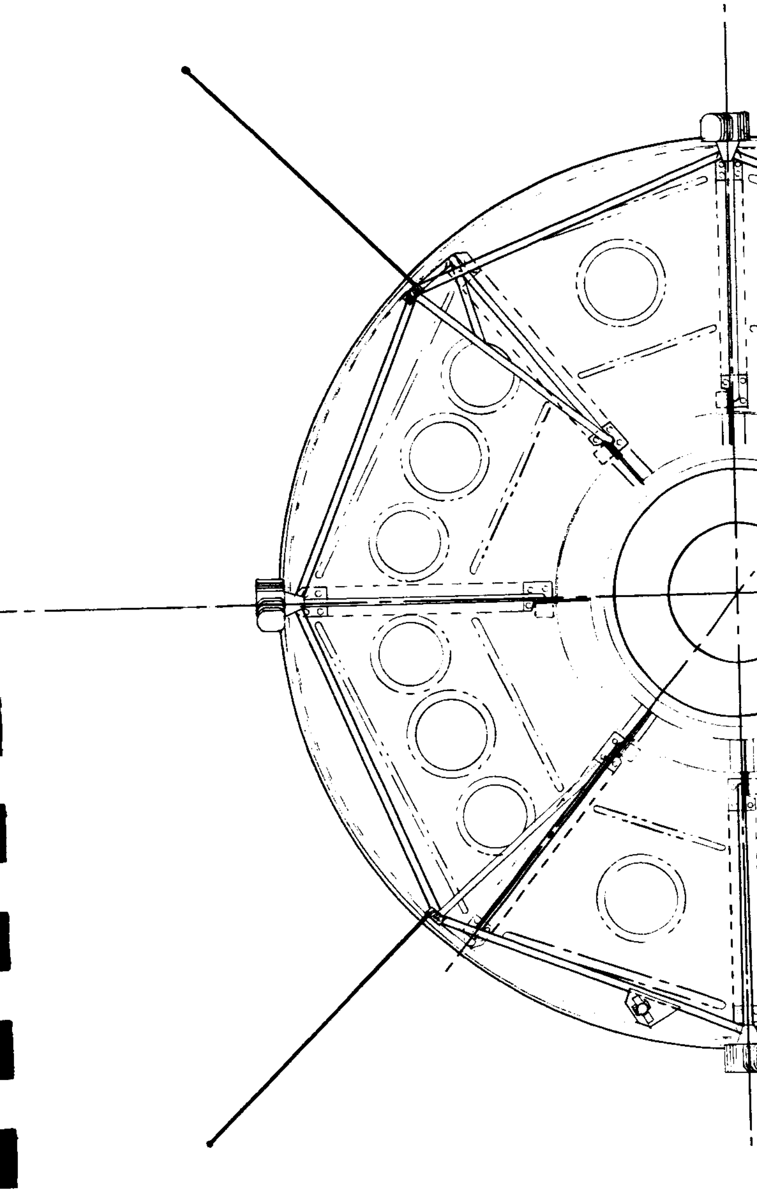

FIGURE A-1. ABL-2

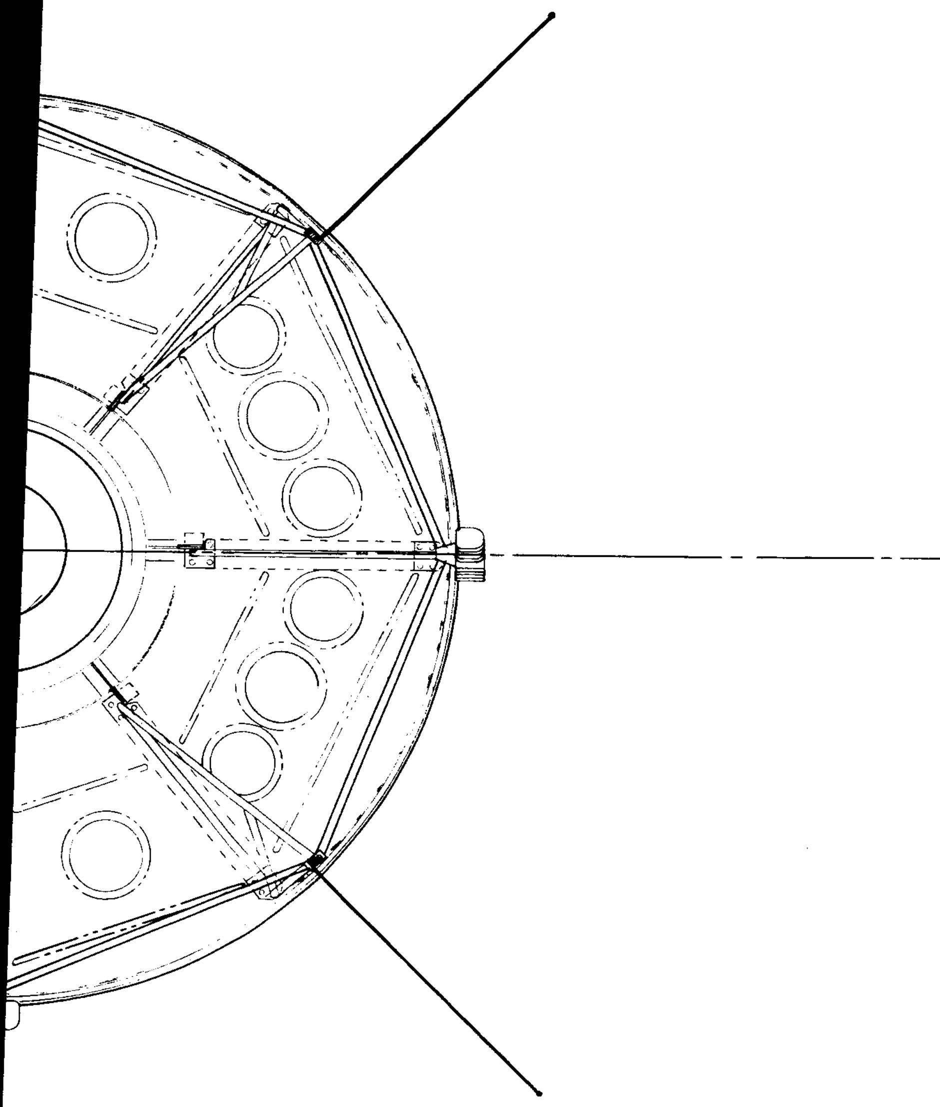

48 ENGINE LAYOUT

2

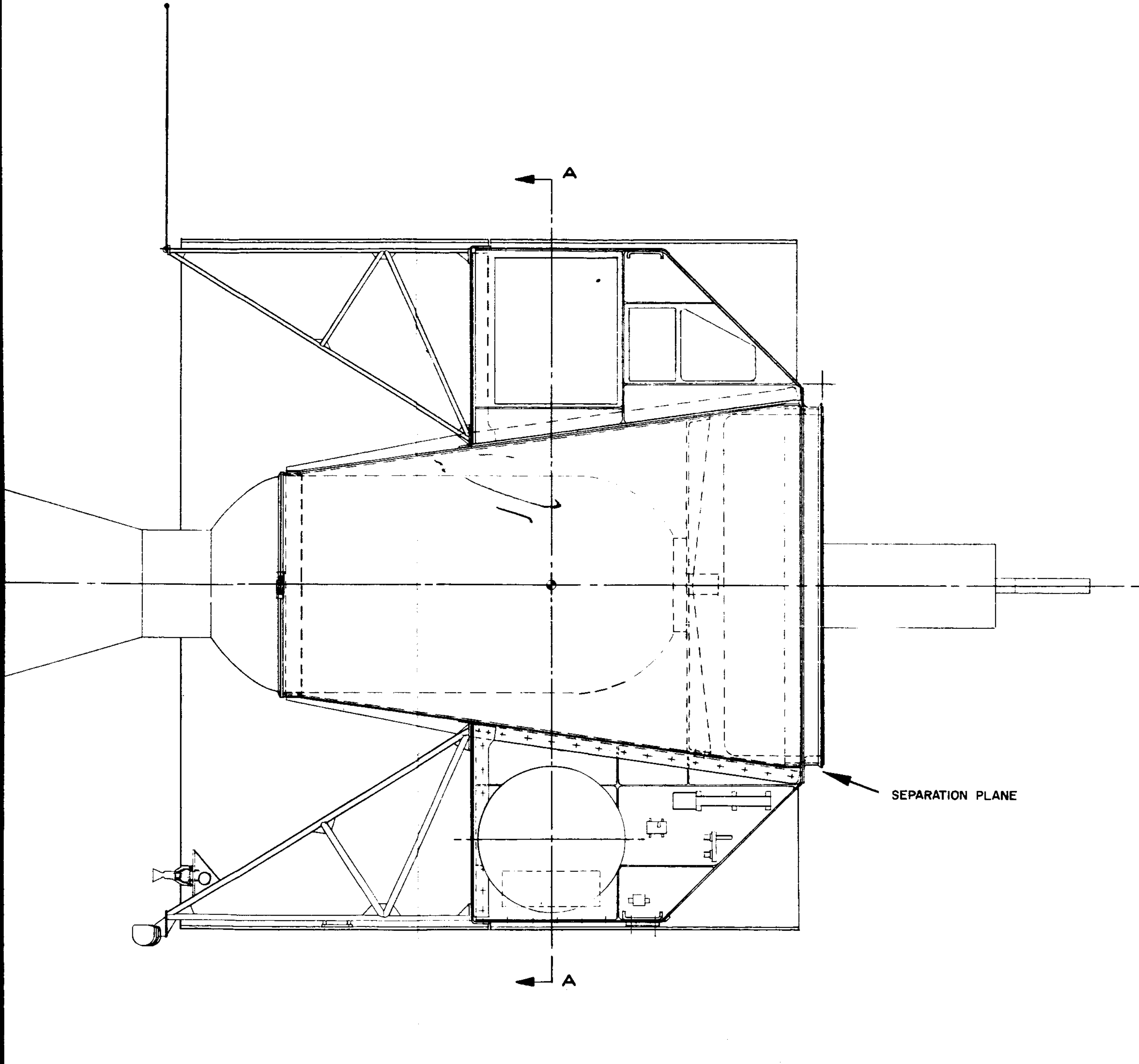

3

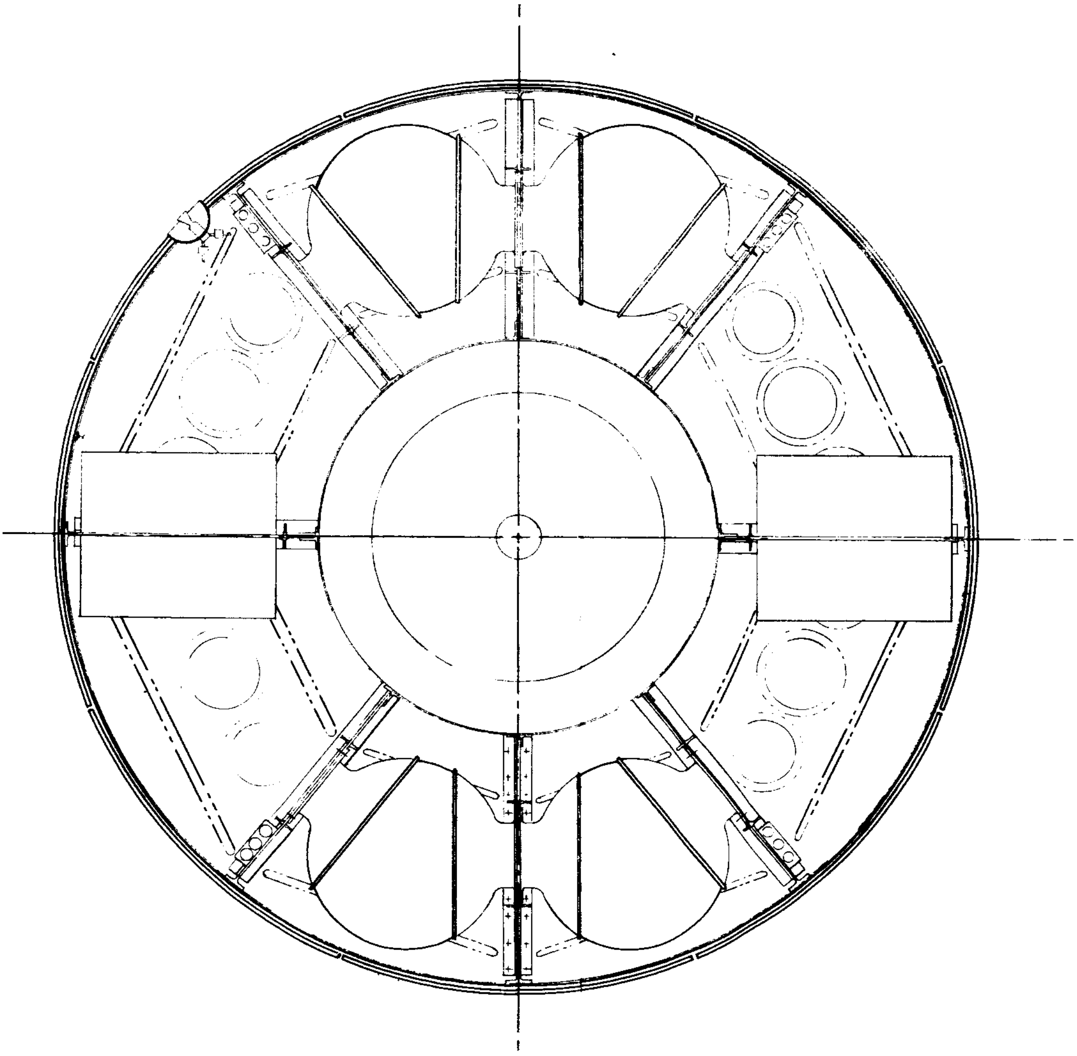

A–A

1) $\Delta V = 6075$ fps (nominal) + 25 fps (foreshortening due to misalignment) = 6100 fps
2) Spacecraft payload weight = 650 pounds
3) Injected weight $\leq$ 1518 pounds (i.e., motor assembly $\leq$ 868 pounds)
4) Vacuum exposure for a period of up to 24 hours must not adversely affect ignition or motor characteristics.
5) Engine assembly must be compatible with vehicle spin of 100 ± 50 rpm and remain operative, within tolerance.
6) Engine assembly must be capable of withstanding the dynamic environment provided by the Advanced Syncom spacecraft during the Atlas-Agena D launch.
7) Maximum case external temperature (portions within spacecraft) = 250° F.
8) Motor, tankage and ancillary equipment must be mountable in the spin-stabilized Advanced Syncom spacecraft with a resultant ratio of moments of inertia $I_R/I_P \geq 1.20$
9) The thrust-time curve should not exhibit any large transients.
10) Propellants used in the bipropellant rocket reaction control system should be employed.
11) System design should permit common tankage to be shared between a unit of the reaction control system and the apogee injection engine, if possible.
12) The engine assembly should permit variable propellant loading to accommodate variations in payload weight up to the maximum of 650 pounds.
13) The requirements should be achieved by an existing or current development engine to minimize the developmental cost and time for adaptation to the Advanced Syncom mission.

System Analysis

A simplified system analysis was performed to determine the suitability of potential engine thrust chamber assemblies and tankage configurations for the Advanced Syncom. System requirements were defined in accordance with the launch vehicle capabilities and mission parameters discussed in References A-1 and A-2. The velocity increment equation

$$\Delta V = g_c \, I_s \ln \left(\frac{M_{T_O}}{M_{B_O}} \right) \text{[fps]}$$

was employed using the following values:

$\Delta V = 6075$ fps (nominal requirement)
+25 fps (required to correct for foreshortening due to misalignment)
= 6100 fps

$g_c = 32.2$ fps (gravitational constant)

$I_s = 305 \frac{lb_{f-sec}}{lb_m}$ (average vacuum I_{sp} per hardware survey)

$M_{T_O} = 1518\ lb_m$ (maximum injected weight per Reference A-1)

$$6100 = 32.2 \times 305 \ln \left(\frac{1518}{M_{B_O}} \right)$$

$$\ln \left(\frac{lb_{f\text{-}sec}}{lb_m} \right) = 0.622$$

$M_{B_O} = \frac{1518}{1.86} = 816\ lb_m$ (maximum burn-out weight)

$W_{P_b} \leq 1518 - 816 = 702\ lb_m$ (maximum weight available for propellants burned)

$W_{P_o} = W_{P_b} + 2$ percent (residual) + 1 percent (mixture ratio mismatch due to calibration tolerances)

$= 1.03\ W_{P_b}$ (total fuel loaded)

$= 723\ lb_m$ (702 lb burned + 21 pounds from contingencies)

Dry weight: engine and tankage assembly = 816 — 650 — 21

$= 145\ lb_m$

$I_T = I_s\, W_{P_b}\ [lb_{f\text{-}sec}]$

$= 305 \times 702$

$= 214{,}110\ lb_{f\text{-}sec}$ total impulse

$T_{B_O} = 214{,}110/1750$

$= 122.5$ seconds (burning time for 1750 lb_f engine)

$T_{B_O} = 214{,}100/2200$

$= 97.5$ seconds (burning time for 2200 lb_f engine)

An inherent potential condition with an all-liquid propulsion system is fuel-sloshing in the tanks. A model has been formulated for computer analysis to obtain data regarding the behavior of the spin axis under various conditions.

STEADYSTATE BEHAVIOR

If no moments are applied to the spinning space vehicle containing liquid fuel tanks, the stable equilibrium condition will be one in which the angular momentum H is fixed while the kinetic energy T is minimized. Since a liquid-fueled vehicle is a highly dissipative system, this equilibrium should be achieved rapidly.

It can be shown that if z is the nominal spin axis and

$$|H|^2 = I_z^2W_z^2 + I_y^2W_y^2 + I_x^2W_x^2 = C^2, I_z > I_y \geq I_x$$

while in addition

$$T = \tfrac{1}{2}(I_zW_z^2 + I_yW_y^2 + I_xW_x^2) = \text{minimum}$$

then the solution is one in which

$$W_z = C/I_z \text{ and } W_y = W_x = 0$$

Furthermore, if I_z is varied, minimum energy occurs for maximum I_z. In the case of a toroidal tank, maximum I_z occurs when the fuel is uniformly distributed. Similarly if two (or more) fuel tanks are symmetrically placed about the spin axis, maximum I_z corresponds to equal distribution of fuel (assuming a cross-feed system exists). As a matter of interest, toroidal tanks have been successfully used as nutation dampers.

DYNAMIC BALANCE

Under conditions of eccentric thrust (during third-stage boost) the fuel mass in each tank (for symmetrically spaced tanks) is approximated by a rigid body hinged at a radius r_1 from the spin axis and located a distance ℓ from the hinge. The moment of inertia of this fuel mass about the spin axis is then treated as if the fuel mass were located a distance $\sqrt{r_1 (r_1 + \ell)}$ from the spin axis. The equilibrium position of this hinged mass under the influence of the combined spin and thrust loads is being analytically examined for destabilizing coupling effects. Preliminary results indicate no destabilizing effects for tanks symmetrically spaced about the spin axis. This approach will be extended to include the toroidal tank configuration and may also be modified to account for higher order mode coupling by adding extra hinges in the analysis if necessary.

SYSTEM CONSIDERATIONS

One consideration in comparing a liquid to a solid engine is the manner in which the impulse is metered and its effect on overall system performance. With the solid engine of Syncom II, the apogee velocity increment is applied by allowing the engine to burn itself out. With an all-liquid system sharing tankage with the reaction control system, this technique would not be applicable. Some method of metering the thrust must be considered which is simple and reliable and will provide satisfactory system performance.

One of the simplest methods is to use a timer. Here the engine is ignited and will burn for a specified time period predetermined by the thrust-time characteristics of the engine and the thrust required to achieve final orbit. Another system is to use an accelerometer aligned along the spin axis to meter the thrust in the same manner as an accelerometer is employed in the Agena D system. If the Agena velocity meter is taken as typical, it is found that the weight breakdown is:

Accelerometer	5 pounds
Accelerometer electronics	3 pounds
Accelerometer readout counter	3 pounds
	11 pounds

Although such an accelerometer system would provide better thrust metering than that achievable with only a timer, the accelerometer system might be heavier. A specific comparison would be a calculation of the propellant required to obviate the final orbit errors caused by a simple timer system.

Referring to Reference A-1, it is found that the root sum squared errors due to Atlas and Agena D systems are as follows:

	Eccentricity	Period, minutes	Inclination, degree	Drift, deg/day
Atlas	0.0025	5.735	0.1392	1.444
Agena D	0.0114	24.358	0.4540	5.929

To calculate the errors due to the third-stage liquid system, it is assumed that the impulse variation is about 3 percent (3σ), which is a conservative estimate of this error for a liquid engine with timer metering for thrust cutoff. An error of only 1.5 percent would be expected in a carefully controlled solid motor or with a velocity metered liquid motor. Consequently, assuming other errors are the same, a comparison is possible, as shown in Table A-4.

To compare the two systems, it is useful to convert the RSS values into the velocity corrections required. The total velocity corrections required are 255.9 fps for an engine system with 1.5 percent impulse variations versus 389.7 fps for an engine system with 3.0 percent impulse variation.

The amount of propellant required to correct these errors can be scaled from the analysis in Reference A-2. The results are as follows:

Impulse	Required, fps	Propellant Required, pounds
1.5 percent variation	255.9	22.1
3.0 percent variation	389.7	33.6

Consequently, in comparing liquid versus solid apogee engines, for the same orbit injection techniques, the results of an error analysis show:

1) Liquid engine with timer requires 11.5 pounds more fuel to adjust the final orbit.
2) Using a liquid engine, with accelerometer, would require approximately the same total system weight, but such utilization might be more complicated.
3) Orbit injection scheme with a liquid engine should be optimized rather than adopt optimum solid motor technique directly.

The storage and environmental temperature limits of the liquid and solid engine are comparable: 0° to 130°F. The at-use temperature limits of the solid motor are undoubtedly narrower, principally because high temperatures would produce a higher thrust and chamber pressure requiring heavier stucture. Thermal control, however, is easier for the solid motor and certainly can be done passively, since it is a dense massive configuration in contrast to the thermally fin-like arrangement of the all-liquid system.

A liquid apogee motor of 2000 pounds thrust will produce accelerations well below 7.5 g. For an efficient solid apogee motor of about 7000 pounds thrust, as contemplated for Syncom II, the maximum static acceleration will be around 12 g. The geometry and flexibility of the boost configuration, however, is such that the vibration loading during boost is expected to be as much as 17 g. Thus a reasonably smooth burning apogee motor combined with the greatly more rigid apogee kick configuration will ensure that the loads encountered during Atlas/Agena boost will remain the critical design loads for either the liquid or solid apogee motor.

The restart capability of a liquid does not appear of great value for the basic Advanced Syncom mission. The expected correction necessary after apogee kick is

TABLE A-4. THIRD-STAGE ERROR ANALYSIS

Source	3σ Value	Eccentricity	Period, minutes	Inclination, degrees	Drift, deg/day
Thrust misalignment	1.25 deg	0.11	4.3	0.2302	6.97
Velocity loss due to spin	6 fps	0.0014	3.01	0.0128	0.75
Total impulse	3 percent (1.5 percent)	0.0334 (0.0167)	77.82 (38.91)	0.3324 (0.1662)	19.50 (9.75)
RSS error		0.0352 (0.0201)	81.60 (45.98)	0.4046 (0.2843)	20.72 (12.01)
Total RSS error (including Atlas/Agena errors)		0.0487 (0.0332)	85.35 (52.34)	0.6238 (0.5534)	22.11 (13.49)
Velocity correction required, fps		82.4 (39.3)	194.6 (119.3)	112.7 (97.3)	201.8 (123.1)

of small enough magnitude to be performed by the low thrust vernier correction system.

Another factor for consideration is the complexity of a liquid system, particularly the complexity of the valves and pressure regulation system.

Engine Survey

Technical discussions were held with four rocket engine companies which either have an engine under development or are in the advanced stages of design. Information was received from Bell Aerosystems, Rocketdyne, Aerojet-General, and the Marquardt Corporation.

Table A-5 summarizes the engines discussed. The configuration studies were conducted to permit accommodating any of the candidate engines.

The thrust chamber assembly proposed by Aerojet has been under development since May 1962 for an Air Force program which was recently cancelled. However, prior to cancellation, engine design feasibility was demonstrated.

The Rocketdyne P-4 drone engine is a low-thrust engine with relatively poor performance parameters.

The thrust chamber proposed by Marquardt is the 1750-pound engine under development as the ullage rocket for the Douglas/NASA S-IV-B booster.

The thrust chamber proposed by Bell and the alternate design proposed by Rocketdyne are currently in the paper design stage and were not considered competitive with the Marquardt or Aerojet engines in development time, cost, or risk.

Configuration Studies

Hughes considered several structural designs using a liquid engine in conjunction with the basic Syncom II structural design approaches with suitable modifications to the attitude control tankage, thrust tube assembly, and general arrangement of electronics.

A structure using spherical tanks was designed to house the combined liquid apogee engine and one unit of the reaction control system (Figure A-2). This structure consists of a cone-shaped thrust tube made

TABLE A-5. CANDIDATE THRUST CHAMBERS FOR ADVANCED SYNCOM APOGEE ENGINE

Parameter	Marquardt MA 118-XAA	Aerojet	Bell	Rocketdyne	
				P-4 Drone	1000-pound
Vacuum thrust, pounds	1750	2200	1750	665	1000
Vacuum specific impulse, second	300 at 30:1	304	307	279	308
Propellant weight for $\Delta V = 6100$ fps at vehicle weight of 1518 pounds	702	698	694	740	692
Thrust chamber assembly weight, pounds	65.5	66.0	58.0	22.3	17.7
Chamber pressure, psia	150	100	150	200	150
Mixture ratio (O/F)	1.62	2.0	1.62	3.0	2.18
Design thrust time, second	260	335	310	Unspecified	213
Advanced Syncom thrust time, second	122.5	97.5	122.5	311	213
Fuel	50 percent N_2H_4 50 percent UDMH	50 percent N_2H_4 50 percent UDMH	50 percent N_2H_4 50 percent UDMH	HYDYNE	MMH
Oxidizer	N_2O_4	N_2O_4	N_2O_4	IRFNA	N_2O_4
Ignition	Hypergolic	Hypergolic	Hypergolic	Hypergolic	Hypergolic
Engine cooling mechanism	Ablative nozzle, radiation extension	Ablative nozzle, radiation extension	Ablative nozzle, radiation extension	Regenerative nozzle, radiation extension	Ablative nozzle, radiation extension
Comments	Under contract for development DAC/NASA for S-IV B ullage rocket	Feasibility demonstrated; under development for USAF since May 1962; recently cancelled	Paper design for S-IV B competition; Bell has 1 year ablative firing experience	Old thrust chamber design; low performance	Paper design only

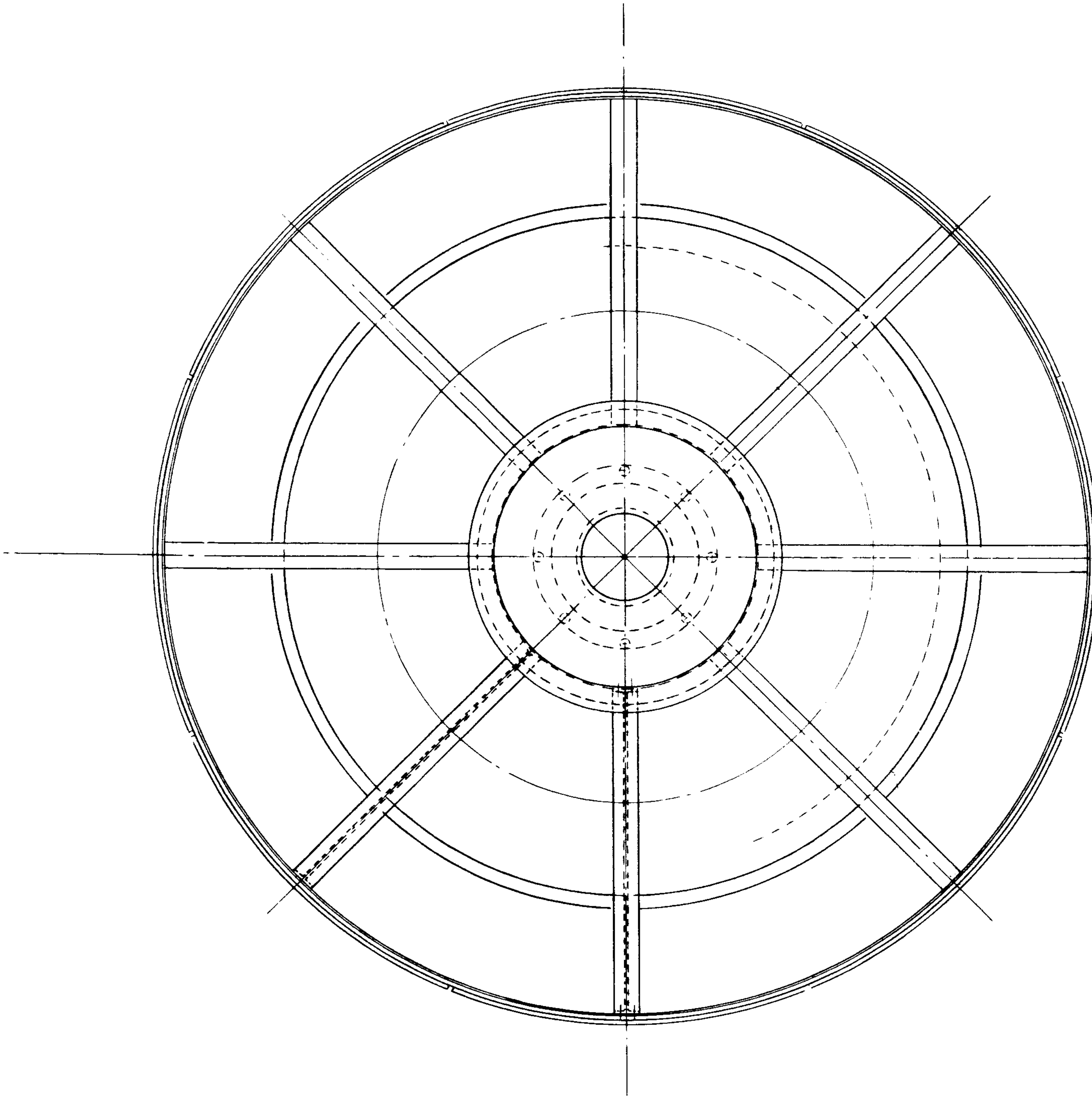

FIGURE A-2. ALTERNATE CONFIGURATION LIQUID APOGEE MOTOR

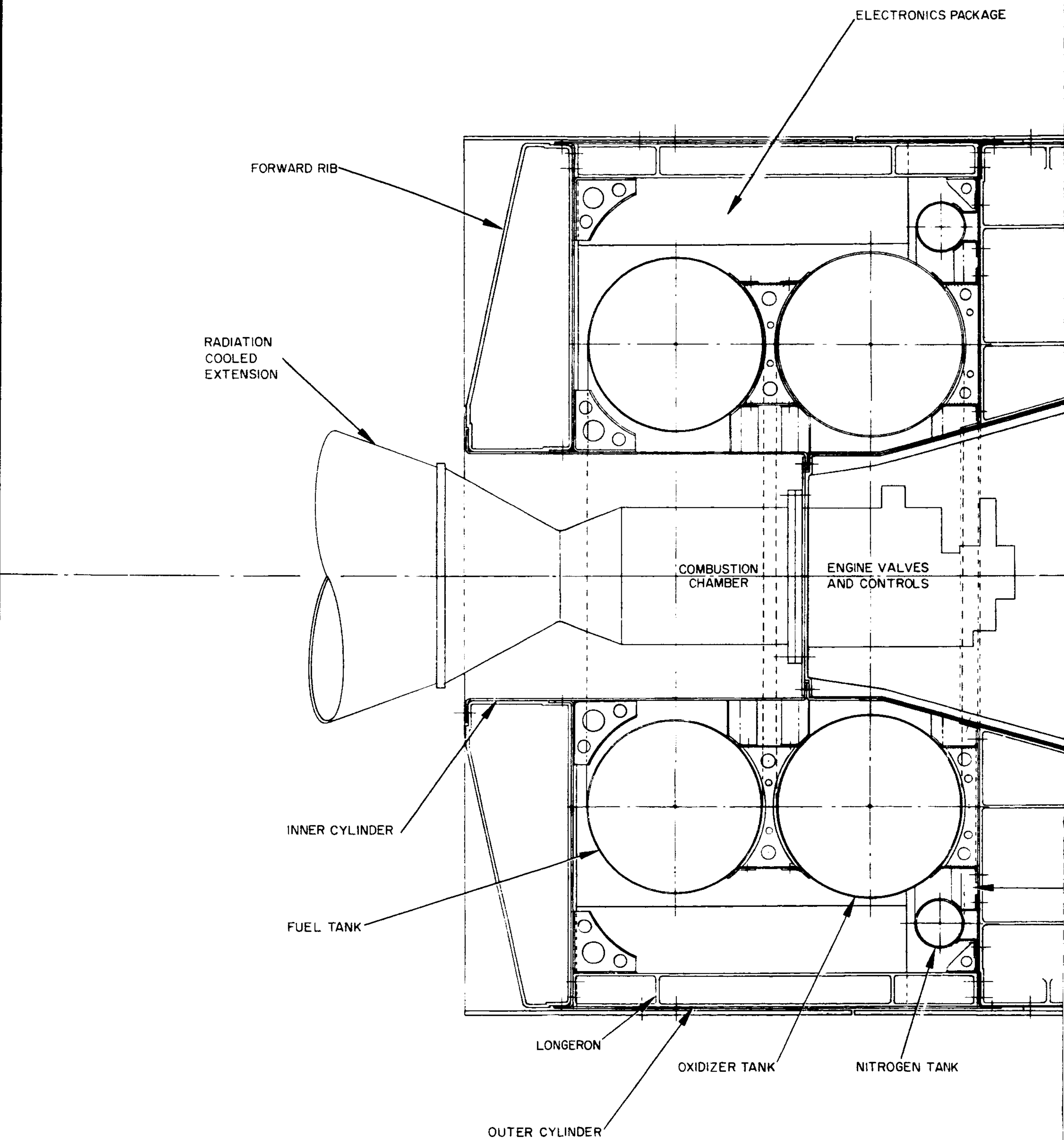
ELECTRONICS PACKAGE
FORWARD RIB
RADIATION
COOLED
EXTENSION
COMBUSTION
CHAMBER
ENGINE VALVES
AND CONTROLS
INNER CYLINDER
FUEL TANK
LONGERON
OXIDIZER TANK
NITROGEN TANK
OUTER CYLINDER

2

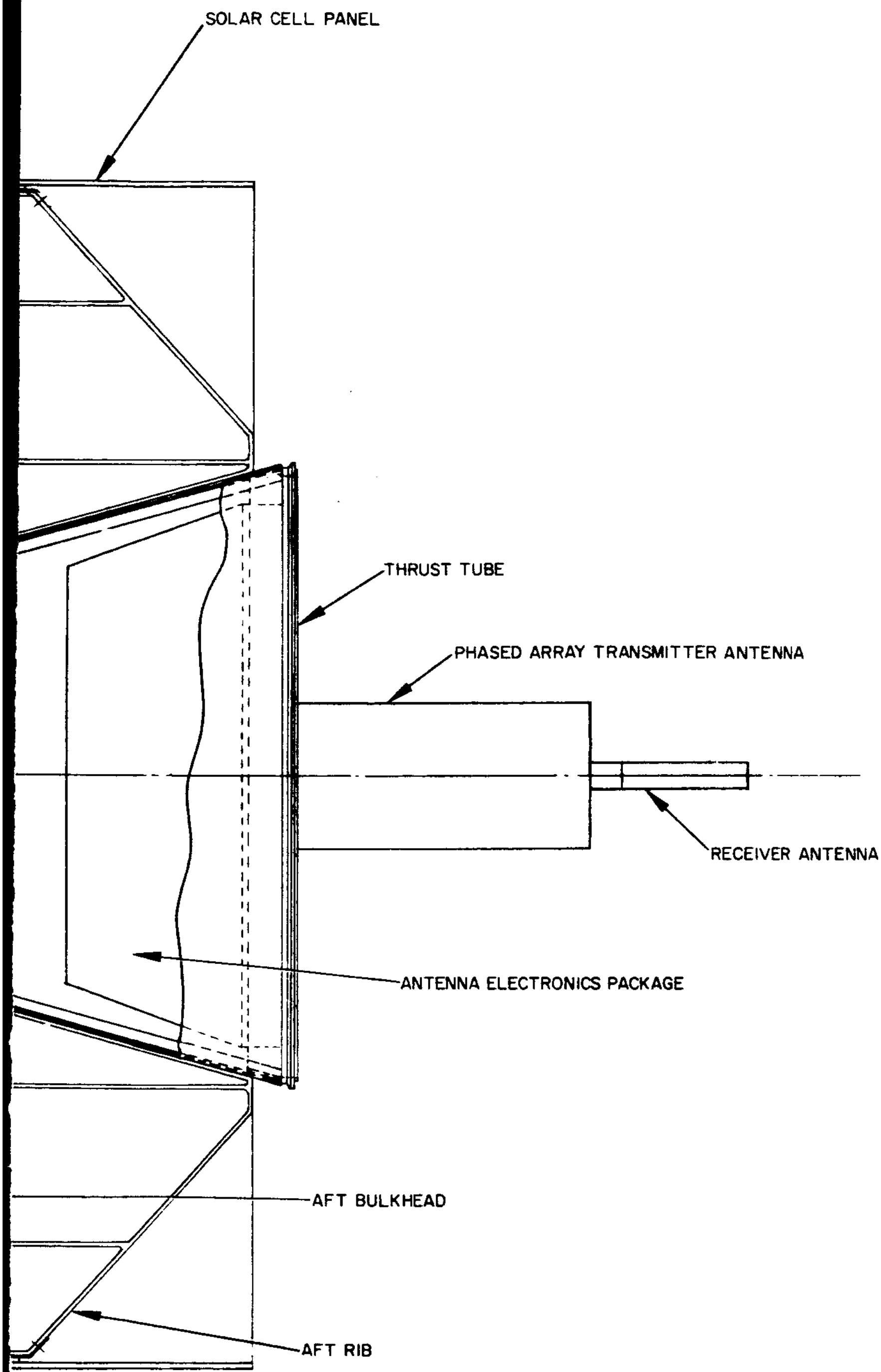
SOLAR CELL PANEL
THRUST TUBE
PHASED ARRAY TRANSMITTER ANTENNA
RECEIVER ANTENNA
ANTENNA ELECTRONICS PACKAGE
AFT BULKHEAD
AFT RIB

3

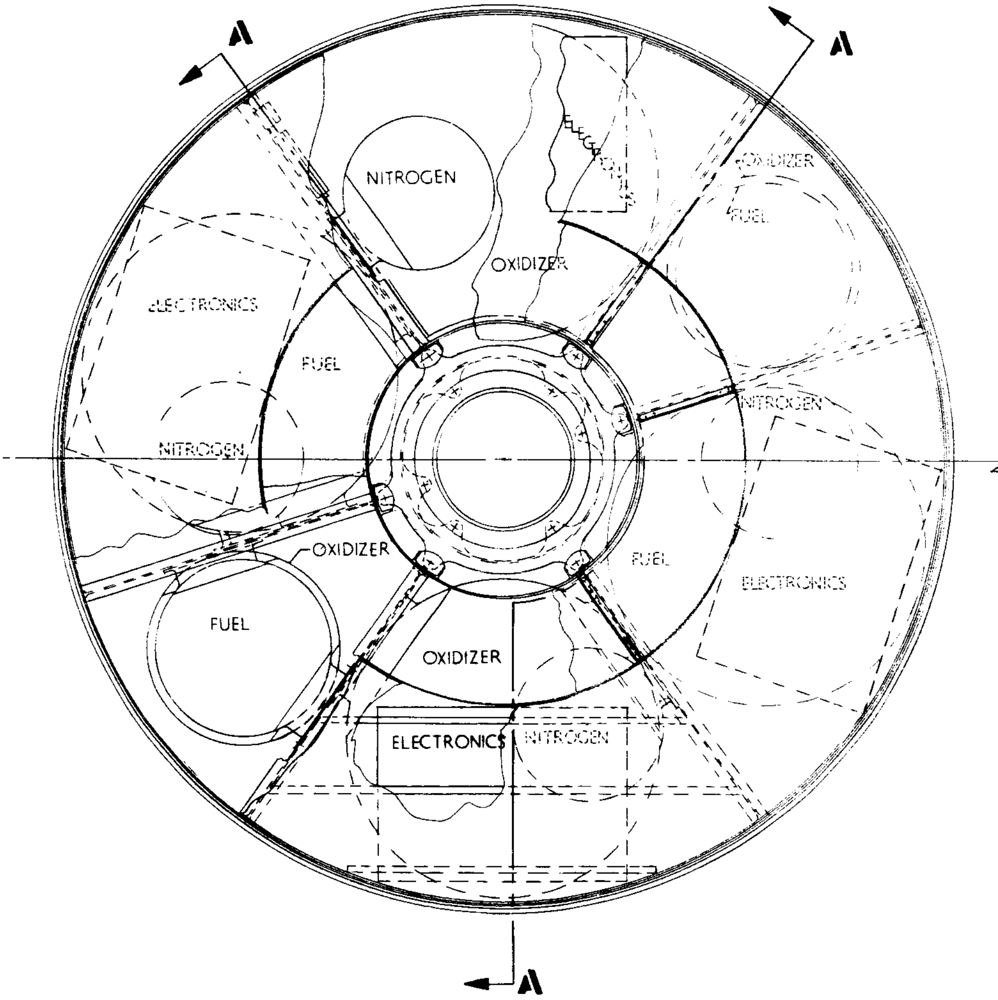

FIGURE A-3. COMB

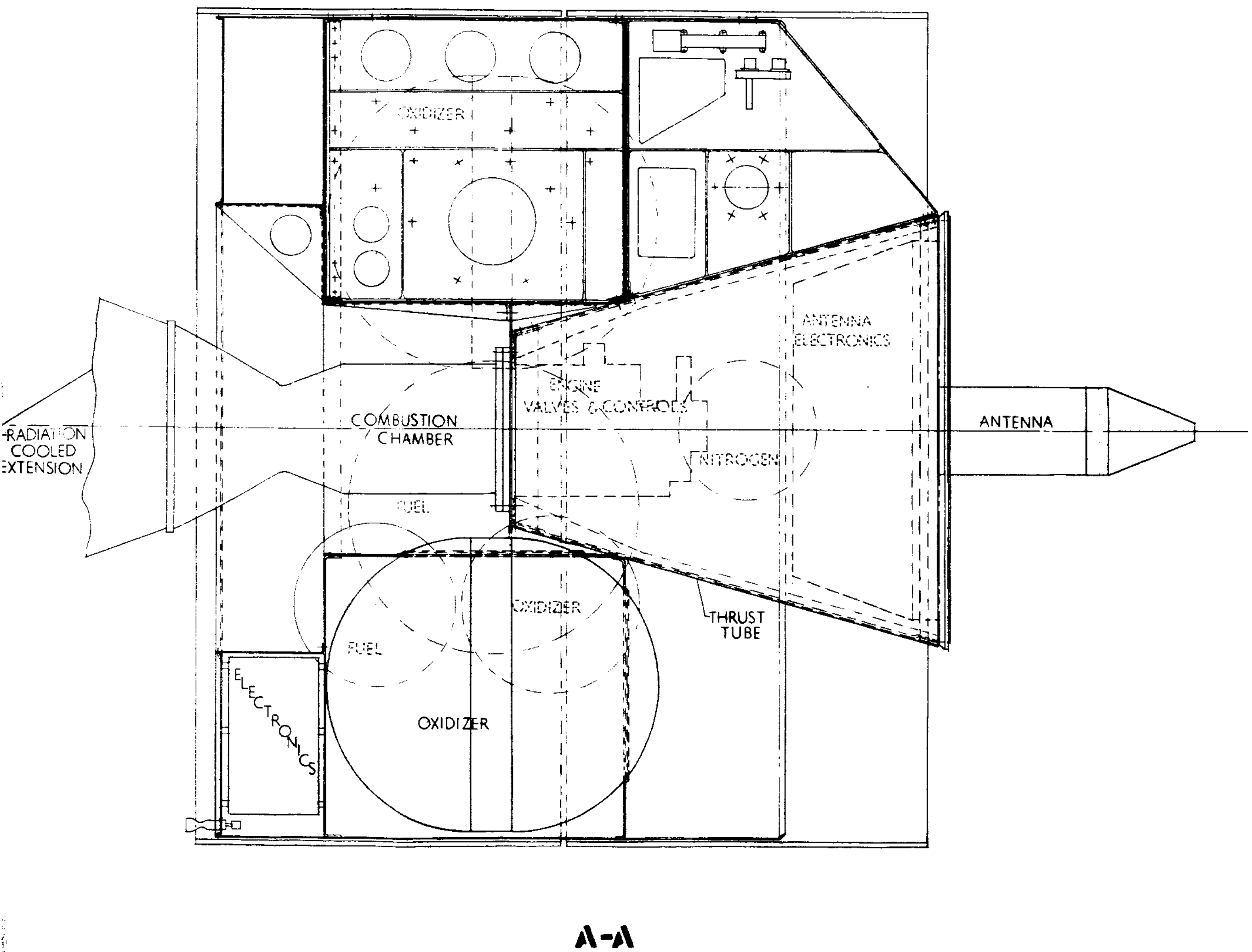

NED LIQUID APOGEE ENGINE AND CONTROL SYSTEM up of aluminum sheet and aluminum-machined rings and stringers, machined aluminum ribs and tank mounting panels, and magnesium bulkheads and rings. The design retains the same solar panels, vernier control jets, and sun sensors as the Syncom II configuration using a solid spherical apogee injection motor.

The tankage consists of four large tanks (two for fuel and two for oxidizer), four nitrogen tanks for the combined apogee motor and one unit of vernier control, and an independent redundant control system unit for stationkeeping control consisting of two oxidizer and two fuel tanks. This configuration presented balance problems and did not meet the ratio of moments of inertia I_R/I_P criteria. Therefore, a layout for a configuration using toroidal tanks was considered (Figure A-3).

The tankage consists of three toroidal tanks (fuel, oxidizer, and nitrogen) for the combined requirements of the apogee motor and redundant vernier control systems. The structure separates into a forward and an aft subassembly. The aft subassembly consists of a cone-shaped thrust tube of aluminum sheet, aluminum machined rings, and eight aluminum stiffeners riveted inside the cone. A flat magnesium sheet (aft bulkhead) is supported by eight radial magnesium aft ribs attached at the periphery of the thrust tube. These ribs carry the weight of the three toroidal tanks and electronic packages. The forward subassembly consists of the inner magnesium ring, forward magnesium bulkhead, and eight magnesium forward ribs. The forward bulkhead is supported by eight radial ribs attached at the periphery of the inner cylinder. The outer cylinder is segmented into eight parts and attached to the aft ribs, longerons, and forward ribs. The segmented cylinder and the eight longerons are removable to provide access to the electronic packages.

One concentric pair of rings is welded to the oxidizer tank and another pair to the nitrogen tank. These rings are attached to the aft bulkhead and aft ribs. The fuel tank is cantilevered from the forward end of the oxidizer tank in a similar pair of rings. The design retains the same solar panels, vernier control jets, and sun sensors as the configuration using a solid-propellant apogee injection motor.

A weight and balance analysis was performed on a configuration using toroidal tanks and the Aerojet engine (worst case). The weights used were those typical of the Syncom II configuration; weight information on the engine was supplied by Aerojet-General Corporation.

The weight breakdown in shown in Table A-6. Table A-7 shows the weight and balance status of this configuration at three points in the trajectory. These numbers may be compared with those for a configuration using the solid apogee engine as reported in Reference A-3. Such a comparison shows that a configuration using a liquid engine is feasible from the weight and balance standpoint.

TABLE A-6. WEIGHT SUMMARY FOR TOROIDAL TANKS

Item	Weight, pounds
Electronics	130.0
Wire harness	20.0
Power supply	119.8
Nitrogen tank	39.0
Oxidizer tank	22.9
Fuel tank	22.9
Pressure regulation	13.0
Miscellaneous controls	13.0
Engine assembly and installation	95.1
Structure	105.6
Miscellaneous hardware, paint, and dynamic balance	20.0
Nitrogen gas residual	18.7
Propellant residual	21.0
Final orbit condition	639.0
Reaction control system fuel	50.0
Reaction control system oxidizer	100.0
Total at apogee burnout	789.0
Apogee fuel	233.0
Apogee oxidizer	465.0
Nitrogen pressurant	31.0
Total injected weight	1518.0

TABLE A-7. WEIGHT AND BALANCE STATUS

Condition	Weight, pounds	Z-Z	I_{zz}	I_{yy}	I_R/I_P
Final orbit condition	639	29.0	52.7	47.8	1.1
Apogee burnout condition	789	29.4	67.0	56.0	1.2
Payload at separation from Agena	1518	30.7	124.0	92.3	1.34

Conclusions

The studies conducted show the feasibility of employing a liquid bipropellant rocket for apogee injection of an Advanced Syncom spacecraft. Tankage arrangements can be devised to permit stable spacecraft configurations, and current developmental engines can be adapted to the application.

The studies to date have concentrated on the simple "alternate" case for accomplishing the basic Syncom orbital injection sequence — that is, considerations of only the comparative merits of liquid or solid propellant rockets for providing the same increment of velocity necessary to circularize the transfer ellipse and remove the inclination of the transfer ellipse. Based on these studies, the solid propellant motor affords a more attractive overall design in simplicity, schedule, and estimated cost for the Syncom II spacecraft. However, additional study should be made of alternate injection schemes, orbiting processes, and spacecraft configurations to increase the synchronous orbit payload weight for an optimized system over that available with the currently planned system.

References

A-1. "Syncom Booster Feasibility Final Report," Lockheed Aircraft Company Report LMSC A057612, 30 September 1962.

A-2. "Initial Project Development Plan, Volume I," Hughes Aircraft Company Report SSD 2380R, August 1962.

A-3. "Monthly Progress Report, Advanced Syncom," Hughes Aircraft Company Report SSD 2537R, October 1962.

APPENDIX B

PRELIMINARY STUDY OF RADIATION INSTRUMENTATION PAYLOAD FOR SYNCOM II

Introduction and Purpose of Measurements

Since a synchronous orbit satellite has a higher altitude (22,300 miles) than those of present-day satellites (except for brief intervals near aphelion), it offers unique advantages for performing high-altitude space physics measurements. First, it provides an excellent platform for long-term studies of the damage of solar radiation and micrometeorites to solar cells and other semiconductor components. Second, its altitude is excellent for studying the transition to the magnetopause and the nature of the outer Van Allen region, including solar particle injection phenomena and the nature of the auroral zone funnel. Third, the satellite will be stabilized in essentially one position for several years, permitting continuous observations of diurnal, solar rotation cycle, and sunspot cycle variations, in which spatial fluctuations can be separated from the temporal.

This section presents the results of a preliminary examination by the Hughes Research Laboratories of what experiments might be performed, the major obstacles apparent, and a tentative payload configuration.

Many properties of space might, of course, be considered. With a limited payload weight, only a limited experiment can be undertaken. The most urgent area at the present which is ideally suited for a Syncom measurement is that of the effects and nature of the particle flux and magnetic field in space.

The highest priority measurement would appear to be the study of radiation effects, both surface and bulk, on semiconductor devices. At synchronous altitude, the radiation flux is enough to cause significant effects only during solar flares. The expected life span of Syncom II will fall on or near the sunspot minimum. For a Fall 1964 launch and a lifetime of 3 to 4 years, only the last year should see any important rise in solar flare disturbances. Therefore, although radiation effects instrumentation is suggested for inclusion, this limitation on its usefulness must be carefully weighed before a final decision is reached.

There is considerable interest in the dynamics of the outer radiation region and especially in its connection to the solar "exosphere." One might study the trapped radiation, protons and electrons; the solar plasma, also composed principally of protons and electrons; and finally, solar-flares protons, or "cosmic rays." The last phenomenon is also limited by relative solar flare inactivity during the sunspot minimum but these events, although rare, do occur and the data from even a few will yield valuable information on solar-earth interaction dynamics (as contrasted to an integrated "total degradation" radiation damage measurement). The objective would be to measure both omnidirectional and directional spectra for both electrons and protons in several energy ranges. A more complete description is given in Particle Detector Payload below.

Only a program that included directional and energy spectra would be worthwhile, since existing and soon forthcoming data should be fairly adequate on total flux. In order to measure the directional spectra of the trapped radiation, the B-field must be known, especially its direction with respect to the detector. In this respect, Syncom II, primarily a communication satellite as contrasted to a measurement satellite, is not ideal. Various time-varying magnetic fields may be expected, both those at frequencies corresponding to satellite rotation (solar cell illumination effects) and those due to various cross-over and leakage phenomena from the RF components. The local magnetic field produced by the satellite must be sensed and compensated. The obvious approach, a magnetometer on a boom, is not feasible for Syncom because of antenna pattern distortion and mass imbalance effects. A promising, but more difficult, approach is discussed in Magnetic Field Measurement, below. In any event, the electromagnetic environment of the satellite must be more accurately known before a final conclusion on the feasibility of field measurement can be made.

Damage caused by micrometeorites has largely been ignored in considerations of space environment problems. This is due partly to a lack of knowledge about the effects, if any, of micrometeorite impingement. The Syncom II spacecraft offers a convenient platform for long-term measurements that will yield information on this phenomenon. The section on particle detector payload below describes the instrumentation for making these measurements.

It is therefore suggested that valuable experiments, both for radiation effects on materials and for geophysical study, can be designed utilizing the unique synchronous orbit characteristics. The limitation on useful geophysical measurements will be magnetic field determination. A promising, but as yet untested, method of overcoming this difficulty is suggested, and a payload package, including the magnetic field sensor, within the probable weight allowance is given.

Field and Particle Environment

PARTICLE FLUXS IN THE OUTER RADIATION ZONE

By now a sizable body of data has been accumulated concerning the general features and behavior of the outer zone. These data are steadily increasing, and with them our general knowledge of the region. So far, however, increased data has decreased detailed understanding because of the forced abandonment of initial, oversimplified conceptions. The available data have been summarized in several places recently, as well as in a continuing series of papers, especially in *The Journal of Geophysical Research.* A resumé of all this material is unnecessary here since detailed knowledge is not required for this stage of payload design.

Perhaps the best recent survey has been issued by Space Technology Laboratories (Reference B-1). Few data exist, however, for distances of 6.5 earth radii (Re) compared to that for the outer zone maximum from 3 to 6 Re. Electron isointensity contours typical of "normal" outer zone conditions are shown in Figure B-1, taken from Reference B-1. These curves are plotted in geomagnetic coordinates, and the geographic equator differs by about 10 degrees from the geomagnetic equator for the expected Syncom position. A typical electron flux is 10^5 electrons/centimeter^2/sec. Electron isointensities after a severe magnetic storm are changed by more than an order of magnitude from nonstorm conditions, as is illustrated in Figure B-2.

A corresponding isointensity plot for protons of noncosmic ray energies is shown in Figure B-3. A typical value will be $\sim 10^6$ protrons/centimeter^2/sec, including low energy components.

Proton energy spectra are shown in Figure B-4, taken on the magnetic equatorial plane. The curve R_o is closest to Syncom conditions, and shows that practically all protons have energies < 1 mev.

The electron energy spectrum is not known accurately at 6.5 Re. In the heart of the belt it is given by the combined data represented in Figure B-5, also from Reference B-1. It is particularly interesting to measure this spectrum, as the point of observation is right in the middle of the auroral zone "funnel."

The pitch angle distribution for electrons is best given by O'Brien (Reference B-2), and is approximately isotropic in the equatorial plane (Figure B-6).

Changes in solar flare protons and Forbush decreases can easily be observed because of the relative ease of penetration near the geomagnetic equator. Cosmic ray reductions of 20 percent in 15 hours and 8 percent in 3 hours due to solar flares may be expected and would be observable.

MAGNETIC FIELD

From the literature (Reference 3), one would expect about 100 to 150γ ($1\gamma = 10^{-5}$g) intensity at 6.5 Re geographic equator, with the sole temporal anomaly being due to solar activity. The field lines will be very nearly parallel to the satellite spin axis ($\pm$ 20 degrees variation).

Magnetic Field Measurement

To interpret radiation data accumulated by Syncom II it is necessary to monitor the magnitude (approximately 10^{-3}g) and direction of the geomagnetic field. For engineering reasons, it is undesirable to mount the magnetometer sensor on a boom at some distance from the main body of the satellite. Consequently, it becomes necessary to discriminate against magnetic noise generated by the electronic equipment aboard, some of it of considerable power rating. Under such circumstances, the most desirable solution would appear to be the use of phase-sensitive detection. A system for accomplishing these measurements is discussed in the following paragraphs.

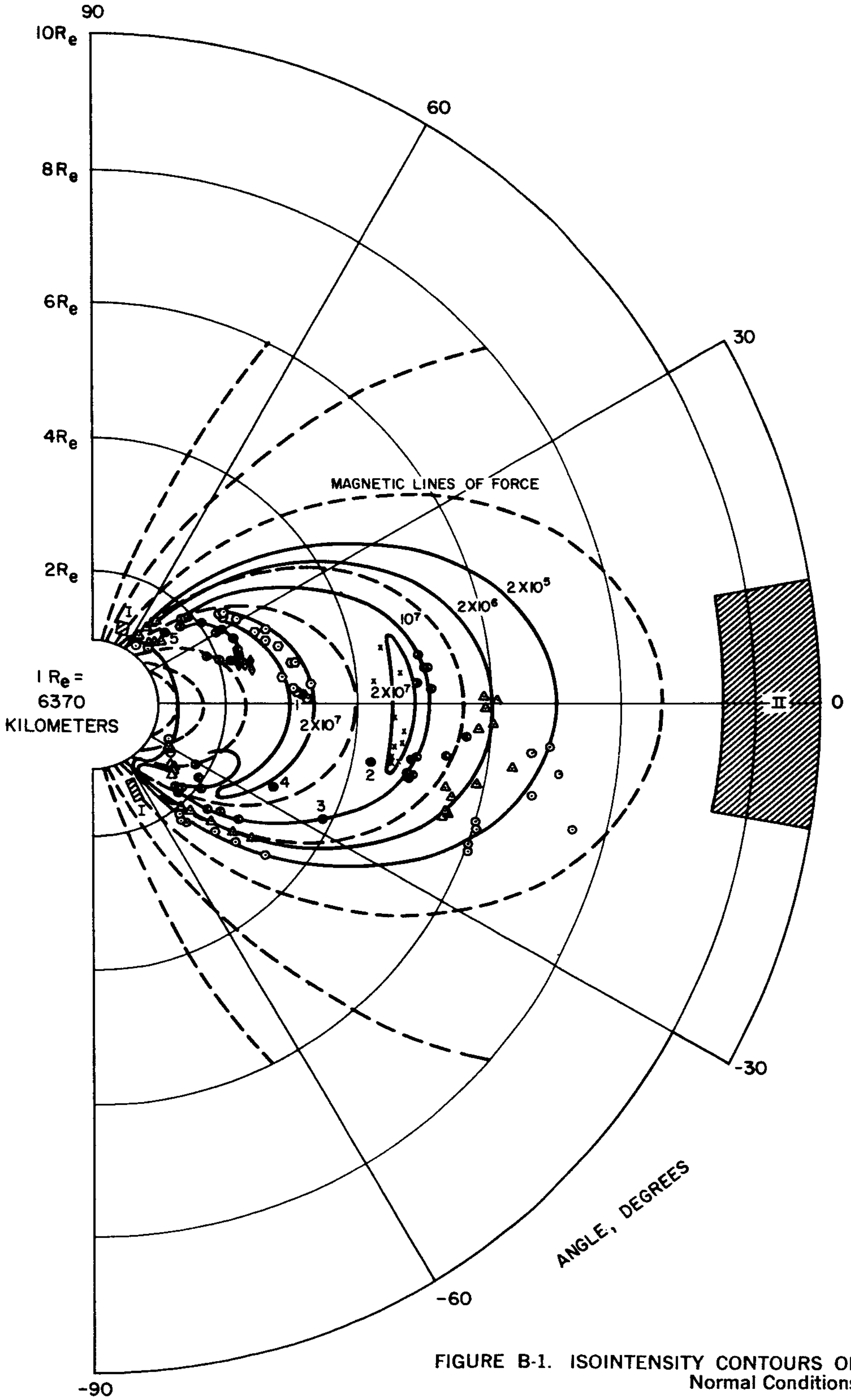

FIGURE B-1. ISOINTENSITY CONTOURS OF ELECTRONS (E > 500 KEV)
Normal Conditions

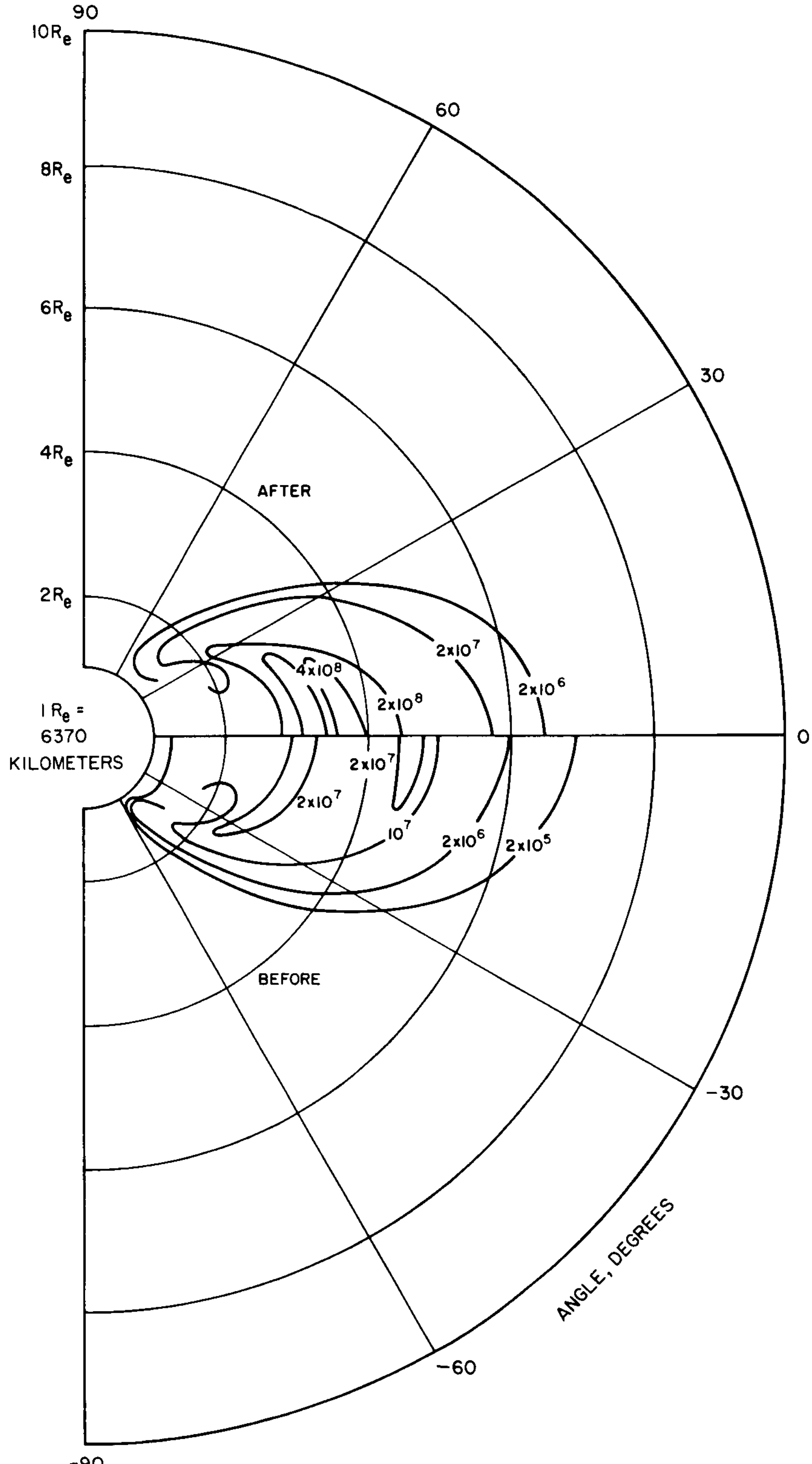

FIGURE B-2. ISOINTENSITY CONTOURS OF ELECTRONS (E > 500 KEV)
Magnetic Storm Conditions

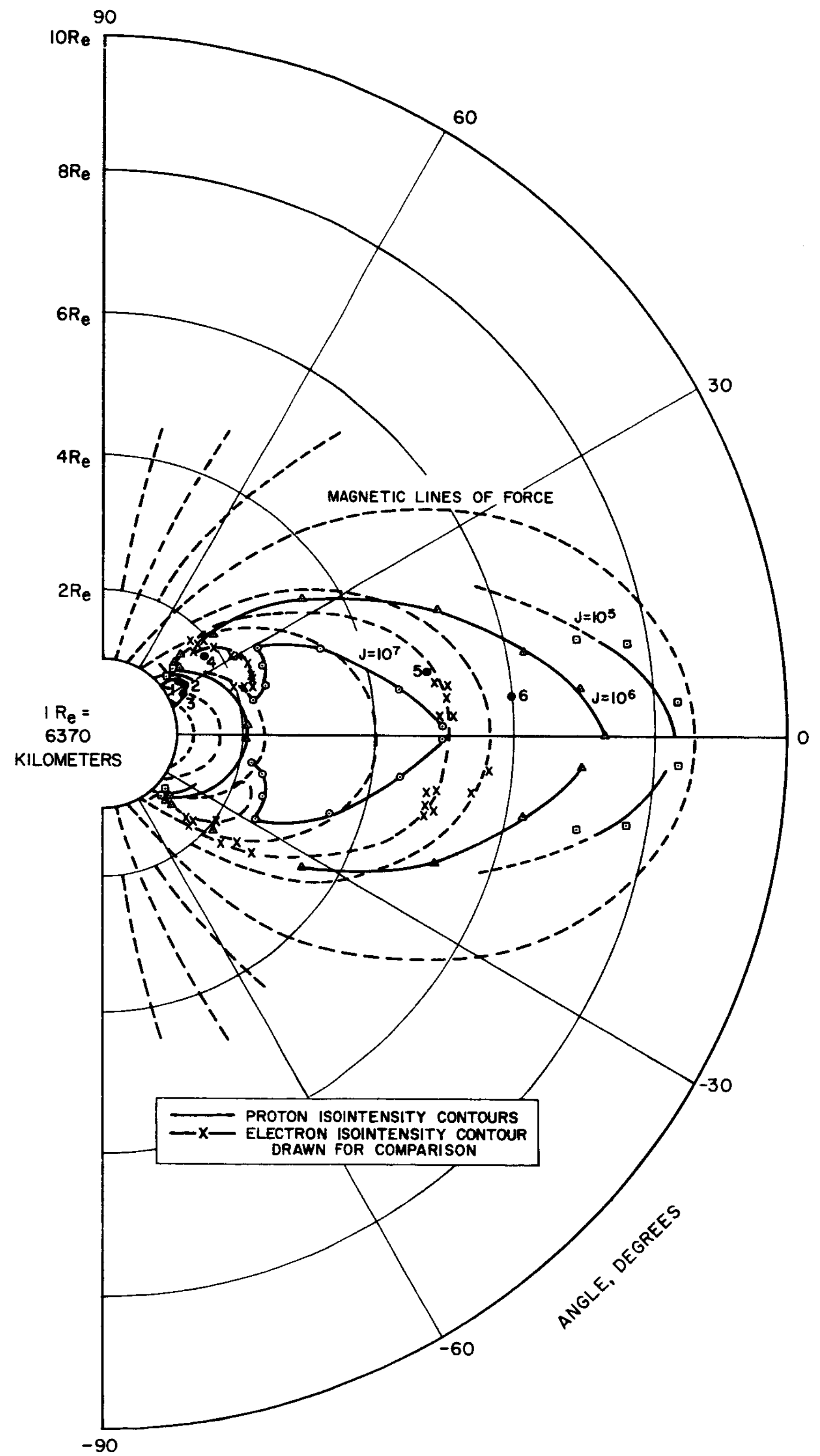

FIGURE B-3. ISOINTENSITY CONTOURS FOR PROTONS

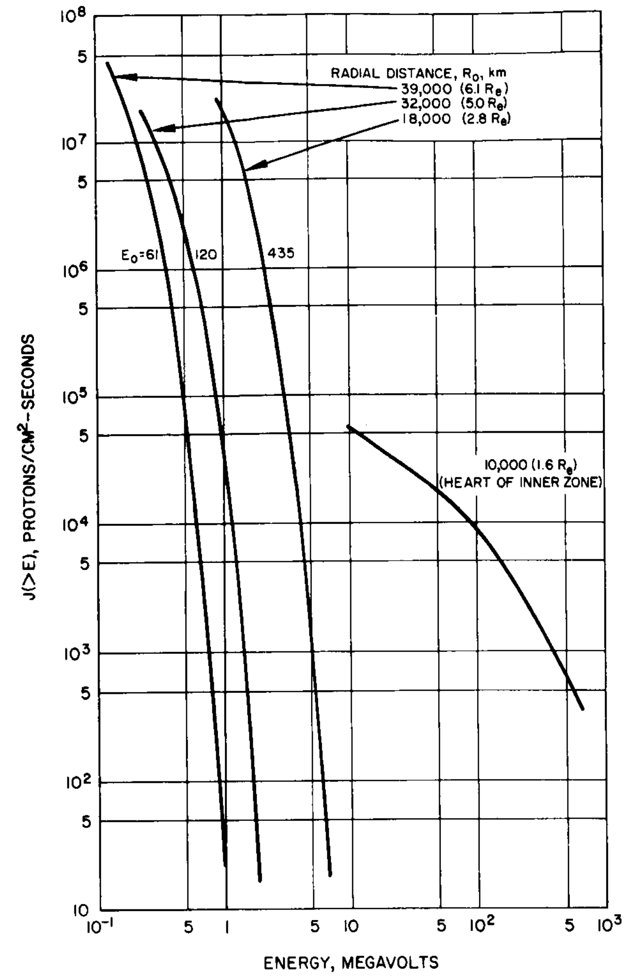

FIGURE B-4. PROTON ENERGY SPECTRA

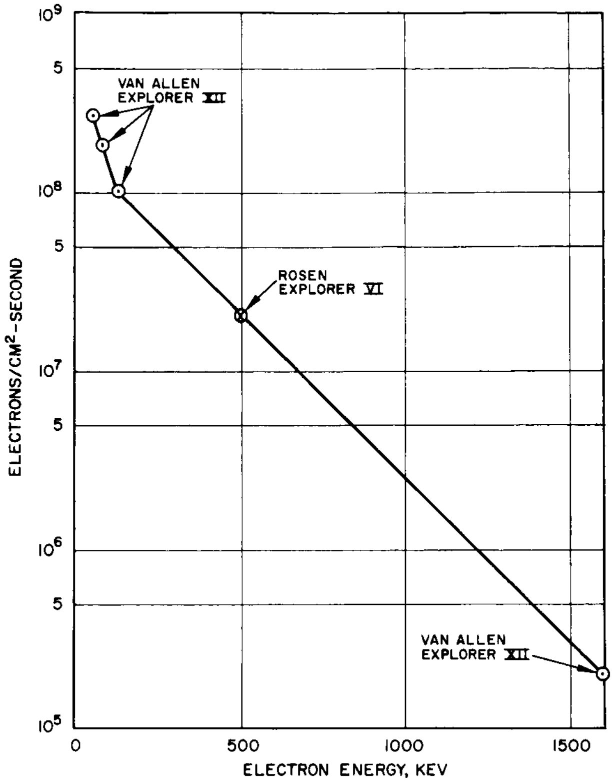

FIGURE B-5. INTEGRAL ENERGY SPECTRA

SENSOR ELEMENT

For measuring fields of the magnitude in question, the flux-gate magnetometer (FGM) appears to be best, particularly because the power demands of the FGM are inconsequential compared to the large amounts available. The great dynamic range of the FGM is also desirable, since magnetic noise of a magnitude quite large compared to the geomagnetic field will not saturate it. A second choice would be a search coil. If full advantage is taken of the cross-sectional area of the satellite (by winding the search coil about the inside of the structure) the output voltage would be about 1 microvolt per turn, and a 100-turn coil would give easily manipulable voltages. The design has the disadvantage, however, of being cumbersome.

THE EQUATORIAL COMPONENT: METHOD I

By rotating the FGM in a given plane,* it is possible to measure the magnitude and direction of the magnetic field component *in that plane.* Since the satellite is already rotating about an axis closely parallel to the earth's axis at about 3 rps, one can take advantage of this rotation by fixing a sensing element in the equatorial plane of the satellite. This element will produce a signal of amplitude proportional to the magnitude of the equatorial component of the geomagnetic field, and of phase depending upon the direction of the component. The freqency of the signal will be equal to the rotation frequency of the satellite. This signal will be superimposed upon noise. The output of the magnetom-

*Or the search coil about an axis perpendicular to the plane.

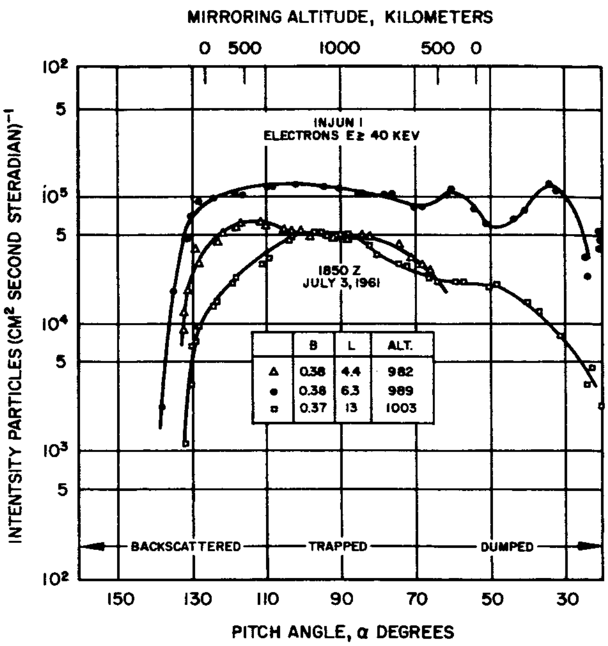

FIGURE B-6. PITCH ANGLE DISTRIBUTION FOR ELECTRONS

eter is fed into a phase-sensitive detector (PSD). It may be convenient to take the reference signal from the antenna-beam rotation circuitry.

By employing a long enough integration time at the output of the PSD, it is believed possible to discriminate very well against noise produced by other electronic equipment, whose frequency differs from that of the reference signal.

There are, however, two potential sources of noise at the same frequency as that of the desired signal. One is due to the fact that as the satellite rotates on its axis, the solar cells on the surface are illuminated in a periodic fashion (at least during daylight hours). The other source is leakage from the antenna beam, which also rotates at the same frequency, but in an opposite sense. In general, these two noise sources will be of a phase different from that of the desired signal, but there will be times when the equatorial magnetic field vector component happens to be parallel to one or the other. At worst, it will be necessary to discard the information at these times. A detailed design study should consider how frequently this will happen and how bad the interference is likely to be. This in turn will depend on the sharpness of the phase shifting network.

A design modification that eliminates this problem will be discussed later.

THE MERIDIONAL COMPONENT

Because of the range of geomagnetic latitudes through which the satellite will pass and the relative orientation of the earth's and the satellite's axes, the magnitude of the equatorial component of the geomagnetic field will generally be of the order of 10 percent of the total field magnitude. It is therefore necessary to measure the field component in a meridional plane of the satellite. For this purpose, another magnetometer element may be mounted in the apparatus, as shown in Figure B-7. A small constant-speed motor drives the system. The gear ratio is chosen so as not to be the ratio of small numbers. This minimizes interference caused by motor noise; any such noise will be at the wrong frequency. The breaker switch automatically provides a reference signal at the same frequency at that of the magnetometer signal; moderate changes in motor speed will not affect the apparatus. Magnetometer power (if needed by the type of magnetometer used) is fed in through slip rings, and the magnetometer output is also taken off slip rings.

The gear ratio and motor speed can be adjusted within the limits set by mechanical reliability. Also, the signal-to-noise ratio of the system can be optimized by choosing the magnetometer rotation speed so that the desired signal is at a frequency different from the known frequencies generated by other equipment. It may be desirable to put blocking filters at the strongest undesired frequencies into the signal circuit before the phase-sensitive detector (PSD).

The rotation speed chosen will probably be large enough that a fairly small search coil will produce a usable voltage. The flux-gate magnetometer, however, is still probably the best choice for a sensing element.

THE EQUATORIAL COMPONENT: METHOD II

Because it is necessary to provide a motor to rotate a magnetometer in the meridianal plane, it may be desirable to use the same motor to drive the equatorial magnetometer, rather than depending upon satellite rotation. This has the advantage of avoiding the possibility of interference from the sources of 3 cps noise, since the rotation speed can be chosen. There is the additional advantage that both magnetometers will

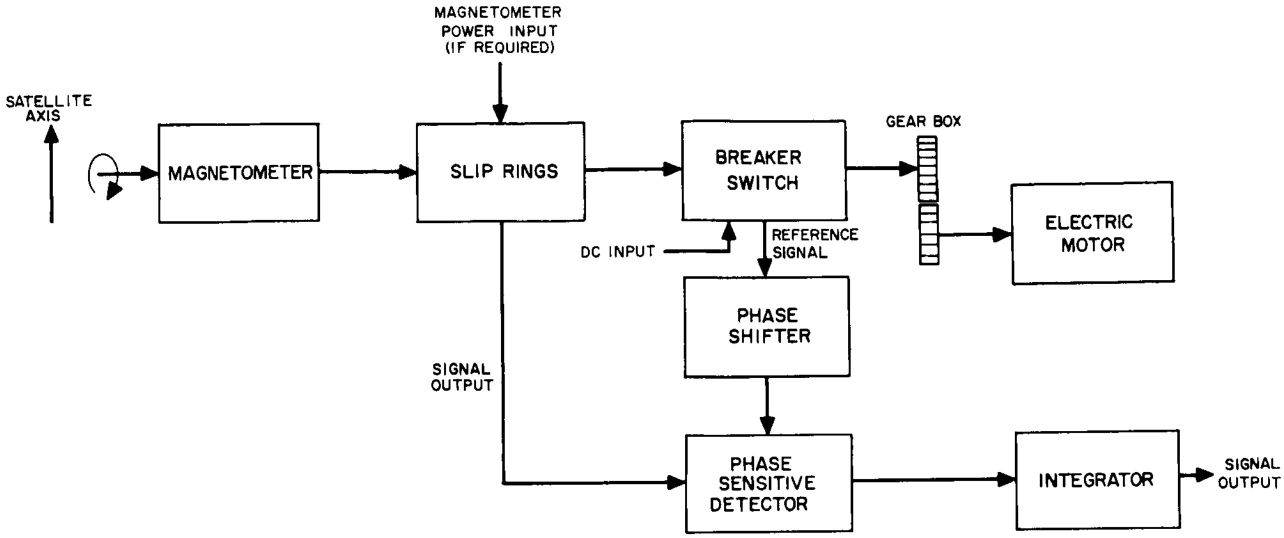

FIGURE B-7. MERIDIONAL PLANE MAGNETOMETER

operate at approximately the same frequency, making possible standardization of electronic systems; the two PSD systems may be similar or identical. The system is depicted schematically in Figure B-8. The meridianal system is the same as that in Figure B-7. The equatorial magnetometer is connected by a right-angle

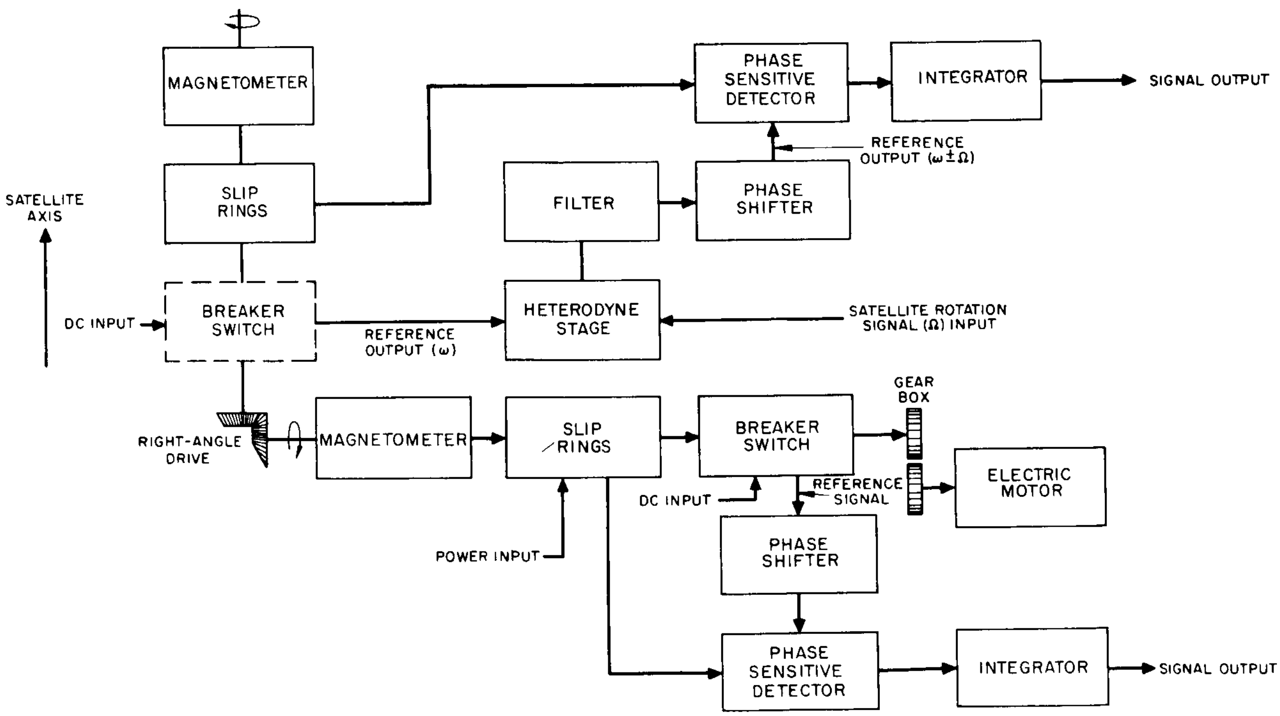

FIGURE B-8. EQUATORIAL PLANE MAGNETOMETER drive. It may be desirable to make the gear ratio slightly different from 1:1 so that any electrical or magnetic coupling between the magnetometers is avoided. If the gear ratio is different from 1:1, it may be most convenient to provide a second breaker switch to generate the reference signal.

Note that the desired signal is not at the shaft rotation frequency ω, but at $\omega \pm \Omega$. Here Ω is the satellite rotation frequency, and the sign depends upon the relative sense of ω and Ω. The following assumes for definiteness that ω and Ω are in the same direction; i.e., the + sign is the correct one.

To provide a reference signal of proper frequency to the PSD, the signal from the breaker is heterodyned with a signal from the antenna beam control circuit and high-pass filter or similar means used to eliminate the unwanted signals at ω, Ω, and $\omega - \Omega$.* The signal at $\omega + \Omega$ is fed into the PSD, together with the magnetometer output.

As the desired signal output of the two magnetometers differs in frequency by Ω, it is probably not necessary to decouple them. In this case, the right-angle drive may have a gear ratio 1:1, and one breaker switch can be eliminated.

Another saving may be effected if the magnetic field changes fairly slowly in time. It may be quite feasible to use one PSD system only, switching back and forth between the magnetometer elements and reference signals with a period long compared with geomagnetic field changes. Whether this is desirable depends upon the weight and complexity of the PSD as compared with the switch. If there is sufficient room aboard the satellite, the switch might be provided as a back-up system in the event of failure of one of the PSDs.

Particle Detector Payload

In measuring the degradation of semiconductor devices during nuclear particle irradiation in space, it is necessary to determine the energy spectrum, as well as the flux, of incident particles, N(E). Aside from the usefulness of determining N(E) for future shielding requirements, these data can be used to separate bulk and surface effects in transistor structures. It has been reported that ionization within the semiconductor device encapsulating package and subsequent formation of surface leakage channels are more serious device degradation mechanisms than the bulk radiation effect caused by lattice damage (Reference B-4). Formation of surface channels would not be a dominant cause of degradation in solar cells because of their mode of operation and encapsulation. Thus, evaluations of radiation effects in the space environment are designed primarily to measure:

1) Effect of bulk damage in solar cells
2) Effect of surface changes in transistor devices
3) Electron spectrum
4) Proton spectrum.

MEASUREMENT OF PARTICLE FLUX

The major component of particle flux ($E > 40$ kev) at Re is electrons; the proton flux is over two orders of magnitude smaller. Since irradiation effects are of interest, only electrons with energy greater than 250 kev will be measured. Lower energy particles can rather easily be removed by shielding. In fact, most solar cells for use in the inner regions have sufficient shielding to remove up to 1 mev electrons. This shielding, however, is probably excessive for the 6 Re particle environment. The proton energy spectrum will be measured for particle energies greater than 1 mev for similar reasons.

The particle measurements discussed here are designed for radiation damage measurements as a first priority. The extension of the energy range to lower and higher values for basic scientific studies can be readily accomplished by adjustments of the detector shielding and pulse height discrimination level. Also the measured energy ranges can be adjusted to be in consonance with other satellite particle measurements. Thus, the Syncom satellite is ideally suited to determining time variations of particle flux in periods of both quiet and active sun.

Choice of Detectors. Although geiger counters (Reference B-5) and scintillation counters have been used successfully on many space missions, the space and weight requirements suggest the use of semiconductor nuclear particle detectors. A further advantage of the

*A typical value of ω might be 1000 rpm, or 16.7 cps. Since $\Omega = 3$ cps, $\omega + \Omega = 19.7$ cps. Given these frequencies, the filter network would appear to present no special problems. It may be desirable to employ a variable filter network which can be adjusted to correct for variations in ω.

use of these devices is the extensive experience within the Hughes Research Laboratories in their use and fabrication (References B-6 through B-9). Use of semiconductor nuclear particle detectors aboard Relay and Telstar also indicate the applicability of this type of detection scheme. The mode of operation of semiconductor particle detectors is such that their characteristics are not so sensitive to irradiation effects as solar cells.

Principles of operation. Nuclear particle detectors under consideration are shallow-diffused silicon p-n junction devices. Application of reverse bias to the junction establishes a region of high electric field strength parallel to the surface and extending below the surface a width W that is proportional to the one-half power of the product of the applied voltage and silicon base resistivity. This high field region comprises the active volume of the device. The output signal is linearly proportional to the amount of energy lost by the particles in the active region. For most particles of interest, the detector pulse height will be of the order of millivolts. The rise and decay of the voltage pulse are determined by the preamplifier time constant. A suitable charge sensitive preamplifier will have a rise time of 0.5 microsecond and an RC clip decay of 1 microsecond. These time constants will determine the maximum count rate before pulse-pileup in the detectors will be a problem. Considerations of pulse-pileup will dictate the choice of the detector area.

Detector design and location. The most reliable detector mounting is to encapsulate the unit in a transistor-like can with a thin kovar diaphragm over an aperture directly above the detector top surface. This transistor can is placed in the shielding housing, which for most experiments is designed to have a conical field of view of 20 to 30 degrees. It should be noted that electron scattering from the cone sides will increase the effective field of view. The most desirable location of the detectors would be to look out perpendicularly to the spin axis. This requirement would necessitate use of 5 to 10 cm^2 of peripheral area. The omnidirectional detectors and high energy detectors would be designed in a different fashion. The omnidirectional detectors will be shallow diffused hemispherical devices (Figure B-9) similar to the type developed for the Air Force Special Weapons Center. In this case the active volume is a hemispherical shell rather than a rectilinear volume. The high energy detectors are silicon p-i-n junctions, whose operation is similar to p-n detectors but which are fabricated using ion drift techniques. Since these p-i-n detectors exhibit a greater sensitivity to radiation, they will be used

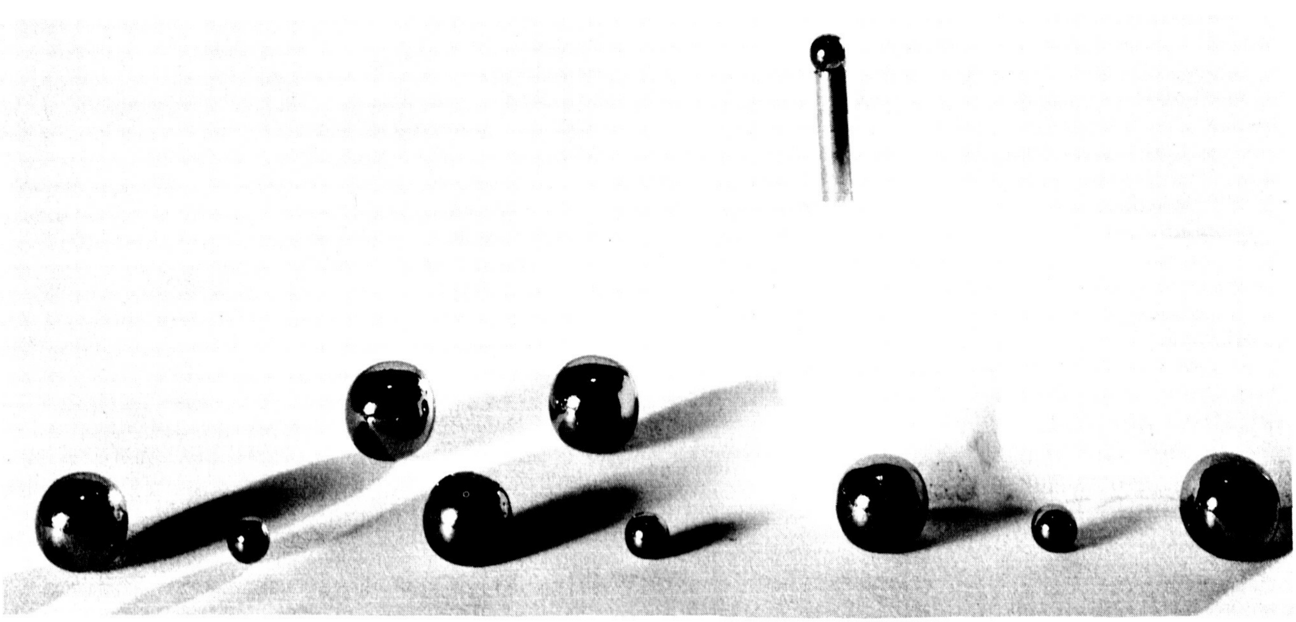

FIGURE B-9. OMNIDIRECTIONAL PARTICLE DETECTOR under moderate shielding conditions so they will "see" only the less intense flux of high energy particles.

Counting circuits. The circuits used with the detector will be similar to those used on Telstar and Relay. However, because of the difficulties experienced on Telstar (Reference B-2) with electrical pickup, each detector will have its preamplifier mounted integrally with the detector shield. The preamplifier will operate in the charge-sensitive rather than voltage-sensitive mode in order to make the system independent of junction capacitance changes. Preamplifier noise levels are typically less than 100 kev in units designed for space application. The pulse from the preamplifier is then introduced into an amplifier and from there into discriminator-logic networks which serve as differential pulse height analyzers. In cases in which stacked detectors are used, a coincidence-anticoincidence network is used. The differential spectrum is fed into rate meters and then sampled for time sharing in the telemetry channel. As in the case with other spinning satellites, the detectors will be gated to turn on when facing the sun and when facing opposite the sun, to determine the count rate in each of the two directions.

Experiment design. Table B-1 illustrates the energy spectrum that can be covered by rather straightforward detector design. As in other outer belt measurements, advantage is taken of the fact that proton fluxes will in general be two orders of magnitude less than the electron flux and no special precautions are taken to exclude those protons that lose an amount of energy equivalent to that lost by the electrons. The very low energy proton spectrum will be removed by 10 mg/cm^2 of aluminum. Since the proton detectors will have a low energy pulse height discrimination cutoff less than the energy that can be lost by a high energy electron in the sensitive volume (neglecting severe multiple scattering), the electron flux will not seriously affect the proton measurement. It should be mentioned that for electron energies above 6 mev, the semiconductor detector efficiency drops with increasing electron energy. This factor will necessitate extensive calibration tests.

TABLE B-1. DETECTOR ENERGY SPECTRUM

Detector	Particle	Energy, mev	Shielding
Omidirectional	Electrons	0.25 to 1	10 mg/cm^2 Aluminum
Omidirectional (p-i-n)	Electrons	1 to 4	1.5 mm Aluminum will pass protrons E> 17 mev.
Directional	Electrons	0.25 to 1 (four differential channels)	10 mg/cm^2 Aluminum
Omidirectional	Protrons	2 to 20	10 mg/cm^2 Aluminum
Directional	Protrons	2 to 20 (four differential channels)	10 mg/cm^2 Aluminum
Directional (stacked units) p-n, p-i-n	Protrons	16 to minimum ionizing (four differential channels)	Thin-thick combination*

*Similar to the configuration built by Hughes Research Laboratories and used by Dr. Harvey Wegner, Los Alamos Scientific Laboratories.

RADIATION DAMAGE

For these experiments, eight n-on-p solar cells will be used: two units without shielding, two with sufficient shielding to exclude 0.5 mev electrons, and two with shielding to exclude electrons below 1 mev; in addition two units with sufficient shielding to exclude 2.5 mev electrons will be used to determine the effect of high energy particles. The output current will be measured when the units are facing the sun. Since the degradation of these units will be rather slow, sampling of output will be time-shared.

Six samples of n-p-n silicon transistors will be used to determine the effect of surface changes. The parameter most sensitive to surface changes is the reverse bias collector current, I_{CBO}. Since the surface effect is minimal under zero bias conditions, the surface change can be separated from the bulk effect by examining I_{CBO} under pulse conditions. Two transistors will operate under zero bias (pulse test), two under steady dc bias, and two under bias but with sufficient shielding to exclude electrons with energy less than 1.5 mev.

The final choice of components for measuring radiation degradation will be made after the semiconductor devices to be used aboard Syncom have been critically evaluated with regard to radiation sensitivity.

Micrometeorite Detection

In evaluating environmental effects on vehicles above the atmosphere, the influence of meteoritic dust is one of the least well known.

METHOD OF DETECTION

A micrometeorite impacting on the surface of an orbiting satellite produces several physical perturbations that may be used for detecting the impact. The impact is accompanied by a transfer of momentum and energy, resulting in a local acceleration, the production of a crater, a light flash, and shock vibrations in the material. This presents a number of possibilities for detecting micrometeorite impact. An effective detection method should include a wide range of sensitivity over a very large effective area, yet be simple, compact, and reliable.

The local acceleration from a particle impacting upon a surface may be measured with a hypersensitive accelerometer. The impulse of the particle propagates through thin sheets of aluminum or steel at a velocity of 5 km/sec, the velocity of sound in these media. A piezo-electric crystal in pressure contact with the surface acts as a transducer, transforming the vibrations from the impulse into an electrical signal. By appropriate electronic amplification, the impact of a microparticle anywhere upon a surface within an area of a square meter may be detected using a single transducer and amplifier. Impacts of hypervelocity particles of mass as low as 10^{-10} gm, i.e., 1 micron diameter, anywhere on the surface can be detected by this method.

The relative amplitude of the impulse may also be measured. For equipment that has been properly calibrated, the mass of the impacting particle may be determined using an assumed mean impacting velocity. Since the mass and rate of impact upon a known area may be measured, the daily accretion rate of interplanetary dust by the earth may be determined. Estimates of the damage to surfaces of satellites may also be made using such data and a proper theory of hypervelocity catering.

The micrometeorite particle detector must have a metallic sounding board for it to effectively measure particle impacts. The Syncom II thermal shield would be a convenient location for this experiment but would require modification of its present all-aluminized glass construction to part aluminum sheet and part aluminized glass. The area of the thermal shield is approximately 2 square meters. Aluminum patches of approximately 0.5 square meter will be placed as shown in Figure B-10.

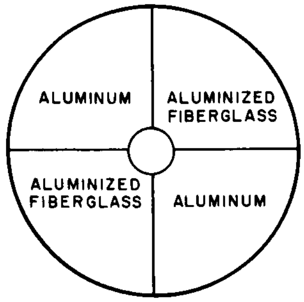

FIGURE B-10. MICROMETEORITE DETECTOR

The transducer would be placed in pressure contact on the under side of the aluminum sheet at its center of mass. The aluminized glass will act as a sound absorber to effectively isolate the two aluminum sounding boards from each other.

References

B-1. Rosen, A., C. A. Eberhard, T. A. Farley, and J. L. Vogl, "A Comprehensive Map of the Space Radiation Environment," Space Technology Laboratories Report No. 8644-6002-RU-000, 28 September 1962.

B-2. O'Brien, B. J., "Lifetimes of Outer Zone Electrons and Their Precipitation into the Atmosphere," J. Geophys. Res., Vol. 67, 1962, p. 3687.

B-3. McIlwain, C. E., "Coordinates for Mapping the Distribution of Magnetically Trapped Particles," J. Geophys. Res., Vol. 66, 1961, p. 3681.

B-4. Peck, D. S., R. R. Blair, W. C. Brown, and F. C. Smits, Bell Sept. Tech. J., Vol. 42, 1963, p. 95.

B-5. O'Brien, B. J., C. D. Laughlin, J. A. Van Allen, and L. A. Frank, J. Geophy. Res., Vol. 67, 1962, p. 1209.

B-6. Mayer, J. W., J. Appl. Physics, Vol. 30, 1959, p. 1957.

B-7. Mayer, J. W., Nat. Acad. of Sciences Pub., Vol. 871, 1961, p. 1.

B-8. Mayer, J. W., I. R. E. Trans. NS-9, 1962, p. 124.

B-9. Mayer, J W.. J. Appl. Physics, Vol. 33, 1962, p.2894.